STRUCTURAL STABILITY RESEARCH COUNCIL

ANNUAL STABILITY CONFERENCE

PROCEEDINGS

2008

STRUCTURAL STABILITY RESEARCH COUNCIL

PROCEEDINGS

2008 Annual Stability Conference

April 2-5, 2008
Nashville, Tennessee

Reports on Current Research Activities

Published by the
Structural Stability Research Council
Missouri University of Science & Technology

DISCLAIMER

The opinions, findings, conclusions, and recommendations expressed herein are those of the authors only and do not necessarily reflect the views of the Structural Stability Research Council, the editors, or the conference sponsors.

ISBN 1-879749-75-0

Proceedings Compiled by
Christina Stratman
SSRC Administrator

STRUCTURAL STABILITY RESEARCH COUNCIL
Missouri University of Science & Technology
301 Butler-Carlton Hall
Rolla, MO 65409-0030
Phone: 573-341-6610
Fax: 573-341-4476
Email: ssrc@mst.edu
Web: www.stabilitycouncil.org

Printed in the United States of America

FOREWORD

Once again I have the pleasure of welcoming you to the Annual Stability Conference. It is an honor for me to serve the Council as Chair and to be able to work with such a great group of professionals as represented by the Executive Committee and Headquarters staff. These folks are truly a credit to the profession and continue to very ably serve the SSRC membership.

The papers and presentations during the conference represent a look at the past, present and future. The majority of the papers are of course reviewing some of the latest research in the field of structural stability. Some, I would argue, are giving us a look into the future at topics of ever increasing importance. The Beedle Award presentation by Professor Don Sherman will give us a look at the past, in which the development of HSS stability provisions in North America is presented. The papers collectively represent key contributions to the body of knowledge in structural stability. I trust you will enjoy reading the papers included and benefit from them. I want to thank SSRC Vice-Chair Ron Ziemian, who chairs the Annual Stability Conference (ASC) Committee, and the other members of the Conference Committee for putting together such an interesting technical program.

The task that gives me the most pleasure during the ASC is the presentation of the The Lynn S. Beedle Award. This award was established by the SSRC Executive Committee to honor the lifelong contributions that Professor Beedle made to the SSRC and to the international structural engineering community as a whole. The recipient of the 2008 Beedle Award is Professor Donald R. Sherman. Dr. Sherman is Professor Emeritus in the Department of Civil Engineering and Mechanics at the University of Wisconsin-Milwaukee. Professor Sherman is recognized with the Beedle Award for his long-term and unfailing contributions to the field of structural stability and in particular for his work on behalf of the Structural Stability Research

FOREWORD

Council for over 30 years. I'm sure you join me in congratulating Professor Sherman for this well-deserved honor!

During the Annual Stability Conference, we also recognize the work of a student with the Vinnakota Award. The Vinnakota Award was established in 1997 by Ramulu S. Vinnakota, long time member of SSRC, in honor of his parents who believed in the importance of education and research. The award is given for the best student authored paper presented at an SSRC Annual Stability Conference. The foresight of Professor Vinnakota in establishing this award has resulted in greater participation by graduate students in the Annual Stability Conference. Several of the past recipients have continued their participation in SSRC activities and are indeed now encouraging the participation of students through their own work as faculty members.

In closing, I would like to acknowledge the continuing support of the American Institute of Steel Construction through their willingness to collaborate with the SSRC and to support the Annual Stability Conference. The integration of the ASC within the overall North American Steel Construction Conference has and continues to be a mutually beneficial collaboration. And finally, I want to acknowledge the excellent work that Mrs. Christina Stratman and Professor Roger LaBoube continue to do on behalf of the SSRC. Their efforts to support our headquarters operation, which is based at the Missouri University of Science & Technology, are greatly appreciated. I know that all within the SSRC family join me in thanking Chris and Roger.

Sincerely,

W Samuel Easterling

W. Samuel Easterling, PhD, PE
SSRC Chair

TABLE OF CONTENTS

TABLE OF CONTENTS

TABLE OF CONTENTS

TABLE OF CONTENTS

INELASTIC BEHAVIOR OF THIN STEEL PLATES SUBJECTED TO CYCLIC COMPRESSION AND TENSION

Iraj H.P. Mamaghani [1]

ABSTRACT

This paper deals with the inelastic analysis and behavior of thin steel plates subjected to in-plane cyclic compression and tension using the finite element method. The modified two-surface plasticity model (2SM) is employed for material nonlinearity in the elastoplastic finite element formulation for plates. The approximate updated Lagrangian formulation of motion is adopted to consider the geometrical nonlinearity. The plate element formulation is implemented in the Finite Element Analysis Program used in the analysis. The plate element formulation employing the 2SM accounts for the important cyclic characteristics of structural steel within the yield plateau and hardening regime, such as the decrease and disappearance of the yield plateau, reduction of the elastic range, and cyclic strain hardening, as well as the spread of plasticity through the thickness and plane of the plate. The cyclic performance of the formulation was found to be good when compared with the results obtained from the elastic perfectly plastic, isotropic hardening, and kinematic hardening material models. Based on the results of an extensive parametric study, the effects of residual stresses, initial imperfection, width-thickness ratio, and loading history, on the cyclic inelastic behavior, strength and ductility, energy absorption capacity, and buckling of steel plates are discussed and evaluated.

---

[1] Assistant Professor, Department of Civil Engineering, University of North Dakota, 243 Centennial Dr., Grand Forks, ND, 58202-8115
Email: irajmamaghani@mail.und.edu

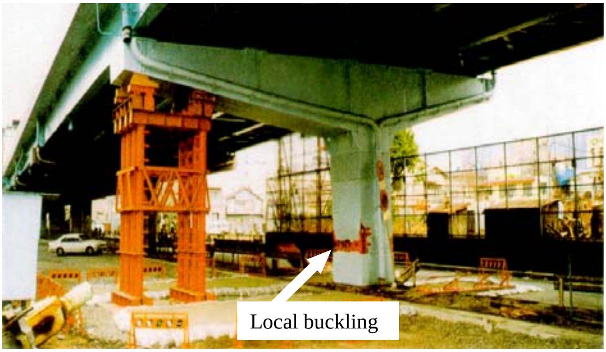

Figure 1. Local buckling of steel bridge pier, Kobe Earthquake, January 1995.

INTRODUCTION

Thin-walled steel structures are vulnerable to damage caused by the coupled instability, i.e., the interaction of local and overall buckling, in the event of a major earthquake. For example, Fig. 1 shows a steel bridge pier of hollow box section, which suffered severe local buckling damage near the base of the pier in the Kobe earthquake. When structural members are composed of thin-walled steel plate elements, the local buckling of the component plates may influence the strength and ductility of those members. To this end, in designing thin-walled steel structures, it is very important to clarify the cyclic inelastic behavior of the component plates.

On the other hand, the stress-strain relationship used in cyclic structural analyses depends on the loading history to which the structure or structural members are subjected. Therefore, advanced computational methods, such as the finite element method (FEM), require an accurate and refined constitutive law to account for the general cyclic behavior of structural steel, which has a characteristic yield plateau followed by strain hardening. The main objective of this study is to use the modified two-surface plasticity model (2SM), recently developed by the author and his coworkers (Mamaghani et al. 1995, Shen et al. 1995), for material nonlinearity to trace the cyclic inelastic behavior of simply supported rectangular thin steel plates using the FEM. An elastoplastic finite element formulation for plates, considering geometrical and material nonlinearities, is developed and implemented in the computer program FEAP (Zienkiewicz 1977) used in the analysis. The 2SM is employed for material nonlinearity. The approximate updated Lagrangian description of motion (AULD) (Washizu 1982) is adopted for geometrical nonlinearity. The formulation accounts for the important cyclic characteristics of structural steel within the yield plateau and strain hardening regime, such as the decrease and disappearance of the yield plateau, reduction of the elastic range, and cyclic strain hardening, as well as the spread of plasticity through the thickness and plane of the plate.

The main parameters concerned in the analysis are: residual stress; initial deflection; width-thickness ratio; and loading history. In what follows, the numerical method used in the analysis is first briefly explained. Later, the cyclic elastoplastic performance of the formulation is discussed and compared with results obtained from the elastic-perfectly plastic (EPP), the kinematic hardening (KH), and the isotropic hardening (IH) material models. Based on the results of analysis, the effect of each material model and aforementioned parameters on the hysteretic behavior (buckling/plastic collapse and energy absorption capacity) of thin plates is discussed and evaluated.

NUMERICAL METHOD

Assuming plane-stress state, the discrete Kirchhoff triangular (DKT) element for plate bending combined with the constant strain triangle (CST) element for plate membrane is employed in this study (Bathe and Ho 1981; Fafard et al. 1989). The material nonlinearity is defined by the 2SM. The AULD, in which the configuration of the structure at the beginning of each incremental loading step is approximated by a flat plate element (Jetteur et al. 1983), is employed for the geometrical nonlinearity. The three points Gauss quadrature integration formula is used to integrate the element stiffness equations for the plate element. A layered approach is employed to consider the plastification of thickness at integration points by assuming seven layers across the plate thickness (Bathe and Ho 1981).

According to the algorithm discussed above, an elastoplastic plate element subroutine was coded and implemented in the computer program FEAP used in the analysis. The Newton-Raphson iterative scheme coupled with the incremental displacement control is employed in the analysis (Zienkiewicz 1977; Owen and Hinton 1980). The incremental uniform displacement is applied on the plate's edge. The displacement convergence criterion is adopted in the analysis and the convergence tolerance is taken as 10^{-3} (Zienkiewicz 1977). The details of the process for numerical analysis can be found in a work by Mamaghani (1996). In what follows, the analyzed plate members and numerical results will be presented and discussed.

Analytical Modeling

Throughout the numerical study, the assumed analytical model for plates is considered as shown in Fig. 2. The plate has an aspect ratio of *a/b* = 0.7, and is taken to be simply supported along the four edges. *a* and *b* are the length and width of the plate. All edges are assumed to remain straight when subjected to in-plane displacement; that is, at $x=-(a/2)$ and $(a/2)$, $w=\theta_x=\theta_z=0$; and at y = 0 and *b*, $w=\theta_y=0$. Such a plate is thought to be modeling component plates in steel hollow box section members (see Fig. 1). The width-thickness ratios of *b/t* = 20, 40, 60, 80 are assumed in the analysis. The initial out-of-flatness of

$$\delta=\delta_0\cos\left(\frac{\pi x}{a}\right).\sin\left(\frac{\pi y}{b}\right) \tag{1}$$

in which $\delta_0=b/450$, is assumed in the analysis (Fig. 2). The assumed value of δ_0 is considered to be an average value in practical unstiffened plates (Usami 1993). The material chosen is structural steel

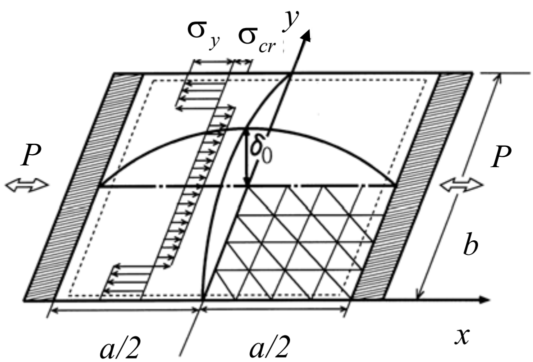

Figure 2. Simply supported rectangular plate modeling flange of the pier.

of grade JIS SS400 (equivalent to ASTM A36) with the properties of the Young's modulus E = 207 GPa, yield stress $\sigma_y = 274$ MPa, Poisson's ratio $\upsilon = 0.29$, length of yield plateau $\varepsilon_{st}^p = 12\varepsilon_y$ (ε_y = yield strain of the material), and plastic modulus at the initial hardening $E_{st}^p = 0.025E$. The 2SM parameters for SS400 are given by Mamaghani (1996) and Shen et al. (1995).

The pattern of assumed residual stress distribution over the cross-section is shown in Fig. 2, and is uniform along the entire length of the plate. The tensile and compressive residual stresses are taken as $\sigma_{rt} = \sigma_y$ and $\sigma_{rc} = 0.33\sigma_y$, respectively. From the symmetry conditions, a quarter of the plate is analyzed, dividing this part into 4×4 elements, as shown in Fig. 2. A forced displacement is imposed along loading edges incrementally, and the increments in reaction forces are calculated at every step. The average in-plane edge strain $\bar{\varepsilon}$ and stress $\bar{\sigma}$ over the cross section are defined as $\bar{\varepsilon} = (\Delta a / a)$ and $\bar{\sigma} = (P / bt)$, where $\Delta a =$

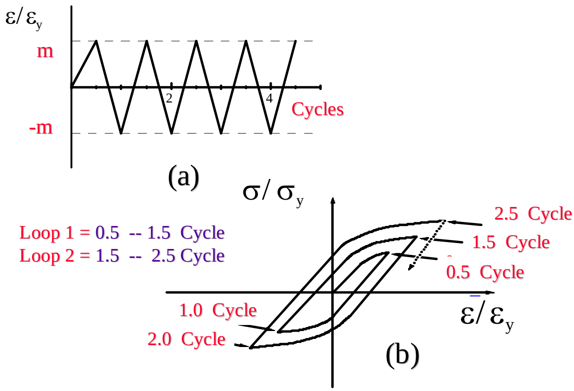

Figure 3. Loading program and definition of cycles and loops.

increment of displacement amplitude along x-axis; P = reaction force along the loading edge; and t = plate thickness. The incremental displacement amplitude of $\Delta a = 1.0\times10^{-4}(a/2) \sim 0.5\times10^{-5}(a/2)$ is adopted in the analysis. Constant displacement amplitude (CDA) loading is used in the analysis, as shown in Fig. 3a. The plate is first subjected to compressive shortening of $m\varepsilon_y$ at the loading edge. This is defined as 0.5 cycles (Fig. 3b). Note that the compressive strain is assumed to be positive. Then, the plate is unloaded in the compression side and reloaded in the tension side until it is stretched up to -$m\varepsilon_y$. This stage of loading is defined as 1.0 cycle. Similarly, the other cycles, 1.5, 2.0, 2.5 and so on, are defined as shown in Fig. 3b. The normalized maximum average strain m, at the loading edge of the plate is defined as

$$m = \frac{\overline{\varepsilon}_{max}}{\varepsilon_y} \tag{2}$$

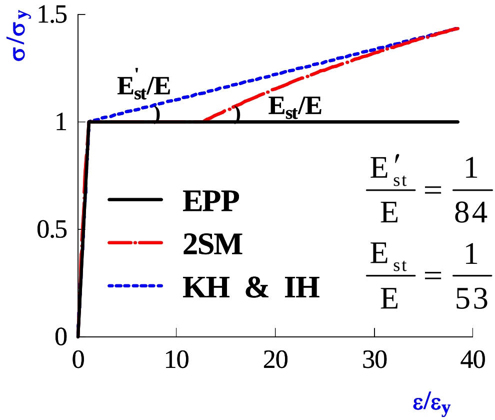

Figure 4. Bilinear stress-strain relationship for steel using different material models.

in which $\bar{\varepsilon}_{max}$ = maximum average strain. Three patterns of loading with *m* = 2, 4, and 6 are adopted for CDA loading, and cycling was performed up to 4.5 cycles.

Figure 4 shows the uniaxial stress-strain relationship under monotonic loading for SS400 steel using the 2SM, EPP, KH, and IH material models. In the present study, based on the experimental results for SS400 steel (Mamaghani et al. 1995), the kinematic and isotropic hardening rates are assumed as E'_{st}/E=1/84, which is considered equal to the slope of the line joining the initial yield point to the loading point corresponding to 5% axial strain obtained by using the 2SM (Fig. 4).

NUMERICAL RESULTS

A series of elastoplastic large deflection analyses are performed on hypothetical specimens of simply supported rectangular plates by imposing in-plane strain cycles of constant displacement amplitudes using the analysis scheme described above. In what follows, numerical results will be presented and discussed.

Effect of Residual Stress

As a typical example, Fig. 5a shows the hysteretic curves obtained using the 2SM for the two specimens with and without residual stresses, respectively. For both specimens the *b/t* ratio is 40 and *m* = 4. The normalized average in-plane stress, $\bar{\sigma}/\sigma_y$, is taken as the ordinate, and the corresponding normalized average edge strain, $\bar{\varepsilon}/\varepsilon_y$, is taken as the abscissa (Fig. 5a). Note that, in what follows, the $\bar{\varepsilon}/\varepsilon_y$ is assumed positive when the plate is subjected to compressive shortening on the loaded edge. Figure 5b compares the analytical averaged axial stress $\bar{\sigma}$-center deflection, *w*, relationship for both specimens. As the edge strain, $\bar{\varepsilon}/\varepsilon_y$, increases, the path of hysteretic curves enters the post buckling range through the elastic limit point, at which yield penetration begins in the most stressed element of the plate (Fig. 5a). Whereas the edge strain increases, the average in-plane load decreases after the peak stress point (Fig. 5a) of the plate is achieved. The results in Fig. 5a indicate that the initial buckling load decreases by 13% due to residual stresses. Figure 5a shows that the initial yielding of the plate occurs earlier when the residual stress is considered in the analysis. This results in a lower stiffness of the stress-strain curve (Fig. 5a). On the other hand, the stress-strain curve without residual stress shows a steeper descending slope due to buckling, and the curves in both cases (with and without residual stress) coincide at the point corresponding with $\bar{\varepsilon}/\varepsilon_y$ =2.0 (Fig. 5a). The obtained results indicate that the residual stresses have almost no effect on the subsequent cyclic behavior (Fig. 5a) and the progress of buckling (Fig. 5b) of the plate.

Effect of Initial Deflection

Figure 6 shows the effect in change of the initial deflection on the cyclic behavior of plates for the two specimens with $\delta_0/b = 1/450$ and $\delta_0/b = 1/150$, respectively. The result in this figure shows that an increase in the initial deflection mainly has the

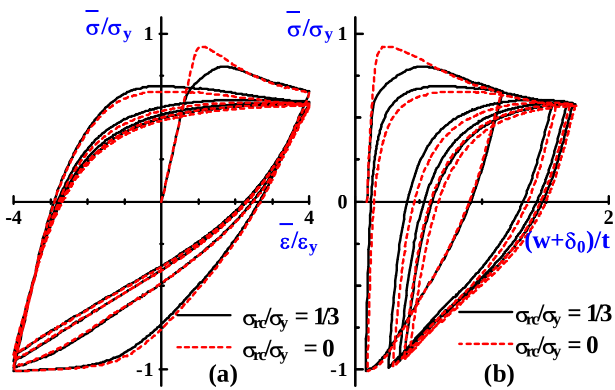

Figure 5. Effect of residual stress: (a) $\bar{\sigma}/\sigma_y - \bar{\varepsilon}/\varepsilon_y$, (b) $\bar{\sigma}/\sigma_y - (w+\delta_0)/t$.

effect of decreasing the initial buckling load and does not significantly affect the subsequent cyclic behavior. It is worth noting that the numerical studies on the cyclic inelastic behavior of steel compression members by Mamaghani et al. (1996a, 1996b) and Banno et al. (1998) show the same behavior as discussed above and indicate that annealing and initial imperfection do not significantly affect overall behavior due to cycling.

Comparison between Two-Surface Model and Other Models

In this section, cyclic behavior of simply supported steel plates is analyzed using the 2SM and bilinear EPP, KH, and IH models. The aim is to compare the effect of each material model on the buckling/plastic collapse behavior of the plates. A typical loading program with CDA of m = 4.0 will be presented and discussed. For comparison, the selected plate parameters (b/t = 40, $\delta_0 = b/450$, and σ_{cr}/σ_y =0.33) are kept the same.

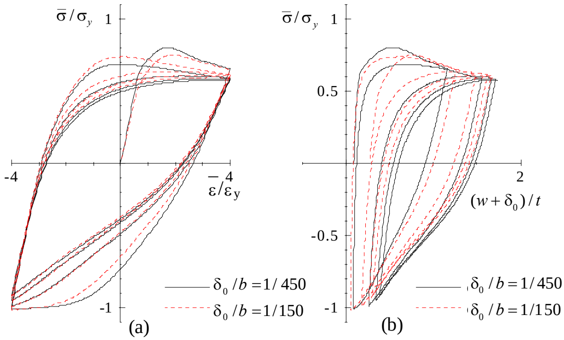

Figure 6. Effect of initial deflection: (a) $\bar{\sigma}/\sigma_y - \bar{\varepsilon}/\varepsilon_y$, (b) $\bar{\sigma}/\sigma_y - (w+\delta_0)/t$.

Figure 7 compares the analytical averaged axial stress $\bar{\sigma}$-averaged axial strain, $\bar{\varepsilon}$, and averaged axial stress $\bar{\sigma}$-center deflection, *w*, relationship for *m* = 4 obtained using the 2SM and bilinear EPP, KH, and IH material models duly normalized. As shown in Fig. 7a, the hysteretic loops have almost the same shape for all models except the 2SM. The loops for the EPP, KH, and IH models show a large elastic range for unloading in the tension side and reloading in compression side. Furthermore, the post-buckling parts of these curves have a steeper descending slope compared to that of the 2SM. Figure 8a compares the change in load-carrying capacity of the plate $\bar{\sigma}_{max}$, during cyclic loading. In the case of the EPP, KH, and IH models, the calculated second and subsequent buckling load capacities are higher than those of the 2SM (see Figs. 7a and 8a). For the IH model, the maximum compressive load during cycling is higher than the other models and increases after 2.5 cycles because of the large cyclic strain hardening. Conversely, the rate of decrease in buckling loads slows down for the other models and tends to converge to 0.6σ_y (Fig. 8a).

One significant feature of the hysteretic loops in Fig. 7a is that all of the models except the 2SM give the second buckling load higher than that of the initial one (see also Fig. 8a). The reason for this is that the EPP and IH models do not consider the Bauschinger effect due to plastic

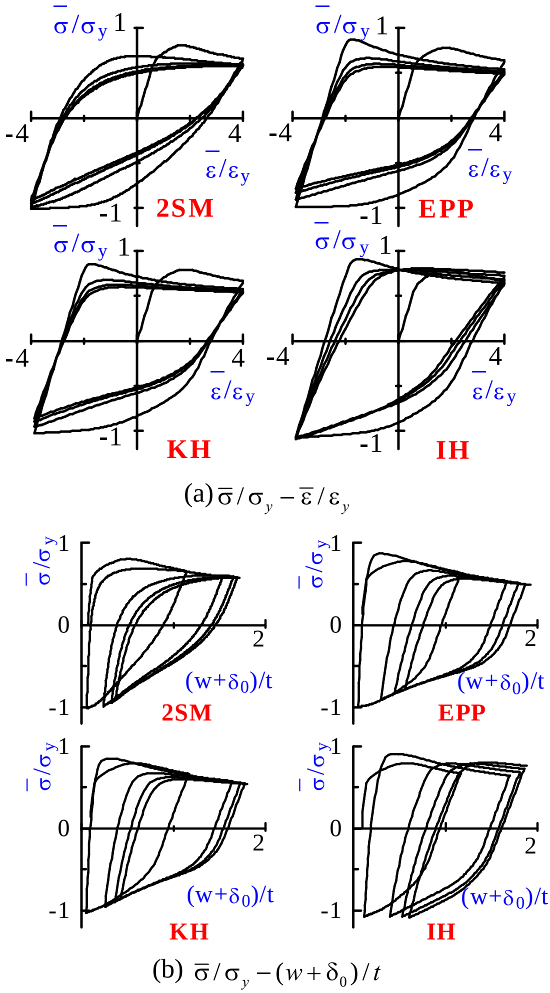

(a) $\overline{\sigma}/\sigma_y - \overline{\varepsilon}/\varepsilon_y$

(b) $\overline{\sigma}/\sigma_y - (w+\delta_0)/t$

Figure 7. Comparison between 2SM and other models.

deformation, and the KH model takes the size of the elastic range to be constant, which does not represent the actual behavior of the structural steel (Mamaghani et al. 1997). In the case of the 2SM, the reduction of elastic range is taken accurately into account (Mamaghani et al. 1995, Shen et al. 1995), which has the effect of softening of the hysteresis curve (reduction in stiffness), leading to lower values of the buckling load. The cyclic compressive load capacities up to 2.5 cycles for the EPP and KH models are almost the same, as shown in Fig. 8a. This is because the strain hardening effect is canceled out by the Bauschinger effect in the KH model. However, the KH model exhibits a higher compressive load capacity due to cyclic strain hardening in subsequent cycles (see Fig. 8a).

Figure 8b compares the progress of residual displacements $(\delta_{rd} + \delta_0)/t$, in the compression side $C \rightarrow T$ (buckling), and in the tension side $T \rightarrow C$, at plate centre, versus the number of cycles, obtained from analyses using the 2SM, EPP, KH, and IH models for CDA (m = 4) loading history. From this comparison, it can be seen that the EPP, KH, and particularly the IH model grossly overestimate the residual displacements compared with the 2SM. As can be noticed from Figs. 7b and 8b, the progress of buckling, which affects significantly the maximum compressive load and subsequent cyclic behavior, is different for each material model. The results in Figs. 7a and 8a also indicate that the maximum yield strength in tension side decreases with an increase in the number of cycles for all models except the IH model. In the case of the IH model, in spite of the higher progress in buckling (see Figs. 7b and 8b), the maximum yield strength in the tension side does not decrease due to the large cyclic strain hardening. It is worth noting that behavior similar to that discussed previously, was observed for the axially loaded pin-ended bracing members with a solid rectangular section (Mamaghani et al. 1996a).

Energy Absorption Capacity

The normalized energy absorption capacity, defined here as E_i/E_e, is one of the objective measures of the overall inelastic behavior of a structural member under cyclic loading (Mamaghani et al. 1997). Therefore, in this section, it is used to describe and evaluate the performance of each material model in the prediction of the hysteretic

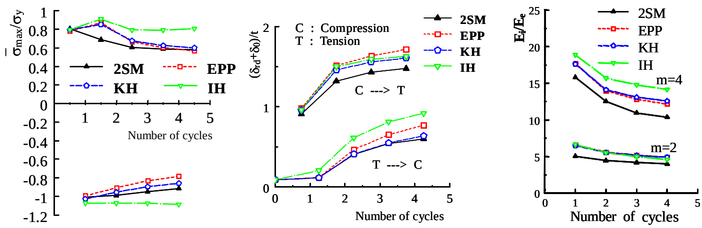

(a) (b) (c)

Figure 8. Comparison between 2SM and other models:
(a) $\bar{\sigma}_{max}/\sigma_y$ - number of cycles; (b) $(\delta_{rd}+\delta_0)/t$ - number of cycles;
(c) E_i/E_e - number of cycles.

behavior for the analyzed plates. E_i is defined as the energy corresponding to the loop i (area enclosed by the $\bar{\sigma}-\bar{\varepsilon}$ curve). As shown in Fig. 3, the loop i = 1 starts at 0.5 cycles and ends at 1.5 cycles; the loop i = 2 is confined between 1.5 and 2.5 cycles, and so on. The elastic strain energy E_e is defined as E_e = $0.5\sigma_y\varepsilon_y$. Using the above definitions, Fig. 8c compares the normalized energy absorption capacities, E_i/E_e, versus the number of loops, obtained from analyses using the 2SM, EPP, KH, and IH models for CDA (m = 2, 4) loading history. From this comparison, it can be seen that the EPP, KH, and particularly the IH model grossly overestimate the energy absorption capacity compared with the 2SM, especially as the number of cycles increases (see Fig. 8c). As shown in Fig. 8c, in the case of CDA with m = 2 (a relatively small displacement), the normalized energy absorption capacity for all models except the 2SM is almost identical; however, in the case of m = 4 (a large displacement), the normalized energy absorption capacity is much higher for the IH model due to the reasons discussed in the previous section. With the progress of deflection (see Figs. 7b and 8b), which has the effect of degrading buckling load (see Figs. 7a and 8a), the normalized energy absorption capacity in the fourth loop decreases by 20-30% compared with the first loop. The normalized energy absorption capacity reduces sharply in the second loop and tends to stabilize following the third loop under CDA (Fig. 8c).

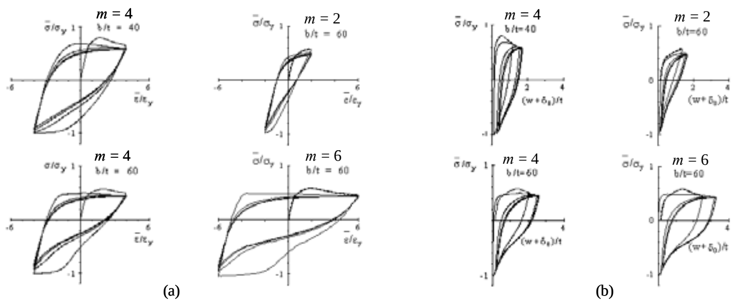

Figure 9. Effect of width-thickness ratio and displacement amplitude: (a) $\bar{\sigma}/\sigma_y - \bar{\varepsilon}/\varepsilon_y$; (b) $\bar{\sigma}/\sigma_y - (w+\delta_0)/t$.

Because the energy absorption capacity is of great interest in seismic design (it reduces the ductility demand on structure), it should be estimated as accurately as possible. From the above comparison between models, it is noticed that all models except the 2SM overestimate the energy absorption capacity. Therefore, the use of the EPP, KH, and IH models in the cyclic analysis of structures may lead to an erroneous estimate of energy absorption capacity. The 2SM, however, gives more promising results and can be used in the cyclic analysis of structures more confidently.

Effect of Width-Thickness Ratio and Displacement Amplitude

In this section, a series of numerical analyses on simply supported steel plates with three values of width-thickness ratios (*b/t* = 40, 60, 80) subjected to three loading programs of CDA (*m* = 2, 4, 6) are carried out to examine the effect of these parameters on the cyclic behavior. In the analysis, both the residual stresses and initial deflection of $\delta_0/b = 1/450$ are considered. Fig. 9 shows the hysteretic curves obtained using the 2SM for the specimens of *b/t* = 40, 60 (*m* = 2, 4, 6). All plates have characteristics of a large thinning out of the hysteresis loops (unstable behavior) up to 2.5 cycles; however, the hysteresis loops tend to stabilize (stable behavior) in subsequent cycles, see Fig. 9a. The change in the normalized compressive load-carrying capacity $\bar{\sigma}_{pi}$ during cyclic loading is shown in Fig. 10. The results in this figure indicate that there is a large reduction in buckling load up to 2.5 cycles,

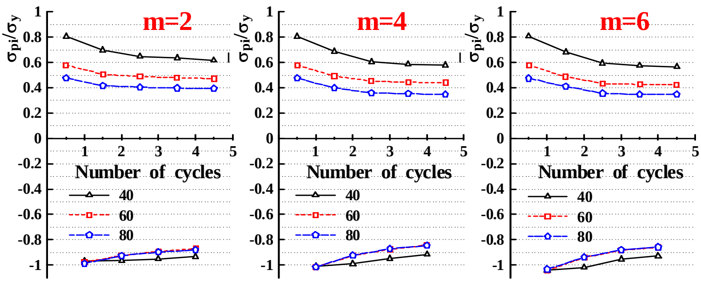

Figure 10. Effect of width-thickness ration (b/t = 40, 60, 80) and displacement amplitude (m =2, 4, 6) on load carrying capacity due to cycling under CDA (2SM).

but it converges to a certain value and does not significantly change in further cycles. The unstable behavior in the early cycles of loading is due to the large progress in buckling (i.e., the increase in deflection of the plate; see Fig. 9b) and the spread of plastic zone, which have the effect of reducing the plate stiffness. As shown in Fig. 9b, buckling of plates mainly occurs in the first compressive loading (0.5 cycles) and increases in the second compressive loading (1.5 cycles). There is no significant change in buckling after 2.5 cycles. Figure 10 shows that with the increase in width-thickness ratio the cyclic load-carrying capacity decreases markedly. The reason for this, as shown in Fig. 9b, is that the size and rate of increase in buckling are larger for the plates with a large width-thickness ratio (thinner plates).

Figure 11 shows the effect of width-thickness ratio (b/t = 40, 60, 80) and displacement amplitude (m = 2, 4, 6) on the normalized energy absorption capacity of plates with the increase in the number of loading cycles under CDA. The absorbed energy for loop i, E_i, is normalized with the absorbed energy in the first loop E_1. The results in Fig. 11 indicate that: (1) the larger the width-thickness ratio, the smaller the normalized energy absorption capacity; (2) the reduction in the normalized energy in the second loop (1.5 to 2.5 cycles) is considerably

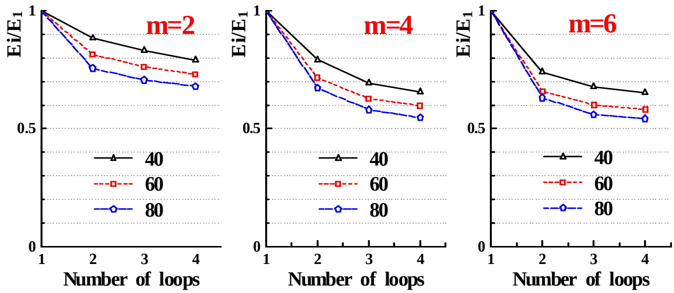

Figure 11. Effect of width-thickness ration (*b/t* = 40, 60, 80) and displacement amplitude (*m* =2, 4, 6) on energy absorption capacity due to cycling under CDA (2SM).

large and tends to stabilize after the third loop for all *b/t* ratios and displacement amplitudes; (3) an increase in the displacement amplitude *m* causes a larger reduction in the normalized energy absorption capacity, especially in the second loop, due to the larger thinning out of the hysteresis loops up to 2.5 cycles when the displacement amplitude is large; and (4) the rate of change in the normalized energy absorption capacity is not noticeably affected by the different values of *b/t* ratios following the second loop.

CONCLUSIONS

This paper deals with the cyclic inelastic behavior and large deflection analyses of simply supported thin steel plates using the finite element method. From the comparison between cyclic elastoplastic performances of different models discussed in this paper, it was concluded that the use of the EPP, KH, and IH models in the cyclic analysis of structures may lead to an erroneous estimate of cyclic behavior (maximum compressive load and energy absorption capacity). The 2SM, however, gives more promising results and can be used more confidently. From this study, it was also found that: (1) residual stress and increase in the initial deflection have mainly the effect of decreasing the initial maximum compressive load (buckling load) and does not significantly affect the subsequent cyclic behavior; (2) the EPP, the KH and particularly the IH models grossly over-estimate the energy absorption capacity compared to the 2SM; (3) the normalized energy absorption capacity reduces sharply in the second loop and tends to stabilize following the third loop under cyclic CDA loading; (4) the energy absorption and compressive load-carrying capacities markedly decrease under cyclic loading because of the increase in the width-thickness ratio. The reason for this is that the size and rate of increase in buckling and the spread of plastic zone are larger for plates with a large width-thickness ratio (thinner plates).

REFERENCES

Banno, S., I. H.P. Mamaghani, T. Usami, E. Mizuno, 1998. Cyclic elastoplastic large deflection analysis of thin steel plates. *Journal of Engineering Mechanics, ASCE*, 124(4), 363-370.

Bathe, K. J., and L. W. Ho, 1981. A simple and effective element for analysis of general shell structures. *Computers and Structures,* Vol. 13, 673-681.

Bradford, M. A., and M. Azhari, 1995. Inelastic local buckling of plates and plate assemblies using bubble functions, *Engineering Structures*, 17(2), 95-103.

Fafard, M., G. Dhatt, , and J. L. Botaz, 1989. A new discrete Kirchhoff plate/shell element with updated procedures, *Computers and Structures*, Vol. 31(4), 591-603.

Jetteur, Ph., S. Cescotto, V. de Ville de Goyet, and F. Frey, 1983. Improved nonlinear finite elements for oriented bodies using an extension of Marguerre's theory, *Computers and Structures*, 17(1), 129-137.

Mamaghani, I. H. P., 1996. Cyclic elastoplastic behavior of steel structures: theory and experiment, *Ph.D. Thesis*, Nagoya University, Nagoya, Japan.

Mamaghani, I. H. P., C. Shen, E. Mizuno, and T. Usami, 1995. Cyclic behavior of structural steels. I: experiments, *J. Engrg. Mech.*, ASCE, 121(11), 1158-1164.

Mamaghani, I. H. P., T. Usami, and E. Mizuno, 1996a. Inelastic large deflection analysis of steel structural members under cyclic loading, *Engineering Structures*, UK, Elsevier Science, 18(9), 659-668.

Mamaghani, I. H. P., T. Usami, and E. Mizuno, 1996b. Cyclic elastoplastic large displacement behaviour of steel compression members, *J. Structural Engineering*, JSCE, Vol. 42A, 135-145.

Mamaghani, I. H. P., T. Usami, and E. Mizuno, 1997. Hysteretic behavior of compact steel box beam-columns. Journal of Structural Engineering, JSCE, Japan, Vol. 43A, 187-194.

Owen, D.R.J., and E. Hinton, 1980. *Finite Elements in Plasticity,* Pineridge Press Limited, Swansea, UK.

Shen, C., I. H. P. Mamaghani, , E. Mizuno, and T. Usami, 1995. Cyclic behavior of structural steels. II: theory, *J. Engrg. Mech., ASCE*, 121(11), 1165-1172.

Usami, T., 1993. Effective width of locally buckled plates in compression and bending, *J. Struct. Engrg., ASCE,* 119(5), 1358-1373.

Washizu, K., 1982. *Variational Methods in Elasticity and Plasticity,* 3rd Ed., Pergamon Press.

Zienkiewicz, O. C., 1977. *The Finite Element Method,* 3rd Ed., McGraw-Hill, New York.

CONTEMPORARY THEORIES OF BUILT-UP COMPRESSION MEMBERS

Ghada Elmahdy[1]

INTRODUCTION

Built-up compression members composed of two steel sections interconnected along one side are treated as built-up members when buckling occurs about the axis passing through the open web. This type of member is often used as bracing members, truss members, or columns in the form of double angles, double channels, double I-sections, or 4-angle members. The main reason for using this type of member as a compression member is to reduce the amount of material needed to produce a member of specific slenderness by using multiple sections spaced apart and interconnected along the open webs. It has long been recognized that this type of member exhibits a decrease in strength with the reduction of the degree of interconnection, or in other words, with an increase in the length of the elements between interconnectors. This decrease in strength is accompanied by an increase in flexibility and can lead to a premature failure of the structure. The purpose of this paper is to explain the phenomena of the behaviour of built-up compression members.

There are two contemporary theories for analysing the effect of buckling of this type of compression member. Either a $P\delta$ analysis is used to determine the effect of the increased flexibility of the member as a result of the interaction between the local $P\Delta$ sway of the individual members between interconnectors and the overall $P\delta$ buckling of the member as a whole. Or a shear analysis is used to account for the increased flexibility of a built-up compression member,

[1] Senior Civil/Structural Engineer, Capital Engineering, Edmonton, Alberta, Canada T5L 2M7.

and consequently the reduced strength of the member.

Obviously, performing a shear analysis on an axially loaded compression member constitutes the resolution of the axial compression force into a component in line with the axis of the member and a component perpendicular to the axis of the member. The presence of an initial out of straightness in the member to instigate the occurrence of buckling is naturally required. This assumption is also in par with the application of a $P\delta$ analysis as illustrated in Fig. 1.

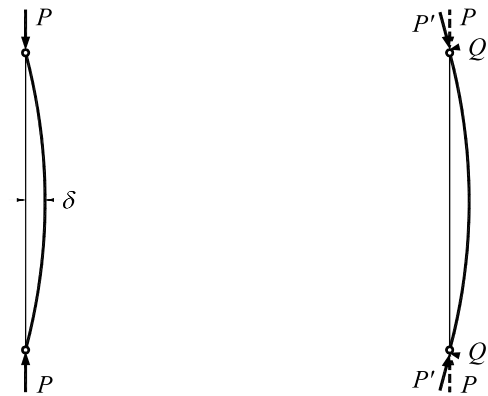

(a) $P\delta$ analysis (b) Shear analysis

Fig. 1 Resolution of Forces for Column Analysis.

In either analysis, the result for built-up compression members is not only the traditional $P\delta$ effect, but an enhanced $P\delta$ effect described as an increased flexibility. The analysis of a built-up compression member using the traditional theory of bifurcation would envelope the additional $P\Delta$ sway effect of the individual members between interconnectors resulting in an increased $P\delta_{inc}$ of the overall column. However, as it has proven difficult to quantify this increase in flexibility of a built-up compression member using a traditional bifurcation method, it is generally accepted that a shear analysis is required to explain and quantify its increased flexibility. In fact, this method has generally been adopted in the form of an equivalent slenderness ratio derived by studying the effect of shear on built-up compression members. The increased deflection in a built-up compression member is illustrated in Fig. 2 for both types of analysis.

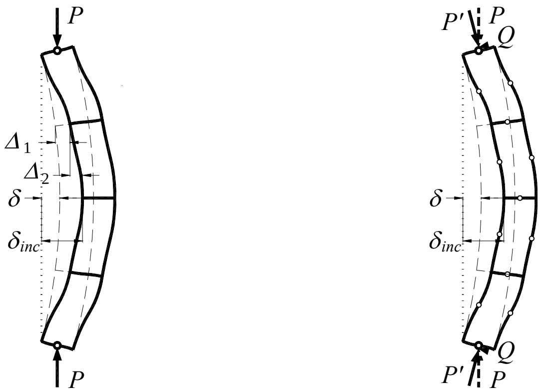

(a) $P\delta + P\Delta$ analysis (b) Shear analysis

Fig. 2 Increased Deflection in Built-Up Compression Members.

$P\delta$ ANALYSIS OF BUILT–UP COMPRESSION MEMBERS

The first impression of an axially loaded built-up compression member is that of a column deflected under the effect of the axial load and any imperfections in a $P\delta$ fashion. Further consideration of the fact that the column is composed of two members interconnected along the open sides leads to the realization that these individual members will also deflect in between connectors in a $P\Delta$ configuration. Superimposing these two effects would create an increased overall midpoint deflection as shown in Fig. 2(a). Based on the analysis of Bažant and Cedolin (1991) the following assumptions of the interaction of local and global buckling of a built-up compression member can be made.

Considering a pinned built-up compression member in which the main members are interconnected by an unspecified web (*i.e.*, batten plates) to maintain the integrity of the column, as shown in Fig. 3, the column has an overall length of L and carries a load of P. The main members are a distance b apart and are interconnected at intervals of a, have an axial stiffness of EA_i and a bending stiffness of EI_y. Two buckling modes can occur, *viz.,* local flexural buckling of the main members and global buckling of the column, shown in Figs. 3(b) and (c), respectively. The local flexural buckling mode has been chosen to reflect the final anticipated $P\Delta$ configuration of this mode of buckling. The flexibility of the interconnectors is small compared to that of the main members so fixed-end conditions are assumed for the local flexural buckling mode. Figure 3(d) shows the simultaneous occurrence of local and global buckling. The buckling modes can be associated with:

(a) a local flange deflection u_1, based on the assumption of fixed-end conditions and the occurrence of side sway,
(b) a global sinusoidal flange deflection u_2, and
(c) a local initial imperfection x_0 taking the shape of the local buckling mode to initiate this mode, such that

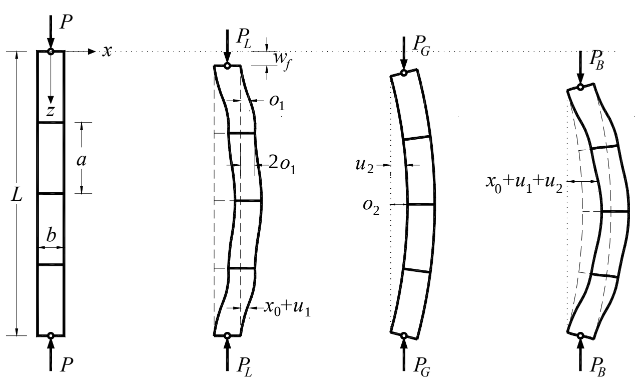

(a) Built-up member (b) Local buckling (c) Global buckling (d) Compound buckling

Fig. 3 Interaction of Local and Global Buckling Modes.

$$u_1 = o_1\left(1\text{-}\cos\frac{\pi z}{a}\right) \qquad u_2 = o_2 \sin\frac{\pi z}{L} \qquad x_0 = \alpha a\left(1-\cos\frac{\pi z}{a}\right) \tag{1}$$

where o_1 and o_2 are midpoint modal amplitudes; and α is an imperfection parameter such that αa represents the amplitude of the initial imperfection at midpoint. No initial global imperfection is included as it is assumed that the local initial imperfection will initiate buckling, and the purpose of this study is to visualize the effect of local flexural buckling on the overall behaviour of the column. However, sinusoidal global deflection is still assumed.

The column can carry a buckling load of P_B, causing an axial force of approximately $\frac{1}{2}P_B$ in each main member. In the local flexural buckling mode the main members may be considered to buckle as a series of fixed-end unbraced columns of length a. Therefore, the elastic local and global flexural buckling loads can be expressed as

$$P_L = \frac{2\pi^2 EI_y}{a^2} \qquad\qquad P_G = \frac{\pi^2 EA_i b^2}{2L^2} \tag{2}$$

and correspond to the buckling loads for the built-up columns shown in Figs. 3(b) and (c), respectively. It should be noted that for the sake of algebraic simplicity the global second moment of area of the column has been taken as $I_o=A_i b^2/2$, neglecting the second moment of area of the individual main members about their own centroidal axes.

(i) Local Buckling Alone

Referring to Fig. 3(b) considering $o_2=0$ gives just local flexural buckling in which the midpoint deflections are magnified by a magnification factor of $1/(1-P_B/P_L)$ giving

$$\alpha a + o_1 = \frac{\alpha a}{1-\dfrac{P_B}{P_L}} \qquad \Rightarrow \qquad o_1 = \frac{\alpha a P_B}{P_L - P_B} \tag{3}$$

The axial shortening per length a due to bending, w_f, can be derived from the expression

$$w_f = \frac{1}{2}\int_0^a \left[\left(x_0' + u_1' \right)^2 - x_0'^{\,2} \right] dz \tag{4}$$

where the prime designates the first derivative with respect to z. Substituting the derivatives of Eq. (1) into Eq. (4) and simplifying gives

$$w_f = \frac{1}{2}\left(\frac{2\pi^2 \alpha o_1}{a} + \frac{o_1^2 \pi^2}{a^2} \right) \int_0^a \sin^2 \frac{\pi\, z}{a} dz \tag{5}$$

Substituting the value of the integral as $a/2$ and substituting o_1 from Eq. (3) gives

$$w_f = \frac{\pi^2 \alpha^2 a P_B}{4\left(P_L - P_B \right)^2} \left(2P_L - P_B \right) \tag{6}$$

Approximately the same result has been derived for slightly flexible end conditions (Elmahdy, 1997).

This axial shortening due to local bending of the flanges reduces the axial stiffness EA_i^* of the flanges, or in other words increases the axial compliance $1/EA_i^*$ such that

$$\frac{1}{EA_i^*} = \frac{1}{EA_i} + \frac{1}{a}\frac{\partial w_f}{\partial P_B} \tag{7}$$

where the second term can be determined by partially differentiating Eq. (6) with respect to P_B and substituting the resulting expression and the second expression of Eq. (2) into Eq. (7) giving the following expression for $1/EA_i^*$

$$\frac{1}{EA_i^*} = \frac{\pi^2 b^2}{2L^2 P_G} + \frac{\pi^2 \alpha^2 P_L^2}{2\left(P_L - P_B \right)^3} \tag{8}$$

This is the modified axial compliance per unit length.

(ii) Interaction of Local and Global Buckling

The general idea of this study is to emphasize, at least theoretically, the influence of local flexural buckling on global buckling. Taking simultaneous local flexural and global buckling into account, the elastic buckling load of the strut P_B, when the global sinusoidal deflection u_2 is nonzero, can be approximately taken as the Euler load of a column with a bending stiffness of $b^2EA_i^*/2$ such that $P_B=\pi^2b^2EA_i^*/2L^2$. Substituting the expression for EA_i^* from Eq. (8) into this and simplifying gives

$$\frac{1}{\lambda_b}-\frac{P_L}{P_G}=\frac{\alpha^2L^2}{b^2(1-\lambda_b)^3} \qquad \text{where} \qquad \lambda_b=\frac{P_B}{P_L} \tag{9}$$

This is the general equation for the interaction of local and global flexural buckling. The relationship between the buckling loads for various ratios of global buckling load to local buckling load for an ideal column is plotted in Fig. 4 taking the local slenderness ratio as constant and gradually increasing the global slenderness ratio. The failure load of the built-up column is now governed by either: (a) global buckling; (b) simultaneous local and global buckling; or (c) local buckling. In the following sections these three buckling modes will be examined to determine the sensitivity of the buckling load to initial imperfections.

Case I: Global Buckling Governs

This case refers to failure of the column due to global buckling before the occurrence of local buckling, but close to it. This situation is illustrated in Fig. 4. In other words $P_G<P_L$ (but close to P_L) such that $P_B\approx P_G$ and $\lambda_b\approx P_G/P_L$. Also, as the local buckling load is close to the global buckling load ($P_L\approx P_G$), it can be deduced from Eq. (2) that $r_y/a\approx b/2L$. Hence, introducing the constant $k_1=b/L$, then substituting this into Eq. (9) and simplifying gives

$$\frac{P_B}{P_G}=\frac{1}{1+\left(\dfrac{\alpha}{\alpha_1}\right)^2} \qquad \text{where} \qquad \alpha_1=k_1\left[\frac{(P_L-P_G)^{3/2}}{P_LP_G^{1/2}}\right] \tag{10}$$

Assuming that α/α_1 is a small quantity taken as x the right hand side of this expression can be expressed by a Maclaurian Series as approximately equal to $1-x^2$. Hence the above expression reduces to

$$\frac{P_B}{P_G} = 1 - \left(\frac{\alpha}{\alpha_1}\right)^2 \qquad \text{where} \qquad \alpha_1 = k_1\left[\frac{(P_L - P_G)^{3/2}}{P_L P_G^{1/2}}\right] \tag{11}$$

Hence, a built-up column that fails by global buckling has a mild sensitivity to an initial imperfection as indicated by the exponent 2.

Case II: Simultaneous Local and Global Buckling Governs

This case refers to failure of the column due to simultaneous local and global buckling, which in Fig. 4 would be at the point of intersection of the two lines. The condition for this to occur is $\lambda_b \approx 1$. Substituting this into Eq. (9) and using the approximation $\lambda_b^{-1}-1 \approx 1-\lambda_b$ gives

$$\frac{P_B}{P_L} = 1 - \left[\frac{\alpha}{\alpha_2}\right]^{1/2} \qquad \text{where} \qquad \alpha_2 = k_1 \tag{12}$$

Thus a built-up column that buckles simultaneously in local and global buckling is severely sensitive to imperfections, which is characterized by the exponent of 1/2. This case represents the optimum design based on the economic aspect of reducing the number of interconnectors.

Case III: Local Buckling Governs

This case refers to a failure load due to local buckling before the global buckling load capacity has been reached, represented by the horizontal line in Fig. 4 such that $P_L < P_G$ (but close to P_G), which implies that $P_B \approx P_L$ giving $\lambda_b \approx 1$. Substituting this into Eq. (9) and simplifying gives

$$\frac{P_B}{P_L} = 1 - \left(\frac{\alpha}{\alpha_3}\right)^{2/3} \qquad \text{where} \qquad \alpha_3 = k_1\left(1 - \frac{P_L}{P_G}\right)^{1/2} \tag{13}$$

Thus the built-up column is said to be strongly sensitive to imperfections which is characterized by the exponent 2/3. The effect of these three sensitivity indices is shown in Fig. 4.

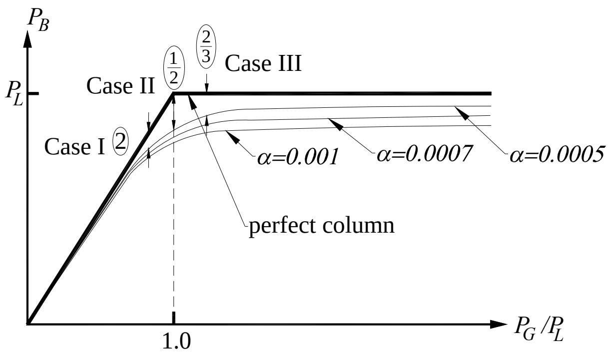

Fig 4. Imperfection Sensitivity for Interaction of Buckling Modes.

As can be seen from the previous study, a $P\delta$ analysis of the effect of the interaction of local and global buckling of a built-up column only results in a realization of the increased flexibility of the column leading to an increase in the sensitivity of the overall buckling load of the column due to initial imperfections. It still remains to be determined the actual reduction in the load carrying capacity of the built-up compression member due to the increased flexibility of this type of member. This has been proven to be most effectively done through a shear analysis of a built-up compression member.

SHEAR ANALYSIS OF BUILT-UP COMPRESSION MEMBERS

The analysis of the effect of shear on a built-up compression member was given by Timoshenko and Gere (1961). Figure 2(b) shows the increased deflection profile of a built-up column due to shear. Unlike solid columns, the effect of a shear force, Q, on the deflection of a built-up column must be considered. This shear for an axially loaded compression member is the component of the vertical axial load perpendicular to the deflected axis of the buckled column. For a built-up column this shearing force is not carried by a solid web, and so a secondary system is required, *viz.,* a frame action for battened columns. As a result of the shearing force in the main members, the lateral deflection of the column is increased. The change in slope of the deflection curve produced by the shearing force is Q/P_d for a column, where P_d is the shear stiffness of the column. Taking the Euler load of the column as $P_E=\pi^2 EI_Y/(KL)^2$ where EI_Y is the flexural stiffness of the integral column and KL is its effective length, gives the expression for the critical load taking into account the effect of shear as

$$P_{cr} = \frac{P_E}{1+\dfrac{P_E}{P_d}} \tag{14}$$

Thus Eq. (14) shows that the critical load is reduced by the ratio $1/(1+P_E/P_d)$.

The effect of the shear force on the critical load depends on the type and arrangement of the secondary system carrying the shear force. For built-up columns, in general, the factor $1/P_d$ is the quantity by which the shear force, Q, is multiplied in order to obtain the additional slope, γ_t, of the deflection curve due to shear. The lateral displacements caused by the shear forces must be evaluated to determine the value of $1/P_d$. As an example, a battened column will be analysed as this represents a built-up compression member that requires the use of an equivalent slenderness ratio, increased to take into account the *flexibility of the interconnector* as stated in the CISC Handbook of Steel Construction’s commentary (2006). This increase is applied to the axis of buckling where the buckling mode of the member involves relative deformation that produces shear forces in the interconnectors (Clause 19.1.4 CAN/CSA-S16-01).

A battened column, as shown in Fig. 5 is actually a frame and it would be proper to analyze it as such. To solve the problem of shear the following assumption can be made. Referring to the deformed axis in Fig. 2(b), points of inflection (*i.e.,* hinges) in the deflection curve can be assumed at the midpoints of the panels and at the midpoints of the battens. Thus, the statically indeterminate system of a built-up column is transferred into a statically determinate system used to determine the effect of the shear force in the column as shown in Fig. 5(b).

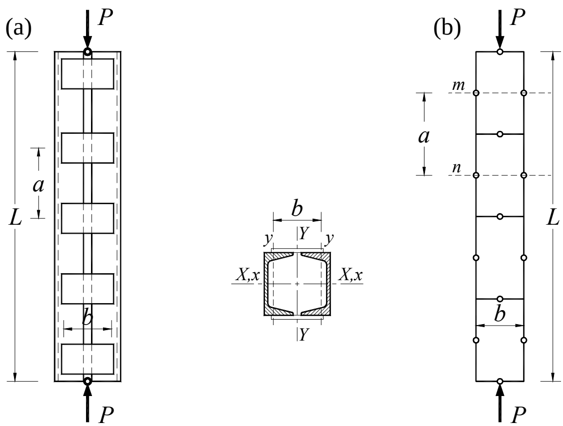

Fig. 5 Statical System of a Battened Column.

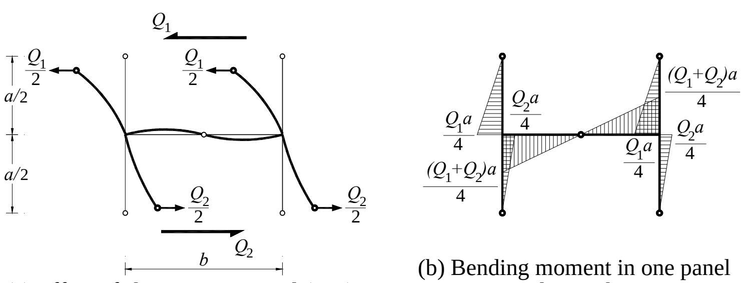

(a) Effect of shear on one panel (m-n)

(b) Bending moment in one panel due to shear

Fig. 6 Statical System of One Panel in Shear.

Considering the effect of shear on one panel (m-n) of length a, the shear force can be assumed to act at the hinges of the main members, half on each member as shown in Fig. 6(a). This would cause the bending moment shown in Fig. 6(b). The lateral deflection in a panel due to shear, as shown in Fig. 7, consists of five components which are the deflections due to:

(a) the flexibility of the batten, δ_1,
(b) the flexibility of the main member, δ_2,
(c) the shear deformation of the batten,
(d) the shear deformation of the main member, δ_3, (δ_3 is composed of (c) and (d)), and
(e) the semi-rigidity of the connection, δ_4.

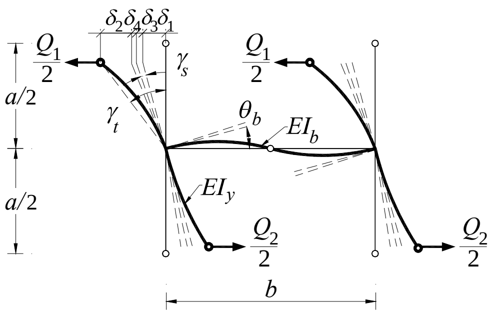

Fig. 7 Total Lateral Deflection of a Panel Due to Shear.

As the value of shear in a column varies along its length (*i.e.,* Q_0, Q_1, Q_2) it will be taken as the general term, Q, usually specified as about 2-2.5% of the axial load by most design standards and specifications. The moment, $Qa/2$, acting at the ends of the batten results in an angle of rotation at each end of the batten, θ_b, which produces a lateral deflection in the main members, δ_1, such that

$$\theta_b = \frac{Qab}{12EI_b} \qquad \Rightarrow \qquad \delta_1 = \frac{\theta_b a}{2} = \frac{Qa^2 b}{24EI_b} \tag{15}$$

where b is the distance between the centroids of the main members; and EI_b is the sum of the flexural rigidities of the battens on one level. The bending of the main member as a cantilever caused by the shearing force $Q/2$ gives the second component of deflection which is

$$\delta_2 = \frac{Q}{2}\left(\frac{a}{2}\right)^3 \frac{1}{3EI_y} = \frac{Qa^3}{48EI_y} \tag{16}$$

where EI_y is the flexural stiffness of one of the main members about its centroidal axis. Thus the angular displacement, γ_b, produced by bending under the effect of the shearing force Q is

$$\gamma_b = \frac{\delta_1 + \delta_2}{a/2} = \frac{Qab}{12EI_b} + \frac{Qa^2}{24EI_y} \tag{17}$$

In addition to δ_1 and δ_2, the contribution of the shear deformation in the batten and the main member caused by the angular displacement must be taken into consideration. The shear force in the batten is Qa/b and the shear force in the main member is $Q/2$, assuming a general value of Q along the column. Hence the corresponding shear strain, γ_s, is

$$\gamma_s = \frac{n_s Qa}{bA_b G} + \frac{n_s Q}{2A_i G} \tag{18}$$

where A_b is the sum of the cross-sectional areas of the battens on one level; A_i is the cross-sectional area of one main member; G is the shear modulus; and n_s is a shape factor which equals 1.2 for rectangular cross sections. The shearing strain, γ_s, gives a lateral deflection of $\delta_3 = \gamma_s a/2$.

Finally, the possibility of lateral deflection due to the semi-rigidity of the connection between the batten plate and the main members can be considered (Lin *et al.*; 1970). From Fig. 6(b) it can be seen that the bending moment acting on the connection of a batten plate to a main member is $M_c = Qa/2$ assuming a general value of Q along the column. If the connection is not fully rigid as in the case of snug-tight bolts, this moment would cause a relative rotation between the batten plate and the main member. The magnitude of this relative rotation depends on the rigidity of the connection, and is directly proportional to the magnitude of the moment. Therefore, the relative rotation can be expressed as $\theta_r = ZM_c$ where Z is a semirigid connection constant (*i.e.,* Z=0 for a rigid connection and $Z=\infty$ for a hinged connection). This would give a lateral deflection of $\delta_4 = ¼a^2ZQ$. Adding the effect of δ_3 and δ_4 to Eq. (17) and dividing by Q gives the expression for $1/P_d$ as

$$\frac{1}{P_d} = \frac{ab}{12EI_b} + \frac{a^2}{24EI_y} + \frac{n_s a}{bA_b G} + \frac{n_s}{2A_i G} + \frac{aZ}{2} \tag{19}$$

It should be noted that the amplification of the lateral deflection due to the axial load in the main members has been neglected.

Substituting Eq. (19) into Eq. (14) and using $P_E = \pi^2 EI_Y/(KL)^2$ gives the following expression for the critical load

$$P_{cr} = \frac{\pi^2 EI_Y}{(KL)^2} \frac{1}{1 + \frac{\pi^2 EI_Y}{(KL)^2}\left(\frac{ab}{12EI_b} + \frac{a^2}{24EI_y} + \frac{n_s a}{bA_b G} + \frac{n_s}{2A_i G} + \frac{aZ}{2}\right)} \tag{20}$$

To express the critical load in the form $P_{cr} = \pi^2 EA/\Lambda_{eq}^2$; where $A=2A_i$ is the integral cross-sectional area; and Λ_{eq} is the equivalent slenderness ratio of the integral cross section about the axis of buckling (*i.e.,* the Y-axis), Eq. (20) must be rearranged such that

$$P_{cr} = \frac{\pi^2 EA}{\Lambda_Y^2 + \frac{\pi^2 Aab}{12I_b} + \frac{\pi^2 a^2}{12r_y^2} + \frac{2\pi^2 An_s a(1+\nu)}{bA_b} + 2\pi^2 n_s(1+\nu) + \frac{\pi^2 EAaZ}{2}} \tag{21}$$

where ν is Poisson's ratio; and r_y is the radius of gyration of a main member about its minor axis (or the axis parallel to the buckling axis). The expression in the denominator is known as the equivalent slenderness ratio of a battened column.

It is now necessary to determine which of the terms in the expression given in the denominator of Eq. (21) have a significant effect on P_{cr}. The first term is of course the slenderness ratio of the integral column and is a fundamental requirement of the equivalent slenderness ratio formula. The following five terms are the secondary effects of additional lateral deflection of the built-up column due to shear. The second and third terms are characterised by the bending deformations in the battens and main members, respectively, due to shear. The fourth and fifth terms represent the shear deformations in the battens and main members, respectively, due to shear. The sixth and final term represents the effect of semi-rigid connections between the main members and the batten plates. Naturally, the role played by the batten plates depends on the dimensions of the batten plates. Most design codes specify minimum dimensions for batten plates in order to eliminate or reduce their effect on the increased flexibility of a built-up compression member; hence, in effect, eliminating the second and fourth terms. A comparison of the individual effects of the second to fifth terms from actual test specimens made by Elmahdy (1997), described later in this paper in the section on previous experimental results, show that undoubtedly the most significant term is the third term representing the bending in the main members due to shear and to a certain extent the fourth term, the shear deformation in the battens, as shown in the chart in Fig. 8. The sixth and final term depends largely on the type of connection between the batten plate and the main member. Its effect is probably best determined using an experimental method for different types of connections.

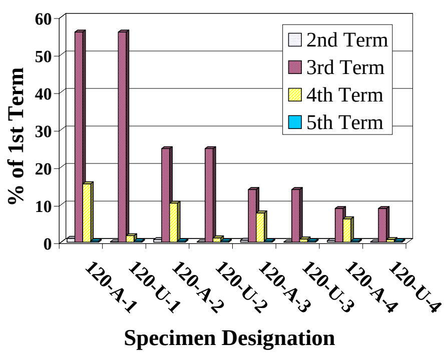

Fig. 8 Terms of Equation (21).

CODE REQUIREMENTS

From the above mentioned theories most international steel design codes, standards, and specifications have set limitations for the slenderness ratio of individual members between interconnectors of built-up compression members to avoid a situation of coupled instabilities, as well as recommendations for the equivalent slenderness ratio of built-up compression members to satisfy the requirements for the effect of shear. The slenderness ratio of individual members between interconnectors, Λ_i, is taken as a fraction of the integral slenderness ratio, Λ_o, as shown in Eq. (22) where b_i is a factor less than one used to ensure that local and global buckling do not occur simultaneously and that the integral buckling load governs.

$$\Lambda_i \leq b_i \Lambda_o \tag{22}$$

To account for the increased flexibility of built-up compression members, the equivalent slenderness ratio is used, which is the slenderness ratio of the member when the buckling mode involves relative deformation that produces shear forces in the interconnectors, taken as

$$\Lambda_{eq} = \sqrt{\Lambda_o^2 + \left(a_i \Lambda_i\right)^2} \tag{23}$$

such that a_i is a factor that represents the effect of additional deflections of the main members and interconnectors in shear, bending, and semi-rigid connections due to the effect of shear.

PREVIOUS EXPERIMENTAL RESULTS

From previous experimental results, the type, dimensions, and number of interconnectors, as well as, the type of connection between the interconnector and the main members have had a significant effect on the value of a_i. Some examples of this are: Temple and Elmahdy (1993, 1995); Zandonini (1985), and Astaneh *et al.* (1985). In fact, each type of interconnector and its connection should probably be calibrated to determine the correct value of a_i for that type of built-up compression member.

A set of test specimens conducted by Elmahdy (1997) in which the behaviour of battened columns was compared with the behaviour of buttoned columns will be outlined to illustrate the two theories mentioned in this paper. The test specimens were composed of two channel C75x6 sections placed back to back spaced apart by 9.53 mm, as shown in Fig. 9. The test specimens were interconnected using one to four interconnectors, either batten plates or button plates (intermittent fillers). The interconnectors were welded along the sides parallel to the longitudinal axis of the specimen. The length of the test specimens was 2233 mm from knife edge to knife edge. The specimens were hinged about the *Y*-axis giving an integral slenderness ratio of 120 about this axis, and fixed about the *X*-axis giving an integral slenderness ratio of 37.7 about this axis. The modulus of elasticity of the test specimens varied from 211 to 215 GPa, and the yield strength of the specimens varied from 351 to 372 MPa as shown in Table 1. For the calculation of the theoretical loads of each test specimen, shown in Table 2, the actual material properties were used, whereas an average of 213 GPa for the modulus of elasticity and 360 MPa for the yield strength were used to generate the column curves.

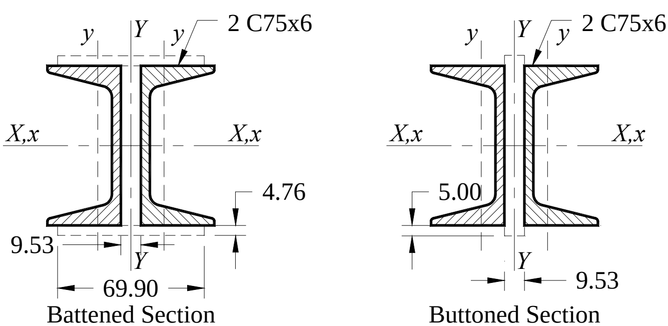

Fig. 9 Cross Section of Test Specimens.

The interaction curve shown in Fig. 10 was generated using Eqs. (11), (12), and (13), and an imperfection parameter of α=0.0005. It can be seen from this figure that the experimental failure loads of the battened and buttoned specimens correlate relatively well with the interaction curve. The experimental results were also plotted against an Euler column curve and the column curve from CAN/CSA-S16-01 (using ϕ=1.0 as resistance factor) for an equivalent slenderness ratio calculated from Eq. (23) once taking a_i =1.00 and once taking a_i =0.65. Figures 11(a) and (b) show these results for both the battened specimens and the buttoned specimens, respectively. The battened specimens correlated better using a_i=1.00, whereas, the buttoned specimens correlated better using a_i =0.65 as specified by Clause 19.1.4 of CAN/CSA-S16-01. However, as there were discrepancies it is recommended that the exact value of a_i be determined experimentally for all types of interconnectors and their connections.

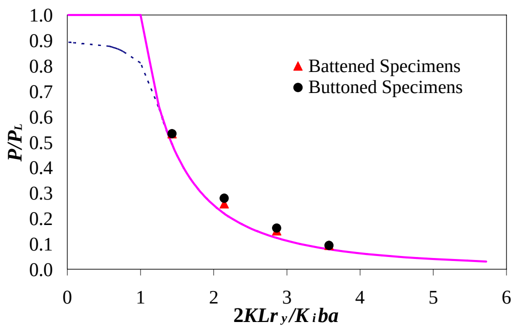

Fig. 10 Interactive Curve with Experimental Failure Loads.

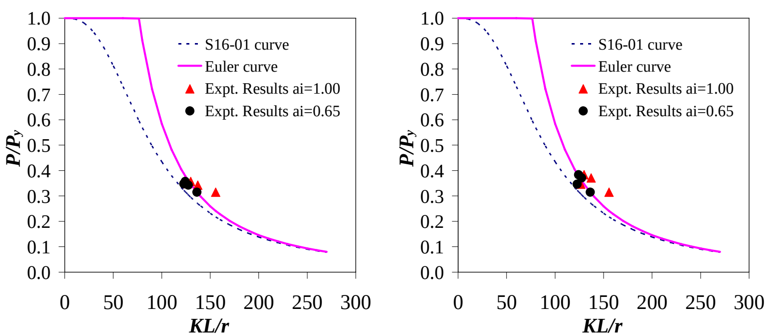

(a) Battened Specimens (b) Buttoned Specimens

Fig. 11 Theoretical Curves and Experimental Failure Loads of Test Specimens.

Table 1 Geometric and Material Properties of Test Specimens.

Specimen Number[a]	a[d] (mm)	Λ_Y	$\Lambda_i = a/r_i$	Λ_{eq}[e] a_i=1.0	Λ_{eq}[e] a_i=0.65	E (GPa)	F_y (MPa)
120-A-1[b]	1000	120	99.0	155.6	136.2	213	353
120-U-1[c]	1000	120	99.0	155.6	136.2	213	353
120-A-2	667	120	66.0	137.0	127.4	215	372
120-U-2	667	120	66.0	137.0	127.4	215	372
120-A-3	500	120	49.5	129.8	124.2	211	351
120-U-3	500	120	49.5	129.8	124.2	211	351
120-A-4	400	120	39.6	126.4	122.7	212	363
120-U-4	400	120	39.6	126.4	122.7	212	363

[a] Specimens are designated by the integral slenderness ratio about the Y-axis, A for battened columns and U for buttoned columns, and the number of interconnectors.

[b] Batten interconnectors have a dimension of 69.9x69.9x4.76 mm (2.75x2.75x3/16 in.).

[c] Button interconnectors have a dimension of 69.9x86.0x9.53 mm (2.75x3.38x3/8 in.).

[d] a is taken as the centre-to-centre distance between interconnectors.

[e] The equivalent slenderness ratio is calculated using Eq. (23) $\Lambda_{eq}=[\Lambda_Y^2 + (a_i\Lambda_i)^2]^{1/2}$.

Table 2 Experimental and Theoretical Failure Loads of Specimens.

Specimen Number	$P_{expt.}$ (kN)	Theoretical Failure Loads (kN)				Experimental/Theoretical Failure Load Ratios			
		a_i=1.0		a_i=0.65		a_i=1.0		a_i=0.65	
		S16-01	Euler	S16-01	Euler	S16-01	Euler	S16-01	Euler
120-A-1	173.0	119.2	132.5	149.3	172.9	1.45	1.31	1.16	1.00
120-U-1	173.1	119.2	132.5	149.3	172.9	1.45	1.31	1.16	1.00
120-A-2	188.1	150.3	172.5	169.3	199.5	1.25	1.09	1.11	0.94
120-U-2	203.8	150.3	172.5	169.3	199.5	1.36	1.18	1.20	1.02
120-A-3	196.2	160.0	188.6	171.6	206.0	1.23	1.04	1.14	0.95
120-U-3	210.6	160.0	188.6	171.6	206.0	1.32	1.12	1.23	1.02
120-A-4	191.1	168.7	199.8	176.8	212.1	1.13	0.96	1.08	0.90
120-U-4	190.4	168.7	199.8	176.8	212.1	1.13	0.95	1.08	0.90

CONCLUSION

Although there are two theories for determining the effect of the increased flexibility of built-up compression members composed of two steel shapes connected together by some type of interconnector, it is the actual shear analysis of built-up compression members that best quantifies the overall behaviour of these members. The $P\delta$ analysis gives an interesting picture of the effect of interaction between local and global buckling and the necessity to avoid the imperfection sensitivity that corresponds with the simultaneous occurrence of these two modes of buckling. However, it does not definitely quantify the overall action of built-up compression members. To determine the effect of each type of interconnector and its connection on the equivalent slenderness ratio, an experimental method of calibration is the recommended course of action to take.

REFERENCES

Astaneh-Asl, A., Goel, S.C., and Hanson, R.D. 1985. Cyclic out-of-plane buckling of double-angle bracing. ASCE Journal of Structural Engineering, **111**(5): 1135-1153.

Bažant, Z.P., and Cedolin, L. 1991. Stability of structures: elastic, inelastic, fracture, and damage theories. Oxford University Press, Inc., New York, NY.

CISC. 2006. Handbook of steel construction (9th edition). Canadian Institute of Steel Construction, Willowdale, Ont.

CSA. 2001. Limit states design of steel structures. Standard CAN/CSA-S16-01, Canadian Standards Association, Rexdale, Ont.

Elmahdy, G.M., 1997. Buckling of built-up columns. Ph.D. Dissertation, Department of Civil and Environmental Engineering, University of Windsor, Windsor, Ont.

Lin, F.J., Glauser, E.C., and Johnston, B.G. 1970. Behaviour of laced and battened structural members. ASCE Journal of the Structural Division, **96**(ST7): 1377-1401.

Temple, M.C., and Elmahdy, G. 1993. Buckling of built-up compression members in the plane of the connectors. Canadian Journal of Civil Engineering, **20**(6): 895-909.

Temple, M.C., and Elmahdy, G. 1995. Local effective length factor in the equivalent slenderness ratio. Canadian Journal of Civil Engineering, **22**(6): 1164-1170.

Timoshenko, S.P., and Gere, J.M. 1961. Theory of elastic stability (2nd edition). McGraw-Hill, Inc, New York, NY.

Zandonini, R. 1985. Stability of compact built-up struts: experimental investigation and numerical simulation. Constuzione Metalliche, Milan, Italy, No. 4, pp. 202-224.

Earthquake Limit States for Curved Steel Bridges

Junwon Seo[1] and Daniel G. Linzell, Ph.D., P.E.[2]

Abstract

To appropriately evaluate bridge performance during an earthquake and perform risk assessments, quantitative seismic assessment criteria is desired. Existing seismic risk assessment limit state information, such as the *slight*, *moderate*, *extensive* and *complete* seismic assessment damage classification levels from the FEMA Hazards U.S. Multi-Hazard (HAZUS-MH) loss assessment package, is largely qualitative. This paper will discuss ongoing research examining quantitative seismic limit states for one particular class of bridges that has received limited seismic response research attention; curved steel I-girder bridges. Limit states are discussed for key components in the structural system and preliminary findings are presented for a three-span continuous curved steel bridge in Pennsylvania. Seismic response is examined through numerical time history analyses and possible failure mechanisms are studied and assessed.

Introduction

In recent decades, the occurrence of three major earthquakes (San Fernando in 1971, Loma Prieta in 1989, and Northridge in 1994)

[1] Ph.D. Candidate, Department of Civil and Environmental Engineering, The Pennsylvania State Univ., University Park, PA 16802, <jus254@psu.edu>
[2] Associate Professor, Department of Civil and Environmental Engineering, The Pennsylvania State Univ., University Park, PA 16802, <DLinzell@engr.psu.edu>

demonstrated possible seismic vulnerabilities that existing bridges may be exposed to. These major seismic events also have provided the impetus for significant improvements in engineering practices for bridge seismic design, analysis, and vulnerability assessment. However, seismic design, analysis and vulnerability assessment criterion for steel bridges has been mainly developed for straight structures (Choi et al., 2004; Nielson et. al, 2006; Padgett, 2007) with little attention being paid to curved bridges (Seo and Linzell, 2007; Wu and Najjar, 2007). This is justifiable given the number of straight steel structures currently in service. This does not mean that research related to the development of curved, steel bridge seismic vulnerability assessment criteria is not needed as curved structures may be more vulnerable to earthquakes than straight steel bridge because of their curvature and resulting torsional and warping behavior. The study discussed herein is attempting to address some aspects of curved, steel, I-girder bridge seismic response.

In general, recent computational approaches examining steel bridge seismic responses have applied "3-D grillage" methods and 3-D finite element methods including shell and solid elements. A "3-D grillage" model utilizes conventional frame elements for all of the idealized grid members accounting for girder, deck, column height etc., to reasonably predict the seismic response of straight steel girder bridges (Choi et al., 2004; Nielson, 2005; Nielson et al., 2006; Padgett, 2007). Similar modeling techniques have been proposed for curved steel bridges, but were applied to static response (Chang et al., 2006). These studies have shown that modeling using a "3-D grillage" method possesses many advantages: 1) clearer explanation of structural behavior for bridge engineers, 2) easier treatment of each components of bridge (e.g., the boundary conditions, bearing, abutment, and column etc.), and 3) much computer run time when compared to 3-D plate-shell finite element models (Choi et al., 2004; Nielson, 2005; Nielson et al., 2006; Chang et al., 2006; Padgett, 2007). Therefore, the "3-D grillage" method is proposed herein as the tool to explore seismic response of representative curved, steel, I-girder, bridges. The proposed analytical method is validated statically using comparisons of predicted girder vertical and lateral bending moments to results obtained from field testing of an in-service, three-span continuous, curved, steel I-girder bridge.

After being acceptably validated and as part of a preliminary component of this research, the “3-D grillage” technique is applied to the same curved steel I-girder bridge to evaluate its seismic vulnerability under representative ground motions, such as the Northridge and El Centro earthquakes. In association with this evaluation vulnerability limit states are discussed for key substructure components in the system, such as support columns, bearings, and abutments. Seismic performance is examined via time history analyses and assessed using damage classification levels from the FEMA HAZUS-MH (FEMA, 1997) loss assessment package.

“3-D Grillage” Model

“3-D grillage” modeling is performed using the OpenSees program (Mazzoni et al., 2006) because of its ease of implementation for earthquake analyses. Following previously published work (Choi et al., 2004; Nielson, 2005, Nielson et. al., 2006; Padgett, 2007), both the concrete deck and the steel superstructure framing are represented using conventional 3-D, 6-DOF frame elements with lumped masses, calculated using tributary dimensions, being placed at each node to represent self-weight. Substructure elements are modeled using varied approaches as summarized in the following paragraphs. Figure 1 is a representative schematic of the “3-D grillage” model.

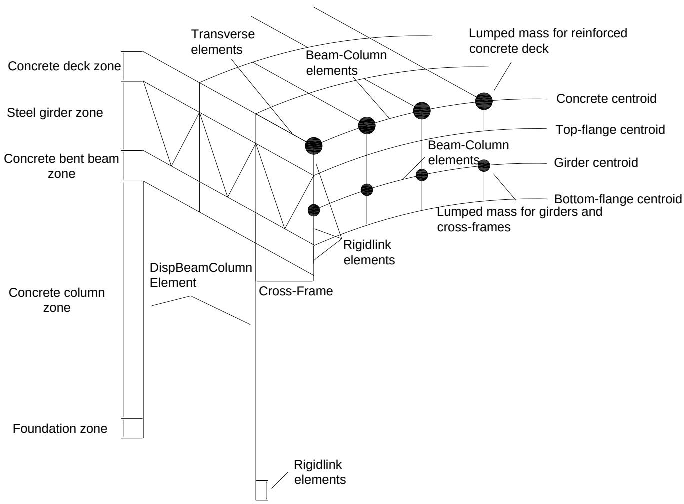

Figure 1 3-D curved bridge grillage model schematic

The superstructure, including the girders and concrete deck, is represented using elastic BeamColumn elements in OpenSees because its anticipated to remain elastic under seismic loading (Choi et al., 2004; Nielson, 2005; Nielson et al., 2006; Padgett, 2007). Section properties of each span are calculated separately for the concrete deck and steel girders. Rigid link elements are used to mimic composite action by coupling girder and concrete deck nodes and are idealized using rigid link rods available in OpenSees. Following the "3D-grillage" approach, rigid links beams are used to couple the top and bottom flanges (Chang et al., 2006). Rigid link rods constrain only translational degrees-of-freedom while rigid link beams constrain translational and rotational degrees-of-freedom (Mazzoni et al., 2006). Cross-frames are idealized using truss elements connected to each top-flange and bottom-flange centroid. Nominal material properties are used for both the concrete and steel, with the concrete having a modulus of elasticity of 2.78e4MPa while the steel has a modulus equal to 2.0e5 MPa.

Included in the computational models for the substructure are the columns, pier caps, abutments and footings. The “3-D grillage” modeling approach is modified to include the substructure based on recommendations by Neilson (2005). The model including substructure is necessary for earthquake assessment since severe damage in the substructure of steel bridge have frequently occurred during three major earthquakes (San Fernando in 1971, Loma Prieta in 1989, and Northridge in 1994)

Columns are generated assuming that their seismic behavior is both geometrically and materially nonlinear. This is accomplished by representing them as Displaced Based BeamColumn elements available in OpenSees.

Pier column and cap reinforced concrete sections are represented using three constitutive models, as shown in Figure 2 for a representative column; one for unconfined concrete, one for confined concrete and one for the reinforcing steel. Unconfined concrete is modeled using a degraded linear uploading/reloading stiffness and residual stress model developed by Karsan and Jirsa (1969). The confined concrete is modeled where the maximum stress and associated strain are given as Kf'_c and $\varepsilon_0 = 0.002K$, respectively, with K calculated using:

$$K = 1 + \frac{\rho_s f_{yh}}{f'_c}\,. \tag{1}$$

Here, f'_c is the unconfined compressive cylinder strength, ρ_s is the ratio of the volume of steel stirrups to the volume of the concrete core measured to the outside of the stirrup and f_{yh} is the yield strength of the stirrups (Park et al., 1982).

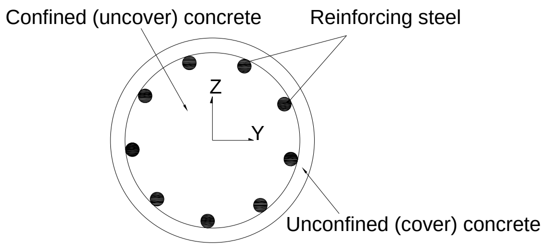

Figure 2: Circular reinforced concrete column

The pier footings are modeled with linear translational and rotational springs (Neilson 2005a). Vertical and horizontal spring stiffness values were determined considering the stiffness of the footing about its strong and weak axes. Figure 3 shows analytical pier model including pier footings and pier caps.

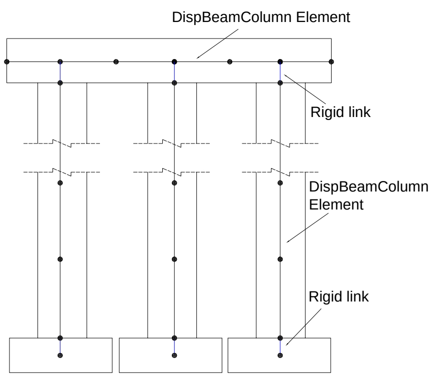

Figure 3 Pier model

Unlike the piers, abutment effects on the seismic response are addressed solely through the incorporation of springs (Nielson 2005a). Tangential spring stiffness values are established by looking at: (1)

active action of the abutment as dictated by the stiffness of the piles upon which it rests; and (2) passive action of the piles and passive soil pressure against the abutment backwall. Pile stiffness is the only component considered when establishing the radial spring stiffness.

Curved Bridge Description

The proposed analytical method is validated statically using comparisons of predicted girder vertical and lateral bending moments to results obtained from field testing of an in-service, three-span continuous, curved, steel I-girder bridge. After validation, the same structure is examined under various seismic events to ascertain its hypothetical seismic vulnerability. The structure has been examined previously by Nevling et al., (2003) and is shown in Figure 4. It is composed of five ASTM A572 Grade 50 steel plate girders and the abutment skew varies between 29° and 52° (south to north) relative to the traffic direction. Figure 5 is a simplified framing plan that details support conditions.

Figure 4 Picture of curved steel I-girder bridge

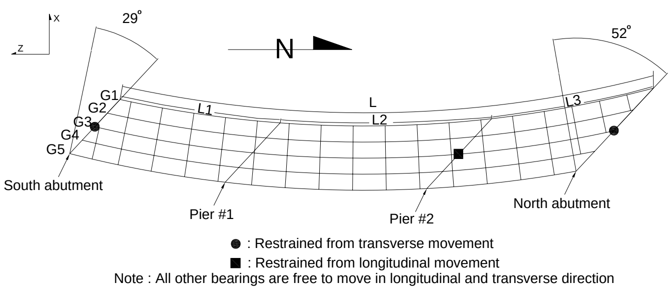

Figure 5 Examined curved steel I-girder bridge (Nevling, 2003)

Elevations, sections and details for the bridge are shown in Figure 6. The bridge has three spans that are 23.5, 30.6 and 23.5 m long, respectively. Girders are spaced 2.39 m center-to-center with two different types of cross frames being placed between them. All girders have 1219 mm x 13 mm webs with 356 mm wide top and bottom flanges of varying thickness. Type A cross frame top and bottom chords are composed of 88.9 x 88.9 x 9.5 mm double angles with diagonals composed of 88.9 x 88.9 x 9.5 mm angles. Type B top chords are composed of WT14 x 49.5s with bottom chords composed of 88.9 x 88.9 x 9.5 mm double angles and diagonals composed of 88.9 x 88.9 x 9.5 mm angles. The radius of curvature is 178.49 m to the exterior girder (G5). The superstructure is supported using multi-column piers with 914.4 mm wide by 1066.8 mm deep reinforced concrete pier caps held up by three 914.4 mm round by 6400 mm tall circular reinforced concrete columns which, in turn, are resting on spread footings with no piles beneath them. Pier columns are spaced horizontally at 4.0 m on center. The foundation wall at the base of the piers is 11.9 m long, 3.4 m wide, and 0.7 m thick. Abutments consist of spread footings on piles with a 1.6 m tall backwall. Design strength for the concrete is assumed to be 20.7 MPa while the reinforcing steel has yield strength of 414 MPa.

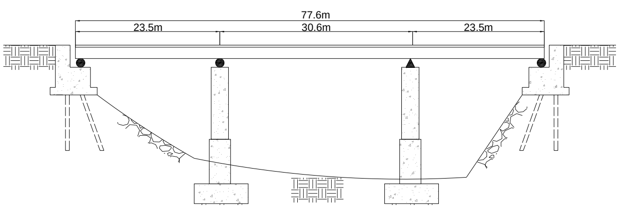

(a) General elevation

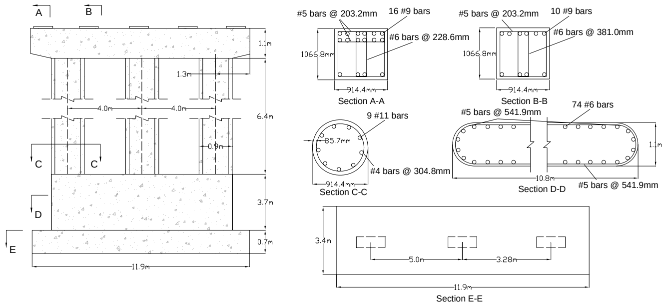

(b) Pier **(c) Concrete reinforcement**

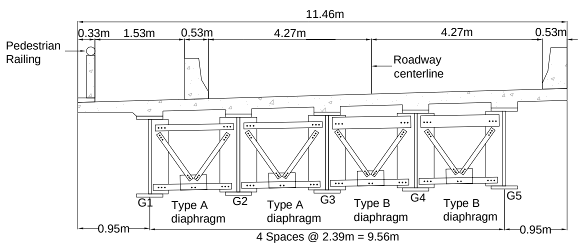

(d) Superstructure Section (Nevling, 2003)
Figure 6: Curved steel I-girder bridge configuration

"3-D grillage" Model Verification

Validation occurred by comparing experimental data from a series of static tests to predictions from the "3-D grillage" model. Since actual seismic field test data for existing curved steel bridges does not exist, static model validation was preliminarily conducted to assess effectiveness of the "3-D grillage" model. Comparisons occurred for vertical and lateral bending moments. Field tests that were compared are summarized in the section that follows.

Field Testing

Static testing was performed by Nevling (2003). The curved bridge was examined using two trucks of known weight placed side-by-side as shown in Figure 7. Truck longitudinal positions shown in Table 1 were selected to induce maximum vertical and lateral bending effects on the interior and exterior girders at instrumented sections shown in Figure 8. Positions were measured along the arc and refer to the location of a lead axle.

Figure 7 Static test truck positions (Nevling, 2003)

Table 1: Summary of single truck load cases (Nevling, 2003)

Test number	Truck Transverse Position, m	Truck Longitudinal Position from South End of Bridge, m
Static 1	0.6 from east parapet	65.2
Static 2	0.6 from east parapet	42.7
Static 3	0.6 from west parapet	46.3
Static 4	0.6 from west parapet	34.7

Comparisons were made to "3-D grillage" model predictions for each of the static tests. Static 1 is presented herein as a representative comparison.

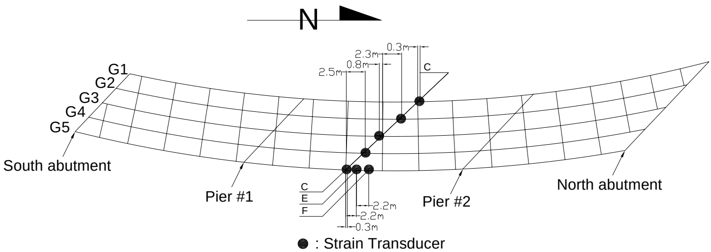

Figure 8 Girder instrument locations (Nevling, 2003)

Static 1

Figure 9 details comparisons between computational and experimental vertical and lateral bending moments. As shown in the figure 9, the "3-D grillage" model can predict vertical and lateral bending moments within an average of 20.8% for Static 1. As shown in Figure 9(a), the "3-D grillage" model tends to predict smaller moments for G2 to G4 and larger values at G5 and G1 for the vertical bending moments. On the other hand, the "3-D grillage" model tends to predict slightly larger values for girder lateral bending moments at all girders than those observed in the field, as shown in Figure 9(b). The maximum percent difference for vertical moments occurs at G3, Section C-C (see Figure 8) as shown in Figure 10(a). The maximum percent difference for lateral moments occurs at G5, Section F-F, as shown in Figure 10(b).

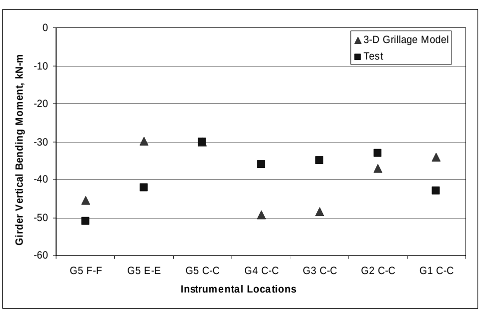

(a) Vertical

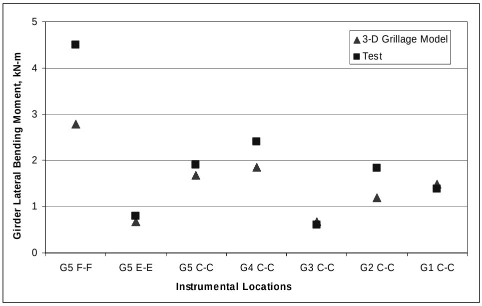

(b) Lateral

Figure 9 Bending moments, Static 1

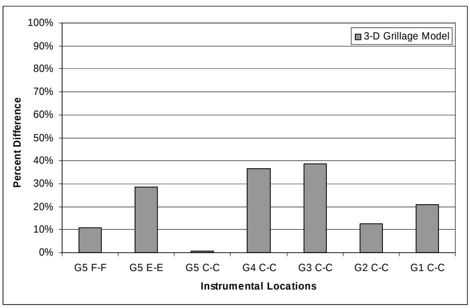

(a) Vertical

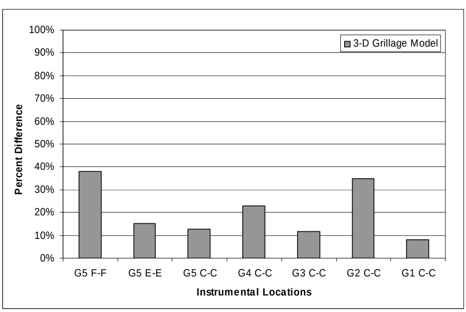

(b) Lateral

Figure 10 Percent difference histogram, Static 1

Curved Bridge Hypothetical Seismic Performance Assessment

This section investigates seismic response using the curved bridge "3-D grillage" model and uses that information to assess its hypothetical seismic vulnerability qualitatively and quantitatively. To accomplish this both quantitative and qualitative criteria are used. Vulnerability is preliminarily assessed qualitatively by applying FEMA HAZUZ-MH loss assessment criteria, developed for straight bridges but applied here as an initial assessment tool. Qualitative description of the four damage states is given in Table 2. These limit states can be used for each substructure component of the bridge.

Table 2 HAZUS' qualitative limit states (FEMA, 2003)

Limit State	Description
Slight	Minor cracking and spalling to the abutment, cracks in shear keys at abutments, minor spalling and cracks at hinges, minor spalling at the column (damage requires no more than cosmetic repair) or minor cracking to the deck.
Moderate	Any column experiencing moderate (shear cracks) cracking and spalling (column structurally still sound), moderate movement of the abutment (<2inch), extensive cracking and spalling of shear keys, any connection having cracked shear keys or bent bolts, keeper bar failure without unseating, rocker bearing failure or moderate settlement of the approach.
Extensive	Any column degrading without collapse - shear failure - (column structurally unsafe), significant residual movement at connections, or major settlement approach, vertical offset of the abutment, differential settlement at connections, shear key failure at abutments.
Complete	Any column collapsing and connection losing all bearing support, which may lead to imminent deck collapse, tilting of substructure due to foundation failure.

Quantitative damage levels were based on previous research that focused on experimental results and interpretation of bridge component behavior to develop substructure damage level quantities that correlated with the qualitative information presented in Table 2 (Nielson, 2005). For this structure these quantities were determined for substructure movements at the bearings and for bending of the pier columns. For the bearings, they focused on radial and tangential displacements. For the columns, they focused on ductility demand based on a curvature ratio calculated as shown in Equation 2 (Nielson, 2005):

$$\mu_c = \frac{\kappa_{\max}}{\kappa_{yield}} \tag{2}$$

where κ_{yield} is the curvature in the column which causes first yield of the outermost reinforcing bar and $\kappa_{\max}$ is the maximum curvature demanded of the column throughout the event. For a straight bridge, the quantitative damage levels associated with HAZUS qualitative limit states were developed by Neilson (2005) and those quantities were applied herein by correcting them for bridge curvature. The resulting values are given in Table 3.

Table 3 Median values for quantitative limit states

	Damage Level			
	Slight	Moderate	Extensive	Complete
Concrete Column Curvature	1.0	1.6	3.2	6.8
Bearing(mm) - Tangential	3.5	11.7	23.5	149.8
Abutment(mm) -Tangential	2.3	4.7	14.7	29.4
Bearing(mm) - Radial	4.9	16.2	32.4	206.4
Abutment(mm) - Radial	3.2	6.5	20.2	40.5

To examine seismic response nonlinear time history analysis was performed with five percent Rayleigh damping being assumed. Ten separate seismic events were applied to the structure, ranging from approximately 0.1g to 1.0g peak ground acceleration (PGA) (Silva, 2000). Each event was applied in the global longitudinal direction initially and then the global transverse direction. Table 4 lists the examined seismic events PGA, peak ground velocity (PGV), peak ground displacement (PGD), and spectral acceleration (S_a).

Table 4 Examined seismic events

Earthquakes	MM/DD/YY	PGA, g	PGV, cm/sec	PGD, cm	S_a, g
Anza-Pinyon	2/25/1980	0.11	3.79	0.26	0.01
Chalfant Valley	7/20/1986	0.207	18.63	4.54	0.24
El Centro	10/15/1979	0.313	79.79	28.13	1.49
Whittier Narrows	10/1/1987	0.414	19.16	2.35	0.12
Kobe	1/16/1995	0.509	37.30	9.52	0.50
Coalinga	5/2/1983	0.592	60.20	8.77	0.46
Superstitn Hills(B)	11/24/1987	0.682	32.50	4.70	0.25
Chi-Chi, Taiwan	9/20/1999	0.821	67.00	23.28	1.23
Northridge	1/17/1994	0.939	76.60	14.95	0.79
San Fernando	1971/02/09	1.16	54.30	11.73	0.62

Maximum quantitative seismic response values and corresponding qualitative damage state for bridge components being examined (i.e., columns and bearings) are presented in Table 5 for each of the ten seismic events. Maximum seismic deformations at the fixed bearing location (see Figure 5) are presented here and are representative of other bearing locations. Results indicate that the global longitudinal seismic direction tends to be the critical direction for column response while deformations at the pier and abutment are not clearly influenced by one direction over another.

As shown in Table 5, under the hypothetical earthquake events column damage states can be moderate to complete. The maximum curvature ductility demand ratio was produced for the Northridge earthquake applied in the global longitudinal direction. Damage states resulting from deformations at the bearing locations vary from slight to complete, with, again, largest damage being caused by the Northridge earthquake applied in the global longitudinal direction. It is of interest to note that when the strongest ground motion, as identified using PGA (i.e., San

Fernando earthquake), was applied to the structure the largest damage did not occur. The same can be said for seismic events having the highest PGV and S_a (i.e., El Centro earthquake). These trends are illustrated in Figure 11, where critical column curvature is plotted against each of the ten seismic event's PGA, PGV and S_a from Table 4.

Table 5 Seismic response and damage state

Earthquakes	Column	Damage State	Bearing, mm	Damage State	Abutment, mm	Damage State
Anza-Pinyon	2.5	Moderate	10	Slight	8	Slight
Chalfant Valley	2.6	Moderate	47	Extensive	26	Extensive
El Centro	18	Complete	130	Extensive	129	Complete
Whittier Narrows	2.6	Moderate	16	Moderate	10	Moderate
Kobe	8.3	Complete	85	Extensive	77	Complete
Coalinga	17.3	Complete	79	Extensive	72	Complete
Superstitn Hills(B)	9.4	Complete	43	Extensive	41	Complete
Chi-Chi, Taiwan	43.5	Complete	216	Complete	195	Complete
Northridge	61.1	Complete	300	Complete	255	Complete
San Fernando	13.2	Complete	107	Extensive	112	Complete

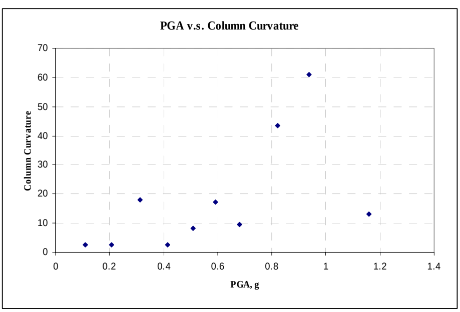

(a) PGA vs. column curvature

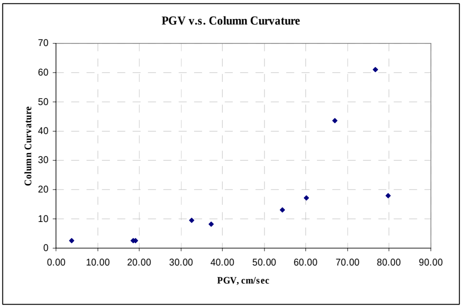

(b) PGV vs. column curvature

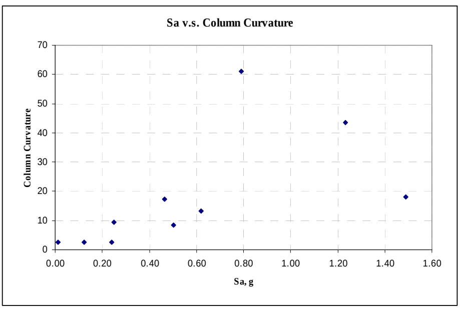

(c) S_a vs. column curvature

Figure 11 Column curvature vs. seismic indices

Conclusion

Summarized herein are preliminary results from computational studies of curved bridge seismic response. The accuracy of "3-D grillage" modeling techniques, modified to include substructure units, was examined statically via comparison with results from field testing of an in-service curved bridge. Comparisons showed that these preliminary models predicted vertical and lateral bending moments approximately 20% of field measured values.

These models were the applied to the same structure to assess its hypothetical seismic vulnerability. Both qualitative and quantitative damage states for select substructure components were examined with the bridge being subjected to ten earthquakes, well know, earthquake time-histories. Results showed varying levels of damage from these earthquakes and also indicated that strongest induced seismic events, as measured using PGA, PGV or S_a, did not necessarily result in critical damage levels.

References

Chang, C. J., White D. W., Beshah, F. and Wright, W. (2006). "Design Analysis of Curved I-Girder Bridge Systems- An Assessment of Modeling Strategies," Annual Proceedings, Structural Stability Research Council, 349-369.

Choi, E., DesRoches, R., and Nielson B. (2004). "Seismic Fragility of Typical Bridges in Moderate Seismic Zones," Engineering Structure, 26, 187–199.

FEMA (1997). HAZUS 97: Technical Manual. Federal Emergency Management Agency, Washington DC.

Karsan, I. D., and Jirsa, J. O. (1969). "Behavior of concrete under compressive loading." Journal of Structural Division ASCE, 95(ST12).

Mazzoni, S., McKenna, F., Scott, M. H., Fenves, G. L., et al (2006). "Open System for Earthquake Engineering Simulation (OpenSees)," Pacific Earthquake Engineering Research Center, Version 1.7.3.

Nevling, D. (2003). "Evaluation of Level of Analysis Methodologies for Horizontally Curved I-Girder Bridges through Comparison with Measured Response of An Inservice Structure," M.S. thesis, Department of Civil and Environmental Engineering, The Pennsylvania State University, PA, 222 pp.

Nielson, B. G. (2005). "Analytical Fragility Curves for Highway Bridges in Moderate Seismic Zones," Ph.D. Dissertation, School of Civil and Environmental Engineering, Georgia Institute of Technology, Atlanta, GA, 373 pp.

Nielson, B. G. and DesRoches, Reginald (2006). "Seismic Fragility Methodology for Highway Bridges," Proceedings of ASCE Structure Congress, St. Louis, MO

Padgett, J. E. (2007). "Seismic Vulnerability Assessment of Retrofitted Bridges using Probabilistic Methods," Ph.D. Dissertation, School of Civil and Environmental Engineering, Georgia Institute of Technology, Atlanta, GA, 253 pp.

Park, R., Priestley, M. J. N., and Gill, W. D. (1982). "Ductility of Square-Confined Concrete Columns," Journal of Structural Engineering, 108(ST4), 929–950.

Seo, J.-W., and Linzell, D. G. (2007). "Seismic Response of a Curved Steel I-Girder using a Simplified Model," Proceedings of New York City Bridge Conference, NYC, NY.

Wolf, J., P. (1985). *Dynamic Soil-Structure Interaction*. Prentice-Hall, Inc, Englewood Cli_s, N.J.

Wu, H., and Najjar, W. S. (2007). "Parametric Seismic Analysis of Curved Steel Box-Girder Bridges with Two Continuous Spans," Proceedings of New York City Bridge Conference, NYC, NY.

Accounting for Residual Stresses in the Seismic Stability of Nonlinear Beam-Column Elements with Cross-Section Fiber Discretization

C. P. Lamarche[1] and R. Tremblay[2]

ABSTRACT

The steel02 material law in the OpenSees finite element program is modified to account for the presence of residual stresses when predicting the buckling response of members using the nonlinear beam-column element. The model is validated against centrally loaded column test results as well as by examination of simple cases. The model is then used to investigate the performance of steel columns in a chevron braced steel frame subjected to strong ground seismic motion.

INTRODUCTION

The OpenSees software framework has been developed for simulating the seismic response of structural and geotechnical systems (Mazzoni et al. 2006). The program features advanced capabilities for modeling and analyzing the nonlinear response of systems using a wide range of material models, elements, and solution algorithms. In particular, the inelastic buckling response of steel columns, beam-columns or diagonal bracing members can be predicted using a nonlinear flexibility based beam-column element (Neuenhofer et al. 1998) in combination with the steel02 model that reproduces the hysteretic response of steel under

---

[1] Ph.D. Candidate, [2]Professor and Canada Research Chair in Earthquake Engineering, Group for Research in Structural Engineering, Department of Civil, Geological and Mining Engineering, Ecole Polytechnique, Montreal, QC Canada H3C 3A7

reversed cyclic loading. Inelasticity is distributed in this beam-column element by using finite length fibers to discretize the member cross-section and a co-rotational formulation is implemented to account for geometric nonlinearities.

In the context of performance-based seismic design, the response of a building structure must be examined under various earthquake levels to establish the probability of attaining limit states including structural collapse. For this ultimate limit state, it is essential to properly reproduce the hysteretic response of the energy dissipative components of the seismic force resisting system and to accurately predict the capacity of the critical components that must withstand the forces imposed during a severe ground shaking. In braced steel frames, the bracing members are expected to undergo several cycles of inelastic buckling and yielding in tension under strong earthquakes. Conversely, beams and columns must remain essentially elastic to maintain structural integrity and continue carrying gravity loads.

OpenSees has already been proven to reproduce accurately the seismic inelastic cyclic response of steel bracing members subjected (Uriz 2005, Aguero et al. 2006). The effect of residual stresses on brace cyclic response is insignificant and was therefore omitted in these past studies. Residual stresses can lead to a reduction of up to 30% in the ultimate compressive strength and stability of structural steel profiles and built-up steel members (Beedle and Tall 1960) and must however be accounted for when evaluating the capacity of columns to resist the combined seismic flexural and axial force demand.

In this study, the steel02 material of the OpenSees platform was modified so that a non-zero initial stress condition can be specified. Residual stress patterns can be then be imposed by assigning different initial stress values to the cross-section fibers following a procedure similar to that presented by Ziemian (1992). Numerical simulations of the monotonic and cyclic buckling response of steel profiles commonly used in practice were carried out to verify convergence and put into contrast the effect of the modification implemented in the program. The model was then validated against results of past experimental tests on built-up members made with welded flamed-cut plates. Finally, nonlinear dynamic analyses were performed to examine the buckling performance of the columns in a two-story chevron braced steel frame subjected to a ground motion record.

IMPLEMENTATION OF RESIDUAL STRESSES IN OPENSEES

The steel02 uniaxial material of OpenSees is based on the modified Giuffre-Menegotto-Pinto (Menegotto and Pinto 1973) hysteretic model proposed by Filippou et al. (1983) to account for isotropic hardening. The response of the steel02 material to a full tension-compression cycle with strain amplitude of 5 times the strain at yield, ε_y,is presented in Fig. 1. The response of the steel02 material without residual stress is illustrated in Fig. 1b. The response including residual stress is presented in Fig. 1c where the offset of the stress-strain state (ε_r,σ_r) at the start is identified. The inclusion of this offset was achieved by modifying the last committed stress and strain variables at the beginning of the steel02 routine embedded in the OpenSees base code.

The modification was intended for flexibility based nonlinear beam-column finite elements using fiber cross-section discretization. This element is based on the Bernoulli assumption, i.e. plane sections remain plane after loading. At each increment of a solution during an analysis, the axial force and bending moments associated to the stress state in each fiber must satisfy equilibrium at every section along the length of the element. Thus, the initial user specified stress pattern in the cross-section must be in a self equilibrium state. Otherwise, the finite element analysis diverges systematically from the start. The sections within a finite element solely have the stress and strain increment associated to each fiber as an input. Furthermore, as previously mentioned, plane sections remain plane after loading. Therefore, the initial strain within the material law is not accounted for at the section level and the stress-strain response that is actually considered in the analysis is illustrated in Fig. 1d.

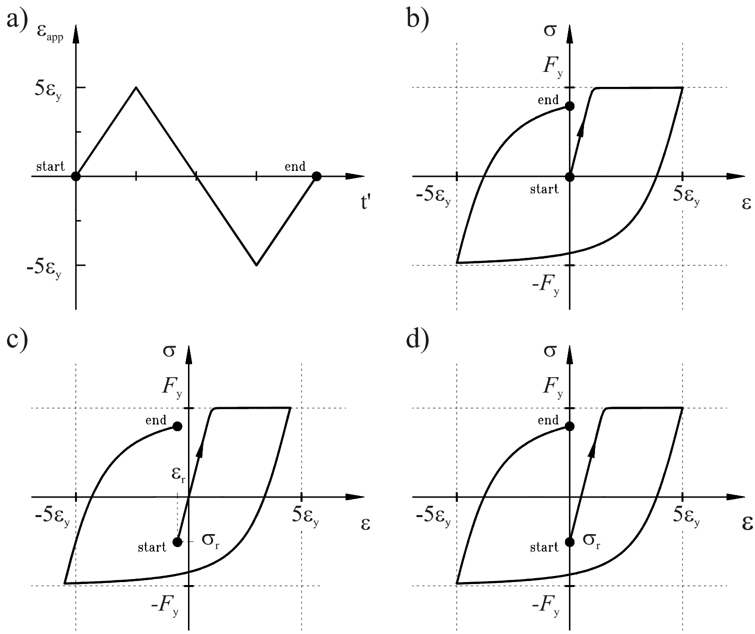

Figure 1. Hysteretic response of the steel02 model with residual stress: a) Applied time history; b) Stress-strain response with no initial stress; c) Stress-strain response with initial stress; and d) Final stress-strain response with initial stress and initial strain set to zero..

NUMERICAL SIMULATIONS: MONOTONIC LOADING

Numerical simulations of the monotonic buckling response of a W250x115 steel column were performed under various conditions to validate the capabilities of the modified model and assess the influence of the modeling parameters on the accuracy of the solution. The member was assumed to be made of ASTM A992 steel with a yield strength, F_y, of 345 MPa. In the analyses, the the Young's modulus of steel, E, was taken equal to 200000 MPa and a kinematic strain hardening ratio E_h / E = 0.01 was assumed. Isotropic hardening properties were disabled as this parameter has no effect under monotonic loading. The effects of initial geometric imperfections and residual stresses were included. Half-sine wave initial member out-of-straightness was assumed with maximum amplitude δ_0 at column mid-height. The residual stress pattern proposed by Galambos and Ketter (1959) was used in the analysis (Fig. 2). A total of 50 fibers were specified to discretize the member cross-section: 20 in each of the two flanges and 10 in the web. The number of elements along the column length, n_e, and the number of integration points (or sections) in each element, n_p, were varied.

Elastic and inelastic buckling responses were examined and buckling was studied about both the weak and strong axes. Pinned conditions were assumed at the member ends and the total member length was adjusted to obtain a member slenderness ratio KL/r = 60 for each buckling mode: L_y = 3972 mm and L_x = 6840 mm. This corresponds to an intermediate slenderness condition for which the effects of residual stresses on compression strength are maximum. The results are presented in Fig. 3. In the figure, the axial load normalized with respect to the elastic buckling load, $P_e = \pi^2 EI/(KL)^2$, is plotted against the lateral deflection at mid span, $\delta_{L/2}$. The buckling axis studied is illustrated in each of the plots.

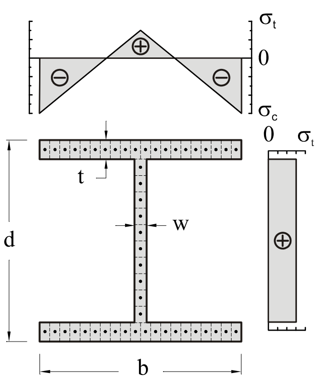

$$\sigma_c = 0.3F_y$$

$$\sigma_t = \frac{bt}{bt+w(d-2t)}\sigma_c$$

Figure 2. Residual stress pattern adopted (Galambos and Ketter 1959).

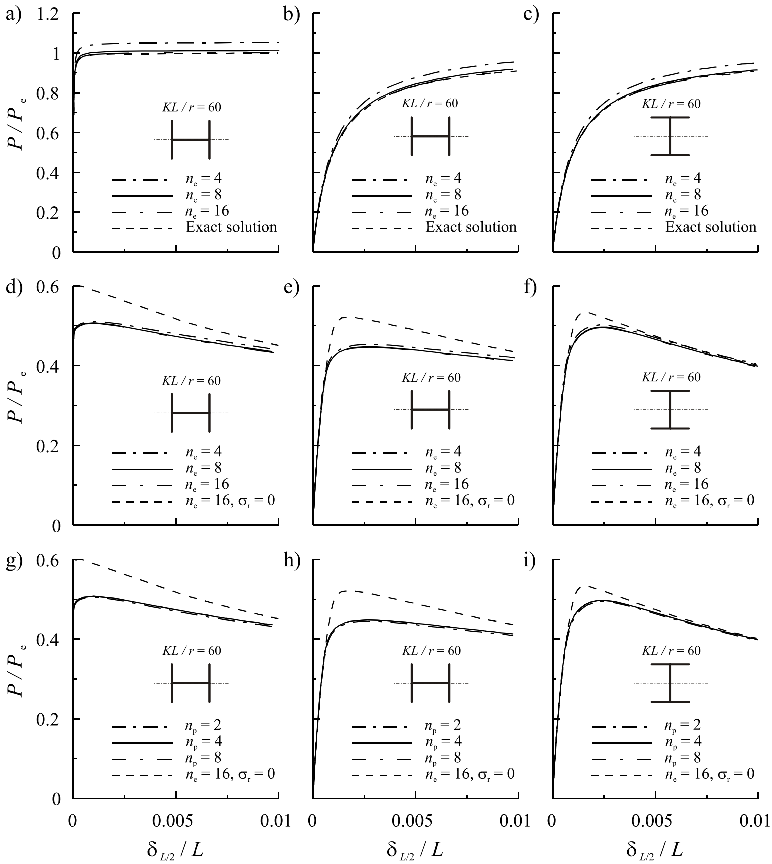

Figure 3. Prediction of the monotonic axial load-lateral deformation buckling response of a W250x115 column.

In the first three graphs of Fig. 3, the material was taken as linear elastic. In Fig. 3a, a very small out-of-straightness $\delta_0/L = 10^{-5}$ was specified and weak axis buckling was studied. Figs. 3b & 3c present the results for weak and strong axis buckling, respectively, when $\delta_0 = L/1000$ is used. That initial imperfection corresponds to the tolerance prescribed in AISC and CSA specifications for W-shape columns (AISC 2005, CSA 2001) and used in previous calibration studies (Surovek-Maleck and White 2004). In all three cases, the number of elements n_e was varied: n_e = 4, 8, and 16. The number of integration points used in each element, n_p, was kept equal to 4. In each graph, the closed form solution, $\delta = \delta_0(1\text{-}P/P_e)$, is also plotted as a reference. For the three cases studied, the response obtained from the OpenSees model are found satisfactory except when n_e = 4. In all other cases, the error was less than 1.5%.

Figs. 3d, 3e & 3f present the results of inelastic buckling simulations for the same values of n_e and the same initial geometric imperfections. The number of integration points per element was kept equal to n_p = 4. Residual stresses were included in all cases except that the results for n_e = 16 and σ_r = 0 are also given for comparison purposes. In Fig. 3d, the out-of-straightness ratio was taken as $\delta_0/L = 10^{-5}$. In Fig. 3e and Fig. 3f, the out of straightness was taken as $\delta_0 = L/1000$. As in the elastic cases, convergence of the finite element analysis was achieved when specifying n_e = 8. The response obtained with n_e = 4 exhibited poorer accuracy. The comparison of the results of the two analyses performed with n_e = 16 very clearly show that residual stresses have a significant effect on the load carrying capacity of the column modeled.

In the last three cases presented at the bottom of Fig. 3, the number of elements used was kept constant to n_e = 8 and the number of integration points per element were varied: n_p = 2, 4, and 6. As done previously, Fig. 3e presents the results for $\delta_0/L = 10^{-5}$ whereas $\delta_0 = L/1000$ was specified for the results presented in Figs 3e & 3f. As shown, using 4 integration points was sufficient to achieve convergence in the analyses in all cases.

As indicated, 50 fibers were used to model the member cross-section in all analyses presented in Fig. 3. The same simulations were repeated using a total of 100 fibers and identical results were obtained, confirming the adequateness of the 50 fibers dicretization pattern.

NUMERICAL SIMULATIONS: CYCLIC LOADING

Two simulations of the cyclic buckling about weak axis were performed for a pinned-pinned W250x58 profile with L = 4000 mm (KL/r = 79.5). One simulation included the residual stress pattern shown in Fig. 2 and the other simulation did not include residual stresses. In both cases, the initial column out-of-straightness was $\delta_0 = L/1000$. The columns were modeled using 8 elements and 4 integration points per element. The section was discretized with 50 fibers: 20 fibers per flange and 10 fibers for the web. In the analysis, the column is initially loaded with a static load corresponding to 40% of the computed ultimate compression strength accounting for residual stresses, P_u = 1575 kN, before applying a cyclic axial displacement sequence producing buckling of the column. The initial static load aims at reproducing gravity load effects in a building column whereas the cyclically applied displacement simulates the seismic demand in the case of a column with insufficient axial capacity. In the analysis, E = 200000 MPa, F_y = 380 MPa and the kinematic and isotropic hardening properties were determined from the cyclic coupon test results by Black et al. (1980) presented in Fig. 4. The kinematic hardening ratio was set equal to $E_h / E = 0.001$ and the isotropic hardening was modeled by shifting linearly the yield asymptotes as a function of the maximum plastic strain reached in the previous cycle, $\varepsilon_{\max}$, using the expression $\sigma_{shift} = a_1 (\varepsilon_{max}/\varepsilon_y - 1)\, \sigma_y$ (Filippou et al. 1983). In this expression, a_1 was set equal to 0.05, ε_{max} is kept equal to ε_y until a larger strain is attained, and $\sigma_y = F_y$

The cyclic displacement sequence imposed on the W250x58 column is presented in Fig 5a. In each cycle, the displacement is first increased until buckling is triggered and then reduced until the load reduces to 0.4 P_u. Five cycles are applied before the column is pushed monotonically to failure. The applied axial load normalized with respect to the column squash load P_y, is plotted against the normalized axial displacement u/L and the out-of-plane displacement $\delta_{L/2}/L$ in Figs. 5b and 5c, respectively. When residual stresses are neglected, the column capacity in the first cycle is overestimated by 15.1%. The influence of residual stresses in subsequent cycles gradually decreases as more yielding develops in the member. The capacity of the column gradually reduces with the cycles. In each cycle, the loops closed nicely and no excessive amount of spurious energy is introduced in the system.

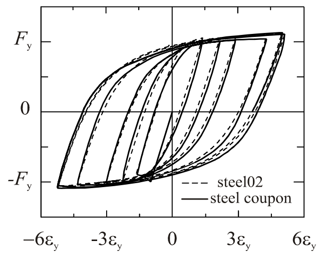

Figure 4. Modeling steel hardening response under cyclic loading (test from Black et al. 1980).

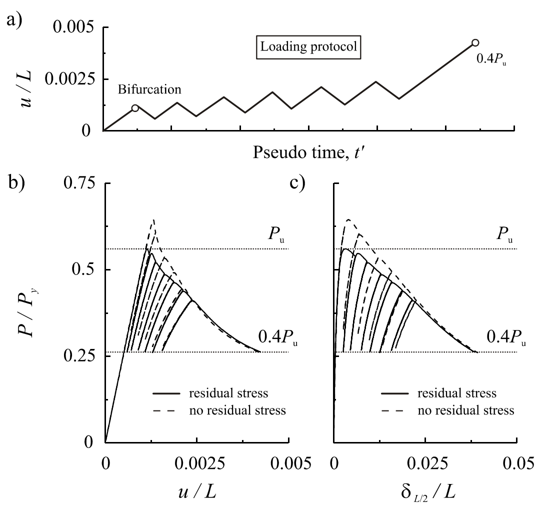

Figure 5. Cyclic buckling response of a W250x58 column: a) Imposed axial displacement sequence; b) Axial load-axial deformation response; and c) Axial load-lateral deformation response.

VALIDATION AGAINST EXPERIMENTAL DATA

The prediction of the pre- and post-buckling behavior of steel columns including initial stresses was validated against tests performed on 14H202 columns at Lehigh University (Kishima et al. 1969). The test columns were made of ASTM A572 (grade 50 ksi) welded flame-cut steel plates. The experimental study included residual stress measurements, tensile coupon tests to determine the base yield stress, stub column tests on short columns, and pin-ended centrally loaded tests on columns having slenderness ratios *KL*/*r* of 60 and 90. The measured residual stresses and cross-section dimensions of the 14H202 columns are presented in Fig. 6.

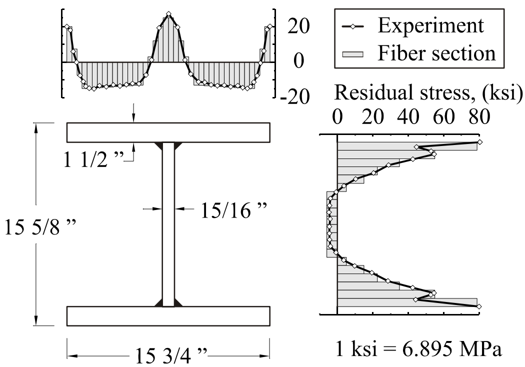

Figure 6. Residual stress pattern of the 14H202 section tested.

In the numerical simulations, the column cross-section was discretized using 100 fibers: 40 for the flanges and 20 for the web. The residual stress pattern adopted in the model is compared to the measured values in Fig. 6. In the finite element model of the columns, 8 elements were used with 4 integration points per element. End conditions were taken as pined-pined and an initial half-sine wave profile was used to represent the column out-of-straightness. The simulation results for the stub column test are presented in Fig. 7a for two cases: without and with residual stresses. The softening effect upon yielding due to the residual stresses is well predicted by the model. In Fig. 7b, the numerical results are compared to the measurements taken during the two centrally loaded column tests. It is noted that buckling developed about the column weak axis in both tests. The same failure mode was observed in the simulations and very good correlation is achieved between test and numerical results when including residual stresses in the analyses.

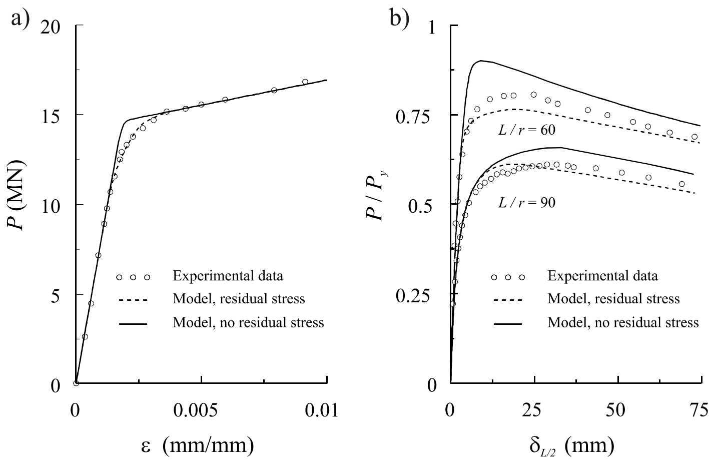

Figure 7. Model validation against test results: a) Stub column test; b) Centrally loaded column tests for KL/r = 60 and 90.

CASE STUDY: TWO-STORY CHEVRON BRACED FRAME

A two-story chevron steel braced frame is used to illustrate the application of the modified OpenSees model for the evaluation of the consequences of column buckling in a building subjected to severe seismic ground motion excitation. In this type of problem, the columns are subjected to complex time varying combinations of axial loads and bending moments during the earthquake motion.

Fig. 8a shows the geometry of the braced frame studied and the selected steel shapes. The frame was designed according to the latest Canadian seismic provisions of NBCC 2005 (NRCC 2005) and CSA-S16S1-05 standard assuming a Type MD (Moderately ductile) braced frame category. A ductility-related force modification factor R_d = 3.0 was used in the design. According to capacity design principles, the bracing members are sized for the combination of gravity and seismic loads and are detailed to undergo for cyclic inelastic response. The beams and columns are then designed to remain essentially elastic when the braces reach their maximum capacity, i.e. they must be able to resist the gravity loads together with the forces induced by yielding and buckling of the bracing members. The bracing members were assumed to be made of square structural tubing conforming to ASTM A500, gr. C (F_y = 345 MPa). The cross-section dimensions and wall thicknesses are given in Fig. 8a. ASTM A992 steel (F_y = 345 MPa) was adopted for the beams and columns.

Two load cases for the column design are illustrated in Figs. 8b and 8c. Case A corresponds to the attainment of the expected buckling capacity of the compression braces at both levels. Case B simulates the situation after buckling of the compression braces and yielding of the tension braces. The corresponding resulting axial loads in the bottom floor column are respectively equal to 1340 and 2140 kN. The latter value was used for the selection of the W250x73 shape. A W250x58 column would have been needed had only Case A been considered in design.

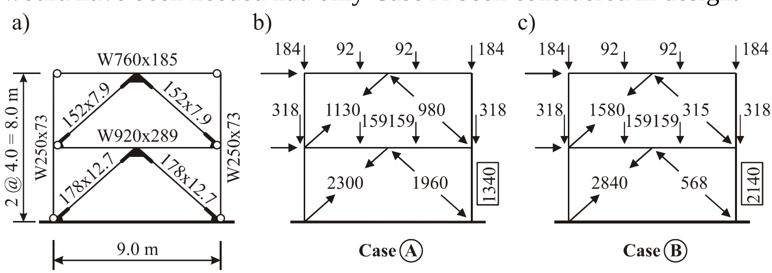

Figure 8. Two-story chevron braced frame: a) Geometry; b) Forces at brace buckling; and c) Forces after brace buckling (forces in kN).

The columns were modeled using 8 nonlinear beam column elements per member and 4 integration points per element. The cross-section of the columns was discretized with 50 individual fibers, i.e. 20 fibers per flange and 10 fibers for the web, and the residual stress pattern presented in Fig. 2 was used. Initial column out-of-straightness with amplitude $\delta_0 = L/1000$ and half-sine wave profiles per story height was considered. The bracing members were also modeled using 8 elements with 4 integration points per element. The cross-section was discretized using 20 fibers (Aguerro et al. 2006) and an initial out of straightness $\delta_0 = L/500$ was considered to obtain compression strength consistent with design assumptions. The dimensions as well as the rotational stiffness and strength of the gusset plates were also modeled using rigid extensions and nonlinear rotational springs. The beams were modeled using 6 nonlinear beam-column elements with 4 integration points per element and 50 fibers per section. Beam-to-column connections and column bases were assumed to be pinned. Initial frame out-of-plumb was ignored in the design and the analysis. In the analysis, an expected steel yield strength R_yF_y = 380 MPa was adopted for all members.

The fundamental periods of the building in its two first modes of vibration are T_1 = 0.41 s and T_2 = 0.18 s. The response of the braced frame is examined under 0.8 times the Castaic, Old Ridge Rd. 90° motion recorded record during the M6.7 Jan. 17, 1994 Northridge earthquake. Fig. 9a shows the first 15 seconds of the scaled horizontal ground acceleration record. The corresponding pseudo-acceleration spectrum S_a is compared to the NBCC 05 design spectrum in Fig. 9b. Nonlinear time step dynamic analysis of the structure was performed using the Newmark average acceleration integration scheme and a time step of 0.005 s. Rayleigh damping corresponding to 3% of critical damping in the first two modes of vibrations was specified in the analysis. The gravity loads considered in design (Fig. 8) were statically applied to the structure before starting the dynamic analysis. Fig. 9c presents the first 15 seconds of the axial load time histories computed in the two columns at the first story. The maximum axial compression load on the left hand side column reached 1974 kN, which is 7.8% lower than the value assumed in design, but compares. As anticipated, the beams and columns remained elastic during the analysis.

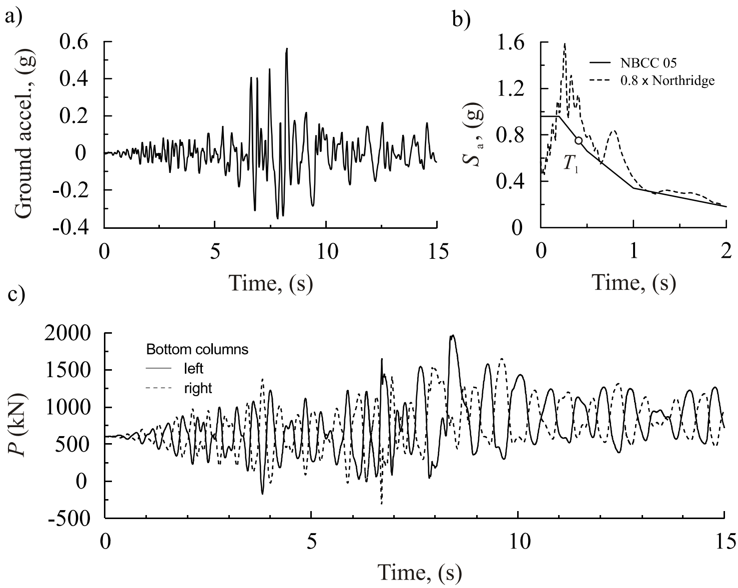

Figure 9. a) Earthquake record, b) Pseudo-acceleration spectra, c) Time history of the compressive forces in the first story W250x73 columns.

The seismic analysis was then redone using a modified computer model with W250x58 columns, thus assuming that only the load Case A of Fig. 8b would have been considered in design. The simulation was performed twice: with and without residual stresses considered in the columns. Fig. 10 shows the computed time history of the horizontal displacements, brace axial loads, and column axial loads at both levels of the frame. These results were obtained for the case with column residual stresses. Fig. 11 shows the hysteretic response obtained in the first level columns. As shown, buckling occurred in both columns when the residual stresses were accounted for in the analysis. In the case where residual stresses were not modeled, the columns exhibited higher capacity and did not buckle during the entire duration of the earthquake.

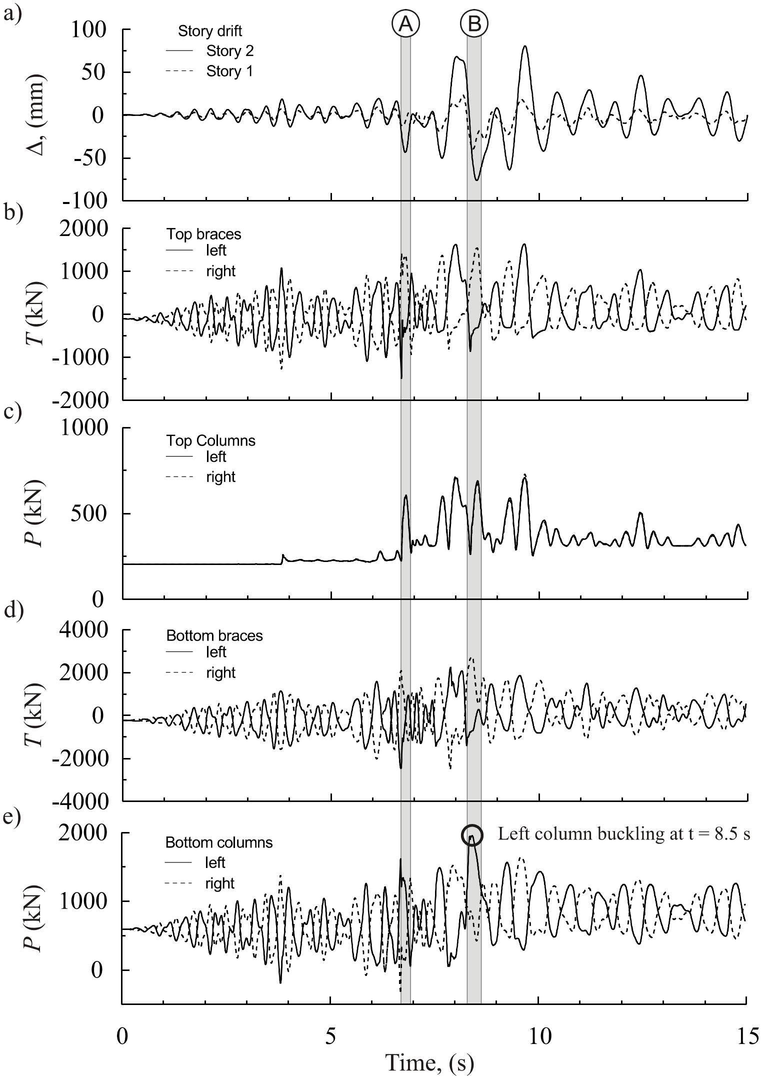

Figure 10. Time history responses with the W250x58 columns.

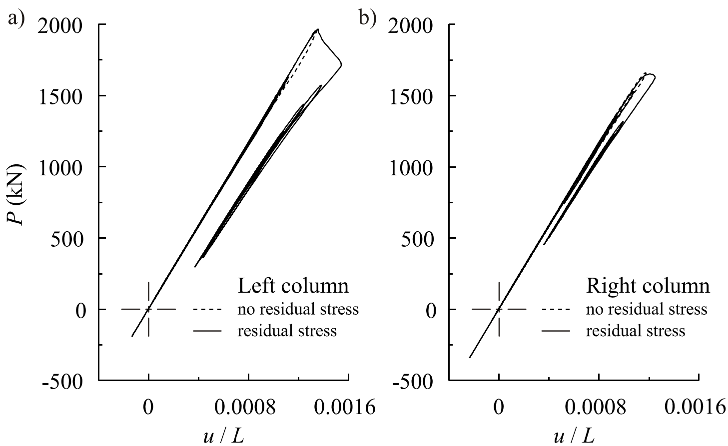

Figure 11. Axial hysteretic column responses: a) Left hand side column, b) Right hand side column.

Fig. 11 shows that the column on the left hand side of the frame experienced the largest demand. Fig 10 is used to illustrate the loading sequence on that particular column. Fig. 10a shows that the lateral displacements at both levels are generally in phase, suggesting that the response was governed by the first mode of the structure and that maximum storey shears developed in the same direction at both levels as assumed in design (Fig. 8). The first critical event affecting the column happened just before time t = 7.0 s, when the braces at both levels buckled after reaching their anticipated compression strength, as illustrated in Figs. 10b and 10d. The left-hand side braces at both levels buckled first, followed by buckling of the two braces on the right-hand side shortly after. This situation corresponds to the design Case A of Fig. 8b and is identified by the first grey region in Fig. 10. In the figure, it is noted that compression forces are negative for the braces and positive for the columns. In Fig. 10c, seismic induced compression forces in both columns at the second story start to peak in phase, indicating that unbalanced brace forces at the roof level are equally transferred to both columns by shear in the roof beam. The forces in the left-hand side column at the first level in Fig. 10e reached a first large compression force peak when the left-hand side braces buckled at the second level. As expected, the column could carry this compressive load without failing.

The next critical event for the left-hand side column depicted graphically in Fig. 10 correspond to the loading Case B of Fig. 8c and led to buckling of the column. At time t = 8.5 s, the right-hand side braces at both levels attained their yield tensile strength while the compression braces on the left-hand side only developed a reduced post-buckling capacity. This resulted in the maximum unbalanced brace forces being transferred by the beams by shear to the columns. Buckling of the left-hand side column occurred at the first level under the peak compression load that developed under that critical loading condition (circled in Fig. 10e). Buckling however only lasted for a brief period of time as the dynamic horizontal inertia forces induced by the earthquake pulled the structure back to a stable state, before the load carrying capacity of the column reduces below the axial load level induced by the gravity loads alone. The seismic demand on the damaged column in the later stage of the earthquake remained below its reduced capacity and the frame could therefore withstand that particular ground motion without total collapse.

Fig. 12 presents snap shots of the out-of-plane deformations and bending moment demand for the left-hand side column at various times during the seismic event. The grey areas in the figure correspond to the envelope of these response parameters. At time t = 8.4 s, just prior to column buckling, the deformed shape corresponds to the initial out-of-straightness slightly amplified by the axial loads. After buckling of the column (t = 8.6 s), the change in deformation is drastic. The shape at t = 40 s is the final resting position after the ground motion had stopped. It is characterized by a double curvature with a significant residual out-of-straightness of approximately L/400 at the top level and L/225 at the bottom level. Nevertheless, the building was still standing as the columns still had sufficient reserve capacity to carry the gravity loads. In Fig. 12b, the bending moment demand during the earthquake remained within 40% of the plastic moment capacity of the column, M_p, Nevertheless, this demand may have detrimental effects on the axial load capacity of the columns and, thereby, should be considered in design.

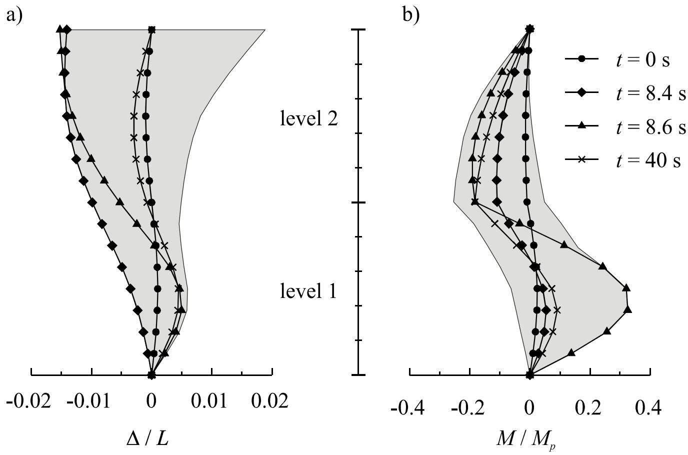

Figure 12. Snap shot and envelope responses of the left-hand side column: a) Horizontal displacements; b) Bending moments.

CONCLUSION

The inclusion of initial stress patterns in nonlinear beam-column using cross-sectional fiber discretization was achieved by modifying the steel02 hysteretic model within the finite element software OpenSees. The formulation and the methodology used to include this feature in the program were described. Numerical simulations of typical steel columns subjected to monotonic and cyclic buckling conditions were also presented. Nonlinear monotonic numerical simulations of full scale centrally loaded columns were performed and compared to laboratory experiments. It was demonstrated that the proposed modifications resulted in a better prediction of the buckling and post buckling behavior of steel columns. Finally, nonlinear seismic analyses were performed to investigate the effect of reducing the columns sizes in a two-story chevron braced steel frames designed according to capacity design principles. The analysis showed that column buckling can occur if these principles are not met. However, seismic demand is typically characterized by successive load reversals and buckling conditions may only exist during very brief periods of time during an earthquake. The building examined in this study could withstand the ground motion without collapse even if column buckling occurred. This behavior suggests that further analytical study be carried out to examine the possibility of relaxing current code capacity design requirements for the columns of braced steel frames. These studies should also examine the influence of the bending moment demand on the columns.

ACKNOWLEDGEMENTS

The financial support from the Fonds québécois de la recherche sur la nature et les technologies (FQRNT) of the Government of Quebec, Canada, and from the Natural Sciences and Engineering Research Council of Canada (Canada Research Chair program) is acknowledged. The authors express their appreciation to F. McKenna and Professor F.C. Filippou from the University of California at Berkeley for their collaboration in the modification of the steel02 code in OpenSees. Lee Gu, from University of Trento, Italy, is also thanked for his advices on the implementation of hysteretic models in finite element codes.

REFERENCES

Agüero, A., Izvernari, C., and Tremblay, R. 2006. Modelling of the Seismic Response of Concentrically Braced Steel Frames using the OpenSees Analysis Environment. Int. J. of Advanced Steel Construction, 2, 3, 242-274.

AISC. 2005. ANSI/AISC 360-05, Specifications for structural steel buildings. American Institute of Steel Construction, Chicago, IL.

Black, R.G. Wenger, W.A.B. and Popov, E.P. 1980. Inelastic Buckling of Steel Struts Under Cyclic Load Reversals. Report No. UCB/EERC-80/40, Earthquake Engineering Research Center, Universty of California, Berkeley, CA.

CSA. 2005. CSA-S16S1-05 Supplement No. 1 to CAN/CSA-S16-01 Limit States Design of Steel Structures. Canadian Standard Association, Toronto, ON.

Filippou, F.C., Popov, E.P., and Bertero, V.V. 1983. Effects of bond deterioration on hysteretic behavior of reinforced concrete joints. Earthquake Engineering Research Center, Report UCB/EERC-83/19, University of California, Berkeley.

Galambos, T.V., Ketter, R.L 1959. Columns under combined bending and thrust. J. of the Eng. Mech. Div., ASCE, 85, pp. 1-30.

Kishima, Y., Alpsten, G. A., Tall, L. 1969. “Residual stresses in welded shapes of flame-cut plates in ASTM A572 (50) steel.” Fritz Engineering Laboratory Report No. 321.2, Lehigh University.

Mazzoni, S., McKenna, F., Scott, M.H., Fenves, G.L. et al. 2006. Open System for Earthquake Engineering Simulation, User Command-Language Manual. Pacific Earthquake Engineering Research, University of California, Berkeley, CA.

Menegotto, M. Pinto, P.E. 1973. Method of analysis for cyclically loaded reinforced concrete plane frames including changes in geometry and non-elastic behavior of elements under combined normal force and bending. Proc. of LABSE, symposium on “Resistance and ultimate deformability of structures acted on by well defined repeated loads”, Lisbon, Spain.

Neuenhofer, Ansgar, F.C. Filippou. 1998. Geometrically nonlinear flexibility-based frame finite element. J. of Struct. Eng., ASCE, 124, 6, pp. 704-711.

NRCC. 2005. National Building Code of Canada 2005, 12th ed., National Research Council of Canada, Ottawa, ON.

Surovek-Maleck, A. and White, D.W. 2004. Alternative approaches for elastic analysis and design of steel frames. I: Overview. J. of Struct. Eng., ASCE, 130, 8, pp. 1186-1196.

Uriz, P. Towards Earthquake Resistant Design of Concentrically Braced Steel Structures. Ph.D. Thesis. Dept. of Civ. Eng., University of California, Berkeley, CA, 2005.

Ziemian, Ronald D. 1992. A verification study for methods of second-order inelastic analysis. Proc. Annual Technical Session, Structural Stability Research Council, Pittsburgh, PA, pp. 315-326.

PERFORMANCE-BASED ANALYSIS OF COMPOSITE STEEL-CONCRETE STRUCTURES UNDER FIRE CONDITIONS

Alexandre Landesmann[1] · *Daniel Lemos Mouço*[2]
Eduardo de Miranda Batista[3]

ABSTRACT

This paper is addressed to the application of a computational tool, denominated as SAAFE Program (System for Advanced Analysis for Fire Engineering), developed to provide an inelastic analysis of steel and composite (steel-concrete) 2D framed-structures under fire conditions. A transient heat transfer analysis model is used to consider the temperature gradient effects due to non-uniform exposure to fire, taking into account the thermo-dependent proprieties of heated materials. The structural behavior is simulated up to the failure by a second-order refined plastic-hinge method, being possible to estimate the correspondent fire elapsed time. The fire resistance of a multi-story composite framed building submitted to a predefined fire scenario is assessed by the proposed approach. Obtained numerical results for the structural behavior are presented, outlining the advantage of considering the structural ductility in the current design practice for steel structures under fire.

[1] Assistant Professor, E-mail: alandes@coc.ufrj.br
[2] M.Sc. Student, E-mail: mouco@coc.ufrj.br
[3] Associate Professor, E-mail: batista@ coc.ufrj.br
Civil Engineering Program, Federal University of Rio de Janeiro (COPPE/UFRJ), POB 68.506, Rio de Janeiro/RJ, 21945-970, Brazil.

DESIGN FOR FIRE CONDITIONS

The incorporation of detailed criteria for design and evaluation of structural steel components, systems and frames for fire conditions, as presented by Appendix 4 of AISC-LRFD (2005), has provided regulatory evidence of current design applications. Due to high cost (Rose *et al.*, 1998), traditional design by qualification testing has been accepted as an alternative approach for providing fire resistance of structural members. Design by analysis methods can be applied for the performance evaluation of individual members or buildings under fire (entire structures or sub-structures). Two approaches are addressed: Simple and Advanced Methods. Simple Methods are more direct to use however, they are not able to describe the actual structural behavior when global deformations are large and the nonlinear behavior becomes relevant. In this simple approach, a uniform temperature field is assumed over the cross-section, modeled by a one-dimensional heat transfer equation. The resistance check is performed for isolated members only. By contrast, Advanced Analysis Methods include both thermal and mechanical responses to the design-basis fire, assessed by computer models. The consideration of a complete structural system, instead of a collection of isolated members, leads to safe and economical fire design. Furthermore, by the global analysis it is possible to estimate more realistically the ultimate strength capacity and to predict the stability behavior of structures under fire conditions. As an alternative to the *FEM* approaches for fire design (Cai *et al.*, 2003), the original Advanced Analysis Concept (Liew *et al.*, 1991, 1993; Liew & White, 1993; Chen *et al.*, 1996; among others), has been extended to study the global performance of framed structures subjected to compartment fires (Liew *et al.*, 1998, 2002). In this context, this paper presents the application of a computational tool, denominated as SAAFE Program (System for Advanced Analysis for Fire Engineering), developed to provide an inelastic analysis of steel and composite (steel-concrete) 2D framed-structures under fire conditions (Landesmann *et al.*, 2005). The accurate representation of the axial and the flexural inelastic mechanical responses, for different temperature distributions, are accounted for by a numerical procedure based on the *Newmark* theory (Chen *et al.*, 1996), with low computational effort. The general summary of this approach is outlined in next section of this paper. Numerical studies are carried out for 12-storey car-park building exposed to a standard time-temperature curve. The computed results are presented, being possible to infer about the applicability of the proposed model.

THERMO-MECHANICAL RESPONSE

Heat transfer analysis

The temperature response of members exposed to fire is performed in the present approach by a 2D nonlinear transient heat transfer analysis modulus of SAAFE, based on FEM (Cook *et al.*, 1989). The thermal temperature-dependent properties of materials, such as the thermal conductivity, specific heat and density are adopted in the proposed procedure as established by part 1.2 of Eurocode 4 (EC4-1.2, 2003). A direct time integration scheme, known as the generalized trapezoidal rule (Cook *et al.*, 1989), is used to determine the temperature (θ) variation. Convective and radiative heat fluxes boundary (vectors {R}) are also accounted for, being adopted 25 W/ºCm² as the convective heat transfer coefficient and the resultant emissivity as 0.5 and 0.7, respectively for steel and concrete surfaces. The transient behaviour is expressed for a predefined time step (Δt), as follows:

$$\left(\frac{1}{\Delta t}[\mathrm{M}]+\omega[\mathrm{C}+\mathrm{H}]\right)\{\theta\}_{n+1}=\left(\frac{1}{\Delta t}[\mathrm{M}]-(1-\omega)[\mathrm{C}+\mathrm{H}]\right)\{\theta\}_{n} +(1-\omega)\{\mathrm{R}\}_{n}+\omega\{\mathrm{R}\}_{n+1} \qquad \text{Eq. (1)}$$

where the following were give, in accordance to Cook *et al.* (1989): a temporal integration factor (ω) is assumed as 2/3; [M] is the lumped mass matrix and, [C+H] represents the conductivity and heat capacity matrixes. Fire exposed members are assumed to be uniformly heated along the entire length and around the entire perimeter of the exposed section. Although the proposed model is able to account for any time-temperature curve, the ASTM E119 (ASTM, 2000) has been adopted as the design-basis fire in the present analysis. Results in temperature domain have been previously contrasted with SAFIR FEM analysis (2001), being observed good agreement.

Material behavior at elevated temperatures

Since the temperature field has been estimated for total fire duration, the structural thermal effects are automatically accounted for by SAAFE program. In this approach, the cross-section FEM mesh, previously adopted in the thermal procedure, is used to estimate new mechanical properties of the cross-section, i.e. the effective strength and stiffness, as a function of the fire elapsed time (also temperature). The compressive stress-strain (σ-ε) relationship for concrete and steel at elevated temperatures, proposed by EC4-1.2 (2003), respectively given by Figure (1a) and (1b) are considered in the analysis.

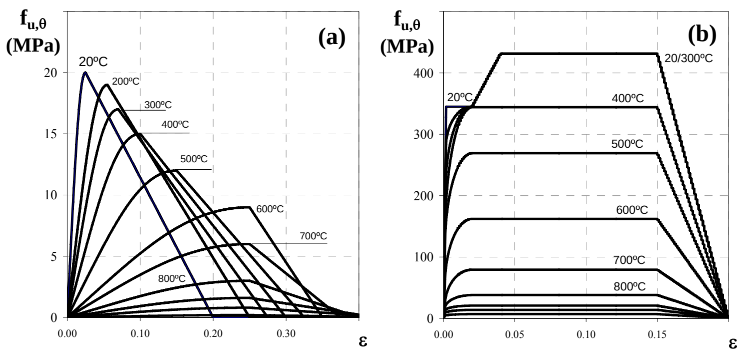

<u>Figure 1</u>: Compressive stress-strain relationship (σ-ε) at high temperatures for: (a) concrete (f_c = 20 MPa, C20); (b) structural steel (ASTM A572 Gr.50, f_y = 345 MPa).

It should be pointed out that the proposed model accounts for concrete softening and loss of resistance after cooling, as well as steel strain-hardening for temperatures below 400°C, which representing a realistic behavior of heated materials.

Flexural behavior

SAAFE adopts a numerical procedure based on the *Newmark* theory to account for the axial and the flexural inelastic mechanical responses, for different temperature distributions. In this procedure, as the FEM mesh is automatically generated from a geometrical pre-processor, which can be used to simulate any kind of cross section. Figure 2 exemplifies a stress-strain distribution for a pure bending loading condition for a concrete encased composite beam.

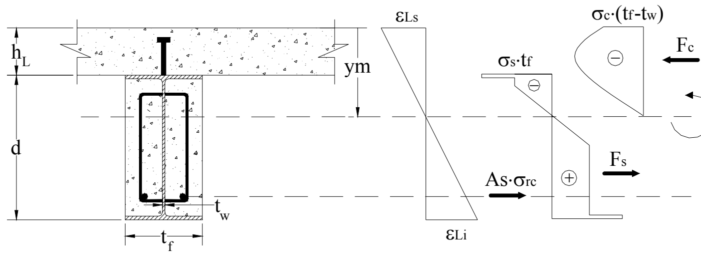

<u>Figure 2</u>: Stress-strain for a concrete encased composite beam.

By assuming the *Bernoulli* hypothesis of plane sections, an incremental strain deformation is imposed for a predefined control fiber (ε_{Ls}). The resulting lowest fiber strain (ε_{Li}) can be evaluated by a numerical procedure for flexural behavior. The curvature (κ) and the neutral axis y_m are obtained as a function of the strain pattern, respectively:

$$\kappa = \frac{\varepsilon_{LS} - \varepsilon_{Li}}{d + h_L}, \quad y_m = \frac{\varepsilon_{LS}}{\kappa} \qquad \text{Eq. (2)}$$

For each predefined time step (Δt), the strain diagram is incrementally increased until the full development of a plastic region over the cross-section (*Mu)*. The correspondent stress pattern is calculated in accordance with the respective material constitutive law (Fig. 1), implicitly accounting for the mean fiber temperature and the residual stress pattern proposed by Sazalai & Papp (2005) for hot-rolled sections. Based on each incremental stress-strain distribution, a non-linear moment-curvature *(M-κ)* curve can be traced. The *3-Parameter Method*, proposed originally by Kish-Chen (Chen *et al.*, 1996) to interpolate experimental results of moment-rotation beam-to-column connections, is use in this paper to represent the inelastic *M-κ* curve. The following parameters are accounted for: *(1)* elastic stiffness (EI_{el}) calculated from the tangent at *M-κ* origin; *(2)* ultimate flexional strength (*Mu*), corresponding to the limit horizontal limit of *M-κ*; *(3)* a *n* shape parameter obtained by the least squares method, is evaluated to represent a smooth transition form the elastic to plastic domain. Applications with the proposed procedure are presented in the following section of this paper. The *M-κ* relationship is defined:

$$M(\kappa)=\frac{\kappa\cdot EI_{el}}{\left(1+\left(\frac{\kappa\cdot EI_{el}}{M_u}\right)^n\right)^{\frac{1}{n}}} \qquad \text{Eq. (3)}$$

The inelastic reduction factor (η) concept, which represents the ratio between inelastic and elastic flexural stiffness, originally presented by Chen *et al.* (1996) for steel structures is implemented in the present paper for composite structures under fire conditions. In this approach, the *M-κ* relationship is used so that η can be performed:

$$\eta=\frac{EI_{in}}{EI_{el}}=\frac{1}{EI_{el}}\frac{dM(\kappa)}{d\kappa}=\frac{1}{\left[1+\left(\frac{\kappa\cdot EI_{el}}{M_u}\right)^n\right]^{1+\frac{1}{n}}} \qquad \text{Eq. (4)}$$

The influence of axial force on the ultimate moment strength are checked in accordance to the AISC/LRFD (2005) recommendations, taking into account the ultimate axial force (P_u), as follows:

$$M=\begin{cases}\left(1-\dfrac{P}{2\cdot P_u}\right)\cdot M_u, \text{for} \quad 0\le\dfrac{P}{P_u}\le 0.2\\[2ex] \dfrac{9}{8}\cdot\left(1-\dfrac{P}{P_u}\right)\cdot M_u, \text{for} \quad 0.2<\dfrac{P}{P_u}\le 1.0\end{cases} \qquad \text{Eq. (5)}$$

Axial behavior

The implemented *Newmark* approach is also performed by SAAFE program to describe the inelastic behavior of steel columns at elevated temperature conditions, under pure axial compression (or for tension). In this approach, the effective tangent modulus (E_t) concept - previously developed to estimate the ultimate strength of compressed members for normal temperature conditions (Chen *et al.*, 1996), is modified and adopted in the present model for fire. A member initial geometrical imperfection is accounted for by prescribing a half sine eccentricity of $L_c/1000$ (L_c is the member length).

The implemented procedure involves an inelastic beam-column ordinary differential equation solution and can be summarized by the following basic steps, repeated for each fire step time: (1) divide the half sine beam-column into a predefined number of stations; (2) impose an incremental the axial load P; (3) evaluate the second-order bending moment; (4) determine the curvature of each station with the *M-P-κ* diagram; (5) evaluate the displacements with the *Conjugate Beam Method*; (6) Repeat steps 3 to 5 until the tolerance is achieved. Equilibrium and compatibility are continuously verified along pre-determined finite number points. The resulting axial-elongation curves (*P-e*) are also represented in a *3-Parameter* form by considering the following: *(1)* elastic stiffness (EA_{el}); *(2)* ultimate axial strength (P_u); *(3) n* shape parameter. Eq. (6) shows the *3-Parameter* fitting for *P-e*.

$$P(e) = \frac{e \cdot EA_{el}}{\left(1 + \left(\frac{e \cdot EA_{el}}{P_u}\right)^n\right)^{\frac{1}{n}}} \qquad \text{Eq. (6)}$$

The tangent modulus can be expressed in terms of inelastic (EA_{in}) and the elastic axial (EA_{el}) stiffness (Liew *et al.*, 1991):

$$\frac{E_t}{E} = \frac{EA_{in}}{EA_{el}} = \frac{1}{EA_{el}} \frac{dP(e)}{de} = \frac{1}{\left[1 + \left(\frac{e \cdot EA_{el}}{P_u}\right)^n\right]^{1+\frac{1}{n}}} \qquad \text{Eq. (7)}$$

P-M interaction curves

The boundary surface approach (Liew *et al.*, 1998, 2002) is used by SAAFE to represent a smooth transition from elastic to inelastic domain. In this procedure, two interaction surfaces are evaluated to capture the load combination of axial force (P) and bending moment (M). The computing *P-M* interaction curves can be plotted for at each time step of fire elapsed time, as presented by Figure 3.

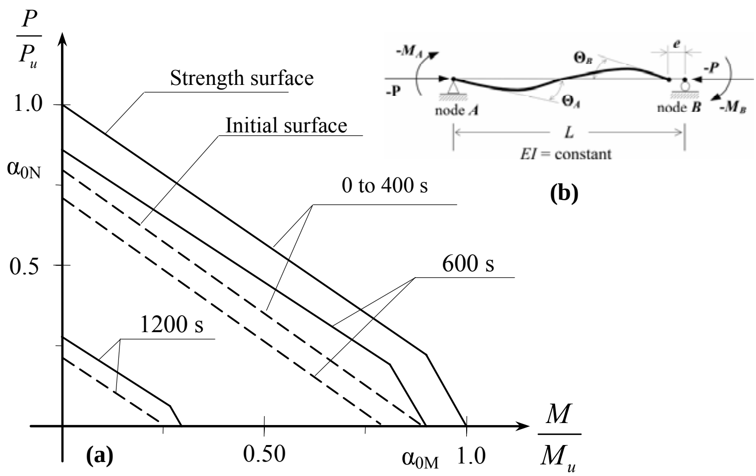

Figure 3: (a) Boundary surface approach: elastic (initial) and inelastic strength curves. (b) beam-column element.

One can observe in Fig. 3 the ultimate strength surface and the initial inelastic surface, obtained in accordance to η inelastic reduction factor. The initial inelastic surface is assumed to be a linear, where the key factors to represent the initial curve are also present, i.e., α_{0M} and α_{0N}, which are performed by the *Newmark* routine, for each time step of the analysis.

Inelastic beam-column element

Both the initial and the ultimate strength surfaces change for each analysis step, since the temperature gradient and the loading combination also change, as the fire temperature becomes more intensive. As a consequence, the resulting interaction surfaces are directly incorporated in the beam-column incremental force-displacement relationship as presented in Eq. (8), where the sub indices *A* and *B* are referred to the ends of the member, as shown in Fig. 3(b).

$$\begin{Bmatrix} \dot{M}_A \\ \dot{M}_B \\ \dot{P} \end{Bmatrix} = \frac{E_t I_\theta}{L_c} \begin{bmatrix} \eta_{\theta.A}\left[S_1 - \frac{S_2^2}{S_1}(1-\eta_{\theta.B})\right] & \eta_{\theta.A}\,\eta_{\theta.B}\,S_2 & 0 \\ \eta_{\theta.A}\,\eta_{\theta.B}\,S_2 & \eta_{\theta.B}\left[S_1 - \frac{S_2^2}{S_1}(1-\eta_{\theta.A})\right] & 0 \\ 0 & 0 & \frac{A_\theta}{I_\theta} \end{bmatrix} \begin{Bmatrix} \dot{\Theta}_A \\ \dot{\Theta}_B \\ \dot{e} \end{Bmatrix} \qquad \text{Eq. (8)}$$

The element force-displacement relationship is expressed in terms of the stability functions, S_1 and S_2, derived from the beam-column equilibrium considerations (Liew *et al.*, 1991; Chen *et al.*, 1996). The stability approach implicitly takes into account for the effect of axial force on the bending stiffness, and hence can be used to predict the P-δ effect. The complete element load-displacement relationship considers a large-displacement small-strain formulation as presented. The equivalent axial (EA_θ) and flexural (EI_θ) stiffness, for fire conditions can be evaluated taking into account each effective segment area k (fiber) and the correspondent temperature-dependent elastic modulus, as follows:

$$EA_\theta = \int_A E_\theta dA\,; \quad EI_\theta = \int_A E_\theta y^2 dA \qquad \text{Eq. (9)}$$

In a similar way, the cross-section ultimate resistances for normal temperature conditions (20°C), *Mu* and *Pu*, are modified taking into account the effective stress limit ($f_{u,\theta}$, where $f_{y,\theta}$ for steel and, $f_{c,\theta}$ for concrete). The equivalent plastic strength, associated respectively with the axial (Pu_θ) and flexional (Mu_θ) strength are determined by Eq. (10).

$$Pu_\theta = \int_A f_{u,\theta} dA\,; \quad Mu_\theta = \int_A f_{u,\theta} |y|\, dA \qquad \text{Eq. (10)}$$

The thermal deformations caused by the temperature increment are taken into account by a restoring forces vector approach (Gatewood, 1957). For a non-uniform temperature distribution along the cross-section, an axial (P_θ) and a flexural (M_θ) restoring forces are evaluated, where ε_θ is the thermal expansion coefficient (EC4, 2003).

$$P_\theta = \int_A \varepsilon_\theta\, E_\theta\, dA\,; \quad M_\theta = \int_A \varepsilon_\theta\, E_\theta\, y\, dA \qquad \text{Eq. (11)}$$

APPLICATION EXAMPLE

General description

A 12-storey car-park building is used in this paper as an application example for the proposed performance-based approach (SAAFE). The loading, geometrical and member definitions for a resistance frame are presented in Figure 4. This 2D frame corresponds to transversal section axes 3, 5 or 7 of Figure 5. The general floor-planning configuration are illustrated by Fig. 5, where one can observe the secondary (*Sec Beam*) and main beams (*Pr Beam*) distribution along a typical 8 m span grid. The bracing system (*Brac.*) corresponding to a *C4* section and the one directional concrete slab are also indicated.

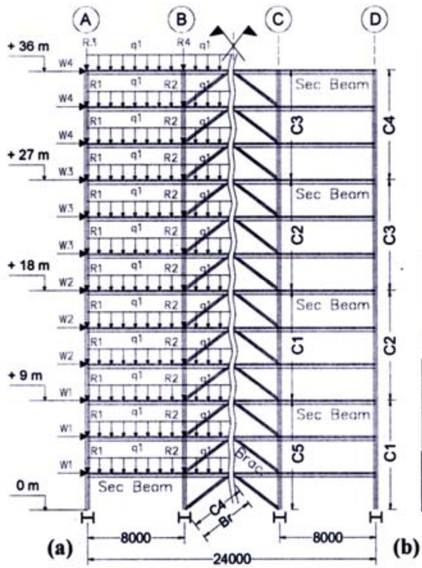

(c) Loading combinations:

Load	$Comb_1$	$Comb_2$	$Comb_3$
q_1 (kN/m)	25.74	18.44	16.20
R_1 (kN)	212.0	150.8	132.5
R_2 (kN)	414.6	292.1	256.9
R_3 (kN)	202.6	141.3	124.4
R_4 (kN)	405.2	282.7	248.8
W_1 (kN)	--	50.0	4.2
W_2 (kN)	--	58.2	4.2
W_3 (kN)	--	63.0	4.2
W_4 (kN)	--	55.2	4.1

(d) Sections:

Columns				
C1	*C2*	*C3*	*C4*	*C5*
W360 x147	W360 x122	HP250 x62	W200 x46	W360 x196

Beam	*Bracing*
W310x32	W200x46

ASTM A572 Gr. 50

NOTE: all dimensions are in *mm*, except where indicated.

Figure 4: Structural definition for the proposed 12-storey resistant frame. (a) Load definition; (b) Geometrical and cross-section definition; (c) resultant load combination; (d) member definition.

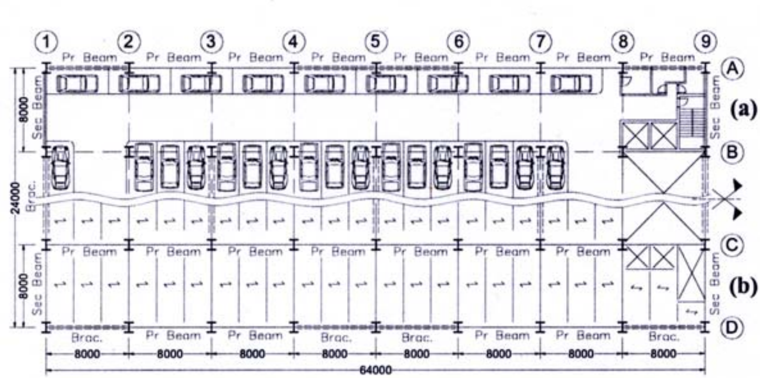

Figure 5: Floor framing definition for the proposed 12-storey. (a) Main parking layout; (b) Beam structural layout.

The beam-to-column connections are assumed to be continuous (fixity) for the interior columns (axes C and B of Fig 4), the exterior connections are considered as pinned (axes A and D of Fig 4). The bracing connections are all assumed to be pinned.

Three selected loading combinations are presented in Eq. (12) for ambient temperature, $Comb_1$ and $Comb_2$ and one fire conditions, $Comb_3$. These resultant load combinations take into account: the nominal dead load (*D* for steel and concrete), the occupancy live load (*L*), wind load (*W*) and, forces due to the design-basis fire (*F*). In addition, a lateral notional load (N_i) is considered for fire combination ($Comb_3$), to be applied at each frame level (*i*), representing 0.2% of the gravity load combination ($Comb_1$) as defined in Appendix 4 of AISC/LRFD (2005). N_i is represented as W for Comb3 in Fig.4 (a, c). It should be point out that the presented combination coefficients are taken according to the Brazilian national regulation (NBR8800, 2007).

$$
\begin{aligned}
Comb_1 &= 1.5L + \left(1.25 \cdot D_{steel} + 1.35 \cdot D_{conc}\right) \\
Comb_2 &= 0.6L + 1.4W + \left(1.25D_{steel} + 1.35D_{conc}\right) \qquad \text{Eq. (12)} \\
Comb_3 &= 0.5L + N_i + F + 1.2\left(D_{steel} + D_{conc}\right)
\end{aligned}
$$

Two options of composite secondary beams (*CB1* and *CB2)* are proposed for the 12-storey building, as presented in Figure 6. They are made of standard W310x31 hot-rolled section, ASTM A572 Gr 50 steel, designed with full interaction with a 100 mm thick concrete slab, pored-in-place (f_c = 20 MPa – characteristic compression). The reinforcement bars in slab are not considered in the beam *CB2* design.

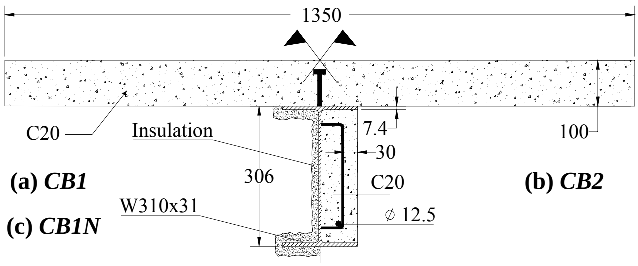

Figure 6: Options for composite beams for 12-storey. (a) CB1 – simple downstand composite beam with insulation layer; (b) CB2 – partially encased beam; (c) CB1N – similar to CB1 without insulation.

The first option *CB1*, as illustrated above (Fig 6.a), is a simple downstand beam. The *CB2* (Fig 6.b) is a partially encased composite beam, filled with a C20 concrete and two reinforcement bars of 12.5 mm of diameter (steel f_y = 500 MPa).

Since the steel section corresponded to options *CB1* are directly exposed to fire, an insulation of 20 mm thick is proposed in order to enhance the fire resistance of the steel members. This insulation is also proposed for the columns. Option *CB1N* corresponds to a *CB1* option without a protection insulation layer. The following insulation properties are taken into account: density of 800 kg/m³, specific heat 1700 J/kg°C and thermal conductivity of 0.17 W/m°C. No protection layer is design for the *CB2* beam option. A fire-design corresponding to the ASTM E119 curve (ASTM, 2000) is postulated to occur at the first floor. The lower part of the beams (level + 3m) and the façade columns (axes A and D of figure 4) are partially exposed to fire, while both interior columns (axes B and C) are completely engulfed by flames.

Temperature response

The temperature evolution for the heated elements is presented in Figure 7, as a function of the fire elapsed time. Three points are selected to represent the temperature across the section height. It also possible to infer about the temperature field for protect and non-protected elements.

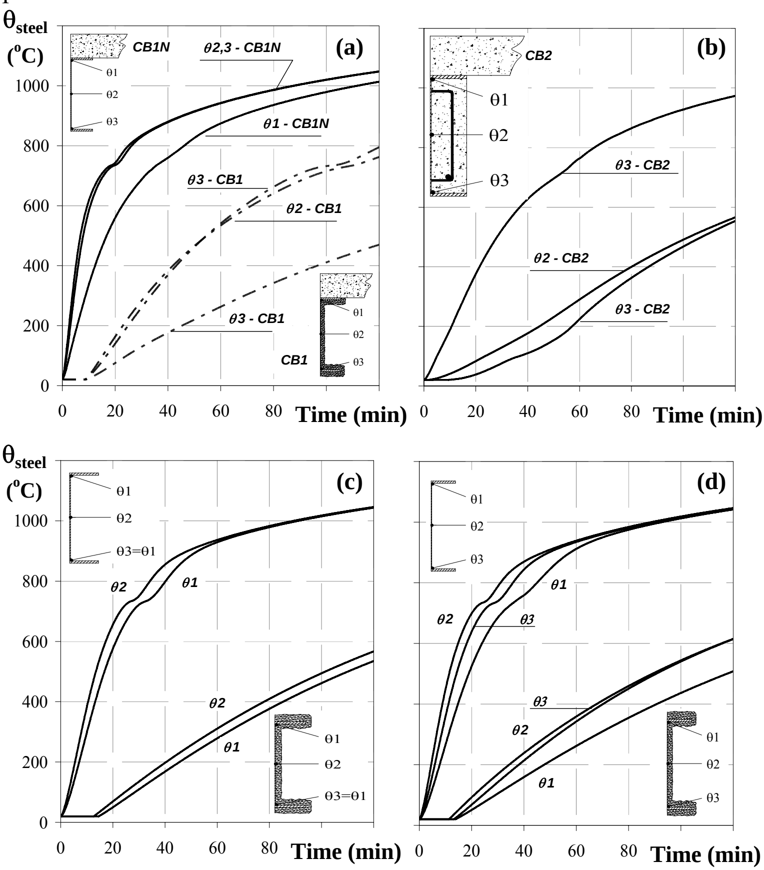

Figure 7: Temperature response for fire-exposed elements. (a) *CB1*; (b) CB2; (c) W360x196 *column C2*; (d) W360x147 *column C1*.

Mechanical response

The moment-curvature curves evaluated by SAAFE for both composite beams (*CB1* and *CB2*), given by Fig 6, are illustrated in Figure 8(a). In addition, results for the steel *W310x31* section are also presented. The inelastic reduction factor (η) obtained by SAAFE as a function of the normalized bending moment are presented in Fig 8(b). It can be observed good correlation with the original η proposed by Chen *et al.* (1996) for steel beams.

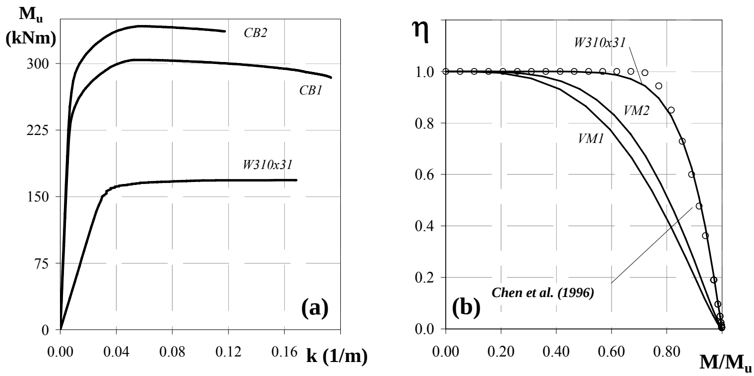

Figure 8: Behavior of beams for the 12-storey building. (a) Moment-curvature curves; (b) inelastic reduction factor.

The presented *M-κ* approach is performed for all the structural elements of the 12-storey building, i.e., the columns, which are not directly exposed to the proposed fire. Obtained results for columns sections indicated no relevant difference in the η factor evaluation, so that an inelastic reduction factor similar to curve plotted by fig 8(a) is adopted.

For fire exposed elements a set of moment-curvature curves and the inelastic reduction factor are obtained as a function of the element temperature (or the fire elapsed time). Figure 9 presents obtained *M-κ* curves for the proposed composite beams. The correspondent normalized flexural stiffness and the normalized ultimate moment as a function of the time are also presented.

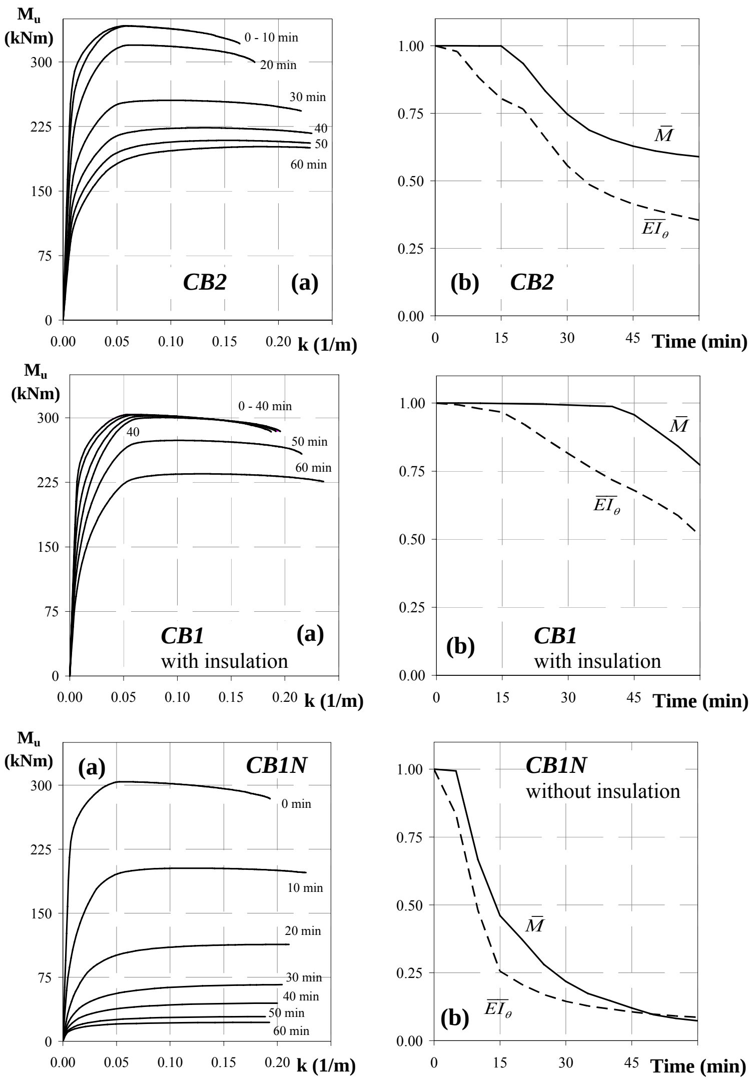

Figure 9: Flexural behavior of composite beams. (a) moment-curvature curves; (b) normalized flexural as a function of time.

Structural behavior

A comparison between the global horizontal (Δ_h) and vertical (Δ_v) displacements, obtained by SAAFE program on the top of the structure, for all the proposed load set combinations (Eq. 12) are present, respectively by Figure 10(a) and 10(b). Where it is possible to track the nonlinear behavior of the frame up to the failure and the correspondent applied load ratio. It should be noted that the presented results in Fig. 10, for *Comb3*, do not account for thermal loading, neither strength nor stiffness reduction due to fire actions, i.e., only mechanical loading are accounted for in this procedure.

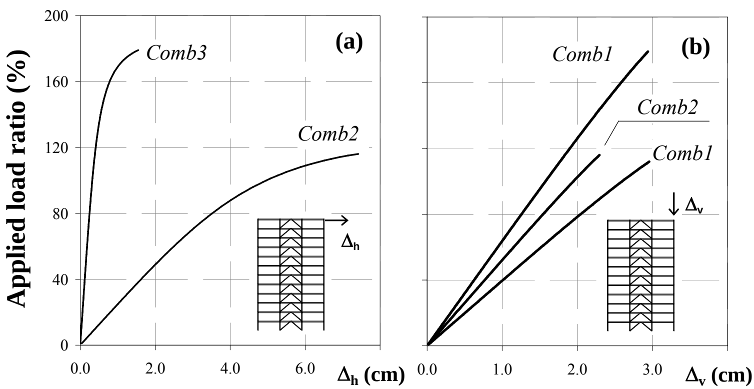

Figure 10: Inelastic behavior of 12-frame for normal temperature conditions. (a) Horizontal and (b) vertical displacement.

The nonlinear structural behavior of the 12-storey frame under the postulated fire condition is presented for the three proposed composite beams options by Figure 11. In this, it is possible to estimate the frame deformed configuration, 30 times majored, for several fire instants up to the ultimate capacity of the building. The performed analysis considered the thermal effects as well as the external loading, as presented by Eqs. (9) to (11). The lateral displacement of heated beam as a function of the fire-time is presented by Fig 11(d). The non-protected condition presents a minimal fire resistance of approximate 15 minutes, where the protected and the concrete encased options present fire-resistant times over 1 hour.

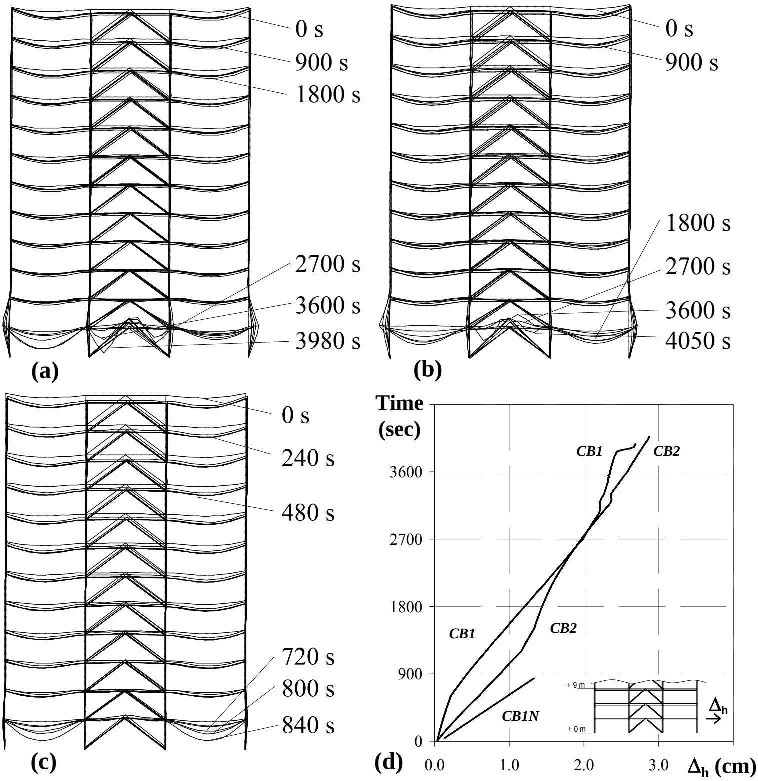

Figure 11: Inelastic behavior of 12-frame under fire conditions. (a) Composite beam option *CB1*; (b) *CB2*; (c) *CB1N*; (d) horizontal displacement as a function of time for proposed beam options.

As presumed the first floor level is very influenced by the thermal action, where plastic deformations are expected on beams. Figure 12 illustrates a plastic diagram for the fire affected structure, where one can observe the amount of plastic-hinge development. Full plastic hinges are indicated for a 1h fire exposure time.

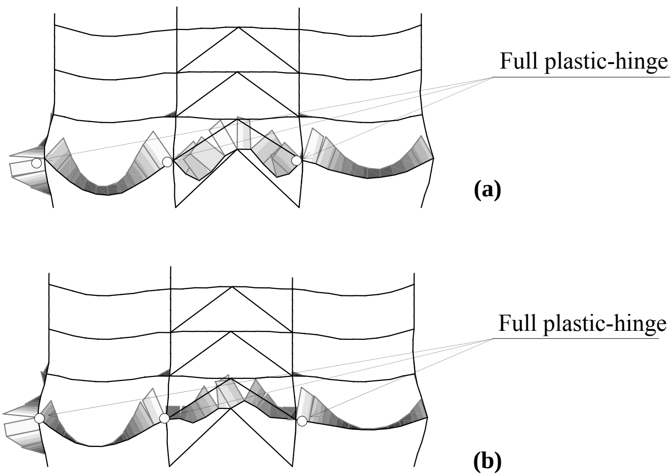

Figure 12: Inelastic distribution on the first floor beams after 1h fire. (a) Composite beam option *CB1*; (b) *CB2*.

CONCLUSIONS

A second-order refined plastic hinge analysis method, used to assess the performance of steel and composite (steel-concrete) structures under fire conditions, is presented in this paper. The computational approach, SAAFE Program (Landesmann *et al.*, 2005) has been developed on the basis of the Advanced Analysis concept (Chen *et al.*, 1996), taking into account the non-linear behavior of material at elevated temperatures, as recommended by part 1.2 of Eurocode 4 (EC4-1.2, 2003).

The model of analysis was applied to study the global behavior of a car-park 2D framed structure exposed to a standard design – basis fire, postulated to occur at the first floor level. The numerical procedure allowed the identification of both local-member and global ultimate limit state of steel framed structures, including the inelastic loading redistribution. This feature represents a more economical and rational fire design than the simplified approach based on individual member capacity checks. The obtained results showed that the developed advanced analysis procedure is able to predict the critical time for different load levels. In addition, the global behavior of framed structures was conveniently followed by the SAAFE computational program.

REFERENCES

AISC/LRFD, "Manual of Steel Construction – Load and Resistance Factor Design Specification for Structural Steel Buildings", American Institute of Steel Construction, Chicago, (2005).

ASTM E119, "Standard Test Methods for Fire Tests of Buildings and Construction Materials", ASTM - American Society for Testing and Materials, West Conshohocken, PA., (2000).

Cai, J., Burgess, I.W., Plank, R.J., "A Generalised Steel/Reinforced Concrete Beam-Column Element Model for Fire Conditions", Engineering Structures, 25(6), 817-833, (2003).

Chen, W.F., Goto Y., Liew, J.Y.R., "Stability Design of Semi-Rigid Frames", 1st, New York, John Willey & Sons, Inc., (1996).

Cook, R.D., Malkus, D.S., Plesha, M.E., "Concepts and Applications of Finite Element Analysis", John Wiley & Sons, New York, 1989.

Eurocode 4 (2003), "Design of Composite Steel and Concrete Structures", prEN 1994-1-1, Comite Europeen de Normalisation (CEN), Brussels, Belgium.

Gatewood, B.E., "Thermal Stress", McGraw Hill Book Co., Inc., New York, (1957).

Landesmann, A., Batista, E.M. and Alves, J.L.D., "Implementation of advanced analysis for steel-framed structures under fire conditions", Fire Safety Journal, v40, n4, pp339-366, (2005).

Liew, J.Y.R., Tang, L.K., Choo, Y.S., "Advanced Analysis for Performance-Based Design of Steel Structures Exposed to Fire", Journal of Structural Engineering, 128(12), 1584-1593, (2002).

Liew, J.Y.R., Tang, L.K., Holmaas, T., Choo, Y.S., "Advanced Analysis for the Assessment of Steel Frames in Fire", Journal of Constructional Steel Research, 47(1-2), 19-45, (1998)

Liew, J.Y.R., White, D.W., Chen, W.F., "Beam-Column Design in Steel Frameworks", Journal of Constructional Steel Research, v. 18, n. 4, pp. 269-308, (1991).

NBR 8800, Brazilian Association of Technical Standards (ABNT), "Project and Execution of Steel Buildings Structures" (in Portuguese), Rio de Janeiro-Brazil, 2007.

Rose, P.S., Bailey, C.G., Burgess, I.W. and Plank, R.J., "The Influence of Floor Slabs on the Structural Performance of the Cardington Frame in Fire", Journal of Constructional Steel Research, 46(1-3), 310-311, (1998).

SAFIR, Franssen, J.–M., Kodur, V.K.R., Mason, J., "User's Manual for SAFIR–2001: A Computer Program for Analysis of Structures Submitted to the Fire", University of Liège, Départment Mécanique des Materiaux et Structures, (2001).

Sazalai, J., Papp, F., "A new residual stress distribution for hot-holled I-shaped sections", Journal of Constructional Steel Research, 61, p.845 – 861, (2005)

White, D. W., Liew, J. Y. R., Chen, W. F., "Toward Advanced Analysis in LRFD". In: Plastic Hinge Based Methods for Advanced Analysis and Design of Steel Frames – An Assessment of the State-of-the-art, Structural Stability Research Council, Scholl of Civil Engineering, Purdue University, West Lafayette, IN, USA. pp. 95-173, (1993).

EXPERIMENTAL STUDY ON ASEISMIC STRENGTHENING METHOD OF STEEL-PIPE PIERS USING ARAMID FIBER SHEET

Masato Komuro[1], Norimitsu Kishi[2], Wai-Fah Chen[3]

INTRODUCTION

In the Great Hanshin-Awaji Earthquake of January 1995, many highway bridges and steel piers suffered severe damages. In order to improve aseismic performance of steel piers against severe quake, many experimental and numerical studies on cyclic elasto-plastic behavior of steel-pipe piers have been conducted in Japan [1-4]. As a result, it was confirmed that the collapse of steel-pipe piers was due to local buckling occurring near footing and/or steel plate stepped area in thickness with the elephant foot bulge mode. It is therefore important to prevent the occurrence of this kind of local buckling or at least to be minimized.

In this paper, we intent to improve aseismic resistant capacity of the steel-pipe piers, by proposing a winding method of Aramid Fiber Reinforced Plastics (AFRP) sheet on steel-pipe piers, the strengthening effects were investigated by conducting monotonic and cyclic loading tests for small steel-pipe pier models.

Moreover, Carbon Fiber Reinforced Plastics (CFRP) sheet has been widely used in the strengthening of concrete structures. However, if CFRP sheet was applied to the strengthening of steel structures, galvanic

[1] Assistant Professor, Muroran Institute of Technology, 050-8585 Japan
[2] Professor, Muroran Institute of Technology, 050-8585 Japan
[3] Professor, University of Hawaii at Manoa, HI, 96822 USA

corrosion may be developed due to direct contact between steel and CFRP sheet. Thus, in this study we tried to apply AFRP sheet to strengthen steel structures.

EXPERIMENTAL OVERVIEW

All pier models are machined in prescribed dimensions using a carbon-steel seamless and hot-formed pressure pipe (JIS G3454 STPG370 90A) with 5.7 mm thickness. The nominal cutting error for prescribed thickness and radius is ± 0.05 mm. The configuration and dimensions of the pier model are shown in Fig. 1. Steel-pipe pier models used in this study are of 96 mm in diameter, 500 mm in height, and 1.5 mm in thickness. The model is made by welding two pipe pieces. In order to prevent the rigid body displacement as much as possible, the basement rigidity is increased by making the basement of model plugged into the 50 mm high pedestal and covered with 9 mm thick pipe.

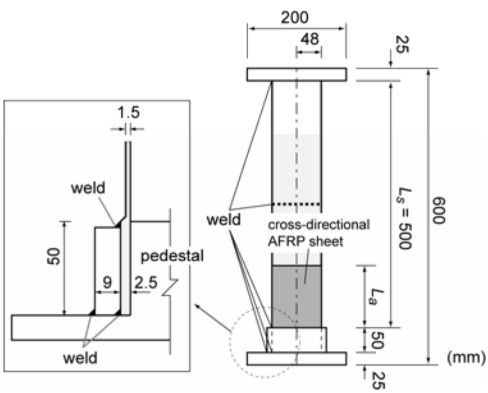

Figure 1. General configuration and dimensions of pier model.

Table 1. List of specimens

Specimen	AFRP sheet		
	No. of layer L_n	Winding height L_a (mm)	Ratio $L_a/L_s{}^{\#}$
L0-A0-m/-c	0	0	0/4
L1/L2/L3-A1-m/c	1/2/3	125	1/4
L1/L2/L3-A2-m/c	1/2/3	285	2/4

L_s: height of steel pier model

Furthermore, both bottom edge of pier model and covered pipe are welded to pedestal, and the top edge of covered pipe is also welded to pier model.

Here, fourteen pipe-pier models were used taking winding height and profiles of AFRP sheet as variable as shown in Table 1. In this table, nominal notation for each pier model was designated using three variables: number of sheet layer; ratio of winding height; and loading method (–m and –c represent static monotonic and cyclic loading test, respectively).

Mechanical properties and stress-strain relation of the steel pier model were obtained by tensile testing according to JIS no.6 test specimens were listed in Table 2 and shown in Fig.2, respectively. Material properties of AFRP sheet used in this experiment are listed in Table 3.

Table 2. Mechanical properties of steel

Yield stress σ_y (MPa)	Tensile stress σ_u (MPa)	Young's modulus E_s (GPa)	Poisson's ratio ν_s	Elongation (%)	Yield strain ε_y (μ)
336	452	206	0.3	44.0	1,633

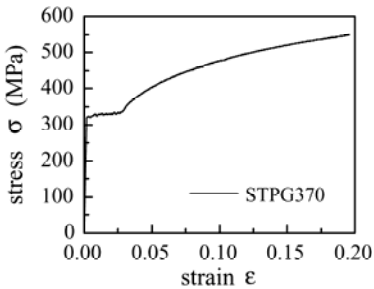

Figure 2. Stress-strain relation of steel.

Table 3. Material properties of AFRP sheet (nominal value)

Mass of AFRPs (kg/m^2)	Tensile stress σ_a (MPa)	Young's modulus E_a (GPa)	Poisson's ratio ν_a	Thickness t_a (mm)	Strain limit ε_a (%)
180	2,060	118	0.4	0.048	1.75

To investigate the strengthening effects of winding AFRP sheet on the maximum lateral load carrying capacity and ductility of the pier model, two types of loading test were applied: static monotonic loading; and static cyclic loading tests. Figure 3 shows the experimental setup used in this study. Lateral load was surcharged using electromotive actuator following a displacement control method. Monotonic loading test was performed until the lateral load H goes down to the H_y as shown in Fig. 4, which is the lateral load when the fiber stress of the bottom of pier model reaches a yielding point and is represented as:

$$H_y = \frac{(\sigma_y - P/A_s)\cdot I_s}{(R + t_s/2)\cdot L} \tag{1}$$

where, σ_y : yield stress ; P : axial compressive load;
R: mean radius, t_s : thickness of steel pier model;
A_s : cross section area; I_s : moment inertia of cross section;
L: loading height (= 631.5 mm)

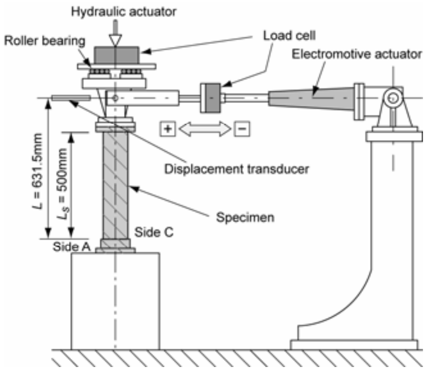

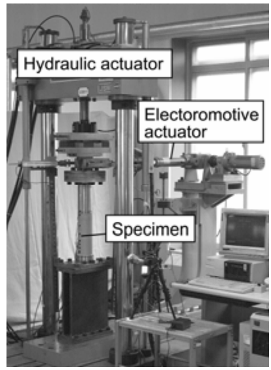

Figure 3. Experimental setup.

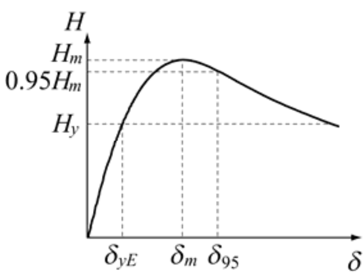

Figure 4. Idealized load-displacement relation under monotonic loading and definition for each parameter.

Cyclic loading test was performed alternatively following the prescribed lateral displacement δ_{yE} as shown in Fig. 5, which is the displacement corresponding to the H_y, and is evaluated by using load-displacement curve obtained from monotonic loading test of bare specimen (L0-A0-m). In this study, lateral load H_y and lateral displacement δ_{yE} were 5.25 kN and 4.898 mm, respectively. Axial compressive load P was set as P = 11.8 kN in this study, which is about 8 % of axial compressive capacity P_y (=$A_s \times \sigma_y$). The loading rate was 0.4 mm/min.

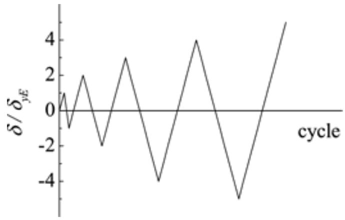

Figure 5. Cyclic loading method.

In these tests, the lateral load H and displacement δ at loading point, and strain gauges installed on the surface of steel and/or AFRP sheets near basement were measured and recorded using digital data recorders. After testing, local buckling modes developed on the basement of specimens were taken by digital camera.

EXPERIMENTAL RESULTS AND DISCUSSIONS

Local Buckling Mode Figure 6 shows the local buckling modes of all specimens after monotonic loading test. From Fig. 6, the local buckling mode of bare steel-pipe specimen (L0-A0-m) was outward buckling mode near the basement, which is widely known as the elephant foot buckling mode (hereinafter, EFB mode).

In the case of winding height L_a = 125 mm (Fig. 6a), the local buckling modes of L1/L2-A1-m specimens were EFB mode near basement the same as bare specimen, causing AFRP sheet to eventually rupture due to hoop tension and it is observed that AFRP sheet was actually ruptured at bending compressive side. In the L3-A1-m specimen, the EFB mode was developed above the border between steel and AFRP sheet. It is for this reason that resistance moment near the border was smaller than applied moment.

In the case of winding height L_a = 285 mm (Fig. 6b), the local buckling modes of L1/L2-A2-m specimens were EFB mode the same as L1/L2-A1-m specimens. However, in the case of L3-A2-m specimen, the rupture of AFRP sheet did not occur and the local buckling mode was inward local buckling deformation near the basement due to confining effect of AFRP sheet, which is similar to the diamond pattern buckling mode (hereinafter, DP mode).

Figure 7 shows the local buckling modes of all specimens after cyclic loading test. From these figures, it was observed that 1) the local buckling modes of L0-A0-c and L1-A*n*-c specimens were EFB mode, 2) the AFRP sheet of L1-A*n*-c specimens was significantly ruptured in both tension and compression sides, and 3) although the local ruptures were observed in L2-A*n*-c specimens, the local buckling modes of L2/L3-A*n*-c specimens were DP mode due to confining effect of AFRP sheet.

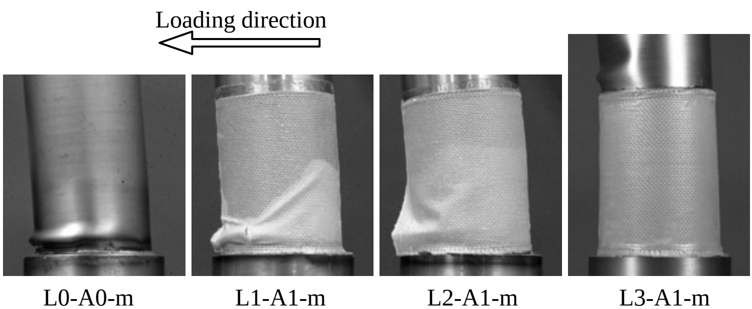

(a) winding height L_a = 125 mm

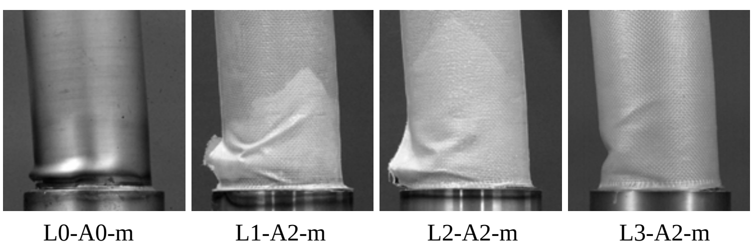

(b) winding height L_a = 285 mm

Figure 6. Local buckling modes after monotonic loading test.

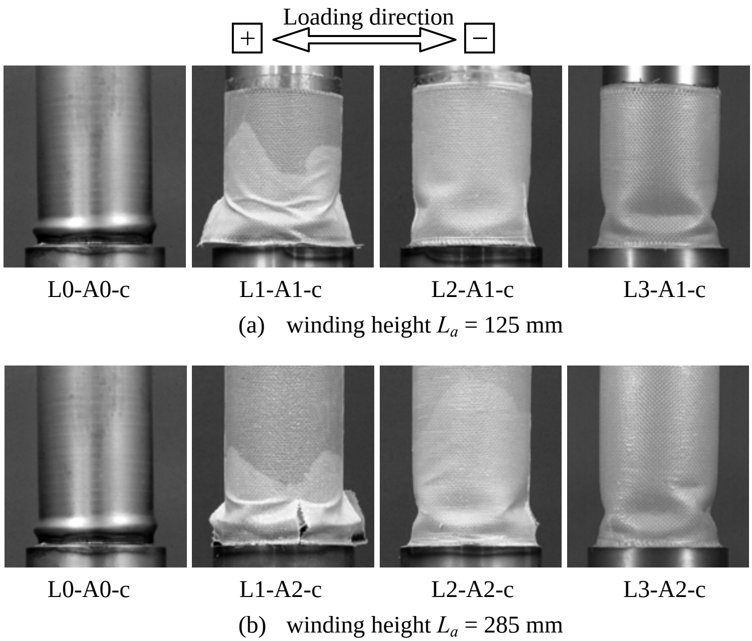

Figure 7. Local buckling modes after cyclic loading test.

Local buckling mode and its height from basement are summarized in Table 4. From this table, although the EFB mode except for L3-A1-m specimen was located about 15 to 20 mm height from basement, the DP mode was located about 25 to 30 mm height. Therefore, it is observed that the height of DP mode was slightly higher than that of EFB mode.

From these results, it is seen that 1) properly winding AFRP sheet near basement of pier-models, local buckling mode was shifted from EFB mode to DP mode due to confining effect of AFRP sheet regardless of loading methods, and 2) in this study, in order to prevent the development of EFB mode due to confining effect of AFRP sheet, the specimen should be winded more than three-layers of AFRP sheet.

Table 4. List of local bucking modes

Specimen	Local buckling mode	Height from basement (mm)	
		Side A	Side C
(a) monotonic loading			
L0-A0-m	EFB	18	-
L1-A1-m	EFB	10	-
L2-A1-m	EFB	22	-
L3-A1-m	EFB	140	-
L1-A2-m	EFB	15	-
L2-A2-m	EFB	13	-
L3-A2-m	DP	30	-
(b) cyclic loading			
L0-A0-c	EFB	17	20
L1-A1-c	EFB	20	36
L2-A1-c	DP	25	27
L3-A1-c	DP	30	26
L1-A2-c	EFB	15	15
L2-A2-c	DP	27	38
L3-A2-c	DP	27	27

Side A: bending compression side at virgin loading (see, Fig. 3)
Side C: bending tension side at virgin loading

Load-Displacement Relation Figure 8 shows the comparison of lateral load and lateral displacement relation under monotonic loading among all specimens. Each lateral load and displacement was normalized by using H_y and δ_{yE}, respectively. From these figures, it is observed that the strengthening effect of AFRP sheet does not influenced much the initial stiffness of steel pipe-pier models because these stiffnesses of all specimens were almost the same. As for the load-displacement relation of bare specimen (L0-A0-m), the lateral load H/H_y was linearly increased until H/H_y = 1.3, and stiffness was gradually decreased with increasing displacement. The maximum load H_m/H_y was about 1.45 at δ/δ_{yE} = 2. After that, the lateral load was gradually decreased due to the development of the EFB mode near basement.

In the case of specimens with AFRP sheet, the lateral load H/H_y was linearly increased until H/H_y = 1.5 and reached the maximum value

(H_m/H_y = 1.6) at δ/δ_{yE} = 2, and kept the same loading level with increasing lateral displacement. The load of L1/L2-A*n*-m specimens was suddenly dropped at δ/δ_{yE} = 3.5 to 5.5. These phenomena were due to rupture of AFRP sheet as shown in Fig. 6. L3-A1-m specimen was gradually decreased from δ/δ_{yE} = 5 due to developing the EFB mode above the border between steel and AFRP sheet. L3-A2-m specimen was kept the same loading level until δ/δ_{yE} = 7 because the rupture of AFRP sheet did not occur and the local buckling mode became DP mode due to confining effect of AFRP sheet, which was different from other specimens.

Figure 9 shows the comparison of strain-displacement relation among three L*n*-A2-m specimens under monotonic loading. Here, the axial strains in bending tension side and circumferential strain in bending compressive side were considered. They were installed at height h = 20 mm from bottom of specimen. From these figures, it was seen that at beginning of loading, the axial strain in bending tension side was lineally increased until about δ/δ_{yE} = 1.5, and then suddenly dropped to zero level due to AFRP sheet was separated from the steel pipe. It is seen that the initial stiffness was not increased by strengthening AFRP sheet.

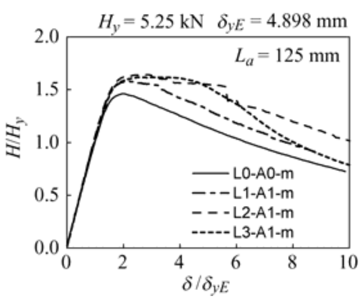

(a) winding height L_a = 125 mm

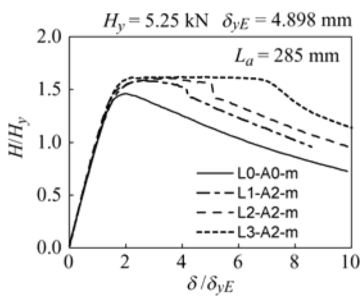

(b) winding height L_a = 285 mm

Figure 8. Comparison of lateral load and lateral displacement relations under monotonic loading.

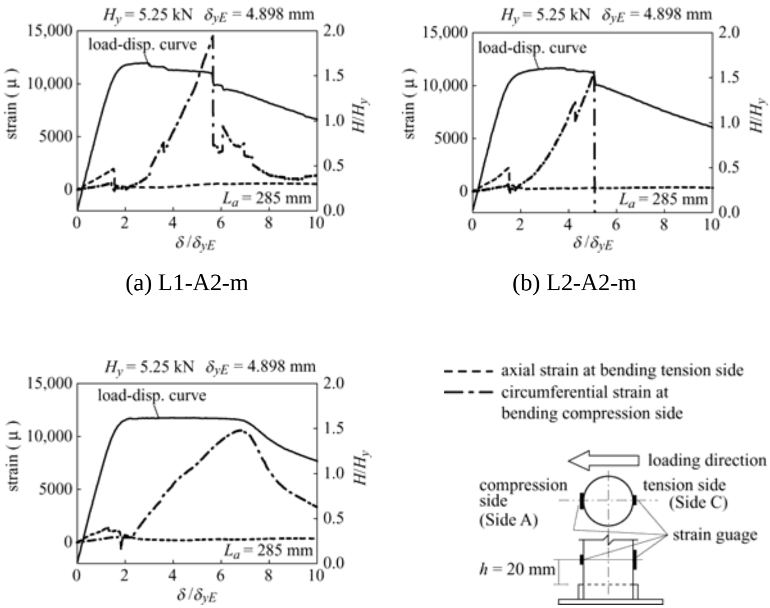

(a) L1-A2-m

(b) L2-A2-m

(c) L3-A2-m

Figure 9. Comparison of strain-displacement relations among Ln-A2-m specimens.

On the other hand, the circumferential strain in bending compression side was gradually increased at beginning of loading. Moreover, the strain was drastically increased from around δ/δ_{yE} = 2 at the maximum loading capacity. It shows that AFRP sheet was resisting the development of outward deformation near basement. Finally, the strains of L1/L2-A2-m specimens were suddenly dropped due to rupture of AFRP sheet. However, the strain of L3-A2-m specimen was gradually decreased from δ/δ_{yE} = 7. This shows that local buckling mode was shifted from EFB mode to DP mode.

Hysteretic loops of load-displacement relations for L0-A0-c and Ln-A2-c specimens are shown in Fig. 10 comparing with the results of monotonic loading. From these figures, it is observed that 1) the maximum load capacity H_m/H_y under cyclic loading had almost the same value of monotonic loading, and 2) the decrease in the lateral load after the maximum load was earlier than that of monotonic loading.

Figure 11 shows the envelopes of hysteretic load-displacement relations. From these figures, it is seen that 1) the larger the volume of winding AFRP sheet, the more improve is the ductility of specimen, and 2) the envelopes for the specimen in the same volume of AFRP sheet were essentially similar regardless of winding height.

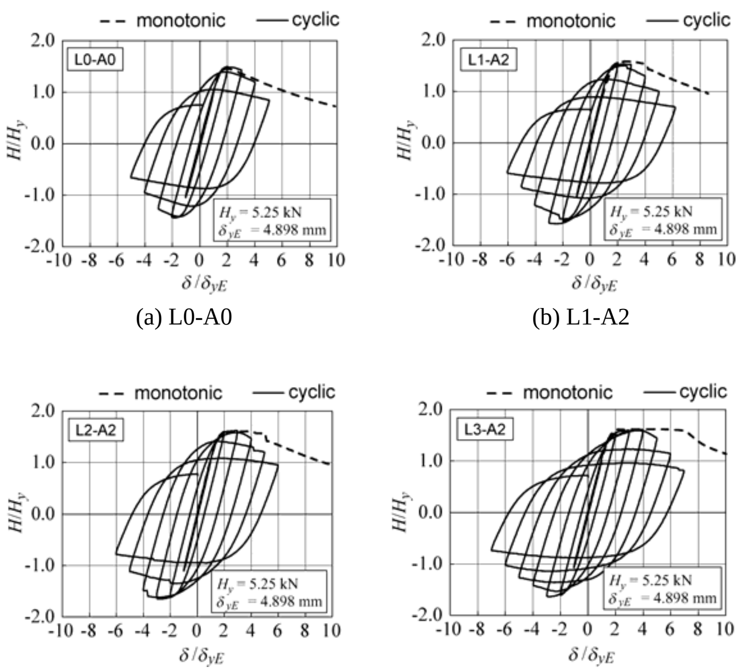

(a) L0-A0

(b) L1-A2

(c) L2-A2

(d) L3-A2

Figure 10. Hysteretic loops of L0-A0 and L*n*-A2 specimens under cyclic loading.

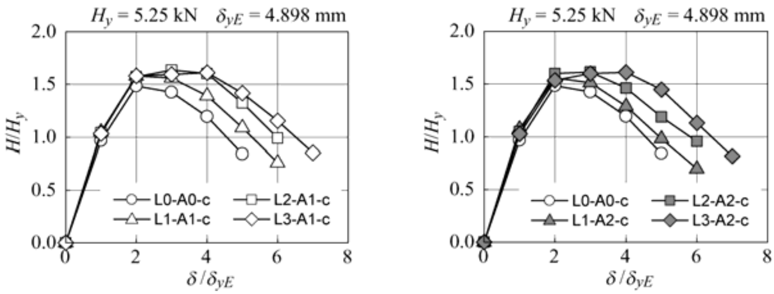

(a) winding height L_a = 125 mm (b) winding height L_a = 285 mm

Figure 11. Envelopes of hysteretic loops for all specimens.

Maximum load H_m and ductility δ_{95} of all specimens are summarized in Table 5. Figure 12 shows the relations between the maximum load ratio H_m / $H_{m\text{-}0}$ and strengthening ratio ρ, and ductility ratio δ_{95} /$\delta_{95\text{-}0}$ and strengthening ratio ρ, in which ρ is the ratio of tensile strength of AFRP sheet to yield strength of steel pier model and is represented as:

$$\rho = \frac{L_n t_a \sigma_a}{t_s \sigma_s} \tag{2}$$

From these results, the maximum load was enhanced 4-13 % by winding AFRP sheet regardless of loading methods. On the other hand, the ductility was depended on the volume of AFRP sheet and loading methods. The ductility of L3-A2-m/c specimens was drastically enhanced by 260 % for monotonic loading and about 150 % for cyclic loading, respectively, comparing with that of bare specimens (L0-A0-m/c). It shows that by properly winding AFRP sheet on steel-pipe piers, the load-carrying capacity of the pier model cannot be improved significantly but its ductility can be increased significantly. L3-A2 specimen was the best among all specimens in which winding height was L_a = 285 mm and strengthening ratio was ρ = 0.6.

Table 5. List of maximum load and ductility

Specimens	Maximum load		δ_{95}	Ductility μ_{95}
	H_m (kN)	H_m/H_y	(mm)	$(=\delta_{95}/\delta_{yE})$
(a) monotonic loading				
L0-A0-m	7.69	1.46 (1.00)	13.7	2.80 (1.00)
L1-A1-m	8.30	1.58 (1.08)	16.4	3.34 (1.19)
L2-A1-m	8.65	1.65 (1.13)	20.2	4.12 (1.47)
L3-A1-m	8.52	1.62 (1.11)	23.7	4.84 (1.73)
L1-A2-m	8.36	1.59 (1.09)	20.2	4.13 (1.48)
L2-A2-m	8.47	1.61 (1.11)	24.9	5.08 (1.81)
L3-A2-m	8.51	1.62 (1.11)	35.6	7.26 (2.59)
(b) cyclic loading				
L0-A0-c	7.87	1.50 (1.00)	14.9	3.04 (1.00)
L1-A1-c	8.30	1.58 (1.05)	16.2	3.31 (1.09)
L2-A1-c	8.76	1.67 (1.11)	19.8	4.05 (1.33)
L3-A1-c	8.45	1.61 (1.07)	21.6	4.40 (1.45)
L1-A2-c	8.20	1.56 (1.04)	15.2	3.11 (1.02)
L2-A2-c	8.55	1.63 (1.09)	16.8	3.43 (1.13)
L3-A2-c	8.47	1.61 (1.07)	22.0	4.48 (1.47)

Note: (   ) means the ratio of L*n*-A*n*-m/c to L0-A0-m/c

CONCLUTIONS

In order to improve the aseismic performance of steel-pipe piers, a winding method of AFRP sheet on steel-pipe piers was proposed. Herein, monotonic and cyclic loading tests were performed to investigate the strengthening effects and ductility of steel pier models with AFRP sheet. To this end, a total of fourteen pipe-pier models were used with several winding height and profiles of sheet as variables. From this study, the following results are obtained:

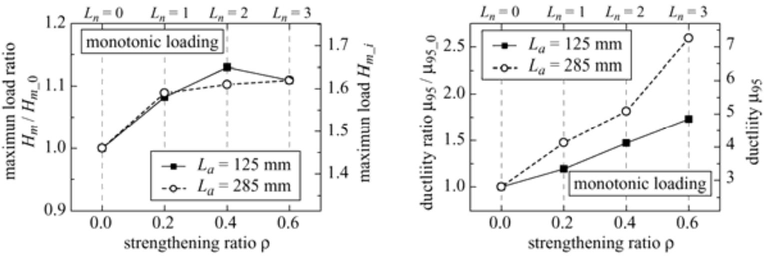

maximum load ductility

(a) monotonic loading

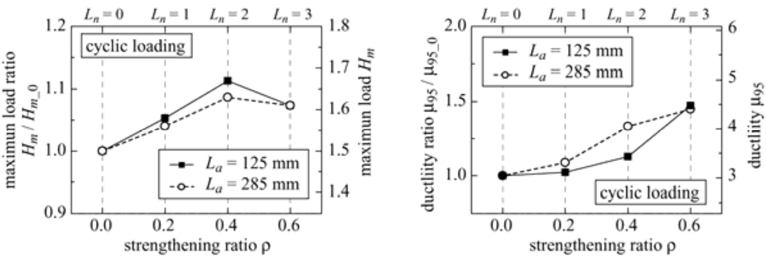

maximum load ductility

(b) cyclic loading

Figure 12. Maximum loading capacity and ductility ratio.

1. By properly winding AFRP sheet near footing area of the steel-pipe model, local buckling mode at collapse is shifted from elephant foot bulge type (EFB) mode to diamond-shape type (DP) mode due to confining effects of AFRP sheet;
2. By winding AFRP sheet on steel-pipe piers, the load-carrying capacity of the pier model cannot be improved significantly but its ductility can be greatly increased; and
3. The L3-A2 specimen was found the best among all specimens in which winding height was L_a = 285 mm and strengthening ratio was $\rho = 0.6$.

REFERENCES

1. Shengbin Gao, Tsutomu Usami, and Hanbin Ge (1998) Ductility evaluation of steel bridge piers with pipe sections, *Journal of Engineering Mechanics*, 124(3), pp.260-267.
2. Yoshiaki Goto, Qingyun Wang, and Makoto Obata (1998) FEM analysis for hysteretic behavior of thin-walled columns, *Journal of Structural Engineering*, 124(11), pp. 1290-1301.
3. H. Koeda, S. Ono, N. Kishi, and Y. Goto (1998) Elasto-plastic behavior of steel-pipe pier models under lateral cyclic loading, *Proceedings of 2nd International Conference on Thin-Walled Structures*, Singapore, pp.787-794.
4. Katsuyoshi Nakanishi, Toshiyuki Kitada, and Hiroshi Nakai (1999) Experimental study on ultimate strength and ductility of concrete filled steel columns under strong earthquake, *Journal of Constructional Steel Research*, 51, pp. 297–319.

AN ASSESSMENT OF THE LEVEL OF LATERAL FLANGE BENDING IN SKEWED AND CURVED GIRDER BRIDGES DUE TO CONCRETE PLACEMENT

Nohemy Y. Galindez[1] *and Karl E. Barth*[1]

INTRODUCTION

This paper presents the results of research aimed at evaluating the levels of lateral flange bending in skewed and curved steel I-girder bridges during deck placement. At this construction stage, exterior girders are most affected by eccentric overhang loading applied by deck forming brackets. This produces torsional effects which are counteracted by internal forces developed primarily in the flanges. These internal lateral forces modify the bending stresses produced by vertical loads, leading in some cases to premature yielding or local buckling of flanges. In skewed and curved girders these effects are amplified by the natural torsion due to the eccentricity of the supports with respect to the loads.

Several past studies have addressed the effects of construction stages on the response of curved bridges (Bell and Linzell, 2007; Howell and Earls, 2007; Chavel and Earls, 2006a & 2006b; Linzell et. al., 2004),

[1] Department of Civil and Environmental Engineering, West Virginia University, Morgantown, WV 26505-6103, Telephone: 304-293-3031 Ext. 2628.

where in most cases numerical evaluations are compared to field or experimental measurements to calibrate models and verify computed predictions on specific bridges. The majority of these research efforts deal with distortions and deflections produced by misalignments of the members on the bridge due to an improper erection procedure; however, a few of them evaluate the lateral stresses produced in the flanges during the deck placement (Shura and Linzell, 2006; Domalik et. al., 2005; Galambos et. al., 2000), but using simplified grillage and frame-element models which results in coarse estimations of the flange-tip stresses. A parametric study published by Davidson et. al. (1996) evaluates the influence of cross-frame spacing, span length, girder depth, number of girders, flange width, girder spacing and degree of curvature into the warping stresses of finite element (FE) models of curved bridges. Shell and beam elements were used to model the webs and the flanges, respectively; therefore, local effects on the flanges were not taken into account. The dead load of the uncured concrete deck is applied to the non-composite section, deck-casting effects are not included since only single span bridges were considered.

As in curved bridges, few referenced works deal with deck-placement issues on skewed bridges (Choo et. al., 2005; Norton et. al., 2003). These works use field measurements to calibrate numerical models for prediction of deformations and stresses; however, little information is given about the lateral-flange-bending behavior produced during the deck placement stage.

Therefore, there is a clear need to study the influence of deck-casting sequences on the lateral flange bending in general skewed and curved steel I-girder bridges to validate or modify the current design specifications. In this work, a comprehensive suite of FE analyses is conducted on representative hypothetical three-span skewed and curved bridges to assess the level of lateral flange bending along the span. Analytical results were compared to predicted values produced from current AASHTO design specifications (AASHTO, 2004). A matrix of parametric variations was developed by varying: radius of curvature, skew angle and central span length. For each hypothetical bridge, lateral flange bending was assessed at each stage in an appropriate deck casting sequence. In each subsequent pouring stage, the respective stiffness of the concrete slab poured in previous steps was modified. The present paper is part of a research work where additional parameters such as number of spans, number of girders, girder spacing and cross-frame orientation (for skewed bridges) would be included along with their effects not only on the lateral flange bending but also on cross-frame forces and web distortions produced during the deck placement.

The results indicate that curved bridges exhibit a significant increase in lateral flange bending in the top flange of the outer girder during intermediate deck placement stages, particularly at positive moment zones where the concrete has not hardened. The lateral flange bending in the bottom flanges also exhibit their maximum values in positive moment regions, however, they are unaffected by the deck casting sequence. Comparisons with current AASHTO specifications show a satisfactory conservatism for straight bridges. Conversely, curved bridges with high curvatures were found to exceed specification requirements for constructibility.

PARAMETRIC STUDY

A parametric study was carried out to investigate the effects of the deck-placement construction stage on the lateral flange bending of skewed and curved bridges. The parametric study is defined by: a. the *parameters* considered as significant in the response of the structure; b. the *design* according to the code provisions of the basic bridge configurations obtained from the parametric evaluation; c. the *models* used to represent the physical behavior of bridge structures; d. the *loads* that represent the real conditions of the construction stage considering the casting-deck sequence; and e. the *analyses* defined for each FE model.

Parameters The selection of the variables considered in this work are intended to cover a wide range of variation in the parameters that govern the practical design of skewed and curved bridges. Subsequent research efforts will refine these ranges and add other variables. However, as a preliminary effort, parameters such as the number of girders (4), the number of spans (3), the girder spacing (12ft), the overhang length (3.6ft), the concrete deck thickness (9in), the material (ASTM A709 Gr.50W) and the ratio of the end-span length to the middle-span length (0.8) were established to form a benchmark bridge. Table 1 contains the parameters considered in this study and their respective values.

Table 1. Parameters and values considered in the parametric study

Parameter	Value
Middle span length (Lm)	150ft – 240ft – 300ft
Ratio of Lm to Radius of curvature (Lm/R)	0.30 – 0.45 – 0.60
Skew angle (θ)	0° - 30° - 45° - 60°

The variation of Lm applies to both skewed and curved bridges; however, there were no considerations of curved bridges with skewed supports. Therefore, a total of 21 different plan view configurations were considered, including the basic straight bridges (θ=0°).

Design Based on the configurations given above, the girders, cross frames and stiffeners of the basic straight bridges were sized according to the design specifications of AASHTO (2004). Changes of section are considered in regions close to the piers; hence, the piece lengths of the girders in the middle and end span (positive moment regions) are 60% and 80% of their respective lengths.

The K-frame cross frames of each configuration were arranged such that their maximum spacing (Lb) in the positive-moment region was close to the maximum traditional value allowed (25ft); in pier regions, the cross frames were set at shorter spacings (17ft – 20ft). For skewed bridges, the cross frames were aligned parallel to the supports; future research will include staggered configurations. The girder plate sizes and the cross-frame spacings of each bridge configuration are given in Table 2 and Table 3, respectively.

Table 2. Girder plate sizes

Lm (ft)	End Span	Pier Zone	Middle Span
150	TF: 18”x1” BF: 18”x1” W: 60”x1/2” L_S: 96ft	TF: 18”x2” BF: 20”x2” W: 60”x1/2” L_S: 54ft	TF: 16”x7/8” BF: 18”x1” W: 60”x1/2” L_S: 90ft
240	TF: 22”x1-1/4” BF: 22”x1-1/4” W: 80”x5/8” L_S: 154ft	TF: 28”x2-3/4” BF: 28”x2-3/4” W: 80”x5/8” L_S: 86ft	TF: 20”x1-1/4” BF: 24”x1-1/4” W: 80”x5/8” L_S: 144ft
300	TF: 28”x1-1/4” BF: 28”x1-1/4” W: 105”x3/4” L_S: 192ft	TF: 32”x2-3/4” BF: 32”x2-3/4” W: 105”x3/4” L_S: 108ft	TF: 26”x”1-1/4 BF: 26”x”1-1/4 W: 105”x3/4” L_S: 180ft

TF: Top Flange; BF: Bottom Flange; W: Web; L_S: Length of the section

Table 3. Cross-frame spacings, Lb (ft)

		End Span		Middle Span	
Bridge Config.	Lm (ft)	M+	M-	M-	M+
ST, SK, CV	150	25	20	20	22
ST, SK, CV	240	25	17	20	25
ST, SK, CV	300	22	20	18	22

ST: Straight; SK: Skewed; CV: Curved

Models FE models were developed for each bridge configuration described above. A MATLAB® program was created to generate the input files (preprocessing) for Abaqus®, where the input variables of the program are the parameters defined above, the mesh geometry described subsequently and the loads. Four nodes shell elements with reduced integration (S4R) were used for the plate girders and the concrete slab. In this preliminary study, the girder flanges were defined with two elements across the width, while six elements were used through the height of the webs. All the girder shell elements are 12-inches long in the longitudinal direction of the bridge; however, the 12-inches length for curved bridges corresponds to the central radius of the bridge, thus the outer-girder elements are longer than the inner-girder ones. The shell elements of the concrete slab are 24in x 24in and are connected to the girder top flanges by multi-point constraints (MPC) which simulate the composite behavior of the deck. The cross frames and the stiffeners were modeled using slender beam elements (B33) considering linear section behavior. Figure 1 shows the FE model of the steel superstructure of a straight bridge. On the other hand, the Von Mises yield criteria, with associated plastic flow rule and isotropic hardening, are used to represent the steel. An isotropic damaged elasticity in combination with isotropic tensile and compressive plasticity is used in the concrete damaged plasticity model to better represent the inelastic behavior of concrete (Barth and Wu, 2006).

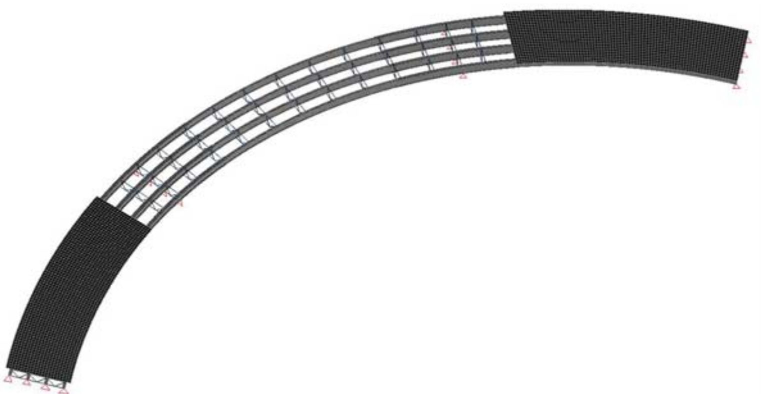

Figure 1. Finite element model of a typical curved bridge at the beginning of the second deck casting stage

Loads The loads considered in the analyses correspond to the construction loads acting during the deck casting process. Permanent dead loads include member self weights. Construction loads include (NSBA, 2003; KDT, 2005):

- *Overhang form brackets*: 50 lbs each, spaced every 3ft
- *Forms*: 15 lb/ft^2

- *Screed rail*: 85 lb/ft
- *Railing*: 25 lb/ft
- *Walkway*: 50 lb/ft^2
- *Finishing machine*: 813 lb/wheel for a total of 8 wheels

The deck casting sequence is comprised of three consecutive stages as shown in Figure 2, where the positive moment regions are poured first. Each pouring stage requires an updated FE model employing different loads and concrete-deck composite conditions; therefore, for each bridge configuration a total of three FE models are run. Within a pouring stage the corresponding concrete weight is applied as a direct vertical load on the non-composite girder sections, but it is extended only up to the middle of that pouring stage length to take into account the effect of the concentrated force produced by the finishing machine. However, the subsequent pouring stages represent the composite action and weight of that already hardened concrete deck by adding shell and *mpc* elements over its corresponding total stage length. The construction loads (except the finishing machine) are applied during the deck casting sequence to the portions of the bridge where the composite behavior of the concrete deck is not yet included. For skewed bridges, the deck placement was considered parallel to the skew angle. The construction joints for curved and skewed bridges are radial and parallel to the supports, respectively.

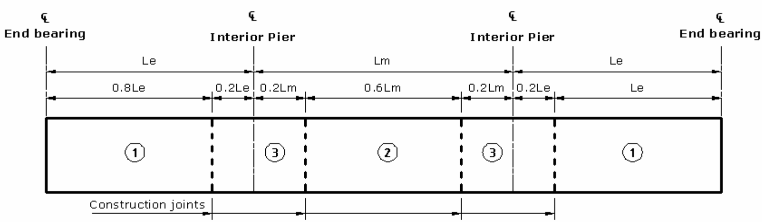

Figure 2. Deck casting sequence

The torsional effects (represented by horizontal forces) are produced by the linear and concentrated forces assumed to be at the end of the overhang length, these forces include the reactions of the distributed loads per unit area over the overhang zone, as shown in Figure 3. The ultimate loads correspond to the Strength Load Combination I of the specifications, which states that the load factors for this specific combination shall not be taken to be less than 1.25 and 1.5 for the weight of the structure and the construction loads, respectively (AASHTO, 2004). Therefore, these recommended values were used for the factored loads presented in this work.

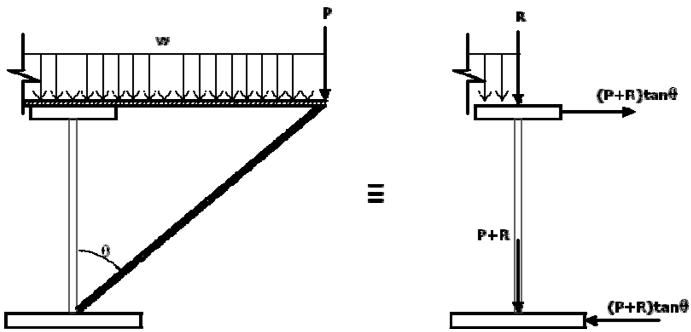

Figure 3. Torsional effects on exterior girders produced by overhang loads

Analyses A static stress analysis is defined for each FE model, where the total load is applied in two steps: gravity and constructional loads. The constructional-load step uses the modified Riks algorithm which takes into account the nonlinear behavior due to material or geometric effects. The Riks method uses the load magnitude as an additional unknown; therefore, it solves simultaneously for loads and displacements. ABAQUS uses the *arc length* as the parameter to quantify the progress of the solution along the static equilibrium path in the load-displacement space. This approach provides solutions regardless of whether the response is stable or unstable (Abaqus, 2004).

RESULTS AND DISCUSSION

Another MATLAB® program was developed to perform the postprocessing of the results obtained for the complete set of FE models (81 models). All the results presented in this paper correspond to the load combination described above which considers the construction loads and the corresponding dead loads.

The effects on the lateral flange bending (LFB) of parameters such as the ratio of curvature (L/R), skew angle (θ), span length (Lm), flange position (top or bottom), girder position (outer or inner for curved bridges) and deck casting sequence (C1, C2 and C3), were evaluated using the specification limit for the lateral bending stress (f_l):

$$\frac{f_l}{F_{yf}} \leq 0.6 \qquad \text{(Eq. 6.10.1.6-1 of AASHTO, 2004)}$$

where F_{yf} is the specified minimum yield strength of the flange.

In addition, the flexural resistance equations for the constructibility limit state (given by Eqs. 6.10.3.2.1, -.2 and -.3 of AASHTO, 2004) in their normalized form (Demand/Capacity) were also used to evaluate the parametric effects.

Curvature and skewness effect The curvature ratio has a considerable effect on LFB as shown in Figure 4a. In regions of maximum moment, the stress values for models with 0.3 and 0.6 ratios of curvature were increased concerning the straight models up to 3 and 6 times, respectively. Conversely, Figure 4b indicates that the skew angle does not affect the LFB stresses of the skewed bridge models considered in the present work. However, it is necessary to study additional geometrical and loading conditions such as staggered cross frame configurations and concrete placing perpendicular to the bridge centerline, to adequately define the effect of skew.

Girder position in curved bridges Figure 5 shows that the most critical LFB stresses correspond to the outer girder where the increments are proportional to the curvature ratio. However, the inner girder exhibits an opposite behavior since the curvature has a beneficial effect on the LFB. This fact suggests that on curved bridges the girder position should be considered as a design parameter. All the subsequent results shown in this paper correspond to the maximum values given by outer girders.

Casting sequence and flange position According to Figure 6, the top flange (TF) presents the highest levels of lateral flange bending in positive moment regions when the concrete is unhardened. However, under the composite action the lateral flange bending practically vanishes on the TF. On the other hand, the bottom flange (BF) exhibits almost the same maximum values of lateral flange bending during the complete deck casting sequence in regions of positive moment. It is also noticed that for both TF and BF the influence of the LFB in the pier zones is minor. These observations are also confirmed by Figure 7, where the normalized flexural equations for constructibility show that the maximum combined effects of main bending and LFB stresses are given in positive moment regions for both TF (during non-composite action only) and BF. In regions either under composite action or close to the piers, only the main bending stresses are significant.

Length effect According to Figure 8, the LFB stresses in straight bridges reduce considerably as length increases while important levels of LFB are exhibited in curved bridges even for long span lengths, principally in positive moment regions. With respect to the main bending stresses, they increase with length for both curved and straight bridges; however, this effect is amplified in the outer curved girders since they are longer than the corresponding straight ones. Therefore, the demand/capacity ratios given by the flexural equations become more critical for curved bridges in the positive moment regions, as shown in Figure 9.

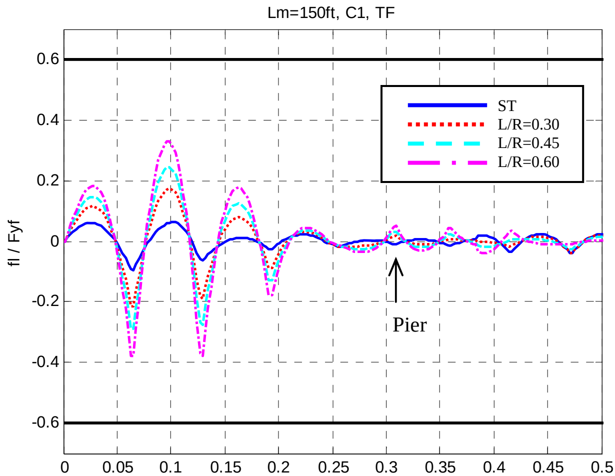

a. Curved Bridge Model

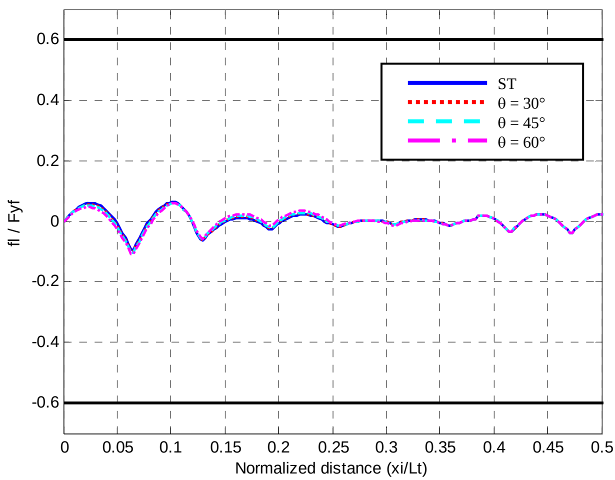

b. Skewed Bridge Model

Figure 4. Curvature and skewness effect on the LFB

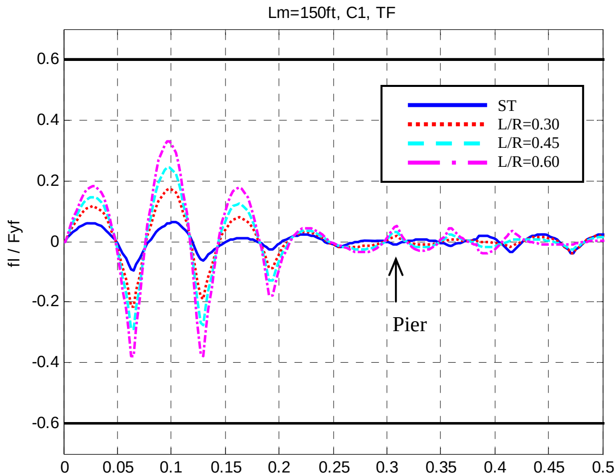

a. Outer girder

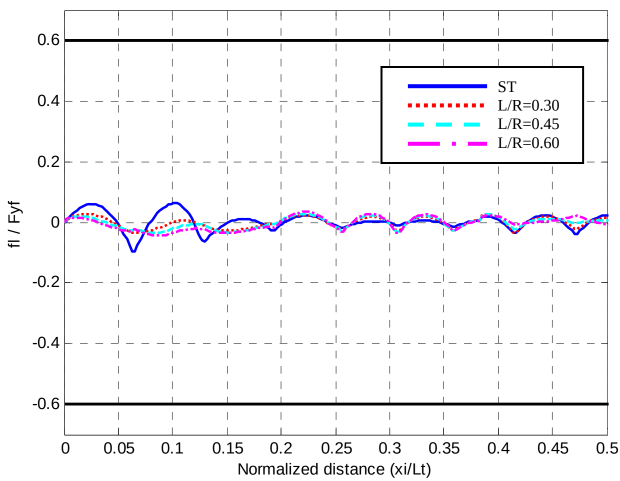

b. Inner girder

Figure 5. Girder position effect on the LFB for curved bridges

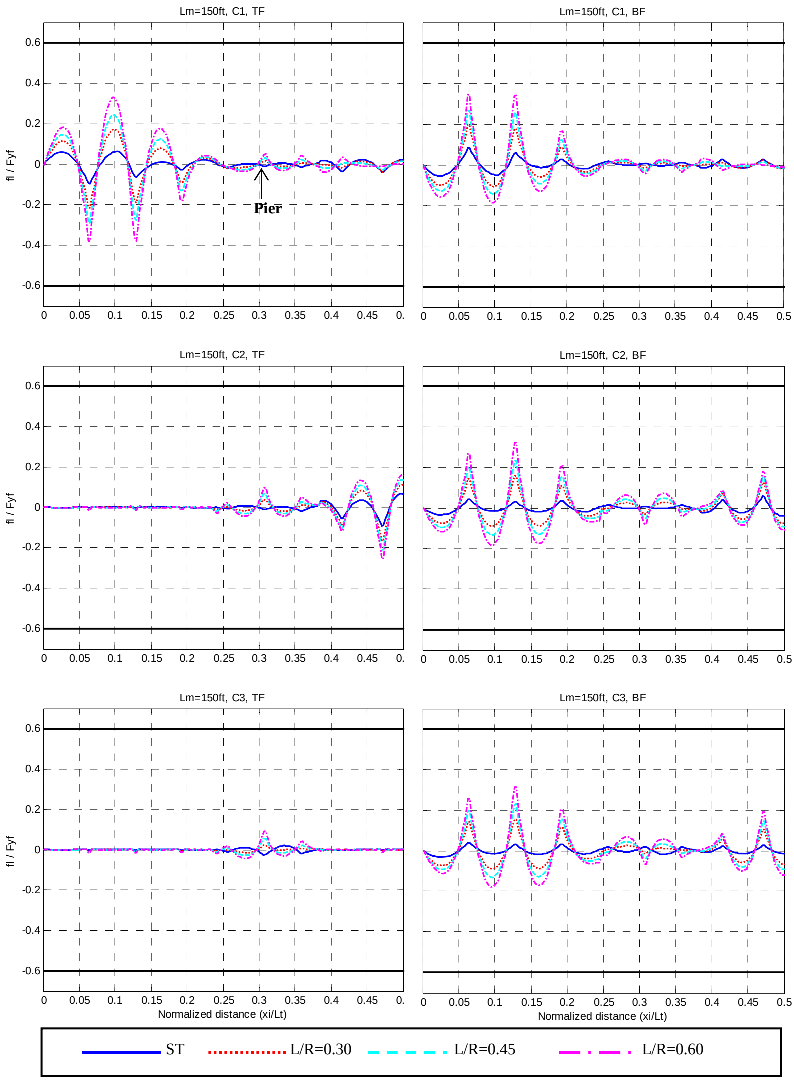

Figure 6. LFB for TF and BF during the deck casting sequence (CV model)

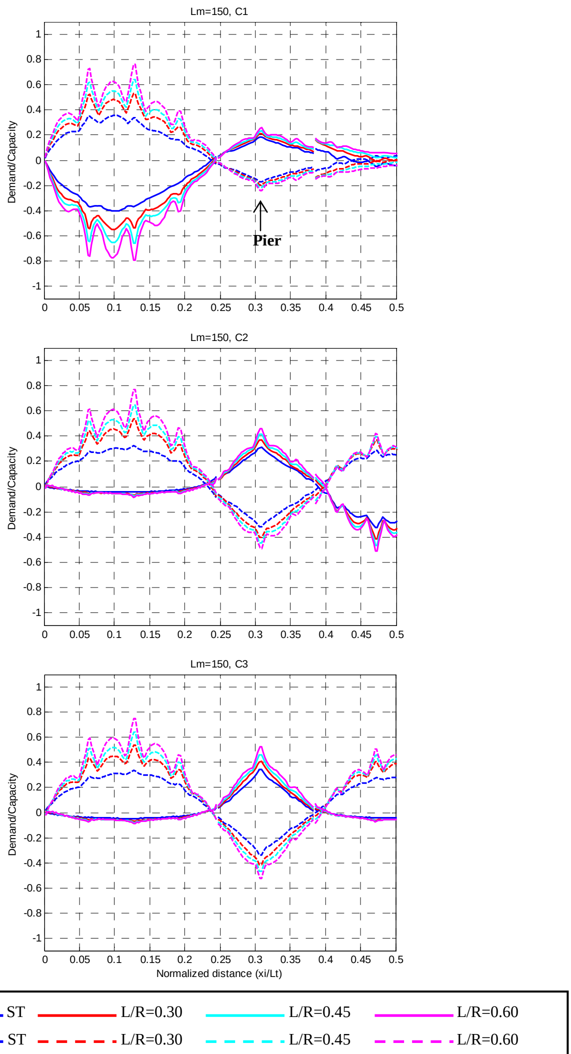

Figure 7. AASHTO equations for TF and BF during the deck casting sequence (CV model)

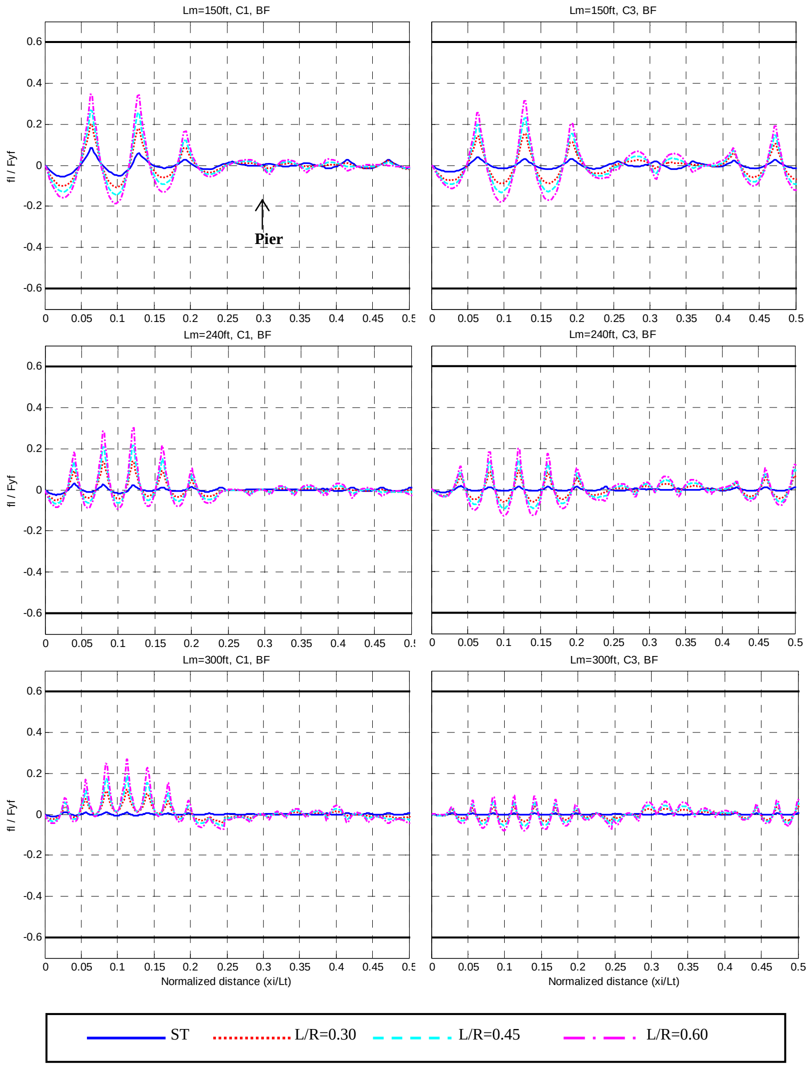

Figure 8. LFB variation for different span lengths

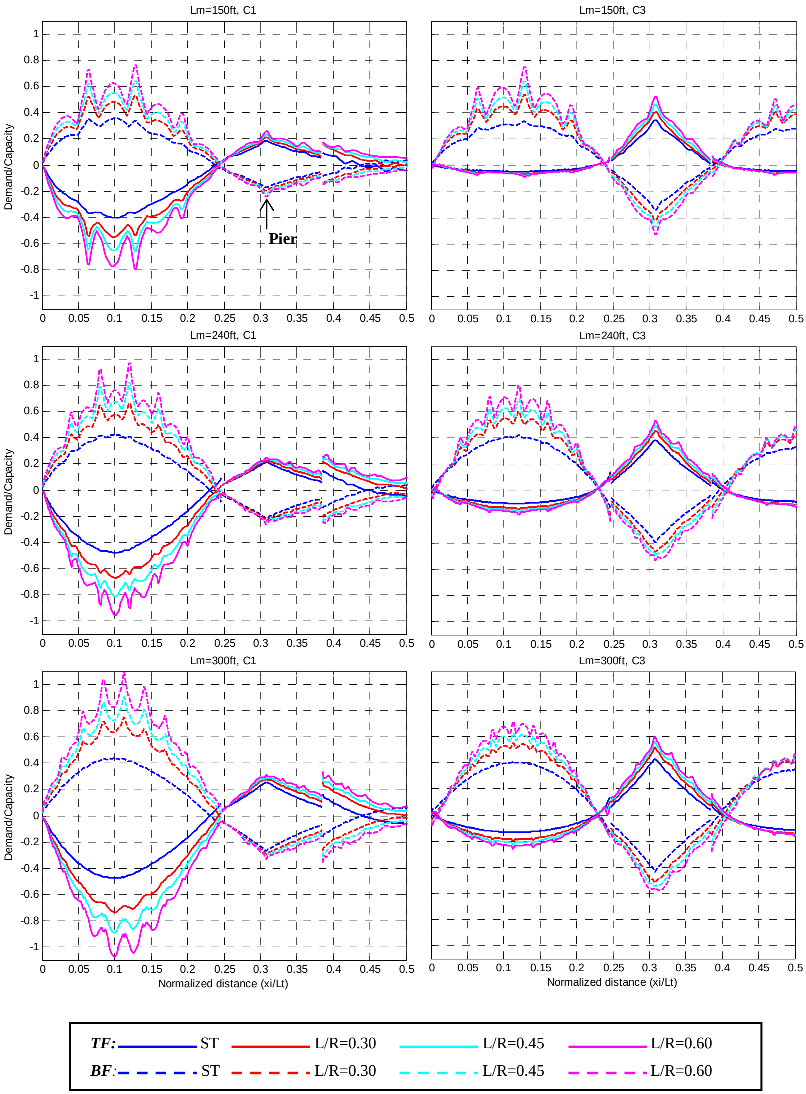

Figure 9. AASHTO equations for different Lm values during C1 and C3

CONCLUSIONS

This paper presents the preliminary results of a study focused on evaluating the levels of lateral flange bending in skewed and curved steel I-girder bridges during deck placement. The primary goal of this preliminary study was to assess key variable to better define a larger parametric study. Additional studies will focus on assessing mesh refinement and considering additional parameters such as number of spans, number of girders, girder spacing and cross-frame orientation (for skewed bridges).

The results of this effort suggest that the curvature ratio has a considerable effect on the lateral flange bending. Curved bridges with high curvatures are prone to exceed the flexural code requirements for constructibility in the positive moment regions, while the corresponding straight bridges exhibit a conservative behavior. Moreover, high levels of lateral flange bending are exhibited on the top flanges in zones of positive moment during intermediate deck casting stages where the concrete is unhardened; however, these stresses disappear under the composite action. The lateral flange bending in the bottom flanges also exhibit their maximum values in positive moment regions, however, they are unaffected by the deck casting sequence. The lateral flange bending effect was found to be negligible in regions close to the piers, which are principally controlled by the main bending stresses. The girder position in curved bridges also affects the stress levels on the flanges since the lateral flange bending is amplified in outer girders while the opposite occurs in inner girders.

A larger goal of this effort is to assess the parametric study not only on the lateral flange bending but also on cross-frame forces and web distortions produced during the deck placement.

REFERENCES

AASHTO (2004) “AASHTO LRFD Bridge Design Specifications, Customary U.S. units.” 3rd Ed, Washington, D.C.

Abaqus (2002) Manuals – Documentation. Version 6.3.1. Hibbit, Karlson & Sorenson, Inc., Pawtucket, RI.

Barth, K., and Wu, H. (2006) "Efficient Nonlinear Finite Element Modeling of Slab on Steel Stringer Bridges." *Finite Elements in Analysis and Design*, Vol. 42, Issue 14: 1304-1313.

Bell, B., and Linzell, D. (2007). "Erection Procedure Effects on Deformations and stresses in a Large-radius, horizontally curved, I-girder Bridge." *Journal of Bridge Engineering*, Vol. 12, No. 4: 467-476.

Chavel, B. W., and C. J. Earls. (2006) "Construction of a Horizontally Curved Steel I-Girder Bridge. Part II: Inconsistent Detailing." *Journal of Bridge Engineering*, Vol. 11. Issue 1: 91-98.

Chavel, B. W., and C. J. Earls. (2006) "Construction of a Horizontally Curved Steel I-Girder Bridge. Part I: Erection Sequence." *Journal of Bridge Engineering,* Vol. 11. Issue 1: 81-90.

Choo, T., Linzell, D., Lee, J., and Swanson, J. (2005) "Response of a continuous, skewed, steel bridge during deck placement." *Journal of Constructional Steel Research*, Vol. 61: 567-586.

Davidson, J., Keller, M., and Yoo, C. (1996) "Cross-frame spacing and parametric effects in horizontally curved I-girder bridges" *Journal of Structural Engineering,* Vol. 122, No. 9: 1089-1096.

Domalik, D., Shura, J., and Linzell, D. (2005) "Design and Field Monitoring of Horizontally Curved Steel Plate Girder Bridge." *Journal of the Tranportation Research Board,* Issue 1928: 83 –91.

Galambos, T., Hajjar, J., Huang, W., Pulver, B., Leon, R., and Rudie, B. (2000) "Comparison of measured and computed stresses in a steel curved girder bridge" *Journal of Bridge Engineering,* Vol. 5, No.3: 191-199.

Howell, T., and Earls, C. (2007). "Curved Steel I-girder bridge response during construction loading: effects of web plumbness". *Journal of Bridge Engineering*, Vol. 12, No. 4: 485-493.

KDT (2005) "Design Manual – Ch.5 Falsework design, analysis and inspection." Kansas Department of Transportation, Version 1, Vol. 3.

Linzell, D., Leon, R., and A. H. Zureick. (2004) "Experimental and Analytical Studies of a Horizontally Curved Steel I-Girder Bridge during Erection." *Journal of Bridge Engineering*, Vol. 9, Issue 6: 521-530.

MATLAB (2004) Documentation. Version 7.0. The Mathworks, Inc., Novi, MI.

Norton, E., Linzell, D., and Laman, J. (2003) "Examination of Response of a Skewed Steel Bridge Superstructure During Deck Placement." *Transportation Research Record,* Issue 1845: 66–75.

NSBA (2002) "Design Example 1: Three-Span Continuous Straight Composite I Girder." Part of *The Steel Bridge Design Handbook*, National Steel Bridge Alliance, Omaha, NE.

Shura, J., and Linzell, D. (2006) "Behavior of a horizontally curved steel plate girder bridge during steel erection and deck placement". TRB Annual Meeting, Washington, D.C.

COMPARISON OF DESIGN METHODS FOR LOCALLY SLENDER STEEL COLUMNS

B.W. Schafer[1] and M. Seif[2]

ABSTRACT
The objective of this paper is to provide a comparison between three Specification approved methods currently applicable to the design of locally slender steel columns. The AISC W-section is selected as the geometry for the comparisons. The local cross-section stability of all W-sections in the AISC Manual is assessed using finite strip analysis and compared with plate buckling solutions in common use. Significant web-flange interaction in local buckling is observed in the majority of sections. The design strength formulas for a locally slender W-section column performed by the AISC Q-factor approach, AISI Effective Width Method, and AISI Direct Strength Method are all provided in a common set of notation. The role of cross-section stability in the prediction equations is highlighted. The potential to use cross-section stability solutions for local stability instead of plate buckling solutions is investigated. Through parametric studies the Q-factor treatment of unstiffened elements is shown to be more conservative than the Effective Width Method, particularly as the unstiffened element becomes more slender. The Q-factor treatment of stiffened elements is generally found to be similar, but slightly less conservative than the Effective Width Method. Also, the Direct Strength Method is shown to sometimes follow different trends than the other methods, particularly with respect to web-flange interaction. The parameters that lead to significant differences between the design methods are the focus of a nonlinear finite element analysis study currently getting underway.

---

[1] Associate Professor, Johns Hopkins University, schafer@jhu.edu
[2] Graduate Research Asst., Johns Hopkins University, mseif1@jhu.edu

INTRODUCTION

In the design of hot-rolled steel structural members typical practice is to avoid locally slender (noncompact) cross-sections. However, this strategy becomes impossible with standard shapes if high or ultra-high yield strength steels are used, since flange and web slenderness limits are a function of yield stress. The Q-factor approach in the American Institute for Steel Construction (AISC) Specification is currently used for designing such slender cross-sections, and has been in-place for a number of years. However, new open source analysis packages now allow local buckling to be determined with full accounting of web-flange interaction, and new design methods have been developed that take advantage of such analysis. With the potential for higher yield stress steels and the availability of new analysis and design methods now seems a good time to take a fresh look at the design of locally slender steel cross-sections.

DEFINITION OF VARIABLES

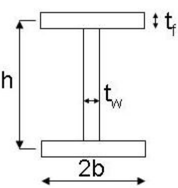

Sketch showing simplified section geometry

b : Half of the flange width ($b_f = 2b$).
t_f : Flange thickness.
h : centerline web height.
t_w : Web thickness.
E : Young's modulus of elasticity.
ν : Poisson's ratio.
L : Length of the member.
r : Governing radius of gyration.
K : Effective length factor.
k_f : Flange local plate buckling coefficient.
k_w : Web local plate buckling coefficient.
P_n : Nominal section compressive strength.
A_g : Gross area of the section.
f_y : Yield stress.
f_e : Global elastic buckling stress, e.g., $\pi^2 E/(KL/r)^2$.
f_{crb} : Flange elastic local buckling stress $= k_f\left(\pi^2 E/\left(12\left(1-\nu^2\right)\right)\right)\left(t_f/b\right)^2$.
f_{crh} : Web elastic local buckling stress $= k_w\left(\pi^2 E/\left(12\left(1-\nu^2\right)\right)\right)\left(t_w/h\right)^2$.
$f_{cr\ell}$: cross-section elastic local buckling stress. e.g. by finite strip

CROSS-SECTION BUCKLING BY FINITE STRIP ANALYSIS

Finite strip analysis was performed for compressive load on the W-sections from the AISC (2005b) Manual of Steel Construction. The analysis was completed using CUFSM version 3.12 (Schafer and Adany 2006). Sections were simplified to their centerline geometry (the increased width in the k-zone was thus ignored). The cross-section local buckling stress (f_{crB}) was identified from the buckling half-wavelength vs. load factor curve. Exact (elastic) plate buckling coefficients are found, for example, by setting $f_{crb}=f_{crB}$ and solving for k_f. The resulting k_f and k_w values are provided in Figure 1. The results of Figure 1 underscore the significant impact of web-flange interaction on local buckling.

The typically cited theoretical limits for the local plate bucking coefficient, k_f, of an isolated flange (an unstiffened element) vary from 0.43, simply supported on one longitudinal edge free on the other longitudinal edge, to 1.3, fixed on one longitudinal edge free on the other longitudinal edge (Galambos 1998). The AISC Specification assumes a k_f value of 0.7 (Salmon and Johnson 1996). Figure 1 shows k_f varies from 0.04 to 0.62 for elastic local buckling. For webs, The theoretical limits for the local plate buckling coefficient, k_w, of an isolated web (a stiffened element) vary from 4 to 7 (simply supported to fixed edges) in pure compression. The AISC Specification assumes a k_w of 5. The exact elastic local buckling k_w values vary from 1.9 to 5.7. As with the flange values, it is clear that web-flange interaction plays a significant role.

For both the web and flange results, not only is their a large difference between the assumed k values and those calculated, but also the calculated values can be outside expected bounds. For example, for the flange numerous k_f values are below 0.43. In these cases web local buckling is driving the flange local buckling. The situation for the flange is worse than simply supported, as the flange must provide rotational stiffness to the web for the section to remain stable. Traditionally, it has been assumed that plate buckling coefficients between simply supported and fixed values provide reasonable bounds (e.g., see Salmon and Johnson 1996), but if local buckling of the entire cross-section is considered a much wider range of k values are possible.

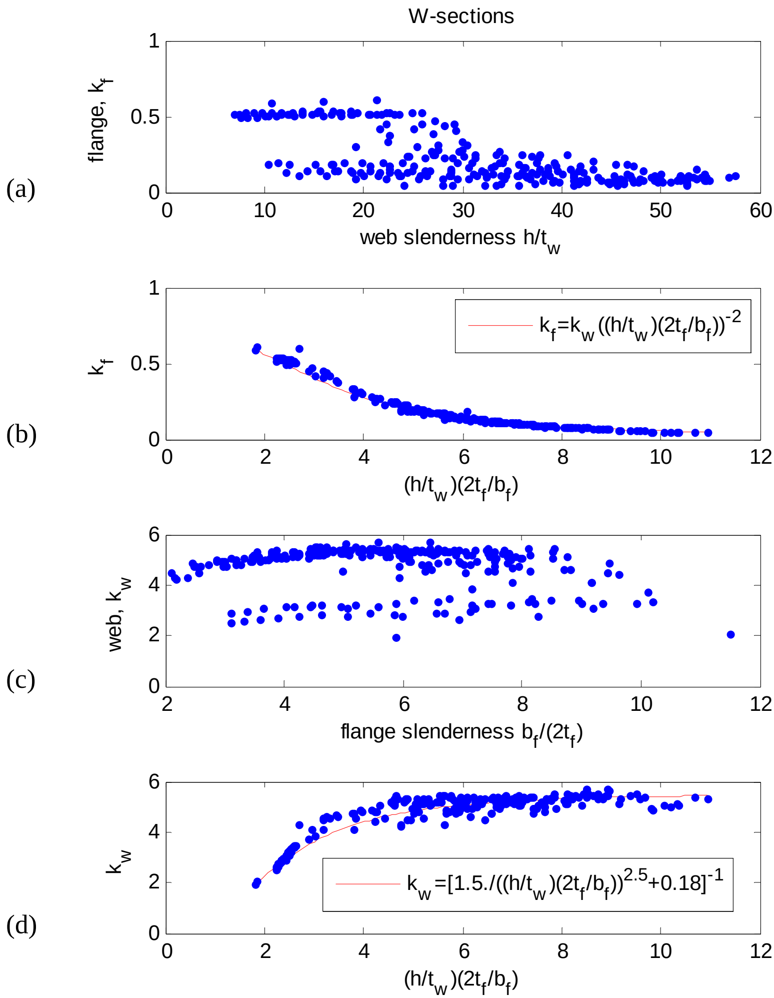

Figure 1 Flange and web local buckling coefficients for AISC W-sections under axial loading.

Given the functional relationships that are revealed in Figure 1(b) and (d) empirical expressions closely matching the finite strip results are possible. Such expressions for W-sections are provided in Schafer and Seif 2007 and for all other AISC Manual sections (WT, C, L, etc) in compression and bending, in Seif and Schafer 2007.

COMPARING THE AISC, AISI, AND DSM DESIGN METHODS

A number of different methods exist for the design of steel columns with slender cross-sections, three of which are detailed here: AISC, AISI, and DSM*. The AISC method, as embodied in the 2005 AISC Specification, uses the Q-factor approach to adjust the global slenderness in the inelastic regime of the column curve to account for local-global interaction, and further uses a mixture of effective width (for stiffened elements) and average stress (for unstiffened elements) to determine the final reduced strength.

The AISI method, from the main body of the 2007 AISI Specification for cold-formed steel, uses the effective width approach. In the AISI method the global column curve is unmodified but the column area is reduced to account for local buckling in both stiffened and unstiffened elements via the same effective width equation. Finally, the DSM or Direct Strength Method, as given in Appendix 1 of the 2007 AISI Specification for cold-formed steel, uses a new approach where the global column strength is determined and then reduced to account for local buckling based on the local buckling cross-section slenderness.

To provide a more definitive comparison between these three methods the formulas are detailed in the subsequent sections for a centerline model of a W-section in compression. The formulas are presented in a common set of notation. Intermediate derivation steps are shown only for the AISC formulas. In addition, the format of presentation is modified from that used directly in the respective Specifications so that (1) the methods may be most readily compared to one another and (2) the key input parameters are brought to light.

---

* Strictly, only the AISC method is applicable to the locally slender hot-rolled steel columns studied here. Comparison of Q-factor and Effective Width methods has been completed by a number of researchers (see, e.g. Galambos 1998 for further discussion). Inclusion of DSM and cross-section local buckling are novel aspects of this paper.

AISC SLENDER COLUMN DESIGN (Q-FACTOR APPROACH)

The AISC procedure for a column with slender elements is summarized in Section E7 of the 2005 AISC Specification. Specifically, the compressive strength for a centerline model of a W-section is:

$$P_n = A_g \begin{cases} Q(0.658)^{Q(f_e/f_y)} f_y & \text{for: } f_e \geq 0.44Qf_y \\ 0.877 f_e & \phantom{\text{for: }} f_e < 0.44Qf_y \end{cases} \tag{1}$$

where:

$$Q = Q_s Q_a \tag{2}$$

and Q_s is a flange reduction factor for unstiffened elements that depends on the flange slenderness as follows:

$$Q_s = 1.0 \qquad \text{if } b/t_f \leq 0.56\sqrt{E/f_y} \tag{3}$$

$$Q_s = 1.415 - 0.74\left(\frac{b}{t_f}\right)\sqrt{\frac{f_y}{E}} \qquad \text{if } 0.56\sqrt{E/f_y} < b/t_f < 1.03\sqrt{E/f_y} \tag{4}$$

$$Q_s = \frac{0.69E}{f_y\left(\frac{b}{t_f}\right)^2} \qquad \text{if } b/t_f \geq 1.03\sqrt{E/f_y} \tag{5}$$

Q_a is a web reduction factor, defined as the ratio between the effective area of the cross section and the total cross sectional area:

$$Q_a = A_{eff} / A_g = h_e t_w / A_g \,, \tag{6}$$

where h_e is defined as

$$h_e = h \qquad \text{if } h/t_w < 1.49\sqrt{E/f} \tag{7}$$

$$h_e = 1.92 t_w \sqrt{\frac{E}{f}}\left[1 - \frac{0.34}{(h/t_w)}\sqrt{\frac{E}{f}}\right] \leq h \qquad \text{if } h/t_w \geq 1.49\sqrt{E/f} \tag{8}$$

and

$$f = P_n / A_{eff} \tag{9}$$

In this form determination of f, and thus h_e and Q_a requires iteration. The AISC Specification notes that f may be conservatively set to f_y. More practically, a reasonable estimate of the f from the iteration may be had without iteration – simply by using the stress from the global buckling column curve with Q = 1, i.e.,

$$\text{estimated } f = \begin{cases} (0.658)^{(f_e/f_y)} f_y & \text{for: } f_e \geq 0.44 f_y \\ 0.877 f_e & \phantom{\text{for: }} f_e < 0.44 f_y \end{cases} \tag{10}$$

This approximation to f is conservative since Eq. 10 will always be greater than the f resulting from Eq. 1 (because Q is strictly less than 1), but Eq. 10's approximation for f is also always less than or equal to f_y.

The AISC expressions may be rewritten to better contrast them with their AISI counterparts and highlight the role of cross-section stability:

$$P_n = A_g \hat{f}_n \tag{11}$$

$$\hat{f}_n = \begin{cases} Q_s Q_a (0.658)^{Q_s Q_a (f_e/f_y)} f_y & \text{if } f_e \geq 0.44 Q_s Q_a f_y \\ 0.877 f_e & \text{if } f_e < 0.44 Q_s Q_a f_y \end{cases} \tag{12}$$

The Q factors may be written directly in terms of the flange and web critical buckling stresses as shown in Eq.'s 13 through 17. Q_s, the flange reduction factor depends on f_{crb} as follows:

$$f_{crb} \geq 2 f_y: \qquad Q_s = 1.0 \tag{13}$$

$$\frac{3}{5} f_y < f_{crb} < 2 f_y: \quad Q_s = 1.415 - 0.59 \sqrt{\frac{f_y}{f_{crb}}} \tag{14}$$

$$f_{crb} \leq \frac{3}{5} f_y: \qquad Q_s = 1.1 \frac{f_{crb}}{f_y} \tag{15}$$

while Q_a, the web reduction factor depends on f_{crh} as follows:

$$f_{crh} > 2f: \qquad Q_a = 1.0 \tag{16}$$

$$f_{crh} \leq 2f: \qquad Q_a = 1 - \left(1 - 0.9\sqrt{\frac{f_{crh}}{f}}\left(1 - 0.16\sqrt{\frac{f_{crh}}{f}}\right)\right)\frac{ht_w}{A_g} \tag{17}$$

Note, that the ratio of the web area to the gross area appears in Eq. 17 due to the AISC methodology where only stiffened elements are treated as being reduced to effective width, and hence effective area.

AISI (AISI – EFFECTIVE WIDTH METHOD)

The AISI Effective Width method is detailed in the 2007 AISI Specification (AISI-S100 2007). The long column (global buckling) design expressions are provided in Section C4.1 of AISI-S100, the effective width reductions follow Section B2.1 for the web (stiffened element) and B3.1 for the flange (unstiffened element). The expressions provided in Table 1 and Table 2 are not in the same format as AISI-S100 but have been derived here for the purposes of comparison.

DSM (AISI – DIRECT STRENGTH METHOD)

The AISI Direct Strength Method (DSM) is detailed in Appendix 1 of the 2007 AISI Specification. The long column (global buckling) design expression is identical to that in C4.1 of the main AISI Specification. The local buckling strength uses the long column strength as its maximum capacity. The DSM expressions provided in Table 1 and Table 2 have been formulated for comparison to the AISC and AISI Effective Width expressions, and are not in the same form as shown in DSM Appendix 1.

DIRECT COMPARISON OF DESIGN EXPRESSIONS

The design expressions for all three methods, in a common notation system, are provided in Table 1 for the general case of a W-section column and Table 2 for a W-section stub column assuming cross-section local buckling ($f_{cr\ell}$) is used in place of isolated plate buckling solutions (f_{crb} and f_{crh}). Although the expressions appear quite different in the format of their original Specification's – in this format (Table 1) they can be seen to have many similarities.

The number of free parameters in slender column design is actually significantly less than one might typically think. Based on Table 1, and performing a simple non-dimensional analysis, the parameters for determining the column strength of an idealized W-section are:

AISC: $P_n/P_y = \mathrm{f}\,(f_e/f_y, f_{crb}/f_y, f_{crh}/f_y, ht_w/A_g)$
AISI: $P_n/P_y = \mathrm{f}\,(f_e/f_y, f_{crb}/f_y, f_{crh}/f_y, ht_w/A_g$ or $2b_ft_f/A_g)$
DSM: $P_n/P_y = \mathrm{f}\,(f_e/f_y, f_{cr\ell}/f_y,)$

The central role of elastic buckling prediction both globally (f_e) and locally (f_{crb}, f_{crh} or $f_{cr\ell}$) in determining the strength of the column is clear. Further, the "direct" nature of the DSM approach is highlighted as DSM only uses ratios of critical buckling values to determine the strength; where AISC and AISI still involve cross-section parameters beyond determination of gross area and critical stress.

Table 1 Comparison of column design equations for a slender W-section in a common notation*

AISC inputs to find P_n A_g = gross area f_e = global buckling stress f_y = yield stress f_{crb} = flange local buckling stress f_{crh} = web local buckling stress ht_w/A_g = web/gross area Comments: shifts the slenderness in the global column curve in the inelastic range only, assumes that unstiffened elements (flange) should be referenced to f_y, only applies an effective width style reduction to stiffened elements (the web), includes an iteration for web stress f.	$P_n = A_g \hat{f}_n$ $\hat{f}_n = \begin{cases} Q_s Q_a (0.658)^{Q_s Q_a (f_e/f_y)} f_y & \text{if } f_e \geq 0.44 Q_s Q_a f_y \\ 0.877 f_e & \text{if } f_e < 0.44 Q_s Q_a f_y \end{cases}$ $Q_s = \begin{cases} 1.0 & \text{if } f_{crb} \geq 2 f_y \\ 1.415 - 0.59\sqrt{\dfrac{f_y}{f_{crb}}} & \text{if } \dfrac{3}{5} f_y < f_{crb} < 2 f_y \\ 1.1\dfrac{f_{crb}}{f_y} & \text{if } f_{crb} \leq \dfrac{3}{5} f_y \end{cases}$ $Q_a = \begin{cases} 1.0 & \text{if } f_{crh} > 2f \\ 1 - \left(1 - 0.9\sqrt{\dfrac{f_{crh}}{f}}\left(1 - 0.16\sqrt{\dfrac{f_{crh}}{f}}\right)\right)\dfrac{ht_w}{A_g} & \text{if } f_{crh} \leq 2f \end{cases}$ $f = \dfrac{P_n}{Q_a A_g} \sim \hat{f}_n$ determined with $Q_s = Q_a = 1$
AISI - Effective Width inputs to find P_n A_g = gross area f_e = global buckling stress f_y = yield stress f_{crb} = flange local buckling f_{crh} = web local buckling bt_f = flange area ht_w = web area Comments: no shift in global column curve, effective width used for stiffened and unstiffened elements.	$P_n = A_{eff} f_n$ $f_n = \begin{cases} (0.658)^{(f_e/f_y)} f_y & \text{if } f_e \geq 0.44 f_y \\ 0.877 f_e & \text{if } f_e < 0.44 f_y \end{cases}$ $A_{eff} = 4\rho_b b t_f + \rho_h h t_w$ $b_e = \rho_b b$ where $\rho_b = \begin{cases} 1 & \text{if } f_{crb} \geq 2.2 f_n \\ \left(1 - 0.22\sqrt{\dfrac{f_{crb}}{f_n}}\right)\sqrt{\dfrac{f_{crb}}{f_n}} & \text{if } f_{crb} < 2.2 f_n \end{cases}$ $h_e = \rho_h h$ where $\rho_h = \begin{cases} 1 & \text{if } f_{crh} \geq 2.2 f_n \\ \left(1 - 0.22\sqrt{\dfrac{f_{crh}}{f_n}}\right)\sqrt{\dfrac{f_{crh}}{f_n}} & \text{if } f_{crh} < 2.2 f_n \end{cases}$
AISI - DSM inputs to find P_n A_g = gross area f_e = global buckling stress f_y = yield stress f_{crB} = local buckling stress Comments: similar to AISI but reductions on whole section and "effective width" equation modified.	$P_n = A_{eff} f_n$ $f_n = \begin{cases} (0.658)^{(f_e/f_y)} f_y & \text{if } f_e \geq 0.44 f_y \\ 0.877 f_e & \text{if } f_e < 0.44 f_y \end{cases}$ $A_{eff} = \rho A_g$ $\rho = \begin{cases} 1 & \text{if } f_{crB} \geq 1.66 f_n \\ \left(1 - 0.15\left(\dfrac{f_{crB}}{f_n}\right)^{0.4}\right)\left(\dfrac{f_{crB}}{f_n}\right)^{0.4} & \text{if } f_{crB} < 1.66 f_n \end{cases}$

* centerline model of W-section (ignores k-zones) in practice AISC and AISI use slightly different k values for f_{crb} and f_{crh}.

Table 2 Comparison of stub column design equations for a slender W-section when cross-section elastic local buckling replaces isolated plate buckling solutions, i.e., $f_{crB} = f_{crb} = f_{crh}$ and when global buckling is assumed to be fully braced.

AISC inputs to find P_n A_g = gross area f_y = yield stress f_{crB} = local buckling stress ht_w/A_g = web/gross area Comments: adoption of f_{crB} for f_{crb} and f_{crh} does not simplify the AISC methodology significantly. Unstiffened and stiffened elements are treated inherently differently in the AISC methodology.	$P_n = Q_s Q_a A_g f_y$ $Q_s = \begin{cases} 1.0 & \text{if } f_{crB} \geq 2f_y \\ 1.415 - 0.59\sqrt{\frac{f_y}{f_{crB}}} & \text{if } \frac{3}{5}f_y < f_{crB} < 2f_y \\ 1.1\frac{f_{crB}}{f_y} & \text{if } f_{crB} \leq \frac{3}{5}f_y \end{cases}$ $Q_a = \begin{cases} 1.0 & \text{if } f_{crB} > 2f_y \\ 1 - \left(1 - 0.9\sqrt{\frac{f_{crB}}{f_y}}\left(1 - 0.16\sqrt{\frac{f_{crB}}{f_y}}\right)\right)\frac{ht_w}{A_g} & \text{if } f_{crB} \leq 2f_y \end{cases}$
AISI – Effective Width inputs to find P_n A_g = gross area f_y = yield stress f_{crB} = local buckling stress Comments: when f_{crB} is used for f_{crb} and f_{crh} the methodology becomes the same as DSM, but with a more conservative local buckling predictor equation.	$P_n = A_{eff} f_y$ $A_{eff} = \rho A_g$ $\rho = \begin{cases} 1 & \text{if } f_{crB} \geq 2.2f_y \\ \left(1 - 0.22\sqrt{\frac{f_{crB}}{f_y}}\right)\sqrt{\frac{f_{crB}}{f_y}} & \text{if } f_{crB} < 2.2f_y \end{cases}$
AISI – DSM inputs to find P_n A_g = gross area f_y = yield stress f_{crB} = local buckling stress Comments: no change from general case	$P_n = A_{eff} f_y$ $A_{eff} = \rho A_g$ $\rho = \begin{cases} 1 & \text{if } f_{crB} \geq 1.66f_y \\ \left(1 - 0.15\left(\frac{f_{crB}}{f_y}\right)^{0.4}\right)\left(\frac{f_{crB}}{f_y}\right)^{0.4} & \text{if } f_{crB} < 1.66f_y \end{cases}$

STUB COLUMN COMPARISON

Since all three methods use the same global buckling column curve (though AISC uses the Q-factor approach which adjusts the slenderness used within the curve) the initial focus of the comparison is on a stub column – and thus local buckling only. Predicted stub column capacities via the three design methods are provided in Figure 2. Since the results are dependent on the cross-section geometry (namely, the ht_w/A_g ratio) some care must be taken when comparing the methods.

Figure 2(a) provides the stub column comparison for the range of geometry typical of heavier W14 columns. For W14 columns all three methods yield nearly the same strength even for cross-sections reduced as much as 40% from the squash load due to local buckling (i.e. P_n/P_y = 0.6). For more slender cross-sections (i.e., $(f_y/f_{crb})^{0.5}$ > 1.2) the AISC method becomes more conservative than AISI and DSM; which essentially provide the same solution for this column.

For a W36 column f_{crb} and f_{crh} are very different (as opposed to a W14 when they are nearly the same), with the web local buckling stress, f_{crh}, being significantly lower than the flange local buckling stress, f_{crb}. In addition, W36 columns have a greater percentage of total material in the web (higher ht_w/A_g than a W14). For the W36's AISC and AISI provide essentially the same solution over the anticipated flange slenderness range. However, DSM which accounts for the web-flange interaction in a very different manner from the other two methods, assumes the W36 remains compact up to higher flange slenderness, but provides a more severe reduction as the flange slenderness increases.

Since the W36 provides a definite contrast between DSM, and AISI and AISC, the analysis is extended over a wider slenderness range in Figure 3. (Note, flange slenderness $(f_y/f_{crb})^{0.5}$ greater than 2 is rare for these sections even at yield stress approaching 100 ksi). For the W36 geometry AISI and AISC provide the same solution even as reductions move from just the web, to include the flange. Only when the flange reduction reaches the final branch of the AISC Q_s curve (f_{crb}<3/5f_y) and the design stress is reduced essentially to its elastic value of 1.1f_{crb} does the AISC method diverge from AISI, and in assuming essentially no post-buckling reserve for the unstiffened element flange, provide a more conservative solution. In contrast, the DSM solution provides a continuous reduction and at high slenderness predicts strength between AISI and AISC.

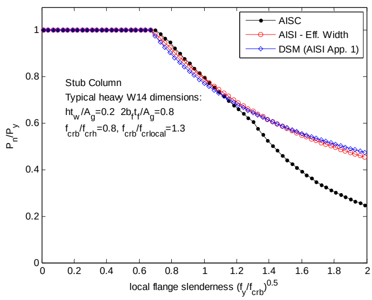

(a) W14 stub column
(flange slenderness varies within W14 series and due to change in f_y)

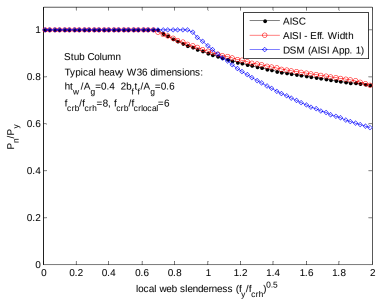

(b) W36 stub column
(web slenderness varies within W36 series and due to change in f_y)

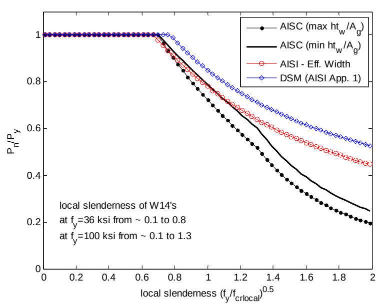

(c) Any W-section stub column, but cross-section local bucking f_{crB} has replaced plate buckling f_{crb}, f_{crh} in the design expressions per Table 2

Figure 2 Predicted stub column capacities

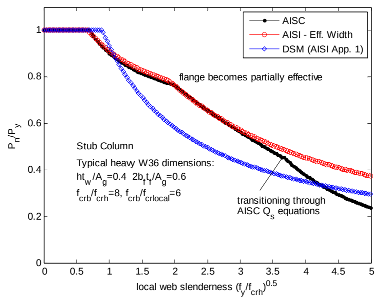

Figure 3 W36 stub column capacity, same as Figure 2(b), but examined over a wider slenderness range to highlight the different predictions

The stub column strength for the case where cross-section elastic local buckling analysis ($f_{cr\mathcal{B}}$) is used instead of the isolated plate solutions (f_{crb} and f_{crh}) is provided in Figure 2(c), while the actual design expressions for this case are provided in Table 2. Figure 2(c) provides an interesting contrast to the previous two plots of Figure 2, as it shows that directly introducing $f_{cr\mathcal{B}}$ into existing AISC or AISI methods may be overly conservative. The DSM solution provides a strictly greater prediction of a columns strength compared with AISI and AISC for a stub column capacity calculated in this manner. The development of the DSM to an expression different than AISI is exactly because comparisons to cold-formed steel columns showed that when cross-section local buckling was used as the parameter stub column strength follows the DSM curve, not the AISI curve. It is postulated that similar conclusions will be reached for AISC W-sections, though the exact change to a similar DSM curve is not yet known.

LONG COLUMN COMPARISONS

The column design expressions for AISC, AISI, and DSM, as summarized in Table 1, are examined for the same three cases as the stub columns in the previous section: W14 columns (Figure 4), W36 columns (Figure 5), and general W-sections where $f_{cr\mathcal{B}}$ is substituted for f_{crb} and f_{crh} (Figure 6). For each case all three methods are examined as the global slenderness ($(f_y/f_e)^{0.5}$) is varied from 0 to 2, and for four different cross-section slenderness values (subfigures (a) – (d)). The cross-section slenderness is systematically increased in the subfigures: (a) provides the results for a fully compact section, (b) for a local slenderness of 0.8, which corresponds approximately to the most slender W14 at f_y=36 ksi, (c) for a local slenderness of 1.3, a locally slender W14 at f_y=100 ksi, and (d) for a local slenderness of 2 which corresponds to a section with high local slenderness – f_{cr}=¼f_y.

The results for the W14 long columns are provided in Figure 5, and the basic conclusions are similar in many respects to the stub column results of Figure 2(a): AISC, AISI, and DSM provide similar capacities except at high local slenderness where AISC provides a much more conservative prediction than AISI or DSM. AISC's Q-factor approach changes the shape of the column curve (i.e., $0.658^{Q(fe/fy)}$ instead of $0.658^{(fe/fy)}$) and the asymptote (Qf_y) for a stub column. Figure 3 shows that the change in shape is not significant as neither AISI nor DSM make this change and the basic results are similar as long as the stub column asymptote is similar. Thus, for the AISC curve the stub column asymptote (Qf_y) is the only change of practical significance. This is not particularly surprising since prior to the adoption of the unified method in AISI, the cold-formed steel specification also used the Q-factor approach. Part of the justification for moving to a unified effective width approach was that the most significant change to the column curve results was the asymptote (stub column value) not the global slenderness change.

Comparison of the W36 columns is also provided in Figure 5. The most interesting results occur for the most slender cross-section, Figure 5(d), which shows that AISC provides the most liberal prediction of the column strength (though still similar to AISI), which is the opposite of the W14's where AISC provided the most conservative prediction. In practice this implies that AISC penalizes slender unstiffened elements (the flange) more than AISI and rewards slender stiffened elements (the web) more than AISI, thus the ratio of the area of stiffened elements to the area of unstiffened elements or the web-to-flange area ratios influence the AISC predictions relative to AISI or DSM a great deal.

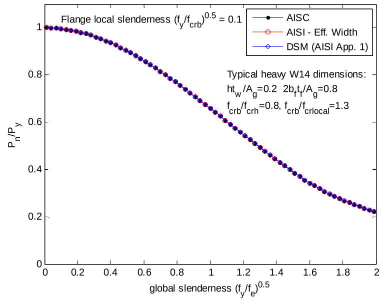

(a) compact: flange slenderness of 0.1, i.e. $f_{crb} = 100f_y$

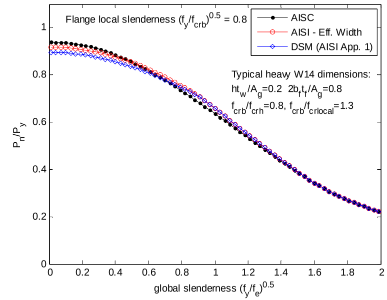

(b) local flange slenderness of 0.8, i.e. $f_{crb} = 1.56f_y$

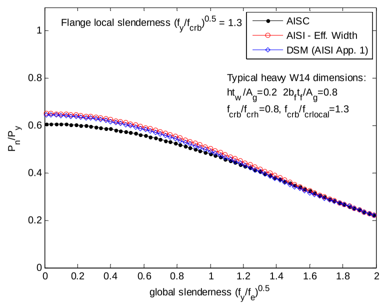

(c) local flange slenderness of 1.3, i.e. $f_{crb} = 0.59f_y$

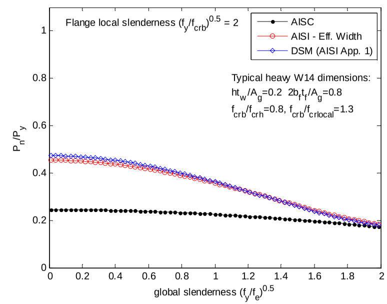

(d) local flange slenderness of 2, i.e. $f_{crb} = 0.25f_y$

Figure 4 Predicted long column capacities of typical W14 columns by the AISC, AISI, and DSM methods for varying flange local slenderness following the formulas of Table 1

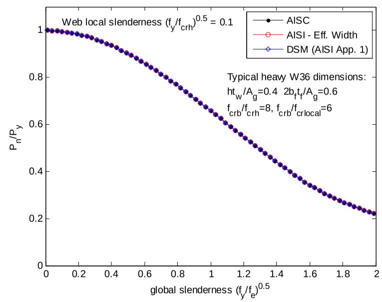

(a) compact: web slenderness of 0.1, i.e. $f_{crh} = 100f_y$

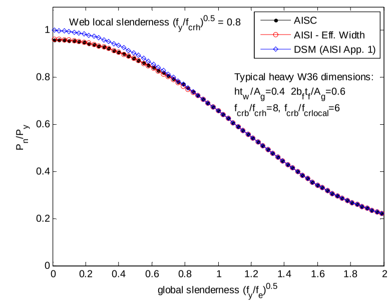

(b) local web slenderness of 0.8, i.e. $f_{crh} = 1.56f_y$

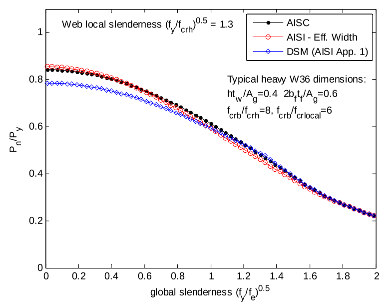

(c) local web slenderness of 1.3, i.e. $f_{crh} = 0.59f_y$

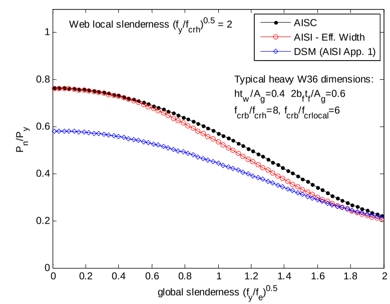

(b) local web slenderness of 2, i.e. $f_{crh} = 0.25f_y$

Figure 5 Predicted long column capacities of typical W36 (as a column) by the AISC, AISI, and DSM methods for varying web local slenderness following the formulas of Table 1

The long column prediction behavior of DSM is similar to what was observed in the stub column predictions of Figure 2(b): DSM provides a higher capacity than AISC or AISI at low web (local) slenderness, but as the web slenderness increases the predicted overall decrease in the capacity is greater than AISC or AISI. Thus, DSM assumes a greater reduction in the slender column strength due to local buckling driven by the web than AISC or AISI. Finally, as is true for all of the long column methods, since the same global buckling column curve is used, at high global slenderness all of the methods eventually converge.

A completely general comparison of the AISC, AISI, and DSM design methods for W-sections is possible if the local cross-section stability solution (f_{crB}) is used in place of the isolated plate buckling solutions (f_{crb} and f_{crh}) - such a comparison is provided in Figure 6. Comparisons between the design methods remain similar to the stub column comparisons of Figure 2(c): DSM predicts a consistently greater strength than AISC or AISI, and AISC is most conservative when the flange (unstiffened element) contributes more to the strength. The DSM column curve is known to fit available cold-formed steel column data better than the AISI Effective Width method, when the plate buckling solutions (f_{crb} and f_{crh}) are replaced by the cross-section local buckling (f_{crB}) solution. The difference in strength predictions at high local slenderness is large – and suggests that the AISC design philosophy may be overly conservative if cross-section stability solutions are adopted with no other change. Further, this conservatism is increasing as higher yield stress cross-sections are considered.

FUTURE WORK

Current efforts include gathering available test data for hot-rolled steel and cold-formed steel to make a statistical comparison of the predictive methods. In addition, we have initiated a parametric study, using ABAQUS, to extend the test database. The role of cross-section details (k-zone, etc.) imperfections, residual stresses, and material yield stress and parameters (strain hardening, etc.) on the results and comparisons will be examined. Particular attention will be placed on understanding the regimes where the AISC and DSM methods give divergent results. The goal of this research is to propose improvements to DSM for its application to locally slender hot-rolled structural steel.

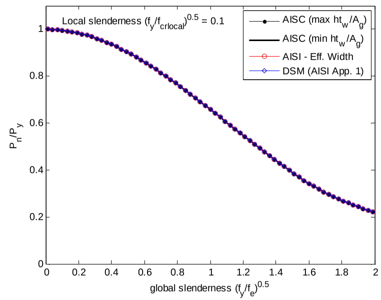

(a) compact: local slenderness of 0.1, i.e. $f_{crB} = 100f_y$

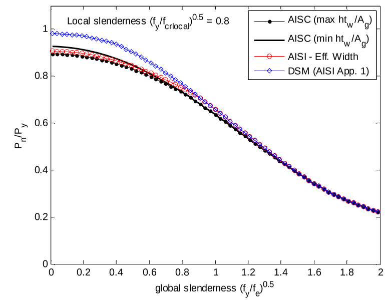

(b) local slenderness of 0.8, i.e. $f_{crB} = 1.56f_y$

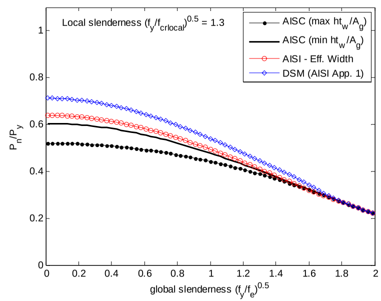

(c) local slenderness of 1.3, i.e. $f_{crB} = 0.59f_y$

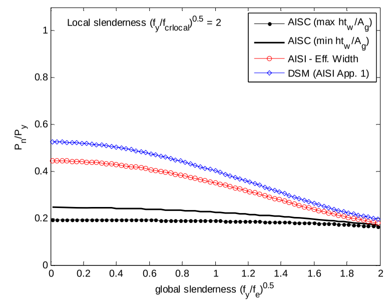

(d) local slenderness of 2, i.e. $f_{crB} = 0.25f_y$

Figure 6 Long column capacities for slender cross-sections. following Table 1, but where cross-section elastic local buckling replaces isolated plate buckling, i.e., $f_{crb} = f_{crh} = f_{crB}$ and AISC ht_w/A_g range reflects range of W14's

CONCLUSIONS

Using the AISC Q-factor and AISI Effective Width approaches it is shown that the design strength of slender steel columns is specified as a function of (a) global buckling stress, (b) web local plate buckling stress, (c) flange local plate buckling stress, (d) yield stress and (e) the ratio of web area to gross area. However, the flange local buckling stress and web local buckling stress are not unique parameters. As shown herein finite strip analysis of W-section columns provides a ready means for incorporating web-flange interaction and replacing the flange and web local plate buckling stress with a single cross-section local bucking stress. The AISI Direct Strength method replaces the five parameters above with only three parameters: (a) global buckling stress, (b) local buckling stress, and (c) yield stress.

Through parametric studies on W-section columns the AISC Q-factor approach and AISI Effective Width Method are shown to provide similar strengths in most practical regimes. However, as the flanges (unstiffened elements) become more slender the AISC Q_s term becomes systematically more conservative than the AISI Effective Width expressions (as it effectively ignores post-buckling reserve). The Direct Strength Method provides similar strength predictions to Q-factor and Effective Width, but predicts a greater influence of web-flange interaction. Replacing the plate local buckling solutions with cross-section local buckling solutions within the existing AISC Q-facotr and AISI Effective Wisth Methods is possible, but is shown to predict capacities systematically lower than the Direct Strength Method. Additional work (primarily nonlinear finite element analysis) to better understand the geometric regimes where the methods provide differing strength capacities and to determine the most efficient and accurate solution for locally slender steel columns is underway.

ACKNOWLEDGMENTS

The authors of this paper gratefully acknowledge the financial support of the AISC, and the AISC Faculty Fellowship program. However, any views or opinions expressed in this paper are those of the authors. The authors would also like to thank Don White for discussions related to material in this paper during the development of the 2005 AISC Specification.

REFERENCES

AISC (2005). Specification for Structural Steel Buildings. American Institute of Steel Construction, Chicago, IL. ANSI/AISC 360-05

AISC (2005b). Manual for Steel Construction. American Institute of Steel Construction, Chicago, IL. 13th Ed., AISC 325-05

AISI (2007). North American Specification for the Design of Cold-Formed Steel Structures. American Iron and Steel Institute, Washington, D.C., ANSI/AISI-S100-07.

Galambos, T. (1998). Guide to Stability Design Criteria for Metal Structures. 5th ed., Wiley, New York, NY, 815-822.

Salmon, C.G., Johnson, J.S. (1996). Steel structures design and behavior: emphasizing load and resistance factor design. Harper Collins College Publishers, New York, NY.

Schafer, B.W., Ádány, S. (2006). "Buckling analysis of cold-formed steel members using CUFSM: conventional and constrained finite strip methods." Proceedings of the Eighteenth International Specialty Conference on Cold-Formed Steel Structures, Orlando, FL. 39-54.

Schafer, B.W., Seif, M. (2007). "Cross-section Stability of Structural Steel." American Institute of Steel Construction, Progress Report No. 1. AISC Faculty Fellowship, 25 June 2007.

Seif, M., Schafer B.W. (2007). "Cross-section Stability of Structural Steel." American Institute of Steel Construction, Letter Report AISC Faculty Fellowship, 12 November 2007.

Lateral Torsional Buckling Strength of Prismatic and Web-Tapered Beams

Yoon Duk Kim[1] *and Donald W. White*[2]

INTRODUCTION

A new MBMA/AISC guide for frame design using web-tapered members (Kaehler et al. 2008) is due to be released in near future. In this guide, the AISC (2005) provisions for prismatic members are extended to address web-tapered and general non-prismatic cases. One of the fundamental concepts employed in this guide is a mapping of elastic buckling strengths to nominal elastic or inelastic buckling resistances for general nonprismatic members. Similar to prior AISC developments detailed by Lee et al. (1981), this mapping is based on the concept of an equivalent prismatic member. However, the mapping is handled explicitly in the new MBMA/AISC developments by considering two fundamental parameters: (1) the ratio of the elastic buckling strength to the required force or stress, γ_e, and (2) the ratio of the required stress to the yield stress f_r/F_y. The term γ_e represents the member overall elastic buckling load level whereas the ratio f_r/F_y focuses the designer's attention on the more highly stressed member locations. Given these two parameters, the ratio of the yield stress to the corresponding elastic buckling stress may be determined as $F_y/F_e = 1 / [\gamma_e(f_r/F_y)]$. The MBMA/AISC design guide utilizes the 2005 AISC member resistance equations expressed in terms of a generalized slenderness $\sqrt{F_y / F_e}$.

Eurocode 3 (EC3) (CEN 2005) Clauses 6.3.2.2 and 6.3.2.3 provide recently updated procedures for calculating prismatic I-section beam LTB resistances. The EC3 resistance equations are expressed in terms of a similar but slightly different generalized slenderness parameter $\sqrt{M_{max} / M_e}$, in which M_{max} is the cross-section flexural capacity in

[1] Ph.D. Candidate, Georgia Tech, Civil and Environmental Engineering, Atlanta, GA 30332-0355
[2] Professor, Georgia Tech, Civil and Environmental Engineering

EC3 and M_e is the elastic LTB strength. The above EC3 clauses provide eight different nominal LTB resistance curves compared to the use of a single base LTB resistance curve in the AISC and MBMA/AISC provisions. Furthermore, EC3 handles the stress gradient "C_b" effect differently than in the AISC provisions.

This paper discusses the ability of the AISC, MBMA/AISC and EC3 procedures to capture general prismatic and web-tapered I-section LTB resistances. First, a brief summary of the different calculation procedures is provided. This is followed by comparisons between nominal strength predictions and experimental results for several representative cases. In addition, full nonlinear finite element analysis (FEA) simulations ("virtual tests") are conducted for a number of these experiments to provide confirmation of the experimental results as well as to demonstrate the ability of refined FEA procedures for prediction of the experimental resistances. All of the members considered in this paper are doubly-symmetric and have compact flanges according to AISC, or Class 1 or 2 flanges according to EC3. The prismatic member comparisons range from compact-web/Class 1 rolled sections to slender-web/Class 4 welded sections and include both uniform moment and moment gradient loadings. The tapered member comparisons involve noncompact/Class 4 webs at the deeper end of the critical unbraced length and include both cases with approximately uniform flange stress as well as with a significant flange stress gradient along the critical unbraced length. For the web-tapered cases, an adaptation of the EC3 prismatic member calculations is employed that is similar to the adaptation of the AISC equations in the MBMA/AISC design guide. Finally, a small number of FEA "virtual tests" are conducted to investigate the LTB behavior of both prismatic and tapered I-section members with Class 4 webs in the limit that the web depth to flange width ratio (h/b_f) becomes large. A number of prior studies have observed the importance of this parameter.

OVERVIEW OF NOMINAL RESISTANCE CALCULATIONS

As noted in the introduction, the AISC and MBMA/AISC LTB resistances are tied in essence to a single base nominal LTB resistance equation. The AISC I-section member flexural resistance calculations are discussed in detail by White (2004) and are based in part on the assessment of more than 767 experimental tests by White and Jung (2004) and White and Kim (2004). In contrast, the EC3 Clause 6.3.2.2 and 6.3.2.3 provisions provide four enhanced LTB resistance curves applicable for rolled and equivalent welded I-section members and four additional more conservative LTB resistance curves that apply to general rolled and welded I-section members. In each of these EC3 clauses, the four resistance curves account for the different behavior of rolled versus welded members as well as of members with relatively wide flanges ($h/b_f \leq 2$) versus relatively narrow flanges ($h/b_f > 2$). The EC3 provisions are discussed in detail by Gardner and Nethercot (2005) and Nethercot and Gardner (2005) and are based on extensive experimental results as well as refined nonlinear FEA simulations (ECCS 2006).

The MBMA/AISC design guide recommends two procedures for calculation of nonprismatic member LTB strengths: a general procedure that applies for any nonprismatic geometry and a specific procedure permitted for members with a single linear taper (no discrete steps in the cross-section geometry within the unbraced length). These procedures give identical results for uniform flange stress cases, but differ somewhat in their predictions when there is a flange stress gradient. In the general procedure, the elastic LTB stress $F_e = \gamma_e f_r$ is calculated including the elastic stress-gradient (C_b) effect. This stress is then substituted directly into the LTB equations (i.e., the mapping from the elastic buckling resistance to the nominal LTB resistance) via the term $\sqrt{F_y / F_e}$ to determine the nominal resistance F_n. In the specific procedure allowed for linearly tapered members, the elastic LTB stress under uniform stress conditions, $F_{e(Cb=1)}$, is used initially for calculating the corresponding base LTB resistance $F_{n(Cb=1)}$. Then the stress-gradient effect is accounted for by multiplying $F_{n(Cb=1)}$ by the C_b factor, i.e., $F_n=C_bF_{n(Cb=1)}$ capped by the cross-section strength. This parallels the calculations for prismatic members in the AISC Specification.

For web-tapered members, the MBMA/AISC guide recommends the calculation of $F_{e(Cb=1)}$ using the cross-section at the middle of the unbraced length as well as the use of an AASHTO (2007) equation for C_b expressed in terms of flange stresses. A detailed discussion of these calculations is provided by Kim and White (2007a). In addition, although end restraint effects are usually neglected in design practice, the consideration of end warping and lateral bending restraint is essential for any meaningful comparison of LTB resistance curves to test results. These effects are accounted for in the current work using an approach discussed by Ozgur et al. (2007), which is an adaptation of the elastic LTB K factor procedures developed by Nethercot and Trahair (1976). These solutions provide a close match to rigorous elastic beam theory eigenvalue buckling results.

The general procedures in EC3 Clause 6.3.2.2 use the same type of approach for handling stress gradient effects as in above general MBMA/AISC procedure. In these methods, the mapping from F_e to F_n is handled in the same way for both stress gradient and uniform flange stress cases. For gradient cases, F_e is calculated using a modification factor ($C_b > 1$ in AISC and a comparable $C_1 > 1$ in EC3). This approach neglects the benefit of the yielding occurring over a shorter member length in the gradient cases. The calculated reduction from F_e to F_n is the same for a given F_e regardless of the flange stress gradient.

On the other hand, the 2005 AISC Specification applies the elastic C_b factor for all inelastic LTB cases, except that the increase in the flexural resistance is capped by the cross-section resistance. It is generally recognized that this is an optimistic solution; however, the predictions are acceptable (Yura et al. 1978, White and Kim 2004).

Lastly, the EC3 Clause 6.3.2.3 procedures, which apply only to rolled and equivalent welded I-sections, give a solution for the moment gradient effects that is intermediate between the above two approaches. This clause utilizes the EC3 C_1 in the same way as in Clause 6.3.2.2. However, the end result is modified by an additional factor denoted by the symbol f. This parameter accounts explicitly for the additional increase in the LTB resistance due to the non-uniform yielding associated with a moment gradient.

FULL NONLINEAR FEA SOLUTIONS

The FEA solutions in this paper are conducted using ABAQUS (Simulia 2007). All the component plates are modeled using the S4R element. A relatively dense mesh of 12 elements through the flange width and 20 elements through the web depth is employed. For tests where measured residual stresses and initial geometric imperfections are available, the FEA models are generated using the measured values. Nominal values are assumed where this information is not available. A nominal residual stress pattern recommended by Kim and White (2007b) is utilized in all cases for the welded I-section members. This residual stress pattern is based on measurements by Prawel et al. (1974) and is self-equilibrating in each plate component. The nominal geometric imperfection is a single-wave compression flange sweep, and the nominal amplitude of the geometric imperfection is taken as $L_b/1000$. Reported yield strengths and geometric dimensions are used in all cases both for the FEA models and for the nominal resistance calculations.

PRISMATIC MEMBER TESTS

The results from three tests by Dux and Kitipornchai (1983), 11 tests by Wong-Chung and Kitipornchai (1986), and six tests by Richter (1988) are considered here as representative uniform bending cases. The tests by Dux and Kitipornchai (1983) and Wong-Chung and Kitipornchai (1986) are simply-supported four point bending tests with a critical middle segment under uniform bending. All of these beams are 250UB37 sections. This section has a compact/Class 1 web with $h/t_w=40$, $b_f/2t_f=6.7$ and $h/b_f=1.7$. These tests have LTB K factors of either 0.66 or 0.91 using the procedures from Ozgur et al. (2007) and Nethercot and Trahair (1976). The tests by Richter (1988) are welded members in which the critical unbraced length as well as the adjacent segments are all subjected to uniform bending. As such, the warping and lateral bending restraint from the adjacent segments is small. The calculated K factors are equal to 1.0 for these tests. These beams have slender/Class 4 webs with $h/t_w=150$, $b_f/2t_f=8.0$ and $h/b_f=4.9$.

Figure 1 shows the experimental, FEA, and nominal strength results for the above rolled section members. The LTB strengths for the selected prismatic tests are calculated using both the AISC and the EC3 procedures. For the rolled section tests, the predictions from both EC3 Clauses 6.3.2.2 and 6.3.2.3 are presented. The LTB resistances based on the EC3 Clause 6.3.2.2 and 6.3.2.3 provisions are denoted by EC3(1) and EC3(2) respectively. It should be noted that the abscissa of

Fig. 1 is $\sqrt{F_y / F_{e(Cb=1)}}$ and the ordinate is M/M_y, in which M is the moment capacity. All the plots in this paper are presented in this normalized form. Figure 1 shows that the experimental test results correlate well with the AISC LTB curve for compact section rolled beams. The two EC3 curves give similar to slightly smaller strengths than the AISC curve. The EC3 (2) strength is slightly higher than the AISC prediction in the inelastic LTB region near the plateau. The FEA simulations generally give LTB resistances that are close to the experimental results and the AISC nominal strength.

Figure 2 shows the experimental and FEA results as well as the design curves for the slender-web welded member tests (Richter 1988). Since these members are not *equivalent welded I-sections* (i.e., their h/t_w and h/b_f values are larger than those of rolled I-sections), the EC3 (2) curve is not shown. Similar to the results for the above rolled I-section member tests, the experimental resistances of these slender-web tests correlate well with the AISC LTB strengths. The EC3 (1) strengths for these slender-web tests is considerably smaller. The FEA predictions are similar to or smaller than the experimental results and the AISC curve for these tests, but are significantly higher than the EC3 predictions. It should be noted that all the residual stresses and geometric imperfections are taken as nominal values in Fig. 2 whereas they are all based on measurements in Fig. 1.

Three rolled section tests by Dux and Kitipornchai (1983), and one welded member test by Shilling and Morcos (1988) are selected as representative moment gradient cases. The tests by Dux and Kitipornchai (1983) are simply-supported three point bending tests with equal unbraced lengths on each side of the load point (C_b=1.75 per AISC and C_1=1.88 per EC3). All these tests are 250UB37 members (h/t_w=40, $b_f/2t_f$=6.7, and h/b_f=1.7). The test beam from Schilling and Morcos (1988) has a slender/Class 4 web with h/t_w=153, $b_f/2t_f$=6.6, and h/b_f=4.4. Only one slender-web moment-gradient prismatic test is considered in this paper since a convenient set of such tests all with the same cross-section and the same nominal LTB resistance does not exist.

Figure 3 shows the moment gradient results for the rolled members. In this figure, two curves are plotted using the AISC equations. The curve

AISC (1) is determined using $F_n = C_b F_{n(Cb=1)}$ as specified in AISC (2005). AISC (2), is obtained by substituting $F_{e(Cb>1)}$ into the AISC equations expressed in terms of $\sqrt{(F_y / F_e)}$ (i.e., the approach used for handling gradient effects in the general MBMA/AISC and EC3 procedures). This is done to highlight the effect of these two approaches.

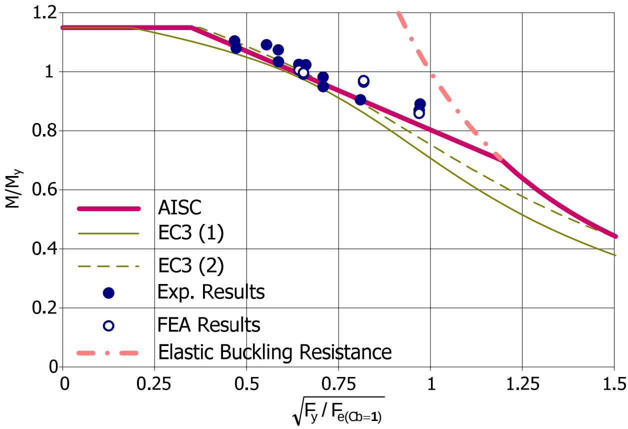

Fig. 1. Uniform bending results, rolled members, h/b_f=1.7.

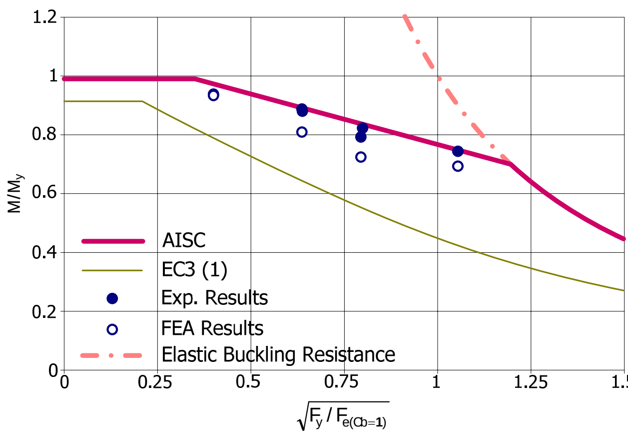

Fig. 2. Uniform bending results, prismatic slender-web cases, h/b_f=4.9.

The AISC(2) curve gives smaller inelastic LTB strengths than the AISC(1) curve. Since these are rolled tests, the EC3(2) curve is generated. This curve accounts for the benefit from the non-uniform yielding along the unbraced length via the parameter f. Figure 3 shows that the experimental results for these rolled tests are similar to or slightly lower than the AISC(1) strengths. These test results and the AISC(1) strengths are significantly greater than the other calculated resistances. Interestingly, the EC3(1) and AISC(2) curves give similar conservative approximations for the inelastic LTB strengths. Figure 3 also illustrates that the EC3 Clause 6.3.2.3 gives EC3(2) strengths that are substantially larger than the general EC3(1) resistances. However, EC3(2) still falls below AISC(1) in the inelastic region. It should be noted that EC3(2) gives slightly higher strengths than AISC(1) for $\sqrt{F_y / F_{e(Cb=1)}} \geq 1.6$. This is because the EC3 modifier C_1 is 1.88 whereas the AISC (1) curve is based on the comparable C_b=1.75.

Figure 4 shows similar results for the slender-web welded member. The LTB of this member is well within the plateau of the AISC(1) curve. The experimental resistance is slightly greater than the AISC(1) strength. The FEA simulation gives an LTB strength that is essentially the same as the experimental result. Similar to the results shown in Fig. 3, the AISC(2) curve gives smaller predictions than AISC(1) in the inelastic LTB region. EC3(1) gives significantly conservative strengths relative to both AISC(1) and (2). EC3(2) is not shown in Fig. 4 since this curve does not apply for a Class 4 web member.

WEB-TAPERED MEMBER TESTS

There are a very limited number of web-tapered beam experiments in which the flexural resistance is governed by LTB. Prawel et al. (1974) tested three simply-supported beams and nine cantilever beams. The discussion in this section is focused on Prawel's simply-supported tests, which are governed by LTB. These members have a linearly-tapered web depth with h_{avg}/t_w=100 and h_{avg}/b_f=2.6 at the mid-span and $b_f/2t_f$=8.0. Based on the web slenderness at their deeper end, the webs of these members are classified as non-compact by the MBMA/AISC procedures. Two of these tests are simply-supported four-point bending tests, in which the critical middle segment is subjected to uniform compression stress. The taper angle β is 4° and 6° for these tests. The other test is a similar stress gradient test with β=6° and vertical load only at its 1/4 span. The FEA simulations of these tests are conducted as discussed above and are presented by Kim and White (2007b).

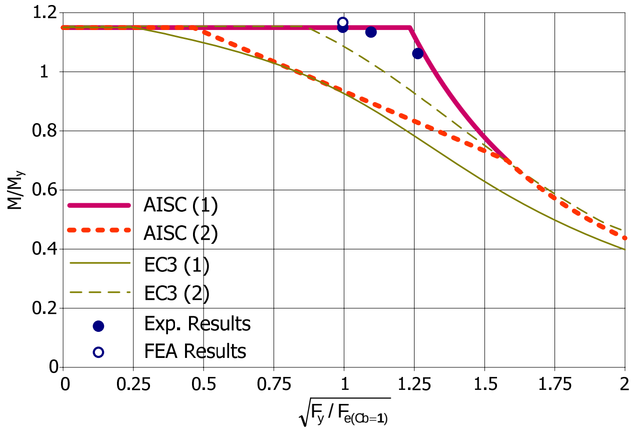

Fig. 3. Moment gradient results, rolled members, h/b_f=1.7.

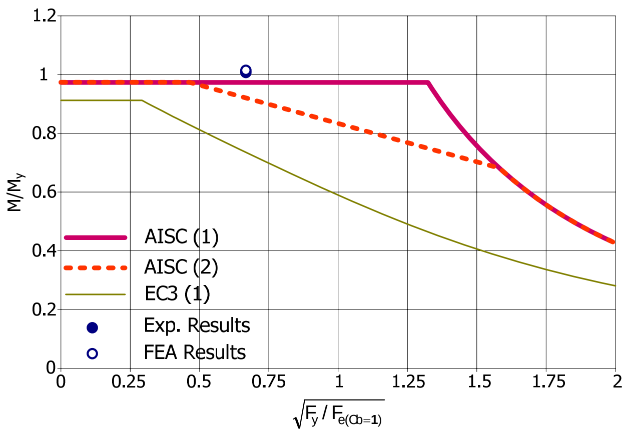

Fig. 4. Moment gradient results, prismatic slender-web case, h/b_f=4.4.

Figure 5 shows the results for the two uniform flange stress cases. The MBMA/AISC(1) curve in this figure is based on the design guide procedure permitted for segments with a single linear taper whereas the MBMA/AISC(2) curve is based on the general design guide procedure. One test result is greater than the MBMA/AISC guide prediction whereas the other test result is slightly smaller than the MBMA/AISC strengths. The FEA solutions give essentially equal conservative LTB strengths for both tests relative to the experimental results and the MBMA/AISC predictions. The EC3(1) curve gives a slightly conservative estimate for the less slender test and significantly conservative prediction for the more slender test.

Figure 6 shows the results for the stress gradient test from Prawel et al. (1974). The value of C_b is determined as 1.31 and is used both in the AISC calculations and for C_1 in the adapted EC3 calculations. The experimental test result falls between the MBMA/AISC (1) and MBMA/AISC(2) resistances. The FEA solution is slightly smaller than the MBMA/AISC(2) strength. The EC3(1) curve again gives a conservative estimate of the member capacity.

NONLINEAR FEA STUDY

As noted in the introduction, the importance of the ratio h/b_f is recognized in a number of previous studies. ECCS (2006) explains that I-section beams with larger h/b_f tend to have reduced LTB resistances. Furthermore, White and Jung (2004) and White et al. (2004) observe substantial reductions in experimental capacities relative to the AISC predictions in a large percentage of cases with $h/b_f > 6$. Nevertheless, the number of physical tests with large h/b_f is small. One useful application of refined full nonlinear FEA models is to better understand the influence of h/b_f on the LTB resistances.

To this end, several simply-supported beams are considered in this section. Both prismatic and web-tapered cases with approximately uniform flange stress as well as with significant stress gradients are studied. Geometries with a linearly-tapered web depth, $h_{avg}/t_w = 100$ at the mid-span, $b_f/2t_f = 6$ and $\beta=10°$ are taken as a starting point for these designs. Values of 3, 4.5 and 6 are selected for the primary variable h_{avg}/b_f, and the yield strength F_y is taken as 55 ksi. For the uniform flange stress tests, L_b is taken equal to 56 r_{tavg}, in which r_{tavg} is the radius of gyration of the compression flange plus one-third of the depth of the web in compression. This gives a value for $\sqrt{F_y / F_{e(Cb=1)}}$ that falls in the middle of the inelastic range of the AISC LTB resistance.

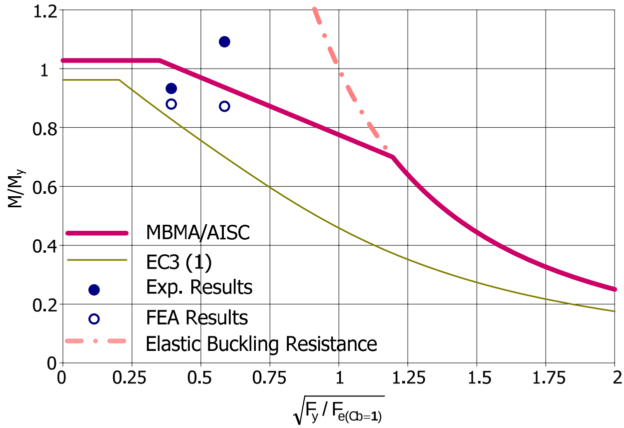

Fig. 5. Uniform stress results, web-tapered tests, h_{avg}/b_f=2.5.

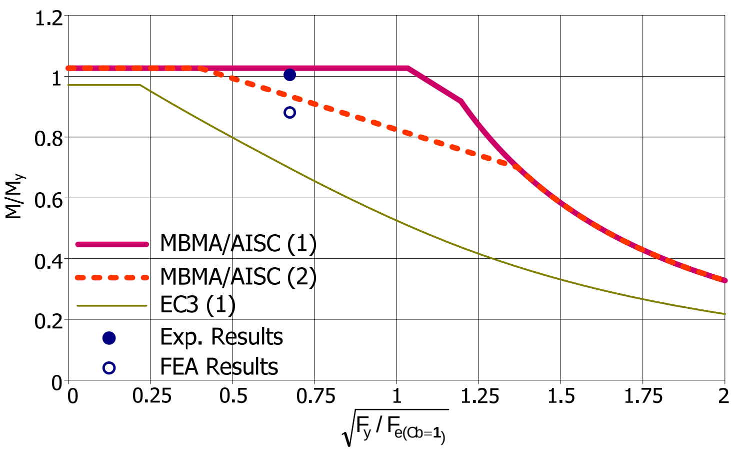

Fig. 6. Stress gradient results, web-tapered test, h_{avg}/b_f=2.5.

For the stress gradient cases, L_b is taken equal to the AISC unbraced length L_r using the mid-span section properties. This results in tapered member calculated LTB strengths, including flange stress gradient effects, that are slightly less than the member cross-section resistance.

Next, for each of the above three tapered beams, a corresponding prismatic member is designed using the cross section at the deep end of the tapered member. The unbraced length of these members is determined such that they have the same F_e as the corresponding tapered tests.

The FEA models are generated as discussed previously using a flange sweep imperfection of $L_b/1000$ and the residual stress pattern suggested by Kim and White (2007b). All of the beams have simply-supported end conditions with zero end warping and lateral bending restraints (ideal "fork" boundary conditions). Open-section thin-walled beam theory kinematics are enforced at the member ends. For the uniform flange stress cases, end-moments are applied such that M/M_y is the same value at both ends of the members. For the stress-gradient cases, the moment is applied only at one end of the member (the deep end for the web-tapered cases); the moment at the opposite end is zero

Figure 7 shows the results for the uniform-stress tapered cases with h_{avg}/b_f=3 and 4.5 and the corresponding prismatic tests. The prismatic beams have h/t_w=144 and 127 and h/b_f=4.3 and 5.7 respectively. It should be noted that each of these sets of prismatic and web-tapered members has the same calculated nominal resistance. This is because the same elastic LTB stress F_e and the same cross-section properties are used to calculate F_n in both the prismatic and web-tapered cases. Figure 7 indicates that the strengths from the FEA “virtual tests” are actually slightly larger for the web-tapered members. These strengths fall approximately mid-way between the MBMA/AISC and EC3(1) curves.

Figure 8 shows the results for the tapered uniform flange stress test with h/b_f=6 as well as the corresponding prismatic test. The corresponding prismatic member has h/b_f=7.1 and h/t_w=118. Similar to the results in Fig. 7, the strength from the virtual test of the tapered member is slightly larger than that from the corresponding prismatic member. However, these test strengths are substantially smaller than the MBMA/AISC and AISC resistances and they are only slightly above the EC3(1) curve. In order to gage the influence of the residual stresses on these resistances, virtual test results for zero residual stress are also shown. The test strengths are significantly larger for these cases; however, they are still slightly smaller than the AISC and MBMA/AISC nominal strengths.

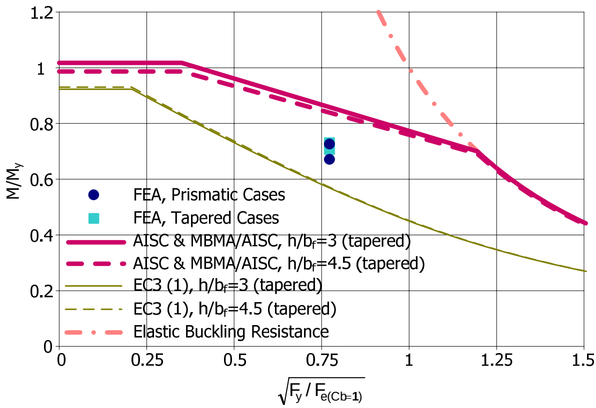

Fig. 7. Uniform stress results, h_{avg}/b_f=3 and 4.5 for tapered tests, h/b_f=4.3 and 5.7 for prismatic tests.

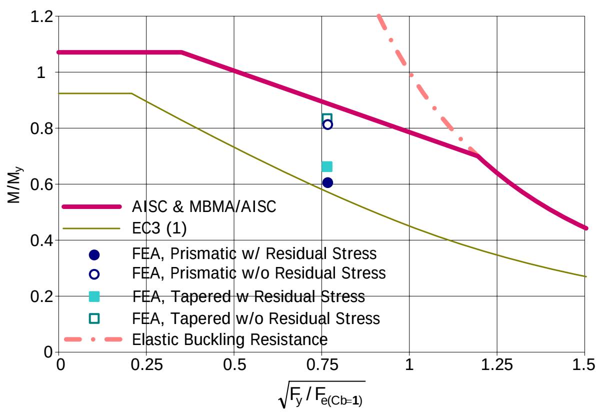

Fig. 8. Uniform stress results, h_{avg}/b_f=6 for tapered test (h/b_f=7.1 for prismatic test).

Figures 9 and 10 show the results from the above stress-gradient tests with $h_{avg}/b_f = 6$ ($h/b_f = 7.7$ and $h/t_w = 129$ for the prismatic beam). The results for the prismatic and tapered tests are shown separately since C_b=1.75 and 1.34 for the prismatic and tapered cases respectively. For both these beams, the full nonlinear FEA simulations indicate significantly smaller LTB strengths than predicted by the AISC-based procedures. Even if zero nominal residual stress is assumed, the LTB strengths for these tests are significantly smaller than the AISC and MBMA/AISC predictions. Conversely, the EC3(1) equations give somewhat conservative strength predictions for these cases.

It appears that for both prismatic and tapered beams with large h/b_f the maximum strength is reached soon after first yielding occurs in the compression flange in the virtual tests. Significant compression flange lateral bending occurs due to the second order amplification of the initial flange sweep imperfection. This results in initial flange yielding at a relatively low applied moment level. ECCS (2006) gives an equation for calculating the first yield resistance based on open-section thin-walled beam theory. Using this equation, the value of M/M_y at the first yield limit is calculated for the prismatic member with zero residual stress considered in Fig. 8. The result is M/M_y=0.81. If the M/M_y value at the first-yield limit state is calculated by taking the compression flange as an equivalent column with a slenderness of L_b/r_t, the result is M/M_y=0.80. In the corresponding virtual tests, this member reaches the first yield in the compression flange at M/M_y=0.75 and reaches a maximum load at M/M_y=0.81. When the nominal residual stresses are included, the ECCS (2006) beam theory solution and the equivalent column solution both predict initial yielding at $M/M_y = 0.64$. Compression flange initial yielding is encountered at $M/M_y = 0.57$ in the virtual test whereas the limit load is reached at $M/M_y = 0.61$. Similar behavior is observed for the corresponding tapered uniform stress case and for the prismatic and tapered members subject to stress gradient. Figure 11 shows the deformed geometry of the stress-gradient web-tapered test with initial residual stresses included and $h/b_f = 6$ at its limit load. It can be seen that yielding in the compression flange has spread through approximately one-half of the flange width at the limit load level. Also, the web-flange juncture is fully yielded at the tension flange due to the high tensile residual stresses in this region.

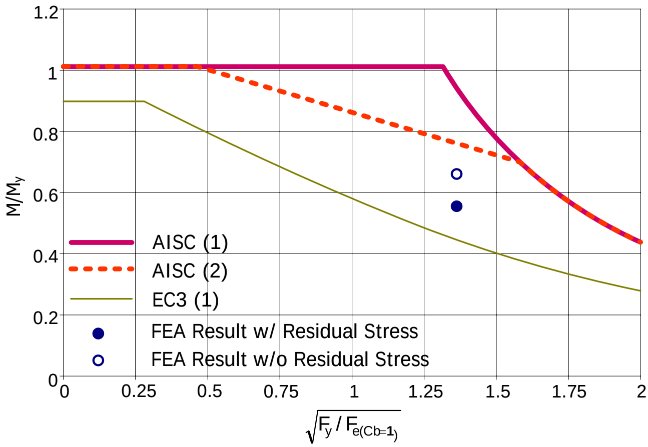

Fig. 9. Stress gradient results, prismatic case with h/b_f=7.7.

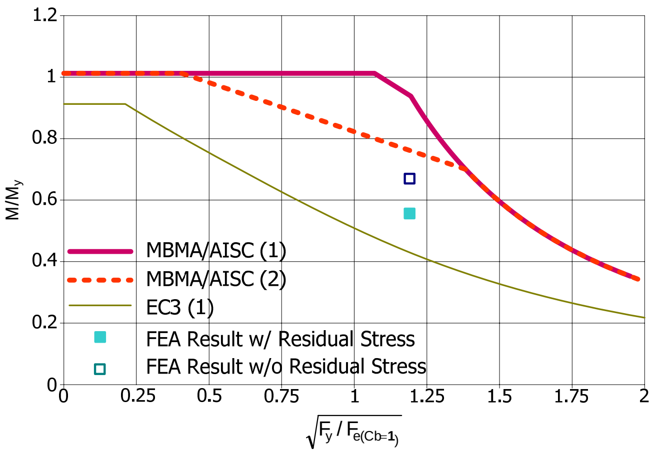

Fig. 10. Stress gradient results, web-tapered case with h_{avg}/b_f=6.

SYNTHESIS OF RESULTS

The limited experimental, FEA and nominal resistance calculation results presented in this paper highlight four important facts:

1) Linearly-tapered I-section members exhibit essentially the same normalized inelastic buckling strengths as prismatic I-section members having:
   a. The cross-section at their deeper end, and
   b. The same F_y/F_e.
2) There is a clear reduction in I-section member LTB resistances for cases with larger h/b_f values.
3) Full nonlinear FEA simulations underestimate the resistances obtained via experimental testing in many cases.
4) In certain instances, the EC3-based nominal resistances are substantially smaller than the experimental, the FEA and the AISC-based resistances.

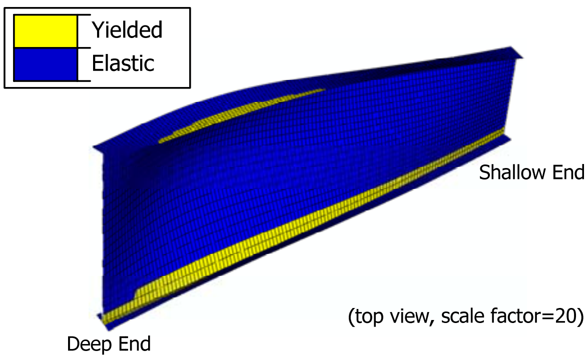

Fig. 11. Deformed configuration showing the mid-thickness spread of yielding at the limit load, stress gradient web-tapered case with $h/b_f = 6$.

There are many simple as well as complex factors behind and implications of each of these facts. Only a few can be summarized here. First, the above equivalency of linearly-tapered members with a specific prismatic I-section member should be obvious. The results presented in fact show a slightly larger resistance of the linearly-tapered members. This is due to slight variations in the attributes and responses along the length of linearly-tapered members that are accounted for approximately in the nominal resistance expressions. The important implication of this approximate equivalency is that research on prismatic and tapered I-section member strengths should not be considered in isolation from one another. The findings of any research that seeks to better quantify the resistance of tapered I-section members should be considered in the context of prismatic I-section members and vice-versa.

The second fact arises clearly from the mechanics of geometrically imperfect I-section beams. This fact is recognized by EC3 via the separate strength curves for $h/b_f \leq 2$ and $h/b_f > 2$, albeit in a very coarse discrete fashion. It appears that members with large values of h/b_f can have a substantial reduction in their physical LTB strengths relative to the AISC LTB nominal resistances. An assessment of experimental test characteristics would indicate that possibly not enough attention has been given to this parameter in prior physical testing. As a result, it is possible that the intended level of reliability is not being provided for I-section members with large values of h/b_f. This can have an important implication on the safety of longer-span structures, where the design economy tends to lead to large values of this parameter. There are numerous mitigating or compensating factors that can occur however. Some of these are discussed below.

The third fact can result from the practice that FEA solutions are typically conducted using a selected geometric imperfection tolerance (e.g., $L_b/1000$) and an idealized nominal residual stress pattern. It is often forgotten that the geometric imperfections and residual stresses in physical beams (and in the physical tests used for development of resistance equations) can have significant scatter. Physical geometric imperfections practically never vary as a simple function along the member length. Also, the residual stress pattern, the yield strengths, etc. are never truly constant along the length. For that matter, the physical yielding of a member subjected to near uniform stress conditions is indeed a discontinuous phenomenon rather than a continuum response. In addition, there are often unavoidable incidental end restraint effects that are unaccounted for even if the most rigorous consideration of the end restraint effects is included in the FEA calculations. Of course, in cases where there is little to no incidental end restraint, one does not attain these benefits. There is significant evidence to show that when the detailed residual stresses, geometric imperfections and boundary conditions are determined and included in the analysis, the correlation between the full nonlinear shell FEA and experimental responses is reasonably good (e.g., see Fig. 1). However, the use of “nominal” or “worst-case” geometric imperfections and residual stresses in FEA models can be overly pessimistic. Also, strength curves developed using a selected near worst-case cross-section will tend to be conservative for members with other cross-sections.

Lastly, a perusal of the substantial documentation behind the development of the EC3 nominal resistance expressions as can be found from the references cited in (ECCS 2006) indicates that the EC3 expressions, using measured (or specified) material properties and geometric dimensions, provide predominantly a lower-bound fit to the physical and numerical test data. Conversely, the AISC resistance equations provide an approximate fit to the mean test resistances across a broad range of parameters. The important end result is that a targeted level of reliability should be achieved using any of the different standards or specifications. Assessment of the reliability implications requires substantial effort beyond the scope of this paper. However, it does appear that there would be substantial benefit to a combined assessment of the data behind both the EC3 and AISC developments.

ACKNOWLEDGEMENTS

The financial support for this research from the Metal Building Manufacturers Association (MBMA) is gratefully acknowledged. The authors are grateful for the input and advice from the MBMA steering groups for their research. Special thanks are extended to Richard C. Kaehler of Computerized Structural Design, S.C. for extensive discussions and feedback. Dr. N. Boissonnade is thanked for his input regarding the EC3 provisions. The opinions, findings and conclusions expressed in this paper are the authors’ and do not necessarily reflect the views of the above individuals, groups and organizations.

REFERENCES

AASHTO (2007). *AASHTO LRFD Bridge Design Specifications,* 4th Edition, American Association of State and Highway Transportation Officials, Washington, D.C.

AISC (2005). *Specification for Structural Steel Buildings,* ANSI/AISC

360-05, American Institute of Steel Construction, Chicago, IL

CEN (2005). *Eurocode 3: Design of Steel Structures, Part 1.1 – General Rules and Rules for Buildings*, EN 1993-1-1, European Committee for Standardization, Brussels, Belgium.

Dux, P.F. and Kitipornchai, S. (1983). "Inelastic Beam Buckling Experiments," *Journal of Constructional Steel Research*, Vol. 3, No. 1:1983, 3-9.

ECCS (2006). *Rules for Member Stability in EN 1993-1-1 – Background Documentation and Design Guidelines,* Report No. 119, Technical Committee 8 – Stability, European Convention for Constructional Steelwork, Brussels, Belgium.

Gardner, L. and Nethercot, D.A. (2005). *Designers' Guide to EN 1993-1-1 Eurocode 3: Design of Steel Structures General Rules and Rules for Buildings*, Thomas Telford Publishing, London, UK, 165 pp.

Kim, Y.-D. and White, D.W. (2007a). "Practical Buckling Solutions for Web-Tapered Members," Proceedings, SSRC Annual Meeting and Technical Session, New Orleans, LA, 259-278.

Kim, Y.-D. and White, D.W. (2007b). "Assessment of Nominal Resistance Calculations for Web-Tapered I-Section Members: Comparison to Results from Experimental Tests and to Finite Element Simulations of Experimental Tests," SEMM Report No. 31, Civil Engineering, Georgia Tech, Atlanta, GA, April, 56 pp.

Kaehler, R.C., White,. D.W. and Kim, Y.-D. (2008). *Frame Design using Web-Tapered Members*, Metal Building Manufacturers Association and American Institute of Steel Construction, to appear

Lee, G.C., Ketter, R.L. and Hsu, T.L. (1981). *The Design of Single Story Rigid Frames*, Metal Building Manufacturers Association, Cleveland, OH, 267 pp.

Nethercot, D.A. and Gardner, L. (2005). "The EC3 Approach to The Design of Columns, Beams and Beam-Columns," *Steel and Composite Structures*, 5(2-3), 127-140.

Nethercot, D.A. and Trahair, N.S. (1976). "Lateral Buckling Approximations for Elastic Beams," *The Structural Engineer*, 54(6), 197-204.

Ozgur, C., Kim, Y.D. and White, D.W. (2007). "Consideration of End Restraint Effects in Tapered Members," SEMM Report No. 32, Civil Engineering, Georgia Tech, Atlanta, GA, 40 pp.

Prawel, S.P., Morrell, M.L. and Lee, G.C. (1974). "Bending and Buckling Strength of Tapered Structural Members," *Welding Research Supplement*, February, 75 -84.

Richter, J.F. (1998). "Flexural Capacity of Slender Web Plate Girders," M.S. Thesis, Univ. of Texas, Austin, May, 133 pp.

Schilling, C.G. and Morcos, S.S. (1988). "Moment-Rotation Tests of Steel Girders with Ultracompact Flanges," Project. 188, Autostress Design of Highway Bridges, AISI, Washington, D.C.

Simulia (2007). ABAQUS Version 6.7/Standard User's Manual, Simulia, Inc., Providence, RI.

White, D.W. (2004). "Unified Flexural Resistance Equations for Stability Design of Steel I-Section Members – Overview," SEMM Report No. 24, Civil Engineering, Georgia Tech, Atlanta, GA, 42 pp.

White, D.W., Barker, M. and Azizinamini, A. (2004). "Shear Strength and Moment-Shear Interaction in Transversely-Stiffened Steel I-Girders," SEMM Report No. 27, Civil Engineering, Georgia Tech, Atlanta, GA, 82 pp.

White, D.W. and Jung, S.-K. (2004). "Unified Flexural Resistance Equations for Stability Design of Steel I-Section Members – Uniform Bending Tests," SEMM Report No. 28, Civil Engineering, Georgia Tech, Atlanta, GA, 127 pp.

White, D.W. and Kim, Y.D. (2004). "Unified Flexural Resistance Equations for Stability Design of Steel I-Section Members – Moment Gradient Tests," SEMM Report No. 26, Civil Engineering, Georgia Tech, Atlanta, GA, 149 pp.

Wong-Chung, A.D. and Kitipornchai, S. (1987). "Partially Braced Inelastic Beam Buckling Experiments," *Journal of Constructional Steel Research*, 7, 189-211.

Yura, J.A., Galambos, T.V. and Ravindra, M.K. (1978). "The Bending Resistance of Steel Beams," *Journal of the Structural Division,* ASCE, 104(9), 1355-1369.

A NEW 3D CO-ROTATIONAL BEAM-COLUMN ELEMENT

Bulent N. Alemdar[1], Donald W. White[2]

INTRODUCTION

Co-rotational formulations have been developed in numerous prior studies. In this approach, the motion of the element is subdivided into rigid body modes and deformation modes. This approach has several advantages: simple kinematic relationships can be utilized in the natural (co-rotational) frame and the number of dofs is reduced in the natural frame. For 3D analysis, special care must be given to the handling of the element rotations. Unlike the displacement components, finite rotations are non-commutative since they belong to a nonlinear differential manifold.

The current study revisits the work of Nour-Omid and Rankin (1991) and elaborates on this work for beam-columns. Closed form element stiffness matrices are derived for efficient computation and ease of implementation. This is a new result of the present work. Furthermore, the current study suggests a modification to improve the element performance. The orientation of the element chord is updated based on an average of the vectors at the element ends. Finally, a new displacement-based second-order element formulation is developed within the natural frame. This formulation addresses the coupling between bending, torsion and axial effects, section warping due to nonuniform torsion, and Wagner effects.

[1] Senior Developer, Bentley Systems, Inc., Structural Engineering Group, 2744 Loker Avenue West, Suite 103, Carlsbad, CA, 92010
[2] Professor, School of Civil and Environmental Engineering, Georgia Institute of Technology, GA 30332-0355

GLOBAL ELEMENT FORMULATION

Representation of Finite Rotations. Three dimensional rotations belong to a special orthogonal (Lie) group, SO(3). The characteristic properties for a member $\mathbf{T}$ in this group are: $\mathbf{T}\mathbf{T}^T = \mathbf{T}^T\mathbf{T} = \mathbf{I}$ and det($\mathbf{T}$) =+1. SO(3) constitutes a nonlinear manifold. The final position after a sequence of rotations can not be obtained by simply adding the rotations (i.e., finite rotations are non-commutative). Another important observation for SO(3) is that the rotation increments (or infinitesimal rotations) are located on a plane defined at the tangent to the actual rotation. The tangent plane at the actual rotation is referred to as so(3) and it forms a linear space for the rotation increments. Figure 1a gives a pictorial representation of finite rotations showing two tangent planes, namely so(3):1 and so(3):2, tangent to SO(3) at **I** and **A** for consecutive rotations of $\boldsymbol{\theta}$ and $\boldsymbol{\delta}\mathbf{w}$. The final rotation is not simply $\boldsymbol{\theta} + \boldsymbol{\delta}\mathbf{w}$ since these rotations are located at different tangent planes. Rather, a more involved updating procedure is required to obtain the final rotation.

The rotational matrix $\mathbf{T}$ can be expressed in different forms, based on parameters such as Euler angles, semi-tangential rotations, or rotational vectors, to name a few. This work adopts a rotational vector representation, $\boldsymbol{\theta}$, for $\mathbf{T}$. Note that $\boldsymbol{\theta}^T = \lfloor \theta_1 \quad \theta_2 \quad \theta_3 \rfloor$, $\theta = \|\boldsymbol{\theta}\|$ and θ_i is a component of rotation vector $\boldsymbol{\theta}$ (i.e., θ_i is not a rotation about an axis). Hence,

$$\mathbf{T}(\boldsymbol{\theta}) = \mathbf{I} + \frac{\sin\theta}{\theta}\tilde{\boldsymbol{\Theta}} + \frac{1-\cos\theta}{\theta^2}\tilde{\boldsymbol{\Theta}}\tilde{\boldsymbol{\Theta}} \tag{1}$$

where $\tilde{\boldsymbol{\Theta}}$ a skew symmetric matrix, constructed from $\boldsymbol{\theta}$:

$$\tilde{\boldsymbol{\Theta}} = \tilde{\boldsymbol{\Theta}}(\boldsymbol{\theta}) = \mathrm{spin}(\boldsymbol{\theta}) = \boldsymbol{\theta}\times = \begin{bmatrix} 0 & -\theta_3 & \theta_2 \\ \theta_3 & 0 & -\theta_1 \\ -\theta_2 & \theta_1 & 0 \end{bmatrix} \tag{2}$$

Equation (1) can be expressed in an alternative form by replacing the sine and cosine terms with their equivalent power series expansions:

$$\mathbf{T}(\boldsymbol{\theta}) = \mathbf{I} + \tilde{\boldsymbol{\Theta}} + \frac{1}{2!}\tilde{\boldsymbol{\Theta}}^2 + \cdots = \mathrm{e}^{\mathrm{spin}(\boldsymbol{\theta})} = \mathrm{e}^{\tilde{\boldsymbol{\Theta}}} \tag{3}$$

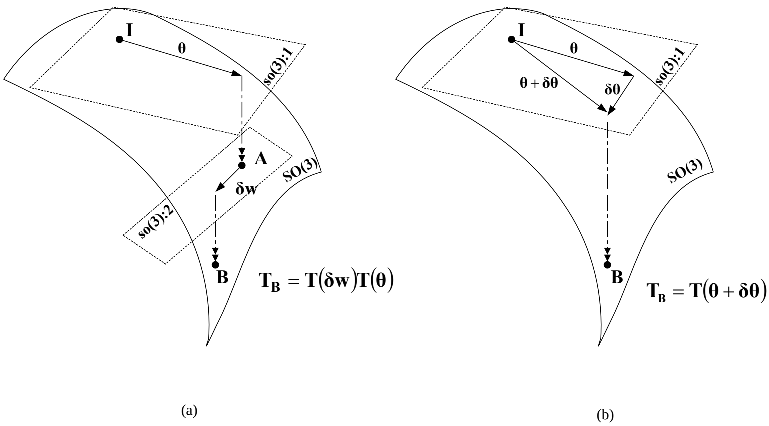

Figure 1 (a) Successive finite rotations on different tangent planes
(b) Mapping current rotations to initial tangent plane

This is called the exponential map. The inverse of the above mapping is

$$\tilde{\boldsymbol{\Theta}} = \mathrm{Log_e}\,\mathbf{T} \tag{4}$$

Spurrier (1978) provides a solution to obtain $\tilde{\boldsymbol{\Theta}}$ from $\mathbf{T}$. Compound rotations are obtained by superposing rotations on existing rotations:

$$\mathbf{T}^{i+1} = \mathbf{T}\,\mathbf{T}^{i} \tag{5}$$

which is also referred to as updating via a left translation (Cardona and Geradin, 1988), or rotation about follower-axis (Argyris at. al., 1979), or a spatial rotation update. The variation of the rotations is obtained by recognizing the following identity (Cardona and Geradin, 1988):

$$\boldsymbol{\delta}\mathbf{T} = \boldsymbol{\delta}\tilde{\boldsymbol{\theta}}\,\mathbf{T} \tag{6}$$

which can be interpreted as superposing skew-symmetric matrices of finite rotation variations on existing rotations. Also, a close look into Eq. (6) leads to the following expression establishing the relationship between the infinitesimal rotation vector, $\boldsymbol{\delta}\mathbf{w}$, located on the tangent plane at the actual rotation and the infinitesimal rotation vector, $\boldsymbol{\delta\theta}$, located on a tangent plane at the initial rotation (identity):

$$\boldsymbol{\delta}\mathbf{w} = \boldsymbol{\Lambda}\,\boldsymbol{\delta\theta} \tag{7}$$

where $\mathbf{\Lambda}$ is given by Alemdar and White (2007). In Fig. (1a), the infinitesimal rotation vectors $\boldsymbol{\delta\theta}$ and $\boldsymbol{\delta w}$ are portrayed graphically on the tangent planes so(3):1 and so(3):2, respectively: so(3):1 is tangent to SO(3) at point **I** (identity) whereas so(3):2 is tangent at point **A** (actual rotation). A proper updating procedure to find final rotations (denoted by point **B**) is followed by either calculating $\mathbf{T}(\boldsymbol{\delta w})\mathbf{T}(\boldsymbol{\theta})$ or by converting $\boldsymbol{\delta w}$ into $\boldsymbol{\delta\theta}$ and then calculating $\mathbf{T}(\boldsymbol{\theta}+\boldsymbol{\delta\theta})$. The former method is a standard updating via a left translation (spatial update) and the later involves mapping infinitesimal rotations calculated on a plane tangent to SO(3) at the actual rotation into infinitesimal rotations on a tangent plane defined at identity (**I**) (see Fig. (1b)). Once the rotations are mapped back to the tangent plane at identity, the final rotations are obtained by $\boldsymbol{\theta}+\boldsymbol{\delta\theta}$. This update is additive since the corresponding tangent plane is a linear space where finite rotations are commutative. The proposed formulation adopts an orthogonal rotation matrix parameterization ($\boldsymbol{\delta w}$) to represent the finite rotation effects. An alternative formulation approach is to adopt $\boldsymbol{\delta\theta}$ as a state variable of the formulation by utilizing Eq. (7) (rotation vector parameterization). This approach is followed in Alemdar and White (2007).

Kinematic Description. The element formulation is developed using three reference systems: a fixed Cartesian global system; a local element system uniquely determined by the element chord base vectors (any kinematic variable written in this system contains rigid body motion modes and deformational modes); and the element natural system, defined by the element base vectors (the kinematic variables in this system contain only deformational modes). To this end, superscript g denotes the global system, superscript e denotes the local system, and an overbar indicates the natural system. If no superscript or overbar is used, the quantity is in the global system. The beam-column element is assumed to be subjected to conservative loads as it moves from its initial state to its current state (Fig. 2). The motion of element is characterized by its end displacements and its end cross-section orientations. The element chord connecting the element end nodes is defined by an orthogonal matrix $\mathbf{E}=\lfloor \mathbf{e}_1 \quad \mathbf{e}_2 \quad \mathbf{e}_3 \rfloor$ which also defines the element local (natural) system. All deformations and local rotations are measured with respect to the element chord. The vectors $\mathbf{e}_i$ are referred to as the element base vectors. These vectors are attached to the element chord and continuously rotate with the element. At its initial state, $\mathbf{E}$ is equal to $\mathbf{E}_o$ (defined by base vectors $\mathbf{e}_{1o}, \mathbf{e}_{2o}$ and $\mathbf{e}_{3o}$). Another orthogonal matrix $\mathbf{T}^g$ is defined for each end node. This matrix defines the cross-section orientation ($\hat{\mathbf{e}}_i = \mathbf{T}^g\, \mathbf{e}_{io}$). The element axial deformations in the natural frame are expressed as:

$$\overline{\mathbf{u}}_2^e = \mathbf{E}^T \left(\mathbf{u}_2^g + \mathbf{X}_2^g - \mathbf{u}_1^g - \mathbf{X}_1^g \right) - \overline{\mathbf{X}}_2^e \tag{8}$$

where $\left\| \overline{\mathbf{u}}_2^e \right\|$ is simply $\mathrm{L} - \mathrm{L}_o$, the difference between element's final and initial chord length. The matrix $\mathbf{T}^g$ can be converted to the element local system utilizing the following expression:

$$\mathbf{T}^e = \mathbf{E}^T\, \mathbf{T}^g\, \mathbf{E} \tag{9}$$

in which the matrix $\mathbf{T}^e$ contains both deformational and rigid body modes and is written in the element local system. To remove rigid body rotations, one needs to recognize the following identity

$$\overline{\mathbf{T}}^g\, \mathbf{E} = \mathbf{T}^g\, \mathbf{E}_o \tag{10}$$

and then pre-multiply both sides with $\mathbf{E}^T$ to obtain

$$\overline{\mathbf{T}}^e = \mathbf{E}^T\, \mathbf{T}^g\, \mathbf{E}_o \tag{11}$$

The orientation of the chord is defined by the base vectors $\mathbf{e}_i$ (see Fig. 2). The choice of these vectors has a significant impact on the simplicity of the formulation. The base vector $\mathbf{e}_1$ can be expressed as:

$$\mathbf{e}_1 = \frac{\mathbf{x}_2 - \mathbf{x}_1}{\mathrm{L}} \tag{12}$$

where $\mathbf{x}_i$ is the position vector at the i[th] end (i.e., $\mathbf{x}_i = \mathbf{u}_i^g + \mathbf{X}_i^g$). A variation in the state variables for $\mathbf{e}_1$ leads to

$$\delta\mathbf{e}_1 = \frac{\mathbf{e}_2}{\mathrm{L}} \left(\delta u_{22}^e - \delta u_{12}^e \right) + \frac{\mathbf{e}_3}{\mathrm{L}} \left(\delta u_{23}^e - \delta u_{13}^e \right) \tag{13}$$

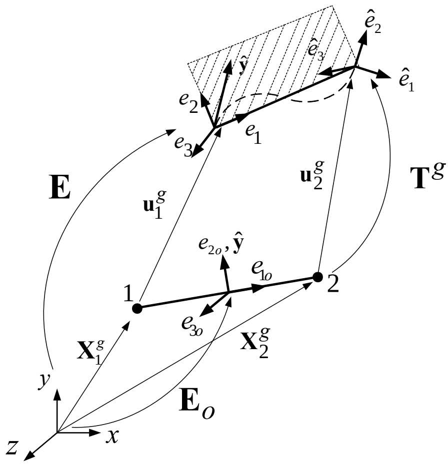

Figure 2. Motion of beam-column element under large displacements and rotations

where u_{ij}^e denotes the displacements at node i and dof j in the element local system. To derive $\mathbf{e_3}$ and its variational form, a new vector $\hat{\mathbf{y}}$ is introduced. Initially, this vector coincides with $\mathbf{e}_{2o}$ and rotates as the element deforms. It is located on the plane of $\mathbf{e}_1$ and $\mathbf{e}_2$, and thus, it is always perpendicular to $\mathbf{e}_3$. The vector $\hat{\mathbf{y}}$ is defined as

$$\hat{\mathbf{y}} = \mathbf{T}^g\, \mathbf{E_o} \begin{Bmatrix} 0 \\ 1 \\ 0 \end{Bmatrix} \tag{14}$$

and it is used to determine the current orientation of the element chord. In this study, $\hat{\mathbf{y}}$ is defined based on an average of the orientations at node 1 and 2. Thus, $\mathbf{e}_3$ and its variations are

$$\mathbf{e}_3 = \frac{\mathbf{e}_1 \times \hat{\mathbf{y}}_{avg}}{\left|\mathbf{e}_1 \times \hat{\mathbf{y}}_{avg}\right|} \tag{15}$$

$$\delta\mathbf{e}_3 = -\frac{\mathbf{e}_1}{\mathrm{L}}\left(\delta u_{23}^e - \delta u_{13}^e\right) + \frac{\mathbf{e}_2}{\hat{y}_{avg2}^e\,\mathrm{L}}\left(\hat{y}_{avg1}^e\left(\delta u_{23}^e - \delta u_{13}^e\right) - \mathrm{L}\,\delta\hat{y}_{avg3}^{\mathrm{e}}\right) \quad (16)$$

Finally, $\mathbf{e}_2 = \mathbf{e}_3 \times \mathbf{e}_1$, which completes the definition of $\mathbf{E}$. The variation of $\hat{\mathbf{y}}$ is needed and can be expressed for node i as:

$$\delta\hat{\mathbf{y}}_i^e = \mathrm{spin}\left(\delta\mathbf{w}_i^e\right)\hat{\mathbf{y}}_i^e = \begin{Bmatrix} -\delta w_{i3}^e\,\hat{y}_{i2}^e \\ \delta w_{i3}^e\,\hat{y}_{i1}^e \\ -\delta w_{i2}^e\,\hat{y}_{i1}^e + \delta w_{i1}^e\,\hat{y}_{i2}^e \end{Bmatrix} \quad (17)$$

In the following, the variation of $\mathbf{E}$ is also needed. Referring to Eq. (6) and noticing that any orthogonal matrix in the global system can be converted to the element local system as in Eq. (9), one obtains

$$\delta\tilde{\mathbf{\Omega}}_E^e = \mathbf{E}^T\delta\mathbf{E} \quad (18)$$

and the vector $\delta\mathbf{w}_E^e$ associated with $\delta\tilde{\mathbf{\Omega}}_E^e$ is expressed as

$$\delta\mathbf{w}_E^e = \begin{Bmatrix} -\mathbf{e}_2^T\,\delta\mathbf{e}_3 \\ -\mathbf{e}_3^T\,\delta\mathbf{e}_1 \\ \mathbf{e}_2^T\,\delta\mathbf{e}_1 \end{Bmatrix} = \mathbf{\Gamma}^T\,\delta\mathbf{q}^e \quad (19)$$

and

$$\mathbf{\Gamma}^T = \begin{bmatrix} 0 & 0 & \frac{\xi_{avg}}{\mathrm{L}} & \frac{\eta_1}{2} & -\frac{\xi_1}{2} & 0 & 0 & 0 & -\frac{\xi_{avg}}{\mathrm{L}} & \frac{\eta_2}{2} & -\frac{\xi_2}{2} & 0 \\ 0 & 0 & \frac{1}{\mathrm{L}} & 0 & 0 & 0 & 0 & 0 & -\frac{1}{\mathrm{L}} & 0 & 0 & 0 \\ 0 & -\frac{1}{\mathrm{L}} & 0 & 0 & 0 & 0 & 0 & \frac{1}{\mathrm{L}} & 0 & 0 & 0 & 0 \end{bmatrix} \quad (20)$$

$$\xi_{avg} = \frac{\hat{y}_{\mathrm{avg1}}^e}{\hat{y}_{\mathrm{avg2}}^e} \quad \xi_1 = \frac{\hat{y}_{11}^e}{\hat{y}_{\mathrm{avg2}}^e} \quad \xi_2 = \frac{\hat{y}_{21}^e}{\hat{y}_{\mathrm{avg2}}^e} \quad \eta_1 = \frac{\hat{y}_{12}^e}{\hat{y}_{\mathrm{avg2}}^e} \quad \eta_2 = \frac{\hat{y}_{22}^e}{\hat{y}_{\mathrm{avg2}}^e} \quad (21)$$

$$\begin{aligned} \left(\delta\mathbf{q}^e\right)^T &= \left\lfloor \delta\mathbf{q}_1^{eT} \quad \delta\mathbf{q}_2^{eT} \right\rfloor \\ \delta\mathbf{q}_i^{eT} &= \left\lfloor \delta u_{i1}^e \quad \delta u_{i2}^e \quad \delta u_{i3}^e \quad \delta w_{i1}^e \quad \delta w_{i2}^e \quad \delta w_{i3}^e \right\rfloor \end{aligned} \quad (22)$$

Also, the variation of $\overline{\mathbf{T}}^e$ is expressed as

$$\delta\overline{\mathbf{T}}^e = \delta\mathbf{E}^T\,\mathbf{T}\,\mathbf{E_o} + \mathbf{E}\,\delta\mathbf{T}\mathbf{E_o} \tag{23}$$

or equivalently,

$$\delta\overline{\mathbf{w}}_i^e = \delta\mathbf{w}_i^e - \delta\mathbf{w}_E^e \tag{24}$$

for node i. Finally, referring to Eq. (11), one can write

$$\delta\overline{\mathbf{u}}_2^e = \text{spin}\left(\overline{\mathbf{x}}_2^e\right)\delta\mathbf{w}_E^e + \left(\delta\mathbf{u}_2^e - \delta\mathbf{u}_1^e\right) \tag{25}$$

Stiffness Matrices. The strain energy Φ can be defined either in the element local system, $\Phi\left(\mathbf{u}^e, \mathbf{w}^e\right)$ or in terms of deformations in the natural system, $\Phi\left(\overline{\mathbf{u}}^e, \overline{\mathbf{w}}^e\right)$. The element internal forces are derived by taking first derivative of Φ with respect to its variables:

$$\mathbf{f}\left(u_{ij}^e, w_{ij}^e\right) = \mathbf{P}^T\,\mathbf{f}\left(\overline{u}_{ij}^e, \overline{w}_{ij}^e\right) \tag{26}$$

where $\mathbf{f}\left(u^e, w^e\right)$ is the element internal forces in the local system, whereas $\mathbf{f}\left(\overline{u}^e, \overline{w}^e\right)$ is the corresponding element forces with respect to the natural frame. The energy conjugate form of Eq. (26) is

$$\delta\mathbf{d}\left(\overline{u}_{ij}^e, \overline{w}_{ij}^e\right) = \mathbf{P}\quad\delta\mathbf{d}\left(u_{ij}^e, w_{ij}^e\right) \tag{27}$$

It is interesting to note that the matrix $\mathbf{P}$ extracts the rigid body modes when it is applied to infinitesimal total displacements and rotations. This matrix is referred to as projector matrix in Nour-Omid an Rankin (1991). Finally, the following transformation is needed to map the quantities from the element local system to the global system:

$$\mathbf{f}\left(u_{ij}, w_{ij}\right) = \begin{bmatrix} \mathbf{E} & & & \\ & \mathbf{E} & & \\ & & \mathbf{E} & \\ & & & \mathbf{E} \end{bmatrix} \mathbf{f}\left(u_{ij}^e, w_{ij}^e\right) = \mathbf{G}\,\mathbf{f}\left(u_{ij}^e, w_{ij}^e\right) \tag{28}$$

$$\delta\mathbf{d}\left(u_{ij}^e, w_{ij}^e\right) = \mathbf{G}^T\,\delta\mathbf{d}\left(u_{ij}, w_{ij}\right) \tag{29}$$

The above equations can be expressed in the following forms:

$$\mathbf{f}\left(u_{ij}, w_{ij}\right) = \mathbf{G}\,\mathbf{P}^T\,\mathbf{f}\left(\overline{u}_{ij}^e, \overline{w}_{ij}^e\right) \tag{30}$$

$$\delta\mathbf{d}\left(\overline{u}_{ij}^e, \overline{w}_{ij}^e\right) = \mathbf{P}\quad\mathbf{G}^T\,\delta\mathbf{d}\left(u_{ij}, w_{ij}\right) \tag{31}$$

A consistent tangent stiffness matrix is derived by taking the variation of Eq. (30). This leads to the following result:

$$\delta\mathbf{f}\left(u_{ij}, w_{ij}\right) = \mathbf{G}\left(\mathbf{K}_{g1} + \mathbf{K}_{g2} + \mathbf{P}^T\,\overline{\mathbf{K}}^e\,\mathbf{P}\right)\mathbf{G}^T\,\delta\mathbf{d}\left(u_{ij}, w_{ij}\right) \tag{32a}$$

or

$$\delta\mathbf{f} = \mathbf{G}\,\mathbf{K}^e\,\mathbf{G}^T\,\delta\mathbf{q} \tag{32b}$$

In the above equation, $\mathbf{K}^e$ is the tangent stiffness matrix written in the element local system whereas $\overline{\mathbf{K}}^e$ is the tangent stiffness matrix in the natural frame, expressed as

$$\delta\mathbf{f}\left(\overline{u}_{ij}^e, \overline{w}_{ij}^e\right) = \overline{\mathbf{K}}^e\,\delta\mathbf{d}\left(\overline{u}_{ij}^e, \overline{w}_{ij}^e\right) \tag{33}$$

It should be noted that various formulations for $\overline{\mathbf{K}}^e$ can be employed within the natural frame. The above development is not affected by the choice of $\overline{\mathbf{K}}^e$. Its derivation is addressed in the next section. The external geometric stiffness matrix $\mathbf{K}_g$ is composed of two parts. The first part is derived as follows:

$$\mathbf{K}_{g1} = -\begin{Bmatrix} \mathrm{spin}\left(\mathbf{f}_1^e\right) \\ \mathrm{spin}\left(\mathbf{m}_1^e\right) \\ \mathrm{spin}\left(\mathbf{f}_2^e\right) \\ \mathrm{spin}\left(\mathbf{m}_2^e\right) \end{Bmatrix} \mathbf{\Gamma}^T = -\mathbf{F}^e\,\mathbf{\Gamma}^T \tag{34}$$

where $\mathbf{f}_i^e$ and $\mathbf{m}_i^e$ are element internal forces and moments, respectively, written with respect to the local system. To derive $\mathbf{K}_{g2}$, the projector matrix $\mathbf{P}$ is needed. The definition of $\mathbf{P}$ is given in Eq. (26) and is expanded here by substituting Eqs. (24) and (25):

$$\mathbf{P}_{ij} = \begin{bmatrix} \mathbf{I}\delta_{ij} + \mathrm{spin}\left(\overline{\mathbf{x}}_i^e\right)\dfrac{\partial \mathbf{w}_E^e}{\partial \mathbf{u}_j^e} - \dfrac{\partial \mathbf{u}_1^e}{\partial \mathbf{u}_j^e} & \mathrm{spin}\left(\overline{\mathbf{x}}_i^e\right)\dfrac{\partial \mathbf{w}_E^e}{\partial \mathbf{w}_j^e} \\ -\dfrac{\partial \mathbf{w}_E^e}{\partial \mathbf{u}_j^e} & \mathbf{I}\delta_{ij} - \dfrac{\partial \mathbf{w}_E^e}{\partial \mathbf{w}_j^e} \end{bmatrix} \tag{35}$$

A closed-form for $\mathbf{P}$ is given in Alemdar and White (2007). Also, using the above equation, an explicit form of $\mathbf{K}_{g2}$ is derived (Alemdar and White, 2007). One observation from $\mathbf{K}_{g1}$ and $\mathbf{K}_{g2}$ is that they not only contain the element forces but they are also related to the element chord orientation through $\hat{\mathbf{y}}$. Also, both matrices are not symmetric. The above lack of symmetry comes from the nature of finite rotations and has been observed in other studies (Crisfield, 1990; Simo and Vu-Quoc, 1986; and Ibrahimbegovic et. al. 1996; Cardona and Geradin, 1988). As indicated in these studies, the symmetric form of the tangent matrix is attained when the element reaches an equilibrium state. The current study uses the symmetric part of the tangent stiffness matrix to reach an equilibrium state. For the problems studied, it is found that this does not have any adverse impact on the convergence behavior.

FORMULATION IN THE NATURAL FRAME

This section develops the equations for a second-order elastic beam-column with a thin-walled open cross-section. It focuses on the deformational components of the element motion, aiming at deriving $\overline{\mathbf{K}}^e$ in Eq. (33). For simplicity, the derivations are carried out without using the superscript e and the overbar. The formulation is based on the following assumptions: Vlasov kinematics; doubly symmetric cross-section (i.e., geometric centroid and shear center coincide); rotations (within the natural frame) approximated by first derivatives of transverse displacements. Based on these assumptions, the element normal strains may be written as follows (Alemdar 2001):

$$\varepsilon = u' + \frac{1}{2}\left(v'\right)^2 + \frac{1}{2}\left(w'\right)^2 - y v'' - z w'' + \frac{1}{2}\left(y^2 + z^2\right)\left(\phi'\right)^2 - y \phi w'' + z \phi v'' \tag{36}$$

where the coordinates y and z are measured with respect to the centroid. The variable u is the axial displacement at the element chord, v and w, transverse displacements measured from the cross-section centroid, and ϕ is the angle of twist. Geometric nonlinear effects are represented by $1/2\left(dv/dx\right)^2$ and $1/2\left(dw/dx\right)^2$. These terms capture the coupling between axial tension-compression and bending. The term

$1/2\left(y^2+z^2\right)\left(d\phi/dx\right)^2$ is referred to as the Wagner strain and captures the effect of torsion on the axial strain. Finally, coupling between bending and torsion is captured via the terms $y\phi\, w''$ and $z\phi\, v''$. Also, the shear strains are defined to vary linearly through the thickness of component plates of the cross section with a zero mid-plane value:

$$\gamma = -2r\phi' \tag{37}$$

where r indicates the distance measured from the mid-plane. Equation (37) is a first-order approximation and gives reasonable results for cross-sections with thin components (Teh and Clarke 1998). The element in this study has seven dofs in the natural frame (see Fig. 3): an axial elongation of the element chord and three rotations relative to the element chord at each end. The principle of virtual displacements is used to derive the element tangent stiffness:

$$\int_{V_o} \delta\hat{\boldsymbol{\varepsilon}}^T \boldsymbol{\sigma} dV - \delta\mathbf{q}^T \mathbf{Q}_{\text{ext}} = 0 \tag{38}$$

where $\boldsymbol{\sigma}$ and $\delta\hat{\boldsymbol{\varepsilon}}$ are the stress and the variation in the strain at a point. The term $\mathbf{Q}_{\text{ext}}$ is the vector of applied forces at the element nodes and $\delta\mathbf{q}$ is the variation of $\mathbf{q} = \lfloor e \quad \theta_1 \quad \theta_2 \quad \theta_3 \quad \theta_4 \quad \theta_5 \quad \theta_6 \rfloor$. The current formulation adopts a linear field for axial elongation and cross-section twist (if warping is not included), and cubic Hermitian functions for the transverse displacements:

$$u = \mathbf{N}_u{}^T \mathbf{q} \quad , \quad v = \mathbf{N}_v{}^T \mathbf{q} \quad , \quad w = \mathbf{N}_w{}^T \mathbf{q} \quad , \quad \phi = \mathbf{N}_\phi{}^T \mathbf{q} \tag{39}$$

$$\begin{aligned}
\mathbf{N}_u^T &= \lfloor N_{u1} \quad 0 \quad 0 \quad 0 \quad 0 \quad 0 \quad 0 \rfloor \\
\mathbf{N}_w^T &= \lfloor 0 \quad 0 \quad 0 \quad N_{v1} \quad 0 \quad 0 \quad N_{v2} \rfloor \\
\mathbf{N}_w^T &= \lfloor 0 \quad 0 \quad N_{w1} \quad 0 \quad 0 \quad N_{w2} \quad 0 \rfloor \\
\mathbf{N}_\phi^T &= \lfloor 0 \quad N_{\phi 1} \quad 0 \quad 0 \quad N_{\phi 2} \quad 0 \quad 0 \rfloor
\end{aligned} \tag{40}$$

$$\begin{gathered}
N_{u1} = \frac{x}{L} \qquad N_{\phi 1} = 1 - \frac{x}{L} \qquad N_{\phi 2} = \frac{x}{L} \\
N_{v1} = -N_{w1} = x - \frac{2x^2}{L} + \frac{x^3}{L^2} \quad N_{v2} = -N_{w2} = -\frac{x^2}{L} + \frac{x^3}{L^2}
\end{gathered} \tag{41}$$

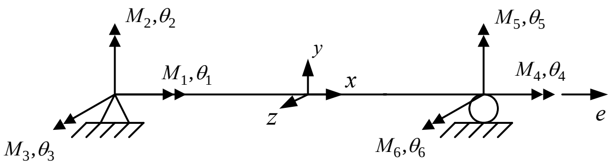

Figure 3. Degrees of freedom and member forces in natural frame

The element formulation based on Eq. (36) exhibits membrane-locking due to the use of the above linear axial and cubic transverse displacement interpolation. To ensure zero axial strain associated with finite bending displacements, a strain smoothing approach (Alemdar, 2001) is adopted. Thus, Eq. (36) is replaced with the following form:

$$\varepsilon = u' + \frac{1}{60}\boldsymbol{\theta}^T \mathbf{X}\boldsymbol{\theta} - y v'' - z w'' + \frac{1}{2}\left(y^2 + z^2\right)\left(\phi'\right)^2 - y\phi\, w'' + z\phi\, v'' \quad (42)$$

where $\boldsymbol{\theta} = \lfloor \theta_1 \quad \theta_2 \quad \theta_3 \quad \theta_4 \quad \theta_5 \quad \theta_6 \rfloor$. The strain variations can be expressed in terms of the generalized section strains $\delta\hat{\mathbf{d}}$ or in terms of end displacements $\delta\mathbf{q}$, i.e.,

$$\delta\hat{\boldsymbol{\varepsilon}} = \begin{Bmatrix} \delta\varepsilon \\ \delta\gamma \end{Bmatrix} = \mathbf{S}\,\delta\hat{\mathbf{d}} = \mathbf{S}\mathbf{N}_{\delta\hat{d}1}\mathbf{N}_{\delta\hat{d}2}\delta\mathbf{q} \quad (43)$$

$$\mathbf{S} = \begin{bmatrix} 1 & -y & z & y^2 + z^2 & 0 \\ 0 & 0 & 0 & 0 & -2r \end{bmatrix} \quad (44)$$

The terms $\mathbf{N}_{\delta\hat{d}1}$ and $\mathbf{N}_{\delta\hat{d}2}$ constructed from the selected interpolation functions are given in Alemdar and White (2007). After substituting Eq. (43) into Eq. (38) and observing the fact that Eq. (38) must be satisfied for an arbitrary choice of $\delta\mathbf{q}$, one obtains

$$\mathbf{g} = \int_0^{L_0} \left(\mathbf{N}_{\delta\hat{d}2}^T \mathbf{N}_{\delta\hat{d}1}^T \mathbf{D}_\Sigma\right) dx - \mathbf{Q}_{ext} \quad (45)$$

where $\mathbf{D}_\Sigma^T = \lfloor P \quad M_z \quad M_y \quad W \quad T_{sv} \rfloor$ is the cross-section internal force vector and it is expressed as

$$\mathbf{D}_{\Sigma} = \int_{A_o} \mathbf{S}^T \boldsymbol{\sigma}\, dA \tag{46}$$

in which $\boldsymbol{\sigma}$ contains the axial and shear stresses at a point on the section, i.e., $\boldsymbol{\sigma}^T = \lfloor \sigma \quad \tau \rfloor$. The section forces W and T_{sv} are the Wagner stress resultant and the St. Venant torque, respectively. Major and minor axis moments are denoted by M_z and M_y, and P is the axial force. Also, the increment in section forces may be expressed as

$$\Delta\mathbf{D}_{\Sigma} = \int_{A_o} \mathbf{S}^T \Delta\boldsymbol{\sigma}\, dA = \int_{A_o} \mathbf{S}^T \mathbf{C}\mathbf{S}\, dA\ \mathbf{N}_{\delta\hat{d}1} \mathbf{N}_{\delta\hat{d}2} \Delta\mathbf{q} \tag{47}$$

$$\Delta\mathbf{D}_{\Sigma} = \mathbf{k}\, \mathbf{N}_{\delta\hat{d}1} \mathbf{N}_{\delta\hat{d}2} \Delta\mathbf{q} \tag{48}$$

where $\mathbf{k}$ is the section tangent stiffness matrix. The matrix $\mathbf{C}$ gives the constitutive relationship between the incremental section stresses and section strains. Any elastic\inelastic material model can be introduced here. In this study, an elastic description is used. Thus, $\mathbf{C} = \{\{E,0\},\{0,G\}\}$ where E and G are the elastic tangent and shear moduli respectively.

Equation (45) is linearized to obtain the element tangent stiffness matrix:

$$\mathbf{K}\,\Delta\mathbf{q} = \mathbf{Q}_{ext}^{i+1} - \mathbf{Q}_{\text{int}}^{i} \tag{49}$$

$$\mathbf{K} = \int_0^{L_0} \mathbf{N}_{\delta\hat{d}2}^T \hat{\mathbf{G}}\, \mathbf{N}_{\delta\hat{d}2} dx + \int_0^{L_0} \mathbf{N}_{\delta\hat{d}2}^T\, \mathbf{N}_{\delta\hat{d}1}^T\, \mathbf{k}\, \mathbf{N}_{\delta\hat{d}1}\, \mathbf{N}_{\delta\hat{d}2}^T\, dx \tag{50}$$

$$\mathbf{Q}_{\text{int}}^{i} = \int_0^{L_0} \left(\mathbf{N}_{\delta\hat{d}1}^{i}\, \mathbf{N}_{\delta\hat{d}2}^{i}\right)^T \mathbf{D}^i\, dx \tag{51}$$

The first term on the right hand side of Eq. (50) is referred to as the element internal geometric stiffness. The matrix $\hat{\mathbf{G}}$ is given in Alemdar and White (2007). The term $\mathbf{K}$ in Eq. (50) is the element tangent stiffness matrix in the natural system, referred to as $\overline{\mathbf{K}}^e$ in Eq. (33). Finally, the right hand side of Eq. (49) is the difference between externally applied force at iteration $i+1$ and the internal forces at the i th iteration.

Incorporating Section Warping. Cross-section warping is added to the above formulation by adding warping strains in Eq. (42). The warping strains are given by $\varpi\phi''$. For doubly-symmetric I-sections, the warping function is $\varpi = \varpi(y,z) = yz$. In this case, the formulation includes two additional warping dofs at each end such that $\mathbf{q} = \lfloor e \quad \theta_1 \quad \theta_2 \quad \theta_3 \quad \theta_{b1}' \quad \theta_4 \quad \theta_5 \quad \theta_6 \quad \theta_{b2}' \rfloor$) and one additional stress resultant section force (the bi-moment). The governing equation for elastic non-uniform torsion of a thin-walled open-section subjected to end torque m_x is

$$\frac{d^4\phi}{dx^4} - p^2 \frac{d^2\phi}{dx^2} = -\frac{m_x}{EC_w} \tag{52}$$

in which C_w is the warping section constant, and $p = \sqrt{GJ / EC_w}$. The corresponding angle of twist can be expressed as:

$$\phi = N_{\phi 1}\theta_1 + N_{\phi 2}\theta_{b1}' + N_{\phi 3}\theta_4 + N_{\phi 4}\theta_{b2}' \tag{53}$$

Alemdar (2001) derived the exact interpolation functions for Eq. (52) in the context of geometrically-linear theory. These functions reduce to the cubic Hermitian functions when p approaches zero. Also, it is noted that p varies between 0.2 and 2.5 and the cubic functions are reasonably accurate for typical rolled I-sections. Thus,

$$\begin{aligned}
\mathbf{N}_u^T &= \lfloor N_{u1} \quad 0 \quad 0 \quad 0 \quad 0 \quad 0 \quad 0 \quad 0 \quad 0 \rfloor \\
\mathbf{N}_w^T &= \lfloor 0 \quad 0 \quad 0 \quad N_{v1} \quad 0 \quad 0 \quad 0 \quad N_{v2} \quad 0 \rfloor \\
\mathbf{N}_w^T &= \lfloor 0 \quad 0 \quad N_{w1} \quad 0 \quad 0 \quad 0 \quad N_{w2} \quad 0 \quad 0 \rfloor \\
\mathbf{N}_\phi^T &= \lfloor 0 \quad N_{\phi 1} \quad 0 \quad 0 \quad N_{\phi 2} \quad N_{\phi 3} \quad 0 \quad 0 \quad N_{\phi 4} \rfloor
\end{aligned} \tag{54}$$

Finally, the matrix $\mathbf{S}$ is modified to

$$\mathbf{S} = \begin{bmatrix} 1 & -y & z & y^2 + z^2 & \varpi & 0 \\ 0 & 0 & 0 & 0 & 0 & -2r \end{bmatrix} \tag{55}$$

Updated forms of $\mathbf{N}_{\delta\hat{d}1}$, $\mathbf{N}_{\delta\hat{d}2}$ and $\hat{\mathbf{G}}$ are given in Alemdar and White (2007). Also, the section resultant forces are updated to include the bi-moments (i.e., $\mathbf{D}_{\Sigma}^{T} = \lfloor P \quad M_z \quad M_y \quad W \quad B \quad T_{sv} \rfloor$).

STATE DETERMINATION

The element state determination is composed of three phases: handling finite rotations by extracting rigid body modes, calculation of element strains and stresses in the natural frame, and calculation of the tangent stiffness matrix and element forces converted to the global system. The following updating procedures apply to iteration m of an increment in a full Newton-Raphson incremental-iterative global solution algorithm.

Handling of Finite Rotations. Once incremental rotations and displacements (i.e., $\Delta\mathbf{w}$ and $\Delta\mathbf{u}$) are obtained from the global solution, the element is updated to its current state. The equations given below are written for node i of the element:

- Update finite rotations:

$$\mathbf{T}_i^{m+1} = \mathbf{T}(\Delta\mathbf{w}_i)\,\mathbf{T}_i^{m} \tag{56}$$

- Update displacements and warping related dofs

$$\mathbf{u}_i^{m+1} = \Delta\mathbf{u}_i + \mathbf{u}_i^{m} \qquad \left(\theta_{bi}^{'}\right)^{m+1} = \Delta\theta_{bi}^{'} + \left(\theta_{bi}^{'}\right)^{m} \tag{57}$$

- Calculate $\hat{\mathbf{y}}_i$ from Eq. (14)
- Calculate $\mathbf{E}^{m+1}$ from $\hat{\mathbf{y}}_{avg}$
- Update $\overline{\mathbf{T}}_i^{e}$ by substituting $\mathbf{E}^{m+1}$ and $\mathbf{T}^{m+1}$ into Eq. (11)
- Obtain $\overline{\boldsymbol{\theta}}_i^{m+1} = \lfloor \overline{\theta}_{i1} \quad \overline{\theta}_{i2} \quad \overline{\theta}_{i3} \rfloor$ from $\overline{\mathbf{T}}_1^{e}$ (see Spurrier, 1978).

State Determination in the Natural Frame. After obtaining $\Delta\mathbf{q} = \lfloor \Delta\mathbf{u} \quad \Delta\overline{\boldsymbol{\theta}} \rfloor$) in the natural frame, the element state determination procedure is carried out as explained below. Note that finite rotation increments ($\Delta\overline{\boldsymbol{\theta}}$) can be obtained from $\Delta\overline{\boldsymbol{\theta}} = \overline{\boldsymbol{\theta}}^{m+1} - \overline{\boldsymbol{\theta}}^{m}$. It is assumed that the rotations in the natural frame are small .

- Calculate $\Delta\hat{\boldsymbol{\varepsilon}}$. For the element formulation including warping effects, this is given as

$$\Delta\hat{\boldsymbol{\varepsilon}} = \left\{ \begin{array}{l} \mathbf{N}_u^{'\,T} + \varpi \mathbf{N}_\phi^{''\,T} - y\left(\mathbf{N}_v^{''\,T} + \mathbf{q}^T \mathbf{N}_\phi \mathbf{N}_w^{''\,T} + \mathbf{q}^T \mathbf{N}_w^{''} \mathbf{N}_\phi^T \right) \\ + z\left(-\mathbf{N}_w^{''\,T} + \mathbf{q}^T \mathbf{N}_\phi \mathbf{N}_v^{''\,T} + \mathbf{q}^T \mathbf{N}_v^{''} \mathbf{N}_\phi^T \right) + \left(y^2 + z^2 \right) \mathbf{q}^T \mathbf{N}_\phi^{'} \mathbf{N}_\phi^{'\,T} \end{array} \right\} \Delta\mathbf{q} +$$

$$\frac{1}{2}\Delta\mathbf{q}^T \left\{ -y\left(2\mathbf{N}_\phi \mathbf{N}_w^{''\,T} \right) + z\left(2\mathbf{N}_\phi \mathbf{N}_v^{''\,T} \right) + \left(y^2 + z^2 \right) \mathbf{N}_\phi^{'} \mathbf{N}_\phi^{'\,T} \right\} \Delta\mathbf{q} + \tag{58}$$

$$\frac{1}{30}\boldsymbol{\theta}^T \mathbf{X} \Delta\boldsymbol{\theta} + \frac{1}{60}\Delta\boldsymbol{\theta}^T \mathbf{X} \Delta\boldsymbol{\theta}$$

In the above, the term $\varpi \mathbf{N}_\phi^{''\,T}$ is omitted if warping is omitted.

- Calculate $\Delta\mathbf{D}_\Sigma$

$$\Delta\mathbf{D}_\Sigma = \int_{A_o} \mathbf{S}^T \Delta\boldsymbol{\sigma}\, dA = \int_{A_o} \mathbf{S}^T \mathbf{C}\, \Delta\hat{\boldsymbol{\varepsilon}}\, dA \tag{59}$$

and update $\mathbf{D}_\Sigma$: $\mathbf{D}_\Sigma^{m+1} = \mathbf{D}_\Sigma^{m} + \Delta\mathbf{D}_\Sigma$

- Calculate $\mathbf{K}^{m+1} = \left(\overline{\mathbf{K}}^e\right)^{m+1}$ from Eq. (50)
- Calculate the forces $\mathbf{Q}_{\text{int}}^{m+1}$ from Eq. (51).

Tangent Stiffness Matrix and Element Forces.

- Calculate $\mathbf{P}^{m+1}$ from $\hat{\mathbf{y}}_{avg}$
- Construct $\mathbf{G}^{m+1}$ from $\mathbf{E}^{m+1}$
- Calculate geometric stiffness matrices, $\mathbf{K}_{g1}^{m+1}$ and $\mathbf{K}_{g2}^{m+1}$
- Update tangent stiffness matrix

$$\mathbf{K}^g = \mathbf{G}^{m+1}\left(\mathbf{K}_{g1}^{m+1} + \mathbf{K}_{g2}^{m+1} + \left(\mathbf{P}^{m+1}\right)^T \left(\overline{\mathbf{K}}^e\right)^{m+1} \mathbf{P}^{m+1} \right)\left(\mathbf{G}^{m+1}\right)^T \tag{60}$$

- Finally convert the forces $\mathbf{Q}_{\text{int}}^{m+1}$ to the global system:

$$\mathbf{Q}_{\text{int}}^{g} = \mathbf{G}^{m+1}\left(\mathbf{P}^{m+1}\right)^T \mathbf{Q}_{\text{int}}^{m+1} \tag{61}$$

EXAMPLES

In the previous sections, the element formulation with and without warping effects are included. These are referred to as the B12 and B14, respectively. In this section, several numerical examples are provided to demonstrate the efficiency and accuracy of the proposed elements. A 7-point Gauss-Lobatto integration rule is used along the element lengths. An arc length solution algorithm with an iterative-incremental full Newton-Raphson solution procedure is used in all the examples.

Lateral Torsional Buckling of an I-Beam. The buckling of a W10x100 beam is studied in this example. The beam is loaded in pure bending about its major axis and a small perturbation moment is applied at one end about its minor axis. The member is simply supported. Figure 4 shows the problem definition and results in terms of the moment normalized by M_{cr} (15057 k-in considering the effect of pre-buckling displacements, Chen and Lui, 1987) versus the normalized mid-span out-of-plane deflection.

Simply Supported Right Angle Frame. The classical solution for buckling load is given by Timoshenko and Gere (1961) as $M_{cr} = 2\pi\sqrt{EI_y GJ}\,/\,L$. The frame is allowed to slide on the x-axis and to rotate around z-axis at its ends. The apex of the frame is constrained to remain in the y-z plane. The problem definition is given in Fig. 5. The frame is subjected to moments at both ends and a small perturbation load is applied along the z-axis at the apex to initiate out-of-plane displacements. The results are compared with other studies in Table 1. Note that 10 elements per member are used in all other studies.

Table 1. Buckling load for the right angle frame

	Buckling Load
Timoshenko and Gere (1961)	622.2
Simo and Vu-Quoc (1986)	615.5
Teh and Clarke (1998)	622.8
Lee et. al. (1994)	618.3
Ibrahimbegovic et. al. (1996)	626.0
Current Element (10 B12 elements per member)	618.7

Cantilever Subjected to a Large Twist Rotation. A 200 mm x 10 mm rectangular beam subjected to large twist is considered here. The beam has E=200000MPa, v=0.25, L=1000mm. The analytical solution is provided by Trahair (2005) as $M = GJ\phi / L + 1/2EI_n(\phi / L)^3$, where ϕ and I_n (17.778E9 mm^6) are the twist rotation at the free end and the Wagner constant respectively. The results are given in Fig. 6 and are compared with the exact nonlinear solution and with a linear solution where the Wagner effects are ignored.

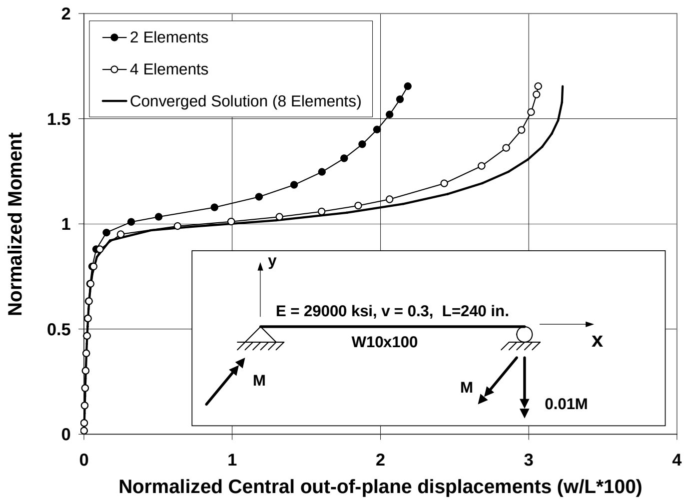

Figure 4. Analysis results for lateral buckling of I-beam (W10x100)

REFERENCES

Alemdar, B. N. and White, D.W., (2007). "A New Co-Rotational Beam Element for Stability Analysis of Three Dimensional Building Frames," Structural Engineering, Mechanics and Materials Report No. 46, School of Civil and Environmental Engineering, Georgia Institute of Technology, Atlanta, GA.

Alemdar, B. N., (2001), Distributed Plasticity Analysis of Steel Building Structural Systems, Ph.D. Thesis, Georgia Institute of Technology, Atlanta, GA.

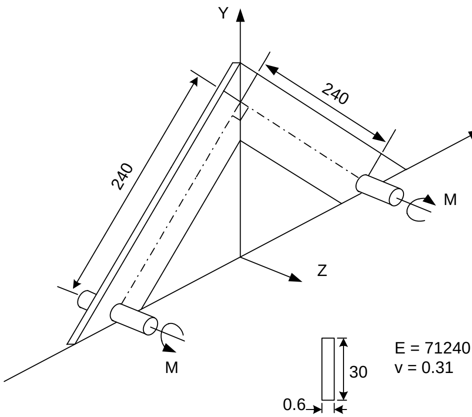

Figure 5. Right angle frame under end moments

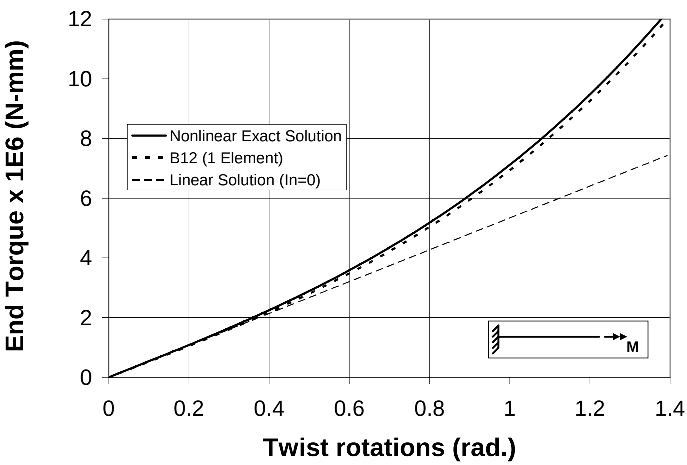

Figure 6. Analysis results for large elastic twist rotations of a cantilever

Argyris, J.H., Balmer, H., Doltsinis, J. St., Dunne, P.C., Haase, M., Kleiber, M., Malejannakis, Mlejenek, H.P., Muller, M., and Scharpf D.W, (1979), "Finite Element Method-the Natural Approach", *Comput. Methods Appl. Mech. Engrg*. 17/18, 1-106

Cardona, A., and Geradin, M. (1988), "A Beam Finite Element Non-Linear Theory with Finite Rotations", *International Journal for Numerical Methods in Engineering*, 26, pp. 2403-2438

Crisfield, M.A., (1990), "A Consistent Co-Rotational Formulation for Non-Linear, Three-Dimensional, Beam-Elements", *Computer Methods in Applied Mechanics and Engineering*, 81 , pp. 131-150

Ibrahimbegovic, A., Shakourzadeh, H., Batoz, J.-L., Al Mikdad, M., Guo, Y.-Q., (1996), "On the role of geometrically exact and second-order theories in buckling and post-buckling analysis of three-dimensional beam structures", *Computers & Structures*, Vol. 61, No. 6, pp. 1101-1114.

Lee, H., Jung, D.-W., Jeong, J.-Ho., and Im, S., (1994), "Finite Element Analysis of Lateral Buckling for Beam Structures", *Computers & Structures*, Vol. 53, No. 6, pp. 1357-1371

Nour-Omid, B., and Rankin, C.C., (1991), "Finite Rotation Analysis and Consistent Linearization Using Projectors", *Computer Methods in Applied Mechanics and Engineering* 93 , pp. 353-384

Simo, J. , Vu-Quoc, L. (1986), "A Three-Dimensional Finite-Strain Rod Model. Part II: Computational Aspects", *Computer Methods in Applied Mechanics and Engineering*, 58, pp. 79-116.

Spurrier, R.A., (1978), "Comment on Singularity-Free Extraction of a Quaternion from Direction Cosine Matrix", *J. Spacecraft*, 15 (4), 255

Teh, Lip H. and Clarke, Murray J., (1998), "Co-rotational and Lagrangian formulations for elastic three-dimensional beam finite elements", *Journal of Constructional Steel Research*, 48, pp. 123-144

Timoshenko S.P. and Gere J.M., (1961), Theory of Elastic Stability, 2^{nd}. New York, McGraw-Hill

Trahair, N.S.,(2005), "Nonlinear Elastic Nonuniform Torsion", *Journal of Structural Engineering*, Vol. 131, No.7, pp.1135-1142

Chen W.F. and Lui, E.M., (1987), Structural Stability: Theory and Implementation, Elsevier.

EXPERIMENTAL STUDY OF OPEN WEB STEEL JOISTS WITH CRIMPED CRITICAL WEB MEMBERS

E.T.Buckley[1], D.W.Dinehart[2], P.S.Green[3], S.P.Gross[2], J.R.Yost[2]

INTRODUCTION AND BACKGROUND

Open web steel joists are manufactured truss like flexural members that are ideal for resisting low levels of load over long spans. These members are typically found in floor or roofing support systems. Joists are typically designed as simply supported and uniformly loaded flexural members that cover long spans to take advantage of their high strength-to-weight ratio. The top chords are almost always in compression and are continuously braced by some type of decking. The bottom chords are generally tension members and are stabilized by horizontal bridging placed at specific locations along the joist. The web members vary between tension and compression members and can be fabricated as bars, single angles, double angles or single angles with crimped ends.

Currently, the design methodology employed by the Steel Joist Institute (SJI, 2005) is based on both allowable stress design (ASD) and load and resistance factor design (LRFD). An LRFD design is performed through the use of resistance factors and by factoring design loads so that the required stress in any given member does not exceed the design stress. An ASD design guarantees that member stresses do not exceed pre-determined allowable stress levels at prescribed service level loads.

When single angle web members are used, a bending moment exists in this member because the load is not applied through the angle's

[1] Structural Engineer, Thornton-Tomasetti, 51 Madison Avenue, New York, NY 10010
[2] Associate Professor, Villanova University, Department of Civil and Env. Eng., 800 Lancaster Avenue, Villanova, PA 19085
[3] Technical Director, Steel Joist Institute, 3127 Mr. Joe White Avenue, Myrtle Beach, SC 29577

centroid. The load is transferred to the web member with an inherent eccentricity because the centroid of the single angle does not intersect with the centroid of the top and bottom chords.

When designing a joist with single angle web members, this eccentricity and resulting bending moment may need to be addressed, since it could reduce the overall load carrying capacity of the entire structural element. In order to eliminate the load eccentricity, the ends of single angle web members may be crimped and oriented such that the member's centroid aligns with the centroid of the chords. From a design standpoint, this method of manufacture is advantageous because it theoretically eliminates the bending stresses that are caused by eccentric loads. It should be noted that crimping the member reduces the weak axis moment of inertia at the crimped locations.

Problem Definition

The motivation behind this study is to better understand the effects of using crimped ends on critical web members for open-web steel joists. The joists supplied for the study were provided by three different manufacturers which allows for comparisons to be made between each manufacturer and the different assembly processes used. These differences in construction and assembly provided a way to identify the joists' overall strengths and weaknesses.

EXPERIMENTAL METHODS

The research conducted consisted of ninety different joists with crimped critical web members made by three separate manufacturers. The colors blue, white and red were given to each manufacturer to distinguish where each joist was assembled so proper comparisons could be made among like joists. Of the ninety joists, each manufacturer produced thirty specimens varying in length, depth, and critical web member size. For each design, two joists were made by each of the three different manufacturers for a total of fifteen different joist designs. Among the fifteen different designs there were three varying lengths. There were thirty joists, each of lengths 8 feet (J1), 22 feet (J2) and 28 feet (J3). The J2 and J3 joists all have a depth of three feet, while J1 has a depth of eighteen inches. There are five different critical web member sizes that are identical among the three joist lengths. The angle sizes of the critical web members are 1.25 in. x 1.25 in., 1.50 in. x 1.50 in., 1.75 in. x 1.75 in., 2 in. x 2 in. and 2.5 in. x 2.5 in. Table 1 shows the test matrix including design loads for each of the fifteen different joist designs. Joist length, depth and critical web member size are the only features of the joist that are required to be identical among all three manufacturers. Often times, joists with the same critical web member size did not have identical other web members or chord sizes. Both the top and bottom chords were manufactured as double angles with one inch chord gaps. Single angles with crimped ends or double angles welded to the exterior of the chords were always used as the non-critical interior web members while double angle or solid round bar was used as exterior web members. The steel angle for all specimens used for the critical web members was cut from the same original length of angle.

Table 1 Text Matrix for crimped web member tests

Joist Series	Span	Depth	Critical Web Size	Design Load (lbs)
J1	8' - 0"	3' - 0"	1.25" x 1.25" x 0.125"	14180
J1	8' - 0"	3' - 0"	1.50" x 1.50" x 0.170"	24232
J1	8' - 0"	3' - 0"	1.75" x 1.75" x 0.170"	29592
J1	8' - 0"	3' - 0"	2.00" x 2.00" x 0.232"	46764
J1	8' - 0"	3' - 0"	2.50" x 2.50" x 0.230"	60790
J2	22' - 0"	3' - 0"	1.25" x 1.25" x 0.125"	2627
J2	22' - 0"	3' - 0"	1.50" x 1.50" x 0.170"	6160
J2	22' - 0"	3' - 0"	1.75" x 1.75" x 0.170"	9910
J2	22' - 0"	3' - 0"	2.00" x 2.00" x 0.232"	19009
J2	22' - 0"	3' - 0"	2.50" x 2.50" x 0.230"	29913
J3	28' - 0"	1' - 6"	1.25" x 1.25" x 0.125"	2630
J3	28' - 0"	1' - 6"	1.50" x 1.50" x 0.170"	6160
J3	28' - 0"	1' - 6"	1.75" x 1.75" x 0.170"	9900
J3	28' - 0"	1' - 6"	2.00" x 2.00" x 0.232"	18940
J3	28' - 0"	1' - 6"	2.50" x 2.50" x 0.230"	30000

All specimens were statically loaded with a point load at midspan to failure. Buckley (2007) provides a detailed description of the testing system, loading rates, data acquisition, and pre-test measurements. A schematic and photograph of the test setup is presented in Figure 1.

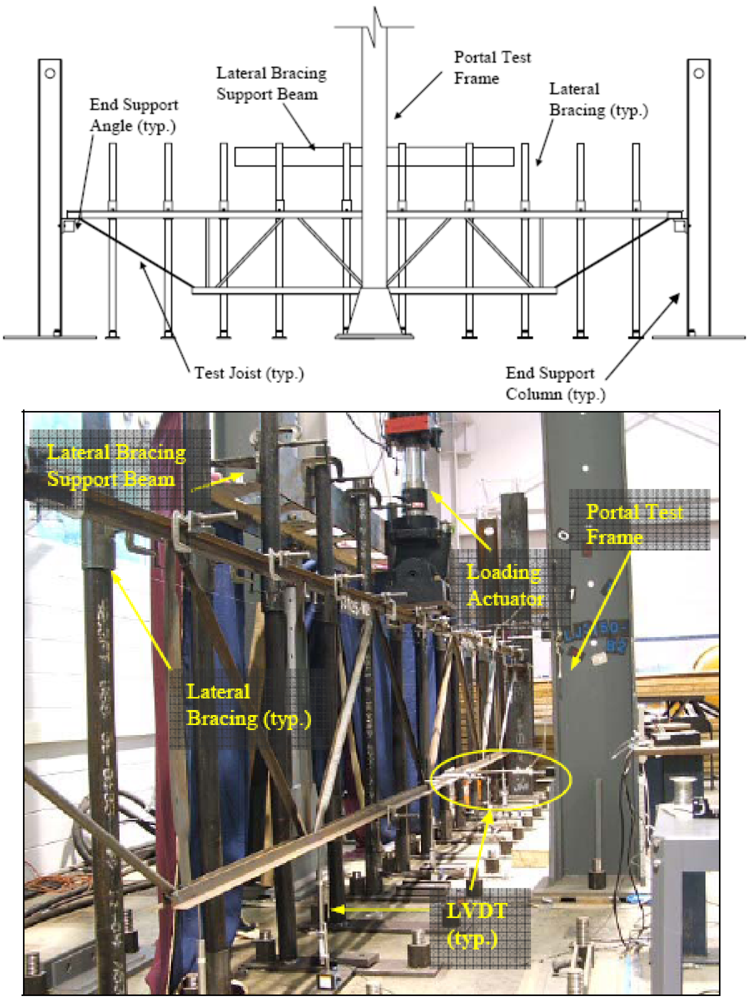

Figure 1 experimental test setup

TEST RESULTS
Failure Types

All 90 joists were tested to failure and midspan deflection was recorded. For the crimped web member joists, 58 out of the 90 specimens failed at the critical web member. There were 29 critical web failures from the J1 series (out of 30 specimens), 18 critical web failures from the J2 series and 11 critical web failures from the J3 series. Figures 2 through 8 depict the different types of failure mechanisms listed in the summary tables. Tables 2 through 4 summarize the critical web member failures for the J1, J2 and J3 joists.

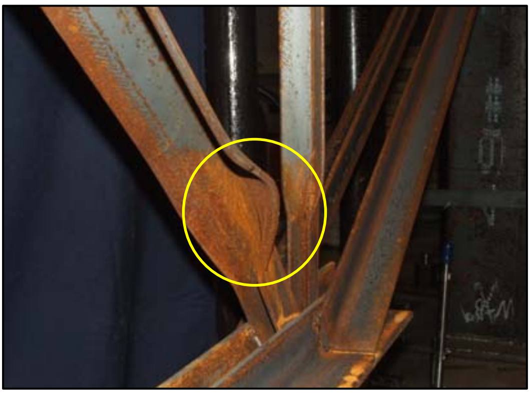

Figure 2 Buckling of the crimp transition zone (J2250-R2)

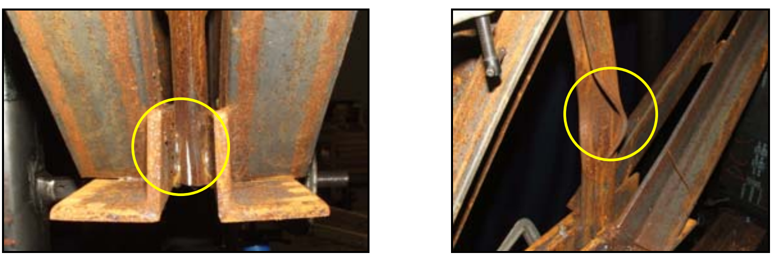

Figure 3 Buckling of crimp transition zone and member fracture (J2200-R1)

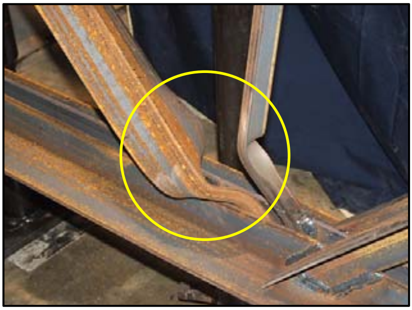

Figure 4 Out-of-plane buckling at the crimp (J3250-W1)

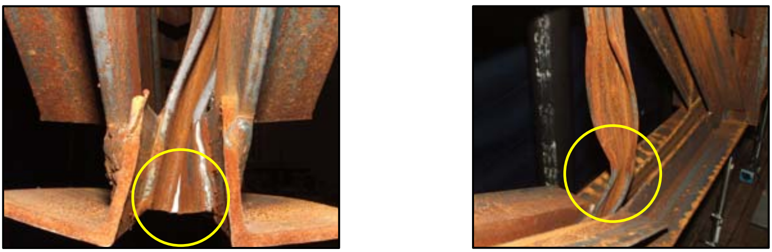

Figure 5 Out-of-plane buckling at crimp and member fracture (J1200-W1)

Figure 6 In-plane buckling of the uncrimped section (J2200-W2)

Figure 7 Out-of-plane buckling of the uncrimped section (J3175-W2)

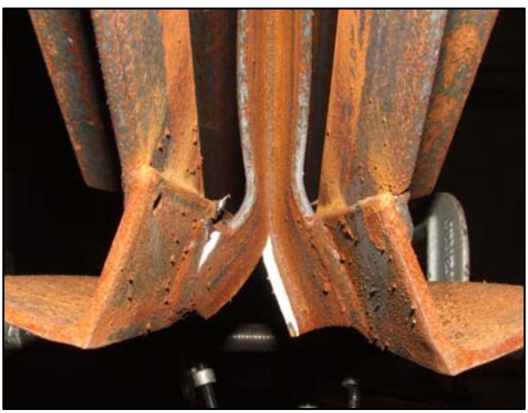

Figure 8 Weld and member fracture at the chord connection (J1175-W1)

Table 2 J1 critical web member failure mechanisms

Test Specimen	Ratio (Exp/Design)	Notes	Failure Mode
J1125-B1	**1.09**	**R**	Buckling of the lower crimp transition zone
J1125-B2	**1.13**	**R**	Buckling of the lower crimp transition zone
J1125-R1	**1.40**	**L**	Buckling of the lower crimp transition zone
J1125-R2	**1.32**	**L**	Buckling of the lower crimp transition zone
J1125-W1	**1.49**	**L**	Buckling of the lower crimp transition zone
J1125-W2	**1.31**	**R**	Buckling of the lower crimp transition zone
J1150-R1	**1.75**	**R**	Buckling of the upper crimp transition zone
J1175-R1	**1.88**	**L**	Buckling of the lower crimp transition zone
J1175-R2	**1.75**	**R**	Buckling of the lower crimp transition zone
J1150-B1	**1.40**	**L**	Out of plane buckling at the lower crimp
J1150-B2	**1.53**	**L**	Out of plane buckling at the lower crimp
J1175-B2	**1.47**	**R**	Out of plane buckling at the lower crimp
J1150-W1	**1.43**	**L**	Out of plane buckling at the lower crimp in addition to weld failure at the bottom chord connection
J1175-W2	**1.56**	**L**	Out of plane buckling at the lower crimp in addition to weld & member fracture at the bottom chord connection
J1200-W1	**1.54**	**L**	Out of plane buckling at the lower crimp in addition to weld & member fracture at the bottom chord connection
J1250-B2	**1.62**	**R**	Out of plane buckling at the lower crimp in addition to weld & member fracture at the bottom chord connection
J1200-W2	**1.66**	**L**	Out of plane buckling at the lower crimp in addition to weld & member fracture at the bottom chord connection of the critical web member & member ***P1***
J1150-W2	**1.40**	**R**	Buckling of the crimp transition zone in addition to weld failure at the bottom chord connection
J1175-B1	**1.44**	**L**	Buckling of the crimp transition zone in addition to weld failure at the bottom chord connection
J1200-R1	**2.01**	**R**	Buckling of the crimp transition zone in addition to weld & member failure at the bottom chord connection
J1250-B1	**1.54**	**L**	Buckling of the crimp transition zone in addition to weld failure at the bottom chord connection
J1250-R1	**1.98**	**L**	Buckling of the crimp transition zone in addition to weld failure at the bottom chord connection
J1250-W1	**1.68**	**L**	Buckling of the crimp transition zone in addition to weld & member fracture at the bottom chord connection of the critical web member
J1175-W1	**1.60**	**L**	Weld and member fracture at the bottom chord connection
J1200-R2	**1.85**	**R**	Weld and member fracture at the bottom chord connection
J1250-W2	**1.98**	**R**	Weld and member fracture at the bottom chord connection
J1200-B2	**1.59**	**L/R**	Weld and member fracture at the bottom chord connection of both critical web members
J1200-B1	**1.51**	**R**	Weld and member fracture at the bottom chord connection in addition to weld failure at the bottom of member ***P6***
J1150-R2	**1.69**	**L**	Fracture along the back heel of the bottom of the angle followed by buckling of the upper crmip transition zone

Table 3 J2 critical web member failure mechanisms

Test Specimen	Ratio (Exp/Design)	Notes	Failure Mode
J2125-R1	**4.37**	**L**	In plane buckling of the uncrimped section
J2200-R2	**2.29**	**R**	In plane buckling of the uncrimped section
J2200-W2	**2.49**	**R**	In plane buckling of the uncrimped section
J2150-R2	**3.17**	**L**	In plane buckling of the uncrimped section
J2125-R2	**4.53**	**R**	Out of plane buckling at the uncrimped section
J2200-B1	**2.18**	**R**	Out of plane buckling at the uncrimped section
J2200-B2	**2.26**	**R**	Out of plane buckling at the uncrimped section
J2200-R1	**2.35**	**L**	Out of plane buckling at the uncrimped section
J2175-B1	**1.41**	**R**	Buckling of the lower crimp transition zone
J2250-R1	**1.39**	**R**	Buckling of the lower crimp transition zone
J2250-R2	**1.30**	**R**	Buckling of the lower crimp transition zone
J2175-B2	**1.97**	**R**	Out of plane buckling at the upper crimp
J2250-B1	**1.66**	**L**	Out of plane buckling at the lower crimp & fracture along the back heel of the critical web member
J2250-W1	**1.72**	**L**	Out of plane buckling of the lower crimp & weld failures at the bottom chord connection of members ***S1*** & ***P1***
J2175-W2	**2.56**	**X-TC / R**	In plane buckling of the top chord & out of plane buckling at the upper crimp
J2200-W1	**2.49**	**X-TC / R**	Local buckling of the top chord & out of plane buckling at the uncrimped secion
J2250-B2	**1.50**	**X-S1 / L**	Fracture along the back heel of ***S1*** & buckling of the lower crimp transition zone of the critical web member
J2250-W2	**1.71**	**X-S3 / L**	Fracture along the back heel of ***S3*** & weld failure at the bottom chord connection of ***S1*** & out of plane buckling at the lower crimp of the left critical web member

Table 4 J3 critical web member failure mechanisms

Test Specimen	Ratio (Exp/Design)	Notes	Failure Mode
J3150-B2	**2.17**	**L**	In plane buckling of the uncrimped section
J3175-B2	**1.83**	**R**	In plane buckling of the uncrimped section
J3200-W1	**2.25**	**L**	In plane buckling of the uncrimped section
J3175-W2	**2.44**	**R**	Out of plane buckling of the uncrimped section and local buckling of the top chord
J3200-R1	**1.47**	**R**	Buckling of the lower crimp transition zone
J3250-B1	**1.93**	**L**	Buckling of the lower crimp transition zone
J3250-B2	**2.01**	**R**	Buckling of the lower crimp transition zone
J3250-R1	**1.39**	**L**	Buckling of the lower crimp transition zone
J3250-R2	**1.36**	**R**	Buckling of the lower crimp transition zone
J3250-W1	**2.13**	**R**	Out of plane buckling at the lower crimp
J3250-W2	**2.10**	**R**	Out of plane buckling at the lower crimp

Load – Deflection Behavior

During each test, applied load data was collected and plotted versus in-plane deflection. Vertical deflection data was recorded using an LVDT at each bottom chord panel point. The *load-deflection* plots for all J2 and J3 joists share the same general behavior as the example plot given in Figure 9. The J1 plots, however, vary for the majority of the tests due to the fact that the joists did not immediately lose capacity after the critical web member initially failed. Figure 10 presents an example of the load-deflection behavior for a J1 specimen. After peak load, a typical J1 joist would slowly begin to shed load due to local buckling. Weld failure and member fracture at the bottom chord connection of the critical web member would then occur.

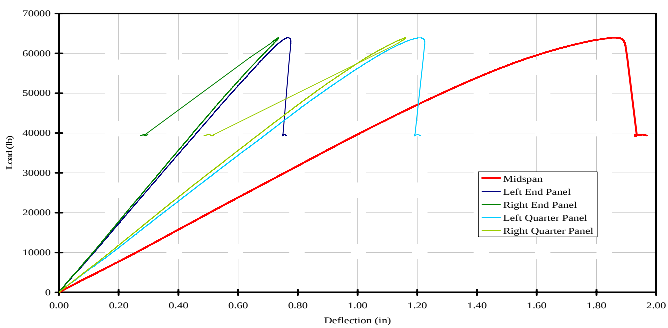

Figure 9 Load-deflection results for J3250-W1

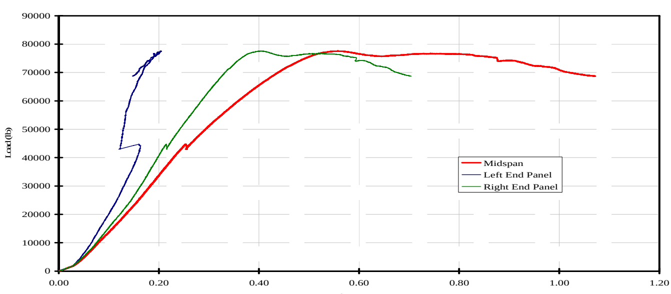

Figure 10 Load-deflection results for J1200-W2

This non-linear behavior following ultimate load is exclusive to the J1 series joists and is most prominent in the joists with the larger web members. This phenomenon is also more pronounced in those joists that failed due to some degree of weld failure or member fracture. There were also several specimens that failed either due to local buckling or member fracture that regained stiffness after the initial local failure. After the local failure, the joists once again began taking load until the critical web member failed in a more global manner.

Non-linearity that occurs when the joist is first loaded is also a characteristic common to the J1 joists and is less obvious in the plots generated for the J2 and J3 series. This initial non-linearity can be attributed to the redistribution of load and leveling that takes place at each joist bearing seat at very low levels of load.

DISCUSSION AND ANALYSIS

Overall Performance

The performance value that was common among all joists tested is divided by the ratio of experimental capacity over the design capacity. In order to evaluate the data collected among different joist sizes and types, this was chosen as the baseline for all comparisons. As mentioned in the previous section, the design capacities that are being used are less accurate than desirable due to the basic analysis used to determine these numbers. The web members were assumed to be concentrically and axially loaded crimped compression members with prismatic section properties of symmetric angular shape. Design capacities will often be less conservative when using this type of fundamental analysis.

Overall performance values for each joist type and manufacturer that failed at the critical web member can be seen in Figure 11, while Figure 12 contains the average loads for all failure types.

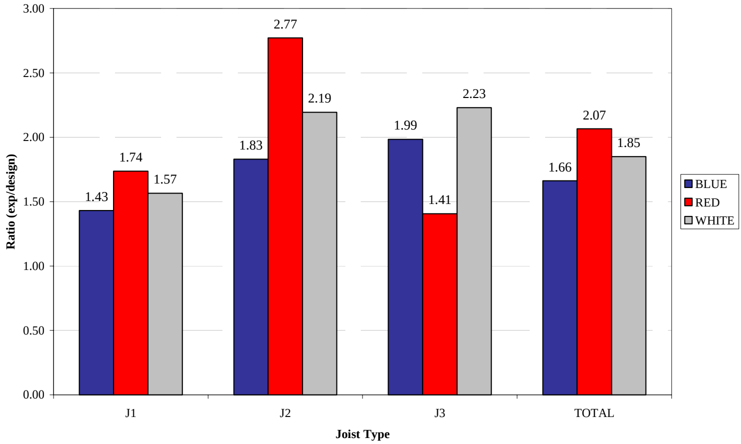

Figure 11 Critical web failures for all joist types

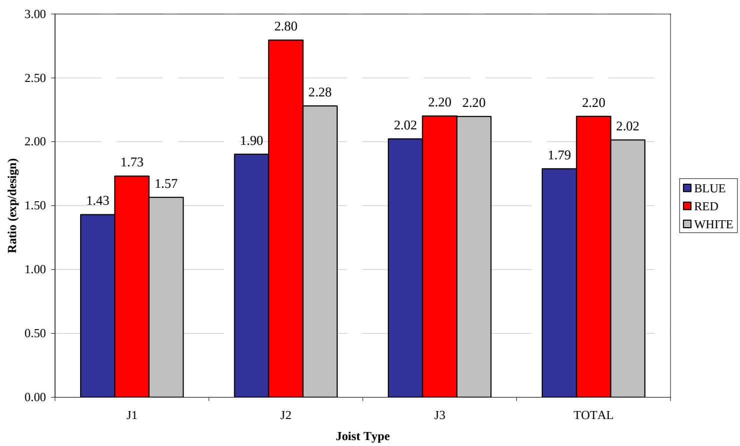

Figure 12 All failures for all joist types

Figures 11 and 12 demonstrate that the red joists failed at the highest average failure ratios for the critical web failures and for all failure types. The red joists that failed due to a critical web member failure averaged a failure ratio 2.07 while the white joists averaged 1.85 and the blue joists averaged 1.66. The red joists of all failure types failed at an average ratio of 2.20 while the white joists averaged 2.02 and the blue joists averaged 1.79. This data shows that in terms of overall performance, the red joists provided more strength than the white or blue joists.

Failure Mode Performance of Critical Web Members

In this section, the 58 critical web member failures will be categorized by seven different failure types. The failure types are buckling at the crimp transition zone, buckling at the crimp transition zone in addition to weld and member fracture, out-of-plane buckling at the crimp, out-of-plane buckling at the crimp in addition to weld and member fracture, in-plane buckling at the uncrimped section, out-of-plane buckling at the uncrimped section and weld and member failure at the bottom chord connection.

Buckling at the crimp transition zone is a local buckling failure that occurs when the transition zone bulges and the web member can no longer maintain its load-carrying capacity. The transition zone can be defined as the location where the web member changes from its crimped shape to its natural angle shape. Table 5 shows a breakdown, in terms of joist type and manufacturer, of the eighteen joists that failed at the crimp transition zone.

Table 5 Buckling of lower crimp transition zone

AVERAGE RATIO = *1.49*					
J1	*9*		**BLUE**	*6*
J2	*4*		**RED**	*10*
J3	*5*		**WHITE**	*2*

Table 5 shows that the J1 series joists are more likely to buckle at the crimp transition zones of the critical web members since they have short effective lengths that make a flexural buckling failure very difficult to achieve. Also evident from this table, is that the red joists are more susceptible to this type of failure while the white joists rarely failed by buckling of the crimp transition zone. When a compression member fails locally it does not reach its ultimate global buckling capacity which explains the relatively low failure loads. The average ratio of experimental capacity versus design capacity for this failure type is the lowest when compared to six different failure modes.

The next failure type to be discussed includes a buckling of the crimp transition zone in addition to a failure of the weld or a fracture at the end of the critical web member. Table 6 shows a breakdown, in terms of joist type and manufacturer, of the seven joists that failed due to member fracture and buckling at the crimp transition zone.

Table 6 Buckling of lower crimp with weld/member failure

AVERAGE RATIO = *1.68*				
J1	*7*		**BLUE**	*2*
J2	*0*		**RED**	*3*
J3	*0*		**WHITE**	*2*

This failure mode occurred only in the J1 series joists and happened exclusively at the bottom chord connections of the critical web member. There was an even distribution of this failure type among the three manufacturers. The failure load ratio for these joists is slightly higher than those of the joists that buckled at the crimp transition zone and experienced no weld failure or member fracture; however, the average ratio is relatively low when compared to the remaining types of critical web member failures. This can once again be attributed to the type of local buckling that caused these joists to fail.

The third failure type is out-of-plane buckling of the critical web member’s crimped section. This type of failure occurs when the crimped section of the web member buckles at the chord connection in its weak direction, out of the plane of the joist. Table 7 shows a breakdown, in terms of joist type and manufacturer, of the eight joists that failed due to buckling at the crimp.

Table 7 Out-of-plane buckling at the crimp

AVERAGE RATIO = *1.86*				
J1	*3*		**BLUE**	*4*
J2	*3*		**RED**	*0*
J3	*2*		**WHITE**	*4*

This is another local buckling failure mode where the distribution among joist types is relatively even. This distribution is not even among manufacturers, as none of the red joists failed in this manner while there were four from both the blue and white groups. The average ratio for this type of failure is higher than the other local buckling modes. This means that this failure mechanism occurs when the joist is closer to reaching its global buckling capacity and therefore can handle more stress. The data indicates that the red joists are much more predisposed to buckling at the crimp transition zone than buckling out-of-plane at the crimp. This could be due to differences in the crimping, welding or manufacturing process of the three joist manufacturers.

The fourth failure mode is out-of-plane buckling of the crimp in addition to a weld failure or fracture at the end of the critical web member. Table 8 shows a breakdown, in terms of joist type and manufacturer, of the seven joists that failed due to member fracture and buckling of the crimp.

Table 8 Out-of-plane buckling at crimp with weld/member failure

AVERAGE RATIO = *1.60*				
J1	*5*		**BLUE**	*2*
J2	*2*		**RED**	*0*
J3	*0*		**WHITE**	*5*

This failure type occurred mostly in the J1 series joists where the member fracture was more of a prevalent characteristic. The two J2 series failures experienced mostly a failure of the welds that occurred due to a violent “folding” of the lower crimped section. Just like the previous failure mode, there were no red joists that failed due to this mechanism.

The fifth critical web member failure mode is buckling of the uncrimped section in the plane of the joist. This is a flexural buckling failure of the entire critical web member. The uncrimped section can be defined as the portion of the web member, between the two transition zones, where the angle has returned to its natural shape. Table 9 shows a breakdown, in terms of joist type and manufacturer, of the seven joists that failed due to flexural buckling of the uncrimped section.

Table 9 In plane buckling in uncrimped section

AVERAGE RATIO = *2.65*				
J1	*0*		**BLUE**	*2*
J2	*4*		**RED**	*3*
J3	*3*		**WHITE**	*2*

This global failure did not occur in the J1 series joists because, as previously mentioned, local buckling occurred before the joist could reach its maximum flexural load-carrying capacity. There was an even distribution among the three manufacturers for this failure type. The longer, more slender members were more susceptible to this failure because of their low flexural buckling capacity compared to their tendency to locally buckle. As expected, the critical web members that failed due to global buckling reached higher capacities than those that buckled locally.

The next failure mechanism is out-of-plane buckling along the critical web member’s uncrimped section. This failure mode is identical to the previous one, with the only difference being the direction the buckling occurs. Table 10 shows a breakdown, in terms of joist type and manufacturer, of the six joists that failed due to out-of-plane buckling of the uncrimped section.

Table 10 Out-of-plane buckling in uncrimped section

AVERAGE RATIO = *2.71*				
J1	*0*		**BLUE**	*2*
J2	*5*		**RED**	*2*
J3	*1*		**WHITE**	*2*

Once again, this global buckling failure did not occur in the J1 series joists but had an even distribution among the three manufacturers. The weak axis of the critical web members is in the plane of the joist, however, these members failed out of the plane of the joist. It is possible that this was caused by initial rotation of the critical web member when it was welded in-between the top and bottom chords. Members that failed in this manner reached a much higher average load ratio than those members that failed locally. As expected, there is a minimal difference in failure ratio between out-of-plane global buckling and flexural buckling in the plane of the joist.

The seventh and final critical web member failure mode is weld failure or member fracture at the bottom chord connection. This type of failure is the only non-buckling mechanism that the critical web members failed in. Table 11 shows a breakdown, in terms of joist type and manufacturer, of the five joists that failed due to weld and member fracture at the bottom chord connection.

Table 11 Weld/member fracture at bottom chord

AVERAGE RATIO = *1.71*				
J1	*5*		**BLUE**	*2*
J2	*0*		**RED**	*1*
J3	*0*		**WHITE**	*2*

This failure mode occurred only in the J1 series joists and was distributed relatively even among the three manufacturers. These joists failed exclusively due to member fracture and/or weld failure where local buckling did not cause the loss of load-carrying capacity. The ratio of experimental capacity divided by the design capacity for this failure mechanism was relatively low and very similar the other joists that failed due to some form of local buckling. The common behavior for this failure type was one in which the critical web member would fracture along the back heel of the angle and the crack would continue to grow and slowly split apart. These joists would not fail suddenly; rather they would slowly lose load-carrying capacity over a period of time and experience relatively large deflections.

Effects of Double Angle End Webs

During this testing program, there were twenty-three failures that occurred due to some form of web member fracture at the bottom chord connection. Each of these failures occurred where a crimped member was sharing a joint with an exterior tension web. All twenty-three of these failures occurred when the exterior web member was constructed using double angles welded to the outside of the bottom chord angles. The other type of member used at this location is a solid round bar welded to the interior of both bottom chord angles. A photograph of this type of failure can be seen in Figure 12.

Figure 12 Fracture of Web Member at Bottom Chord Connection

SUMMARY AND CONCLUSIONS

This study consisted of the testing of 90 open-web steel joists with crimped end critical web members. There were 30 eight foot joists, 30 twenty-two foot joists and 30 twenty-eight foot joists manufactured by three different SJI member companies. Based on the results of the crimped angle web member joist study, several conclusions can be made. The failure mode data suggests that the non-critical joist members were not designed with a low enough stress ratio to ensure all of the failures would occur at the desired members. This is the result of critical web members reaching higher failure ratios than anticipated. This study also showed that, joists which failed locally, i.e. crimp transition zone failure, buckling at the crimp and member or weld fracture, did not reach failure loads as high as those reached by joists that failed globally due to flexural buckling. Failures were categorized into seven different categories.

REFERENCES

E. T. Buckley (2007) *Experimental Study of Open Web Steel Joists with Crimped Critical Web Members*, Villanova University Masters Thesis, Villanova, PA.

Steel Joist Institute 42nd Edition Catalog (2005) Steel Joist Institute, Myrtle Beach, SC.

ACKNOWLEDGEMENTS

The authors are very grateful for the financial support of the Steel Joist Institute. Special thanks are given to the three participating SJI member companies that manufactured the test specimens. The authors also thank Carlos Molina-Hutt and Bryan Enslein, undergraduate research fellows, for their assistance in the experimental testing phase of the project.

GBT-BASED POST-BUCKLING ANALYSIS OF THIN-WALLED STEEL MEMBERS AND FRAMES

C. Basaglia[1], *D. Camotim*[2] *and N. Silvestre*[3]

ABSTRACT

This paper presents the development and illustrates the application of two beam finite element formulations based on Generalized Beam Theory (GBT) that are intended to analyze the (i) local and global post-buckling behavior of thin-walled steel isolated members, possibly exhibiting localized restraints (*e.g.*, due to bracing), and (ii) the global post-buckling behavior of thin-walled steel frames – in both cases, one takes into account the presence of unavoidable initial geometrical imperfections. Initially, one briefly reviews the main concepts and procedures involved in establishing the GBT system of non-linear equilibrium equations. Then, one adresses the steps involved in (i) discretizing these equations by means beam finite element formulations that incorporate the influence of either non-standard support conditions (isolated members) or joint behavior (frames), and (ii) solving the ensuing system of non-linear algebraic equations, adopting an incremental-iterative approach combining Newton-Raphson's method with a load control strategy. Finally, the application and capabilities of the proposed GBT beam finite element formulations are illustrated through the presentation and discussion of numerical results concerning (i) the distortional post-buckling behavior of lipped channel columns with and without a mid-web displacement restraint and (ii) the in-plane and spatial global post-buckling behavior of a simple "L-shaped" frame built from plain channel members. In order to validate the developed GBT-based beam finite element formulations, most of the results obtained are compared with values yielded by beam and shell finite element analyses carried out in the commercial code ANSYS.

[1] Ph.D. Student, [2]Associate Professor and [3]Assistant Professor, Department of Civil Engineering, IST/ICIST, Technical University of Lisbon, Av. Rovisco Pais, 1049-001 Lisboa, Portugal.

INTRODUCTION

The structural efficiency of slender steel frames built from equally slender (locally and globally) thin-walled members can only be adequately assessed after acquiring in-depth information concerning their buckling and post-buckling behaviors, a task that involves (i) identifying the relevant buckling modes, (ii) evaluating the associated bifurcation stress and (iii) determining the corresponding post-buckling equilibrium paths and ultimate strengths. This information plays also a crucial role in the development, validation and calibration of methodologies (formulae and/or procedures) to design those thin-walled steel frames efficiently (*i.e.*, safely and economically). However, since these frames are very frequently built from open-section thin-walled members, which exhibit an extremely low torsional stiffness and are highly susceptible to local (local-plate and/or distortional) and global deformations, the assessment of their structural behavior constitutes a rather complex task (*e.g.*, Kim & Kang 2002). Indeed, in the context of numerical analysis, this task can only be rigorously performed by resorting to shell finite element models (*e.g.*, Boissonnade & Degée 2005), an approach that requires an enormous computational effort (including data input and result interpretation) and is still absolutely prohibitive for routine applications, even when they involve frames with only a few members.

It is now well established that one-dimensional models (beam finite elements) based on Generalized Beam Theory (GBT) are very computationally efficient and illuminating numerical tools to perform elastic buckling and post-buckling analyses of isolated thin-walled members − GBT is a beam theory enhanced with folded-plate concepts that was originally conceived by Schardt (1989) and has been extensively upgraded in the last few years (*e.g.*, Camotim *et al.* 2004, 2006, 2008). In particular, it is now possible to assess the (i) first-order and buckling behavior of members and frames with arbitrary cross-section geometries, support conditions and loadings and (ii) post-buckling behavior of isolated members. Note, however, that the post-buckling analyses involved only members subjected to uniform internal forces and moments and exhibiting standard support conditions (*e.g.*, Silvestre & Camotim 2003, 2006) − thus, the authors are currently extending the non-linear GBT formulation to cover the post-buckling behavior of (i) isolated members with non-standard support conditions, such as localized displacement restraints (Basaglia *et al.* 2007a and Camotim *et al.* 2007) and (ii) thin-walled frames. Concerning the application of

GBT (or any other beam models) to thin-walled frames, the major difficulties lie in the appropriate treatment of the joints, involving the simultaneous consideration of (i) the transmission of warping due to torsion, distortion and shear deformation, and (ii) the compatibility between the transverse (membrane and flexural) displacements of the connected member end sections. However, the authors have partially overcome these difficulties, since their efforts have already led to the development of GBT-based finite element approaches to analyze the local-plate, distortional and global buckling behavior of plane and space frames (Basaglia *et al*. 2006, 2008).

The objective of this work is to report on the current state of an ongoing investigation aimed at extending the scope of the available geometrically non-linear GBT beam finite element formulation, making it possible to analyze also (i) the *local and global* post-buckling behavior of thin-walled steel members with arbitrary loading and support conditions and (ii) the *global* post-buckling behavior of thin-walled steel frames[2]. In particular, one addresses (i) the determination of the non-linear finite element and overall (member/frame) non-linear finite stiffness matrices, which incorporate the effect of the non-standard support conditions or the frame joints, and (ii) the numerical strategy adopted to solve the system of (discretized) non-linear equilibrium equations. In order to illustrate the application and provide a better grasp of concepts and procedures involved in the proposed GBT-based approach, one presents and discusses numerical results concerning (i) the distortional post-buckling behavior of lipped channel columns with and without a mid-web displacement restraint and (ii) the in-plane and spatial global post-buckling behavior of a simple "L-shaped" frame built from plain channel members. For validation purposes, most of the results obtained are compared with values yielded by ANSYS (SAS 2004) shell and beam finite element analyses.

CROSS-SECTION ANALYSIS – A BRIEF OVERVIEW

Since the member cross-section displacement field is expressed as a linear combination of mechanically meaningful deformation modes, GBT analyses lead to the establishment of equilibrium equations written in a very convenient

---

[2] Due to current software limitations, which will be overcome in the near future, it is not yet possible to analyze the *local* post-buckling behavior of thin-walled steel frames – nevertheless, it is worth mentioning that the development of the corresponding GBT formulation is progressing well.

(modal) form, whose computational efficient solution provides in-depth insight on the member structural response.

Consider the prismatic member with the supposedly arbitrary unbranched open cross-section depicted in figure 1, also showing the global (X, Y, Z) and local (x, s, z) coordinate systems – u, v, w are the corresponding displacement components (x, u are always the longitudinal axis and warping displacement).

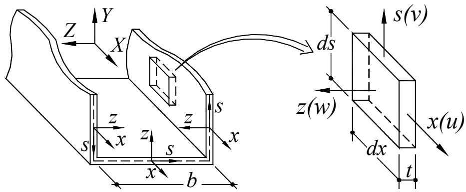

Figure 1. Arbitrary unbranched open cross-section and global and local coordinate axes and displacements

According to GBT, the member mid-surface displacement field reads

$$u(x,s)=u_k(s)\phi_{k,x}(x) \quad v(x,s)=v_k(s)\phi_k(x) \quad w(x,s)=w_k(s)\phi_k(x) \quad , \qquad (1)$$

where (i) $(.)_{,x}\equiv d(.)/dx$, (ii) the summation convention applies to subscript k, (iii) functions $u_k(s)$, $v_k(s)$, $w_k(s)$, yielded by a GBT cross-section analysis, characterize deformation mode k and (iv) $\phi_k(x)\equiv\phi_k(X)$ are mode amplitude functions defined along the member length (*e.g.*, Silvestre & Camotim 2002, 2003).

The GBT cross-section discretization of member formed by n walls (i) involves $n+1$ natural and m intermediate nodes (note that the free end nodes count as both natural and intermediate), and (ii) leads to the determination of (ii$_1$) $n+m+1$ *conventional* deformation modes, (ii$_2$) $n+m-2$ *shear* modes and (ii$_3$) $m+2n-2$ *transverse extension* modes – the amplitudes of these deformation are the (discretized) cross-section degrees of freedom. The conventional modes, based on Vlasov's assumption of null membrane shear strains, constitute the core of GBT and comprise (i) *4* rigid-body modes (extension, major/minor axis bending, torsion), (ii) n-3 distortion modes and (iii) m local-plate modes. The shear modes account for the *non-linear* variation of warping along the cross-section mid-line (no in-plane cross-section deformation involved). The transverse extension modes involve only in-plane displacements due to the wall transverse bending.

Figures 2(a)-(b) show the dimensions, elastic constants (Young's modulus and Poisson's ratio) and GBT discretizations of the lipped and plain channel cross-sections dealt with in this work – the corresponding cross-section analyses lead to sets of $N=50$ and $N=4$ deformation modes − figure 3 shows the main features of the ones most relevant to the analyses carried out next, *i.e.*, those with significant contributions to the deformed configurations associated with (i)

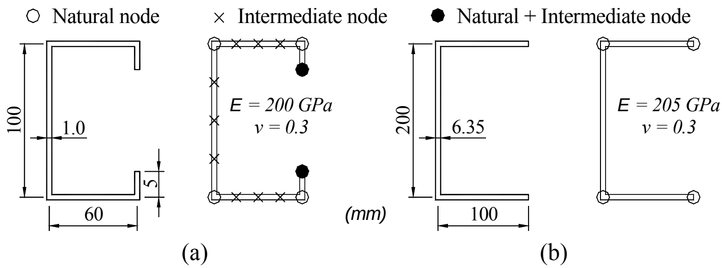

Figure 2. (a) Lipped and (b) plain channel cross-section geometry and GBT discretization adopted

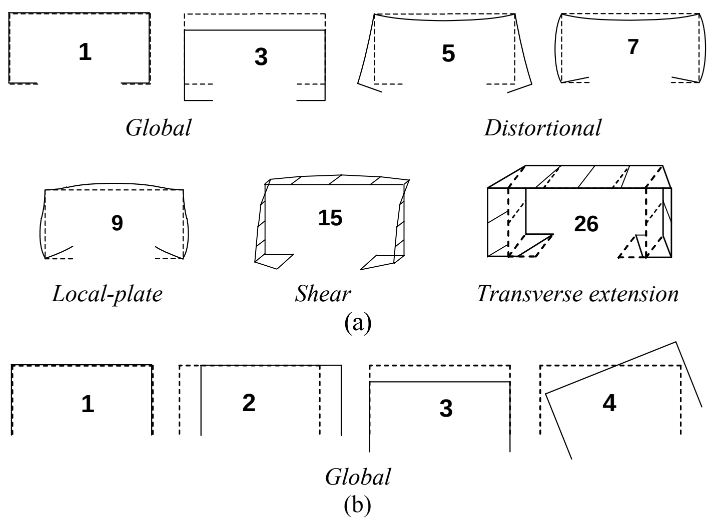

Figure 3. Main features of the most relevant (a) lipped and (b) plain channel deformation modes

the lipped channel column post-buckling behavior (*5* conventional, *1* shear and *1* transverse extension) and (ii) the plain channel "L-shaped" frame global post-buckling behavior (only the four rigid-body modes).

MEMBER LOCAL AND GLOBAL POST-BUCKLING ANALYSIS

After performing the cross-section analysis, *i.e.*, determining the deformation mode shapes and evaluating the corresponding mechanical properties, it is possible to express the member equilibrium in *modal* form. Indeed, designating by δU and $\delta \Pi$ the first variation of the member strain energy and the virtual work of the applied (external) loads, the usual application of the principle of virtual work leads to

$$\delta U+\delta \Pi=\int_V \sigma_{ij}\,\delta\varepsilon_{ij}\,dV+\delta\Pi_q+\delta\Pi_Q=\sum_{p=1}^{3}(\delta U_p-\delta\overline{U}_p)+\delta\Pi_q+\delta\Pi_Q=0 \quad , \quad (2)$$

where (i) V is the volume of the n-plate member, (ii) the bar identifies the strain energy term stemming from the initial geometrical imperfections, (iii) σ_{ij} and ε_{ij} are the stress and strain tensor components, (iv) δU_p are the first variations of the strain energy linear ($p=1$), quadratic ($p=2$) and cubic ($p=3$) terms, and (v) $\delta\Pi_q$ and $\delta\Pi_Q$ are the virtual works done by the distributed and concentrated loads. The δU_p and $\delta\overline{U}_p$ expressions are of the form (only the first terms are shown, for illustrative purposes[3])

$$\delta U_1=\int_L (C_{kh}\phi_{k,xx}\delta\phi_{h,xx}+B_{kh}\phi_k\delta\phi_h+D_{kh}\phi_{k,x}\delta\phi_{h,x}+\ldots)\,dx \quad , \quad (3)$$

$$\delta U_2=\int_L (C_{kjh}\phi_{k,xx}\phi_{j,x}\delta\phi_{h,x}+\tfrac{1}{2}C_{hjk}\phi_{k,x}\phi_{j,x}\delta\phi_{h,xx}+\ldots)\,dx \quad , \quad (4)$$

$$\delta U_3=\int_L (\tfrac{1}{2}C_{kijh}\phi_{k,x}\phi_{i,x}\phi_{j,x}\delta\phi_{h,x}+\ldots)\,dx \quad , \quad (5)$$

$$\delta\overline{U}_1=\int_L (C_{kh}\overline{\phi}_{k,xx}\delta\phi_{h,xx}+B_{kh}\overline{\phi}_k\delta\phi_h+D_{kh}\overline{\phi}_{k,x}\delta\phi_{h,x}+\ldots)\,dx \quad , \quad (6)$$

---

[3] Due to space limitations, it is not possible to present here the full expressions – the interested reader may find them in the work of Silvestre & Camotim (2003).

$$\delta\overline{U}_2 = \int_L (C_{kjh}\overline{\phi}_{k,xx}\phi_{j,x}\delta\phi_{h,x} + \tfrac{1}{2}C_{hjk}\overline{\phi}_{k,x}\overline{\phi}_{j,x}\delta\phi_{h,xx}\ldots)\,dx \quad , \quad (7)$$

$$\delta\overline{U}_3 = \int_L (\tfrac{1}{2}C_{kijh}\overline{\phi}_{k,x}\overline{\phi}_{i,x}\phi_{j,x}\delta\phi_{h,x} + \ldots)\,dx \quad , \quad (8)$$

where the tensor ***C***, ***B*** and ***D*** components are cross-section modal mechanical properties associated with the resistance to longitudinal extensions, transverse extensions and shear strains, respectively. While the second-order tensor components (C_{kh}, D_{kh}, B_{kh}) characterize the cross-section linear behavior, the third (C_{kjh}, etc.), fourth (C_{kijh}, etc.) and higher-order (*h.o.t.*, not shown in (3)-(8)) ones are associated with its geometrically nonlinear behavior. Note that the global modes **1** (axial extension – C_{11} is the axial stiffness), **2**+**3** (major and minor axis bending – C_{22} and C_{33} are the bending stiffness values) and **4** (torsion – C_{44} and D_{44} are the warping and St. Venant torsion stiffness values) are characterized by $B_{kh}=0$, since they involve only cross-section rigid-body motions. On the other hand, all the remaining deformation modes ($k\geq$**5**) exhibit (i) primary and secondary warping displacements and/or (ii) cross-section in-plane deformation, thus leading to non-null C_{ik}, D_{ik}, B_{ik} components, with no obvious mechanical interpretation – this feature lack is shared by all higher-order mechanical properties (even the rigid-body mode ones).

The virtual work done by the distributed ($\delta\Pi_q$) and concentrated ($\delta\Pi_Q$) loads is obtained through the expressions[4]

$$\delta\Pi_q = -\int_L\int_b (q_x\delta u + q_s\delta v + q_z\delta w)\,ds\,dx \quad (9)$$

$$\delta\Pi_Q = -Q_i\delta\phi_{i,x}\Big|_{x=0}^{x=L} - Q_i'\delta\phi_i\Big|_{x=0}^{x=L} \quad , \quad (10)$$

where (i) q_x, q_s, q_z and δ_u, δ_v, δ_w are the distributed loads and corresponding virtual displacements, (ii) Q_1, Q_2, Q_3, Q_4 are the axial force, bending moments (about the major/minor axes) and bimoment, and (iii) Q_2', Q_3', Q_4' are the transversal loads (along the major/minor axes) and torsion moment.

From (2), is a straightforward matter to obtain the member GBT system of

[4] In these expressions only loads akin to the rigid-body deformation modes are dealt with. Moreover, (i) no distributed moments are considered, (ii) all concentrated loads act at the member end sections and (iii) all transverse loads are deemed applied at the cross-section shear centre.

non-linear differential equilibrium equations (one per deformation mode),

$$
\begin{aligned}
& C_{kh}(\phi_k - \overline{\phi}_k)_{,xxxx} - D_{kh}(\phi_k - \overline{\phi}_k)_{,xx} + B_{kh}(\phi_k - \overline{\phi}_k) - \\
& - C_{kjh}(\phi_{k,xx}\phi_{j,x} - \overline{\phi}_{k,xx}\phi_{j,x})_{,x} + \tfrac{1}{2} C_{hjk}(\phi_{k,x}\phi_{j,x} - \overline{\phi}_{k,x}\overline{\phi}_{j,x})_{,xx} + \\
& + \tfrac{1}{2} C_{kijh}(\phi_{k,x}\phi_{i,x}\phi_{j,x} - \overline{\phi}_{k,x}\overline{\phi}_{i,x}\phi_{j,x})_{,x} + h.o.t. = q_h \qquad , \quad (11)
\end{aligned}
$$

where (i) the initial geometrical imperfections shape are expressed in modal form and (ii) q_h are the (modal) distributed loads − one has $q_h=0$ for $h>3$.

Beam Finite Element Formulation. In isolated members with arbitrary end, intermediate and localized support conditions, the solution of the system (11) can be obtained by means of a GBT-based beam finite element formulation analogous to the one developed and implemented by Silvestre & Camotim (2003) – the modal amplitude functions $\phi_k(x)$ are approximated by linear combinations of (i) Lagrange cubic polynomial primitives (axial extension and shear modes) and (ii) Hermite cubic polynomials (transverse extension and all remaining conventional modes). Therefore, one has

$$\phi_k(x) = \psi_\alpha(x) d_{k\alpha} \quad \overline{\phi}_k(x) = \psi_\alpha(x) \overline{d}_{k\alpha} \qquad , \quad (12)$$

where (i) ψ_α are Hermite polynomials or primitives of Lagrange ones, (ii) $d_{k\alpha}$ are generalized displacements and (iii) the bar identifies again the initial geometrical imperfections. The ensuing (discretized) system of non-linear algebraic equations is then numerically solved by means of an incremental-iterative approach combining Newton-Raphson's method with a load control strategy[5] – the (symmetric) element tangent stiffness matrix $\boldsymbol{T}^{(e)}$ is obtained by differenting the various components of the finite element internal force vector $\boldsymbol{f}^{(e)}$, thus yielding

$$T^{(e)} = \frac{\partial f_1^{(e)}}{\partial d_k^{(e)}} + \frac{\partial}{\partial d_k^{(e)}} (f_2^{(e)} + f_3^{(e)} - \bar{f}_2^{(e)} - \bar{f}_3^{(e)}) \qquad , \quad (13)$$

where

$$f_p^{(e)} = \frac{\partial U_p^{(e)}}{\partial d_{k\alpha}^{(e)}} \quad \Leftrightarrow \quad f^{(e)} = f_1^{(e)} + f_2^{(e)} + f_3^{(e)} - \bar{f}_1^{(e)} - \bar{f}_2^{(e)} - \bar{f}_3^{(e)} \quad . \quad (14)$$

---

[5] This means that no equilibrium path descending branches can be determined – this limitation will be soon overcome, as an arc-length control strategy is currently being implemented.

Then, the member global internal force vector $\boldsymbol{f}_M$ and stiffness matrix $\boldsymbol{T}_M$ are obtained by (i) assembling their finite element counterparts and (ii) accounting for taking into account the end, intermediate and localized support conditions, which obviously have the net effect of reducing the number of degrees of freedom involved in the analysis (*i.e.*, the dimension of vector $\boldsymbol{d}_M$).

Localized Support Conditions. In order to incorporate non-standard support conditions, namely intermediate localized displacement restraints, into the analysis, one must impose appropriate *constraint conditions* that vary from case to case (Basaglia *et al.* 2007a and Camotim *et al.* 2007). For illustrative purposes, consider the full restraint of the transverse flexural displacement $\tilde{\delta}_Z$ (see fig. 4) of a member mid-surface point P located within a wall, *i.e.*, corresponding to a cross-section *intermediate* node (see fig. 2) – its location is defined by $x{=}x_P$ and $s{=}s_P$. Then, the constraint condition reads

$$\tilde{\delta}_Z(x_P,s_P)=\sum_{j=1}^{N} w_j(s_P)\phi_j(x_P)=0 \qquad , \quad (15)$$

where $w_j(s_P).\phi_j(x_P)$ is the contribution of mode j to the restrained displacement.

The constraint conditions are included into the member internal force vector and stiffness matrix through the operations

$$\tilde{f}_M=[\Omega_M]^T f_M \qquad \tilde{T}_M=[\Omega_M]^T T_M[\Omega_M] \qquad , \quad (16)$$

where the member transformation matrix $[\Omega_M]$, defined by

$$\{\tilde{d}_M\}=[\Omega_M]^T\{d_M\} \qquad , \quad (17)$$

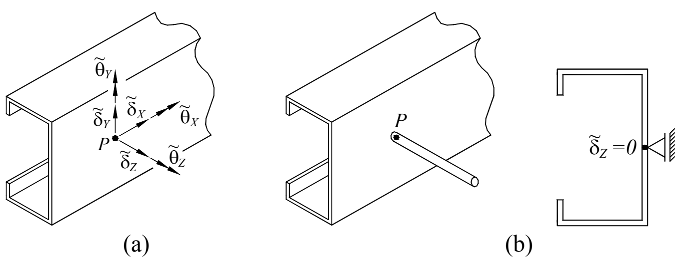

Figure 4. Point P (a) displacements and rotations and (b) full transverse flexural displacement restraint (along Z)

provides the degree of freedom reduction ($\boldsymbol{d}_M \Rightarrow \tilde{\boldsymbol{d}}_M$) stemming from the constraint conditions − matrix $[\Omega_M]$ incorporates the displacements values at point P associated with the various deformation modes: $u_k(s_P)$, $v_k(s_P)$ or $w_k(s_P)$.

After having the member internal force vector and tangent stiffness matrix, performing the member post-buckling analysis involves the successive solution of non-linear equation systems

$$\Delta\tilde{\boldsymbol{f}}_M = \tilde{\boldsymbol{T}}_M \, \Delta\tilde{\boldsymbol{d}}_M \quad , \quad (18)$$

that governs the member incremental equilibrium (from a known equilibrium state) – $\Delta\tilde{\boldsymbol{f}}_M$ and $\Delta\tilde{\boldsymbol{d}}_M$ are vectors whose components are generalized force and displacement increments. As mentioned earlier, these non-linear systems are solved iteratively by means of Newton-Raphson's method. After each iteration, one must obtain the displacement increment vector $\Delta\boldsymbol{d}_M$, in order to update the member deformed configuration and obtain the tangent stiffness matrix to be used in the next iteration – thus, transformation $\Delta\tilde{\boldsymbol{d}}_M \Rightarrow \Delta\boldsymbol{d}_M$ (*i.e.*, the inverse of (17)) must be performed. The incremental-iterative approach employed to determine the member non-linear (post-buckling) equilibrium paths presented in this work is not further addressed here – a detailed account of the procedures involved in its implementation can be found in the work of Silvestre & Camotim (2003).

Illustrative Example: Lipped Channel Column with Localized Restraint. One analyzes simply supported (end sections locally/globally pinned and free to warp) uniformly compressed lipped channel columns with length $L=300mm$ and the cross-section dimensions shown in figure 2(a), together with the GBT cross-section discretization adopted. A longitudinal discretization into six finite elements was used to determine the column (i) critical buckling mode shape and associated buckling load and (ii) post-buckling behavior.

Two different columns are analyzed, without and with a localized restraint involving the flexural displacement of the mid-span mid-web point. Their buckling analyses yielded the following results: (i) $P_{cr}=17.44kN$ with a virtually "pure" distortional critical buckling mode (*97.0%* participation of mode **5** – see fig. 3(a)), for the unrestrained column, and (ii) $P_{cr.R}=19.56kN$ with a predominantly distortional critical buckling mode (*64.3%* contribution from mode **5** combined with *35.7%* joint participation of modes **7**+**9** – see fig. 3(a)).

Figure 5 display the post-buckling equilibrium paths (P vs. v, where v is the vertical displacement of the mid-span flange-lip corners) concerning the unrestrained and restrained columns and yielded by geometrically non-linear (i) *shell* (ANSYS) and (ii) *beam* (GBT) finite element analyses − the columns contain critical-mode initial geometrical imperfections with the amplitude defined by v_0=+0.15mm (outward flange-lip motions) or v_0=−0.15mm (inward flange-lip motions), where v_0 is the initial v value. It is worth noting that the restrained column GBT results were obtained by means of analyses including four deformation mode sets. As for figures 6(a)-(b), it shows the unrestrained and restrained column deformed configurations (inward and outward flange-lip motions) yielded by ANSYS analyses and all corresponding to P=22.0kN.

The close observation of the post-buckling results presented in figures 5 and 6(a)-(b) prompts the following remarks:

(i) In both the unrestrained and restrained columns, virtually "exact" post-buckling behaviors are provided by GBT-based analyses including

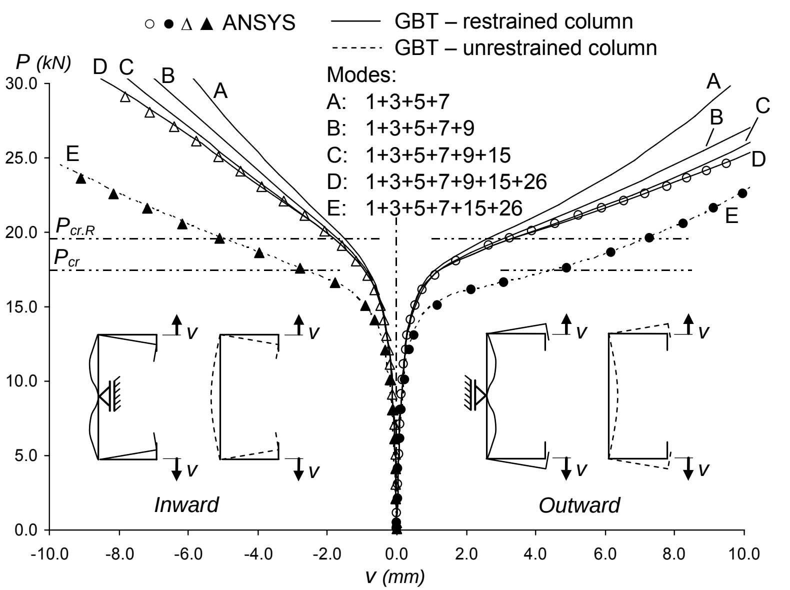

Figure 5. Equilibrium paths of the unrestrained and restrained lipped channel columns yielded by the ANSYS and GBT post-buckling analyses

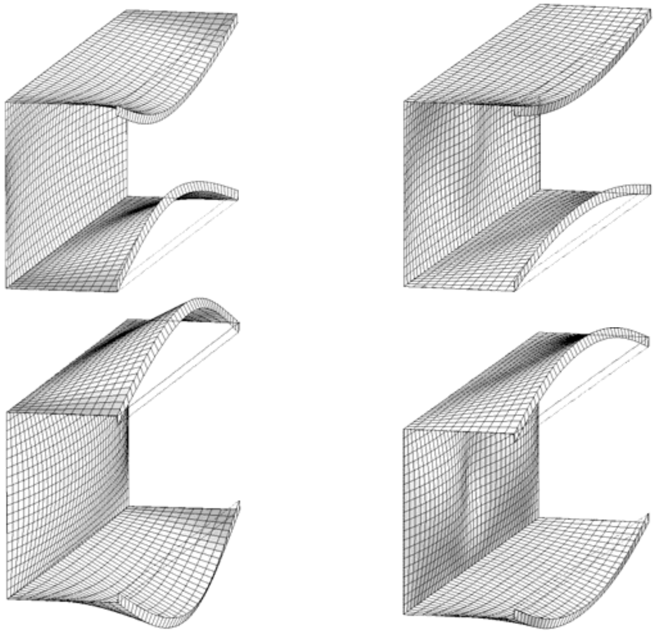

Figure 6. ANSYS deformed configurations (inward and outward flange-lip motions) of the (a) unrestrained and (b) restrained columns ($P=22.0kN$)

modes **1**+**3**+**5**+**7**+**15**+**26** and **1**+**3**+**5**+**7**+**9**+**15**+**26**, respectively – within the range $10<v<10mm$, the differences never reach *3.0%*. Moreover, note that the GBT analyses involve only a small fraction of the number of degrees of freedom required by their ANSYS counterparts: about *95* (restrained columns) or *84* (unrestrained columns) against over *11300*.

(ii) In the restrained columns, the sole inclusion of the conventional modes (**1**+**3**+**5**+**7**+**9**) leads to accurate results only up to the applied critical load level. But adding shear mode **15** to the analysis improves the accuracy significantly − the differences between the GBT and ANSYS values are then quite small until $P=1.2P_{cr.R}$, ("exact" value underestimated by *4.5%*).

(iii) Figure 5 shows that the lateral restraint reduces the inward and outward flange-lip corner maximum displacements to *43.8%* and *67.3%* of the corresponding unrestrained values, for $P=22.0kN$. It is also interesting to notice that the dominant single half-wave distortional behavior "forces" the restrained column webs to deform symmetrically (see fig. 6(b)).

(iv) The comparison between the inward and outward unrestrained column curves depicted in figure 5 clearly shows a non-negligible post-buckling asymmetry with respect to the v sign – the inward column post-buckling behavior is stiffer and, therefore, associated with higher strength values. This phenomenon was first unveiled by Prola & Camotim (2002), on the basis of spline finite strip post-buckling analysis results. More recently, this asymmetry was further investigated by Camotim & Silvestre (2004), who found out, by means of GBT post-buckling analyses, that it stemmed mostly from shear effects related to non-linear warping, which alter considerably the evolutions of the flange-lip displacement profile and stress distributions as post-buckling progresses.

(v) In the restrained columns the post-buckling asymmetry addressed in the previous item is clearly more pronounced (see fig. 5) – this is most likely due to the fact that the web restraint (*i.e.*, stiffening – it now exhibits two half-waves, as shown in fig. 6(b)) renders the flange-lip deformation more relevant (the flanges and lips become relatively "weaker") – recall that the flange-lip shear deformation is precisely the "key player" in the column distortional post-buckling asymmetry.

FRAME GLOBAL POST-BUCKLING ANALYSIS

Since one deals exclusively with *global* post-buckling analysis, only the first four (rigid-body) deformation modes have to be considered – this means that, out of matrices ***C***, ***D*** and ***B*** appearing in system (11), only the first two need to be are retained (there is no longer cross-section in-plane deformation). Therefore, one has

$$\begin{aligned} & C_{kh}(\phi_k-\overline{\phi}_k)_{,xxxx}-D_{kh}(\phi_k-\overline{\phi}_k)_{,xx}- \\ & -C_{kjh}(\phi_{k,xx}\phi_{j,x}-\overline{\phi}_{k,xx}\phi_{j,x})_{,x}+\tfrac{1}{2}C_{hjk}(\phi_{k,x}\phi_{j,x}-\overline{\phi}_{k,x}\overline{\phi}_{j,x})_{,xx}+ \\ & +\tfrac{1}{2}C_{kijh}(\phi_{k,x}\phi_{i,x}\phi_{j,x}-\overline{\phi}_{k,x}\overline{\phi}_{i,x}\phi_{j,x})_{,x}+h.o.t.=q_h \end{aligned} \quad , \quad (19)$$

and it is worth mentioning that the non-linear GBT formulation employed in this work may be viewed as a novel application of Vlasov's classical thin-walled beam theory – in fact, it can be argued that it just provides its "translation" into the unique GBT "modal language"[6].

After performing the (beam) finite element discretization of the frame, one must handle separately the degrees of freedom associated with (i) the member internal nodes or end supports and (ii) the nodes corresponding to frame joints. In the former, one considers always GBT (modal) degrees of freedom, *i.e.*, values and derivatives of the (discretized) amplitude functions $\phi_k(x)$ – this can be done because the compatibility between them is trivially ensured, as in isolated member (Silvestre & Camotim 2003). The same is not true for the joint nodes, where guaranteeing the compatibility between the GBT degrees of freedom of the converging finite element end sections it is not a straightforward matter – this stems from their modal nature and the fact that they are referred to distinct (member) coordinate systems. In order to overcome this difficulty, one must first "transform" the modal degrees of freedom into *nodal* generalized displacements of the point where the joint is assumed to take place (often the intersection of the connected member centroidal axes), a task carried out by resorting to a "*joint element*" concept (*e.g.*, Basaglia *et al.* 2008). Next, one addresses the concepts and procedures involved in determining the frame overall internal force vector $\boldsymbol{f}_F$ and tangent stiffness matrix $\boldsymbol{T}_F$, on the basis of their GBT-based beam finite element counterparts:

(i) To ensure displacement compatibility at the "joint element", one uses the frame transformation matrix $[\Omega_F]$, relating the GBT (member) and nodal (joint) degrees of freedom, which is defined by the expressions

$$\{\tilde{\xi}\} = [\Omega_F]^T \{d_M\} = \begin{bmatrix} [R_{\tilde{Y}+\tilde{Z}}][R_X][L] & \\ & 1 \end{bmatrix}^T \{d_M\}$$

$$\{\tilde{\xi}\} = \begin{bmatrix} U_{\tilde{X}} & U_{\tilde{Y}} & U_{\tilde{Z}} & \Theta_{\tilde{X}} & \Theta_{\tilde{Y}} & \Theta_{\tilde{Z}} & \Theta'_{\tilde{X}} \end{bmatrix}^T \qquad , \quad (20)$$

where (i_1) $\{\tilde{\xi}\}$ is the global mode nodal generalised displacement sub-vector (referred to axes $\tilde{X}-\tilde{Y}-\tilde{Z}$ – see fig. 7(a)), (i_2) $\{d_M\}$ contains the GBT degrees of freedom, (i_3) matrix $[R_{\tilde{Y}+\tilde{Z}}]$ describes the transformation associated with successive rotations about axes $\tilde{Z}$ (first) and $\tilde{Y}$ (second), defined by matrices $[R_{\tilde{Z}}]$ and $[R_{\tilde{Y}}]$, (i_5) matrix $[R_X]$ corresponds to the

[6] The authors are currently working on extending the non-linear GBT formulation to include also the local deformation modes – this issue will be further addressed in the paper.

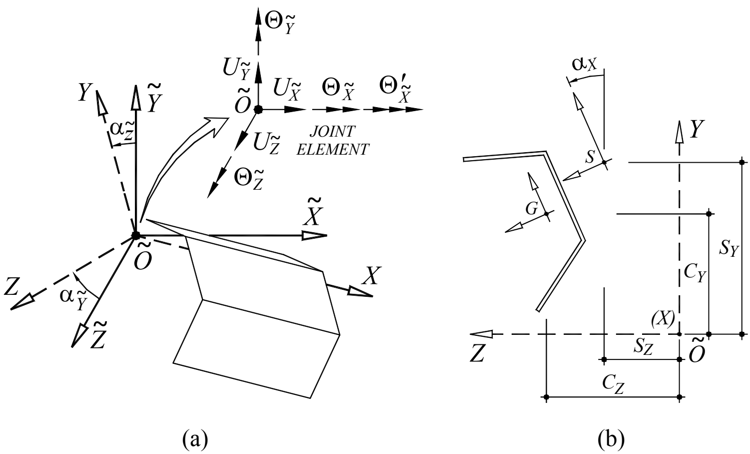

Figure 7. (a) “Joint element” and global coordinate systems, and (b) member cross-section (local) coordinate system and relative positions of G, S and $\tilde{O}$

rotation about the member axis X (see fig. 7(b)), and (i$_4$) $[L]$ is a translation matrix relating the converging element/member generalized displacements (originally referred to longitudinal axis passing through the cross-section centroids G or shear centres S) to parallel reference axes passing through point $\tilde{O}$, where the joint is deemed “materialised” (see fig. 7(b)). Finally, note that the development of the rotation matrices $[R_{\tilde{Z}}]$, $[R_{\tilde{Y}}]$ and $[R_X]$ has already been presented in detail by the authors (Basaglia *et al.* 2008) and also that $\{\tilde{\xi}\}$ is obtained from the GBT degrees of freedom vector $\{d_M\}$ by means of an ordered rotation sequence: first about the member axis X, then about the global axis $\tilde{Z}$ and lastly about the global axis $\tilde{Y}$ – altering this rotation sequence will certainly lead to erroneous results.

(ii) By using the transformation matrix defined in (20), one obtains, in the most general case, *7* degrees of freedom per connected member end node. These sets of degrees of freedom must satisfy the relations

$$\{\tilde{\xi}\}_{b_r} = \begin{bmatrix} [I]_{6x6} & \\ & \Gamma \end{bmatrix} \{\tilde{\xi}\}_{a_{r+1}} \quad , \quad (21)$$

where $[I]$ is the identity matrix and Γ is a constant relating the torsional rotation derivatives, *i.e.*, quantifying the “(torsion) warping transmission” at the frame joint under consideration – a detailed explanation of this concept can be found in the work of Basaglia *et al.* (2008)[7].

(iii) Through the use of operations

$$\widetilde{f}_F = [\Omega_F]^T f_F \qquad \widetilde{T}_F = [\Omega_F]^T T_F [\Omega_F] \qquad , \quad (22)$$

one readily obtains the frame tangent stiffness matrix $\widetilde{T}_F$, which (iii_1) ensures the degree of freedom compatibility at all nodes and (iii_2) is associated with "mixed degrees of freedom" – GBT degrees of freedom (d_{ki}) in the member internal nodes or end supports and "conventional" generalized displacements ($\widetilde{\xi}_i$) in the joints connecting those members.

Once the frame global internal force vector and tangent stiffness matrix are obtained, the determination of frame post-buckling equilibrium paths requires the successive solution of non-linear equation systems of the form

$$\boldsymbol{\Delta\widetilde{f}_F} = \boldsymbol{\widetilde{T}_F}\ \boldsymbol{\Delta\widetilde{d}_F} \qquad , \quad (23)$$

which describe the frame incremental equilibrium from a known equilibrium state – $\boldsymbol{\Delta\widetilde{f}_F}$ is the generalized force increment vector and $\boldsymbol{\Delta\widetilde{d}_F}$ is a "mixed" vector combining increments of joint nodal displacement and GBT degrees of freedom. In order to solve the system (23) one adopts the approach already used for the isolated members: iteration based on Newton-Raphson's method and a load control strategy. However, because one ends up with a "mixed" displacement increment vector, is indispensable, in order to obtain a fully modal representation of the frame deformed configurations, to "transform back" the joint nodal degrees of freedom into GBT modal ones – in other words to "invert" the operation defined in the equation system (20).

Illustrative Example: "L-Shaped" Frame with Plain Channel Members. In order to validate and illustrate the application and capabilities of the proposed GBT-based non-linear beam finite element approach, one now presents and discusses numerical results concerning the global elastic post-buckling behavior of the simple "L–shaped" frame depicted in figure 8, which is formed by two fixed-ended equal-length orthogonal plain channel members *A* and *B* (L_A=L_B=*500cm*) (i) with identical cross-sections (dimensions given

[7] Although the torsion warping transmission concepts and results were developed in the context of frame global *buckling* analysis, they all remain valid when performing *post-buckling* analyses.

in fig. 2(b)) and (ii) connected with flange continuity. The frame is acted by a vertical load (*P*) applied at the joint and one analyses both the frame in-plane and spatial global post-buckling behaviors. The GBT results are (i) obtained with discretizations of *6* finite elements per member and (ii) validated through comparisons with values yielded by ANSYS analyses involving member discretizations into BEAM3 (in-plane) and BEAM189 (spatial) elements.

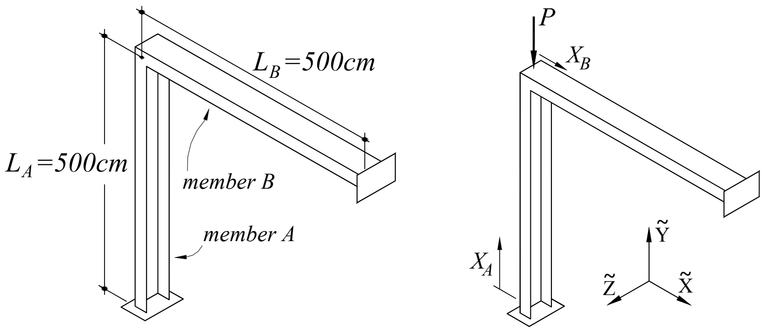

Figure 8. "L– shaped" frame geometry, loading and end support conditions

One begins by addressing the frame *in-plane* post-buckling behavior, which involves only contributions from the GBT deformation modes **1** (axial extension) and **3** (minor axis bending) – GBT and ANSYS buckling analyses yielded practically identical critical load values: $P_{cr.GBT}=619.08kN$ and $P_{cr.ANSYS}=618.39kN$ (*0.11%* difference). Figure 9(a) shows the post-buckling equilibrium paths (P/P_{cr} vs. w/L_A – w is the column mid-span displacement due to the applied load) of two frames differing only in the "sign" of the critical-mode initial geometrical imperfection: either positive ($w_0=+1.0cm$) or negative ($w_0=-1.0cm$), depending on whether beam *B* bends upwards or downwards − w_0 is the column initial mid-span displacement. Moreover, figure 9(b) shows the GBT-based frame deformed configurations corresponding to $P/P_{cr}=0.94$.

The observation of the in-plane post-buckling results presented in figures 9(a)-(b) leads to the following comments:

(i) The fixed-ended "L-shaped" frame exhibits a slightly asymmetric post-buckling behavior, with the unstable branch associated with positive w values (beam upward bending) – this behavior is qualitatively similar to the one obtained for the well-known Roorda's frame (*e.g.*, Roorda 1965

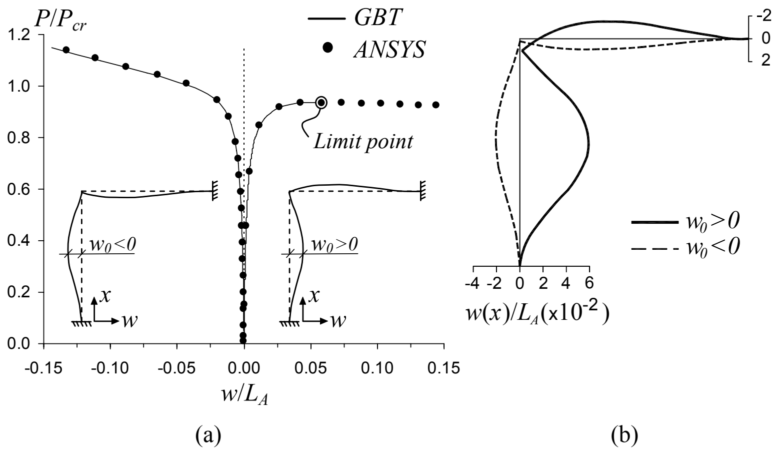

Figure 9. Frame in-plane post-buckling behavior: (a) equilibrium paths and (b) deformed configurations ($P/P_{cr}=0.94$)

or Silvestre & Camotim 2005), which has pinned end supports – in quantitative terms, the asymmetry Roorda's frame is more pronounced, most likely due to the lower stiffness of the two members.

(ii) Because the incremental-iterative numerical solution implemented employs a load control strategy, the GBT analysis can only determine the frame post-buckling equilibrium path associated with $w_0>0$ (beam upwards bending) up to its limit point, which occurs for $P/P_{cr}=0.94$ and corresponds to a w value about three times higher than the one of the equilibrium path associated with $w_0<0$ (see figs. 9(a)-(b)).

(iii) There is a virtually perfect agreement between the equilibrium paths yielded by the GBT and ANSYS analyses – of course, taking into account that the latter cannot capture a descending branch.

Next, one investigates the spatial global post-buckling behavior of the same "L-shaped" frame. Since the members can now freely deform out-of-plane, one must also include modes **2** (major axis bending) and **4** (torsion) in the GBT post-buckling analyses – note that, due to the presence of mode **4**, it was necessary to incorporate in the analysis the *complete* and *direct* warping transmission at the frame joint ($\Gamma=1$ – see Basaglia *et al.* 2008). Concerning the frame critical buckling behavior, the GBT and ANSYS analyses yielded once more practically coincident critical load values: $P_{cr.GBT}=521.35kN$ and $P_{cr.ANSYS}=521.51kN$ (*0.03%* difference) – the corresponding buckling mode exhibits a highly predominant contribution from mode **2** (*93%*) and also a non-negligible participation of mode **4** (*7%*). Figure 10 shows again the post-buckling equilibrium paths (P/P_{cr} vs. w – w is now the joint out-of-plane displacement due to the applied load[8]) of two frames differing only in the critical-mode initial geometrical imperfection "sign": positive ($w_0=+1.0cm$) or negative ($w_0=-1.0cm$) for joint "forward" or "backward" motions − w_0 is the joint initial out-of-plane displacement. Finally, figure 11 provides GBT-based (i) deformed configurations and (ii) modal participations of the column and beam mid-span and joint cross-sections, for $P/P_{cr}=0.77$ and $w>0$. The following conclusions stem from the analysis of these post-buckling results:

(i) The frame spatial post-buckling behavior is clearly unstable symmetric – this means that, due to the use of the load control strategy, the GBT analysis can only determine the two frame post-buckling equilibrium paths up to their limit points, which occur for $P/P_{cr}=0.78$.

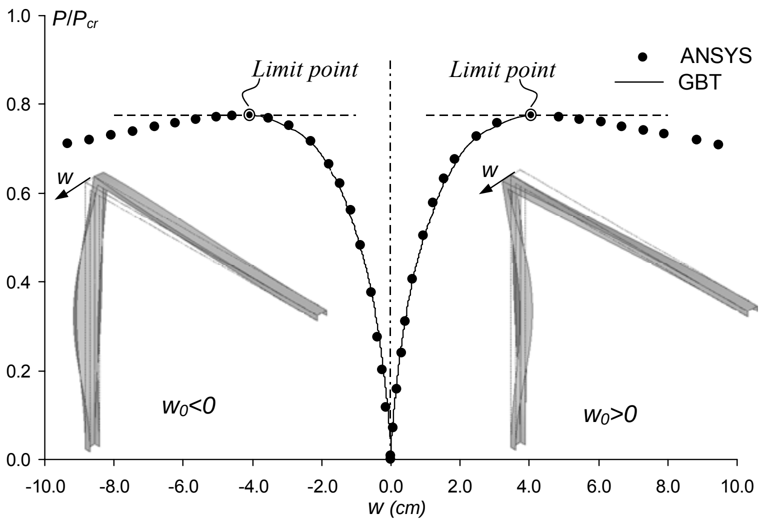

Figure 10. Frame spatial post-buckling behavior: equilibrium paths and initial geometrical imperfection shapes

[8] By joint it is meant the "intersection of the column and beam centroidal axes".

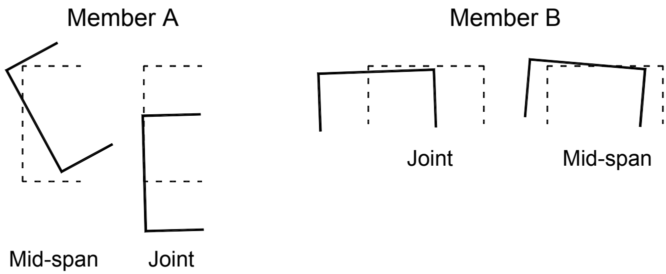

Member	Cross-section	Mode **1**	Mode **2**	Mode **3**	Mode **4**
A	Mid-span	5.46	64.76	23.02	6.76
	Joint	9.87	89.22	0.64	0.27
B	Mid-span	0.46	90.07	7.46	2.01
	Joint	0.64	89.14	9.87	0.35

Figure 11. GBT deformed configuration and modal participations (%) of the column and beam mid-span and joint cross-sections ($P/P_{cr}=0.78$ and $w>0$)

(ii) There is again an excellent agreement between the equilibrium paths obtained through the GBT and ANSYS analyses – or, to be more precise, between their ascending branches (up to the limit load).

(iii) The frame post-buckling deformed configuration involves flexural-torsional deformations in both members, as shown in figure 11. It is interesting to notice a relevant contribution of mode **3** (particularly in the column mid-span region), since this mode does not participate in the frame critical buckling mode (or the initial geometrical imperfections).

(iv) The deformed configurations of the column and beam mid-span cross-sections provide evidence that the former exhibits larger deformations – this is not surprising at all, since only the column is loaded.

CONCLUSION

This paper presented the main steps and procedures involved in the derivation and numerical implementation of two GBT-based geometrically non-linear beam finite element formulations, intended to analyze (i) the local and global post-buckling behavior of thin-walled steel isolated members, possibly with localized displacement restraints, and (ii) the global post-buckling behavior of thin-walled steel frames – in both cases, one took into account the presence of unavoidable initial geometrical imperfections. In particular, one addressed the establishment of the GBT systems of non-linear equilibrium equations, as well as their finite element discretizations, which incorporate the influence of either non-standard support conditions (isolated members) or the joint behavior (frames). The solutions the ensuing systems of non-linear algebraic equations were obtained by means of an incremental-iterative approach combining Newton-Raphson’s method with a load control strategy.

In order to illustrate the application and capabilities of the developed GBT-based beam finite element approach, one presented and discussed numerical results concerning (i) the distortional post-buckling behavior of lipped channel columns with and without a mid-web displacement restraints and (ii) the in-plane and spatial global post-buckling behaviors of a simple “L-shaped” frame built from plain channel members. For validation purposes, most of these results were compared with values yielded by conventional shell (isolated members) and beam (frames) finite element analyses carried out in the code ANSYS – an excellent agreement was found in all cases.

Finally, one last word to mention that the authors are presently working on the development of a FORTRAN code to implement the non-linear GBT-based beam finite element formulation presented in this paper, which will replace the symbolic MAPLE implementation employed until now. The ensuing substantial increase in computational capacity will make it possible to analyze the local and global post-buckling behavior of thin-walled steel frames with several members and exhibiting arbitrary load and support conditions (including localized displacement restraints to model bracing effects) − the outcome of this research effort will be reported in the near-to-intermediate future.

ACKNOWLEDGEMENTS

The first author gratefully acknowledges the financial support of *CAPES Foundation* (Brazil), through scholarship nº BEX 3932/06-0.

REFERENCES

Basaglia C, Camotim D, Silvestre N and Bebiano R (2007a). GBT-based buckling analysis of thin-walled members with arbitrary loading and support conditions, *Book of Abstracts of 18th ASCE Engineering Mechanics Conference* (EM2007 – Blacksburg, 3-6/6), 206. (full paper in CD-ROM Proceedings)

Basaglia C, Camotim D and Silvestre N (2007b). GBT-Based analysis of the local-plate, distortional and global buckling behavior of thin-walled steel frames, *Proceedings of Structural Stability Research Council Annual Stability Conference* (New Orleans, 18-21/4), 391-412.

Basaglia C, Camotim D and Silvestre N (2008). Global buckling analysis of plane and space thin-walled frames in the context of GBT, *Thin-Walled Structures,* **46**(1), 79-101.

Boissonnade N and Degée H (2005). Analysis of tapered steel frames using beam elements and comparison with shell modelling, *Proceedings of 4th European Conference on Steel and Composite Structures* (EUROSTEEL 2005 – Maastricht, 8-10/6), B. Hoffmeister and O. Hechler (eds.), 1.4–33-40.

Camotim D and Silvestre N (2004). GBT distortional post-buckling analysis of cold-formed steel lipped channel columns and beams, *Program and Book of Abstracts of 17th ASCE Engineering Mechanics Conference* (EM2004 – Newark, 13-16/6), 38-39. (full paper in CD-ROM Proceedings)

Camotim D, Silvestre N, Gonçalves R and Dinis PB (2004). GBT analysis of thin-walled members: new formulations and applications, *Thin-Walled Structures: Recent Advances and Future Trends in Thin-Walled Structures Technology* (International Workshop – Loughborough, 25/6), J. Loughlan (ed.), Canopus Publishing Ltd., Bath, 137-168.

Camotim D, Silvestre N, Gonçalves R and Dinis PB (2006). GBT-based structural analysis of thin-walled members: overview, recent progress and future developments, *Advances in Engineering Structures, Mechanics & Construction* (SMCD 2006 – Waterloo, 14-17/5), M. Pandey, W.-C. Xie, L. Xu (eds.), Springer, 187-204.

Camotim D, Silvestre N, Basaglia C and Bebiano R. (2007). GBT-based buckling analysis of thin-walled members with non-standard support conditions, *submitted for publication*.

Camotim D, Basaglia C and Silvestre N (2008). GBT buckling analysis of thin-walled steel frames, *proceedings of the Fifth International Conference on Coupled Instabilities in Metal Structures* (CIMS 2008 – Sydney, 23-25/6), accepted for publication.

Kim SE and Kang KW (2002). Large-scale testing of space steel frame subjected to non-proportional loads, *International Journal of Solids and Structures*, **39**(26), 6411-6427.

Prola L and Camotim D (2002). On the distortional post-buckling behavior of cold-formed lipped channel steel columns, *Proceedings of Structural Stability Research Council Annual Stability Conference*, (Seattle 24-26/4), 571-590.

Roorda J (1965). Stability of structures with small imperfections, *Journal of the Engineering Mechanics Division* (ASCE), **91**(1), 87-106.

Schardt R (1989). *Verallgemeinerte Technishe Biegetheorie*. Springer-Verlag, Berlin. (German)

Silvestre N and Camotim D (2002). First-order generalised beam theory for arbitrary orthotropic materials, *Thin-Walled Structures*, **40**(9), 755-789.

Silvestre N and Camotim D (2003). Non-linear generalised beam theory for cold-formed steel members, *International Journal of Structural Stability and Dynamics*, **3**(4), 461-490.

Silvestre N and Camotim D (2005). An asymptotic-numerical method to analyze the post-buckling behavior, imperfection-sensitivity and mode interaction in Frames", *Journal of Engineering Mechanics* (ASCE), **131**(6), 617-632.

Silvestre N and Camotim D (2006). Local-plate and distortional postbuckling behavior of cold-formed steel lipped channel columns with intermediate stiffeners, *Journal of Structural Engineering* (ASCE), **132**(4), 529-540.

SAS (Swanson Analysis Systems Inc.) (2004). *ANSYS Reference Manual* (version 8.1).

Imperfection sensitivity and reliability using simple bar-spring models for stability

Zeinoddini, V.M.[1], Graham-Brady, L.L.[2], Schafer, B.W.[3],

ABSTRACT

The objective of this paper is to demonstrate how simple bar-spring models can illustrate elementary and advanced structural behavior, including stability, imperfection sensitivity, and plastic collapse. In addition, the same bar-spring models also provide a ready means for assessing structural reliability. Bar-spring models for a column (both post-buckling stable and unstable), a frame, and a plate are all developed. For each model the influence of geometric imperfections are explicitly introduced and the ultimate strength considering plastic collapse of the supporting springs derived. The developed expressions are compared to material and geometric nonlinear finite element analysis models of analogous continuous systems, using MASTAN for the column and frame and ABAQUS for the plate. The results show excellent qualitative agreement, and surprisingly good quantitative agreement. The developed bar-spring models are used in Monte Carlo simulations and in the development of first order Taylor Series approximations to provide the statistics of the ultimate strength as used in structural reliability calculations. Good agreement between conventional first order second moment assumptions and the Monte Carlo simulations of the bar-spring models is demonstrated. It is intended that the developed models provide a useful illustration of basic concepts central to structural stability and structural reliability.

---

[1] Graduate Res. Asst., Johns Hopkins University (vahidzm@jhu.edu)
[2] Associate Professor, Johns Hopkins University (lori@jhu.edu)
[3] Associate Professor, Johns Hopkins University (schafer@jhu.edu)

INTRODUCTION

The stability behavior of columns, frames, and plates can be well approximated and understood through simple analytical models employing rigid bars and springs (e.g., Chajes 1969). The models in Chajes' work demonstrate wonderfully the bifurcation and post-buckling behavior of a variety of structural systems. Most importantly, the solutions are in simple closed-form equations that can be readily studied by the engineer for a deeper understanding of the behavior.

In this work, the models of Chajes are extended to consider (a) initial geometric imperfections, (b) yielding of the springs, and (c) reliability of the strength predictions from the developed bar-spring models. Solutions are provided in closed-form and compared to known nonlinear elastic solutions for the continuous problem, as well as material and geometric nonlinear finite element analysis using MASTAN or ABAQUS. The comparisons show the accuracy of these simple models, even for relatively large nonlinearities. Further, the models provide an explicit means to characterize imperfection sensitivity, i.e., loss in peak capacity as a function of imperfection size.

Ultimately the quantity of interest for the design engineer is not the imperfection sensitivity, but rather what capacity can the structure safely be designed for? Imperfection sensitivity is reflected as variance in the predicted capacity, but all the inputs (E, I, etc.) potentially influence the statistics of the capacity and must be considered in any determination of the structure's reliability. The developed bar-spring models are shown to provide a convenient way to assess reliability through classic first-order Taylor Series approximations and Monte Carlo simulation. Standard first order second moment methods commonly used in structural reliability are employed and compared to the simulations. The developed resistance factors are consistent with those used in practice.

It is hoped that the solutions herein will be useful to engineers trying to understand basic structural stability behavior including collapse and reliability. In addition, it is hoped that the material is useful for educators in structural stability and structural reliability courses.

COLUMN MODELED BY A POST-BUCKLING STABLE BAR-SPRING SYSTEM

Bar-spring system

Consider the stability behavior and load-deflection response of a simple bar-spring model of an axially loaded pin-ended column consisting of two rigid bars connected via a rotational spring as shown in Figure 1.

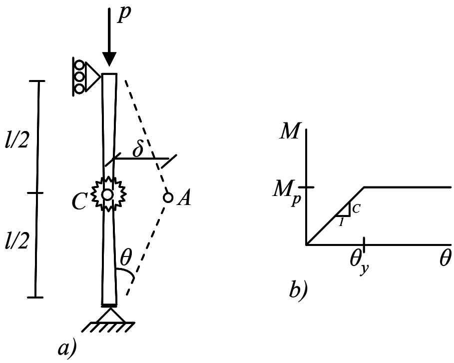

Figure 1: Post-buckling stable bar-spring model of a column

Elastic stability

The stability of this bar-spring model is assessed using a simple equilibrium solution, whereby equilibrium in the deformed configuration is examined. For the model of Figure 1, in the deformed state, moment equilibrium about point *A* results in:

$$p\delta = C2\theta \tag{1}$$

Given the relationship between sidesway, δ, and rotation θ:

$$\sin\theta = \delta/(l/2) \tag{2}$$

the moment equilibrium may be written as

$$p(l/2)\sin\theta = C\cdot 2\theta \tag{3}$$

Small deflections: For small deflections (rotations) sin $\theta \approx \theta$ and:

$$p\theta = \frac{4C}{l}\theta \tag{4}$$

therefore the critical buckling load is found as:

$$p_{cr} = 4C/l\,. \tag{5}$$

The bar-spring model may be related to a continuous pin-ended column of length, l, and stiffness EI, by setting p_{cr} of Eq. 5 to the Euler buckling load (π^2EI/l^2) and solving for C, resulting in:

$$C = \frac{\pi^2 EI}{4l} \tag{6}$$

Large deflections: For large deflections (rotations) and employing the definition of Eq. 5, Eq. 3 simplifies to:

$$p = p_{cr} \frac{\theta}{\sin\theta} \tag{7}$$

The large deflection bar-spring solution of Eq. 7 may be compared with the actual large deflection solution of the continuous system (Wang 1953) as shown in Figure 2. Both the discrete bar-spring model and the continuous system are post-buckling stable, and the solutions are similar for relatively large displacements ($\delta/l < 0.3$).

Elastic stability with imperfections

If the bar-spring model has an initial imperfection δ_0, which does not engage the rotational spring, then the moment equilibrium at point A is

$$p(\delta + \delta_0) = C2\theta \tag{8}$$

For small initial imperfections

$$\delta_0 \cong \theta_0(l/2) \tag{9}$$

Substituting Eq. 9 into Eq. 8 and recognizing the earlier δ-θ relation of Eq. 2 provides the large deflection solution with initial imperfections:

$$p = p_{cr} \frac{\theta - \theta_0}{\sin\theta} \tag{10}$$

Plastic collapse

Members can yield as well as buckle. If the rotational springs are elastic-plastic and yield at rotation θ_y, the moment equilibrium of Eq. 3, for the case of a yielded rotational springs, results in:

$$p = p_{cr} \frac{\theta_y}{\sin\theta} \tag{11}$$

The equilibrium solutions for perfect (Eq. 7), imperfect (Eq. 10), and yielded (Eq. 11) bar-spring models of Figure 1 are depicted in Figure 3.

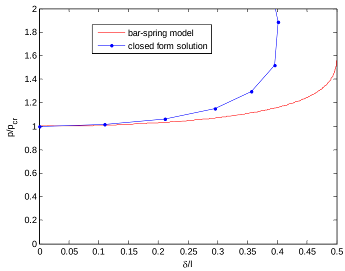

Figure 2: Comparison between bar-spring model and analytical solution for continuous column

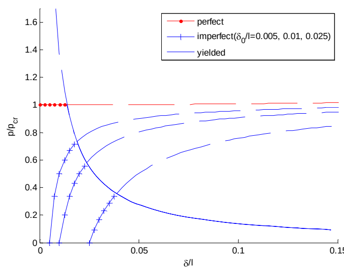

Figure 3: Behavior of post-buckling stable bar-spring model

Yielding also may be associated with a continuous system (i.e., an Euler column) assuming classical plastic hinge behavior. Total rotation of the cross-section at yield is θ_y^* where

$$\theta_y^* = 2\theta_y \tag{12}$$

Equating the moment in the rotational springs to the plastic moment of the section, M_p, and noting $M_p = Z\sigma_y$:

$$\theta_y^* = M_p / C = Z\sigma_y / C \tag{13}$$

Imperfection sensitivity

Imperfection sensitivity is defined here as the loss in peak load carrying capacity due to imperfections. Since this bar-spring model is post-buckling stable the peak load carrying capacity of a perfect column without imperfections occurs when $\theta = \theta_y$ (when the yielding curve intersects the equilibrium curve for no imperfections) and results in

$$p_{max}(perfect) = p_{cr}\frac{\theta_y}{\sin\theta_y} = p_{cr}\frac{\sin^{-1}(2\delta_y / l)}{2(\delta_y)/l} \tag{14}$$

and when initial imperfections are considered

$$p_{max}(imperfect) = p_{cr}\frac{\theta_y}{\sin(\theta_y + \theta_0)} = p_{cr}\frac{\sin^{-1}(2\delta_y / l)}{2(\delta_y + \delta_0)/l} \tag{15}$$

The loss in strength due to imperfection θ_0 (or δ_0) is the difference (Δp) in Eq. 14 and 15, or:

$$\frac{\Delta p}{p_{cr}} = \frac{\theta_y}{\sin\theta_y} - \frac{\theta_y}{\sin(\theta_y - \theta_0)} \cong 1 - \frac{1}{1+\theta_0/\theta_y} \tag{16}$$

For a continuous column Eq. 16 can be modified to a more convenient form, by utilizing Eq. 9, 12, and 13 resulting in the following expression for imperfection sensitivity:

$$\frac{\Delta p}{p_{cr}} \cong 1 - \frac{1}{1+p_{cr}\delta_0/M_p} \tag{17}$$

Example and comparison with continuous system

To provide an illustrative example and a comparison with a continuous column, nonlinear finite element analysis (FEA) of a 12 ft long, pin-ended, W4x13 hot-rolled steel column with the properties as listed in Figure 4 was performed. This column was modeled with an initial sideway imperfection of (*l*/2)/100 using beam elements in MASTAN (McGuire et al 2000). Material and geometric nonlinear analysis was performed. The nonlinear FEA results are compared with the bar-spring model in Figure 4. Although the predicted peak load exhibits a small difference the basic load-deflection response including the influence of imperfections and yielding collapse are captured in the bar-spring model.

<u>W4x13 column</u>
l = 144 in.
I = 11.3 in^4
E= 29000 ksi
σ_y = 50 ksi
Z = 6.26 in^3
M_p =314 kip-in.
θ_y =0.0275 rad

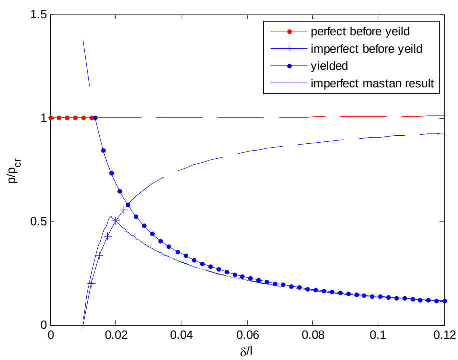

Figure 4: Bar-spring model and MASTAN results for a simple column

COLUMN MODELED BY A POST BUCKLING UNSTABLE BAR-SPRING SYSTEM

Bar-spring system

Here the stability behavior and load-deflection response of a simple bar-spring model of a column consisting of two pinned rigid bars stabilized via a translational spring, as shown in Figure 5, is considered.

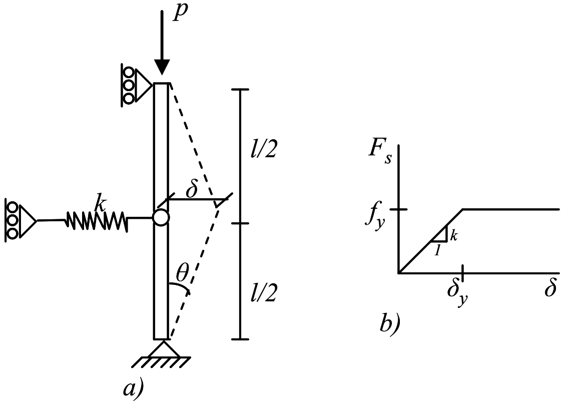

Figure 5: Post-buckling unstable bar-spring model of a column

Elastic stability

Moment equilibrium about the middle joint results in:

$$p\delta = \frac{k\delta}{2}\frac{l}{2}\left(\sqrt{1-\frac{4\delta^2}{l^2}}\right) \tag{18}$$

Which simplifies to a *p*-*δ* relation of

$$p = kl/4\sqrt{1-4(\delta/l)^2} \tag{19}$$

and a critical load of:

$$p_{cr} = kl/4 \tag{20}$$

To find the stiffness (k) of the spring the model is assumed to have the same critical load as a continuous pin-ended Euler column, resulting in:

$$k = \frac{4\pi^2 EI}{l^3} = \frac{4}{l}p_{cr} \tag{21}$$

Elastic stability with imperfections

If an initial imperfection δ_0 exists, which does not engage the spring, then the *p-δ* relation becomes:

$$p = p_{cr}\left(1-\frac{\delta_0}{\delta}\right)\sqrt{1-4\left(\frac{\delta}{l}\right)^2} \tag{22}$$

Plastic collapse

If the supporting spring is elastic-plastic and yields at δ_y, then:

$$p = p_{cr}\left(\frac{\delta_y}{\delta}\right)\sqrt{1-4\left(\frac{\delta}{l}\right)^2} \tag{23}$$

In which δ_y is assumed to be the displacement at which $p\delta_y$ is equal to the plastic moment of the section, therefore:

$$\delta_y = \frac{M_p}{p} = \frac{Z\sigma_y}{kl/4} \tag{24}$$

Figure 6 provides the *p-δ* results for the perfect, imperfect (with different imperfection magnitudes), and yielded bar-spring models.

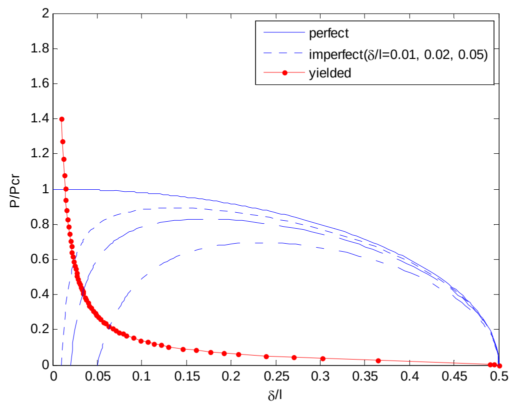

Figure 6: Behavior of post-buckling unstable bar=spring model

Imperfection sensitivity

Since this model is post buckling unstable the peak load carrying capacity of a perfect column is the critical load:

$$P_{max}(perfect)=P_{cr} \tag{25}$$

When there is initial imperfection the maximum load will be:

$$p_{max}(imperfect)=\frac{kl}{4}\left(1-\frac{\delta_0}{\delta_m}\right)\sqrt{1-4\left(\frac{\delta_m}{l}\right)^2} \tag{26}$$

δ_m is the displacement at the maximum load and either occurs due to yielding (as in Figure 6) or elastic instability.

$$\delta_m = \min\left(\delta_y + \delta_0 \text{ (yielding)}, \sqrt[3]{\delta_0 l^2/4} \text{ (buckling)}\right) \tag{27}$$

The loss of strength due to the imperfection may then be found as:

$$\frac{\Delta p}{p_{cr}}=1-\left(1-\frac{\delta_0}{\delta_m}\right)\sqrt{1-4\left(\frac{\delta_m}{l}\right)^2} \tag{28}$$

Example and comparison with continuous system

Similar to the previous section the developed equations are compared to a nonlinear beam element model of the continuous column as shown in Figure 7. The results are similar to Figure 6 since the peak load occurs under relatively small deformations. The basic load-deflection response including the influence of imperfections and yielding collapse are captured in the bar-spring model.

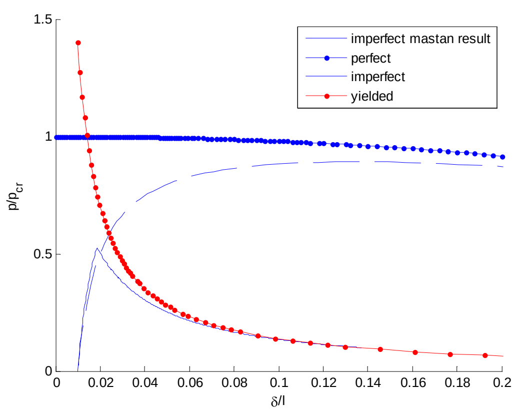

Figure 7: comparison of bar-spring model of the column with unstable post buckling with MASTAN results

MULTI-BAY FRAME MODELED BY BAR-SPRING SYSTEM

The next model considered is that of a laterally supported frame, shown for the continuous system and the bar-spring model, in Figure 8.

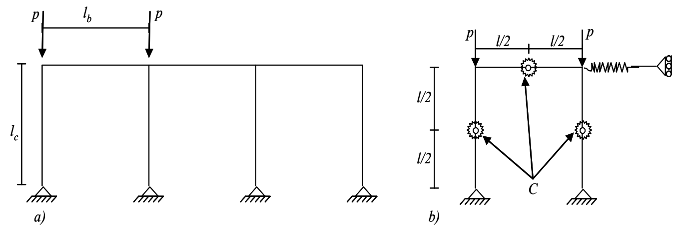

Figure 8 Simple frame and related bar-spring model

Bar-spring system

As demonstrated in Figure 9 deformation in this model can be represented as a combination of a sway mode and a symmetric mode.

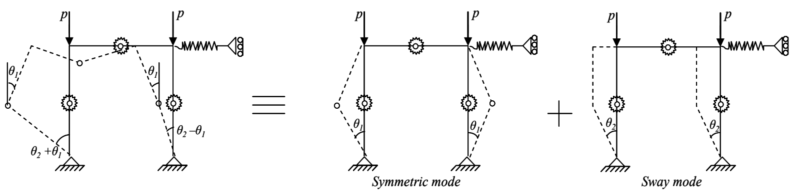

Figure 9: decomposition of deformations for bar-spring model of a frame

In this example the energy method is used to find the equilibrium equation. The total energy (Π) in the deformed shape of Figure 9 is

$$\Pi = C(6\theta_1^2 + \theta_2^2) + \tfrac{1}{2}kl^2 \sin\theta_2 - 2pl(2 - \cos\theta_1 \cos\theta_2 - \cos\theta_1) \quad (29)$$

By taking the partial derivatives of Eq. 29 with respect to θ_1 and θ_2, and equating the resulting expressions to zero, it is found that:

$$p = \frac{2C\theta_2 + kl^2 \cos\theta_2 \sin\theta_2}{2l \cos\theta_1 \sin\theta_2} \quad (30)$$

In which θ_1 and θ_2 have the following relation:

$$12C\theta_1 \cot\theta_1 \sin\theta_2 = 2C\theta_2(\cos\theta_2 + 1) + kl^2 \cos\theta_2 \sin\theta_2(\cos\theta_2 + 1) \quad (31)$$

With these equations one can find the critical load and *p-θ* relationship for the symmetric deformation mode and sway deformation mode.

Symmetric deformation mode

Elastic stability: substitute $\theta_2=0$ in Eq. 30 and the equilibrium equation for the symmetric mode is obtained as:

$$p = \frac{3C}{l}\frac{\theta_1}{sin\,\theta_1} \quad \text{and} \quad p_{cr} = \frac{3C}{l} \tag{31}$$

The translational spring has no influence on the solution, and the result is functionally the same as the post-buckling stable column result.

Elastic stability with imperfections: for an initial imperfection of magnitude θ_{10} in the symmetric mode, the p-θ relationship is:

$$p = p_{cr}\frac{\theta_1 - \theta_{10}}{sin\,\theta_1} \tag{32}$$

Plastic collapse: as before, assuming elastic-plastic springs which yield at θ_{1y}, the p-θ relationship in the fully yielded cases is as follows

$$p = p_{cr}\frac{\theta_{1y}}{sin\,\theta_1} \tag{33}$$

Imperfection sensitivity: the maximum loads for the perfect and imperfect models are found when $\theta_1=\theta_{1y}$ resulting in:

$$p_{max}(\,perfect\,) = p_{cr}\frac{\theta_y}{sin\,\theta_y} = p_{cr}\frac{sin^{-1}(2\delta_y\,/\,l)}{2(\delta+\delta_0)/\,l} \tag{34}$$

$$p_{max}(imperfect\,) = p_{cr}\frac{\theta_y}{sin(\theta_y+\theta_0)} = p_{cr}\frac{sin^{-1}(2\delta_y\,/\,l)}{2(\delta+\delta_0)/\,l} \tag{35}$$

and the loss of strength due to the imperfection is

$$\frac{\Delta p}{p_{cr}} = \frac{\theta_y}{sin\,\theta_y} - \frac{\theta_y}{sin(\theta_y-\theta_0)} \cong 1 - \frac{1}{1+\theta_0\,/\,\theta_y} \tag{36}$$

which can be written in terms of section properties as

$$\frac{\Delta p}{p_{cr}} \cong 1 - \frac{1}{1+p_{cr}\delta_0\,/\,M_p} \tag{37}$$

Sway mode:

Elastic stability: substituting $\theta_1=0$ in Eq. 30 results in:

$$p = \frac{C}{l}\frac{\theta_2}{\sin\theta_2} + \frac{kl}{2}\cos\theta_2 \tag{38}$$

in which the critical buckling load may be written as

$$p_{cr} = p_{cr1} + p_{cr2} \text{ where } p_{cr1} = \frac{C}{l} \text{ and } p_{cr2} = \frac{kl}{2} \tag{39}$$

Elastic stability with imperfections: for sway imperfection θ_{20}:

$$p = p_{cr1}\frac{\theta_2 - \theta_{20}}{\sin\theta_2} + p_{cr2}\frac{\sin\theta_2 - \sin\theta_{20}}{\tan\theta_2} \tag{40}$$

In the sway mode both the rotational (C) and transitional (k) springs are involved, and both springs affect the post buckling behavior. When C/kl^2 is greater than 1.5 the model is strictly post-buckling stable.

Plastic collapse: assuming elastic-plastic behavior for the springs and a yield rotation of θ_{2y}, (note: $\theta_{2y}=M_p/C$) the p-θ relation results in:

$$p = \frac{C}{l}\frac{\theta_{2y}}{\sin\theta_2} + \frac{kl}{2}\frac{\sin(\theta_{2y}+\theta_{20}) - \sin\theta_{20}}{\tan\theta_2} \tag{41}$$

Imperfection sensitivity: assuming the peak load carrying capacity occurs when $\theta_2 = \theta_{2y}$ (i.e., assuming C/kl^2 is large enough or θ_{2y} small enough that the intersection of the plastic collapse load and the elastic equilibrium equations determines the peak load) then the strength for the perfect and imperfect models is:

$$p_{max}(\mathit{perfect}) = \frac{C}{l}\frac{\theta_{2y}}{\sin\theta_{2y}} + \frac{kl}{2}\frac{\sin\theta_{2y}}{\tan\theta_{2y}} \tag{42}$$

$$p_{max}(\mathit{imperfect}) = \frac{C}{l}\frac{\theta_{2y}}{\sin(\theta_{2y}+\theta_{20})} + \frac{kl}{2}\frac{\sin(\theta_{2y}+\theta_{20}) - \sin\theta_{20}}{\tan(\theta_{2y}+\theta_{20})} \tag{43}$$

Loss in strength due to θ_{20} (Δp) is the difference between Eq. 42 and 43. Assuming θ_{20} and θ_{2y} are small (i.e., $\theta_{20}, \theta_{2y} < 0.1$ true in common structures), then the drop in strength is found to be:

$$\frac{\Delta p}{p_{cr}} = \frac{\theta_{2y}}{\sin\theta_{2y}} - \frac{\theta_{2y}}{\sin(\theta_{2y}-\theta_{20})} \cong 1 - \frac{1}{1+\theta_{20}/\theta_{2y}} \tag{44}$$

Noting $\theta_{20}\approx\delta_0/(l/2)$, $\theta_{2y}=M_p/C$ and $C=1.82EI/l$ (based on equating buckling loads for an *l*x*l* sway frame of uniform stiffness *EI*) Δp equals:

$$\frac{\Delta p}{p_{cr}} \cong 1 - \frac{1}{1+\dfrac{3.64EI\delta_0}{M_p l^2}} \tag{44}$$

Example and comparison with continuous system

A translational spring stiffness, *k*, of 522.8 lb/in. is found for the configuration shown in the Figure 9 assuming l = 12 ft, and using W4x13 members (Figure 4). In addition, for this configuration C = 4213 kip-in./rad and θ_{2y} = 0.075 rad. To illustrate the influence of imperfections, consider $\delta_o = l/200$, recognizing $\theta_{20}\approx\delta_o/(l/2)$ then Eq. 42 results in a p_{max}(*perfect*) of 66.88 kips and Eq. 43 in a p_{max}(*imperfect*) of 49.04 Kips. The impact of imperfections on the strength of the model is pronounced. For $\delta_o=l/200$ the bar-spring model is explicitly compared to a corresponding nonlinear beam element model of the continuous system in MASTAN, as shown in Figure 10. The basic load-deflection behavior of the model agrees well, and even the predicted peak load shows surprisingly little difference between the continuous model and the bar-spring model.

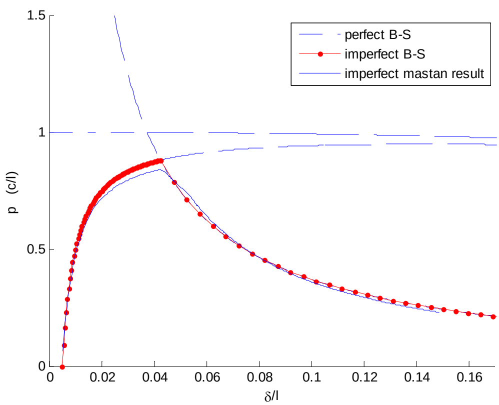

Figure 10: comparison of bar-spring model with MASTAN results for a frame with lateral support

PLATE

Bar-spring system

Consider a bar-spring model of a thin square plate, simply supported at the edges (Figure 11). The rotational springs in the model represent the bending stiffness of the plate and the translational springs represent the transverse membrane stiffness of the plate.

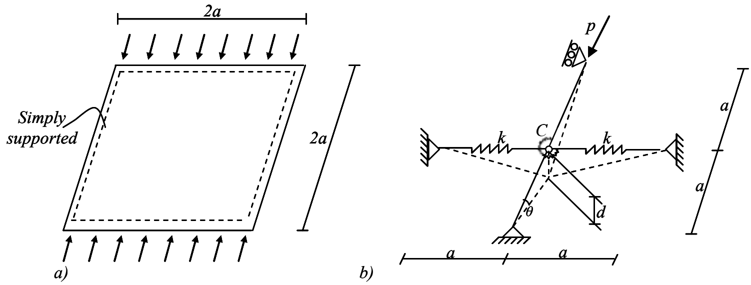

Figure 11 a) simply supported plate and b) bar spring model

Elastic stability

The total potential energy of the model in the deformed state is:

$$\Pi = 4C\theta^2 + ka^2\left(\frac{1}{cos\,\theta} - 1\right)^2 - 2pa(1 - cos\,\theta) \tag{45}$$

Differentiation with respect to θ leads to the equilibrium expression:

$$p = \frac{4C}{a}\frac{\theta}{sin\,\theta} + \frac{ka}{cos^2\,\theta}\left(\frac{1}{cos\,\theta} - 1\right) \text{ and } p_{cr} = \frac{4C}{a} \tag{46}$$

The first term of Eq. 46 reflects the bending behavior of the plate and is post-buckling stable, but only weakly so for practical θ. The second term of Eq. 46 is strongly post-buckling stable and highlights the influence of transverse membrane stiffness on post-buckling. The rotational stiffness, C, may be found by equating the critical buckling stress of the plate to the model:

$$f_{cr} = 4\frac{\pi^2 D}{(2a)^2 t}, \quad p_{cr} = f_{cr}2at, \text{ therefore } C = \frac{\pi^2 D}{2} \tag{47}$$

where $D = Et^3/(12(1-\nu^2))$. The membrane action is considered as a portion, α, of the axial stiffness (EA/L) of the plate:

$$k = \alpha E2at / a = \alpha 2Et \tag{48}$$

Elastic stability with imperfections

If we consider an out-of-plane initial imperfection, d_o, in the center of the plate and noting that $d_o = asin\theta_o$, then Eq. 46 becomes:

$$p = \frac{4C}{a}\frac{\theta - \theta_0}{sin\,\theta} + \frac{ka}{cos^2\,\theta}\left(\frac{1}{cos\,\theta} - \frac{1}{cos\,\theta_0}\right) \tag{49}$$

Plastic collapse

Similar to the previous models, assuming an elastic-plastic behavior for the springs where yielding initiates at θ_y (and $d_y = asin\theta_y$):

$$p = \frac{4C}{a}\frac{\theta_y}{sin\,\theta} + \frac{ka}{cos^2\,\theta}\left(\frac{1}{cos(\theta_y)} - 1\right) \tag{50}$$

Here it is assumed (simplistically) that the rotational and translational springs yield at the same time, and that θ_o does not engage the spring.

Imperfection sensitivity

The maximum loads for the perfect and imperfect models are:

$$p_{max}(\,perfect\,) = \frac{4C}{a}\frac{\theta_y}{sin\,\theta_y} + \frac{ka}{cos^2\,\theta_y}\left(\frac{1}{cos\,\theta_y} - 1\right) \tag{51}$$

$$p_{max}(\,imperfect\,) = \frac{4C}{a}\frac{\theta_y}{sin\,\theta_m} + \frac{ka}{cos^2\,\theta_m}\left(\frac{1}{cos\,\theta_y} - 1\right) \tag{52}$$

where the intersection of the plastic collapse load and elastic equilibrium expression occurs at θ_m, found from the following:

$$p_{cr}\frac{\theta_y}{sin\,\theta_m} + \frac{ka}{cos^2\,\theta_m}\left(\frac{1}{cos(\theta_y)} - 1\right) = p_{cr}\frac{\theta_m - \theta_0}{sin\,\theta_m} + \frac{ka}{cos^2\,\theta_m}\left(\frac{1}{cos\,\theta_m} - \frac{1}{cos\,\theta_0}\right) \tag{53}$$

For small θ_0 and θ_y, the loss of strength due to imperfections ($\Delta p = p_{max}(perfect) - p_{max}(imperfect)$) simplifies to

$$\Delta p = p_{cr}\left(1 - \frac{\theta_y}{\theta_m}\right) + ka(\theta_y^4 - \theta_m^2\theta_y^2) \tag{54}$$

and although ka is mach bigger than p_{cr} ($4c/a$), the second term in Eq. 54 is negligible because it involves rotations to the fourth power, so:

$$\frac{\Delta p}{p_{cr}} \cong \left(1 - \frac{\theta_y}{\theta_m}\right) \text{ or } \frac{\Delta p}{p_{cr}} \cong \left(1 - \frac{d_y}{d_m}\right) \tag{55}$$

Example and comparison with continuous system

The developed bar-spring model is compared to a simply supported square plate (a = 2.5 in., t = 0.05 in.) with end loading, modeled in ABAQUS. The ABAQUS model uses a fine mesh of S9R5 thin shell elements, and employs the von Mises yield criteria with an elastic-plastic stress-strain relation (E=29500 ksi and σ_y=50 ksi). Note, in this case α=½ (Eq. 48) and the yielding of the bar-spring model was empirically modified to d_y/a = 0.035 to match the ABAQUS results. An initial imperfection of d_o = 0.05 in. in the first buckling mode of the plate was employed. The results of Figure 12 show that the bar-spring model is capable of accurately capturing the basic behavior (given some calibration).

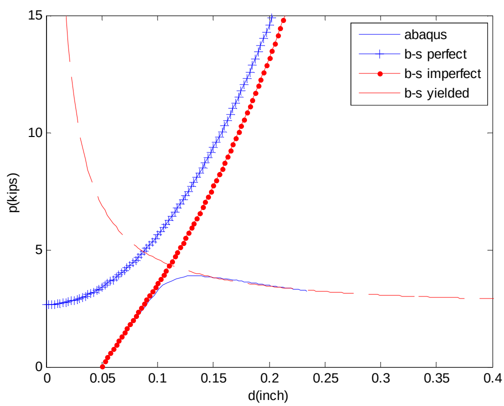

Figure 12: Bar-spring and ABAQUS model of plate with imperfection

RELIABILITY

The simple bar-spring models of the previous sections are shown to provide reasonable reproductions of the stability and collapse behavior of columns, frames, and plates. In this section we explore the reliability predictions that may be developed from the same models, but now allowing the model parameters to be random variables. Since the bar-spring models reduce the solutions to variables (instead of functions) their use is particularly amenable to elementary reliability calculations.

Column with stable post-buckling

The maximum capacity of the bar-spring model of the column with stable post-buckling behavior is found in Eq. 15 and may be written as:

$$P = p_{cr}\frac{sin^{-1}(2\delta_y / l)}{2(\delta_y + \delta_0)/l},\ p_{cr} = \frac{\pi^2 EI}{l^2},\ \text{and}\ \delta_y = \frac{Z\sigma_y l^2}{\pi^2 EI} \tag{56}$$

where E, I, Z, and σ_y, are assumed to be lognormal random variables, and δ_o is assumed to follow a uniform distribution. For reliability considerations we seek the statistics of random variable P, the strength. A conventional solution is the application of a first-order Taylor Series expansion to Eq. 58 about the mean (μ) values, i.e.:

$$P = P\left(\mu_{E,}\mu_{\sigma_y,}\mu_{I,}\mu_{Z,}\mu_{\delta_o}\right) + \frac{\partial P}{\partial E}\left(E - \mu_E\right) + \ldots + \frac{\partial P}{\partial \delta_o}\left(\delta_o - \mu_{\delta_o}\right) \tag{57}$$

Consider n as designating the nominal or specified properties (e.g., see Figure 4, n_E = 29000 ksi, etc.) and μ for the mean and V for the coefficient of variation, then: $\mu_E = n_E$, $V_E = 0.06$, $\mu_{\sigma y} = 1.05n_{\sigma y}$, $V_{\sigma y}$ = 0.10 (Galambos 1978), $\mu_I = n_I$, $V_I = 0.05$, $\mu_Z = n_Z$, $V_Z = 0.05$ (Yura et al. 1978), and $\mu_{\delta o} = l/1470$ with a range (δ_o is a uniform random variable) of $l/1400$ to $l/900$ (Bjorhovde 1978, Galambos 1998). The Taylor Series expansion of Eq. 57 then results in:

$$P = 149.09 - 2.41\bar{\delta}_o + 0.666\bar{\sigma}_y + 8.57\bar{E} + 7.21\bar{I} + 0.33\bar{Z} \tag{58}$$

where the overbar denotes that each variable has been transformed to a mean of 0 and variance of 1, i.e., $\bar{X} = (X - \mu_X)/(V_X\mu_X)$ for random variable X. Since Eq. 58 is a linear function its moments may be readily evaluated, providing an estimated μ_P = 149.09 and V_P = 0.0766. In addition the coefficients of Eq. 58 provide a sense of which variables are the most influential on the solution.

Direct Monte Carlo (MC) simulation is the other means used to determine the statistics of P. A simulation consisting of 10^6 samples was performed and is summarized in Figure 13a, along with a normal and lognormal distribution fit to the simulation data. For this simple example the first order Taylor series and the simulation provide the same mean and coefficient of variation to several significant figures, i.e., the MC results are: $\mu_P = 149.09$ and $V_P = 0.0761$.

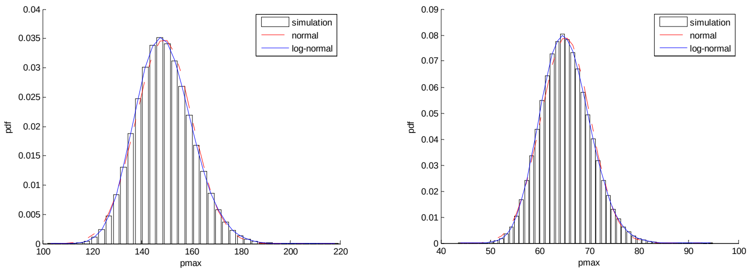

(a) post-buckling stable column (b) multi-bay frame

Figure 13 Simulation results for bar-spring models

A first order Taylor Series and MC simulation was also performed on the post-buckling unstable column. However, for this combination of imperfections and yield stress the statistics of *P* are essentially identical to the post-buckling stable model. By MC simulation $\mu_P = 148.9$ and $V_P = 0.0767$ for the post-buckling unstable column.

Multi-bay Frame- sway mode

The strength of the multi-bay frame in the sway mode is defined by Eq. 43. Making similar transformations to those of Eq. 44 (i.e., converting *C* to a function of *EI*, *k* to a function of *EI*, θ_{2o} to a function of δ_o, and θ_y to a function of *Z* and σ_y) the strength *P* may be written as a function of random variables *E*, *I*, *Z*, σ_y and δ_o (while *l* remains deterministic). Assuming the same distributions as before, the first order Taylor Series expansion results in:

$$P = 65.20 - 0.40\overline{\delta}_o + 0.09\overline{\sigma}_y + 3.86\overline{E} + 3.21\overline{I} + 0.05\overline{Z} \qquad (59)$$

With $\mu_P = 65.20$ and $V_P = 0.077$ from Eq. 59. MC simulation with 10^6 samples is shown in Figure 13b and provides an estimated $\mu_P = 65.17$ and $V_P = 0.077$. As with the column model the Taylor Series and MC simulation are in nearly identical agreement.

Plate

The maximum strength of the plate bar-spring model is provided in Eq. 52, but requires the solution to the rather complicated nonlinear expression of Eq. 53 to find θ_m, or equivalently d_m, (the displacement where the elastic equilibrium and plastic collapse equations intersect). Solution to d_m also requires d_y, but yielding is more complicated in the plate model and no explicit form is provided. Instead, d_y is selected as the deterministic value previously determined for the example problem (i.e., $d_y/a = 0.0375$). For the MC simulation E, and d_o are set as lognormal random variables with $\mu_E = 29500$ ksi, $V_E = 0.06$, and $\mu_{do} = 0.5t$, $V_{do} = 0.66t$, and a and t are assumed deterministic with $a = 2.5$ in., and $t = 0.05$ in.. Simulation results for 100,000 samples are provided in Figure 14, and estimated $\mu_P = 4.66$, and $V_P = 0.085$.

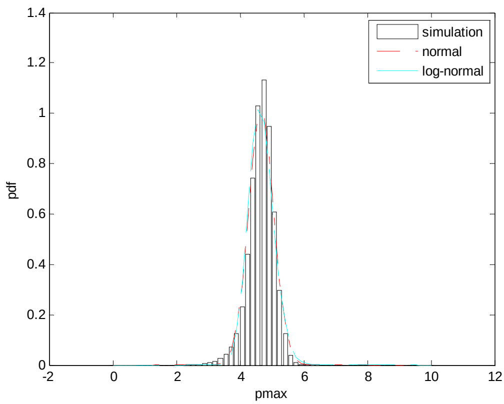

Figure 14 Simulation results for plate model

A first order Taylor Series expansions is also performed on the plate model, but since closed form expressions as a function of the random variable δ_o is not possible, finite differences are used to approximate the coefficients of the Taylor series, this results in:

$$P = 4.64 - 0.3756\overline{\delta}_o + 0.28\overline{E} \tag{60}$$

and estimated statistics of $\mu_P = 4.64$, and $V_P = 0.10$. Agreement between the two methods is quite good even for the more complicated functions used in the plate solution.

Resistance factors for codes

The bar-spring model results may also be used to generate approximations for the resistance factors used in code formulations, such as Load and Resistance Factor Design (LRFD). Using standard LRFD reliability format, select $g=\ln(P/Q)$ as the indicator function, where P is the resistance, Q the demand, and $g<0$ indicates failure. Limit the probability of failure by selecting $g=0$ to be a given number of standard deviations ($\beta\sigma$'s, e.g., $\beta = 3$) from the mean, via:

$$E\left[ln\left(P/Q\right)\right] = \beta\sigma_{ln(P/Q)} \tag{61}$$

For first order, second moment approximations of P and Q:

$$ln\left(\mu_P / \mu_Q\right) = \beta\sqrt{V_P^2 + V_Q^2} \tag{62}$$

Further simplifying $\sqrt{V_P^2 + V_Q^2} \sim \alpha\left(V_P + V_Q\right)$ with α=0.55:

$$\mu_P = e^{\beta\sqrt{V_P^2+V_Q^2}}\mu_Q \cong e^{\alpha\beta\left(V_P+V_Q\right)}\mu_Q \text{ so } e^{-\alpha\beta V_P}\mu_P = e^{\alpha\beta V_Q}\mu_Q \tag{63}$$

Given the standard LRFD format, the resistance factor is found as

$$\phi \mathrm{P_n} > \gamma Q \text{, assuming } \mu_P = P_n \text{, then } \phi = e^{-\alpha\beta V_P} \tag{64}$$

Thus, from Eq. 64 we may provide estimates of ϕ for all of the bar-spring models (assuming α=0.55, β=3) as given in Table 1. The results provide ϕ factors similar to those in common use. Further, all of the models have similar ϕ values, because they have similar V_P.

Table 1 Calculated resistance factors (ϕ) for bar-spring models

ϕ	MC Simulation	1st order Taylor
Column	0.881	0.882
Multi-bay frame	0.880	0.880
Plate	0.873	0.847

CONCLUSIONS

Simplified bar-spring models including geometric imperfections and elastic-plastic springs are developed for columns, frames, and plates. Comparison of the discrete bar-spring models to material and geometric nonlinear FE models of the analogous continuous systems (column, frames, and plate) show good overall agreement. Closed-form expressions for the maximum capacity and for the imperfection sensitivity of each of the bar-spring models are developed. The developed bar-spring models are also used to assess the reliability of columns, frames, and plates. It is shown that the bar-spring models agree well with the classic first order second moment reliability methods and developed resistance factors are consistent with those used in practice.

ACKNOWLEDGMENTS

This material is based upon work supported by the National Science Foundation (NSF) under Grant No. 0528318. Any opinions, findings, and conclusions or recommendations expresses in this material are those of the authors and do not necessarily reflect the views of the NSF.

REFERENCES

Chajes, A. (1969). "Stability behavior illustrated by simple models." ASCE, *J. of the Structural Division*, 95 (ST6) 1153-1172.

Galambos, T.V. (1998). Guide to Stability Design Criteria for Metal Structures. John Wiley & Sons, 5th Ed.

Galambos, T.V., Ravindra, M.L. (1978). "Properties of Steel for use in LRFD." ASCE, *J. of the Structural Division*, 104 (9) 1459-1468.

McGuire, W., Gallagher, R.H., Ziemian, R.D. (2000). Matrix Structural Analysis. John Wiley & Sons, 2nd Ed.

Wang, C.T. (1953). Applied Elasticity. McGraw-Hill.

Yura, J.A., Galambos, T.V., Ravindra, M.K. (1978). "The bending resistance of steel beams." ASCE, *J. of the Structural Division*, 104 (9) 1355-1370.

System Buckling of I-Shaped Girders

Todd Helwig[1], Joseph Yura[2], Reagan Herman[3], and Chong Zhou[4]

ABSTRACT

The lateral torsional buckling capacity of steel girders is often increased by reducing the unbraced member length with cross-frames or other torsional braces provided at discrete locations along the girders. The objective of providing cross-frames is to create a brace point so that the girders buckle between the cross-frames and the capacity of the individual girders can be evaluated using the spacing between the cross-frames. However, twin girder systems are also susceptible to failures in which both girders behave as a system and buckle in a half-sine curve shape along the girder length at load levels that can be substantially lower than those predicted using existing design solutions. Such failures have been observed both in the laboratory and in the field. Even systems with several girders can experience problems related to this system buckling mode during construction since girders are often erected in pairs. The system failures are a function of the in-plane stiffness of the girders and are relatively insensitive to the spacing between the intermediate cross-frames or their stiffness. A general discussion of the failure mode is provided by presenting results from finite element analyses for twin

[1] Assistant Professor, Dept. of Civil Engineering, University of Texas at Austin
[2] Professor Emeritus Dept. of Civil Engineering, University of Texas at Austin
[3] Research Assistant Professor, Dept. of Civil and Env. Engineering, The Johns Hopkins University
[4] Graduate Research Assistant, Dept. of Civil and Env. Engineering, University of Houston

girders buckling as a system. A closed-form solution for estimating the buckling moment of the global system mode is also presented. This solution can be used by engineers as a limit on existing design methods for systems that are susceptible to the system buckling mode.

INTRODUCTION

Lateral torsional buckling is a failure mode that involves a lateral movement of the cross-section and a twist of the girder. The buckling capacity of the girders can be increased by providing bracing along the girder length to control either lateral movement of the compression flange or twist of the girder cross-section. Braces such as cross-frames fit into the category of torsional bracing since they control twist of the members.

The general design philosophy of stability bracing for multi-girder systems is to reduce the unbraced length of the girders so that the buckling behavior of the individual members can be isolated from the rest of the structural system. Although braces can be adequately proportioned to act as a brace point for many systems, twin girders with cross-frames are also susceptible to a global failure mode in which the two girders buckle as a system in a half-sine curve over the girder length. Systems with more than two girders can also experience problems related to the global system buckling mode during construction since girders are often erected in pairs. Three- and four-girder systems with relatively close girder spacing can fail in a system mode; however the problem is most frequently encountered with twin girder systems. Such failures have been observed in the laboratory and also in the field. One of the global failure modes occurred in Texas during a bridge-widening involving a twin girder with several cross-frames. The failure of a single box girder during construction, despite having several internal K-frames, is also attributed to a similar mode of failure. The buckling capacity of girder systems that fail in this global mode is relatively insensitive to the size and spacing between cross-frames. The current bracing solutions for cross-frames and diaphragms that are typically employed by engineers do not include the global mode, which can potentially lead to unsafe designs in buildings, bridges, and other structures.

This paper presents finite element results that demonstrate the global buckling mode in twin girder systems. A design equation that predicts the global buckling capacity is also presented. This expression can be used by design engineers to identify potential problems since it provides an upper limit on current bracing design solutions.

Background information on torsional bracing systems is presented in the following section followed by an overview of the finite element model and the scope of the analyses. Finite element results that demonstrate the buckling behavior of twin girder systems are then reviewed. Results are presented for girders that buckle between brace points as well as girders that buckle in the global system mode. Comparisons between the finite element analysis (FEA) results and the design expression for predicting the global mode are provided and a design example is presented in the appendix.

BACKGROUND

Adequate stability bracing must possess sufficient stiffness and strength (Winter 1960). The American Institute of Steel Construction (AISC) Specification (2005) includes provisions for the stiffness and strength requirements for torsional beam bracing. The stiffness equation in the Specification is based upon a simplification of the following expression (Yura 2001):

$$M_{cr} = \sqrt{C_{bu}^2 M_0^2 + \frac{C_{bb}^2 \overline{\beta_T} E I_{y\cdot eff}}{2C_t}} \le M_s \quad \text{or} \quad M_y \tag{1}$$

where: M_o = buckling capacity of the beam with no intermediate bracing and uniform moment loading; C_{bu} = moment gradient factor for the beam with no intermediate bracing; C_{bb} = moment gradient factor for the beam with full bracing; E = modulus of elasticity of the girders, $\overline{\beta_T}$ = continuous torsional bracing system stiffness; $I_{y\cdot eff}$ = effective weak axis cross-sectional moment of inertia = $I_{yc}+(t/c)I_{yt}$; I_{yc} = moment of inertia of compression flange about axis through the web; I_{yt} =

moment of inertia of tension flange about axis through the web; c = distance between cross section centroid and centroid of compression flange; t = distance between cross section centroid and centroid of tension flange; C_t = 1.2 top flange loading factor (equal to 1.0 for loading at centroid or uniform moment); M_s = moment corresponding to beam buckling between braces; and M_y = beam yield moment.

The expression in (1) was developed assuming continuous torsional bracing, $\overline{\beta}_T$. For systems braced by discrete cross-frames, the continuous brace stiffness can be replaced using the relationship, $\overline{\beta}_T = n\beta_T / L$, where n is the number of intermediate (between supports) torsional braces with a stiffness of β_T, and L is the span of the girder. The design expression that is given in the AISC Specification (2005) has conservatively neglected the first term under the radical in (1), which represents the capacity of the beam with no intermediate bracing. Also, the AISC Specification (2005) equations assume top flange loading (C_t = *1.2*) and are specifically applicable for doubly symmetric sections and therefore use I_y instead of $I_{y\text{-}eff}$. The expression shown in (1) is a general expression that is applicable for doubly and singly-symmetric I-shaped members.

There are a number of factors that affect the torsional brace stiffness, β_T. These factors include the stiffness of the brace, cross-sectional distortion, and also the in-plane stiffness of the girders. The stiffness behavior of bracing systems is generally governed by the classic equation for springs-in-series. Therefore the following relationship is used to determine the torsional brace stiffness of the system, β_T :

$$\frac{1}{\beta_T} = \frac{1}{\beta_b} + \frac{1}{\beta_{\text{sec}}} + \frac{1}{\beta_g} \tag{2}$$

where: β_b is the stiffness of the brace, β_{sec} accounts for distortion in the girder cross section, and β_g accounts for the in-plane stiffness of the girders. The stiffness of the torsional bracing system, β_T, will be smaller than the smallest of the three terms on the right side of (2).

The stiffness of the brace depends on the cross-frame or diaphragm system that is employed. Stiffness expressions for a variety of cross-frame geometries can be found in Yura (2001). A stiffness expression for the cross-sectional distortion is also provided in Yura (2001) as well as in the AISC Specification (2005). Many cross-frames essentially extend from the top of the girder to the bottom of the girder so cross-sectional distortion does not affect the bracing behavior and the β_{sec} term can be assumed to be infinity. The effect of the in-plane stiffness was discussed in Helwig et al. (1993), which provided the following expression for twin girders:

$$\beta_g = \frac{12S^2EI_x}{L^3} \tag{3}$$

where: S is the spacing between the twin girders, E is the modulus of elasticity of the beams, I_x is the strong-axis moment of inertia, and L is the span of the beam. While the expression in (3) was developed for twin girders, a general expression for the in-plane girder stiffness for systems with more than two girders was presented in Yura (2001). Although the in-plane girder stiffness does affect the stiffness of the torsional bracing system, the provisions in the AISC Specification do not account for this effect since the in-plane stiffness is often relatively large for systems with three or more girders. However, for twin girder systems the in-plane stiffness can often dominate the system stiffness given by (2). Although accounting for the effect of the in-plane stiffness of the girders in (2) can often identify problems where the brace system will not be adequate, requiring the additional stiffness term specifically for twin girders may not be desirable for many engineers. An alternative approach is to utilize a solution that will identify when the girders may be susceptible to the global system failure mode. A solution is presented later in the paper that provides the engineer with a design moment for the system buckling mode that can be applied as an upper limit of (1) in a manner similar to the limits M_s and M_y currently used in (1). This moment limit approach is attractive from a design perspective since the engineer knows the design moment and can use the proposed limit to solve for the required in-plane moment of inertia to ensure adequate capacity to avoid the global failure mode.

FINITE ELEMENT MODEL

The finite element program ANSYS (2003) was used to study the buckling behavior of twin girder systems with cross-frames for bracing. Linear elastic materials were utilized in all analyses. The cross-sections of the girders that were studied are shown in Fig. 1. Section #1 is a doubly symmetric section, while Section #2 is a singly symmetric section. Analyses were conducted with two orientations for the singly-symmetric section: A) the small flange subjected to compression; and B) the large flange subjected to compression. An indication of the degree of monosymmetry of a section can be determined from the ratio $\rho = I_{yc}/I_y$, where I_y is the weak axis moment of inertia and I_{yc} is the moment of inertia of the compression flange about the weak axis. For a doubly-symmetric section the value of ρ is 0.5. Section #2 in Fig. 1 has a ρ-value of 0.2 when the small flange is in compression and 0.8 when the large flange is in compression.

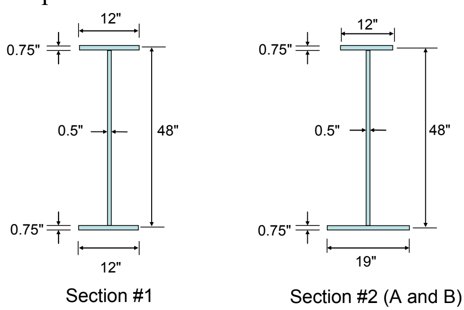

Figure 1: Cross sections studied.

The cross sections of the girders were modeled using 8-node shell elements. Two shell elements were used to model each flange and four elements were used through the web depth. The number of element divisions along the girder length was typically selected so that the element aspect ratios were as close to unity as possible. Shell elements were also used to model transverse web stiffeners at supports and at the locations of point loads.

Twin girder systems with simple supports were analyzed with loading that caused compression in the top flange. Although twist was restrained by cross-frames at the ends of the girders, the cross-sections were free to warp. In addition to uniform moment, two types of transverse loads were considered in the investigation: a single point load applied at midspan, and a uniform distributed load applied along the member length. Analyses were conducted with points of load application located at the top flange, midheight, and bottom flange.

The torsional bracing that was used in the analyses consisted of cross-frames such as the one depicted in Fig. 2. The cross-frame was a "tension-only" system that was modeled with a single diagonal. Although most cross-frames have two diagonals, the members that are employed often consist of angles, which have relatively low buckling strengths. The "tension-only" cross-frame system conservatively neglects the compression diagonal and its relatively low buckling strength. The cross-frames were full depth members that framed into the girders at the top and bottom of the web. Since the cross-frames connected directly to the flange-to-web juncture, cross-sectional distortion did not affect the brace behavior. Although span-to-depth ratios of 15~25 were considered, the results presented in this paper will focus on systems with span-to-depth ratios of 20. Similar trends were observed with the other span-to-depth ratios that were analyzed. Several different spacings between the cross-frames were studied.

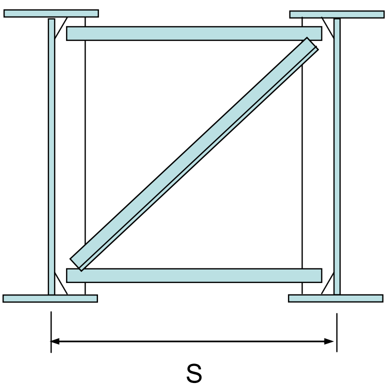

Figure 2: Tension-only cross frame.

FEA RESULTS

Doubly-Symmetric Sections

This segment of the paper focuses on results for doubly symmetric Section #1 from Fig. 1. Results for the singly-symmetric Section #2 are presented in the following section. As mentioned in the discussion of the finite element model, the girders were subjected to a variety of loading conditions and cross-frame spacings. Although the majority of

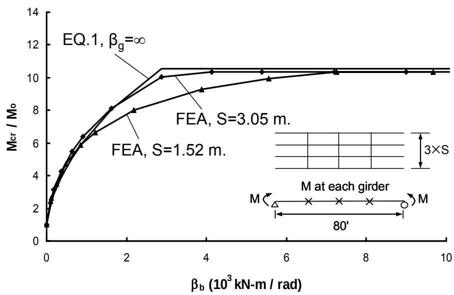

Figure 3: Buckling moment versus brace stiffness for 4-girder system.

the FEA results that are presented focus on twin girder systems, cases with three- and four-girder systems were also considered. Figure 3 shows a comparison of FEA results for a system with four girders and uniform moment loading. The girders have a span-to-depth ratio (*L/d*) of 20 and three intermediate lines of cross-frames as depicted in the plan view of the four-girder system shown on the figure. The buckling capacity of the beams is graphed on the vertical axis versus the brace stiffness of each cross-frame on the horizontal axis. The buckling moment, M_{cr}, on the vertical axis was normalized by M_o, which is the uniform moment buckling capacity of A girder with no intermediate (between supports) bracing. FEA results are shown for girder spacings of 3.05 m (10 ft.) and 1.52 m (5 ft.). There is relatively little difference between the FEA results for the different girder spacings. The two FEA solutions are within 15% of each other for the majority of the values of the brace stiffness considered. The reason for the difference is due to effects of the in-plane stiffness, which become more significant for closer girder spacings. However, both girders buckle between the brace points at values of M_{cr}/M_o of approximately 10.

A graph of (1), which has reasonable agreement with the FEA results, is also shown in Fig. 3. There are more cross-frames per girder in the four girder system (¾ cross-frame per girder) compared to the two-girder system (½ cross-frame per girder). Therefore, an effective brace stiffness of $1.5\beta_b$ [$=\beta_b\times(3/4)/(1/2)$] was used in evaluating β_T for the four girder system in (1). The effect of the in-plane stiffness of the girders was neglected in evaluating the torsional brace stiffness in (1). Since most designers do not consider the effect of the in-plane stiffness, using a β_g of infinity is consistent with most current design procedures. As mentioned in the background section, the in-plane stiffness is relatively large for systems with more than two girders and can often be neglected.

Although the in-plane girder stiffness had a relatively small effect on the FEA results for the four-girder system shown in Fig. 3, this factor does have a significant effect on the twin girder system. This is demonstrated in Fig. 4, which shows a graph of the FEA results for a twin girder system spaced at 3.05 m and 1.52 m. The difference in the buckling capacity of the systems for the two different girder spacing is quite dramatic. The behavior of the system with the wider 3.05 m girder spacing followed the behavior that is typically expected, in which the buckling capacity increased with stiffer braces until finally the girders buckled between the cross-frame locations. The girders with the smaller spacing, on the other hand, always buckled in a half-sine curve mode shape regardless of the brace stiffness that was provided.

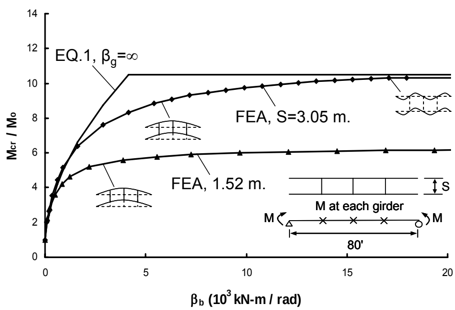

Figure 4: Buckling moment versus stiffness for twin girder.

When the girders buckle between the braces, the girders tend to behave independently of one another. However, since the girders don't buckle between the braces with the closer girder spacing, the two girders tend to behave as a unit that is relatively insensitive to the size and spacing of the bracing. This is demonstrated in Fig. 5, which shows twin girder systems with the 1.52 m girder spacing. The number of intermediate braces was varied from 1 to 5 as shown in the plan-view sketches in the figure. For the case of a single intermediate cross frame, the bracing was effective enough to force the girders to buckle between the brace

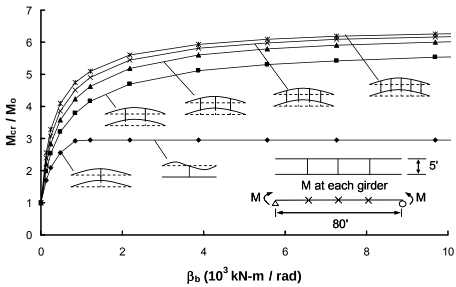

Figure 5: Insensitivity of system failure mode to brace spacing.

points. However, the systems with two or more intermediate braces never buckled between the braces. In addition, for the systems with two or more intermediate braces, although the spacing between the braces was dramatically reduced as additional intermediate braces were added, the buckling behavior was not significantly affected. The insensitivity to the brace spacing when the twin girders buckle as a system is contrary to the conventional wisdom for solving buckling problems. The reason that the braces are so ineffective in the systems with the close girder spacing is because the in-plane girder stiffness, β_g, dominates the system stiffness in (2). When β_g is smaller than the stiffness required to force the girders to buckle between the brace points, the twin girders will always buckle in the system mode (half sine curve), regardless of the size or number of intermediate cross-frames provided.

An expression to predict the buckling capacity of twin girders in the global system mode has been developed and presented in Yura et. al (2008). The buckling capacity of one of the girders in the system (global) mode is:

$$M_{cr,global} = \frac{C_{bu}\pi}{L}\sqrt{E\left(2I_{yc}\right)GJ + \frac{\pi^2 E^2 \left(I_{y\,eff}\right) I_x S^2}{4C_t L^2}} \tag{4}$$

where: $M_{cr,\,global}$ is the buckling moment of a single girder in the global mode; C_{bu}, C_t, E, I_x, I_{yc}, $I_{y\cdot eff}$, S, and L are as previously defined; G is the shear modulus of elasticity; and J is the torsional constant. The expression in (4) is valid for both doubly- and singly-symmetric sections. For a doubly-symmetric section, $I_{y\cdot eff}$ and $2I_{yc}$ are simply equal to the section's moment of inertia about the weak axis (I_y).

Although the two girders work together as a system to resist the moment in the global buckling mode, (4) is expressed in terms of the moment on one girder. The capacity in (4) is expressed for one girder to be consistent with the design forces per girder that engineers typically work with, as well as expressions such as (1), which are used to evaluate the buckling behavior of a single girder. The warping stiffness of the I-girders was conservatively neglected in (4) since the contribution is relatively small; however the full expression including the warping term is provided in Yura et. al (2008).

A plot of the FEA results for the twin girder systems with 3.05 m and 1.52 m spacings are shown with (1) and (4) in Fig. 6. As discussed previously, (1) provides a reasonable predication of the capacity for the system with the wider girder spacing, where the girders buckle between the braces, but dramatically overestimates the capacity of the girders with the closer spacing. For the girders with the closer spacing, which fail in the system mode, the proposed global buckling expression in (4) shows good agreement with the FEA results for the closer 1.52 m girder spacing.

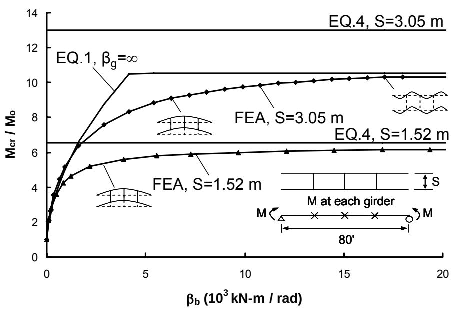

Figure 6: Buckling moment vs. brace stiffness and proposed equation.

The system buckling expression in (4) provides an upper limit on the capacity predicted by (1) so as to avoid unsafe situations where the girders buckle in the global system mode. The limit that is provided by (4) would be applied in a similar fashion to the limits M_y and M_s that are currently used on (1). Although using the expression in (3) for β_g can provide an indication of the in-plane stiffness problem for girders that are susceptible to the system buckling mode, the limit given by (4)

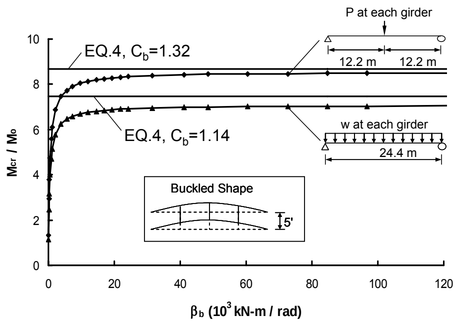

Figure 7: Effect of moment gradient on system mode buckling.

provides a relatively simple method of predicting the system mode capacity. If the girders do not have adequate stiffness, the expression can be used to solve for either the required I_x or S to avoid the system mode of failure. The effects of moment gradient on the buckling capacity are typically handled with a C_b factor. The bracing solution shown previously in (1) employed two C_b factors, one of which represented the behavior of the girder with no intermediate bracing (C_{bu}), and the other corresponding to the fully braced girder (C_{bb}). The results presented so far for the system mode of buckling have focused on systems with uniform moment loading, for which the C_{bu} factor in (4) was equal to 1. For cases with variable moment the moment gradient factor will be greater than unity. Although intermediate braces are provided, the buckled shape of the girders in the system mode has the same basic shape (half sine-curve) as the girders with no intermediate bracing. Therefore, the moment gradient factor that should be used in (4) is the C_b for the unbraced girder (C_{bu}). The AISC Specification provides an expression for calculating C_b, which for the case of a uniform distributed load yields a C_{bu}=1.14, and for a midspan point load gives C_{bu}=1.32. For centroidal loading, the C_t factor is 1. The accuracy of the expression for a uniform load and midspan point load are shown in Fig. 7. The critical buckling moment is graphed on the vertical axis versus the torsional brace stiffness of each brace. The vertical axis has been normalized by M_o, which is the buckling capacity of one of the girders with uniform moment loading and no intermediate bracing. The transverse loads were applied at midheight of the girders. The twin girders had a spacing of 1.52 m (5 ft.) with three intermediate braces. As before, the twin girders fail in the system mode with a buckled shape consisting of a half-sine curve along the girder length. In addition to the finite element results, the expression in (4) is graphed using the corresponding values of C_{bu} for the two load cases of a midspan point load and a uniformly distributed load. The expression in (4) shows good agreement with the finite element results for the global failure mode of systems with moment gradients. In addition to applying the transverse loads at midheight, top and bottom flange loadings were also considered. The impact of load height effects are discussed in the SSRC (Structural Stability Research Council) Guide (1999) and also by Helwig et. al. (1997). Gravity loads applied at the top flange tend to cause an overturning torque as the girders begin to twist, which results in a decrease in the buckling capacity relative to midheight loading. Loading applied at the bottom flange, on the other hand, tends to cause a restoring torque, which results in an increase in the buckling capacity relative to midheight loading. The SSRC Guide (1999) provides solutions consisting of a modified C_b factor that accounts for the effects of load height on individual I-shaped girders. Figures 8 and 9 show the FEA results for girders in a twin girder system buckling

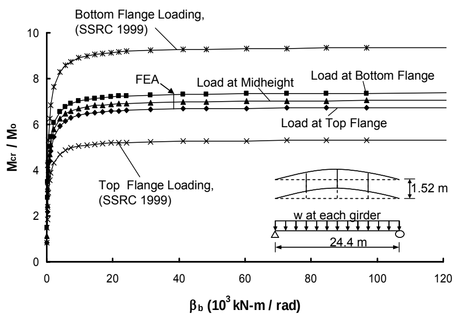

Figure 8: Insensitivity of system mode to load height effects – distributed load.

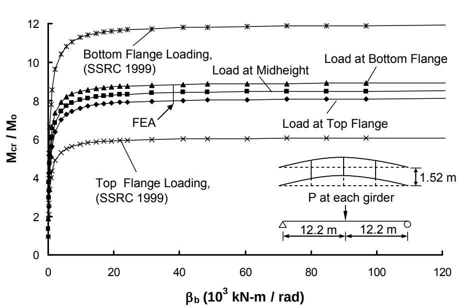

Figure 9: Insensitivity of system mode to load height effects – point load.

in the system mode for the respective cases of uniform and midspan point loads applied at the top flange, midheight, and bottom flange. The SSRC solutions for girders with top flange and bottom flange loading are also shown in the figures. The SSRC solutions, which are based on individual girder response rather than a global system response, show significant load height effects with a large difference between the buckling capacity for top flange and bottom flange loading. Although the FEA solutions for the twin girders buckling in the system mode show that top and bottom flange loading have an effect on the buckling capacity relative to midheight loading, the effect is relatively minor. The C_t factor was incorporated into the last term under the radical of (4) to reflect the small load height effect shown in Figs. 8 and 9. As shown in Fig. 10, use of the appropriate C_b factor for uniform and midspan point loads, respectively, with the C_t factor in Eq. 4 shows very good agreement with FEA results for the doubly-symmetric Section #1.

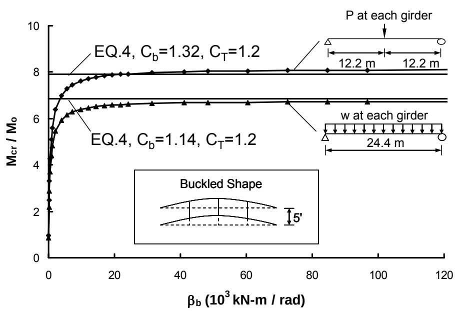

Figure 10: Comparison of Eq. (4) for top flange loading.

Singly-Symmetric Sections

The results presented so far have focused on the doubly-symmetric Section #1. Analyses were also conducted on the singly-symmetric Section #2 shown in Fig. 1. The singly-symmetric section was analyzed with loading that caused the small flange to be in compression (Section #2A – $\rho = 0.2$) and with loading that subjected the large flange to compression (Section #2B – $\rho = 0.8$). Figure 11 shows a graph of the buckling capacity of Sections 2A and 2B with uniform moment loading. The twin girders had a spacing of 1.52 m (5 ft.) and four

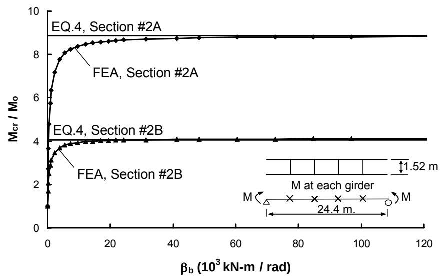

Figure 11: Buckling moment vs. brace stiffness for singly-symmetric section #1.

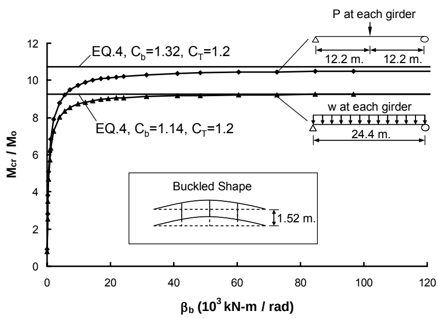

Figure 12: Effects of top flange loading on singly-symmetric section – ρ=0.2.

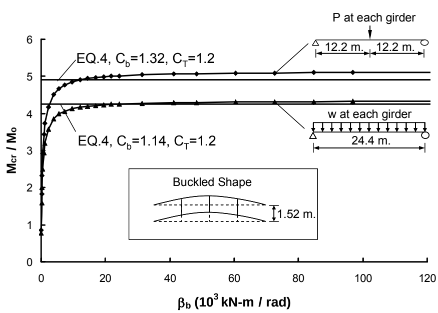

Figure 13: Effects of top flange loading on singly-symmetric section – ρ=0.8.

intermediate braces. As the torsional brace stiffness was increased, Section 2A, with the smaller compression flange, had a significantly larger relative increase in buckling capacity compared to Section 2B, however both girder systems failed in the global system mode. The corresponding graphs of (4) show good agreement with the FEA solutions and provide good estimates of the system buckling capacity for both singly symmetric section orientations.

Analyses were also conducted on the singly symmetric sections with top flange loading. Figures 12 and 13 show FEA results for Sections #2A and #2B, respectively, with top flange loading. Equation (4), with the appropriate C_b factor for each loading case and 1.2 for the C_t

factor, is also plotted in the figures. The expression in (4) again shows good agreement with the FEA solutions for both the singly symmetric section orientations.

SUMMARY

Twin girder systems are particularly susceptible to a global system failure mode of buckling that is relatively insensitive to the size and spacing of the braces. In this global failure mode, the cross-frame locations do not act as a brace point and both girders buckle as a system in a half-sine curve along the girder length. Current design methods for torsional beam bracing may miss the potential for this global buckling mode. The global mode can occur at load levels that are substantially lower than those predicted by conventional buckling solutions, and this system failure mode becomes more critical as the girder spacing is reduced. A solution was presented that provided good estimates of the buckling moment corresponding to the system failure mode. The solution showed good agreement with results for both doubly- and singly-symmetric sections with a variety of load cases. This expression can be used to identify the potential for a system buckling problem, and to determine the required in-plane moment of inertia or girder spacing to obtain a safe design.

REFERENCES

1. American Institute of Steel Construction (2005) Specification for Structural Steel Buildings, Chicago, IL.

2. ANSYS (2003), "Finite Element Program Users Manual, Version 8.0", ANSYS, Inc., Houston, PA.

3. Helwig, T. A., Frank, K. H., and Yura, J. A. (1993), "Bracing Forces in Diaphragms and Cross Frames," Structural Stability Research Council Conference, April 6-7, Milwaukee, Wisconsin, pp. 129-140.

4. Helwig, Todd A.; Frank, Karl H.; and Yura, Joseph A. (1997), "Lateral-Torsional Buckling of Singly-Symmetric I-Beams," *ASCE Journal of Structural Engineering*, V. 123, No. 9, Sept., pp. 1172-1179.

5. SSRC (1998) Structural Stability Research Council, *Guide to Stability Design Criteria for Metal Structures*, 5th Ed. (1998). T. V. Galambos, ed., John Wiley & Sons, Inc., New York, N.Y.

6. Winter, G. (1960), "Lateral Bracing of Columns and Beams," ASCE Transactions Vol. 125, pp. 809-825.

7. Yura, J. A. (2001), "Fundamentals of Beam Bracing," *Engineering Journal*, American Institute of Steel Construction, 1st Quarter, pp. 11-26.

8. Yura, J. A., Helwig, T. A., Herman, R. S., and Chong, Z. (2008), "Global Lateral Buckling of I-shaped Girder Systems", *ASCE Journal of Structural Engineering*, Under review.

A UNIQUE BUCKLING MODE FOR COLD-FORMED STEEL FRAMED SHEAR WALL WITH SHEET STEEL SHEATHING

Cheng Yu[1]

ABSTRACT

A cold-formed steel framed shear wall with sheet steel sheathing may fail in shear buckling of the sheathing, local buckling or distortional buckling of the framing member under compression, and fastener failures. A distortional buckling mode on the boundary studs under tension was observed in a test program conducted at the University of North Texas. In the monotonic tests on shear walls with tight fastener spacing pattern, it was found that the flanges of the boundary tension studs were distorted by a bending moment. The moment was caused by the eccentric axial loading at the hold-down. The distorted boundary studs can be the failure mechanism for shear walls however this unique buckling mode has not been considered in design. This paper presents the observed unique buckling mode on the tension studs, analyzes the specific circumstances that allow the occurrence of this unique mode of failure, and provides recommendations for the shear wall design to avoid this unexpected buckling mode.

[1] Assistant Professor, Department of Engineering Technology, University of North Texas, Denton, TX 76207. (cyu@unt.edu)

INTRODUCTION

The cold-formed steel (CFS) framed shear wall with sheet steel sheathing is a code approved structural practice in the U.S. The current International Building Code (IBC 2003) [1], Uniform Building Code (UBC 1997) [2], and the American Iron and Steel Institute Standard for Cold-Formed Steel Framing (AISI 2004a) [3] provide provisions for the CFS shear walls and specify the nominal strength for both wind loads and seismic loads for 0.018-in. and 0.027-in. sheet steel shear walls. The published shear strengths were based on the tests conducted by Dr. Reynaud Serrette and his team at Santa Clara University in 1997 and 2002 [4, 5]. In Serrette's tests, the observed failure modes for sheet steel shear walls included the buckling of the sheathing, the pull-out of the fasteners, and the buckling of the boundary studs under compression. In order to obtain the shear strength of CFS shear walls with thicker sheet steel sheathing, a test program was recently performed at the University of North Texas (UNT). The UNT research was focused on 0.030-in. and 0.033-in. steel sheet shear walls with 2:1 and 4:1 aspect ratios (height/width), and 0.027-in. steel sheet shear walls with aspect ratio of 2:1. This research also investigated the CFS shear wall with different fastener spacing configurations. Three different fastener spacing configurations were included in the test matrix: 6-in., 4-in., or 2-in. on center for the fasteners on the panel edge, and the fastener spacing was 12-in. on center for all tests. The test program consisted of two series of tests: the monotonic tests for determining the shear strength for the wind loads, and the cyclic tests for determining the shear strength for the seismic loads.

Besides the three possible failure modes described by Serrette [4, 5], a different failure mode of the distortional buckling on the back-to-back boundary studs under uplifting/tension force was also discovered in the UNT research. It was found that this unique buckling mode primarily observed in monotonic tests on the CFS shear walls with 2-in. fastener spacing on the panel edge. This paper emphasizes the details of the this unique buckling mode and the finite element method is used for the analysis beyond the experiments.

TEST PROGRAM

Setup of Monotonic Test

The shear wall tests were performed on a 16-ft span, 12-ft high adaptable structural steel testing frame. Figure 1 illustrates the schematic of the test setup. The wall was bolted to the base beam and loaded horizontally at the top. The base beam was 5-in. × 5-in. structural steel tubing was attached to a W16×67 structural steel beam. The out-of-plane displacement of the wall was prevented by a series of steel rollers on the front side and three individual rollers on the back side of the wall top. The rollers also worked as a guide for the loading beam "T" shape as shown in Figure 2. The "T" shape was attached to the top track member of the wall by 2 - No. 12 × 1 ½-in. hex washer head (HWH) self-drilling tapping screws placed every 3-in. on center. The anchorage system for monotonic tests consisted of three Grade 8 ½-in. diameter shear anchor bolts with standard cut washers (ASME B18.22.1) [6] and one Simpson Strong-Tie® S/HD10S hold-down with one Grade 8 ½-in. diameter anchor bolt installed on the inside of the boundary studs on the loaded side. The hold-down is a steel hardware installed at the bottom of the shear wall studs to provide uplift resistance against the overturning force due to the lateral load applied at the top of the wall. Figure 3 shows a typical hold-down.

The testing frame was equipped with one MTS® 35-kip hydraulic actuator with ±5-in. stroke. A 10-kip universal compression/tension load cell was placed to connect the top of the lever to the "T" shape for force measuring. Five position transducers were employed to measure the horizontal displacement at the top of wall, the vertical displacements of the two boundary studs, and the horizontal displacements of the bottom track, as shown in Figure 2.

The monotonic tests were conducted in a displacement control mode at a constant speed of 0.3 in. per minute for the displacement of the top of the wall. The testing procedure was in accordance with ASTM E564-06 "Standard Practice for Static Load Test for Shear Resistance of Framed Walls for Buildings" [7]. A preload of approximately 10% of the estimated peak load was applied first to the specimen and held for 5 minutes to seat all connections. After the preload was removed, the incremental loading procedure started until failure using a load increment of 1/3 of the estimated peak load. For each specimen configuration, two identical tests were conducted. For the monotonic testing, a third specimen would be tested if the shear strength or stiffness of the second specimen tests is not within 15% of the result of the first specimen tested.

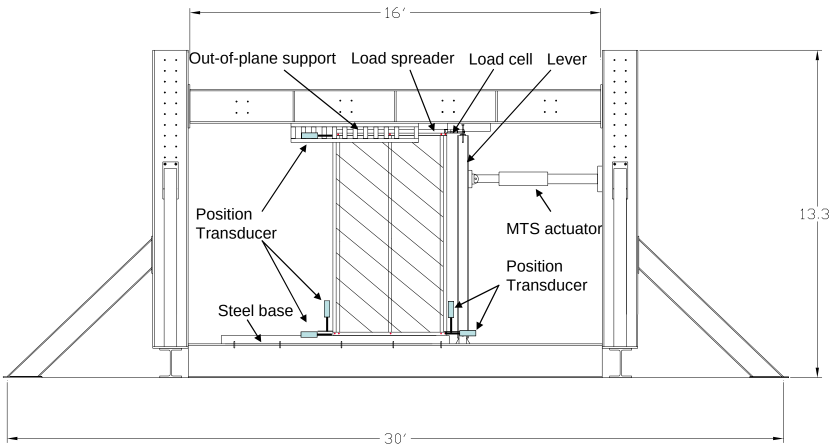

Figure 1 Testing frame with a 4-ft × 8-ft wall assembly installed

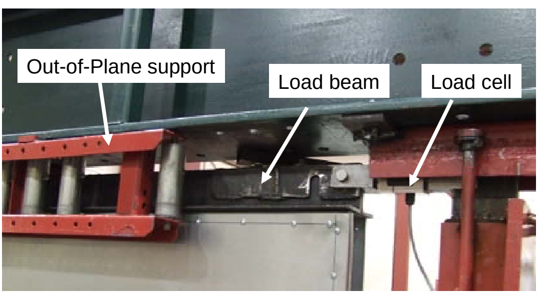

Figure 2 Close up of the top of the wall

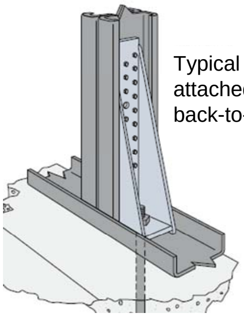

Figure 3 Typical hold-down (photo from Simpson Strong-Tie®)

Test Specimens

Figure 4 shows the dimensions of the sheathed steel framed shear wall assembly for the monotonic tests. The framing members were assembled using No. 8 × ½-in. modified truss head self-drilling screws. Double C-shaped studs (back-to-back) were used for both boundary studs of the wall. The webs of the boundary studs were stitched together using 2 - No. 8 × ½-in. modified truss head self-drilling screws spaced at 6-in. on center. 0.043-in. and 0.033-in. SSMA (Steel Stud Manufacturers Association) standard framing members were chosen for the wall assembles. For the monotonic tests, one Simpson Strong-Tie® S/HD10S hold-down was attached to the tension boundary studs from the inside by using a total of 15 - No. 14 × 1-in. HWH self-drilling screws. For all specimens, the hold-down was raised 1 ½-in. above the flanges of the bottom track.

The sheet steel sheathing was installed on one side of the wall with No. 8 × ½-in. modified truss head self-drilling screws. The typical screw panel edge and field location schedule is shown in Figure 5. The screw spacing of 6-in., 4-in., or 2-in. on the panel edges and 12-in. in the field of the panel was investigated, and the sheathing screws were installed on the outer flange of the boundary studs for all the tests.

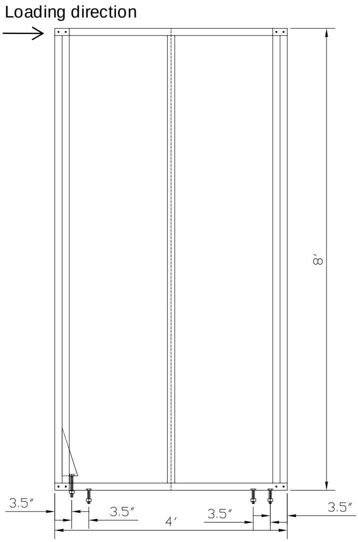

Figure 4 Wall for monotonic test

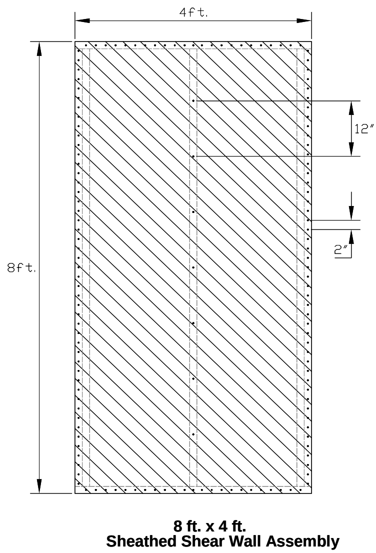

Figure 5 Typical fastener spacing

THE UNIQUE BUCKLING MODE

Test Results

In the monotonic tests on 4-ft. × 8-ft. CFS walls with 2-in. perimeter fastener spacing, it was found that the boundary studs which were subject to uplifting/tension force buckled on the flanges near the hold-down. Figure 6 shows the deformed shape of a CFS wall with 0.033-in. sheet steel sheathing when the shear wall reached the peak load. The fastener spacing on the panel edge was 2-in. on center. The buckling mode can be characterized as the distortional buckling because the flanges rotated about the junction line between the web and the flanges. On the other side, the boundary studs under compression were intact. The unique buckling mode on the tension studs was also observed on 0.030-in. and 0.027-in. sheet sheathed walls with 2-in. perimeter fastener spacing as shown in Figure 7. However this buckling mode was not observed on shear walls with 4-in. and 6-in. perimeter fastener spacing. Table 1 summarizes the wall configurations which demonstrated this unique buckling mode in the monotonic tests.

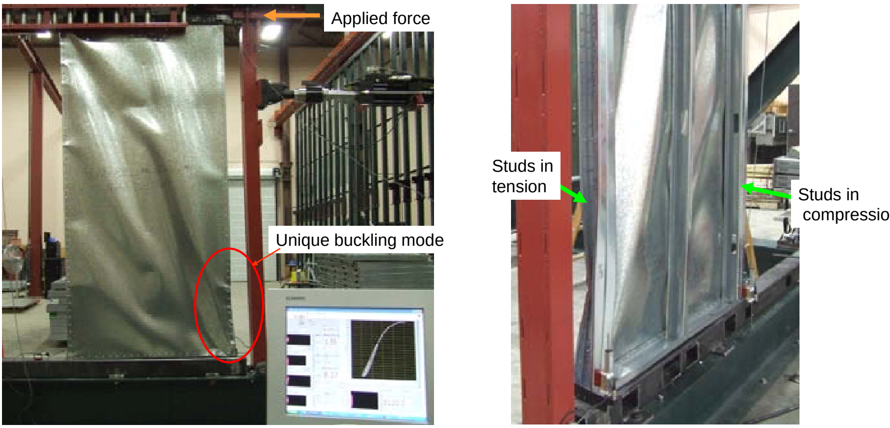

(a) front view (b) back view

Figure 6 Unique buckling mode on 0.033-in. sheet steel wall

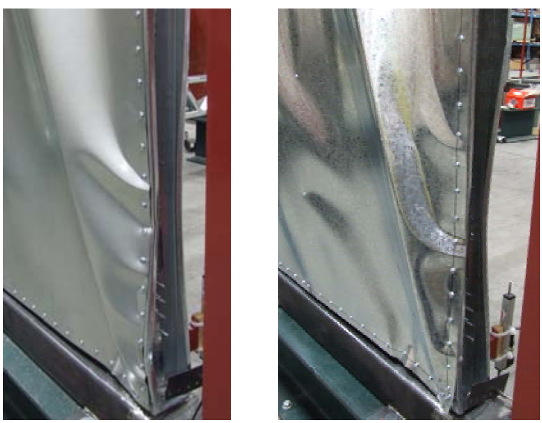

0.030" sheathing 43 mil framing **0.027" sheathing 33 mil framing**

Figure 7 Unique buckling mode on 0.030-in.and 0.027-in. sheet steel walls

Table 1 Summary of specimens demonstrating the unique buckling mode

Sheet steel sheathing	Studs	Tracks	Fastener spacing Perimeter/Field (in./in.)
0.033-in.	350S162-43	350T150-43	2/12
0.030-in.	350S162-43	350T150-43	2/12
0.027-in.	350S162-33	350T150-33	2/12

Note: all specimens were 4-ft. × 8-ft.

The details of the components of the steel sheet walls listed in Table 1 are given as follows:

Studs:

- 350S162-33 SSMA structural stud, 0.033-in. 3-1/2-in. × 1-5/8-in. made of ASTM A1003 Grade 33 steel, placed in 2-ft. o. c. for 0.027-in. steel sheet walls.
- 350S162-43 SSMA structural stud, 0.043-in. 3-1/2-in. × 1-5/8-in. made of ASTM A1003 Grade 33 steel, placed in 2-ft. o. c. for 0.030-in. and 0.033-in. steel sheet walls.

Tracks:

- 350T150-33 SSMA structural track, 0.033-in. 3-1/2-in. × 1-1/2-in. made of ASTM A1003 Grade 33 steel for 0.027-in. steel sheet walls.
- 350T150-43 SSMA structural track, 0.043-in. 3-1/2-in. × 1-1/2-in. made of ASTM A1003 Grade 33 steel for 0.030-in. and 0.033-in. steel sheet walls.

Sheathing:

- 0.033-in. thick ASTM A1003 Grade 33 steel.
- 0.030-in. thick ASTM A1003 Grade 33 steel.
- 0.027-in. thick ASTM A1003 Grade 33 steel.

Steel sheet was installed on one side of the wall assembly.

Framing and Sheathing Screws:

- No. 8×18-1/2-in. modified truss head self-drilling tapping screws. Spacing at panel edge is 2-in. o.c. Spacing in the field of the sheathing is 12-in. for all specimen configurations.

The occurrence of the distortional buckling on the tension studs indicated that compressive stress was developed at flanges although the boundary studs were subject to a net tension force on the cross-section. The author concluded that the compressive stress was primarily caused by the hold-down which applied eccentric axial forces to the boundary studs. The hold-down was fastened to the stud web and bolted to the base. The bolt which held the hold-down in place was installed eccentrically from the centroid of the boundary studs. The distance between the bolt and the web of the studs was 1 ½-in. The eccentricity was the original setup of the hold-down and it was not avoidable. On the other hand, the sheathing was fastened to the studs along the outer flange as illustrated in Figures 6, 7, 8 which caused additional loading eccentricity for the studs. Due to eccentric axial loads, a bending moment was developed on the boundary studs thus generating compressive stresses on the outer flanges. Furthermore, the moment was applied to the weaker axis of the boundary studs. Therefore when the bending moment was significantly large enough, the buckling would occur on the tension studs close to the hold-down. In the tests, the shear walls with 2-in. perimeter fastener spacing had the highest shear strength compared to the other walls with 4-in. or 6-in. fastener spacing therefore the resultant moment by the eccentric axial force was the highest on walls with 2-in. fastener spacing. This explains why the unique buckling mode was primarily observed on the shear walls with 2-in. perimeter fastener spacing but not on walls with 4-in. or 6-in. fastener spacing on the panel edge.

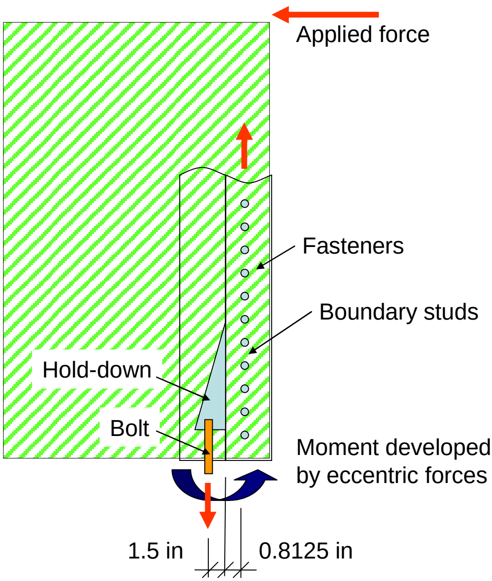

Figure 8 Moment generated on the tension studs

Finite Element Analysis

To verify the conclusion that the distortional buckling on the tension studs was caused by the eccentric axial loads, a finite element model on a 0.043-in. back-to-back studs using SSMA 350s162-43 member was developed in ABAQUS [8]. Figure 9 shows the FE model. For purpose of simplicity, only the back-to-back boundary studs, the hold-down, and the bolt were modelled. 8-node quadratic shell element (S8R5 in ABAQUS) was used for the studs, and 10-node quadratic solid element (C3D10M in ABAQUS) was used for the hold-down and the bolt. In the FE model, the bottom cross-section of the bolt was fixed and an axial force was applied to the centroid of the top cross-section of the 8-ft high boundary studs to simulate the uplifting force in the test. The additional loading eccentricity by the sheathing fasteners was ignored in the model. The nonlinear material properties were considered in the FE model. Figure 10 shows the stress distribution and the deformation shape when the studs reached the peak load. The same distortional bucking mode as observed the actual tests was also found by the FE model, in which the flanges of the boundary studs distorted. the outer flanges closed in while the inner flanges opened up. The FE results also confirmed that compressive stresses were developed on the outer flanges even the studs were subjected to a net tension force across the section, and the compressive stresses could lead buckling of the studs.

The tests and FE analysis indicated that the buckling may occur on the boundary studs on the uplift side due to the eccentric loading caused by the hold-down. And this unique buckling mode can happen even the studs were designed to be able to resist the overturning/compression force. In the tests, the specimens listed in Table 1 did not failed in the boundary studs in compression.

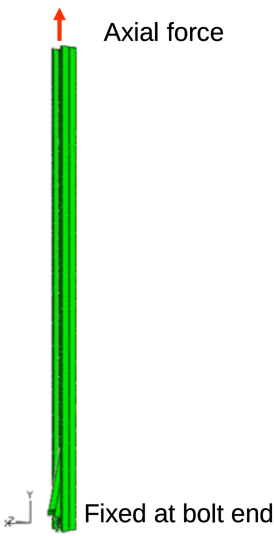

Figure 9 FE model

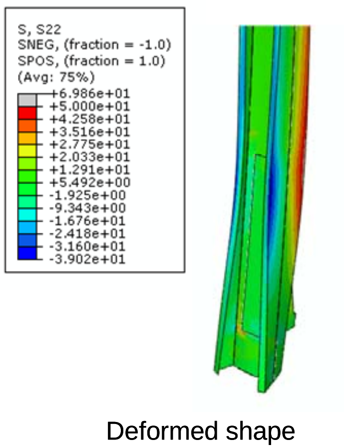

Figure 10 Stress distribution and buckling shape

CONSIDERATION IN DESIGN

The discovered unique buckling mode has not been considered in design. In order to avoid the potential failure by this unique mode, two possible solutions may be utilized in practice. First solution is to use appropriate/thicker studs for higher resistance against the bending moment caused by the eccentric loads. Second solution is to use appropriate fastener installation pattern to reduce the loading eccentricity.

Solution 1 – choosing appropriate stud members

The bending moment on the tension studs can be estimated according to the wall configurations and then the appropriate stud member can be selected by calculation.

Here a design example is provided. Assume one designs a 4-ft. × 8-ft. CFS framed Type I shear wall using 33 ksi 0.027-in. sheet steel sheathing on one side and No. 8 screws spaced at 2-in./12-in. o.c. for the sheathing. The fastener installation pattern is illustrated in Figure 5. The pre-selected framing members are 33ksi SSMA 350S162-33 studs and 33ksi SSMA 350T150-33 track. The assembly configuration is same as that shown in Figure 4. Assume the required allowable unit shear strength is 215 plf (ASD).

Required Shear Strength

According to the AISI (2004a) [3], the nominal shear strength of the shear wall R_n = 1170 plf. CFS shear wall safety factor for wind loads Ω = 2.0.

Available shear strength (ASD) $v_a = 1170 / \Omega$ = **585 plf > 215 plf. OK.**

Required Axial Compression Strength for the Boundary Studs

The axial strength of the boundary back-to-back studs should be checked as well, the procedure can be found in the Section C4 of the North American Specification for the Design of Cold-Formed Steel Structural Members (NASPEC 2001) [9]. The selected studs members are SSMA 350S162-33, the two members are fastened for 6-in. o.c. The boundary studs are unbraced.

Shear wall moment arm
d = (4 ft × 12)-(1.5 in. + 1.625 in. + 1.625 in.)= 43.25 in.

Required overturning/compression strength
T = (215 × 4 ft) × 96 / 43.25 = 1909 lbs = 1.909 kip

Nominal axial strength of the double studs
a = 6 in.
r_i = 0.617 in. (for single C stud)
r = 0.812 in. (for double back-to-back studs)

$$\left(\frac{KL}{r}\right)_m = \sqrt{\left(\frac{KL}{r}\right)_o^2 + \left(\frac{a}{r_i}\right)^2} = \sqrt{\left(\frac{8\times 12}{0.812}\right)_o^2 + \left(\frac{6}{0.617}\right)^2} = 118.6$$

$$F_e = \frac{\pi^2 E}{(KL/r)^2} = \frac{3.14^2 \times 29500}{(118.6)^2} = 20.7 \text{ ksi}$$

$$\lambda_c = \sqrt{\frac{F_y}{F_e}} = \sqrt{\frac{33}{20.7}} = 1.263$$

$$F_n = \left(0.658^{\lambda_c^2}\right) F_y = \left(0.658^{1.263^2}\right) 33 = 16.9 \text{ kip}$$

$$P_n = A_e F_n = 0.4434 \times 16.9 = 7.49 \text{ kip}$$

The definitions of above notations refer to Section C4 of NASPEC (2001) [9].

Safety factor for studs Ω = 1.8

Available axial compression strength P_a=7.49/1.8 = **4.163 kip >1.909 kip. OK**

IBC (2003) and AISI (2004) stipulate that minimum 0.033-in. framing members are required. Therefore the selected wall assembly meets the requirements by the code and it gives adequate shear strength. The shear anchorage and the hold-down should be examined as well, the procedures are skipped here.

Required Section Strength of the Boundary Studs Against the Unique Buckling Mode

Additionally, the potential failure by the buckling on the tension studs needs to be checked as well. This is the additional check beyond the existing design procedure. The moment is applied to the weaker axis (Z-Z in Figure 11), and the double studs fail in distortional buckling. The recommended procedure follows:

The overturning force resisted by the hold-down bolt T = 1.909 kip

The sheathing fasteners were installed along the center line of the outer flange which is 1.625-in. wide, and the distance between the bolt and the centroid of the studs is 1.5-in. Therefore it can be conservatively assumed that the moment arm d = 1.5+1.625/2 = 2.3125-in.

The required bending strength about Z-Z axis

$M_Z = 1.909 \times 2.3125 = 4.414$ kip-in.

The distortional buckling strength can be determined by the Direct Strength Method specified in Appendix 1 Design of Cold-Formed Steel Structural Members Using the Direct Strength Method, 2004 Edition (AISI 2004b) [10].

The elastic distortional buckling moment is obtained by the finite strip software CUFSM [11]. Figure 11 shows the distortional buckling shape of the back-to-back C-sections in CUFSM.

$M_y = 7.04$ kip-in.

$M_{crd} = 21.18$ kip-in.

$$\lambda_d = \sqrt{\frac{M_y}{M_{crd}}} = \sqrt{\frac{7.04}{21.18}} = 0.577 < 0.673$$

The nominal bending strength $M_{nd} = M_y = 7.04$ kip-in.

The definitions of above notations refer to AISI (2004b) [10].

Safety factor for studs $\Omega = 1.8$

The available bending strength

$M_a = M_{nd} / \Omega =$ **3.911 kip-in. < 4.414 kip-in. Fail**

Therefore thicker stud members need to be used to resist the moment generated by the eccentric forces. 33ksi SSMA 350S162-43 is chosen.

$M_y = 8.78$ kip-in.

$M_{crd} = 75.3$ kip-in.

$$\lambda_d = \sqrt{\frac{M_y}{M_{crd}}} = \sqrt{\frac{8.78}{75.3}} = 0.342 < 0.673$$

$M_{nd} = M_y = 8.78$ kip-in.

The available bending strength

$M_a = M_{nd} / \Omega =$ **4.878 kip-in. > 4.414 kip-in. OK**

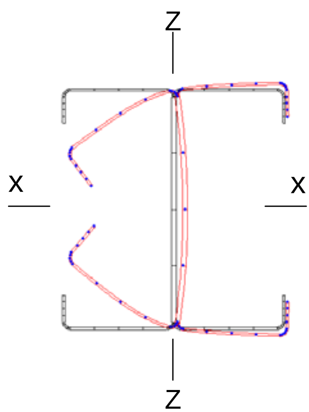

Figure 11 Distortional buckling mode calculated by CUFSM

The design example shows that the distortional buckling strength of the boundary studs on the weaker axis may control the capacity of the shear wall because of the bending moment generated by the hold-down. In the multiple-story buildings, the eccentric loading on the studs at lower stories may be beneficially reduced by the weight of the above stories, however it is still expected to check the potential failure mode discovered in this research.

Solution 2 – using appropriate fastener installation pattern

In this research, the sheathing fasteners on the boundary studs were installed along the center line of the outer flange as the standard setup. This configuration is also common in practice.. As discussed in the previous sections, this original fastener pattern caused additional loading eccentricity. Therefore two alternative fastener patterns, (1) fasteners on inner boundary studs; (2) fasteners staggered on boundary studs, were also investigated in this test program. The two alternative patterns were shown in Figure 12. Two monotonic tests were performed to study the alternative fastener pattern, both tests used 0.043-in. frame with 0.030-in. sheet steel sheathing, and 2-in./12-in. fastener spacing. Test 1 and 2 used the alternative fastener pattern (1) and (2) respectively. The test results showed that both alternative fasteners patterns yielded higher (approximately 7%) shear strength than the original fastener pattern. The distortional buckling mode on the tension studs was no longer evident for the two alternative configurations. Figure 12 shows the deformation of the tension studs when the shear wall reached its peak load in the monotonic test. The alternative pattern (1) caused the least loading eccentricity therefore the least distortion on the stud flanges was observed compared to the other two fastener installation patterns.

It can be concluded that both alternative fastener installation patterns could reduce the loading eccentricity by the hold-down therefore they are recommended. It is also suggested that the sheathing fasteners and the hold-down be installed on the same side of the boundary studs when the circumstance is allowed.

Table 2 Test results for 4-ft. × 8-ft. CFS shear wall with 0.030-in sheathing and 2-in./12-in. fastener spacing

Fastener installation pattern	Original	Alternative (1)	Alternative (2)
Tested shear strength of wall	1054 plf	1091 plf	1151 plf

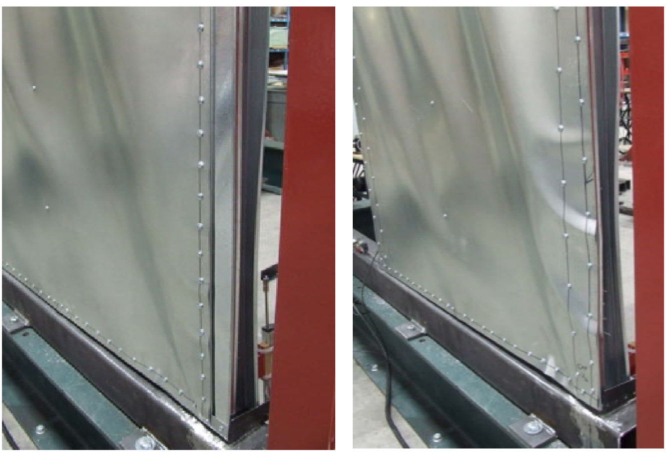

(a) alternative fastener pattern (1) (b) alternative fastener pattern (2)

Figure 12 Deformation at the tension studs at peak load

CONCLUSIONS

A unique bucking mode on the boundary studs in tension was observed in shear wall tests on cold-formed steel wall assembles with 0.033-in., 0.030-in., or 0.027-in. sheet steel sheathing and 2-in. fastener spacing on the panel edge. Finite element model was developed to investigate the stress distribution and deformation shape. It was found that the unexpected buckling was caused by eccentric axial loading which was generated by the hold-down and the sheathing fasteners. The discovered buckling mode may control the failure of the shear wall assemblies therefore it should be considered in the design. A design procedure to predict the stud strength resisting the unique buckling failure was provided in this paper. Two alternative fastener installation patterns were also studied and recommended for practice due to a reduced loading eccentricity for the boundary studs.

REFERENCES

[1] 2003 International Building Code, International Code Council, Inc., Washington DC, USA, 2003.

[2] 1997 Uniform Building Code, International Code Council, Inc., Washington DC, USA, 1997.

[3] Standard for Cold-Formed Steel Framing – Lateral Design 2004 Edition, American Iron and Steel Institute, Washington, DC, USA, 2004a.

[4] Serrette, R.L., Additional Shear Wall Values for Light Weight Steel Framing, *Report No. LGSRG-1-97,* Santa Clara University, Santa Clara, CA, USA, 1997.

[5] Serrette, R.L., Performance of Cold-Formed Steel-Framed Shear Walls: Alternative Configurations, *Report: LGSRG-06-02*, Santa Clara University, CA, USA, 2002.

[6] ASME B18.22.1 (1998), Plan Washers, American Society of Mechanical Engineers, New York, NY, USA, 1998.

[7] ASTM E564-06 (2006), E564-06 Standard Practice for Static Load Test for Shear Resistance of Framed Walls for Buildings, American Society for Testing and Materials, West Conshohocken, PA, USA, 2006.

[8] ABAQUS version 6.7, Dassault Systems Simulia Corp., Providence RI, USA, 2007.

[9] North American Specification for the Design of Cold-Formed Steel Structural Members, 2001 Edition, American Iron and Steel Institute, Washington DC, USA, 2001.

[10] Appendix 1 Design of Cold-Formed Steel Structural Members Using the Direct Strength Method, 2004 Edition. American Iron and Steel Institute, Washington DC, USA, 2004b.

[11] CUFSM version 2.6, by Ben Schafer, Department of Civil Engineering, Johns Hopkins University. http://www.ce.jhu.edu/bschafer/cufsm/.

FLANGE ANCHORING MECHANISM DEVELOPED IN PLATE GIRDERS UNDER SHEAR

***Sung C. Lee*[1], *Doo S. Lee*[2], *Chan S. Park*[3] and *Chai H. Yoo*[4]**

ABSTRACT

In the classical tension field theories it is implicitly assumed that the tension field cannot develop in the web panel without recourse to the anchoring mechanism of the flanges and/or adjacent panels. This paper revisits the anchoring mechanism developed by the flanges during postbuckling of plate girder web panels under shear. The appreciation of the flange anchoring mechanism in practical plate girders differs

---

1 Member of SSRC. Professor, Dept. of Civil and Environmental Eng., Dongguk Univ., Seoul 100-715, Korea (Corresponding Author). E-mail: sclee@dongguk.edu
2 Post-Doctoral Researcher, Dept. of Civil and Environmental Eng., Dongguk Univ., Seoul, Korea
3 Graduated Student, Dept. of Civil and Environmental Eng., Dongguk Univ., Seoul, Korea
4 Member of SSRC. Auburn Univ., Auburn, Alabama

from theory to theory. It is found that a complete development of the anchoring mechanism by the flanges not only requires heavy flanges but also incompressible transverse stiffeners that are necessary to keep the flanges from moving towards the web during the flange anchoring action. No matter how heavy the flanges are, the anchoring mechanism hardly develops without incompressible transverse stiffeners. In practical plate girders the contribution the anchoring mechanism to the postbuckling shear strength is negligibly small mainly due to lack of the axial rigidity of the transverse stiffeners.

INTRODUCTION

All the classical tension field theories summarized in SSRC (1998) assume that the tension field cannot develop in the web panel without recourse to the anchoring mechanism developed by the flanges and/or adjacent panels. This is due to the fundamental assumption implicitly used in the classical theories: the diagonal compression developed at pre-buckling stage shown in Fig. 1 (c) cannot increase once elastic buckling takes place. The diagonal stresses are the principal stresses. The equilibrium is obviously violated without the diagonal compression under additional shear applied after elastic buckling as shown in Fig 2 (b), which necessitates the development of normal stresses shown in Fig. 3. The vertical and horizontal normal stresses are to be anchored by the flanges and adjacent panels, respectively.

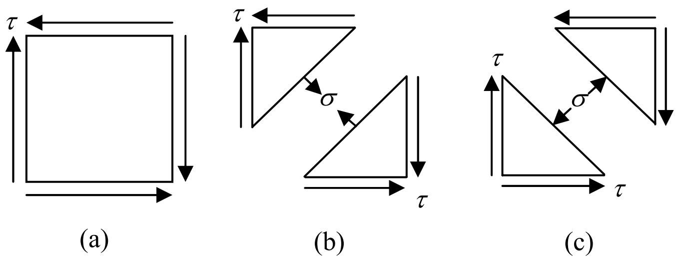

Fig. 1 Stress development at prebuckling stage: (a) Shear stress; (b)

Diagonal tension; and (c) Diagonal compression.

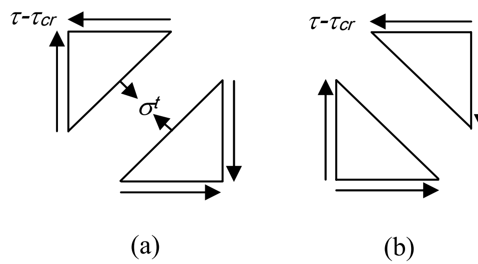

Fig. 2 Incomplete stress state after buckling: (a) Diagonal tension; (b) No diagonal compression.

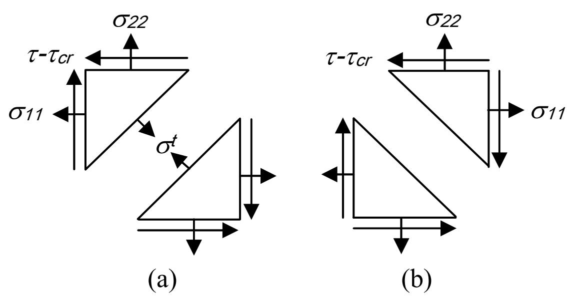

Fig. 3 Complete stress development after buckling: (a) Diagonal tension; (b) No diagonal compression.

On the other hand, Lee and Yoo (1998) found that even a laterally supported panel (panel simply supported at all the edges) without any external anchors was able to develop the postbuckling strength quantitatively almost equivalent to those observed in tests of normal plate girders. Most recently, Yoo and Lee (2006) unveiled what was behind the postbuckling mechanism of the simply supported panel without any anchors to resist the normal stresses shown in Fig. 3. Contrary to the classical theories, the diagonal compressions continuously increase near the edges of the simply supported panel after buckling as shown in Fig. 4. The tension field is possible in the simply supported panel due to the increments of the diagonal compressions without recourse to external anchor systems such as the flanges and adjacent panels.

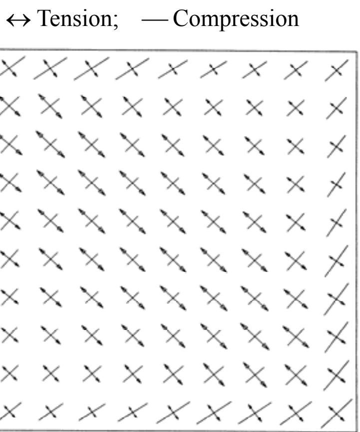

Fig. 4 Distribution of proncipal stresses under pure shear at ultimate stage. (adopted from Yoo and Lee 2006)

Therefore, it appears that there exist two independent sources of the tension field developed in the web panel: (1) the anchoring mechanism developed by means of the flanges and/or adjacent panels; and (2) the function of lateral supports, i.e., the increments of the diagonal compressions after elastic buckling near the laterally supported edges. The flanges used in normal plate girders are rigid enough to provide the web panels with the simple supports. The transverse stiffeners are also designed to function as the simple support. The fact that the postbuckling strengths observed in plate girders agree well with those of simply supported panels with the same dimensions necessarily implies that the function of the lateral supports is dominant over the anchoring mechanism. This paper summarizes two companion papers (Lee et al. 2007a and 2007b) which explained why the flange anchoring mechanism cannot be so active in practical plate girders.

WEB PANEL WITH IDEAL RIGID ANCHORS

Lee et al. (2007a) analyzed Model S-SR shown in Fig. 5, where roller supports were added to the top and bottom edges of a simply supported panel. The roller supports can play the role of ideal rigid anchors to withstand the vertical normal stresses shown in Fig. 3. The slenderness ratio of the panel is 150: width and thickness of the panel are 2000 mm and 13.33 mm, respectively. Material properties are: the elastic modulus, E = 200 GPa; the Poisson's ratio, μ = 0.3; and the yield strength is 345 MPa. Model S-SR is expected to be able to fully develop the anchoring mechanism in the vertical direction.

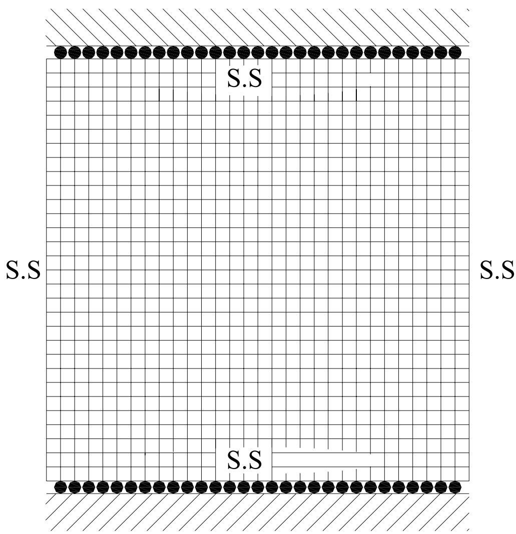

Fig. 5 Boundary condition of Model S-SR

Table 1 comparatively shows the results. Model S-S designates a simply supported panel with the same dimensional and material properties as those of Model S-SR. It is of interest to note that an enormous postbuckling strength was developed in Model S-SR. The postbuckling strength of Model S-SR is 2.48 times higher than that of Model S-S. The overall shear strength surprisingly amounts to as much as 80.2 % of the shear yield strength.

Table 1. Postbuckling strength pf Model S-SR

	Model S-S	Model S-SR	Model S-SR / Model S-S
V_{cr}	2,013.8 kN	2,013.8 kN	1.00
V_u	2,876.9 kN	4,157.7 kN	1.45
$V_{P.B}$	863.1 kN	2,138.4 kN	2.48

Note. Shear yield strength ($\frac{F_y}{\sqrt{3}}Dt_w$)=5,310.3 kN

FURTHER INVESTIGATION OF ANCHORING MECHANISM

Next, Lee et al. (2007a) investigated Model S-FR shown in Fig. 6. The vertical edges are simply supported but the top and bottom edges are free to move in the lateral direction. Instead, the rigid anchors installed in Model S-SR are provided at the laterally unsupported top and bottom edges. This type of the boundary condition is not likely to exist in the real world because if the flanges are heavy enough to function as the rigid anchors, they can also provide the simply supports. Yet, the investigation of Model S-FR is essential in order to assess the postbuckling capability of the rigid anchor.

The laterally unsupported top and bottom edges resulted in a decrease in the elastic buckling strength of Model S-FR as can be seen from Table 2. It is of interest to see that the sum (1,251.6 kN) of individual postbuckling strengths of Model S-S (863.1 kN) and Model S-FR

(388.5 kN) is much less than the postbuckling strength (2,138. 4 kN) developed in Model S-SR. The deformed shape at failure is shown in Fig. 7. Severe out-of-plane deformations occurred along the top and bottom edges. It appears that Model S-FR collapsed much earlier than Model S-SR due to an early loss of the out-of-plane stability.

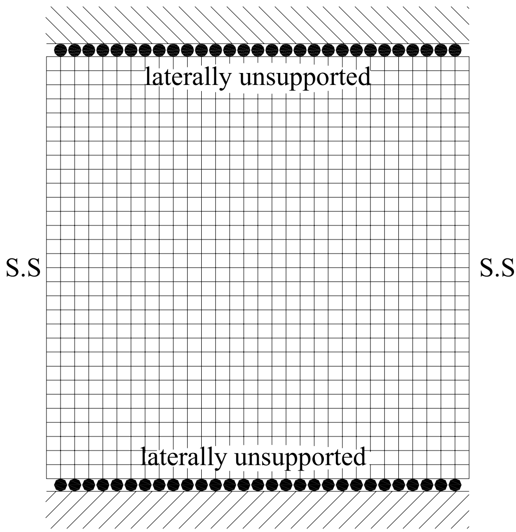

Fig. 6 Model S-FR

Table 2. Postbuckling strength pf Model S-FR

	Model S-FR	Model S-S
V_{cr}	966.5 kN	2,013.8 kN
V_u	1,355.1 kN	2,876.9 kN
$V_{P.B}$	388.5 kN	863.1 kN

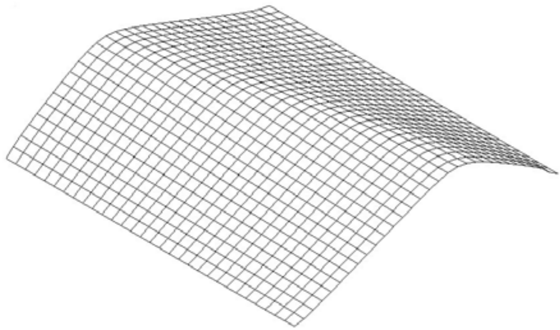

Fig. 7 Deformed shape of Model S-FR at ultimate stage.

This finding dictates that the rigid anchors are not able to fully exert their potential capability unless the lateral supports are simultaneously provided. It is evident now that the lateral supports have two functions: (1) they are able to develop their own tension field as discovered by Yoo and Lee (2006); and (2) they assist the anchoring mechanism to be fully developed by keeping the rigidly anchored edges from laterally deforming.

FLANGE RIGIDITY REQUIRED FOR ANCHORING MECHANISM

Lee et al. (2007a) also investigated the minimum bending rigidity of the flanges required to be able to function as the ideal rigid anchors analyzing Model S-STF shown in Fig. 8. The flanges are modeled with beam elements. The panel is simply supported at all the edges and shear forces are applied along the edges. The flanges are simply supported at both ends, i.e., the transverse stiffeners are assumed to be incompressible. The flanges and the panel are linked with rigid truss elements so that only the vertical normal stresses shown in Fig. 3 are transmitted from the web panel to the flanges during the anchoring mechanism.

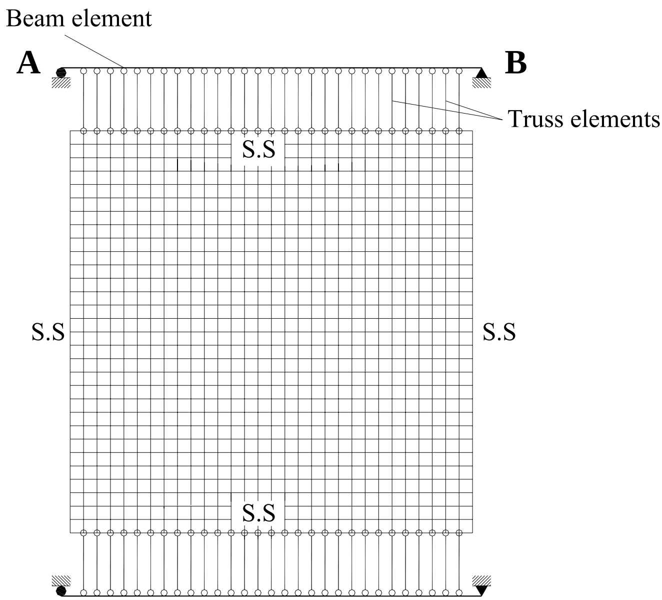

Fig. 8 Model S-STF.

Table 3. Postbuckling strength pf Model S-STF (unit: kN)

	Model S-S	Model S-STF					Model S-SR
t_f / t_w	-	1.0	3.0	5.0	20.0	45.0	-
V_{cr}	2,014	2,014	2,014	2,014	2,014	2,014	2,014
V_u	2,877	2,903	2,952	3,043	3,776	4,153	4,158
$V_{P.B}$	863	889	938	1,029	1,762	2,139	2,144
$V_{P.B(FA)}$	-	26	75	166	899	1,276	-

Note. $V_{P.B(FA)}$ is the contribution of flange anchoring mechanism

The bending rigidity of the flanges in Model S-STF varies by means of changing the flange thickness. As thickness of the flanges increases, the postbuckling strength also increases approaching that of Model S-SR as shown in Table 3. The flanges with t_f /t_w = 45.0 may be considered to be practically rigid in the model. It is of interest to note that the contribution of the normal flanges (t_f /t_w = 3.0 and 5.0) to the postbuckling strength through the anchoring mechanism is unexpectedly high.

BEHAVIOR OF TRANSVERSE STIFFENER

It needs to be reminded that in Model S-STF the transverse stiffeners are assumed as incompressible bodies. The transverse stiffeners must posses not only a sufficient axial strength to withstand the reactions developed at the simple supports but also a sufficient axial rigidity to keep both ends of the flanges from moving towards the panel during the anchoring action. Otherwise, the anchoring mechanism is not likely to fully develop even with the rigid flanges. Lee et al. (2007a) found that no matter how heavy the flanges are, the anchoring mechanism hardly develops if the simple supports of the flanges in Model S-STF are replaced with normal transverse stiffeners. In normal plate girders, the contribution of the flange anchoring mechanism to the shear strength is negligibly small because transverse stiffeners are too flexible to keep both ends of the flanges from moving towards the panel during the anchoring action. In order to initiate the flange anchoring action, the transverse stiffeners should have an enormous axial rigidity which cannot be achieved in practical designs.

FLANGE BENDING STRESSES RESULTED FROM ANCHORING ACTION

It has long been known that the severe flange deformations shown in

Fig. 9 stem from bending during the anchoring action. This led to a number of classical failure theories that involved plastic hinge mechanisms. However, a practically meaningful anchoring action cannot take place in normal plate girders because the transverse stiffeners are not incompressible as discovered in the companion paper. This finding means that the bending stresses developed in the flanges due to the anchoring action may not be high enough to form the plastic hinges. Lee et al. (2007a) also found that with the normal transverse stiffeners, the bending stress developed through the anchoring mechanism is negligibly low when compared to the yield stress regardless thickness of the flange. It is safe to say that the failure mode accompanied by severe flange deformations shown in Fig. 9 is not due to the anchoring action.

Fig. 9 Flange deformations (adopted from Jung 1996).

EXPERIMENTAL INVESTIGATION

Although a large number of experimental studies had been carried out on the ultimate shear behavior of plate girders, it was never clearly reported when the flanges actually began to undergo noticeable deformations. Lee et al. (2007b) tested four plate girders in order to trace the flange deformations. The dimension and material properties are given in Table 4.

Table 4. Dimensions and mechanical propoerties of test girders

	Model 1	Model 2	Model 3	Model 4
d_o (mm)	700	800	720	800
D (mm)	700	800	720	800
t_w (mm)	5.0	5.0	4.0	4.0
F_{yw} (MPa)	321.0	321.0	335.0	335.0
b_f (mm)	220	240	220	240
t_f (mm)	16.0	16.0	12.0	12.0
F_{yf} (MPa)	287.0	287.0	248.0	248.0
d_0/D	1.0	1.0	1.0	1.0
D/t_w	140	160	180	200

Fig. 10 shows deformed shape of Model 1 at several loading steps. It is of interest to note that any discernable flange deformations had not taken place until the loading step passed the ultimate strength point. Fig.11 shows normal strains measured on the top surface of the top flange of in close proximity to the plastic hinge-like point. It can be seen that not only the strains almost linearly increased up to the ultimate point but the strains at the ultimate point are lower than the yield strain. If the flanges had been subjected to substantial local bending moments due to the anchoring action during postbuckling, the compressive strains should have exhibited a sudden increase as soon as the elastic buckling took place. These results confirm that the flange stresses developed by the anchoring action in normal plate girders are negligibly small. The flanges began to undergo increasingly large deformations exhibiting plastic hinge-like modes as the strain passed the yield strain during unloading. Now it is evident the plastic hinge-like mode has nothing to do with the anchoring action.

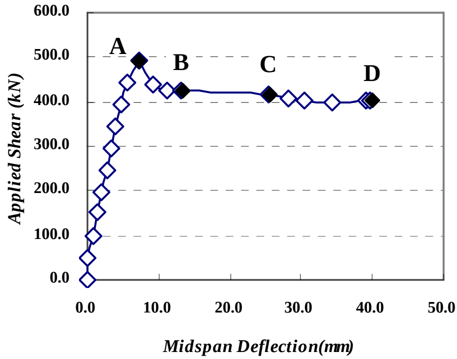

(a)

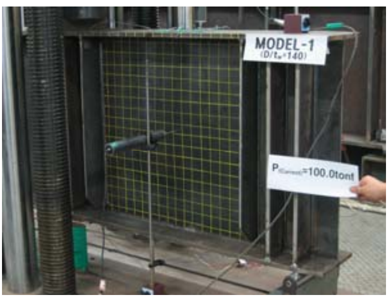

(b)

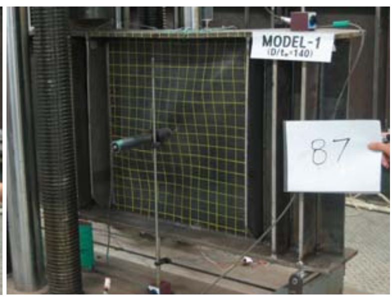

(c)

(d)

(e)

Fig. 10 Deformed shape of Model 1: (a) Shear versus midspan deflection: (b) Step A; (c) Step B; (d) Step C; (e) Step D

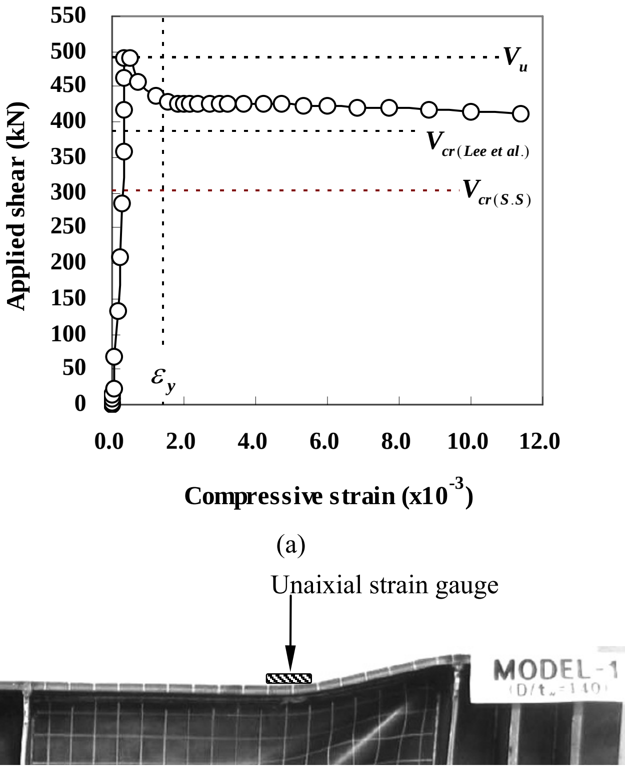

(a)

(b)

Fig. 11 Normal strains measured on the top flange surface of Model 1: (a) Compressive strains on the top flange; (b) Location of Unaxial strain gauge.

TRACE OF PLASTIC HINGE-LIKE FAILURE MODE

In order to trace the source leading to severe flange deformations exhibited in Figs. 9 and 10, Lee et al. (2007b) analyzed a plate girder shown in Fig. 12, where some part of the web panel were cut out along the tension diagonal. The cut-out part was determined in an average sense considering the yield zones at the ultimate strength point and the final loading step. Fig. 13 shows the deformed shape at the ultimate point, which looks similar to the final shape shown in Fig. 10. Therefore, it is evident that the plastic hinge-like failure mode take places when the flanges resist the direct shear transferred from the web beyond the ultimate strength point.

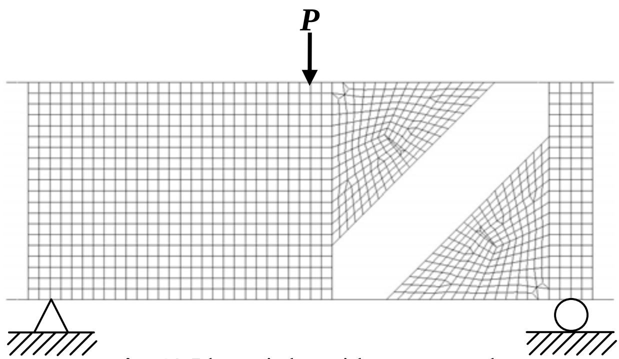

Fig. 12 Plate girder with cut-out web.

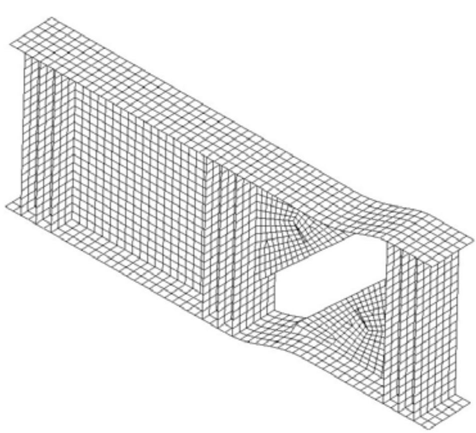

Fig. 13 Deformed shape of plate girder with cut-out web.

INVESTIGATION OF HORIZONTAL ANCHORING ACTION

Basler (1963) first implicitly assumed that adjacent panels of the interior web panel were able to function as rigid anchors. This seemingly valid assumption is a necessary consequence of the then knowledge that the anchoring mechanism is the unique source of tension field action. Since Basler believed that the flanges used in normal plate girders were, in general, too flexible to function as rigid anchors, it was impossible for him to explain the postbuckling mechanism developed in the web panel without recourse to the anchoring action of adjacent panels. Basler, therefore, assumed that tension field stresses do not develop along the flanges as shown in Fig. 14.

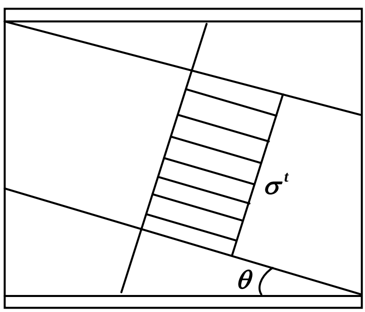

Fig. 14 Tension field theory for plate girder (adopted from Balser 1963).

If the anchoring mechanism takes place in the interior web panel by means of adjacent panels as assumed by Balser, normal stresses will necessarily develop during postbuckling along the vertical edges of the interior panel as shown in Fig. 15. It is so obvious that the horizontal equilibrium cannot be satisfied in the left-hand and right-hand free body diagrams as long as the normal stresses are present. This fact means that the horizontal anchoring action of adjacent panels is never possible.

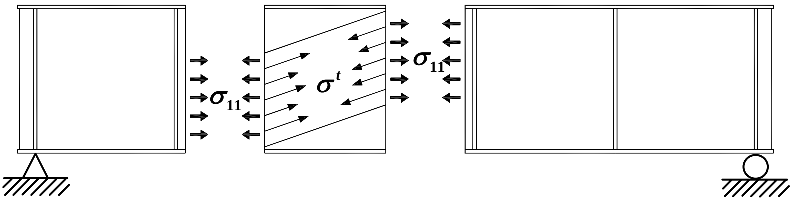

Fig. 15 Normal stresses in interior panel resulting from horizontal anchoring action.

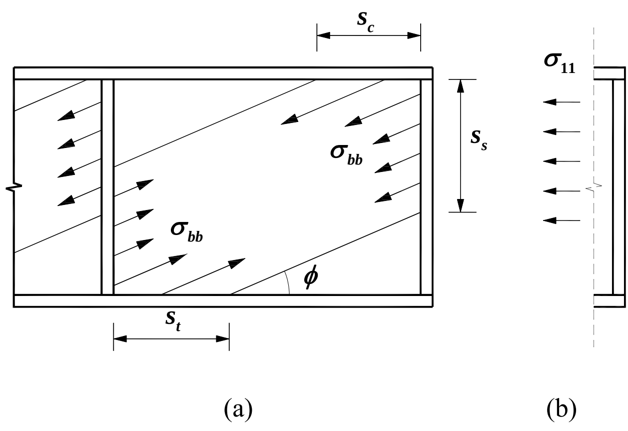

Fig. 16 Tension field stresses of end panel: (a) Tension field stresses (adopted from Eurocode 3 1993); (b) Horizontal components of tension field stresses.

Euro Code 3 (1993) stipulates that an end stiffener should meet an additional criterion to be able to anchor the tension field when the tension field contribution is included in the design shear resistance of end panels. Fig. 16 (a) shows tension field stresses in an end panel given in the Euro Code 3. Fig. 16 (b) shows horizontal components of the tension field stresses acting on the end stiffener. The horizontal equilibrium cannot be satisfied as long as the horizontal normal stresses are present. No matter how heavy the end stiffener is, the anchoring action never takes place. The additional criterion imposed on the end stiffener, therefore, should be repealed. Instead, end panels can develop the tension field like interior panels through the postbuckling mechanism of lateral supports unveiled by Yoo and Lee (2006) if the end stiffener has a rigidity to function as the simple support during postbuckling. No differentiation is necessary between end and interior panels in the shear design of plate girders.

SUMMARY AND CONCLUDING REMARKS

Lee et al. (2007a and 2007b) revisited the anchoring mechanism that is assumed to be the unique source of the web postbuckling strength in the classical tension field theories. The findings can be summarized as follows:

(1) When two opposite edges of a simply supported panel are provided with rigid anchors that are capable to keep the edges from moving inwards the panel, the anchoring mechanism can fully develop resulting in an enormous increment of the postbuckling strength.

(2) The lateral supports contribute to the postbuckling strength in two ways. They not only have their own postbuckling mechanism unveiled by Yoo and Lee (2006) but also help the anchoring mechanism develop up to a potential capacity by preventing a premature failure caused by the out-of-plane instability.

(3) Even with the flanges that are heavy enough to function as the rigid anchor, the anchoring mechanism cannot completely develop unless the flanges are supported by incompressible transverse stiffeners.

(4) The primary reason why the anchoring mechanism by the flanges contributes little to the postbuckling strength in ordinary plate girders is that the transverse stiffeners used are axially too flexible to be treated as incompressible.

(5) Axial forces developed in the transverse stiffeners attached on ordinary plate girders due to the anchoring mechanism are negligibly small.
(6) Severe flange deformations are not due to the anchoring action of the flanges but due to the direct shear force acting on the flange cross-sections.
(7) The horizontal anchoring mechanism cannot develop even in interior panels because adjacent panels are not able to function as the rigid anchors.
(8) The anchoring mechanism is virtually nonexistent in practical plate girders. That is to say, the tension field developed in the web panel is mostly attributable to the postbuckling mechanism developed by the function of lateral supports discovered by Yoo and Lee (2006).
(9) It is recommended that the provision in AISC (2001) and AASHTO LRFD (2004) that prohibits the use of the postbuckling strength in exterior panels be repealed and the additional criterion burdened on the end stiffener in Euro Code 3 (1993) should be removed.

APPENDIX 1. REFERRENCES

1. *AASHTO LRFD Bridge Design Specifications*, 3rd ed. (2004). American Association of State Highway and Transportation Officials, Inc., Washington, D.C.
2. ADINA (2001). *Theory and Modeling Guide*: Volume 1, Report ARD 00-7, ADINA R & D, Inc.
3. *AISC Manual of Steel Construction, Load and Resistance Factor Design*, 3rd ed. (2001). American Institute of Steel Construction, New York, N.Y.
4. Basler, K. (1963). "Strength of plate girders in shear." *Transactions,* ASCE, 128(II), 683-719. (Also as paper No. 2967, *J. Struct. Div.*, ASCE, October 1961, 87(7), 151-181.
5. Eurocode 3: Design of steel structures, (1993). European Committee for Standardization, Brussels, Belgium.
6. Jung, J. S. (1996). “Experimental study on ultimate behavior of plate girder webs under shear.” Ph.D. Dissertation, Dongguk Univ., Seoul, Korea. (in Korean)

7. Lee, S. C., Davidson, J. S., and Yoo, C. H. (1996). “Shear buckling coefficients of plate girder web panels.” *Comput. Struct.*, 59(5), 789-795
8. Lee, S. C., and Yoo, C. H. (1998). "Strength of plate girder web panels under pure shear." *J. Struct. Engrg.*, ASCE, 124(2),184-194.
9. Lee, S. C., Lee, D. S., and Yoo, C. H. (2007a). “Further Insights into Postbuckling of Web Panels. I: Flaw in Flange Anchoring Mechanism.” *J. Struct. Engrg*., ASCE, Submitted for a possible publication.
10. Lee, S. C., Lee, D. S., Park, C. S., and Yoo, C. H. (2007b). “Further Insights into Postbuckling of Web Panels. II: Other Myths.” *J. Struct. Engrg*., ASCE, Submitted for a possible publication.
11. SSRC (1998). *Guide to Stability Design Criteria for Metal Structures*, edited by Galambos, T.V., 5th ed., John Wiley & Sons, New York, NY.
12. Yoo, C. H., and Lee, S. C. (2006). “Mechanics of web panel postbuckling behavior in shear.” *J. Struct. Engrg*., ASCE, 132(10), 1580-1589.

APPENDIX 2. NOTATIONS

b_f = width of the flange;

D = depth of the girder;

d_0 = transverse stiffener spacing;

E = modulus of elasticity;

F_y = mill specified minimum yield stress;

F_{yf} = mill specified minimum yield stress of the flange;

F_{yw} = mill specified minimum yield stress of the web;

S_c = anchoring length of tension field along the compression flange;

S_s = anchoring length of tension field along the end post of end panel;

S_t = anchoring length of tension field along the tension flange;

t_f = thickness of the flange;

t_w = thickness of the web;

V_{cr} = elastic shear buckling strength;

$V_{cr(Lee\ et\ al.)}$= elastic shear buckling strength calculated according to Lee et al.(1996);

$V_{cr(S.S)}$ = elastic shear buckling strength of plate with simple-simple boundary;

$V_{P.B}$ = postbuckling strength;

$V_{P.B(FA)}$ =postbuckling strength due to the contribution of flange anchoring mecahnism;

V_u = ultimate shear strength(V_u=V_{cr}+$V_{P.B}$);

ε_y = yield strain;

μ = Poisson's ratio;

σ = normal stress or principal stress;

σ_{11} = horizontal normal stress;

σ_{22} = vertical normal stress;

σ_{bb} = tension field stress;

σ^t = diagonal tensile stress;

τ = shear stress;

τ_{cr} = elastic shear buckling stress;

ϕ = inclination of tension field.

Flexural Stiffness Limits for Frame Members of Steel Plate Shear Wall Systems

Mehdi Dastfan[1] *and Robert G. Driver*[2]

ABSTRACT

Steel plate shear walls consist of a boundary frame of beams and columns, supplemented by thin infill plates that tend to buckle at relatively low loads. When designed and detailed properly, these walls are capable of dissipating large amounts of energy, with stable hysteresis behaviour. To maximize efficiency in this regard, a relatively uniform post-buckling tension field should be developed, which requires proper anchorage provided by the surrounding frame members. In the current editions of both the Canadian and American design standards for steel structures, a general equation for determining the required stiffness of the columns is provided to ensure the formation of a relatively uniform tension field in the panels. An assessment of the origin of this equation shows that it is not suitable for the columns near the top and base of the wall. Moreover, the Canadian standard provides a stiffness requirement for the top beam that in most common cases cannot be met. In this paper, the effects of the stiffnesses of the top beam (or bottom beam, if present) and the adjacent columns are investigated simultaneously using a commercial finite element analysis program, and a design method is proposed for determining suitable, but practical, flexural stiffnesses for these members.

[1]Ph.D. Candidate, Dept of Civil and Env. Engg., University of Alberta, Edmonton, AB, Canada

[2]Professor, Dept of Civil and Env. Engg., University of Alberta, Edmonton, AB, Canada

INTRODUCTION

Steel plate shear walls are known to be an effective means of resisting lateral forces on buildings and are particularly suitable for seismic applications. This system consists of a vertical steel infill plate connected to a surrounding frame of beams and columns to transfer lateral loads to the foundation. Although heavily stiffened infill plates have sometimes been used in the past to maximize inelastic cyclic performance, for reasons of economics most recent steel plates shear wall projects have employed unstiffened plates. A large body of research has demonstrated that thin unstiffened plates perform very well under extreme cyclic lateral loads.

In most unstiffened SPSWs, the infill plate is thin enough to buckle at relatively low levels of lateral loading. Therefore, the infill plate must be properly anchored to the surrounding frame to develop a post-buckling tension field and the beams and columns must possess enough flexural stiffness for the buckled plate to perform efficiently. Figure 1 shows the tension field in an unstiffened shear wall schematically.

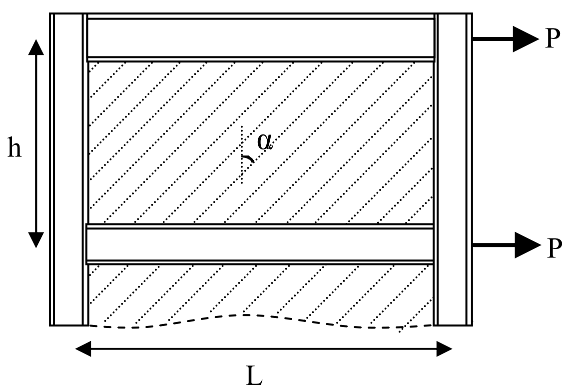

Figure 1. Tension field development after buckling of infill plate

BACKGROUND

Wagner (1931) conducted an analytical study on elastic metal I-girders with thin webs loaded in shear and developed a method for determining the moment of inertia of the flanges required to develop a sufficiently uniform tension field in each panel. In the derivation, he defined a flange flexibility parameter that was used to establish the relationship between the flange stiffness and the deviation of the web tension field from the ideal (uniform) case. As this parameter forms the basis of the current column stiffness requirements in the steel plate shear wall provisions of both standard S16 of the Canadian Standards Association (CSA. 2001) and the AISC Specification (AISC. 2005), the symbols and terms used in all subsequent discussions are changed from the original work for consistency with the context of steel plate shear walls. The flange flexibility parameter, therefore, takes the form of a column flexibility parameter, ω_h, expressed as follows:

$$\omega_h = h\sin\alpha \sqrt[4]{\left(\frac{1}{I_L} + \frac{1}{I_R}\right)\frac{w}{4L}} \tag{1}$$

where h is the storey height, α is the angle of inclination of tension field from vertical, I_L and I_R are the moments of inertia of the left and right columns, respectively, w is the infill plate thickness, and L is the wall width to the centres of the columns (see Figure 1).

Because of the flexural deformation of the columns between floor beams due to the tension field forces themselves, the tension field is not uniform; as the columns deform inward, a variation of strain (and therefore stress) across the infill plate develops. One of the ways that Wagner characterized the extent of the tension field stress non-uniformity is through the parameter C_2, which is a function of ω_h, for determining the maximum panel stress, $\sigma_{t,max}$, from the mean panel stress, $\sigma_{t,mean}$:

$$\sigma_{t,max} = (1 + C_2)\sigma_{t,mean} \tag{2}$$

The parameter C_2 is plotted as a function of ω_h in Figure 2.

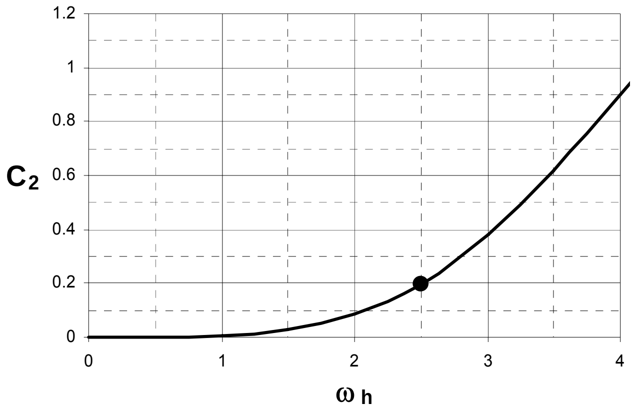

Figure 2. Parameter C_2 as a function of ω_h

Kuhn *et al.* (1952) simplified the equation for ω_h by taking the angle of inclination of the tension field, α, to be slightly less than 45° (*i.e.*, $\sin\alpha = 0.7$) and replacing the sum of the reciprocals of the column stiffnesses by four times the reciprocal of the sum (exact only for equal column stiffnesses):

$$\omega_h \approx 0.7h \sqrt[4]{\frac{w}{L(I_L + I_R)}} \tag{3}$$

With the further assumption that the two column stiffnesses, I_c, are equal, this equation has been adopted in North America (CSA. 2001; AISC. 2005) for use in establishing the minimum stiffness of steel plate shear wall columns required to ensure an approximately uniform tension field. It takes the following form:

$$\omega_h = 0.7h \sqrt[4]{\frac{w}{2LI_c}} \tag{4}$$

In order to select an appropriate upper limit on ω_h, it was assumed that the columns should be stiff enough so that the maximum stress in the tension field is no more than 20% greater than the average tensile stress across the panel. In other words, C_2 should not exceed 0.2 and, therefore, ω_h must not exceed 2.5, as shown in Figure 2. This flexibility limit leads to a minimum column moment of inertia, I_c, as follows:

$$I_c = 0.00307 \frac{wh^4}{L} \tag{5}$$

OBJECTIVES AND METHODOLOGY

An assessment of the assumptions made in the derivation of Equation 1, as discussed in the next section, reveals that it is not suitable for the columns near the top or the base of the wall. This is because one end of each tension "strip" anchored in these regions is connected to the top beam or the foundation rather than to a column at both ends. The current edition of Canadian standard S16 (CSA. 2001) attempts to address the need for a minimum stiffness of the top beam by requiring that its moment of inertia be high enough so that the variation of tensile stress across the panel width does not exceed 20%. Not only does this require an iterative solution, but in most common cases the requirement simply cannot be met. Therefore, the objectives of this work were to:

- study the original derivation that has led to the accepted column flexibility parameter for steel plate shear walls, ω_h;
- develop a new flexibility parameter suitable for the top and bottom of the shear wall, where the original assumptions do not apply;
- include in the new parameter the interaction of the behaviours of both the top or bottom beam and the adjacent columns;
- establish an upper limit to the new flexibility parameter that produces column and beam stiffnesses that will achieve efficient overall performance of the wall; and
- verify the limit through a detailed analytical investigation.

In this paper, a new boundary member flexibility parameter, ω_L, is developed for use at the top and base of a steel plate shear wall using the logic behind the equation for ω_h (Equation 1). Numerous realistic steel plate shear walls with various panel aspect ratios, h/L, plate thicknesses, w, and values of ω_h were modelled and analyzed using the commercial finite element analysis program ABAQUS to examine the influence of the parameter ω_L on the uniformity of the tension field and select an appropriate upper limit for use in design.

DEVELOPMENT OF PARAMETER ω_L

As described in the following, a close look at the original equation for ω_h (Equation 1) reveals that it represents a measure of the released strain in the tension strips. This release is due to the flexural deformations of the columns that arise from the distributed load applied by the anchored tension strips themselves, as shown in Figure 3, where σ_t is the tension field stress and q_c is its component perpendicular to the column in the form of a distributed force.

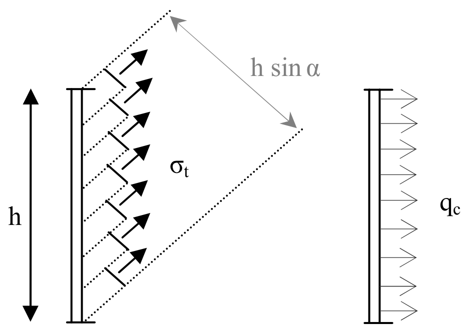

Figure 3. Distributed load along column applied by anchored tension strips

The perpendicular distributed load along the column, q_c, can be found as follows:

$$q_c = \frac{\sigma_t wh \sin\alpha \sin\alpha}{h} = \sigma_t w \sin^2\alpha \tag{6}$$

The flexural deflection of the column, δ_c, due to q_c is proportional to:

$$\delta_c \propto q_c \frac{h^4}{I_c} \Rightarrow \delta_c \propto w \frac{h^4}{I_c} \sin^2\alpha \tag{7}$$

The shortening of a tension strip connected at its ends to the left and right columns, δ_{strip}, due to the deformations of those columns is:

$$\delta_{strip} = (\delta_{c_L} + \delta_{c_R})\sin\alpha \tag{8}$$

The released strain in the strip because of this shortening is:

$$\varepsilon_{released} = \frac{\delta_{strip}}{l_{strip}} \Rightarrow \varepsilon_{released} \propto (\frac{h^4}{I_L} + \frac{h^4}{I_R}) \frac{w \sin^4\alpha}{L} \tag{9}$$

where l_{strip} is the length of the tension strip, which is equal to $L/\sin\alpha$.

By comparing Equations 1 and 9, it can be concluded that they are related to each other:

$$\omega_h = \sin\alpha \sqrt[4]{\left(\frac{h^4}{I_L} + \frac{h^4}{I_R}\right)\frac{w}{4L}} \quad \Rightarrow \omega_h \propto \varepsilon_{released} \tag{10}$$

In the top and bottom panels of steel plate shear walls, however, the tension field is not anchored to the columns at both ends, so the equation for ω_h is not directly applicable. Therefore, the parameter ω_L must account for the effects of flexural deformation of both the anchoring beam and the column, depicted in Figure 4. As with ω_h, this parameter should represent the released strain in the strips and an analogous expression can be derived in the same way.

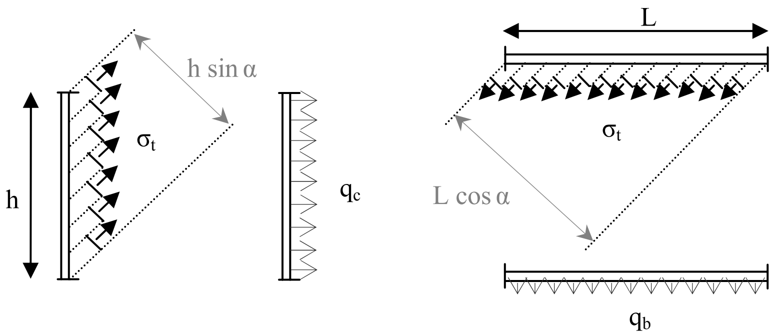

Figure 4. Distributed load along boundary members applied by anchored tension strips

The perpendicular distributed load along the beam, q_b, applied by the anchored tension strips can be calculated as:

$$q_b = \frac{\sigma_t wL\cos\alpha\cos\alpha}{L} = \sigma_t w\cos^2\alpha \tag{11}$$

The flexural deflection of the beam, δ_b, due to q_b is proportional to:

$$\delta_b \propto q_b \frac{L^4}{I_b} \Rightarrow \delta_b \propto w\frac{L^4}{I_b}\cos^2\alpha \tag{12}$$

The shortening of the strips due to a combination of δ_c and δ_b (Equations 7 and 12) can be calculated as follows:

$$\delta_{strip} = \delta_c\sin\alpha + \delta_b\cos\alpha \tag{13}$$

And the released strain due to this shortening is:

$$\varepsilon_{released} = \frac{\delta_{strip}}{l_{strip}} \Rightarrow \varepsilon_{released} \propto \left(\frac{h^4}{I_c} + \frac{L^4}{I_b}\cot^3\alpha\right)\frac{w\sin^4\alpha}{L} \tag{14}$$

Similar to the treatment of ω_h (see Equation 10), the parameter ω_L can be formulated as:

$$\omega_L = \sin\alpha \sqrt[4]{\left(\frac{h^4}{I_c} + \frac{L^4}{I_b}\cot^3\alpha\right)\frac{w}{4L}} \tag{15}$$

For simplicity, and consistent with the observation that the value of α in conventional steel plate shear walls is generally close to, but slightly less than, 45°, Equation 15 can be written in a simplified form as:

$$\omega_L = 0.7 \sqrt[4]{\left(\frac{h^4}{I_c} + \frac{L^4}{I_b}\right)\frac{w}{4L}} \tag{16}$$

ESTABLISHMENT OF LIMITS FOR ω_L

To determine a suitable upper limit for ω_L, numerous steel plate shear walls of varying proportions were modelled and analyzed using ABAQUS under a shear load that gave the same mean tension field stress (the anticipated yield stress of the plate material) in the panels for each model. The walls were meshed using four-node finite strain reduced integration shell elements and all beams and columns were made up of two-node beam elements. For an initial imperfection of the infill plate, a small out-of-plane displacement was applied at the centre of each plate. The bending moment at both ends of all beams was released to ensure that the entire applied shear was carried by the plate.

Figure 5 shows the percentage decrease in the average stress over the portion of the tension field anchored by the beam as compared to the overall average stress in the plate. Trend lines are also shown in the figure for models grouped according to the value of ω_h. Since the parameters ω_h and ω_L are not independent, for the same value of ω_L a lower beam stiffness will result for a lower value of ω_h (*i.e.*, a higher column stiffness). It was determined that lowering ω_h and/or ω_L below 1.0 produced no further improvement in the stress uniformity, thereby identifying the best-case scenario.

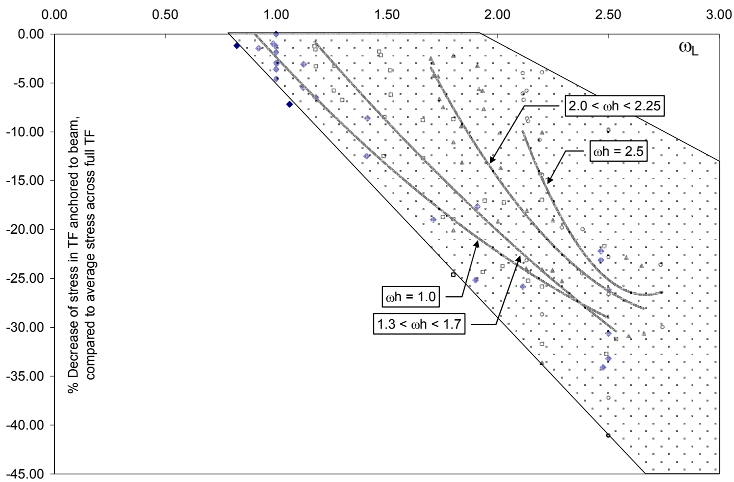

Figure 5. Non-uniformity of tension field stress as a function of ω_L

Figures 6, 7, and 8 show the stress distributions across the plate diagonal for several combinations of ω_h and ω_L for panel aspect ratios of 2.0, 1.0 and 0.67, respectively. It should be noted that there is an unavoidable non-uniformity in the tension field stress across the panel and even an infinitely stiff beam will not result in a perfectly uniform stress. An upper limit of 2.5 results in a sufficiently uniform tension field at the top of the wall, which is not particularly influential to the overall system behaviour. However, the need for an efficient tension field is seen as being greater in the bottom panel, and thus, an upper limit of 2.0 on ω_L is proposed.

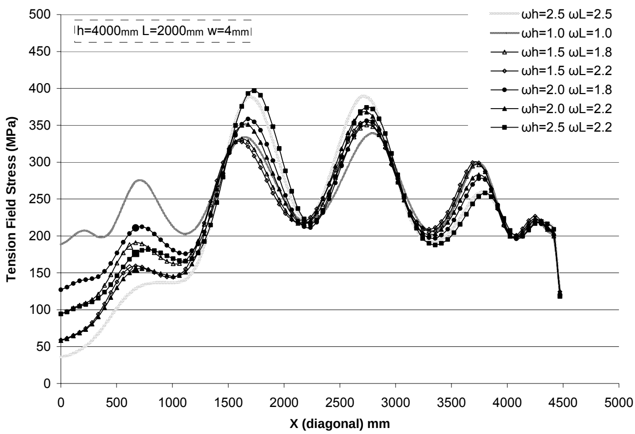

Figure 6. Variation of tension field stress for different combinations of ω_h and ω_L (h/L = 2.0)

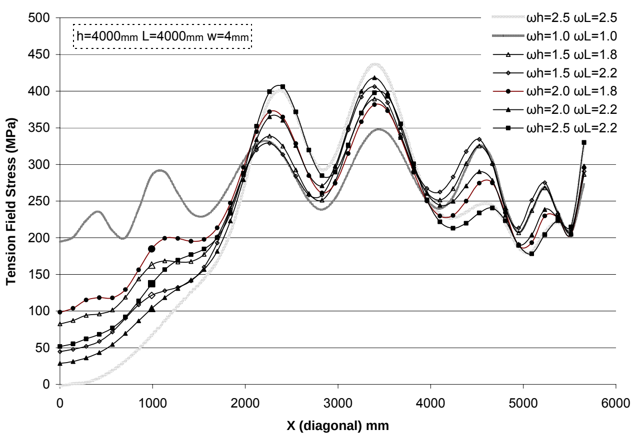

Figure 7. Variation of tension field stress for different combinations of ω_h and ω_L (h/L = 1.0)

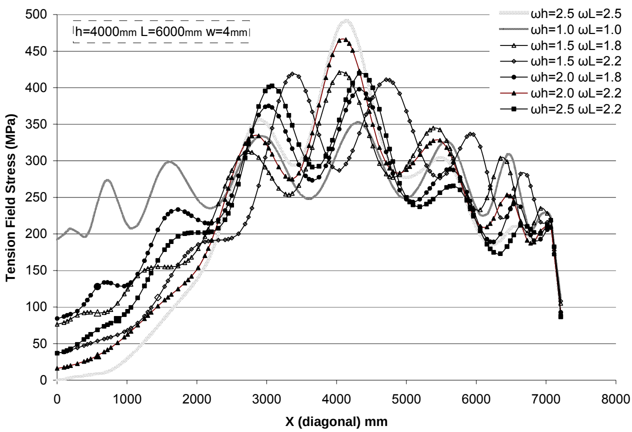

Figure 8. Variation of tension field stress for different combinations of ω_h and ω_L (h/L = 0.67)

Since the minimum permissible column stiffness is obtained from ω_h, and since ω_L is a function of both the beam and the column stiffnesses, to avoid obtaining a negative beam stiffness from Equation 16, a lower limit must also be set for ω_L. (That is, if the target value of ω_L is set too low, the beam would have to deflect in the opposite direction of the tension field force in order to obtain the desired stress uniformity.) By dividing ω_L by ω_h, the relationship between these two parameters can be shown as follows:

$$\frac{\omega_L^4}{\omega_h^4} = \frac{\dfrac{h^4}{I_c} + \dfrac{L^4}{I_b}}{2\dfrac{h^4}{I_c}} \tag{17}$$

To find the lower limit for ω_L, the stiffness of the beam is set to be less than infinite. Therefore, Equation 17 can be written as:

$$\frac{\omega_L^4}{\omega_h^4} \geq \frac{1}{2} \quad \Rightarrow \quad \omega_L \geq 0.84\omega_h \tag{18}$$

It should be emphasized that the requirements described here for the establishment of the beam stiffness are only to address the issue of tension field uniformity. Obviously the beams must also possess sufficient strength for these forces, as well as sufficient strength and stiffness to resist all other applied loads as well.

Examples of hot-rolled wide-flange top beam sections, for which both parameters ω_h and ω_L are equal to 2.5, are tabulated in Table 1 for steel plate shear walls with different aspect ratios and an infill plate thickness of 4 mm. Table 1 indicates that reasonable sizes of top beams result from this method. At the base of the wall, anchor beams would be much heavier due to the lower limit on ω_L and the possible presence of a thicker infill plate. As an economical solution at the bottom panel, the infill plate can alternatively be anchored directly to the foundation.

Table 1. Hot-rolled wide-flange sections for top beams ($\omega_h = \omega_L = 2.5$)

h (mm)	L (mm)	Aspect Ratio (h/L)	Thickness (mm)	Top beam
4000	2000	2.0	4	W360×39
4000	4000	1.0	4	W610×125
4000	6000	0.67	4	W610×307

CONCLUSIONS

A new boundary member flexibility parameter, ω_L, has been developed based on the logic behind the widely-accepted column flexibility parameter ω_h in order to achieve a sufficiently uniform tension field in the top and bottom panels where ω_h does not apply. The new parameter accounts for the flexibility of both the top or base beam and the adjacent columns on the panel behaviour. Limits on the value of ω_L have been proposed to ensure a sufficiently uniform tension field in the extreme panels, supported by a detailed finite element investigation.

Based on the results of these analyses, upper limits for ω_L of 2.5 and 2.0 were selected for the top and bottom panels, respectively. The proposals in this paper have been adopted into the current draft of the 2009 edition of the Canadian design standard for steel structures, S16.

ACKNOWLEDGMENTS

Funding for this research was provided by the Alberta Ingenuity Fund from the Alberta Heritage Foundation and the Honorary Izaak Walton Killam Scholarship from the University of Alberta.

REFERENCES

AISC. (2005) "Seismic Provisions for Structural Steel Buildings", ANSI/AISC 341-05, American Institute of Steel Construction, Chicago, IL.

CSA. (2001) "Limit States Design of Steel Structures", CAN/CSA S16-01, Canadian Standards Association, Toronto, Ontario.

Kuhn, P., Peterson, J.P., and Levin, L.R. (1952) "A Summary of Diagonal Tension, Part I: Methods of Analysis", , Technical Note 2661, National Advisory Committee for Aeronautics, Washington, DC.

Wagner, H. (1931) "Flat Sheet Metal Girders with Very Thin Metal Web, Part III", , Technical Note 605, National Advisory Committee for Aeronautics, Washington, DC.

Performance-Based Fire Resistant Design for Concrete-Filled HSS Columns

Kodur V.K.R.[1] and Fike R.[2]

Abstract:
The use of concrete filling offers a practical alternative for achieving the required stability of steel Hollow Structural Section (HSS) columns under fire conditions. However, the current prescriptive-based approach, has a number of constraints that in many applications restrict the utilization of concrete filling for achieving the required fire resistance. To overcome such constraints, a performance-based methodology for fire resistance design is presented in this paper. A set of numerical simulations were carried out to investigate the effect of realistic fire scenarios, loading, and stability based failure criterion on the fire resistance of concrete filled HSS columns. Results from the parametric studies show that fire scenario and load level have significant influence on the resulting fire resistance. It is demonstrated that by adopting a performance-based approach, it is possible to show that concrete filled HSS columns can provide fire resistance sufficient to withstand complete compartment burnout, while maintaining structural integrity.

Keywords: Column stability, HSS-Columns, Standard fire, Design fire, Concrete-filling, Fire resistance, Performance-based design

[1]Kodur V.K.R., Professor, Department of Civil and Environmental Engineering, Michigan State University
[2]Fike R., Graduate Student, Department of Civil and Environmental Engineering, Michigan State University

1. INTRODUCTION

Steel Hollow Structural Sections (HSS) are very efficient in resisting compression, torsional, and seismic loads, and are widely used as compressions members in the construction of framed structures. Structural stability under fire exposure is one of the primary considerations in the design of high-rise buildings, and hence, building codes normally require fire protection for HSS columns to maintain overall structural stability in the event of fire. Providing such external fire protection to HSS columns involves additional cost, reduces aesthetics, increases weight of the structure, and decreases usable space. Also, durability of fire proofing (adhesion and cohesion to steel) is often a questionable issue, and hence, requires periodic inspection and regular maintenance, which in turn, incurs additional costs during the lifetime of the structure [1,2].

Often these HSS sections are filled with concrete to enhance the stiffness, torsional rigidity, and load-bearing capacity. The two components of the composite column complement each other ideally. The steel casing confines the concrete laterally, allowing it to act as in tri-axial compression and develop its optimum compressive strength, while the concrete, in turn, enhances resistance to elastic local buckling of the steel wall and global buckling of the column. In addition, a higher fire resistance is obtained without using external fire protection for the steel, thus increasing the usable space in the building and removing the need for application and maintenance of the fire protection. Properly designed concrete-filled columns can lead economically to the realization of architectural and structural design with visible steel, but without any restrictions on fire safety [3-5].

Design guidelines for achieving fire resistance through concrete filling have been incorporated into codes and standards [6-8]. However, the current fire guidelines are limited in scope and restrictive in application since they were developed based on ASTM E-119 [9] standard fire test, and are valid only for the standard fire exposure conditions. In many applications, such as atriums, schools, and airports, where exposed steel is highly desired, the current prescriptive provisions can not be applied due to limitations on column size, load, and fire exposure. Thus designers can not take advantage of concrete-filling option for achieving fire resistance in HSS columns.

This paper presents a performance-based methodology for fire safety design of Concrete Filled HSS (CFHSS) columns. A review of the fire performance of CFHSS columns is presented, and the drawbacks and limitations of the current fire resistance evaluation approaches are discussed. Results from the numerical studies on a set of CFHSS columns exposed to various fire and loading scenarios are presented. The analysis is carried out using finite element based computational model SAFIR, wherein the material and geometric non-linearity and stability-based failure criterion are considered. Results from the analysis are used to present a framework for performance-based fire engineering methodology.

2. PERFORMANCE-BASED DESIGN

Recently there has been an increased impetus on moving toward a performance-based approach for fire safety design [10,11]. This is mainly due to the fact that the current prescriptive-based approach has serious limitations restricting the use of alternate, cost effective solutions for providing fire resistance. There are two basic methods by which performance-based fire safety design can be accomplished: tests can be performed wherein the structural performance of the system to be built is evaluated, or, numerical/computational simulations can be used to evaluate the system to be built. Due to the high cost, time, and effort associated with full scale fire testing, the first option is mostly used to validate numerical models. The second option of numerical models allows the consideration of most significant factors that influence fire resistance. The most important factors to be considered in performance-based fire safety design are fire scenario, load conditions, and failure condition [12]. These main components are discussed here:

2.1 Fire Scenario

The current practice of evaluating fire resistance of CFHSS columns is based on standard fire tests or models, in which the column is exposed to a standard fire as specified in standards such as ASTM E-119 [9] or ISO 834 [13]. While standard fire resistance tests are useful benchmarks to establish the relative performance of different CFHSS columns under standard fire condition, they should not be relied upon to determine the survival time of CFHSS columns under realistic fire scenarios. Nor does the standard heating condition bear any resemblance to the often less severe heating environments encountered in real fires.

Figure 1 illustrates various time-temperature curves for standard and some realistic (design) fire scenarios [15]. In the standard fires (ASTM E-119 fire and hydrocarbon fire) [9,14], the fire size is the same (irrespective of compartment characteristics), temperature increases with time throughout the fire duration, and there is no decay phase. However, in real fires, the fire size is a function of compartment characteristics, such as ventilation, fuel load, and lining materials, and there is a decay phase as clearly shown in Figure 1 (design fires FV02 - FV12) [15]. In the decay phase of the realistic fire scenarios, the cross section of the column enters the cooling phase, in which the concrete and/or steel recovers part of its strength and stiffness, and thus, the fire resistance of the column increases.

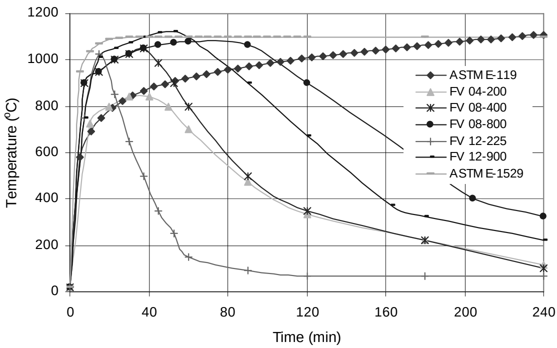

Figure 1: Time-temperature relationships for various fire scenarios

2.2 Load Level

The current codes of practice for evaluating fire resistance through standard fire tests are generally based on a load ratio of about 50%. Load ratio is defined as the ratio of the applied load on the column under fire conditions to the strength capacity of the column at room temperature. Load ratio depends on many factors including the type of occupancy, the dead load to live load ratio, the safety factors (load and capacity factors) used for design under both room temperature and fire conditions. The loads that are to be applied on CFHSS columns, in the event of fire, can be estimated based on the guidance given in ASCE-07 standard [16] (1.2 dead load + 0.5 live load) or through actual calculations based on different load combinations. Based on ASCE-07 [16] and AISC LRFD Manual [7], and for typical dead to live load ratios (in the range of 2 to 3), the load ratio for CFHSS columns ranges between 30% and 50%.

Further, the load ratio might influence the fire resistance of CFHSS columns calculated based on realistic failure criteria. Thus, for innovative, realistic and cost effective performance-based fire safety design, it is important to evaluate the fire resistance of CFHSS columns based on actual load levels.

2.3 Failure Criterion

Many tests and numerical analysis procedures use a temperature limiting criterion to define failure. It is commonly assumed that once the steel section reaches a critical temperature of 538°C, approximately 50% of the room temperature strength is lost [17], and failure is eminent. While sufficient for traditionally protected steel sections, the effect of the concrete core is not captured by the thermal failure criterion. To correct this, stability of the column under fire conditions needs to be considered. Columns can fail globally either by buckling or crushing depending on slenderness. Depending on factors such as the end conditions, buckling or crushing could occur well after the limiting temperature of 538°C is reached. If a column is adequately restrained on both ends via a fixed-fixed connection, fire resistance can be enhanced appreciably due to redistribution of moments between critical sections. Additionally, local stability should be accounted for. CFHSS columns can fail locally without collapse due to crushing of the concrete on the inside, or local buckling of the steel wall [18-20].

3. STATE-OF-THE-ART

Alternate approaches for achieving fire resistance of CFHSS columns have been studied for the last three decades. Methods such as filling the HSS columns with liquid (water) and concrete, are the most popular approaches studied by researchers [3,21,22]. However, the use of concrete-filling is the most attractive and feasible proposition developed by researchers.

3.1 Experimental and Numerical Studies

The fire resistance tests on CFHSS columns were predominantly carried out at the National Research Council of Canada (NRCC), a few organizations in Europe, and more recently in China. The experimental program at NRCC consisted of fire tests on about 80 full-scale CFHSS columns [3,23-26]. Both square and circular HSS columns were tested, and the influence of various factors, including type of concrete filling (PC, RC, and FC), concrete strength, type and intensity of loading, and column dimensions were investigated under the ASTM E-119 [9] standard fire exposure condition. The tests reported by other European and Chinese studies [22,27,28] are similar to NRCC tests, but the fire exposure was that of the ISO 834 [13] standard fire; whose time-temperature curve is similar to that of ASTM E-119 [9].

The numerical studies, primarily carried out NRCC, consisted of development of mathematical models for predicting the fire behavior of circular and square CFHSS columns [29-31]. In these models, the fire resistance is evaluated in various time steps, consisting of the calculation of the temperature of the fire to which the column is exposed, the temperatures in the column, its deformations, and strength during exposure to fire, and finally, its fire resistance. Full details on the development and validation of these models are given in references [20,24,29].

Data reported from NRCC tests and numerical studies can be used to illustrate the behaviour of concrete-filled HSS columns under fire conditions. Figure 2 shows the variation of the axial deformation as a function of time for 3 typical HSS columns filled with one of three types of concrete, namely: plain concrete (PC), steel fiber reinforced concrete (FC) and bar reinforced concrete (RC) [23]. The three columns had similar dimensions and loading conditions, and the results can be used to illustrate the comparative fire behaviour of the three types of concrete filling.

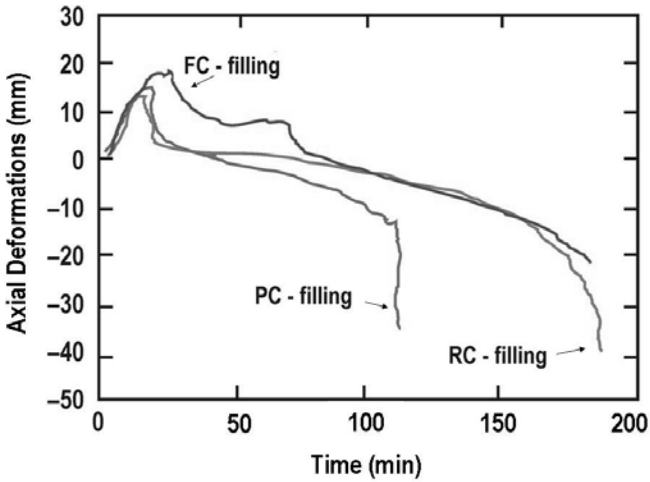

Figure 2: Axial deformation in CFHSS columns as a function of time

At room temperature, the load is carried by both the concrete and the steel. When the column is exposed to fire, however, the steel carries most of the load during the early stages because the steel section expands more rapidly than the concrete core. At higher temperatures, the steel section gradually yields as its strength decreases, and the column rapidly contracts at some point between 20 and 30 minutes after exposure to fire. At this stage, the concrete-filling starts carrying more and more of the load. The strength of the concrete decreases with time, and ultimately, when the column can no longer support the load, failure occurs either through buckling or compression. The elapsed time that it takes for the column to fail is the measure of its fire resistance. The behavior of the column, after steel yields, is dependent on the type of concrete-filling. Both FC and RC-filled HSS columns have higher fire resistance than PC-filled HSS columns.

It can be seen in Figure 2 that the deformation behaviour of the FC-filled steel column is similar, during the later stages of the test, to that of the RC-filled steel column. The initial higher deformations in the FC-filled HSS column might be due to higher thermal expansion of steel fiber-reinforced concrete. The fire resistance of the RC-filled HSS column is higher than that of the FC-filled HSS column, which in turn is higher than the PC-filled HSS column.

3.2 Design Equation for Evaluating Fire Resistance

Based on the results from experimental and numerical studies [19,29,32], the most important parameters that influence the fire resistance of CFHSS columns are: type of concrete filling (plain, bar-reinforced, and fiber-reinforced), outside diameter or width of the column, load on the column, effective length of the column, concrete strength, type of aggregate, and eccentricity of load.

Using the results from computer-simulated parametric studies, as well as fire resistance tests, a unified design equation has been developed for calculating the fire resistance of circular and square HSS columns filled with any of the three types of concrete [32-34]. The equation expresses the fire resistance of a CFHSS column, as a function of influencing parameters:

$$R = f \frac{(f'_c + 20)}{(KL - 1000)} D^2 \sqrt{\frac{D}{C}} \tag{1}$$

Where: R = fire resistance in minutes, f'_c = specified 28-day concrete strength in MPa, D = outside diameter or width of the column in mm, C = applied load in kN, K = effective length factor, L = unsupported length of the column in mm, f = a parameter to account for the type of concrete filling (PC, RC, and FC), the type of aggregate used (carbonate or siliceous), the percentage of reinforcement, the thickness of concrete cover, and the cross-sectional shape of the HSS column (circular or square), values of which can be found in reference [31].

The above equation has been validated by comparing the predictions with those obtained from the computer programs as well as with fire tests conducted at different laboratories [5,29,31]. The fire resistances obtained using the equation are somewhat more conservative (about 10-15%) than those obtained from the tests, particularly for the range of higher fire resistances.

3.3 Limitations

The above developed equation though providing an innovative and cost effective approach for visualizing exposed steel, is limited in scope and restrictive in application since it was developed based on ASTM E-119 [9] standard fire tests, and is valid only for narrow range of column dimensions, loads, and other design variables. Table 1 gives some of the limitations of the above-developed approach, and the range of variables encountered in field applications. It can be seen that the current design equation is valid only over a narrow range of column parameters such as lengths up to 4 m, diameter up to 400 mm, concrete strengths up to 55 MPa, and only for ASTM E-119 [9] standard fire exposure. Therefore, the design equation, and relevant solutions, cannot be used under the recently introduced performance-based codes, which provide rational, cost-effective and innovative fire safety solutions.

Table 1: Current design limitations and range of parameters encountered in practical applications

Parameter	**Current Limitation**	**Practical Applications**
Column shape	square and circular	square, circular and rectangular
Column size	400 mm	600 mm and beyond
Column length	4 m	6-10 m
Concrete strength	55 MPa	100 MPa
Fire scenarios	ASTM E-119	design fires and hydrocarbon fires
Load level	strength of concrete core	service loads
Eccentric loads	not allowed	always present

In many applications, such as atriums, schools, and airports where exposed steel is highly desired, the lengths and sizes of columns are beyond those allowed in the current design equations, and thus, the architects and designers can not take advantage of high fire resistance ratings (and other advantages) that can be achieved from CFHSS columns. Also, the limitations of the above research for only ASTM E-119 [9] fire exposure, hinders the use of HSS columns in offshore structures and oil platform applications. Thus, the full potential for the use of these CFHSS columns has not been realized.

Due to above limitations, a number of opportunities for the use of CFHSS columns are being lost. Further, in places where CFHSS columns are used, external fire protection is still provided, without taking advantage of inherent fire resistance present in this composite system.

4. NUMERICAL STUDIES

To overcome the above limitations, a set of numerical studies were carried out to develop an approach for performance-based design of CFHSS columns. The analysis was carried out using a FEM based computer program SAFIR, and by exposing different types of CFHSS columns to various fire and loading scenarios. Some of the details associated with the analysis are discussed here.

4.1 Computer Program

The computer program SAFIR is capable of modeling: multiple materials in a cross section, cooling phase of a fire, large displacements, effects of thermal strains, non-linear material properties according to Eurocode 3, and residual stresses [35]. Additionally, SAFIR allows the user to input any time-temperature relationship to facilitate the use of design fire scenarios.

In SAFIR, the thermal and structural analysis are performed independently. The thermal model consists of 2D solid elements where the fire exposed sides and the exposure types are specified by the user. The thermal model in SAFIR neglects heat transfer in the longitudinal direction and the effect of hydraulic migration in concrete.

For structural analysis, SAFIR uses a fiber-based approach wherein each of the solid elements in the thermal model is considered to be a fiber in the structural model. A stress and temperature dependent stiffness matrix is established that incorporates each of the fibers. Due to the increasing temperature in the column, the stiffness decreases to a point where the column can no longer support the applied load, and failure occurs. Through the use of beam elements to simulate columns, both crushing and buckling failure of the columns can be captured. Limitations of the structural model include the assumption that there is no slip between the steel and the concrete.

4.2 Columns Selected

The validity of SAFIR was established by comparing the predictions from the program with test data from the literature. For this purpose, five CFHSS columns tested at NRCC under the standard fire scenario were selected. All pertinent information for the plain CFHSS columns is provided in Table 2 [19,31,36-38]. In the designation of columns (ex: RP-355), the first letter (R) represents section shape (Round or Square), second letter (P) denotes filling type (Plain Concrete), and the number (355) denotes the diameter or width of the section.

Table 2: Test parameters and fire resistance values for CFHSS columns

Column ID	**DIA or Width (mm)**	**Length (mm)**	**AISC Factored Load (KN)**	**Load Ratio**	**Fire Resistance (min)**	
					Test	**SAFIR**
RP-168	168.3	3810	1197	0.13	81	82
RP-273	273.1	3810	3508	0.15	143	128
RP-355	355.6	3810	5120	0.37	170	164
SP-152	152.4	3810	1409	0.20	86	74
SP-178	177.8	3810	1976	0.28	80	72

4.3 Computer Model Validation

For validation of SAFIR, the above selected columns were analyzed under ASTM E-119 fire exposure. The thermal and structural response, as well as the ultimate failure times generated by SAFIR were compared with measured test data.

Comparison of the predicted temperatures from SAFIR with test data indicated a good agreement between test and SAFIR temperatures at different locations on the steel surface and in the concrete core. In the majority of cases, the temperature in the steel shell was within 5% of that observed from tests for the duration of the simulation. Concrete temperatures, however, initially were under estimated up to 100^{o}C, at which point they then began to be over estimated. This is due to SAFIR only considering the energy to evaporate water at 100^{o}C, and not its subsequent condensation in, and heating of, the central core. This causes SAFIR to neglect the re-vaporization of the water in the central core, and consequently higher temperatures are predicted.

The structural response from SAFIR was validated by comparing the predicted axial deformations with those measured in tests. For column SP-178 the maximum deflection achieved in testing was 18.3mm, while that observed from SAFIR was 18.0mm. There is however a considerable time lag present in the majority of simulations, the response from SAFIR is shifted such that maximum deflections are reached at a later stage in the test. This is due to the assumption that there is no slip between the steel and the concrete in SAFIR. This causes the steel section to rupture the concrete along the entire length of the column in the simulation, while in reality slip may occur allowing the steel section to expand freely.

The predicted and measure values of fire resistance for the 5 CFHSS columns are tabulated in Table 1. A comparison of the fire resistance values indicate that the SAFIR predictions are in good agreement with measured fire resistance values. Due to the inherent variability of laboratory testing and assumptions made within a computational model, the results presented here are in reasonable agreement and the models, (both the thermal and structural) constructed here are deemed acceptably conservative to continue with the parametric study.

5. PARAMETRIC STUDIES

The validated computer program SAFIR was used to carry out a set of parametric studies to quantify the effect of critical parameters on fire resistance of CFHSS columns. For this purpose, 11 CFHSS columns were selected (see Table 3) for the study. Five of these are test columns shown in table one, while the remaining six had varying design parameters with respect to length, concrete strength, cross section, and load ratio.

Table 3: Fire resistance of columns under different fire scenarios

	Analysis-Fire Exposure					
Column	FV04-200	FV08-400	FV08-800	FV12-225	FV12-900	ASTM E-1529
RP-168	-	-	49	-	45	41
RP-273	-	-	-	-	-	89
RP-355	-	-	-	-	-	119
RP-355L	-	-	59	-	53	49
RP-406	-	52	46	-	42	36
RP-406L	-	-	93	-	-	82
SP-152	-	-	48	-	45	40
SP-178	-	-	50	-	47	89
SP-355L	-	-	66	-	60	56
SP-406	-	-	48	-	43	38
SP-406L	-	-	-	-	-	98

5.1 Effect of Fire Scenario

The effect of fire scenario was studied by analyzing a set of CFHSS columns under various fire scenarios. To accomplish this, the design fires shown in Figure 1 were used. To simulate the "cool-short fire" a ventilation factor of 0.04 and a fuel load of 200 MJ/m^2 was chosen (FV04-200). To simulate hotter fires, two fires were chosen with a ventilation factor of 0.08 and fuel loads of 400 MJ/m^2 and 800 MJ/m^2 respectively (FV08-400, FV08-800). The FV08-100 fire represents a short fire, while FV08-400 and FV08-800 represent medium and long duration fires respectively. Finally, short and long duration hot fire scenarios were simulated using a ventilation factor of 0.12 and a fuel load of 225 MJ/m^2 and 900 MJ/m^2 respectively (FV12-225 and FV12-

900). The time temperature relationships used in these fires was obtained from Magnusson and Thelandersson charts [15]. Standard fire scenarios for both building and hydrocarbon fire scenarios were taken from ASTM E-119 [9] and ASTM E-1529 [14] respectively. It can be seen in Figure 1 that all of the design fires have a maximum temperature followed by a decay phase, while there is no decay phase in the two standard fires.

Results from the thermal analysis using SAFIR indicate that the fire scenario has a significant effect on internal temperatures attained in the columns. This is illustrated in figures 3 and 4 where temperatures on the steel surface and at mid-depth of concrete are plotted for column RP-273 under different fire exposures.

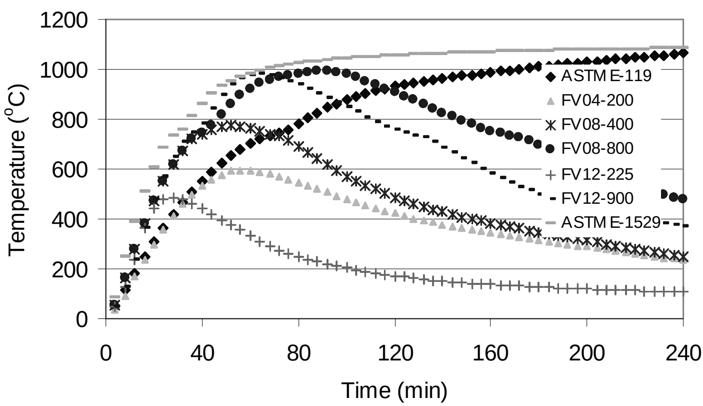

Figure 3: Temperatures at steel surface for column RP-273 exposed to different fire scenarios

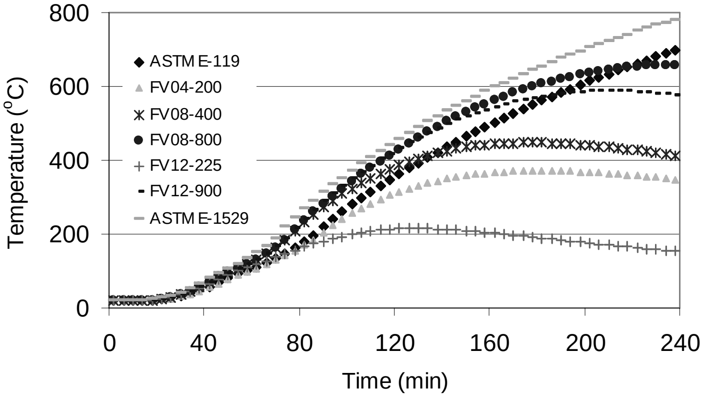

Figure 4: Temperatures at center of concrete core for column RP-273 under different fires

It can be seen in Figure 3 that three of the five design fires produce higher initial temperatures in steel than the ASTM E-119 [9] fire. This effect is continued in concrete temperatures also, (Figure 4) though to a lesser degree. The presence of the decay phase in the design fires however causes the temperature in all locations of the column to be less than that for the ASTM E-119 fire at the end of the simulation period. Column stability is maintained in design fires despite the more severe initial temperatures due to the decay phase of the fire allowing cooling of the steel before sufficient concrete strength is lost to induce failure.

To illustrate the effect of fire scenario on the structural response, axial deformations resulting from a severe and mild fire exposure are compared in Figure 5 for column RP-273. Under both fire scenarios, the column expands due to the rising temperatures from fire. After the rising phase, the contraction phase starts which is primarily due to the steel shell reaching maximum thermal expansion. The gradual contraction continues for a significant duration of time without resulting in failure. The shape of the contraction curve is influenced by the fire characteristics in the cooling phase. It can be seen from Figure

5 that failure of the column under severe fire occurs in about 2 hours, while no failure resulted even after 4 hours of exposure under a mild fire.

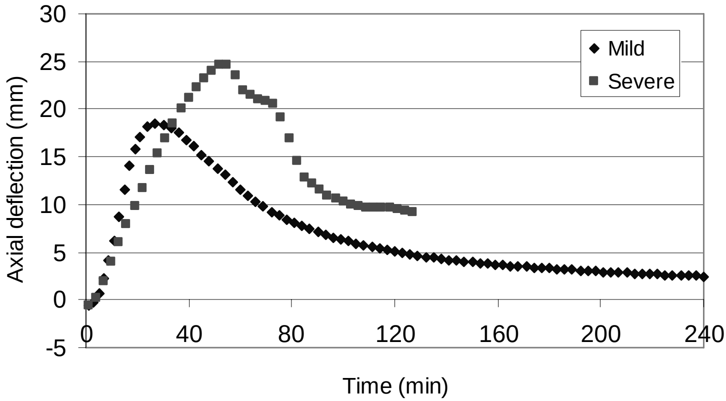

Figure 5: Axial deformation as a function of time for column RP-273

Table 3 shows the resulting failure (fire resistance) times for the columns under different fire exposure scenarios. Boxes occupied by a "-" indicate that no failure was observed during the 4 hour simulation period. It can be seen from the table that no failure was observed in the majority of cases except those under severe fire exposure (FV12-900). This analysis clearly illustrates that higher fire resistance can be obtained for CFHSS columns under most design fires.

5.2 Effect of Load Ratio

The effect of load ratio on fire resistance was evaluated by subjecting column SP-355 to design fire FV800-08 for a range of load ratios. Load ratio was varied from 20% to 100%. Figure 6 shows the variation of fire resistance with load ratio for plain CFHSS columns. A load ratio of 30% or less will provide fire resistance sufficient to withstand complete burnout of the compartment. However, the fire resistance decreases with increasing load ratio beyond 30%. This can be attributed to the fact that concrete filling generally provides a load bearing capacity of about 30% of the overall composite column. In a fire scenario, the steel shell looses its strength very quickly and, concrete carries most of the load. Thus, for load ratios higher than 30%, the concrete filling has to be strengthened either through the use of bar-reinforcement or through the use of steel fibers to achieve higher fire resistance.

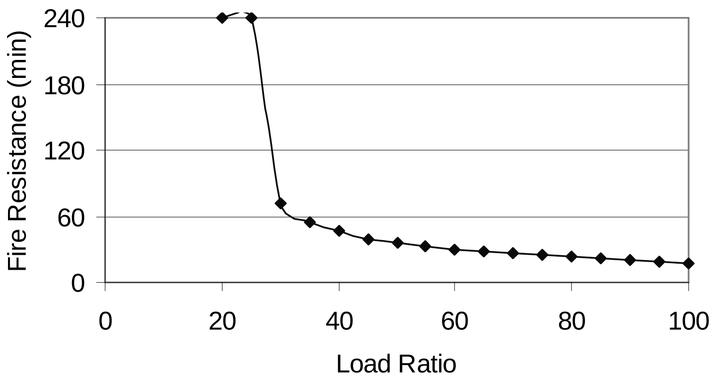

Figure 6: Effect of load ratio on fire resistance for column SP-355

5.3 Effect of Length

To evaluate the effect of column length on fire resistance, column RP-355 was subjected to design fire FV800-08 for four length scenarios. In order to eliminate variance resulting from load ratio, the load on the column was altered for every case to account for the increase in effective length such that the load ratio was held constant at 30%. Figure 7 displays the results of this investigation. Plain concrete filling can be used to obtain a fire resistance of one hour for lengths up to 7m. After 8m, there is a sharp drop off indicating that the failure mechanism has changed from crushing to buckling. In many instances, the fire resistance requirement is greater than one hour which makes the use of plain concrete-filling impractical. In such circumstances the use of either steel fiber reinforced or bar reinforced concrete filling is a viable option.

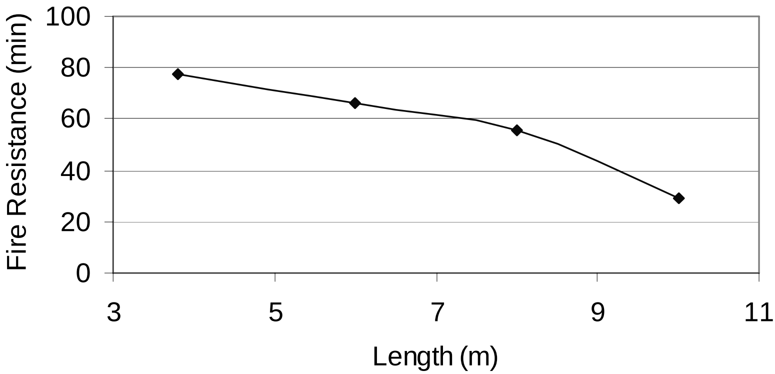

Figure 7: Effect of length on fire resistance for column RP-355

5.4 Effect of Concrete Filling

The effect of concrete filling on fire resistance was evaluated by analyzing HSS columns with three types of concrete filling, namely: plain concrete (RP-355), bar reinforced concrete (RB-355), and steel fiber reinforced concrete (RF-355). The fire resistance predictions obtained from the analysis are plotted as a function of column length in Figure 8. It can be seen from the figure that for columns lengths up to 8m, bar and steel fiber reinforced CFHSS columns provide high fire resistance (up to four hours) as compared to that of plain concrete-filled HSS columns (about 1 hour). However, the fire resistance of bar and fiber reinforced concrete filled HSS columns decreases rapidly beyond 8m of length. This could be attributed to a change in failure mode from crushing to buckling for the longer columns. These results illustrate that it is possible to achieve fire resistance up to 4 hours in HSS columns of longer length (up to 8m) through the use of bar or steel fiber reinforced concrete filling.

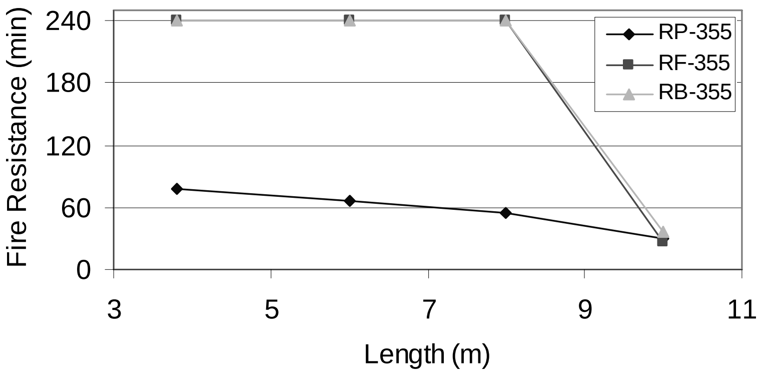

Figure 8: Effect of type of concrete filling on fire resistance of HSS columns

6. PERFORMANCE –BASED DESIGN

For fire safety design, the performance-based approach is becoming popular since cost-effective and rational fire safety solutions can be developed using this approach [7,11]. One of the key aspects in any performance-based design is the fire resistant design of structural members. For evaluating fire resistance, numerical models that can simulate the response of structural members under realistic fire, loading and restraint scenarios can be used. The main steps involved in undertaking a rational approach for performance-based design are:

a) identifying proper design (realistic) fire scenarios and realistic loading levels on HSS columns under consideration;
b) carrying out detailed thermal and structural analysis by exposing the CFHSS column to fire conditions; and
c) developing relevant practical solutions, such as: use of different types of concrete filling, to achieve required fire resistance.

6.1 Development of Fire Scenario and Loading

The design fire scenarios for any given situation should be established either through the use of parametric fires (time-temperature curves) specified in Eurocodes [17] or through design tables [15] based on ventilation, fuel load, and surface lining characteristics. The ventilation factor (F_v) can be established using the relationship:

$$F_v = \frac{A_v}{A_t}\sqrt{H_v} \tag{2}$$

Where A_v is the area of the window opening (m^2), A_t is the total internal area of the bounding surface (m^2), and H_v is the height of the window opening (m) [39]. Next, the fuel load in MJ should be determined per m^2 of the total bounding surface (not just the floor surface area). Typical fuel loads for common compartment uses are readily available [12,39] and can be used for this relatively simplistic calculation. Figure 1 shows typical standard and real fire exposure curves that can be generated for performance-based fire safety design. The presence of sprinklers can be accounted for in developing fire scenarios.

The loads that are to be applied on concrete-filled HSS columns, in the event of fire, should be estimated based on the guidance given in ASCE-07 standard [16] (1.2 dead load + 0.5 live load) or through actual calculations based on different load combinations.

6.2 Structural Analysis Under Fire Exposure

Once the fire scenarios and load level are established, the next step is to avail of a computer program for the analysis of CFHSS columns exposed to fire scenario. The computer program should be able to trace the response of the CFHSS column in the entire range of loading up to collapse under fire. Computer programs such as SAFIR (as demonstrated in this paper) or ANSYS can be adopted for the analysis. Using the computer program, a coupled thermal-structural analysis shall be carried out at various time steps. In each time step, the fire behavior of a CFHSS column is estimated using a complex, coupled heat transfer/strain equilibrium analysis, based on theoretical heat transfer and mechanics principles. The analysis shall be performed in three steps: namely, calculation of fire temperatures to which the column is exposed, calculation of temperatures in the column, and calculation of resulting deflections and strength, including an analysis of the stress and strain distribution.

The program, used in the analysis, should be capable of accounting for non-linear high temperature material characteristics, complete structural (column) behavior, various fire scenarios, high temperature creep, different concrete types (concrete with and without steel fibers), and failure criteria. In the analysis, geometric nonlinearity which is an important factor for slender columns (that are used in many practical applications), shall be taken into consideration. Thus, the fire response of the column shall be traced in the entire range of behavior, from a linear elastic stage to the collapse stage under any given fire and loading scenario. Through this coupled thermal-structural analysis, various critical output parameters, such as temperatures, stresses, strains, deflections, and strengths have to be generated at each time step.

The temperatures (in the concrete, and reinforcement), strength capacities, and computed deflections of the column shall be used to evaluate failure of the column at each time step. At every time step the failure of the column shall be checked against a pre-determined set of failure criteria, which include thermal and structural (including buckling) considerations. The time increments continue until a certain point at which the thermal failure criterion has been reached or the strength (or deflection) reach their limiting state. At this point, the column becomes unstable and will be assumed to have failed. The time to reach this failure point is the fire resistance of the column.

6.3 Development of Practical Alternatives

Results from the analysis can be utilized to develop practical solutions for achieving required fire resistance in CFHSS columns. Such solutions include changing the type of concrete filling to be used for achieving certain fire resistance for given design conditions. Other factors such as the type of aggregate in the concrete, reinforcement in the column, or load level can be varied to achieve the required fire resistance in HSS columns. As an example, while plain concrete filling can provide 1 hour fire resistance in HSS columns, by switching to steel fiber reinforced concrete filling, up to 3 hours of fire resistance can be obtained through a performance-based approach.

6.4 Design Implications

The approach presented here, is capable of tracing the behavior of CFHSS columns from the initial pre-fire stage to the failure of the column under realistic fire scenarios, load level, and for any failure criteria. Using computer programs, a designer can arrive at a performance-based fire safety design of a CFHSS column for any realistic conditions and column properties such as fire scenario, load level, failure criteria, concrete filling type, column size, and length. Thus, the use of this approach will lead to an optimum design that is not only economical, but is also based on rational design principles. Further, the approach can be applied to conduct parametric studies, which can then be used to develop rational fire safety design guidelines for incorporation into codes and standards.

Through implementation of the design process outlined here, structural safety and integrity will be improved, construction time and cost will be reduced, and exposed structural steel can be achieved. Applications for these columns could include airports, schools, detention facilities, and high-rise buildings where structural stability in fire is paramount, and relatively high fire resistance is required.

7. CONCLUSIONS

Based on the results of this study, the following conclusions can be drawn:

- The current fire resistance provisions, developed based on limited standard fire tests under "standard fire scenarios", are prescriptive and simplistic in application, and thus, can not be applied for rational fire safety design of CFHSS columns under performance-based codes.

- Load level has significant influence on the fire resistance of CFHSS columns. The fire resistance of CFHSS columns drastically reduces for load levels greater than 30-35%.
- Type of fire exposure has significant effect on fire resistance of CFHSS columns. Thus, the failure, and the fire resistance of CFHSS columns under most design fire scenarios are higher than that under ASTM E-119 [9] standard fire exposure scenario.
- Through the use of relevant concrete filling and adopting a performance-based approach to fire design, it is possible to maintain stability of HSS columns under most design fire exposures for a practical length of time.
- The limiting criterion, used for determining failure, has significant influence on the fire resistance of CFHSS columns. The conventional failure criterion, such as limiting steel temperature can not be applied to CFHSS columns. The strength and deformation failure criteria should be considered for evaluating fire resistance of CFHSS columns.

8. ACKNOWLEDGMENT

The research, presented in this paper, is primarily supported by the American Institute of Steel Construction through AISC Faculty Fellowship Award to Prof. Kodur.

9. REFERENCES

1. FEMA (2002), “World Trade Center Building Performance Study: Data Collection, Preliminary Observations, and Recommendations”, Federal Emergency Management Agency, Washington, DC.
2. NIST (2005), “Final Report of the National Construction Safety Team on the Collapse of World Trade Center Towers”, NCSTAR1, National Institute of Standards and Technology, Gaithersburg, MD 20899.
3. Kodur V.K.R. and Lie T.T. (1995), “Experimental Studies on the Fire Resistance of Circular Hollow Steel Columns Filled With

Steel Fibre Reinforced Concrete", IRC Internal Report No. 691, National Research Council of Canada.
4. Klingsch W. and Wuerker K. (1985), "New Developments in Fire Resistance of Hollow Section Structures, Symposium on Hollow Structural Sections in Building Construction", ASCE, Chicago, Illinois, USA.
5. Twilt L., Hass R., Klingsch W., Edwards M. and Dutta D. (1996), "Design Guide 4 for Structural Hollow Section Columns Exposed to Fire", 1st edition, CIDECT.
6. ASCE/SFPE 29 (1999), "Standard Calculation Method for Structural Fire Protection", American Society of Civil Engineers, Reston, VA.
7. AISC (2005), "Steel Construction Manual 13th Edition", American Institute of Steel Construction, Chicago, IL.
8. NBC (2005), "National Building Code of Canada", National Research Council of Canada, Canada.
9. ASTM (2001), "Standard Methods of Fire Test of Building Construction and Materials", Test Method E119-00, American Society for Testing and Materials, West Conshohocken, PA.
10. Meacham, B.J. and Custer, R.P.L., (1992) "Performance-based Fire Safety Engineering: An Introduction of Basic Concepts", Journal of Construction Steel Research Institute, Vol. 7, pp. 35-54.
11. Kodur, V.K.R. (1999), "Performance-Based Fire Resistance Deign of Concrete-Filled Steel Columns", Journal of Construction Steel Research Institute, Vol. 51, pp. 21-36.
12. Parkinson, D.L. and Kodur, V.K.R. (2007), "Performance-Based Design of Structural Steel for Fire Conditions – A Calculation Methodology", International Journal of Steel Structures Vol. 7, No. 3, pp. 219-226.
13. ISO 834 (1975), "Fire Resistance Tests – Elements of Building Construction", International Organization for Standardization, Geneva, Switzerland,
14. ASTM (2001), "Standard Methods of Fire Test of Building Construction and Materials", Test Method E1529-93, American Society for Testing and Materials, West Conshohocken, PA.
15. Magnusson, S.E. and Thelandersson, S. (1970), "Temperature-Time Curves of Complete Process of Fire Development;

Theoretical Study of Wood Fuel Fires in Enclosed Spaces", Civil Engineering and Building Series 65, Acta, Polytechnica, Scandinavia.
16. ASCE 7-05 (2005), "Minimum Design Loads for Buildings and Other Structures", American Society of Civil Engineers, Reston, VA.
17. Eurocode 1 (2005), ENV 1993 1-2: "General Rules – Structural Fire Design", European Committee for Standardization.
18. Kodur, V.K.R. (2005), "Achieving Fire Resistance Through Steel Concrete Composite Construction", Proceedings of 2005 Structures Congress, NY.
19. Kodur V.R. and Lie T.T. (1996), "Fire Resistance of Circular Steel Columns Filled With Fiber-reinforced Concrete", Journal of Structural Engineering, ASCE Vol. 122, No. 7, pp. 776-782.
20. Kodur, V.K.R. and Lie, T.T. (1997), "Evaluation of Fire Resistance of Rectangular Steel Columns Filled With Fiber-Reinforce Concrete", Canadian Journal of Civil Engineering, Vol. 24, pp. 339-349.
21. Bond G.V.L. (1975), "Fire and Steel Construction, Water cooled Hollow Columns", Constrado, Croydon.
22. Klingsch W. and Wittbecker F.W. (1988), "Fire Resistance of Hollow Section Composite Columns of Small Cross Sections", Bergische Universität, Wuppertal, Germany, pp. 103.
23. Kodur V.K.R. and Lie T.T. (1995), "Fire Performance of Concrete-filled Hollow Steel Columns", Journal of Fire Protection Engineering, Vol. 7, No. 3, pp. 89-98.
24. Lie T.T. and Chabot M. (1992), "Experimental Studies on the Fire Resistance of Hollow Steel Columns Filled With Plain Concrete", IRC Internal Report No. 611, National Research Council of Canada.
25. Lie, T.T. and Caron, S.E. (1988), "Fire Resistance of Circular Hollow Steel Columns Filled with Carbonate Aggregate Concrete: Test Results", IRC Internal Report No. 573, National Research Council of Canada.
26. Lie, T.T., Irwin, R.J., and Chabot, M (1991), "Factors Affecting the Fire Resistance of Circular Hollow Steel Columns Filled With

Plain Concrete", IRC Internal Report No. 612, National Research Council of Canada.

27. Grandjean G., Grimault J.P. and Petit L. (1981), "Determination de la durée au feu des profils creux remplis de béton", Rapport final, Commission des Communautés Européennes, Recherche Technique Acier, Luxembourg.
28. Finnish Constructional Steelwork Association (1989), "Fire Technical Design Manual for Composite Columns with Concrete Filled Hollow Steel Sections", Helsinki, pp. 66.
29. Kodur V.K.R. (1997), "Design Equations for Evaluating Fire Resistance of SFRC-filled Steel Columns", ASCE Journal of Structural Engineering, Vol. 124, No. 6, pp. 671-678.
30. Lie T.T. and Chabot M. (1990), "A Method to Predict the Fire Resistance of Circular Concrete Filled Hollow Steel Columns", Journal of Fire Protection Engineering, Vol. 2, No. 4, 111-126.
31. Lie T.T. and Kodur V.K.R. (1996), "Fire Resistance of Steel Columns Filled With Bar-reinforced Concrete", Journal Structural Engineering, ASCE, Vol. 122, No. 1, pp. 30-36.
32. Lie T.T. and Stringer D.C. (1994), "Calculation of Fire Resistance of Steel Hollow Structural Steel Columns Filled With Plain Concrete", Canadian Journal of Civil Engineering, Vol. 21, No. 3, pp. 382-385.
33. Kodur V.R. (1999), "Performance-based Fire Resistance Design of Concrete-filled Steel Columns", Journal of Constructional Steel Research Institute, Vol. 51, pp. 21-36.
34. Kodur V.R. and MacKinnon D.H. (2000), "Fire Endurance of Concrete-filled Hollow Structural Steel Columns", AISC Steel Construction Journal, Vol. 37, No. 1, pp. 13-24.
35. Franssen, Jean –Marc (2005), "SAFIR: A Thermal/Structural Program for Modeling Structures Under Fire", Engineering Journal Vol. 42, No. 3, pp. 143-155.
36. Lie, T.T. and Chabot, M. (1992), "Experimental Studies on the Fire Resistance of Hollow Steel Columns Filled with Plain Concrete", IRC Internal Report No. 611, National Research Council of Canada.

37. Lie, T.T. and Irwin, R.J. (1995), "Fire Resistance of Rectangular Columns Filled with Bar-Reinforced Concrete", Journal of Structural Engineering, Vol. 121, No. 5, pp. 797-805.
38. Chabot, M. and Lie, T.T., (1992), "Experimental Studies on the Fire Resistance of Hollow Steel Columns Filled with Bar-Reinforced Concrete", IRC Internal Report No. 628, National Research Council of Canada.
39. Buchanan, A.H. (2005), "Structural Design for Fire Safety", John Wiley and Sons Ltd., New York, NY.

SHEAR STRENGTH OF HORIZONTALLY CURVED COMPOSITE I-GIRDERS

N E Shanmugam[1], M A Basher[2], A R Khalim[3]

ABSTRACT

The paper deals with steel-concrete composite I- girders curved in plan. Finite element modeling of the composite action in the girders is presented in the paper. Details of the finite element modeling and the non-linear analysis are given along with the information obtained on the behavior of the girders. The accuracy of the modeling is assessed first by comparing the finite element results in respect of curved steel plate girders and straight composite plate girders tested by other researchers. The modeling is then used for the analysis of horizontally curved composite I-girders. Effects of parameters such as curvature, steel flange width and web panel width that affect the behavior of composite girders are considered in the analyses.

INTRODUCTION

Horizontally curved I-girders are often employed in the construction of modern highway bridges. The capacity of curved girders is notably decreased due to the existence of the initial curvature. As the curvature increases, excessive deflections may occur. Such deflections are caused by the tendency to include more vertical and rotational rigid body motion in the displacement field. The vertical displacement and the rotation are not independent but coupled in the horizontally curved

---

[1] Professor, [2] Research student, [3]Associate Professor, Department of Civil and Structural Engineering, Universiti Kebangsaan Malaysia, 43600 UKM Bangi, Selangor D E, Malaysia

I-beams. At the design stage these girders are assumed to act independent of the deck slabs resting on them even though the deck slabs are connected to the girders by means of shear connectors. The advantage of composite action between the steel girders and concrete deck is not considered. The present study is concerned with such composite action in horizontally curved I-girders.

An experimental investigation on full-scale horizontally curved steel plate girders has been carried out to study their overall behavior and to determine the shear strength by Zureick et al (2002). Web plate slenderness (d/t) approximately equal to the largest value permitted for transversely stiffened members in AASHTO (2004) and panel aspect ratio b/d = 1.5 and 3.0 were tested to failure. Shanmugam et al. (2003) investigated the ultimate load behavior and load carrying capacity of medium size plate girders curved in plan. Web openings may need to be provided in these structural members. Lian and Shanmugam (2003) carried out experimental and finite element studies on horizontally curved plate girders containing centrally located circular web openings. Parametric studies have been carried out and simple design method proposed (Lian and Shanmugam, 2004). Jung and White (2006) have reported results obtained from the finite element analyses of the full-scale curved girders tested by Zureick et al (2002). Both the elastic shear bucking and the full nonlinear maximum shear strength responses have been considered.

Slender steel-concrete composite plate girders are used extensively for the construction of short and medium span bridges (Laane and Lebet, 2005). Allison et al [1982] carried out an experimental investigation on steel-concrete composite plate girders under combined shear and negative bending. Shanmugam and Baskar (2003a, 2003b, 2006) studied both experimentally and numerically the effects of combined shear and bending on composite plate girders. Parametric studies using finite element modeling were carried out and a method to determine the shear capacity proposed. This paper is concerned with horizontally curved composite I-girders. Finite element method has been used to investigate the elastic and ultimate load behavior and, parametric studies carried out. Details of the finite element modeling and the results obtained from the analyses are presented herein.

FINITE ELEMENT ANALYSIS

Finite element software LUSAS has been used in the analysis. Three-dimensional models were developed by idealizing the flange, web, and stiffener plates in plate girders using QSL8 semi-loof thin shell element in the LUSAS element library. Concrete slab was idealized by stress elements which are three dimensional hexahedral isoparametric solid continuum elements (HX20) with higher order models capable of modeling curved boundaries. This solid element has 20 nodes with three degrees of freedom at each node representing the three global directions in which it may move. Generally, the shell element can accommodate curved geometry with varying thickness and anisotropic and composite material properties. The element formulation takes account of both membrane and flexural deformations.

The plate girders were modelled as simply supported girders by choosing Z-axes as the vertical axis. The pin-supported condition was simulated by fixing translation in X, Y and Z direction, whilst the rotation about X, Y and Z-axis was left free. Roller conditions were simulated by allowing translations in the X direction only and rotation about the axis being left free.

Material properties and Initial imperfections

In the modelling, steel plate girders were modelled using ungraded Mild Steel in LUSAS material library. Young's Modulus 209 kN/mm^2 and Poisson's ratio equal to 0.3 are defined in the computer pachage. The nonlinear material model used Von Mises yield criterion, an associated flow rule and isotropic hardening, giving three distinct regimes - elastic, perfectly plastic and multi-linear strain hardening respectively.

A perfectly straight and undeformed model will provide different answers from a model with imperfect geometry. In LUSAS an imperfection can be built into the initial model by manually defining the appropriate geometry or it can be arrived at by loading a previous results file, selecting the load case of interest and choosing the LUSAS Data file command and selecting the deformed mesh factor option to create a model having deformed geometry appropriate to the eigenvalue or load case chosen. In this study, initial imperfection of the girders was obtained from the buckling analysis whereby the deformed mesh from the first eigenvalue used for the nonlinear analysis.

Finite element mesh
Regular mesh with element size of 80mm x 80mm defined in the Attributes options tabs are assigned to all surfaces of the plate girders. The mesh shown in Figure 1 was chosen based on convergence studies to determine the optimal mesh that gives a relatively accurate solution and one that takes low computational time. It has been found that the mesh chosen is capable of producing results close to the actual behaviour of the girder.

Loading
Feature based loads are assigned to the model geometry and are effective over the whole of the feature to which they are assigned. Prescribed loads with total prescribed displacement instead were used in this analysis. A Prescribed Displacement defines a nodal movement by either a total or incremental prescribed displacement in global (or

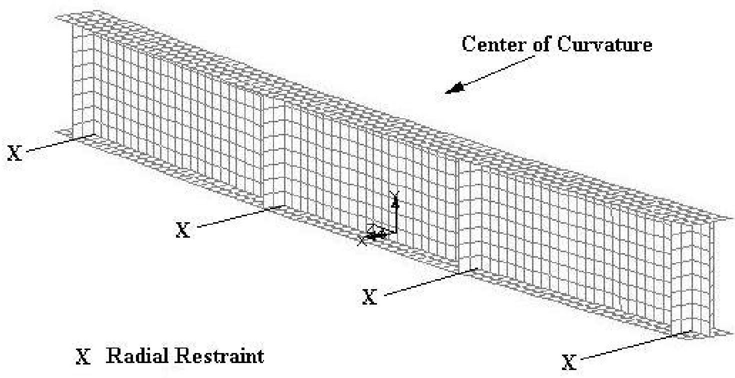

Figure 1 Typical finite element modelling used in the analyses

transformed) axis directions. Variables loaded with a nonzero prescribed variable will automatically be restrained in the required direction.

In *LUSAS*, incremental-iterative solution procedure is used. In this procedure, the total required load is applied in a number of increments. With each increment, a linear prediction of the nonlinear response is made, and subsequent iterative corrections performed in order to restore equilibrium by the elimination of residual forces. The iterative corrections are referred to some form of convergence criteria that indicate to what extent an equilibrium state has been achieved. The nonlinear solution is based on the Newton-Raphson procedure.

Accuracy of the finite element modelling

It is important to establish the accuracy of the finite element modeling before undertaking the analysis of the horizontally curved composite plate girders. Neither experimental nor analytical results could be found for comparison in the literature for such girders. Horizontally curved steel plate girder tested by Zureick et al. (2002) and straight composite plate girders tested by Shanmugam and Baskar (2003, a,b) were, therefore, considered for comparison and to assess the finite element modeling using LUSAS.

Zureick et al (2002) carried out full-scale tests on four steel plate girders identified in the text as S1, S2, S1-S and S2-S of 11.58 m chord length. Transverse stiffeners along the girder length were positioned such that the panel aspect ratio was 3 in the case of S1 and S2 and 1.5 in the case of S1-S and S2-S. The overall depth of the girders was around 1.22 m whilst the top and bottom flanges of around 22.9 mm thick varied in width from 546.6 mm as in the case of S1 and S1-S and, 556.3 mm for S2 and S2-S. The girders S1 and S1-S had a nominal radius of 63.63 m whilst the corresponding value for the girders S2 and S2-S was 36.58 m. The cross-sectional dimensions of the girders are shown in Figure 2 and the overall geometry of the girders in Figure 3. Test set-up and applied loading in the tests are shown in Figure 4. Also shown in Figure 4 are shear force and bending moment diagrams corresponding to the applied loading.

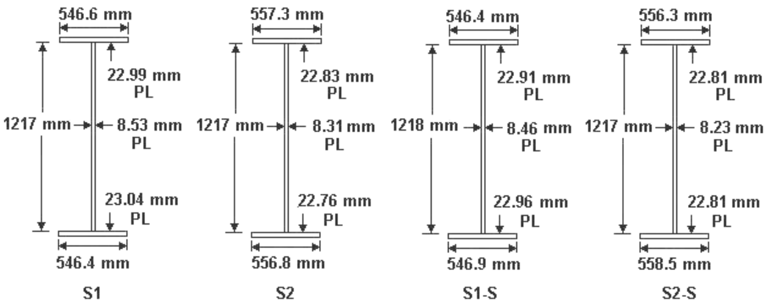

Figure 2 Dimensions of the test girders by Zureick et al (2002)

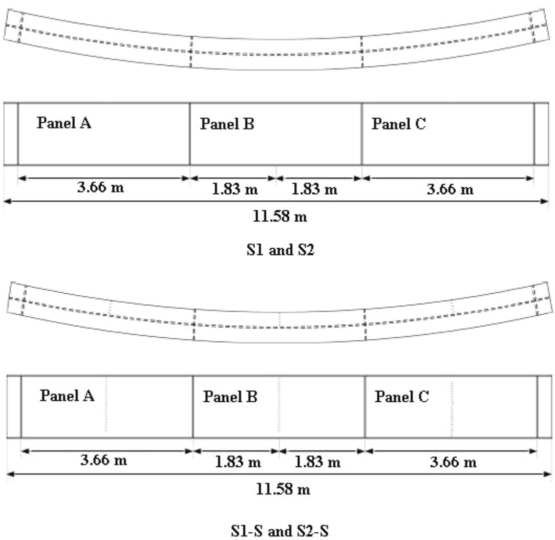

Figure 3 Overall Geometry of the test girders (Jung & White, 2006)

Further details of the test girders may be found in the reference (Jung and White 2006). Typical girder S2-S was analyzed using LUSAS and, load-deflection plots are shown in Figure 5. In the figure, experimental results along with the ABAQUS results given by Jung and White (2006) are also plotted for comparison. It can be seen from the figures that the load-deflection plots obtained from the analyses by LUSAS lie very close to the corresponding experimental and ABAQUS curves thus establishing the accuracy of the computer package LUSAS.

Studies similar to the above were carried out on straight composite plate girders (Shanmugam and Baskar, 2003,a,b). Ten medium-scale composite girders were tested to failure and these girders are identified in the text as CPG1 to CPG10.

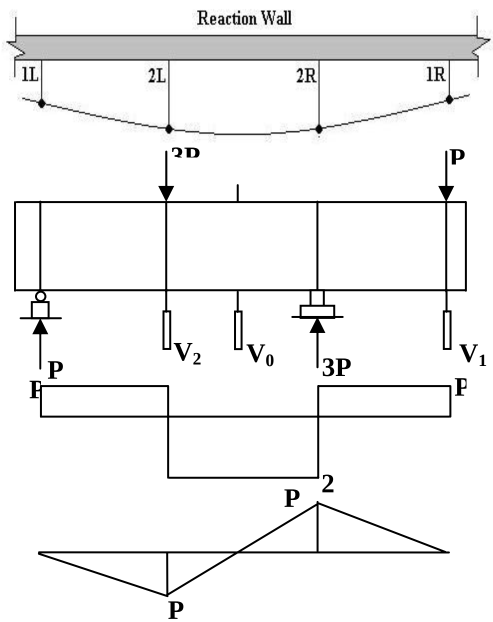

Figure 4 Test Set-up and applied loading (Jung and White, 2006)

Two different web-depth to thickness (*d/t*) ratios viz. 250 and 150 and two different moment/shear ratios were considered. The panel aspect ratio of the web was restricted to 1.5 in all girders. In all composite girders the bond between steel girder and deck slab was achieved by means of shear studs, 19mm dia, 100mm long, welded in two rows.

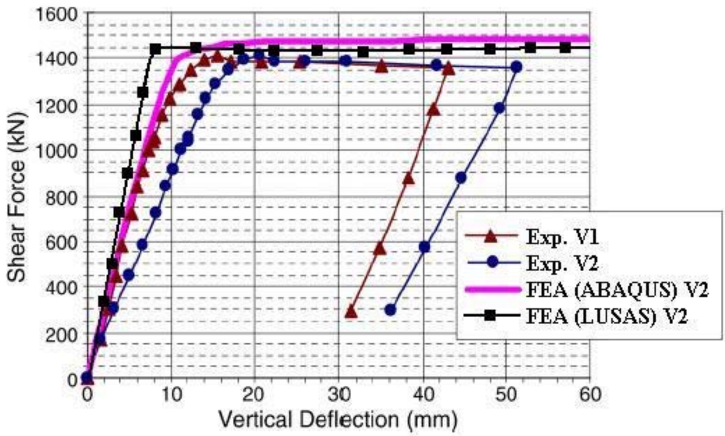

Figure 5 Load-deflection plots for girder S2-S (Zureick et al., 2002)

The width of deck slab was taken as 1000mm with an overall depth of 200mm. The slab width was 1200mm in some girders. Typical girders, CPG5 and CPG6, were analyzed using LUSAS and the corresponding load-deflection plots are given along with the experimental results in Figures 6. It can be seen from the figures that LUSAS predictions lie very close to the experimental results thus proving the validity of the LUSAS analyses of straight composite plate girders.

The results given above in respect of horizontally curved steel plate girder and straight composite girders establish the accuracy of the finite element modeling using LUSAS and the ability of the analyses to account for the horizontal curvature as well as the composite action between the concrete slab and steel plate girders. Having established the accuracy of the modeling using LUSAS it was decided to use the computer package for the analyses of horizontally curved composite plate girders.

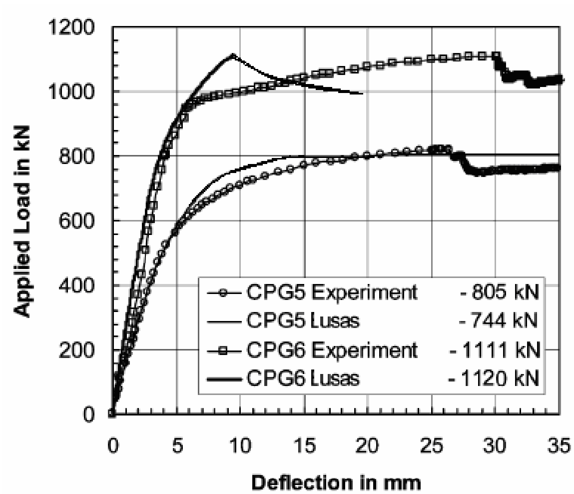

Figure 6 Load-Deflection Plots for CPG5 & CPG6 (Baskar et al., 2003)

HORIZONTALLY CURVED COMPOSITE PLATE GIRDERS

The four steel plate girders, S1, S2, S1-S and S2-S tested by Zureick et al. (2002) are taken as the steel part of the composite girders analysed in this study. To each of these four steel girders, concrete slab of 200 mm thick and 2400mm wide is added at the top flange to act compositely with the steel part. The dimensions of the slab were chosen as per AASHTO recommendations for a composite girder. Full interaction in the composite action is assumed. The resulting four composite girders are identified herein in the text as C1, C2, C1-C and C2-C corresponding to S1, S2, S1-S and S2-S, respectively.

Girder C1 corresponds to the steel girder S1 tested originally by Zureick et al. (2002) to examine the shear strength of a curved web panel of aspect ratio equal to 3. The ratio the web panel length to the radius of curvature was kept as 0.0575; subtended angle of 0.0575 between the cross frame locations, slightly greater than one-half of the maximum value of 0.1 permitted by AASHTO in the unified provisions for design of straight and curved I-girders was adopted (Jung and White, 2006). Girder C1-C was identical to C1 but had an additional intermediate stiffener located at the center of each panel between bearing stiffeners. The resulting web panel ratio in this case was, therefore, equal to 1.5. Girder C2 was similar to C1 but differed only in the radius as 36.58 m thus giving a panel length to radius of curvature ration of about 0.1. This value is close to the AASHTO requirement $L_b / R \leq 0.10$. Girder C2 – C was identical to C1 – C but had a radius of 36.58 m and panel aspect ratio of 1.5. Figure 7 shows the cross-section of a typical composite girder. A detailed finite element modeling was prepared for each of the girders; the finite element mesh of a typical girder is shown in Figure 8. The type of elements used for steel part of the girder and for concrete slab was same as those described earlier in this paper.

The support and loading conditions adopted for the analyses of composite girders are same as those used for steel girders by Zureick et al. (2002) and shown in Figure 4. The vertical support conditions provided for the physical model have been simulated by restraining the corresponding displacements at the nodes along a line across the width of the bottom flange. At the roller support, the girders are free to move along the tangential direction. Suitable restraints by means of truss elements were provided to the girder corresponding to the tube braces used to prevent the lateral torsional buckling of the girders as shown by 1L, 1R, 2L and 2R in Figure 4. Concentrated loads 3P and P as shown in Figure 4 were simulated in the analyses by beans of displacement control. Nominal residual stresses and imperfections for the steel part of the girder have been assumed in the analyses. The results obtained from the finite element analyses using LUSAS are presented for typical girders herein.

RESULTS AND DISCUSSION

The finite element analyses provided detailed output in terms of displacements, stresses, strains, moments and forces. However, for brevity only the most relevant results are presented herein for discussion. Load-vertical deflection plots corresponding to the mid-span (V_2) are shown in Figures 9 and 11 and load-radial deflection plots measured at mid-depth of the central panel in Figures 10 and 12 for typical girders. In each of the figures variations of radial displacement corresponding to the respective steel girders (Jung and White, 2006) are also presented for comparison.

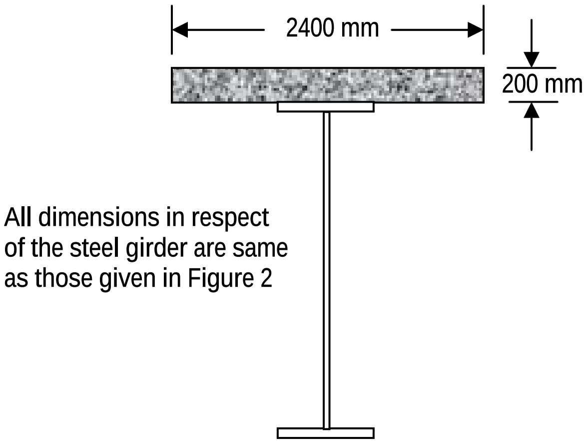

Figure 7 Cross-section of composite girders

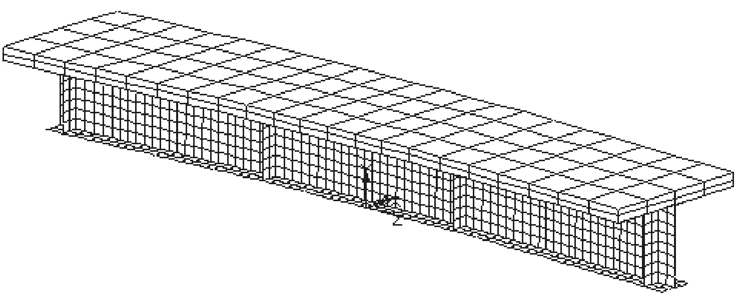

Figure 8 Typical finite element mesh for composite girders

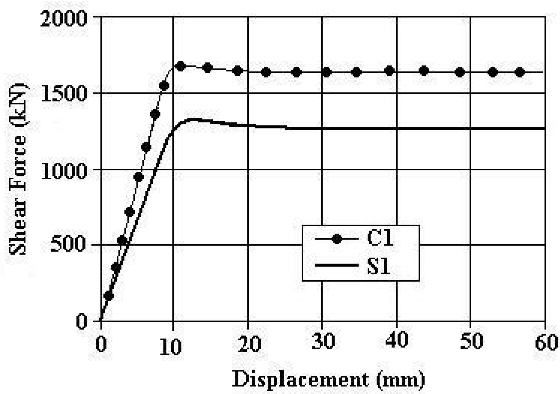

Figure 9 Load-deflection plot for the girder C2

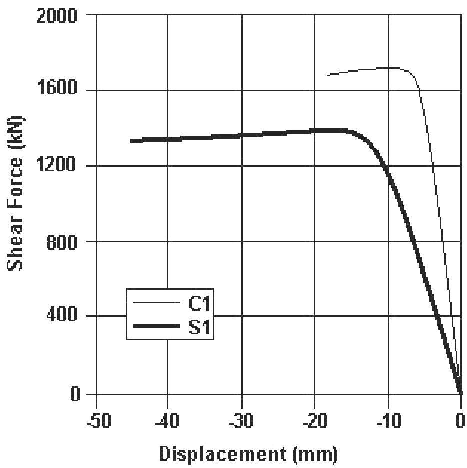

Figure 10 Radial deflection for C1

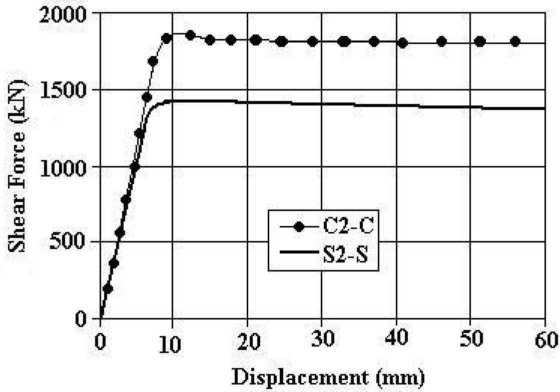

Figure 11 Load-deflection plot for the girder C2 - C

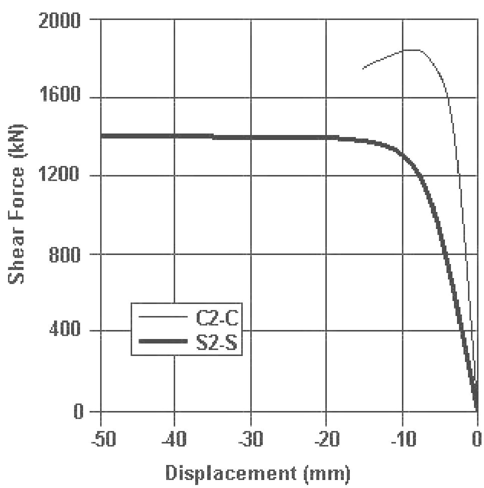

Figure 12 Radial deflection for the girder C2 - C

Elastic behaviour at the initial stages is observed for all the girders and, it becomes nonlinear soon after reaching the ultimate condition. The behaviour of the composite girders is similar to that of the steel girders and enhancement in stiffness and ultimate load-carrying capacity compared to steel girders can be witnessed in all the composite girders. Composite girders exhibit significant gain in the ultimate load capacity, ranging from 28% to 30% over the corresponding values for steel girders. The gain should be attributed to the contribution due to the presence of concrete slab and the composite action. There is some increase in stiffness in respect of the girders C1, C1-C and C2 in particular though not significant. It can be seen that the behaviour of the composite girder is stiffer and stronger compared to the corresponding steel girders.

After the onset of buckling in web panels the girder continues to carry larger load. As the load is increased hence the shear in the webs, out-of-plane deformations continue to grow. Tension field action in the web panels experiencing larger shear force sets in and it grows further with the increase in load. Figure 13 shows such tension field in the composite girder C1 in which the middle panel subject to larger shear force developed tension field first followed by the outer panels. The figure shows two views of the girder, one corresponding to the state soon after reaching the failure load and the other well beyond the failure load. The middle web panel under larger shear appears to have suffered extensive buckling soon after reaching the failure load. As the displacement is increased beyond the failure load, the adjacent web panels are subject to larger deformation, conspicuous from the deflected shape of the web panels as shown in the figure. Load beyond the ultimate condition leads gradually to collapse of the girder. Since the top flange was restrained by concrete slab no buckling could be noticed in the flange except that the flanges bent due to excessive deformations at ultimate load conditions. It should, however, be remembered that full interaction has been assumed between concrete slab and the steel beam and, the behaviour could be different under partial interaction conditions.

Figure 14 shows the load-vertical deflection plots in which the girders having same radius of curvature are grouped together in order to highlight the panel size effect on the behaviour of these girders. Transverse stiffeners in the case of C2 are spaced at 3.66 m centre to

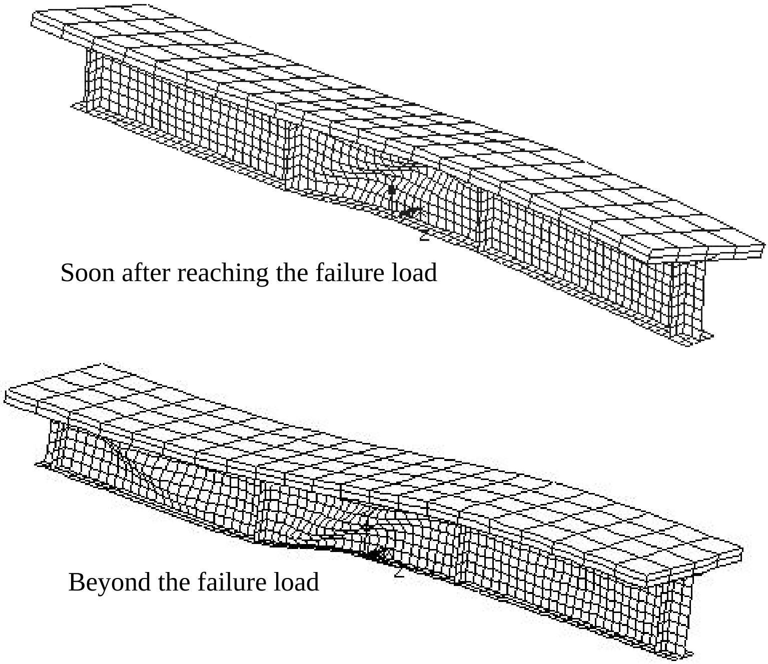

Figure 13 Views after failure of the girder C1

centre whereas in C2-C the spacing is closer, 1.83 m. Thus the effect of web panel size is apparent in the figures in which the girders with smaller panel aspect ratio exhibit larger load carrying capacity and slightly stiffer behaviour. The ultimate load in the case of girders having closely spaced stiffeners is around 13% to 18% higher than that for the girders with widely spaced transverse stiffeners. This type of behaviour is obvious because of the inherent buckling behaviour of these panels under shear loading. Similar observations have been made in the steel girders also (Jung and White, 2006).

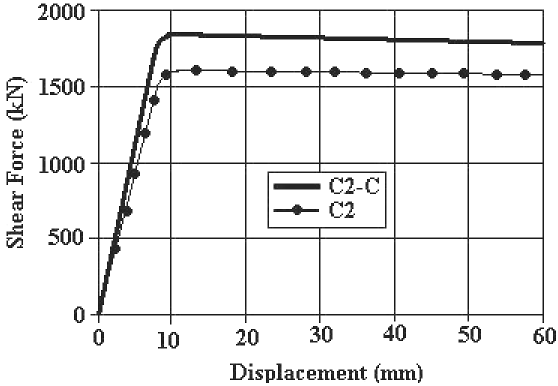

Figure 14 Panel size effect on the behaviour of composite girders

Studies were also carried out to investigate the effect of curvature on the behaviour of composite girders. Figure 15 shows the results obtained from studies on girder C1 in which the radius of curvature was varied from 50 m to 100 m. Results corresponding to a straight composite girder and the girder C1 are also shown in the figure. It is evident from the figure that the curved girders carry less load compared to the straight one and, the drop in load carrying capacity decreases with increase in radius of curvature. For example, the maximum shear at failure for straight girder is 2318 kN and the corresponding value for the girder with radius of curvature equal to 100 m is 2098 kN, a drop of around 10%. The girder with radius curvature of 50 m could carry only 1,578 kN, a drop of around 30% compared to the straight girder.

Figures 16 and 17 show the moment-shear interaction diagrams for the girders C2 and C2-C, respectively. Moment-shear interaction behavior for steel girders S_2 and S_2-S is also shown in the respective figures. Results corresponding to the flange widths, varying from 203.2 mm to 546.6 mm, are presented in these figures. In the analyses with different flange widths, the bearing and intermediate stiffener widths are adjusted to suit the flange dimensions. The maximum shear and

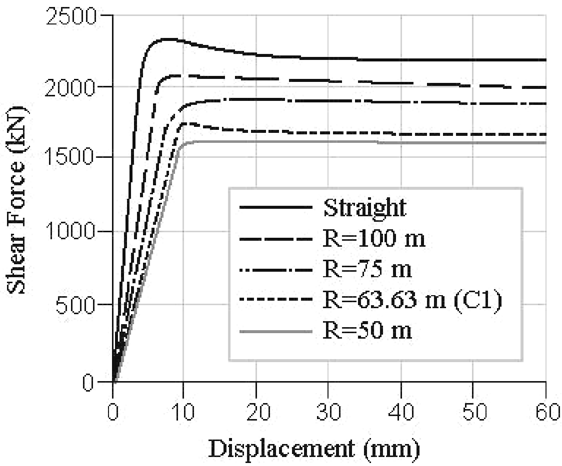

Figure 15 Effect of radius of curvature on composite Girders.

moment obtained from the finite element analyses are normalized with respect to nominal shear resistance V_n and $M_{n(1/3\ rule)}$ as per the recommendations by the American Association of State Highway and Transportation Officials (AASHTO). The simple equation for major axis bending strength provided by AASHTO accounts for the influence of (or interaction with) flange lateral bending. From the finite element results V_{max} can be obtained as the maximum shear force and, the maximum moment for each girder is calculated as $M_{max} = (V_{max}/2)L_b$.

It can be seen from the figures that the normalized shear capacities (V_{max}/V_n) decrease by around 17% as the flange width is reduced from 546.6 mm to 203.3 mm. The nominal shear resistance V_n , independent of flange width, is not affected by the change in the flange width. It should, therefore, be noted that the variation in normalized shear capacities is entirely due to the drop in the maximum shear developed within the inner panel as a result of reduced flange width. Shear-moment interaction for the girders with the change in flange width appears to be influenced significantly by web panel width as shown in the figures. Comparison of Figures 16 and 17 shows that the drop in

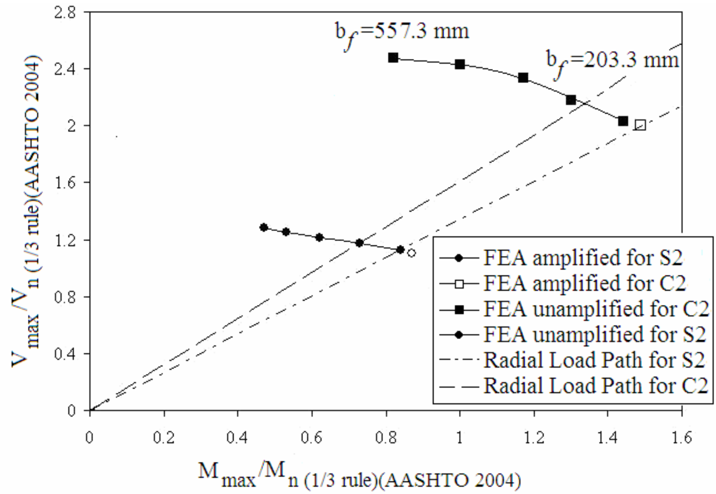

Figure 16 Moment – Shear Interaction for the Girder C2

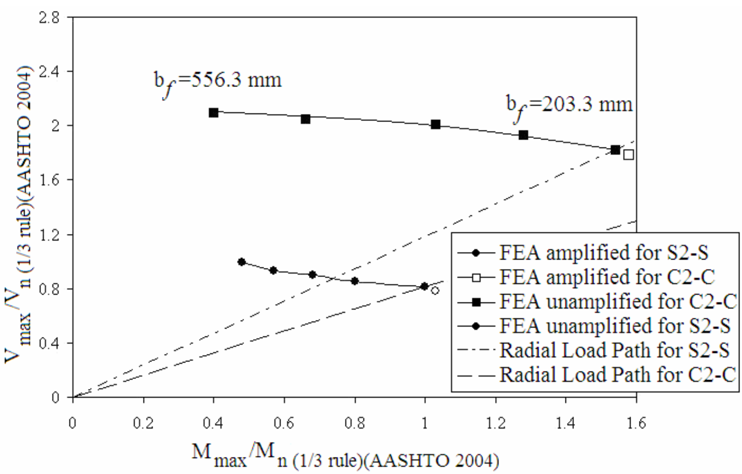

Figure 17 Moment – Shear Interaction for the Girder C2-C

shear capacity, around 17%, occurs with corresponding increase in moment ($M_{max}/M_{n(1/3\ rule)}$) ratio. It is seen that the V_{max}/V_n is larger than the ratio $M_{max}/M_{n(1/3\ rule)}$. The reduction in M_{max} calculated as $(V_{max}/2)L_b$ is small. However, the value of $M_{n(1/3\ rule)}$, compared to the value of V_n, is affected considerably by the flange size. As a result the computed values of $M_{max}/M_{n(1/3\ rule)}$ ratio is significantly larger for smaller flange widths. It can also be noticed in all cases that the amplification factor has negligible influence on shear-moment interaction behaviour. Comparison of the results for composite and steel girders show significant increase in shear capacity for composite girders.

CONCLUSIONS

The studies presented herein show that the elasto-plastic finite element package (LUSAS) employed is capable of predicting the elastic as well as ultimate load behaviour of steel- concrete composite plate girders with sufficient accuracy. The accuracy of the analyses is based on the comparison of the finite results for steel girders and straight composite girders tested earlier by other researchers. Further analyses have been carried out on composite plate girders curved in plan by varying radius of curvature, web panel widths and steel flange widths. It is apparent from the results that accounting of composite action between the concrete deck and steel section yields in larger load carrying capacity. Tension field action in web panels, similar to those observed in straight plate girders, is also observed in horizontally curved composite plate girders. The increase in radius of curvature provides larger load carrying capacity i.e. straight girders carry larger loads compared to the curved ones. It is obvious from the results that larger flange widths provide greater resistance to lateral bending besides giving larger moment capacity.

REFERENCES

Zureick, A. H., White, D. W., Phoawanich, N. and Park, J, “Shear strength of horizontally curved steel I girders – experimental tests.

Final report to Professional Services Industries, Inc. and Federal Highway Administration, March, 2002.
AASHTO, LRFD bridge design specifications. 3rd ed. 2005 Interim provisions, Washington (DC): American Association of State and Highway Transportation Officials; 2004.
Shanmugam, N.E., Mahendrakumar, M. and Thevendran, V., "Ultimate Load Behaviour of Horizontally Curved Plate Girders", Journal of Constructional Steel research, UK, Vol. 49, No. 4, 2003, 509-529.
Lian, V.T. and Shanmugam, N.E., "Openings in Horizontally Curved Plate Girders", Thin-Walled Structures, UK, Vol. 41, No. 2-3, 2003, 245-269.
Lian, V.T. and Shanmugam, N.E., "Design of Horizontally Curved Plate Girder Webs Containing Circular Openings", Thin Walled Structures, UK, Vol. 42, No. 5, 2004, 719-739.
Jung, S.K. and White, D.W., "Shear strength of horizontally curved steel I girders – finite element analysis studies", Journal of Constructional Steel research, UK, Vol. 62, No. 4, 2006, 329-342.
Lääne Ahti, Lebet Jean-Paul, Available rotation capacity of composite bridge plate girders under negative moment and shear, Journal of Constructional Steel Research 61, 305–327, 2005.
Allison, R.W., Johnson, R.P., and May, I.M., (1982). "Tension field action in composite plate girders." Proc. of the Instn. of Civil Engrs, London, V.73, part 2, June, 255- 276
Baskar, K. and Shanmugam, N.E., (2003a). "Steel-concrete Composite Plate Girders Subject to Combined Shear and Bending." Journal of Constructional Steel Research, Vol. 59, n. 4., 531-557.
Shanmugam, N.E. and Baskar, K., (2003b). "Steel-concrete Composite Plate Girders Subject to Shear loading." Journal of Structural Engineering, ASCE, Sep., Vol. 129, n. 9, 1230-1242.
Shanmugam, N.E. and Baskar, K., "Design of Composite Plate Girders under Shear Loading", International Journal of Steel and Composite Structures, Vol. 6, No. 1, 2006, 1-14.

Zureick, A. H., White, D. W., Phoawanich, N. and Park, J, “Shear strength of horizontally curved steel I girders – experimental tests. Final report to Professional Services Industries, Inc. and Federal Highway Administration, March, 2002. **(Page 2, 5, 8, 9)**

AASHTO, LRFD bridge design specifications. 3rd ed. 2005 Interim provisions, Washington (DC): American Association of State and Highway Transportation Officials; 2004. **(Page 2)**

Shanmugam, N.E., Mahendrakumar, M. and Thevendran, V., “Ultimate Load Behaviour of Horizontally Curved Plate Girders”, Journal of Constructional Steel research, UK, Vol. 49, No. 4, 2003, 509-529. **(Page 2)**

Lian, V.T. and Shanmugam, N.E., “Openings in Horizontally Curved Plate Girders”, Thin-Walled Structures, UK, Vol. 41, No. 2-3, 2003, 245-269. **(Page 2)**

Lian, V.T. and Shanmugam, N.E., “Design of Horizontally Curved Plate Girder Webs Containing Circular Openings”, Thin Walled Structures, UK, Vol. 42, No. 5, 2004, 719-739. **(Page 2)**

Jung, S.K. and White, D.W., “Shear strength of horizontally curved steel I girders – finite element analysis studies”, Journal of Constructional Steel research, UK, Vol. 62, No. 4, 2006, 329-342. **(Page 2, 6, 7, 11, 15)**

Lääne Ahti, Lebet Jean-Paul, Available rotation capacity of composite bridge plate girders under negative moment and shear, Journal of Constructional Steel Research 61, 305–327, 2005. **(Page 2)**

Allison, R.W., Johnson, R.P., and May, I.M., (1982). “Tension field action in composite plate girders.” Proc. of the Instn. of Civil Engrs, London, V.73, part 2, June, 255- 276 **(Page 2)**

Baskar, K. and Shanmugam, N.E., (2003a). "Steel-concrete Composite Plate Girders Subject to Combined Shear and Bending." Journal of Constructional Steel Research, Vol. 59, n. 4., 531-557. **(Page 2, 5, 7)**

Shanmugam, N.E. and Baskar, K., (2003b). "Steel-concrete Composite Plate Girders Subject to Shear loading." Journal of Structural Engineering, ASCE, Sep., Vol. 129, n. 9, 1230-1242. **(Page 2, 5, 7)**

Shanmugam, N.E. and Baskar, K., "Design of Composite Plate Girders under Shear Loading", International Journal of Steel and Composite Structures, Vol. 6, No. 1, 2006, 1-14. **(Page 2)**

DESIGN OF TAPERED BEAM-COLUMNS

Xian-Xing Li [1]

INTRODUCTION

Tapered steel members, especially used in rigid gable frames or pitched portal frames, are very popular worldwide. The reason for the wide use of tapered member is due to its high strength-to-weight ratio, high stiffness-to-weight ratio, and speed of erection. Although solution of tapered steel members has become an industrial standard, recognized design rules have not been successfully developed. For example, no provision in North-American steel design codes is available to cover the design of tapered members.

The difficulty and complexity of analysis of tapered members has drawn many researchers' efforts to develop efficient and direct solutions for structural design. Andrade et al (2005), Galambos (1998), and Li (2007) have summarized some of these research works in this field. The fundamental work of Lee et al. (1972, 1981) on the axial compressive buckling and lateral-torsional buckling behaviors of tapered members had been adopted in Appendix F7 of AISC ASD Specification and Commentary (1989). However, this procedure involves series of design charts as aids, which are laborious for design uses and difficult for computer application. Furthermore, this approach is only applicable for the web-tapered members with equal flanges and to the cases where restraining members framing to the restrained columns are free of axial compressions. These are seldom the cases in practice for most metal building applications involving tapered beams and columns.

---

[1] Ph.D., P. ENG., Senior Engineer, SNC-Lavalin Inc., 2275 Upper Middle Road East, Oakville, ONT L6H 0C3, Canada.

Although some of the basic ASD rules for tapered members were transferred to Appendix F3 of the AISC LRFD Specification and Commentary (2002) without a true Limit States basis, these provisions were not included in the new 2005 AISC Specification.

According to Lee et al (1972, 1981) and AISC (1989, 2002), the allowable bending stress due to elastic lateral-torsional buckling is interpolated from two extreme scenarios: one when the smaller end is thin and deep in which the St. Venant's torsional resistance should govern, and the other when the smaller end is thick and shallow in which the warping resistance should control. Therefore, the accuracy of this approach for general configurations between them is compromised. It was found by Li (2007) that this procedure may yields results that are considerably overestimated for elastic lateral-torsional buckling but are significantly underestimated for inelastic lateral-torsional buckling.

On the other hand, restraining members framing to the end of restrained member in a rigid frame are generally subjected to significant axial compressions, which may considerably deteriorate the restraining stiffness. In this case, none of them is a fully effective restraining member to stabilize other restrained members. Therefore, appropriate structural stability analysis is required for rigid frames, without independent consideration by simply separating columns and girders.

In common structural practices, member tapering is a combination of both web and flange tapering in depth, width, and thickness. To reflect the general tapering of all elements of a tapered member, the existing taper concept, which is based on the web depth taper ratio, is to be extended to cater for any kinds of practical tapering configurations.

The purpose of this paper is to develop a general closed-form solution based on the equation formulation and the philosophy of Limit States Design. The axial compressive and flexural resistances as well as their interaction of general tapered beam-columns are investigated and proposed. This proposed procedure is to allow for the conventional analysis and design rules for the prismatic members to be easily extended to the tapered members.

TAPERED COLUMNS

The factored axial compressive resistance of a tapered column can be determined based on the smallest cross-section and the equivalent effective length factor as used by Lee, et al (1972, 1981) and AISC (2002). In this paper, the smallest cross-section is redefined as the one being of the smallest moment of inertia within the member length instead of the cross-section depth. The factored axial compressive resistance of tapered members is proposed to follow the same design criteria for prismatic columns as adopted in AISC (2002) as follow:

$$C_r = \phi A_0 F_y \left[0.658^{\lambda_e^2} \right] \qquad for\ \lambda \le 1.5 \qquad (1a)$$

$$C_r = \phi A_0 F_y \left[\frac{0.877}{\lambda_e^2} \right] \qquad for\ \lambda > 1.5 \qquad (1b)$$

in which, λ_e = equivalent slenderness parameter, defined as

$$\lambda_e = \frac{K_e L}{r_0} \sqrt{\frac{F_y}{\pi^2 E}} \qquad (2)$$

where, subscript 0 denotes the smallest cross-section. A_0, r_0 = effective area and radius of gyration of the smallest cross-section of the member, respectively; K_e, L = equivalent effective length factor and unsupported length of the tapered member, respectively. The axial compressive resistance can be expressed in any other formulae used for prismatic columns specified in steel design codes with the slenderness parameter being substituted by the proposed one, i.e., Eq. (2). Eqs. (1) are used for calculating compressive resistance with in-plane buckling. For out-plane buckling, the column between lateral bracing supports can be approximated as prismatic member which generally doesn't control. Also, the section compactness requirements on the member elements of the smallest cross-section follow the steel design codes.

A rigid frame consists of rigidly jointed tapered members. As an example, a rigid gable frame with tapered members is shown in Fig. 1. Because all members in the gable frame are subjected to significant axial compressions resulted from roof loads, none of them can be considered as a fully effective restraining member. In order to have stability analysis done, however, the rigid frame must be separated into some independent unites to which traditional structural stability analysis methodologies can be applied.

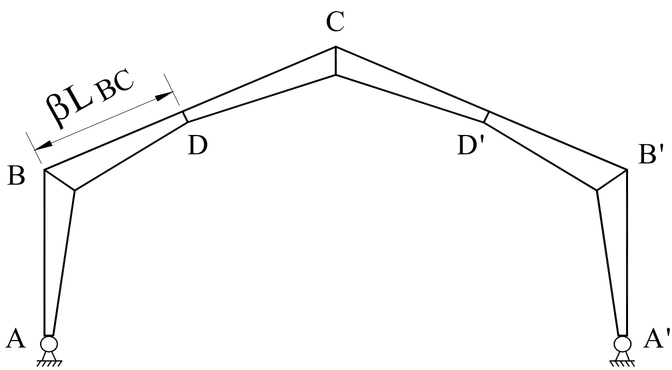

Fig. 1. Rigid gable frame with tapered members

Consider a rigid frame in sidesway permitted condition and subjected to pure axial compressions. From an axial compressive buckling mode, the rigid frame can be separated into several independent pieces with rigid joint referred to as basic stability unites, with the separation points being placed at the inflection points of the buckling mode. A basic stability unit is an independent unit owing to no flexural restraining effects transferring across inflection points. There are no post-buckling bending moments at the end of each component. For a typical rigid gable frame symmetric about the apex as shown in Fig. 1, the basic stability unit consists of the physical column “AB” with simple support at the base “B” and the physical girder “BC” with the apex “C” being an inflection point of the anti-symmetric buckling mode. The anti-symmetric buckling is associated with a far lower buckling load than the symmetric buckling mode for this kind of rigid frame (Timoshenko et al., 1961, and Galambos, 1998). However, a basic stability unit can consist of a column and multiple girders rigidly jointed together, such as for rigid frame with multiple spans.

For a basic stability unit, the effective length factors, K_{ec} for the physical column and K_{eg} for physical girder g, can be expressed as

$$K_{ec} = \frac{\pi}{\chi} \tag{3}$$

$$K_{eg} = \frac{\pi}{\omega_g \chi} \tag{4}$$

where χ and ω_g = effective length parameter of the column and effective length factor ratio of the column to the girder g, respectively, which are determined subsequently.

Each jointed member in the basic stability unit can be equivalently and approximately replaced by a prismatic member having the same smallest cross-section and the same rotational stiffness at the rigid joint in question, $\psi \cdot L$, by using the length conversion factor, ψ. With the aid of the four-moment equation (Bleich, F., 1952) applied to the column-girder joint with modified member lengths and the equilibrium equation applied to the column with actual length, the following overall stability condition of the basic stability unit is derived:

$$\left[\frac{\psi_c \chi}{\tan(\psi_c \chi)} + \psi_c - 1\right] \sum \frac{\psi_g^2 \omega_g^2}{\eta_g \left[1 - \frac{\psi_g \omega_g \chi}{\tan(\psi_g \omega_g \chi)}\right]} - \psi_c{}^2 = 0 \tag{5}$$

in which $\sum$ denotes the summation over all physical girders, i.e., the members in the basic stability unit except the physical column. As a simplification, Eq. (5) can be closely approximated by the following equation:

$$\varpi^2 \left[\frac{\psi_c \chi}{\tan(\psi_c \chi)} + \psi_c - 1\right] + \psi_c{}^2 \eta \left[\frac{\varpi \chi}{\tan(\varpi \chi)} - 1\right] = 0 \tag{6}$$

In Eqs. (5) and (6), η_g = flexural stiffness ratio of the girder g; η = total flexural stiffness ratio of the girders; and ϖ = equivalent effective length factor of girders. They are defined as follow together with ω_g:

$$\eta_g = \frac{I_{c0} / (\psi_c L_c)}{I_{g0} / (\psi_g L_g)} \tag{7a}$$

$$\omega_g = \sqrt{\frac{P_g L_g^{\,2} / I_{g0}}{P_c L_c^{\,2} / I_{c0}}} \tag{7b}$$

$$\frac{1}{\eta} = \sum \frac{1}{\eta_g} \tag{7c}$$

$$\varpi = \max(\psi_g \omega_g) \tag{7d}$$

where, P_c, P_g, L_c, L_g, I_{c0}, I_{g0}, ψ_c and ψ_g = axial compression forces, member lengths, moments of inertia of the smallest cross-sections, and length conversion factors of the physical column and the physical girder g, respectively. The axial compression forces should be determined in a single load cases combination in question during the structural analysis of a rigid frame.

The general taper ratio of a tapered member is defined based on the moments of inertia of two extreme sections as follow:

$$\tau = I_{xL} / I_{x0} \tag{8}$$

where I_x = moments of inertia about major axis. The subscripts 0 and L denote the corresponding quantities at the smallest and largest cross-sections within the overall member, respectively. The general taper ratio synthetically combines the effects of the web depth and thickness tapering as well as the flange width and thickness tapering.

The length conversion factor of a tapered member, ψ, is similar to the Equivalent Length Conversion concept (Lee et al. 1981) which is for tapered members with far end pinned or fixed and is determined by the corresponding charts. In this paper, the length conversion factor is proposed with a simple formula for the convenient use. Based on the computational investigation of the moment-rotation relationship for various tapering configurations and the examination of the resulting fitted functions, the length conversion factor, ψ_c and ψ_g, can be conservatively approximated by the following function:

$$\psi = \frac{\beta^{0.7}}{\tau_N{}^{0.7}} + \frac{1-\beta^{0.7}}{\tau_F{}^{0.3}} \tag{9}$$

in which, subscripts N and F denote the near end which is the rigid joint and the far end which is the inflection point, respectively.
$\beta\,(0 \le \beta \le 1)$ = location factor of the smallest cross-section, defined as the ratio of the distance between the near end (rigid joint) and the smallest cross-section to the overall member length, as shown in Fig. 1.

The exact solution of Eq. (5) can be obtained by using try-and-error method or iteration techniques. However, it is rather expressed by approximate explicit equation for the design purpose. Based on the investigation of curve-fitting functions, the solution of Eq. (6) can be represented by the following approximation with small error:

$$\frac{\pi}{\chi} = \sqrt{4\psi_c + \frac{16}{5}\psi_c\eta + \varpi^2} \tag{10}$$

As an example of a basic stability unit consisting of a physical column and a physical girder which is typical for rigid gable frame, the values of χ computed from the exact solution of Eq. (5) and the approximate solution of Eq. (10) are shown in Fig. 2 for the cases of $\psi_c = 0.2$, $\psi_g\omega_g = 2.0$ and $\psi_c = 1.0$, $\omega_g = 0.0$. The explicit expression of approximate solution of Eq. (10) provides the results in good agreement with exact solutions and remains on the conservative side.

The following example of a rectangular rigid frame under pure axial compressions, as shown in Fig. 3, is used to demonstrate the efficiency and accuracy of the proposed procedure for the effective length factors. This type of rectangular rigid frame is a basic case used by Lee et al. (1972, 1981) to establish the series of design charts for calculating effective length factors of tapered columns, where the top girder and bottom girder, if any, represent the restraining members. In the proposed procedure, the girder under axial compression is not assumed to be an independent restraining member.

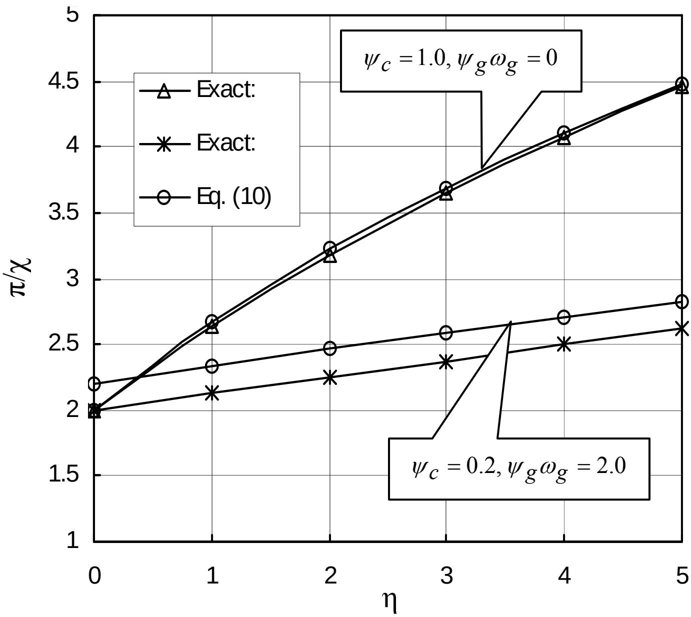

Fig. 2. Effective length factor for rigid gable frames

The columns and top girder are subjected to axial compressions, P and $2P$, respectively. Because the girder midspan is an inflection point of the anti-symmetric buckling mode, the basic stability unit consists of the column and the adjacent half-length of the girder. The proposed effective length factors of Eqs. (3) and (4) are used to obtain the critical buckling load of the column. In this case, $\psi_c = 0.325$, $\eta_g = 3.077$, $\omega_g = 1.414$, $K_{ec} = \pi / \chi = 2.549$, and $(P_c)_{cr} = \pi^2 EI_{c0} / (K_{ec} L_c)^2 =$ *116* KN. The nonlinear finite element method (NFEM) gives $(P_c)_{cr}$ =*127* KN. The predicted value is in good agreement with NFEM result. By considering the girder as an independent restraining member and using the design charts of Lee et al (1981), $K_c = 2.10$, hence $(P_c)_{cr} =$ *171* KN, which is *35%* bigger than the NFEM result. It can be seen that the top girder doest not restrain the columns with full effectiveness.

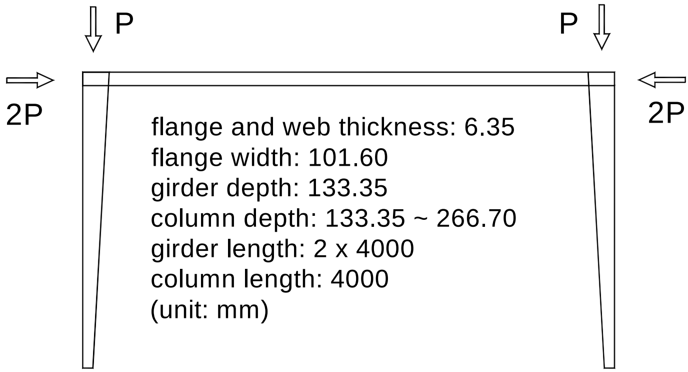

Fig. 3. Rectangular rigid frame

For the top girder, $K_g = 1.803$, $\left(P_g\right)_{cr} = \pi^2 EI_{g0} / \left(K_g L_g\right)^2 = 232$ KN. The ratio of critical compression loads is the same as applied loads, which means that the girder and column will buckle simultaneously. The buckling capacity is dependent up on each other.

Shown in Fig. 4 is an example to demonstrate the accuracy and efficiency of the proposed procedure for the axial compressive resistance. The top end (as rigid joint) is restrained by a guide with rotation inhibited. The guide can be regard as a special restraining girder having an infinite moment of inertia. The bottom end (as far end) is pinned. The predicted axial compressive resistances using the proposed procedure and NFEM results are plotted against the location factor of the smallest cross-section, β . In the NFEM model, the initial out-of-straightness of the column and residual stress pattern are not included. The material is assumed to be the elasto-perfectly plastic, i.e., the beneficial strain hardening is ignored to compensate for the loss of resistance due to the imperfections. It can be seen from Fig. 4 that the predictions of the axial compressive resistance by the proposed approach are in good agreement with the NFEM results. The accuracy of the proposed axial compressive resistance is in an acceptable range, but on the conservative side.

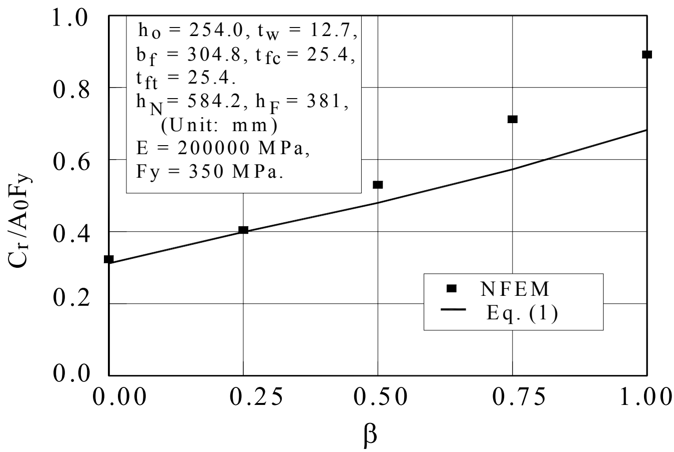

Fig. 4. Axial compressive resistance (see Table 1 for symbols)

It is also noticed from Fig. 4 that the prediction error of the axial compressive resistance increases with the decrease of the effective length factor, or slenderness parameter, as a result of the increase of the location factor of the smallest cross-section, β (in this case, β =1.0 corresponds to λ_e = 1.07). This conservatism provides additional compensation for the strength reduction effect of member imperfections. It has been clear that the influence of member imperfections is especially marked for intermediate slenderness parameters (in the vicinity of λ = 1.0), where plastic squashing and elastic buckling interact the most.

TAPERED BEAMS

Lateral-torsional buckling generally controls the flexural resistance of laterally unsupported beams. The flexural resistance of a tapered beam can be expressed in the similar formulae as for prismatic beams. A general design approach with AISC-type equations for tapered beams has been proposed by Li (2007). This approach is applicable for general combined tapering of web and flanges. The limiting unbraced lengths for the elastic lateral-torsional buckling and full cross-section yielding were explicitly derived.

A simplified approach for flexural resistance is proposed herein. The maximal bending moment for elastic lateral-torsional buckling can be assumed as the bending moment not exceeding two third of the cross-sectional resistance as used for prismatic beams adopted in CAN/CSA-S16.1-04. The factored flexural resistance is then expressed as follow:

When $M_u > 0.67M_{\text{sec}}$

$$M_r = 1.15\phi M_{\text{sec}}\left(1 - \frac{0.28M_{\text{sec}}}{M_u}\right) \le \phi M_{\text{sec}} \tag{11a}$$

When $M_u \le 0.67M_{\text{sec}}$

$$M_r = \phi M_u \tag{11b}$$

in which, M_{sec} and M_u = cross-sectional and elastic lateral-torsional buckling moment resistances about major principal axis, respectively, of the section in question within the unbraced length. The cross-sectional moment resistance is determined by considering local flange buckling and local web buckling due to slenderness of beam elements. For compact section with $I_{yc} \ge I_{yt}$, it equals to the full cross-section yielding resistance, M_p. For cross-sections with non-compact web only, it can be conservatively taken as initial yielding moment, M_y.

Although members in a rigid gable frame can be of multiple piecewise tapering both in flanges and webs along the entire length as fabricated, it can be reasonably assumed that the unbraced member segment between lateral-torsional supports is only of linear web tapering. The elastic lateral-torsional buckling resistance of a tapered beam can the be expressed as the same equation as used by Li (2007):

$$M_u = C_m C_L \alpha_z M_{crs0} \tag{12}$$

where $C_m =$ moment diagram modification factor as proposed by Li (2007); C_L = level loading application factor as proposed by Li (2007); $\alpha_z = 1 + (\tau_s - 1)z / L_b$, moment distribution factor where z = location of the cross-section in question, which is the coordinate along the beam longitudinal axis with coordinate zero placed at the smaller end of the tapered beam segment. M_{crs0} = fundamental buckling moment at the smaller end of the unbraced beam segment with singly symmetric section, which can be derived based on the formulation by Li (2007):

$$M_{crs0} = M_{\beta 0} + \sqrt{M_{\beta 0}^2 + M_{cr0}^2} \tag{13}$$

in which, M_{cr0} , $M_{\beta 0}$ = fundamental lateral-torsional buckling moment and asymmetry differential buckling moment at the smaller end, respectively, which are expressed by

$$M_{cr0} = \frac{\pi}{\alpha_s L_b} \sqrt{EI_y GJ_0 + \left(\frac{\pi E}{L_b}\right)^2 I_y C_{w0}} \tag{14}$$

$$M_{\beta 0} = \frac{13 E h_0}{3(\alpha_s L_b)^2} \left(I_{yc} - I_{yt}\right) \tag{15}$$

in which, I_y, I_{yc}, I_{yt} = moments of inertia of the cross-section, the compression and tension flanges about minor-axis of the cross-section, respectively; h = distance between flange centroids instead of the clear distance of flanges; L_b = unbraced member length between adjacent lateral-torsional bracings. In Eqs (14) and (15),

$$\alpha_s = \sqrt{\frac{1+\tau_s}{2}} \ , \quad \tau_s = \frac{I_{xL} / y'_{cL}}{I_{x0} / y'_{c0}} \tag{16}$$

where τ_s = cross-section modulus taper ratio; I_x and y'_c = moment of inertia about the major-axis and distance from center of gravity of the cross-section to the centroid of compression flange, respectively. The subscripts 0 and L in Eqs. (12) through (16) denote the smallest and the largest cross-sections within the unbraced length, respectively.

In the derivation of Eq. (15), a more precise approximation to the asymmetry coefficient, β_x, is proposed and incorporated as follow:

$$\beta_x = \frac{0.87\, h\left(I_{yc} - I_{yt}\right)}{I_y} \tag{17}$$

To demonstrate the accuracy and efficiency of the proposed approach, Fig .5 depicts the comparison of the flexural resistances at the larger end between the predictions of Eqs. (11) with $\phi = 1.0$ and the corresponding simulations by NFEM for the example as shown. The tapered beam has singly symmetric I-shaped section with member tapering on the web element. The elasto- perfectly plastic material is assumed. The member is simply supported and subjected to an end moment applied to the larger end. Appendix F3 of AISC (2002) is not applicable for the case of singly symmetric sections. It can be seen from the Fig. 5 that the proposed approach predicts the results being in good and conservative agreement with the NFEM results.

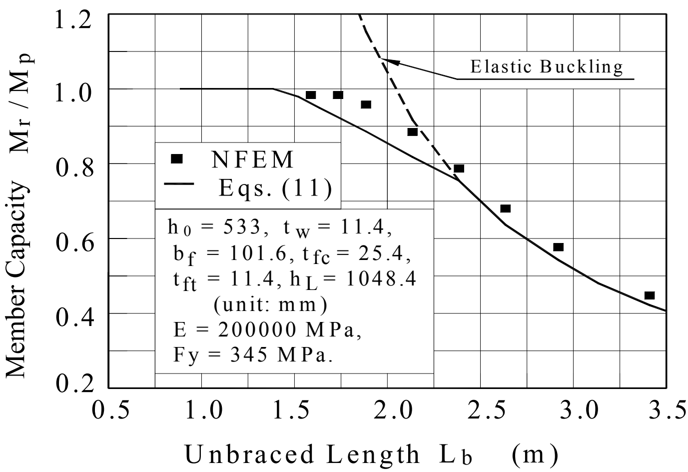

Fig. 5. Inelastic buckling moments for singly symmetric sections (see Table 1 for symbols)

As another example, the tapered beam with doubly symmetric section is investigated. The web depth taper ratio, the material, and the support conditions remain the same as the previous example in Fig. 5. The flexural resistance predicted by the NFEM, the equations in Appendix F3 of AISC (2002), and the proposed approach with $\phi = 1.0$, respectively, are shown in Fig. 6. It can be seen that the proposed predictions are in close agreement with the NFEM results. The comparison between these predictions shows that the predictions of AISC (2002) are sometimes unconservative for elastic lateral-torsional buckling, but considerably conservative in the case of inelastic lateral-torsional buckling, as was found by Li (2007).

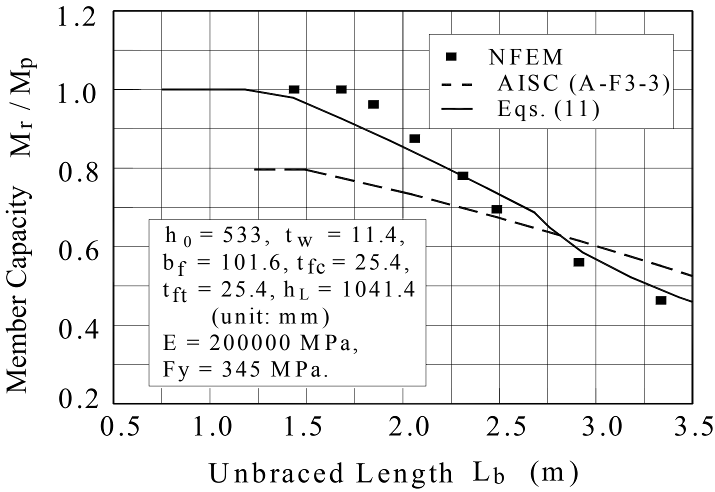

Fig. 6. Inelastic buckling moments for doubly symmetric sections (see Table 1 for symbols)

TAPERED BEAM-COLUMNS

A tapered beam-column subjected to combined axial compression and bending moment must account for the limit states: cross-sectional failure, overall buckling failure, and lateral-torsional buckling failure. The strength of the tapered beam-columns can be expressed by interaction equations accounting for the different limit states. By referencing steel design codes for prismatic members, the same interaction equation is proposed for tapered beam-columns in the following general form:

$$\frac{U_c C_f}{C_r} + \frac{U_x M_{fx}}{M_{rx}} + \frac{U_y M_{fy}}{M_{ry}} \leq 1.0 \tag{18}$$

where C_r = ultimate compressive resistance. For in-plane lateral buckling, Eqs. (1) are used for the calculation. The flexural resistance, M_r, is calculated from Eqs (11). U_c, U_x, and U_y are the interaction factors depending on the limit states and cross-section compactness. These factors are proposed to remain same as for prismatic members. For AISC (2005) with $0 \le I_{yc}/I_y \le 0.9$, $U_c = 1$ & $U_x = U_y = 8/9$ for $C_f / C_r \ge 0.2$; $U_c = 1/2$ & $U_x = U_y = 1$ for $C_f / C_r < 0.2$.

The axial compressive resistance of a tapered member is a global design parameter that is determined based on the smallest cross-section but applicable to every cross-section within the member length on which the equivalent effective length factor is calculated. For any cross-section being designed within this length, it is neither modified by its cross-section area nor by its moment of inertia.

In order to validate and demonstrate the application and capability of the proposed procedure, a design example for a rigid gable frame is illustrated in Appendix. The interaction ratios for three critical segments of the tapered column and the girder are listed in tables. The failure load based on the nonlinear finite element analysis is also provided. The prediction of the strength of the structure designed based on the proposed procedure is reasonable and remains on the conservative side as compared with the NFEM result, which is the ratio of the applied load level to the factored failure load level. It can be seen that the proposed closed-form solution for tapered members is developed with straightforward calculations, which is analogous to the design procedure for prismatic members. Therefore, the proposed solution is user-friendly for and readily applicable to structural design.

CONCLUSIONS

A closed-form solution for the design of tapered steel beam-columns has been proposed. This approach, equation-formulated and derived from the stability theories and conventional design rules for prismatic members, can be used for design of general tapered members.

Following conclusions and comments were drawn:

1. Tapered steel members with combined general tapering on flange width, flange thickness, web depth, and web thickness, can be systematically analyzed by the introduction of the general taper ratio, τ , and taper ratio of section modulus, τ_S .

2. Columns and girders in rigid frames may not able to independently restrain jointed members due to the fact that the large axial force deteriorates the restraining stiffness.

3. The effective length factor of tapered column in a rigid frame is determined by introducing the concept of the basic stability unit. A rigid frame subjected to pure compression forces can be separated into a series of independent basic stability unites based on buckling mode.

4. The axial compressive resistance is proposed based on the same formula as for prismatic members with the slenderness parameter being substituted by the proposed one.

5. Equations for calculation of inelastic lateral-torsional buckling resistance of tapered beams are proposed which are similar to the formulae used for prismatic beams with doubly symmetric sections. These equations are in simple forms and yield good results.

6. The interaction equation of tapered beam-columns subjected to combined axial compressions and bending moments follows the same equation as for prismatic members, which gives rational results.

7. The proposed procedure follows the same philosophy as for prismatic members and is readily applicable to design practices without limitation of cross-sectional symmetry (single or double). It simply extends the conventional design procedure for prismatic members to tapered members.

REFERENCES

AISC 2005. Load and Resistance Factor Design Specification for Structural Steel Buildings. American Institute of Steel Construction, Chicago, IL.

AISC 2002. Load and Resistance Factor Design Specification for Structural Steel Buildings. American Institute of Steel Construction, Chicago, IL.

AISC 1989. Specification for Structural Steel Buildings: Allowable Stress Design and Plastic Design. American Institute of Steel Construction, Chicago, IL.

Andrade, A. and Camotim D. 2005. Lateral-Torsional Buckling of Singly Symmetric Tapered Beams: Theory and Application. ASCE Journal of Engineering Mechanics, 131(6): 586-597.

Bleich, F. 1952. Buckling Strength of Metal Structures. McGraw-Hill Book Co.

CAN/CSA-S16.1-04. Limit States Design of Steel Structures. Canadian Standards Association, Rexdale, Ontario.

Galambos, T. V. 1998. Guide to Stability Design Criteria for Metal Structures. John Wiley & Sons, Inc.

Lee, G. C., Ketter, R. L., Hsu, T. L. 1981. Design of Single Story Rigid Frames. Metal Building Manufactures Association, Cleveland, Ohio.

Lee, G. C., Morrell, M. L., and Ketter, R. L. 1972. Design of Tapered Members. Welding Research Council Bulletin, No. 173.

Li, X. X. 2007. Flexural Strength for General Lateral-Torsional Buckling. ASCE Journal of Structural Engineering, 133(5): 674-682.

Timoshenko, S. P. and Gere, J. M. 1961. Theory of Elastic Stability, McGraw-Hill Book Co.

APPENDIX - ILLUSTRATION OF APPLICATION

Following illustrated is a design example of a symmetric rigid gable frame with tapered steel members as shown in Fig. 1. Singly symmetric I-shaped sections are used for the columns and girders. The yield stress of steel is F_y = 350 MPa, and the resistance factor is taken as ϕ = 0.9. The roof girder slope is 2:12. The factored uniformly distributed load on the frame girders is 27.5 kN/m. The lateral restraints are provided such that overall lateral buckling about weak axis due to axial compression is not critical and excluded in this example.

The size and geometry of the members, design parameters for compression, and axial compressive resistances are summarized in Table 1. The factored forces with second-order effects, design parameters for bending, and flexural resistances are summarized in Table 2. The design parameters required for the proposed procedure are hand-calculated. In Table 2, the design checks are based on three critical sections: 1) the larger end of the top segment of the column; 2) the larger end of the knee segment of the roof girder; and 3) the smaller end of the crown segment of the girder. The results of the interaction ratios for these three critical sections are shown in Table 2. The maximum interaction ratio is 0.95 for the roof girder.

Failure analysis using nonlinear finite element method (NFEM) (COSMOSM 2.85) is also carried out. The material is assumed to be elastic-perfectly plastic. Geometrical nonlinearity is included. Rigid lateral restraints are attached to both flanges at locations with L_b specified in Table 2. A 0.5 kN lateral force is applied to the compression flange of each member segment to initiate possible side sway mode failure. Member imperfections on geometry and material are not included.

The theoretical ratio of the applied load level to the factored failure load level is 0.78. As expected, the predicted maximum interaction ratio, 0.95, is bigger than the theoretical ratio by NFEM. This is because the interaction equation accumulates all kinds of possible conservative estimates regarding the interaction factors, the axial compressive and flexural resistances, and ignoring restraining effects of adjacent segments. However, the predicted overall strength by the proposed procedure still corresponds well with the failure load by NFEM and remains on the conservative side. It is necessary to make certain allowance for those effects present in real steel structures, e.g., initial lack of straightness, residual stresses, lateral and torsional bracing stiffness, etc., that have not been considered in NFEM.

Table 1. Size and geometry of members, design parameters for compression, and axial compressive resistances

Member	h_0 (mm)	h_L (mm)	t_w (mm)	b_{fc} (mm)	b_{ft} (mm)	t_{fc} (mm)	t_{ft} (mm)	Length (mm)
AB	482.5	1532.5	18	350	350	40	25	8000
DB	782.5	1532.5	18	350	350	40	25	14000
DC	790	1025	14	350	350	30	20	16000
Member	τ_N	τ_F	ψ	A_0 (mm^2)	L (mm)	K_e	λ_e	C_r (kN)
AB	12.81	1.0	0.168	30850	8000	2.307	1.148	5597
CB	5.68	1.78	0.522	28210	30000	0.880	1.046	5621

Symbols: h_0, h_L = distance between flange centroids at the smallest and the largest cross-sections, respectively; t_w = web thickness; b_{fc}, t_{fc} = compression flange width and thickness, respectively; and b_{ft}, t_{ft} = tension flange width and thickness, respectively; τ_N, τ_F = taper ratio at the near and the far end, respectively; A_0 = cross-sectional area of the smallest section; L = overall member length; K_e = equivalent effective length factor; λ_e = equivalent slenderness parameter; C_r = factored compressive strength.

Table 2. Factored forces, design parameters for bending, flexural resistances, and interaction ratios

End segment of	M_f (kN-m)		C_f (kN)	L_b (mm)	h_0 (mm)	τ_s	C_m	C_L
	Start	End						
AB	4254	6807	825	3000	1106	1.434	1.034	1.0
DB	3264	6807	944	6000	1179	1.332	1.137	0.995
DC	1509	1147	877	6000	912	1.111	1.0	0.996
Critical section of	M_{crs0} (kN-m)	M_u (kN-m)	$M_{\sec}$ (kN-m)	M_r (kN-m)	U_c	U_x	Interaction Ratio	
AB	32405	48343	9374	8436	0.5	1.0	0.88	
DB	9081	13684	9374	7841	0.5	1.0	0.95	
DC	5583	5560	3757	3152	0.5	1.0	0.56	

Symbols: M_f = factored bending moment; C_f = factored axial compression; L_b = unbraced member length; τ_s = cross-section modulus taper ratio; C_m = moment diagram modification factor; C_L = level loading application factor; M_{crs0} = fundamental lateral-torsional buckling moment at the smaller end; M_u = cross-sectional resistance; $M_{\sec}$ = elastic lateral-torsional buckling moment resistance; M_r = factored flexural resistance; U_c, U_x = interaction factors for compression and bending.

POST-BUCKLING BEHAVIOR OF COLD-FORMED STEEL LIPPED CHANNEL COLUMNS AFFECTED BY DISTORTIONAL/GLOBAL MODE INTERACTION

Pedro Borges Dinis[1] and Dinar Camotim[2]

ABSTRACT

This paper reports the results of a numerical investigation concerning the elastic and elastic-plastic post-buckling behavior of cold-formed steel lipped channel columns affected by distortional/global (flexural-torsional) buckling mode interaction. The results presented and discussed were obtained by means of analyses performed using the finite element code ABAQUS and adopting column discretizations into fine 4-node isoparametric shell element meshes. The columns analyzed (i) are simply supported (locally/globally pinned end sections that may warp freely), (ii) have cross-section dimensions and lengths that ensure equal distortional and global (flexural-torsional) critical buckling loads, thus maximizing the distortional/global mode interaction effects, and (iii) contain critical-mode initial geometrical imperfections exhibiting different configurations, all corresponding to linear combination of the two "competing" critical buckling modes. After briefly addressing the lipped channel column "pure" distortional and global post-buckling behaviors, one presents and discusses in great detail a fair number of numerical results concerning the post-buckling behavior of similar columns experiencing strong distortional/global mode interaction effects. These results consist of (i) elastic (mostly) and elastic-plastic non-linear equilibrium paths, (ii) curves or figures providing the evolution of the deformed configurations of several columns (expressed as linear combination of their distortional and global components) and, for the elastic-plastic columns, (iii) figures enabling a clear visualization of (iii_1) the location and growth of the plastic strains and (iii_2) the characteristics of the failure mechanisms more often detected in the course of this research work.

[1] Assistant Professor and [2]Associate Professor, Department of Civil Engineering, ICIST/IST, Technical University of Lisbon, Av. Rovisco Pais, 1049-001 Lisbon, Portugal.

INTRODUCTION

Most cold-formed steel members display very slender thin-walled open cross-sections, a feature making them highly susceptible to several instability phenomena, namely (i) *local* (local-plate or distortional) and (ii) *global* (flexural or flexural-torsional) buckling – see figures 1(a)-(d). Moreover, depending on the member length and cross-section shape/dimensions, any of these buckling modes can be critical. However, since several commonly used cold-formed steel member geometries may lead to rather similar distortional and global buckling stresses, the corresponding post-buckling behavior (elastic or elastic-plastic), ultimate strength and failure mechanism are likely to be strongly affected by the interaction between these two buckling modes.

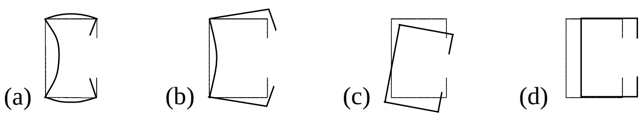

Figure 1. Lipped-channel column (a) local-plate, (b) distortional, (c) flexural-torsional and (d) flexural (cross-section) buckling mode shapes

It has been well known for quite a long time that cold-formed steel members exhibit stable *local-plate* and *global* elastic post-buckling behaviors with clearly different post-critical strength reserves: rather high in the first case and quite low in the second. On the other hand, fairly recent studies have shown that (i) the *distortional* post-buckling behavior fits somewhere in the middle of the two previous ones (in kinematic and strength terms) and (ii) exhibits a non-negligible asymmetry with respect to the direction of the flange-stiffener motion (outward or inward) – *e.g.*, see the works of Kwon & Hancock (1993), Prola & Camotim (2002), Camotim & Silvestre (2004) or Silvestre & Camotim (2006).

Concerning the mode interaction phenomena that may affect the column post-buckling behavior and strength, the ones stemming from the nearly simultaneous occurrence of local-plate and global buckling are, by far, the better understood – this is attested by the fact that their effects are already taken into account by virtually all current hot-rolled and cold-formed steel design codes, either through the well-known "plate effective width" concept or by means of the much more recent (but increasingly popular) "Direct Strength Method" (*e.g.*, Schafer 2005, 2008). On the other hand, the influence of local-plate/distortional mode interation effects on the post-buckling behavior and strength of lipped channel columns has attracted the attention of several researchers in the recent past (*e.g.*, Schafer & Peköz 1999, Yang & Hancock 2004, Ungureanu & Dubina 2004, or Dinis *et al.* 2005, 2007) – it is worth noting that some of the investigations carried out have already led to the development and calibration of novel applications (design curves) of the Direct Strength Method (*e.g.*, Yang & Hancock 2004, Hancock *et al.* 2007, Camotim *et al.* 2008 or Silvestre *et al.* 2007, 2008a,b).

However, to the authors' best knowledge, there are no existing studies addressing the influence of the distortional/global buckling mode interaction on the post-buckling behavior and ultimate strength of cold-formed steel columns (or any other members, for that matter)[1]. Therefore, the aim of this paper is to present and discuss a set of numerical results concerning the (i) post-buckling behavior (elastic and elastic-plastic), (ii) ultimate strength and (iii) failure mode nature of cold-formed steel lipped channel columns affected by distortional/global (flexural-torsional) mode interaction. In order to enable a thorough assessment of all possible mode interaction effects, one analyzes columns with (i) the cross-section dimensions and material properties given in table 1, which ensure that the distortional buckling load is considerably lower than its local-plate counterpart, and (ii) a carefully selected length value, in order to guarantee that the distortional (D – multiple half-waves) and global (G – single half-wave) buckling loads coincide[2].

Table 1. Lipped channel column cross-section dimensions and elastic constants

b_w (mm)	b_f (mm)	b_s (mm)	t (mm)	E (GPa)	ν
150	110	17.5	2.4	210	0.3

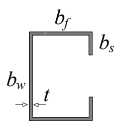

[1] Nevertheless, one must mention that a very recent work of Hancock *et al.* (2007) includes a very brief allusion to the distortional/global buckling mode interaction – however, this is done in the context of the analysis of columns with a rather complex (one may even say somewhat "artificial") cross-section shape and without presenting any further results or comments.

[2] Moreover, the selection of the column cross-section dimensions has also to satisfy two additional conditions: (i) competing ("pure") buckling modes with odd half-wave numbers, so that the maximum deformation occurs at mid-span (although this feature is by no means essential, it renders the presentation of the results much easier) and (ii) no higher-order distortional buckling mode "close" to the distortional/global modes under consideration – this last condition was particularly hard to enforce (for the cross-section dimensions chosen, there is a *12%* buckling load gap).

One analyzes a fairly large number of columns that only differ in the initial geometrical imperfection configuration – the various configurations consist of linear combinations of the competing distortional and global buckling mode shapes with amplitudes (mid-span flange-lip corner vertical displacements) of (i) *10%* of the wall thickness *t* (distortional mode) and (ii) *L/1000* (global mode). All numerical results presented were yielded by finite element analyses carried out in the code ABAQUS (HKS 2002) that (i) adopt member discretizations into fine 4-node isoparametric shell element meshes (element length-to-width ratio roughly equal to *1* – fig. 2(b) illustrates the meshes used) and (ii) model the simply supported conditions by imposing null transverse displacements at all end section nodes – for a detailed account of all modeling issues, the reader is referred to the works of Dinis & Camotim (2006, 2008) or Dinis *et al.* (2007).

Initially, one performs column buckling analyses, in order (i) to select the most appropriate member length (*i.e.*, the one maximizing the D/G interaction) and also (ii) to obtain the associated buckling mode shapes, required to define the initial geometrical imperfections. Next, one addresses the pure distortional and global elastic post-buckling behaviors, which are deemed not affected by D/G interaction. Finally, one presents and discusses the results concerning the column post-buckling behavior and ultimate strength under D/G interaction, which comprise (i) several elastic (mostly) and elastic-plastic non-linear post-buckling equilibrium paths, (ii) curves and figures providing the evolution, along the elastic paths, of the deformed configurations of several columns (expressed as a combination of their distortional and global components) and, for the elastic-plastic columns, (iii) figures enabling a clear visualization of (iii_1) the location and growth of the plastic strains and (iii_2) the characteristics of the failure mechanisms more frequently detected in the course of this research work – by analyzing members with different yield stresses, one may also assess how the D/G mode interaction effects vary with the yield-to-critical stress ratio.

BUCKLING BEHAVIOR – LENGTH SELECTION

The curves shown in figure 2(a) provide the variation, with the column length L (logarithmic scale), of (i) the ABAQUS critical load P_{cr} and (ii) the single-wave buckling load $P_{b.1}$, yielded by finite strip analyses performed with CUFSM$_{2.6}$ (Schafer 2003). As for figure 2(b), it shows the ABAQUS distortional and flexural-torsional buckling mode shapes of the $L=222\,cm$ column. These buckling results prompt the following remarks:

(i) The ABAQUS buckling curve exhibits three distinct zones, corresponding to (i_1) 1-4 half-wave local-plate buckling, (i_2) 1-3 half-wave distortional buckling and (i_3) single half-wave global buckling.

(ii) The black and white dots identify the practically coincident minimum single half-wave distortional critical loads yielded by the $\text{CUFSM}_{2.6}$ and ABAQUS analyses ($P_{cr.D}=203.7\,kN$), which correspond to $L_D=76\,cm$.

(iii) As clearly shown in figure 2(a), the $L_{D/G}=222\,cm$ has *practically identical* distortional and global critical loads ($P_{cr.D}=203.6\,kN$ and $P_{cr.G}=203.9\,kN$)[1], associated with three and single half-wave buckling modes (see fig. 2(b)). Obviously, the post-buckling behavior and ultimate strength of such column will be highly affected by *distortional/global* mode interaction.

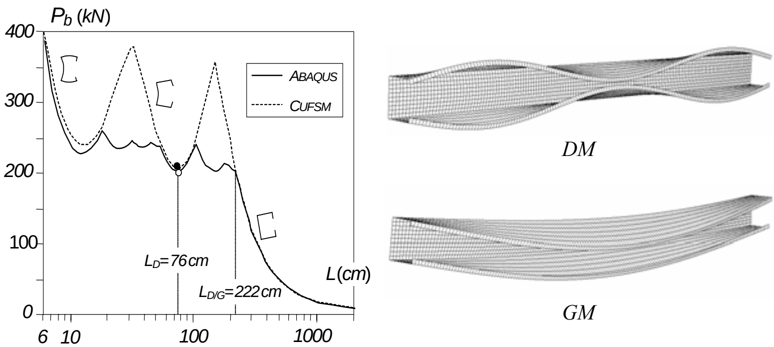

(a) (b)

Figure 2. (a) Column buckling curves and (b) distortional and global (flexural-torsional) buckling mode shapes of the $L_{D/G}=222\,cm$ column

DISTORTIONAL AND GLOBAL POST-BUCKLING BEHAVIORS

One begins by presenting numerical results concerning the *pure* distortional and global column post-buckling behaviors (*i.e.*, without D/G mode interaction). Six columns are analyzed, with three lengths: (i) $L_D=76\ cm$ ($P_{cr}=203.6\,kN$), (ii) $L_{G.1}=300\,cm$ ($P_{cr}=119.9\,kN$) and (iii) $L_{G.2}=900\,cm$ ($P_{cr}=28.9\,kN$) – note that the $L_{G.1}$ and $L_{G.2}$ columns have critical loads equal to *59%* and *10%* of the one

[1] Despite the extreme closeness of the distortional and global buckling loads, the ABAQUS analyses never yielded "combined" buckling modes – such combined modes were obtained for columns with equally close local-plate and distortional buckling loads (*e.g.*, Dinis *et al.* 2007).

associated with D/G interaction ($L_{D/G}$=*222 cm*). For each length, the columns contain either *positive* or *negative* critical-mode geometrical imperfections, *i.e.*, (i) L_D columns with distortional imperfections of magnitude ±*10%* of the wall thickness *t* (positive and negative mean mid-span *inward* and *outward* flange-lip motions), and (ii) L_G columns with global imperfections with mid-span *web chord rotations* equal to ±*0.016 rad*[1] (positive and negative mean *clockwise* and *counterclockwise* rotations).

Figures 3(a)-(b) show the upper portions ($P/P_{cr}>0.6$) of the post-buckling equilibrium paths (i) P/P_{cr} *vs.* v/t (v is the mid-span top flange-lip corner vertical displacement), for the two L_D columns, and (ii) P/P_{cr} *vs.* β (β is the mid-span web chord rotation), for the four L_G columns – also shown are a few deformed configurations of column mid-span cross-sections at advantage post-buckling stages. These post-buckling results lead to the following conclusions:

(i) The L_D and $L_{G.2}$ columns exhibit the expected stable distortional and global post-buckling behaviors (*e.g.*, Camotim *et al* 2005): while the L_D columns exhibit a fair amount of post-critical strength reserve and a clearly visible asymmetry (the inward column is a bit stiffer), the $L_{G.2}$ ones display little post-critical strength and perfectly symmetric equilibrium paths.

(ii) However, the $L_{G.1}$ columns have an unexpected unstable symmetric post-buckling behavior – the equilibrium path limit points occur for $P/P_{cr}\approx 0.87$.

(iii) In order to try to understand why the L_G columns exhibit two different post-buckling behaviors, it was decided to perform buckling analyses

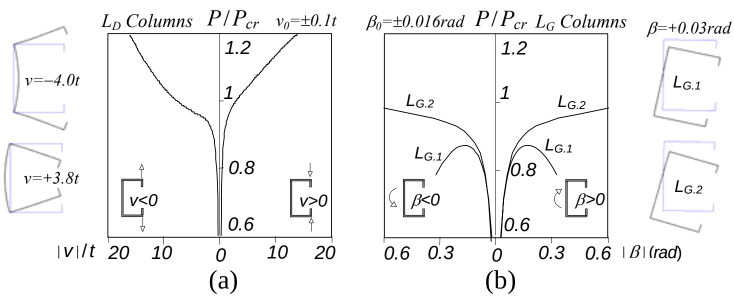

Figure 3. (a) Distortional (P/P_{cr} *vs.* v/t) and (b) global (P/P_{cr} *vs.* β) column elastic post-buckling behaviors

[1] Note that, in the $L_{G.1}$ columns, this magnitude corresponds to a global initial imperfection associated with mid-span flange-lip corner vertical displacements equal to *L/1000* (*i.e.*, *3 mm*).

of those columns using Generalized Beam Theory (GBT – *e.g.*, Camotim *et al.* 2004), hoping that its modal features would shed new light on this issue – indeed, this was the case! The curves shown in figure 4(a) provide the variation of the buckling load P_b with the column length L (L>*100 cm*): (iii$_1$) one yielded by ABAQUS analyses and already shown in figure 2(a), and (iii$_2$) the other obtained from GBT analyses including *6* single half-wave deformation modes (*4* global and *2* distortional) – dashed curve. As for figure 4(b), it displays the GBT-based column *modal participation diagram* (for single half-wave buckling) – it shows the contributions of each GBT deformation mode to the column buckling modes[1]. Finally, figures 4(c) shows the buckling mode shapes yielded by the GBT analyses for the columns with lengths *L=222*, *300*, *900 cm*, as well as the in-plane shapes of the *3* deformation modes participating in them. The following conclusions can be drawn from these GBT-based buckling results:

(iii.1) The GBT curve descending branch involves, in fact, two distinct buckling modes: (iii$_1$) *distortional-flexural-torsional* ones (**2**+**4**+**6**),

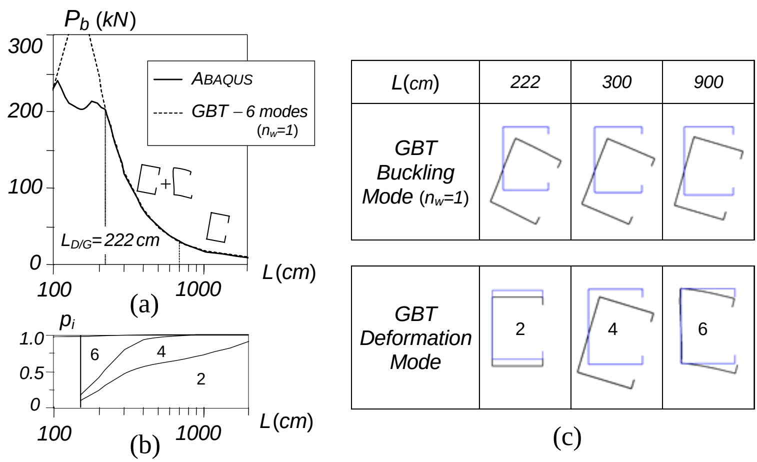

Figure 4. GBT-based column buckling behavior: (a) P_b *vs.* L curves (L>*100 cm*), (b) modal participation diagrams (n_w=*1*) and (c) in-plane shapes of *3* column buckling modes (*L=222*, *300*, *900 cm*) and participating deformations modes

[1] The participations of the deformation mode *k* in the column buckling modes are obtained from the corresponding mid-span cross-section deformed configurations (*e.g.*, Camotim *et al.* 2004).

for $150<L\leq700\ cm$, and (iii$_2$) *flexural-torsional* ones (**2**+**4**), for $700<L<2000\,cm$ – note that the participation of the anti-symmetric distortional mode **6** progressively fades as the column length grows, until it finally vanishes for $L\approx700\,cm$.

(iii.2) Since the $L_{G.1}$ and $L_{G.2}$ columns are located inside the two length ranges identified in the previous item, their buckling modes have different natures: (iii$_1$) *47.0%, 33.1%* and *19.9%* of modes **2**, **4**, **6** ($L_{G.1}$), and (iii$_2$) *70.2%* and *29.8%* of modes **2**, **4** ($L_{G.2}$).

(iii.3) The participation (or not) of mode **6** provides the explanation for the different post-buckling behaviors exhibited by the $L_{G.1}$ and $L_{G.2}$ columns – its presence is responsible for the surprising unstable post-buckling behavior of the $L_{G.1}$ columns depicted in figure 3(b). However, the mode **6** contribution to the column critical buckling mode would remain virtually undetected in the absence of the GBT analysis – this statement can be clearly attested by looking at the member and cross-section deformed configuration shown in figures 2(b) and 4(b), which were obtained by means of ABAQUS shell finite element and CUFSM$_{2.6}$ finite strip analyses[1].

(iii.4) In the GBT nomenclature, the $L_{G.1}$ column critical buckling mode is designated as "mixed", since it "mixes" deformation modes of different natures (**2**+**4** and **6** – global and distortional). Note that the existence of "mixed" buckling modes *is not a buckling mode interaction* phenomenon, which corresponds to the simultaneous (or nearly so) occurrence of two or more critical buckling modes.

(iii.5) In the $L=222\ cm$ columns, two critical buckling modes occur simultaneously: (iii$_1$) a three half-wave pure symmetric distortional one and (iii$_2$) a single half-wave "mixed" (distortional-flexural-torsional) one, combining *30.2%* of mode **2**, *22.0%* of mode **4** and *46.4%* of mode **6** (*i.e.*, with a predominance of mode **6**) – the latter was previously termed "global" (a designation that will be retained for the sake of simplicity). Therefore, the D/G buckling mode interaction phenomenon investigated next really involves the two competing critical buckling modes described above.

---

[1] The sole "sign" of the presence of the anti-symmetric distortional mode **6** is a practically imperceptible web double-curvature bending (see fig. 4(b)) that can only be detected if one knows about it beforehand. Moreover, the authors have confirmed that mode **6** participates in the so-called "global" buckling modes of lipped channel columns with virtually any cross-section geometry.

POST-BUCKLING BEHAVIOR UNDER D/G MODE INTERACTION

One now investigates the elastic and elastic-plastic post-buckling behaviors of simply supported $L=222\ cm$ columns ($P_{cr}=203.6\ kN$), which are strongly affected by the interaction between nearly coincident distortional (three half-waves) and "global" (single half-wave) buckling modes[1].

Initial Geometrical Imperfections. A very important issue in mode interaction investigations is to assess how the initial geometrical imperfection shape influences the post-buckling behavior and strength of the structural system under scrutiny. Indeed, the commonly used approach of including critical-mode imperfections ceases to be well defined, due to the presence of two competing buckling modes that may be combined arbitrarily. Thus, in order to obtain column equilibrium paths that (i) cover the whole D/G critical-mode imperfection shape range and (ii) can be meaningfully compared, one adopts the following approach, which accounts for the fact that the two competing ("pure") buckling modes exhibit odd half-wave numbers:

(i) To determine the "pure" critical buckling mode shapes, normalized to exhibit unit mid-span flange-lip corner vertical displacements: (i_1) a distortional mode with $v_D=1\ mm$, associated with a mid-web flexural displacement (measured with respect to the web chord) of $w_D=0.265\ mm$ and (i_2) a "global" one also with $v_G=1\ mm$, implying a mid-span web chord rotation equal to $\beta_G=0.005\ rad$.

(ii) To scale down the above pure modes, thus leading to the following magnitudes for the distortional and "global" imperfections: $v_{D.0}=0.1\ t$ and $v_{G.0}=L/1000$ (in this particular case, $0.1\ t=0.24mm$, $L/1000=2.22\ mm$).

(iii) A given initial geometrical imperfection shape is obtained as a linear combination of these scaled buckling modes shapes, with coefficients $C_{D.0}$ and $C_{G.0}$ satisfying the condition $(C_{D.0})^2+(C_{G.0})^2=1$. A better visualisation and "feel" of the initial imperfection shape is obtained by considering the unit radius circle drawn in the $C_{D.0}$-$C_{G.0}$ plane that is shown in figure 5(a): each "acceptable" imperfection shape lies on this circle and corresponds to an angle θ, measured counterclockwise from the horizontal ($C_{D.0}$) axis and defining a $C_{G.0}/C_{D.0}$ ratio ($C_{D.0}=cos\,\theta$ and $D_{G.0}=sin\,\theta$). Figure 5(b)

---

[1] As seen just before, this interaction really involves a three half-wave symmetric distortional buckling mode and a "mixed" buckling mode combining anti-symmetric distortion, major axis flexure and torsion (distortional-flexural-torsional mode).

provides the pure D and G initial imperfection shapes (θ=*0°*, *90°*, *180°* and *270°*) – note that (iii[1]) θ=*0°* and θ=*180°* correspond to *inward* and *outward* flange-lip motions, and that (iii[2]) θ=*90°* and θ=*270°* are associated with clockwise and counterclockwise cross-section rotations. In this work, one considers (mostly) initial imperfections corresponding to *15°* intervals.

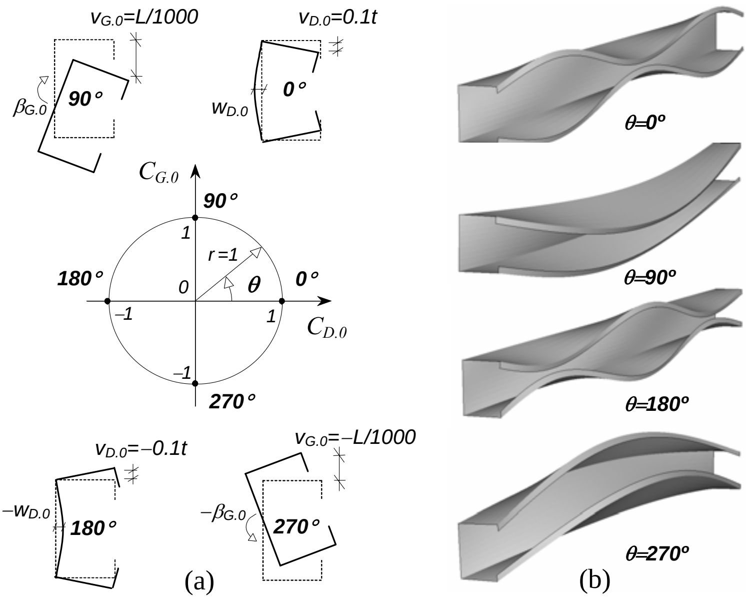

Figure 5. (a) Initial imperfection representation in the $C_{D.0}$-$C_{G.0}$ plane and (b) initial imperfection shapes for θ=*0°*, *90°*, *180°* and *270°*

Elastic Mode Interaction. Initially, one presents post-buckling results concerning columns with *13* initial imperfection shapes corresponding to $0 \leq \theta \leq 180°$ and separated by *15°* intervals[1] – moreover, in order to clarify some behavioral aspects, the θ=*1,26,27,179,181,349°* columns were also analyzed.

[1] Except for the *181°* and *349°* columns, addressed next, no post-buckling results concerning columns with initial imperfection shapes defined by $180<\theta<360°$ are presented – since the column post-buckling behavior is symmetric with respect to the deformed configuration *global* component sign, regardless of whether there is mode interaction or not (see fig. 3(b)), the $0 \leq \theta \leq 180°$ column results provide all the necessary information.

Figures 6(a)-(b) show the upper parts of the most representative column post-buckling equilibrium paths (i) P/P_{cr} *vs.* w/t, where w is the mid-web flexural displacement (measured with respect to the web chord), and (ii) P/P_{cr} *vs.* β, where β is the mid-span web chord rigid-body rotation. As for figure 6(c), it shows the limit deformed configurations of the θ=*27-179°* and θ=*1-26°* columns, which correspond to the curve descending branches (advanced post-buckling stages). In order to shed some light on issues raised by the close scrutiny of the curves shown in figures 6(a)-(b), more post-buckling results are presented in figures 7 to 12 – they consist of (i) equilibrium paths previously displayed in figure 6(a), complemented by illuminating column mid-span cross-section deformed configurations, (ii) ultimate load values and also (iii) figures providing the evolution of mode coupling along those equilibrium paths.

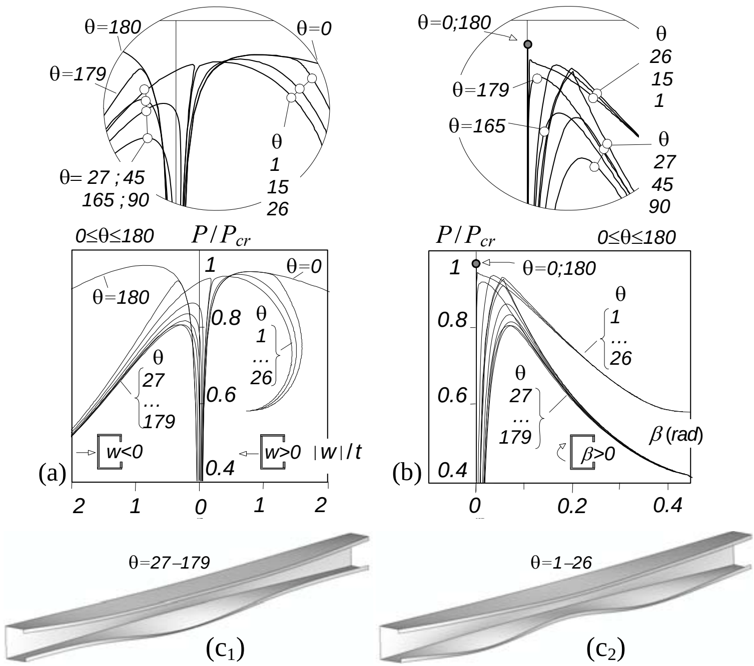

Figure 6. (a) P/P_{cr} *vs.* w/t and (b) P/P_{cr} *vs.* β equilibrium paths of columns with $0 \le \theta \le 180^o$ initial imperfections, and (c) limit deformed configurations of the (c_1) θ=*27-179°* and (c_2) θ=*1-26°* columns (curve descending branches)

The close observation of the post-buckling results presented in figures 6(a)-(c) leads to the following remarks (and also further results):

(i) All column equilibrium paths (P/P_{cr} *vs.* w/t and P/P_{cr} *vs.* β) exhibit well-defined limit points, which occur almost always for very small w/t and β values. The exceptions are the $\theta=0, 180^o$ column equilibrium paths (pure distortional initial imperfections), which have limit points associated with (i_1) slightly larger w/t values and (i_2) null β values – they correspond to a *singular* post-buckling behavior that will be addressed further ahead.

(ii) The comparison between the equilibrium paths P/P_{cr} *vs.* β of (ii_1) the $\theta=90^o$ column (pure "global" initial imperfections with $\beta_0=0.005\,rad$), shown in figure 6(a), and (ii_2) the $L_{G.1}$ column ($\beta_0=0.016\,rad$), depicted in figure 3(b), shows clearly the adverse effect (*strength erosion*) due to the D/G mode interaction. Indeed, in spite of the considerably smaller initial imperfection magnitude (about one third), the limit point exhibited by the $\theta=90^o$ column equilibrium path corresponds to a lower applied load level ($P/P_{cr}=0.81$ vs. $P/P_{cr}=0.87$).

(iii) The equilibrium paths displayed in figure 6(a) can be grouped in three categories, each one corresponding to a different post-buckling behavior – they are identified next and addressed separately in the sequel:

  (iii.1) $\theta=0, 180^o$ *Equilibrium Paths*, corresponding to pure distortional initial imperfections. As mentioned before, these two columns exhibit a *singular* post-buckling behavior, characterized by the fact that their cross-sections exhibit no rigid-body rotations (*i.e.*, $\beta=0$).

  (iii.2) $1\leq\theta\leq26^o$ *Equilibrium Paths*, corresponding to predominantly distortional initial imperfections with outward outer half-waves.

  (iii.3) $27\leq\theta\leq179^o$ *Equilibrium Paths*, corresponding to all the remaining initial imperfection shapes.

  At this stage, it is worth noting that the first two equilibrium paths concern a rather unexpected L/G interactive behavior, which will be the last to be dealt with. Moreover, the equilibrium paths belonging to the last two categories merge into common post-buckling curves associated with (iii_1) clockwise mid-span web chord rotations and (iii_2) either inward ($27\leq\theta\leq179^o$) or outward ($1\leq\theta\leq26^o$) mid-span web bending – since the $27\leq\theta\leq179^o$ category includes the vast majority of equilibrium paths, thus providing a more meaningful characterization of the D/G mode interaction effects, it will be addressed first. Then, one tackles the $1\leq\theta\leq26^o$ category, which constitutes another particular case.

Columns with $27 \leq \theta \leq 179^o$ initial geometrical imperfections

These equilibrium paths correspond to initial geometrical imperfections whose global components involve always clockwise cross-section rigid-body rotations (in view of the global post-buckling symmetry, it is not necessary to consider counterclockwise rotations)[1] – such component is either (i) the only one (θ=90^o) or (ii) combined with a distortional one exhibiting inward ($27 \leq \theta < 90^o$) or outward ($90 < \theta \leq 179^o$) mid-span flange-lip motions[2]. The joint observation of all these equilibrium paths leads to the following remarks:

(i) They all merge into a common curve, which corresponds to a deformed configuration that may be deemed associated with a "coupled buckling mode" shape. In order to provide a better visualization of this concept and, at the same time, quantify the amount of "coupling", figure 7 shows the evolution, along those equilibrium paths, of a "mode coupling ratio" defined as C_G/C_D and relating the amplitudes of the column deformed configuration global and distortional components. These amplitudes are obtained from the mid-span web (i_1) chord rotation β and (i_2) mid-point flexural displacement w, adopting the following simplifying assumptions:

  (i.1) The column deformed configuration can be completely expressed as a linear combination of the global and distortional buckling mode shapes, normalized with respect to $v_{G.0}$=$2.22\ mm$ ($L/1000$) and $v_{D.0}$=$0.24\ mm$ ($0.1t$) – these values correspond to $\beta_{G.0}$=$0.0111\ rad$ and $w_{D.0}$=$0.0564\ mm$.

  (i.2) The β and w values associated with a given deformed configuration stem exclusively from its global and distortional components.

  (i.3) In view of the above assumptions, one readily determines the global and distortional participation factors, by means of the expressions C_G=$\beta/\beta_{G.0}$ and C_D=$w/w_{D.0}$. Then, all C_G/C_D curves depart from a unit-radius circle on the C_G-C_D plane (see detail), with initial slopes that depend on the initial imperfection shape.

---

[1] Recall that the GBT buckling analysis showed that these "global" components combine (i) a clockwise torsion rotation, (ii) a downward major axis bending displacement and (iii) downward flange-lip motions associated with anti-symmetric distortion. Since they are all "linked" through the buckling mode shape, it suffices to mention only the torsion rotation β (the most "visible" one).

[2] Although one always quotes the nature of the mid-span flange-lip motions (for simplicity reasons), it should be noted that the key feature of the initial geometrical imperfections is the nature of the flange-lip motions of the *two outer* half-waves – it provides the explanation for several qualitative aspects of the column D/G interactive behavior.

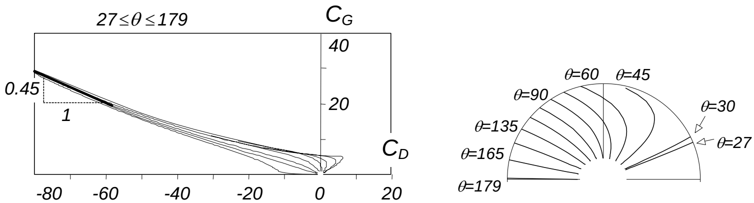

Figure 7. Evolution of the mode coupling ratio C_G/C_D along the various equilibrium paths associated with $27 \leq \theta \leq 179^o$

The C_G/C_D curves shown in figure 7 provide valuable information about the column D/G mode interaction behavior (for $27 \leq \theta \leq 179^o$). Indeed, as post-buckling progresses, all of them tend to a practically straight line with slope defined by $\Delta C_G \approx -0.45 \Delta C_D$ (negative C_D values stand for distortional deformed configuration components with *outward* mid-span flange-lip motions – see figs. 5(a)-(b))[1]. Then, it seems reasonable to view this straight line as the representation of the column "*coupled buckling mode*", which combines participations of (i_1) a three half-wave distortional component with *outward* mid-span flange-lip motions and (i_2) a single half-wave global component that are roughly equal to one and two thirds of the total deformed configuration (*31%* and *69%*, to be precise) – this coupled buckling mode shape can be visualized in figure 6(c_1)[2].

(ii) All equilibrium paths exhibit a *limit point* prior to merging into the "common curve" and one observes that, generally speaking, the column limit load decreases as the initial imperfection global component becomes more dominant – this can be confirmed by looking at the table included in figure 8, which provides the variation of the column ultimate load ratio P_u/P_{cr} with its initial imperfection shape (*i.e.*, with θ). However, one observes that the minimum ultimate load ($P_u/P_{cr}=0.803$) occurs for the $\theta=105^o$ column, *i.e.*, the one combining *96.5%* and *25.9%* of the pure global and distortional imperfections[3] – nevertheless, one must mention

[1] When interpreting this coupled buckling mode shape, the reader should be always aware of the global and distortional buckling mode normalizations – they correspond to mid-span flange-lip corner vertical displacements equal to *2.22mm* (global) and *0.24mm* (distortional), *i.e.*, the former is more than nine times the later.

[2] The mid-span cross-section deformed configuration associated with this coupled buckling mode shape can also be viewed in figures 9(c) ($\theta=179^o$ – IV) and 11(b) ($\theta=27^o$ – IV).

[3] It is interesting to notice that 105^o is very close to the average between 27^o and 179^o.

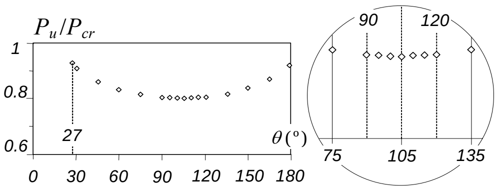

θ (°)	P_u/P_{cr}	θ (°)	P_u/P_{cr}
27	0.928	105	0.803
30	0.909	120	0.807
45	0.864	135	0.819
60	0.836	150	0.839
75	0.817	165	0.870
90	0.807	179	0.920

Figure 8. Variation of P_u/P_{cr} with the initial imperfection shape ($27 \leq \theta \leq 179^o$)

that the P_u/P_{cr} value remains practically constant for $90 \leq \theta \leq 120^o$ (0.5% between the minimum and maximum values – see curve detail in fig. 8), *i.e.*, analyzing a column with a pure global initial imperfection ($\theta=90^o$) will certainly provide a rather accurate estimate of the minimum P_u/P_{cr} value – in other words, the pure global initial imperfection may be viewed, for practical purposes, as the *most detrimental* one, in the sense that it maximizes the strength erosion due to the D/G mode interaction[1].

(iii) Although it is evident that the initial imperfection global component plays a crucial role in the column post-buckling behavior (note that all equilibrium paths exhibit limit points), it is also obvious that there must exist a plausible explanation for the qualitative and quantitative differences exhibited by the $90 < \theta \leq 179^o$ and $1 \leq \theta < 90^o$ column equilibrium paths, clearly visible in figures 6(a)-(b) – (iii_1) while the former tend to the common curve in a "regular" fashion (the amplitudes of both the global and distortional components grow monotonically), (iii_2) the latter either tend to that same common curve "irregularly" ($27 \leq \theta < 90^o$ – occurrence of distortional component reversals) or do not tend to it at all ($1 \leq \theta < 27^o$ – they tend to another common curve, which will be addressed later).

(iv) All the distinct post-buckling behaviors described in the previous item stem from the influence exerted by the outer half-wave flange-lip motions (distortional feature) on the major axis flexure (global feature). Indeed, (iv_1) while inward flange-lip motions reduce the cross-section major moment of inertia, thus facilitating the occurrence of the corresponding flexure, (iv_2) the outward flange-lip motions have precisely the opposite effect. This assessment justifies (or is confirmed by) the following facts:

(iv.1) The "regularity" of the $90 < \theta \leq 179^o$ column equilibrium paths, due to the *converging* effects of the initial imperfection global and

[1] Even if this assessment concerns only the $27 \leq \theta \leq 179^o$ interval, it is valid for any θ – as shown in figures 6(a)-(b) and discussed ahead, the $\theta=0, 180^o$ and $1 \leq \theta \leq 26^o$ column ultimate loads are higher.

distortional components.

(iv.2) The distortional component amplitude reversals occurring in the $27<\theta\leq 90^o$ column equilibrium paths, due to the *opposing* effects of the initial imperfection global and distortional components, with the former prevailing over the latter.

(iv.3) The "peculiarity" of the $1<\theta\leq 26^o$ column equilibrium paths, due to the *opposing* effects of the initial imperfection global and distortional components, with the latter prevailing over the former.

(iv.4) The "equality/symmetry" between the equilibrium paths and mid-span cross-section deformed configurations concerning the column pairs θ=*179,181^o* and θ=*1,359^o*, clearly shown in figures 9(a)-(c) – for clarity, the first three cross-section deformed configurations of every column are amplified *20*, *5* and *3* times, respectively. It is worth noting that the initial imperfections in each pair have the same distortional component and opposite-sign global components.

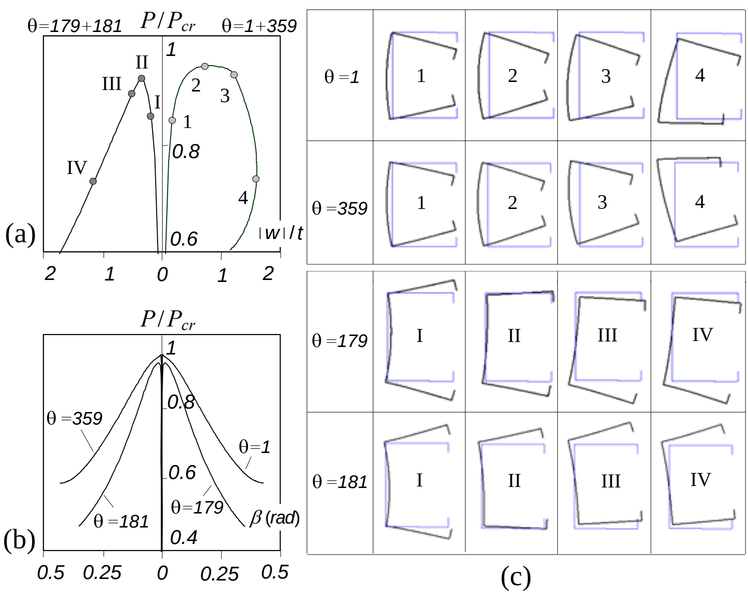

Figure 9. (a) P/P_{cr} *vs.* w/t and (b) P/P_{cr} *vs.* β equilibrium paths and (c) mid-span cross-section deformed configuration evolution (θ=*1,359^o* and θ=*179,181^o*)

Columns with $1 \leq \theta \leq 26^o$ initial geometrical imperfections

These equilibrium paths correspond to initial geometrical imperfections whose global components involve clockwise cross-section rigid-body rotations (as before) combined with a highly predominant distortional one exhibiting inward mid-span flange-lip motions ($C_{D.0}>0.899$). From the close observation of these few equilibrium paths it is possible to draw the following conclusions:

(i) As the ones dealt with previously ($27 \leq \theta \leq 179^o$), they all merge into a common curve – this merging occurs only in their descending branches (after the limit points) and the common curve corresponds to the deformed configuration shown in figure 6(c_2)[1]. However, the characteristics of this deformed configuration change continuously as post-buckling progresses, as attested by the equilibrium paths shown in figures 6(a)-(b) (particularly the latter) and also by the evolution of the mode coupling ratio C_G/C_D displayed in figure 10(a) – indeed, one notices that the amplitudes of the deformed configuration distortional components start decreasing, at a growing rate, along the P/P_{cr} *vs.* w/t equilibrium path descending branches (see fig. 6(a)), which implies also a global component growth rate increase, clearly visible in the corresponding P/P_{cr} *vs.* β equilibrium paths (their common curve becomes almost horizontal – see fig. 6(b))[2]. Therefore, no coupled buckling mode shape can be inferred from (or linked to) the common curve concerning these equilibrium paths.

(ii) Whenever the initial outer half-wave outward flange-lip motions are large enough (*i.e.*, for $\theta<27^o$), their post-buckling growth (amplification)

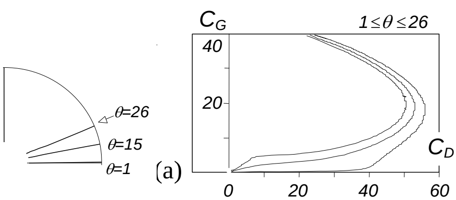

θ (°)	P_u/P_{cr}
1	0.944
15	0.937
26	0.928

(b)

Figure 10. (a) Evolution of the mode coupling ratio C_G/C_D along the various equilibrium paths and (b) variation of P_u/P_{cr} with θ ($1 \leq \theta \leq 26^o$)

[1] The mid-span cross-section deformed configuration associated with this coupled buckling mode shape can also be viewed in figures 9(c) ($\theta=1^o$ – IV) and 11(b) ($\theta=26^o$ – IV).

[2] Since the outer half-wave outward flange-lip motions decrease, the occurrence of major axis flexure becomes "easier", which explains the global component (*i.e.*, β) growth rate increase.

"retards" the dominant appearance of the (destabilizing) deformed configuration global component. This leads to slightly higher limit loads (see table in fig. 10(b) and compare its values with those appearing in fig. 8) that tend to occur for visibly larger *w* values (*e.g.*, compare the limit point locations of the $\theta=1^o$ and $\theta=179^o$ column P/P_{cr} *vs.* w/t equilibrium paths).

(iii) The amplitude reversals of the column deformed configuration distortional components cease abruptly, as shown in figure 6(a). Indeed, no further equilibrium states could be detected, most likely because the column outer half-wave flanges-lips were about to "snap" from an outward position to an inward one – obviously, such dynamic behavior could not be captured by the ABAQUS (static) geometrically non-linear analyses carried out.

(iv) To enable a better grasp of the qualitative and quantitative differences between the two sets of column equilibrium paths dealt with ($27\leq\theta\leq179^o$ and $1\leq\theta\leq26^o$), figure 11 shows the $\theta=26, 27^o$ column (iv_1) P/P_{cr} *vs.* w/t equilibrium paths and (iv_2) mid-span cross-section deformed configuration evolution. Despite the tiny initial imperfection difference, the two column post-buckling behaviors are quite distinct – *e.g.*, (iv_1) the equilibrium path shapes and (iv_2) the distortional components of the mid-span cross-section deformed configurations along the descending branches (the $\theta=26^o$ and $\theta=27^o$ column flange-lip assemblies move inward and outward).

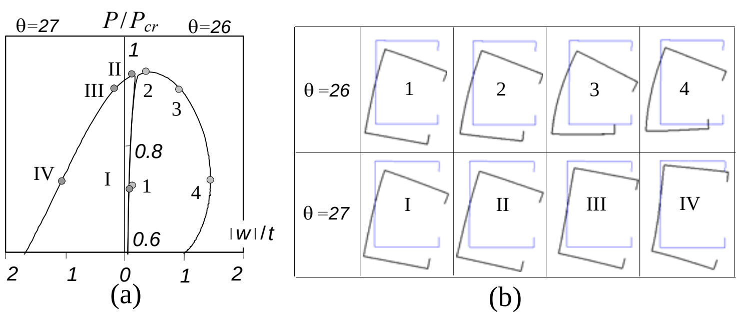

Figure 11. (a) P/P_{cr} *vs.* w/t equilibrium paths and (b) mid-span cross-section deformed configuration evolution ($\theta=26^o$ and $\theta=27^o$)

<u>Columns with $\theta=0, 180^o$ initial geometrical imperfections</u>

Finally, one addresses the equilibrium paths of the columns containing *pure distortional* initial geometrical imperfections, which exhibit rather peculiar post-buckling behaviors, both characterized by (i) the highest limit load values (P_u/P_{cr}=*0.945*, *0.961*, for θ=*0*, *180°*), (ii) much less pronounced limit points (see fig. 6(a)) and (iii) the total absence of torsional rotations (see fig. 6(b)). This is rather surprising, since (i) there are no D/G mode interaction effects of the type found for all other initial imperfection shapes (no torsional rotations) but, at the same time, (ii) the two column equilibrium paths are not similar to the purely distortional ones shown in figure 3(a) (occurrence of limit points).

Then, in order to understand the nature of the singular column post-buckling behavior described above, it is convenient to look at figures 12(a)-(b), showing (i) the two column equilibrium paths, (ii) mid-span cross-section deformed configurations (amplified *twice*) at three equilibrium states and also (iii) the column overall deformed configurations at the descending branch states. Indeed, it is possible to observe that:

(i) The θ=*0°* and θ=*180°* column P/P_{cr} *vs.* w/t equilibrium paths are slightly different – in particular, the former column exhibits a lower limit load.

(ii) While the first mid-span cross-section deformed configurations (1 and I) are "purely distortional", the second and third ones (1-2 and II-III) indicate the presence of minor axis flexure (web in tension) – this is clearly confirmed by the column overall deformed configurations shown in fig. 12(b), which correspond to the equilibrium states 3 and III.

(iii) Therefore, the θ=*0°* and θ=*180°* columns are affected by a different type of distortional/global mode interaction phenomenon, which (iii$_1$) involves only minor axis flexure and (iii$_2$) is not caused by the closeness of two buckling loads. Indeed, this mode interaction stems from the occurrence of

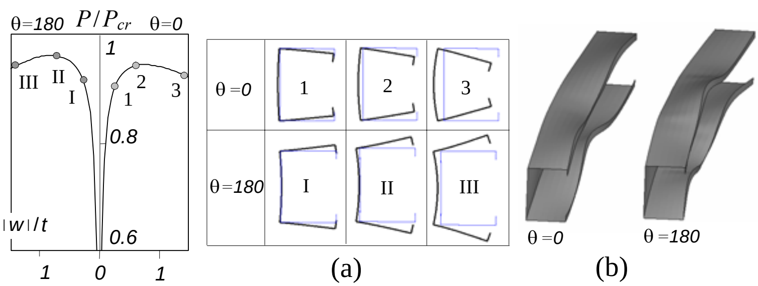

Figure 12. (a) P/P_{cr} *vs.* w/t paths and mid-span cross-section deformed configuration evolution, and (b) post-peak deformed configurations (θ=*0°*,*180°*)

horizontal shifts (towards the web) of the column cross-section *effective centroids*, responsible for the development of minor axis flexure (the axial compression become gradually more eccentric) – these effective centroid shifts stem from the progressive "weakening" (axial stiffness drop) of the flange-lip assemblies, due to the presence of rather high longitudinal compressive normal stresses (*e.g.*, Young & Rasmussen 1999)[1].

(iv) The lower limit load exhibited by the $\theta=0^o$ column is due to the fact that it is associated with two half-waves involving outward flange-lip motions, which develop higher compressive stresses than their inward counterparts (*e.g.*, Prola & Camotim 2002 or Silvestre & Camotim 2006)[2].

(v) This distortional/global mode interaction phenomenon did not occur in the column *single half-wave* distortional post-buckling presented in figure 3(a) (the equilibrium paths exhibit no limit points) – this is due to the much shorter column length (about one third of the one considered now), which corresponds to a much higher global (minor axis flexure) buckling load and, therefore, precludes the occurrence of interaction (the cross-section "weakening" is insufficient to trigger it).

Elastic-Plastic Mode Interaction. In this section, one presents a few results dealing with the elastic-plastic post-buckling behavior of simply supported lipped channel columns experiencing D/G mode interaction. These results concern columns (i) containing the *13* initial imperfection shapes dealt with before ($0\leq\theta\leq 180^o - 15^o$ intervals) and (ii) exhibiting *three* yield-to-critical stress ratios, namely $f_y/\sigma_{cr}\approx 1.1, 1.7, 2.5$, corresponding to yield stresses equal to $f_y=235, 355, 520MPa$ – recall that $\sigma_{cr}=209.5MPa$. For comparative purposes, one presents again some elastic results obtained earlier, which may be viewed as corresponding to an infinite yield stress (*i.e.*, $f_y=f_y/\sigma_{cr}=\infty$).

Figure 13(a) shows the upper portions ($P/P_{cr}>0.6$) of four equilibrium paths P/P_{cr} *vs.* w/t, which describe the post-buckling behaviors of columns containing pure global initial imperfections ($\theta=90^o$) and exhibiting different yield-to-critical stress ratios – the choice of this particular initial imperfection shape is

[1] This type of distortional/global mode interaction is qualitatively similar to the well-know local-plate/global one, which is currently incorporated in virtually all steel design codes through the "plate effective width" concept.

[2] This limit load difference only exists because the number of distortional half-waves is *odd*, which brings about the different behaviors exhibited by the outward and inward ones. Moreover, this difference will obviously decrease as the (odd) half-wave number increases.

due to (i) space limitations, on one hand, and (ii) the fact that the elastic $\theta=90^o$ column was found to exibit one of the lowest limit loads[1]. As for figure 13(b), it concerns the column with $f_y/\sigma_{cr}\approx 1.1$ and displays four plastic strain diagrams, corresponding to equilibrium states located along the post-buckling path (as indicated in fig. 13(a)) and including the column collapse mechanism. Finally, table 2 provides the column ultimate load ratios (P_u/P_{cr}) asociated with all the θ and f_y value combinations considered in this study. The observation of these results prompts the following remarks:

(i) Out of the four sets of columns analyzed, (i_1) only the ones with $f_y/\sigma_{cr}\approx 1.1$ exhibit a (minute) elastic-plastic strength reserve and (i_2) the ones with $f_y/\sigma_{cr}\approx 2.5$ remain elastic up until the ultimate (limit) load is reached. Moreover, the columns with $f_y/\sigma_{cr}\approx 2.5$ are the sole to exhibit (a very small amount of) ductility prior to failure – in the columns with $f_y/\sigma_{cr}\approx 1.7$, the onset of yielding triggers the column failure.

(ii) In all θ=*26-179*^{o} columns, yielding starts at the bottom lip mid-span zone, as illustrated in figure 13(a) (diagram *I* – θ=*90* column). Collapse occurs almost immediately after and is caused by the full yielding of the mid-span bottom web-flange corner, leading to the formation of a "distortional plastic hinge" that precipitates the collapse of the mid-span bottom flange-lip assembly (see diagram *II* in fig. 13(b), which also shows a yield line crossing the whole mid-span cross-section bottom flange). Along the equilibrium path descending branch yielding spreads progressively along the lower web and bottom flange-lip central regions, while all other column areas remain elastic (see diagrams *III* and *IV* in fig. 13(b)).

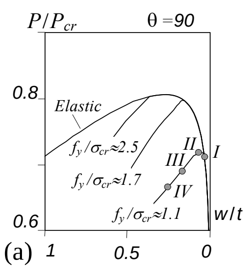

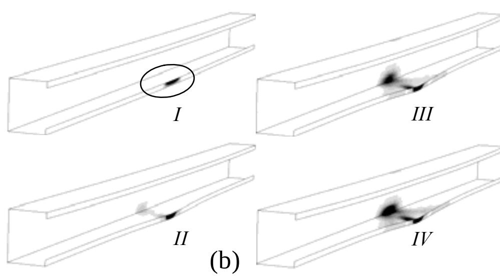

Figure 13. (a) P/P_{cr} *vs.* w/t elastic-plastic equilibrium paths of $\theta=90^o$ columns and (b) plastic strain and deformed configuraton evolution for $f_y/\sigma_{cr}\approx 1.1$

[1] Recall that the $\theta=105^o$ column has the lowest limit load, differing *0.5%* from the $\theta=90^o$ column one.

Table 2. Variation of the ultimate load ratio P_u/P_{cr} with θ and f_y/σ_{cr}

θ (°)	f_y/σ_{cr} 1.1	1.7	2.5	∞	θ (°)	f_y/σ_{cr} 1.1	1.7	2.5	∞
0	0.850	0.931	0.945	0.945	90	0.721	0.797	0.807	0.807
15	0.826	0.921	0.937	0.937	105	0.711	0.792	0.803	0.803
30	0.807	0.912	0.909	0.909	120	0.716	0.797	0.807	0.807
45	0.797	0.863	0.864	0.864	135	0.726	0.807	0.819	0.819
60	0.764	0.831	0.836	0.836	150	0.754	0.831	0.839	0.839
75	0.740	0.811	0.817	0.817	165	0.792	0.864	0.870	0.870
90	0.721	0.797	0.807	0.807	180	0.854	0.940	0.960	0.961

(iii) In all of the θ=*1-27°* columns, the plastic strain evolution (not shown) is qualitatively quite similar to the one described in the previous item. There is one important difference, though: yielding starts and spreads around the column regions located near the outer half-wave crests, where the largest distortional deformations occur (see fig. 6(c_2)).

(iv) The ultimate load ratio values given in table 2 show that the variation of P_u/P_{cr} with θ is qualitatively similar for all the column sets. Indeed, one observes that (iv_1) the θ=*105°* column always exhibits the lowest values and that (iv_2) there is very little variation within the $90 \leq \theta \leq 120°$ interval (the maximum and minimum P_u/P_{cr} are never more than *1.4%* apart) – this confirms that, for practical purposes, one may consider the pure global initial imperfection (θ=*90°*) as the *most detrimental* one[1].

(v) The *strength erosion* associated with the distortional/global modal interaction effects is quite considerable. For the θ=*90°* column, one has ultimate strengths corresponding to *29%* (f_y=*235MPa*), *21%* (f_y=*355MPa*) and *20%* (f_y>*355MPa*) drops with respect to the critical buckling load – it is interesting to notice there is no benefit in having a yield stress much larger than f_y=*355MPa*, since the column collapse is totally governed by elastic distortional/global mode interaction effects.

(vi) The features addressed in the previous two items are bound to have far-reaching implications in the design of cold-formed steel columns that experience D/G interaction, mostly because the (uncoupled) distortional and global post-buckling behaviors are looked upon as stable (even if only marginally) – no adverse mode interaction effects have ever been reported.

[1] It is worth recalling that a pure outward distortional initial imperfection was found to be the most detrimental in the context of simply supported lipped channel columns affected by local-plate/distortional mode interaction (Dinis *et al.* 2005, 2007).

CONCLUSION

This work dealt with a numerical (shell finite element) investigation on the elastic and elastic-plastic post-buckling behavior of simply supported cold-formed steel lipped channel columns affected by distortional/global buckling mode interaction. The analyses, performed in the code ABAQUS, involved columns containing several initial imperfections with shapes obtained by combining differently the two competing distortional (three half-waves) and global (one half-wave) buckling modes with amplitudes equal to (i) *10%* of the wall thickness *t* (dirtortional mode) and (ii) *L/1000* (global mode).

Initially, one addressed the lipped channel column (i) buckling behavior and (ii) uncoupled distortional and global post-buckling behaviors, a task that (i) made it possible to select the most appropriate column length (*i.e.*, the one maximizing the D/G interaction effects) and (ii) ended up disclosing a few unexpected (and surprising) features. Then, one presented and discussed several numerical results concerning the elastic post-buckling behavior of lipped channel columns (i) having the selected length (*i.e.*, experiencing strong D/G mode interaction effects) and (ii) containing critical-mode initial imperfections with various configurations and the same amplitude (linear combinations of the two competing buckling mode shapes). These results consisted of (i) non-linear equilibrium paths and (ii) figures providing the evolution, along those paths, of column and cross-section deformed configurations. Finally, the paper closed with a few post-buckling results of elastic-plastic columns with (i) the same geometry and initial imperfection shapes and (ii) three yield stress values. Besides the non-linear equilibrium paths and deformed configuration evolution, one addressed also (i) issues related to the onset and spread of plasticity, as well as (ii) the variation of the column ultimate strength with the initial imperfection shape and yield stress value.

Among the various conclusions drawn from this investigation, the following ones deserve to be specially mentioned:

(i) A GBT analysis revealed that a large portion of the column critical buckling curve descending branch corresponds to *distortional-flexural-torsional* buckling modes with relevant anti-symmetric distortional components – this contradicts the general belief that such column lengths are associated with global buckling. Thus, the columns analyzed in this work are affected by the interaction between (i_1) three half-wave symmetric distortional and (i_2) single half-wave (anti-symmetric) distortional-flexural-torsional modes.

(ii) The participation of the anti-symmetric distortional mode just mentioned provided the explanation for the surprising unstable "global" post-buckling behavior exhibited by the intermediate-to-long lipped channel columns.

(iii) The equilibrium paths describing the post-buckling behaviors of the columns affected by distortional/global ("global" means "distortional-flexural-torsional") mode interaction exhibit features that vary considerably with the initial imperfection shape. Those equilibrium paths can be grouped in three categories, depending on whether the initial imperfection shape is (iii_1) pure distortional, (iii_2) predominantly distortional with outward outer half-waves or (iii_3) none of the above – this last category comprises the vast majority of the post-buckling paths and led to the identification of a "coupled buckling mode", defined by $\Delta C_G \approx -0.45 \Delta C_D$.

(iv) A key aspect concerning the distortional/global mode interaction is the influence exerted by the outer half-wave flange-lip motions (distortional feature) on the major axis flexure (global feature). Indeed, (iv_1) while inward flange-lip motions reduce the cross-section major moment of inertia, thus facilitating the occurrence of the corresponding flexure, (iv_2) the outward flange-lip motions have precisely the opposite effect[1].

(v) The columns containing pure distortional initial imperfections are affected by a different type of distortional/global mode interaction phenomenon, which (v_1) involves only minor axis flexure and (v_2) is not caused by the closeness of two buckling loads – it is due to the occurrence of horizontal shifts of the column cross-section *effective centroids*, stemming from the "weakening" (axial stiffness drop) of the flange-lip assemblies brought about by high compressive normal stresses.

(vi) Regardless of the initial imperfection shape, all elastic equilibrium paths exhibit limit points that take place below the critical applied load level. Concerning the elastic-plastic post-buckling behavior, it was found that (vi_1) the *strength erosion* due to distortional/global modal interaction effects is considerable, (vi_2) there is virtually no elastic-plastic strength reserve and/or ductility (the onset of yielding often triggers column failure) and, for yield stresses a bit larger than $f_y=355\,MPa$, (vi_3) the column collapse is totally governed by elastic distortional/global interaction.

---

[1] This aspect is particularly relevant because the (symmetric) distortional buckling mode exhibits three half-waves (*2* outward and *1* inward or vice-versa) – if the mode has an even or larger odd half-wave number, it should play a much lesser role (this issue is currently under investigation).

(vii) For practical purposes, pure global initial imperfections may be taken as the most detrimental ones, in the sense that they lead to the lowest ultimate loads, both in the elastic and elastic-plastic columns.

Some of the features just described are bound to have far-reaching implications in the design of cold-formed steel columns experiencing distortional/global interaction, mostly because (i) the uncoupled distortional and global post-buckling behaviors are now looked upon as stable (even if only marginally) and (ii) no adverse mode interaction effects between them had ever been reported. The authors are currently investigating the influence of this mode interaction phenomenon in the post-buckling and ultimate strength behaviors of lipped channel columns with other cross-section dimensions and support conditions – the completion of this task should pave the way towards the development and validation of a direct strength approach to design this type of columns.

REFERENCES

Camotim D and Silvestre N (2004). GBT distortional post-buckling analysis of cold-formed steel lipped channel columns and beams, *Program and Book of Abstracts of 17th ASCE Engineering Mechanics Conference* (EM 2004 – Newark, 13-16/6), 38-39. (full paper in CD-ROM Proceedings)

Camotim D, Silvestre N, Gonçalves R and Dinis PB (2004). GBT analysis of thin-walled members: new formulations and applications, *Thin-Walled Structures: Recent Advances and Future Trends in Thin-Walled Structures Technology* (International Workshop – Loughborough, 25/6), J. Loughlan (ed.), Canopus Publishing Ltd., Bath, 137-168.

Camotim D, Silvestre N and Dinis PB (2005). Numerical analysis of cold-formed steel members, *International Journal of Steel Structures*, **5**(1), 63-78.

Camotim D, Dinis PB and Silvestre N (2008). Local/distortional mode interaction in lipped channel steel columns: post-buckling behaviour, strength and DSM design, *Proceedings of Fifth International Conference on Thin-Walled Structures* (ICTWS 2008 – Brisbane, 18-20/6), submitted for publication.

Dinis PB and Camotim D (2006). On the use of shell finite element analysis to assess the local buckling and post-buckling behaviour of cold-formed steel thin-walled members, *Book of Abstracts of III European Conference on Computational Mechanics: Solids, Structures and Coupled Problems in*

Engineering (III ECCM – Lisboa, 5-9/6), C.A.M. Soares *et al.* (eds.), Springer, 689. (full paper in CD-ROM Proceedings)

Dinis PB and Camotim D (2008). On the shell finite element analysis of the local-plate and distortional buckling and post-buckling behaviour of cold-formed steel thin-walled members, *submitted for publication*.

Dinis PB, Silvestre N and Camotim D (2005). Analysis of the local-plate/distortional mode interaction in cold-formed steel lipped channel columns, *Proceedings of Tenth International Conference on Civil, Structural and Environmental Engineering Computing* (Rome, 30/8-2/9), B. Topping (ed.), Civil-Comp Press, 371-372. (full paper in CD-ROM Proceedings)

Dinis PB, Camotim D and Silvestre N (2007). FEM-based analysis of the local-plate/distortional mode interaction in cold-formed steel lipped channel columns, *Computers & Structures*, **85**(19-20), 1461-1474.

Hancock GJ, Yap D and Yang D (2007). Interaction buckling in high strength cold-formed steel compression members, *Proceedings of the 6th International Conference on Steel & Aluminium Structures* (ICSAS'07 – Oxford, 24-27/7), R. Beale (ed.), 14-25.

HKS (Hibbit, Karlsson & Sorensen Inc.) (2002). ABAQUS Standard (vrs. 6.3-1).

Kwon Y and Hancock GJ (1993). Postbuckling analysis of thin-walled channel sections undergoing local and distortional buckling, *Computers & Structures*, **49**(3), 507-516.

Prola L and Camotim D (2002). On the distortional post-buckling behavior of cold-formed lipped channel steel columns, *Proceedings of Structural Stability Research Council Annual Stability Conference*, (Seattle 24-26/4), 571-590.

Schafer BW (2003). *CUFSM* (version 2.6) www.ce.jhu.edu/bschafer/cufsm.

Schafer BW (2005). *Direct Strength Method Design Guide*, AISI (American Iron & Steel Institute), Washington DC.

Schafer BW (2008). Revtew: the direct strength method of cold-formed steel member design, *Journal of Constructional Steel Research*, accepted for publication.

Schafer BW and Peköz T (1999). Laterally braced cold-formed steel members with edge stiffened flanges, *Journal Structural Engineering* (ASCE), **125**(2), 118-127.

Silvestre N and Camotim D (2006). Local-plate and distortional post-buckling behavior of cold-formed steel lipped channel columns with intermediate stiffeners, *Journal of Structural Engineering* (ASCE), **132**(4), 529-540.

Silvestre N, Camotim D and Dinis PB (2007). DSM design of fixed lipped channel columns against local-plate/distortional interactive buckling, *Proceedings of the 6th International Conference on Steel & Aluminium Structures* (ICSAS'07 – Oxford, 24-27/7), R. Beale (ed.). 752-759.

Silvestre N, Camotim D and Dinis PB (2008a). Direct strength prediction of lipped channel columns experiencing local-plate/distortional interaction, *Advanced Steel Construction – an International Journal*, accepted for publication.

Silvestre N, Camotim D and Dinis PB (2008b). Direct strength approach to the design of lipped channel steel columns against local/distortional interactive buckling, *submitted for publication*.

Ungureanu V and Dubina D (2004). Recent research advances on ECBL approach – Part I: plastic-elastic interactive buckling of cold-formed steel sections, *Thin-Walled Structures*, **42**(2), 177-194.

Yang D and Hancock GJ (2004). Compression tests of high strength steel columns with interaction between local and distortional buckling, *Journal of Structural Engineering* (ASCE), **130**(12), 1954-1963.

Young B and Rasmussen KJ (1999). Shift of effective centroid in channel columns, *Journal of Structural Engineering* (ASCE), **125**(5), 524-531.

LATERAL TORSIONAL BUCKLING OF CHANNEL SECTIONS LOADED IN BENDING

Dagowin B. la Poutré [1]

ABSTRACT

Although channel sections are very common in engineering practice, no structural design standard gives design criteria for lateral torsional buckling of channels loaded in bending and torsion, the most common load case. This paper deals with the LTB of hot-rolled channel sections loaded in bending and torsion. Several different section depths, loading positions and spans were studied.
At first a review of the current state of the art of design criteria for LTB of channel sections is presented. Next, the elastic stability determined analytical will be treated. Then the plastic strength of channel sections loaded in bending and torsion is investigated numerically. Finally, the full non-linear inelastic stability for LTB is investigated in which the influence of imperfections and residual stresses are incorporated. The nonlinear FE-analyses represent the actual buckling loads, with which a design criteria for stability of channel sections loaded in bending is deducted. Comparisons to other design criteria are made and the current design proposal proves to be accurate.

1 INTRODUCTION

Hot-rolled channel sections are very common elements in structural engineering. They posses clear advantages over wide flange beams due

[1] Bernard Ingenieure ZT-GmbH
Bahnhofstrasse 19, A-6060 Hall in Tirol, Austria
+43-5223-5840-125, E-Mail: Dagowin.Lapoutre@bernard-ing.com

to the lacking flanges on one side of the web. This advantage can be expoided in a structural sense, i.e. enabling easy connections to other structural elements such as columns, or in an aesthetic sense, creating flush edges when the channel is used on an edge with flanges inwards.

Channel sections loaded in bending posses structural properties which are rather different from wide flange beams. The shear center and centroid do not coincide and both are not on a material point of the cross section, Figure 1. For channels loaded in bending, the most common point of load application is the web, which will be called eccentric loading hereafter. All eccentrically loaded channels are subject to an initial torsional load, next to bending, which will make the cross section twist. The applied load remains vertical and, due to the twisted position, will causes bi-axial bending. This effect is enhanced further and the section will not reach its major axis bending capacity, but fail in lateral torsional buckling. The behavior is non-linear and it is no longer possible to determine the ultimate load by hand analysis.

When loaded at the shear center, the sections will deflect only and not twist. At a critical load, the sections will buckle suddenly in a lateral torsional mode. Figure 2 shows the load-deflection diagram for both centrically (shear center) and eccentrically (web) loaded channels. The centrically loaded sections show a linear load-deflection behavior, and then buckle suddenly. The eccentrically loaded section show a non-linear load-deflection behavior. They fail more gradually and the ultimate load is characterized as limit point.

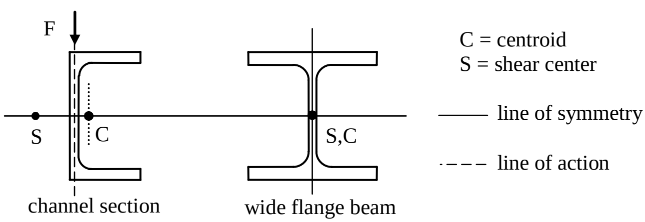

Figure 1. Channels vs. wide flange beams.

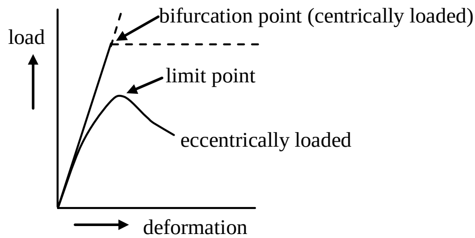

Figure 2. Bifurcation (shear center) and limit point (web) failure.

Although these sections are very common, there are no provisions for eccentric loading in structural standards to design for stability. It is the object of this paper to investigate what design methods are available in the literature and to draft a possible design check for the LTB of channel sections. This paper is limited to stability of channels loaded in bending and torsion only.
This paper was motivated as part of the effort for the sixth editions of The Guide to Stability Design Criteria of Task Group 15 - Beams, to draft a section on stability criteria for channels.

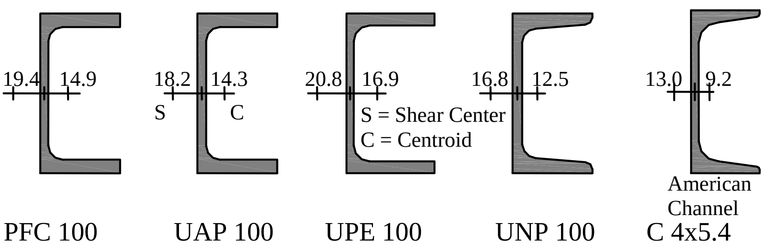

Figure 3. Different series of hot-rolled channels (dimensions in mm).

Two main types of hot-rolled channel sections can be distinguished: channels with tapered flanges and channels with flanges with parallel surfaces. For each type there are again different series. Figure 3 shows a few different types:

- PFC (Parallel Flange Channels) from Corus,
- UAP from Arcelor-Mittal, which were discontinued in 2005,
- UPE introduced by Salzgitter and adopted by other mills,
- UPN being standard European channels, and
- American Standard Channels.

Tolerances of European channels are given by EN 10279, 2000, and American channels by A 6/A 6M, 1993.
Parallel flange channels have clear advantages over taper flange channels from the point of view of construction. No tapered washers are needed when the flanges are bolted and stiffeners can be cut at right angles. However, from a structural point of view, tapered flanges are better, which can be explained by the following:
For channels where the flanges stay out to the right (as chosen in the depiction of Figure 3), the location of the shear center is further to the left of the web when more material is located to the right of the web. It is clear that tapered channels have more material close to the web and therefore have the shear center closer to the web, as illustrated for sections with comparable depths by Figure 3, reducing the eccentricity of any load applied at the web.

2 STATE OF THE ART

Despite its popularity as structural element, there is relatively little published on the stability of hot-rolled channel sections. A review is given of publications on experiments, elastic section properties, plastic strength, analytical research, and standards.

2.1 Stability experiments

Hill, 1953, studied the elastic lateral torsional buckling of aluminum channels loaded by uniform bending to verify analytical equations for elastic stability. Differences between the experimental and analytical results were attributed to the boundary conditions. Hill proposed to use the same equations for LTB for I and channel sections.
La Poutré, et al., 2000, performed a series of four point bending test on

hot-rolled UPE 160 channels, where the point of load introduction was varied over the depth from the top flange, axis of symmetry, to the bottom flange. Reference tests were performed with loads applied at the shear center. The test program served to calibrate an FE-model for LTB of channels and good correlation was shown by La Poutré, 1999. Gijben, 2000, performed four point bending tests on UNP 160 and IPE 160 sections loaded at the shear center. The difference with the experiments by La Poutré, et al., 2000, was that the support conditions were varied to find ideal supports in testing. Two of the three tested support configurations worked well and the results were in line with analytical buckling loads.

While for wide flange beams many studies can be found on the residual stress distribution due to hot-rolling, these studies are rare for channels. For the UPE 160 channels used in the experiments of La Poutré, Boon, 2001, determined the residual stresses with the hole drilling and the sectioning methods. He compared the results with each other and came to the conclusion that the sectioning method is more robust. The measured residual stresses showed a quite irregular pattern. To derive smooth, theoretical patterns, such as the known ones for wide flanges beams, more tests are needed.

As part of a recent research program (Sedlacek, et al., 2004) to study the LTB of wide flange beams and channel sections, a large series of tests were performed on hot-rolled channel sections by three German universities. All universities used UPE 200 sections in three point bending and the tests were performed to validate an FE-Model with which the stability of these sections was investigated. At the University of Aachen-RWTH, the plastic strength of channels loaded by just bending, bending and torsion, and bi-axial bending and torsion was studied. All results can be found in Sedlacek, et al., 2004. At the Technical University of Berlin, LTB of channels loaded by bending and torsion was studied. A full account of the experiments can be found in Sedlacek, et al., 2004, and partial results were published by Lindner & Glitsch, 2004. At the University of Bochum, channels loaded by normal force, bending and torsion were studied. A full account of the experiments can be found in Sedlacek, et al., 2004, and partial results were published by Kindmann & Wolf, 2004.

2.2 Elastic section properties

The section properties of hot-rolled sections used to be determined based on thin-walled theory, i.e. the center lines of the sections were considered to determine the moments of inertia, the torsional constant and the warping constant. However, hot rolled sections comprise rather thick plates and fillets, and some thickness effects contribute to the section properties as well, especially to the torsional and warping constants. For the torsional constant of channels, there are very good analytical approximations, such as by Young, 1989, and SCI-P-210, 1996. However, with the Finite Element Method, more precise solutions to the section properties can be obtained. Wagner, et al., 1999, studied the section properties of UNP sections numerically and compared them with analytical results and found differences up to 20%. Kraus, 2005, compared analytical and numerical section properties of UAP and UPE sections and found differences up to 3.5%. Although these difference seem large, they occur mainly for sections with a small depth, for larger depths they diminish. In this paper, the analytical section properties will be used, while they are more accessible.
Tabulated section properties for Parallel Flange Channels are given by SCI-P-210, 1996, for UPE and UAP by Kraus, 2005, for UPN by Wagner, et al., 1999, and for American Standard Channels by the AISC Manual of Steel Construction, 1999.

2.3 Plastic strength

One of the early papers on the analytical plastic strength of I-sections loaded by bi-axial bending and normal force was by Rubin, 1978. With a novel method, which could be adopted for channels as well, a large plastic capacity could be used for the interaction of loads. The German steel construction standard DIN 18800 Teil 2, 1990, adopted nearly identical interaction curves. Two decades later, Kindmann & Frickel, 1999, claimed that the method of Rubin and DIN 18800 gave values up to 20% larger than the actual plastic strength and should no longer be used. What followed was a heated debate in the journal Stahlbau after which the validity of the interaction equations was kept upright. Parallel to this debate, Roes, 2001, investigated the analytical plastic strength of channel sections loaded in bending and mixed (i.e. St.-Venant and warping restraint) torsion. The analytical plastic strength was improved when compared with Kindmann & Frickel, but still rather conservative (up to 40%) when compared with plastic FEA. It was also shown that applying analytical methods to determine the plastic strength of channels becomes rather complex.

2.4 Eigenvalue

Timoshenko & Gere, 1961, found that the elastic lateral torsional buckling load (eigenvalue) for channel sections loaded by pure bending can be determined with the same analytical expressions as for doubly symmetric wide flange beams. In the Guide to Stability Design Criteria for Metal Structures (Galambos (Ed.), 1998), this finding was recognized and in Section 5.2, dealing with elastic LTB of beams, it is stated in 5.2.3 Monosymmetric Beams that “the methods and formulas in Section 5.2.2. (…) apply to doubly symmetric beams of uniform section, … , and for channels where bending about the major axis is in the plane of the shear center”.

Other studies showed analytically (Melcher, 1994, 1999) and numerically (La Poutré, et al., 2002) that the eigenvalue of channels loaded by a shear force, with a line of action passing through the shear center, can be determined with the same equations as used for wide flange beams.

So it is established in the literature that the elastic LTB can be determined for channels with the same equations as for wide flange beams.

2.5 Inelastic LTB – centric loading

A distinction needs to be made between centric and eccentric loading. In Stability of Metal Structure, A World View (Beedle (Ed.), 1990), it was found that a few older standards had provisions for LTB which were valid not only for doubly symmetric I-sections but also for channel sections. These Standards were SNIP II-23-81 from the USSR published in 1982 and BSK from Sweden published in 1987. In recent standards, no design clauses for LTB of centrically loaded channels were found.

In La Poutré, et al., 2002, it was shown that Eurocode 3 gives good results for centrically loaded channels compared with FEA ultimate loads. It was concluded that the design method of this standard can be extended beyond double symmetric sections to mono symmetric channel sections loaded at the shear.

2.6 Inelastic LTB – eccentric loading

For eccentrically loaded channels, the first study in recent times concerned with the inelastic LTB of hot-rolled channels was published by Höß, et al., 1992 and more elaborately by Wagner, et al., 1996. They concluded that, if the ultimate loads were plotted against buckling curves, there was little correlation between the two. Instead of using buckling curves, they proposed tables with ultimate loads for channel sections.

La Poutré, et al., 2002, studied LTB of hot-rolled channel sections and proposed a Merchant-Rankine design equation for eccentric loading. In this equation, the eigenvalue for centric loading $F_{eig,loc}$ was used, where the index 'loc' indicates that the location at the top flange, axis of symmetry or bottom flanges should be entered. $F_{pl,web}$ indicates that the plastic strength for a load applied at the web should be entered in the equation. This plastic strength can be determined accurately with FEA only (2.3 Plastic strength). This design equation yielded conservative results and a modification was proposed (Eq. 1) by adding a constant μ to the design equations. (where μ = 0.06 for top flange loading, μ = 0.11 for axis of symmetry loading, and μ = 0.15 for bottom flange loading). Thus the actual buckling loads were approached and the equation was less conservative.

$$F_{MR*,loc} = \frac{1}{1/F_{eig,loc} + 1/F_{pl,web}} + \mu \cdot F_{pl,web} \qquad (1)$$

Based on a large series of tests and FE-Simulations, Lindner & Glitsch, 2004, proposed Equation 2 to design doubly symmetric section loaded by bi-axial bending and channel sections loaded eccentrically.

$$\frac{M_y}{\chi_{LT} \cdot M_{y,pl}} + C_{mz} \cdot \frac{M_z}{M_{z,pl}} + k_{zw} \cdot k_w \cdot \alpha \cdot \frac{B_w}{B_{w,pl}} \leq 1 \qquad (2)$$

In this equation, χ_{LT} is a non-dimensional reduction factor for buckling, M_y the applied major axis bending moment and $M_{y,pl}$ the major axis plastic capacity. The second term is zero while no minor axis bending is applied initially and B_w is the bi-moment due to the restraint of warping (see La Poutré, 1999, for equations), and $B_{w,pl}$ the plastic bi-moment capacity. The constants $k_{zw} = 1 - M_z/M_{z,pl} = 1$ because $M_z = 0$, $k_w = 0.7 - 0.2 \cdot B_w/B_{w,pl}$, and $\alpha = 1/(1 - M_y/M_{cr})$ where M_{cr} is the eigenvalue. The bi-moment capacity can be determined with Equation 3 (Kindmann, 1996, and Roes, 2001). Solving Eq. 2 directly for the maximum applicable bending moment M_y is not possible due to the factor α which has M_y in the denominator. Therefore the M_y needs to be determined iteratively.

$$B_{w,pl} = \frac{1}{4} A_f \cdot b_0 \cdot h_0 \cdot f_y \cdot \left(1 + \frac{A_w}{2 \cdot A_f} - \frac{A_w^2}{16 \cdot A_f^2}\right) \tag{3}$$

Kindmann & Frickel, 2002, modified the provisions from the German steel design standard DIN 18800 (Eq. 4) to design channels for LTB.

$$\frac{M_y}{\kappa_{LT} \cdot M_{y,pl}} \le 1 \tag{4}$$

In which: $\kappa_{LT} = \left(1 + \bar{\lambda}_{MT}^5\right)^{-0.4}$ and $\bar{\lambda}_{MT} = \bar{\lambda}_M + \bar{\lambda}_T$

To the non-dimensional slenderness for LTB $\bar{\lambda}_M$, a component $\bar{\lambda}_T$ is added to account for torsion, thus increasing the non-dimensional slenderness $\bar{\lambda}_{MT}$ for channels. With an increased slenderness, the non-dimensional reduction κ_{LT} is also greater. Furthermore the slenderness is limited to 0.5 or above and divided in three ranges as follows:

$$
\begin{aligned}
&0.5 \le \bar{\lambda}_{MT} < 0.75: && \bar{\lambda}_T = 1.11 - \bar{\lambda}_M \\
&0.75 \le \bar{\lambda}_{MT} < 1.14: && \bar{\lambda}_T = 0.69 - 0.44 \cdot \bar{\lambda}_M \\
&\bar{\lambda}_{MT} \ge 1.14: && \bar{\lambda}_T = 0.19
\end{aligned}
$$

2.7 Standards

Despite the fact of the common occurrence in engineering, no structural steel design standard has provisions for checking the stability of channel sections loaded in bending and torsion. The AISC Manual of Steel Construction, 1999, has provisions for the major axis strength, but no clauses for the stability. The same applies for Eurocode 3 (EN 1993-1-1, 2006).

3 CURRENT RESEARCH

3.1 Load case and material law

The load case studied is four point bending with the loads applied at a quarter span, Figure 4a. The major bending moment for this load case is given by $M_y = F \cdot L/4$. The point of load application at the cross section was varied, Figure 4b. The load applied at the axis of symmetry was to study the interaction of initial torsion with bending. This was compared with load applied at the top and bottom flange respectively to investigate the amplifying and diminishing effects respectively of these load locations. Standard parallel flange European channels of the UPE series were selected and two depths, 200 and 400 mm, were studied at six different spans ranging from 6 to 36 times the depth of the section.
A multi linear material law was used with an elastic, a perfectly plastic, and a hardening branch, Figure 5a. The strain at ultimate strength ε_u was 15 times the strain at the proportional limit ε_y, which complies with the demanded for minimum ductility by Eurocode 3. The steel grade studied was S235 with a yield strength $f_y = 235$ N/mm^2.

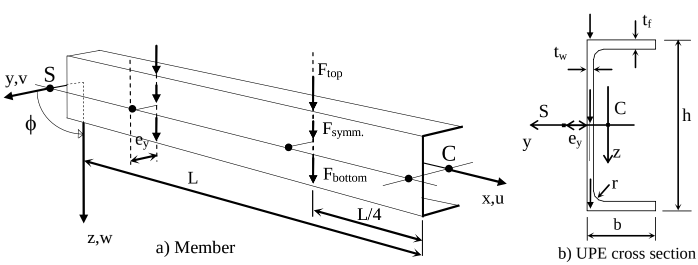

Figure 4. Studied load cases

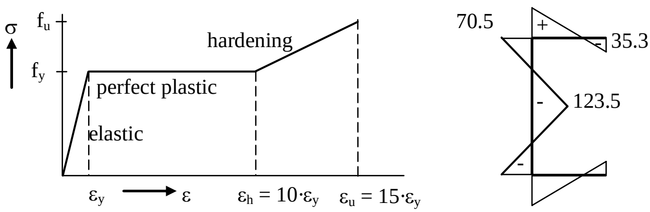

(a) multi-linear material law (b) residual stress distribution

Figure 5. Material law and residual stress distribution used for the FE-analyses.

As stated in the state of the art, residual stress patterns for hot-rolled channel section are rare in the literature. The study of Boon, 2001, gives a rather scattered pattern and instead a theoretical distribution, proposed by Sedlacek, et al., 2004, was used, Figure 5b.

3.2 Input values for design

To determine the non-dimensional slenderness, the eigenvalue and plastic strength are needed. The eigenvalue for centrically loaded channel sections can be determined analytically with the same equations as used for doubly symmetric I-sections. Furthermore, it was found by La Poutré, et al., 2002, through FE-analysis that there is no appreciable difference in the eigenvalue if the load is applied at the shear center or at the web. Therefore, the eigenvalue for eccentrically loaded channel sections can be determined with the equations for centrically loaded sections. In this paper, the equations from the Austrian National Applications Document (NAD) of Eurocode 3, B 1993-1-1, 2007, were used. These equations used to be in the older editions of Eurocode 3, but were removed upon finalization. The analytical results were compared with FE-results and they compared very well for larger spans. Only for very short spans (L/h = 6), where shear force plays an important role, the numerical eigenvalues were about 10% less. The results are given in Tables 1 and 2.
As has been found from the literature, determining the plastic strength for channels loaded in bending and torsion analytically becomes very complex and yields conservative results. Therefore the plastic strength was determined with FE-Analysis, in which material nonlinearity was

used but no large displacements (geometric linearity). The ultimate bending moments will be referred to as M_{MNA} and are given by Tables 1 and 2

3.3 Nonlinear Finite Element Analysis

The channels were modeled with the finite element program Ansys. The cross section comprises six 4-node shell 181 elements for the web and flanges. The fillets of the actual section contribute to the bending stiffness but cannot be modeled with shell elements. Nevertheless they are important for the stiffness of the section. Instead of fillets, beam elements were used to compensate for the fillets, a procedure described in detail in the SSRC contribution of 2003 (La Poutré, et al., 2003). There, the described procedure was used for wide flange beams, but can easily be adapted for channels. In the length of the channels, 44 elements were used which results in a aspect ratio smaller than the advised minimum aspect ratio of 1/20th. Figure 6 shows the FE-model, where the beam elements, which make up for the fillets, at the flange-web junction can clearly be seen.

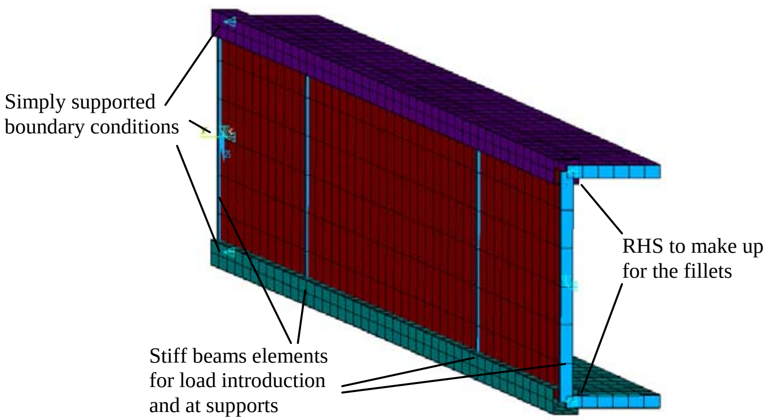

Figure 6. FE-Model of channel section.

A lateral imperfection with a sinusoidal shape with a maximum amplitude of v_{max} = L/1000 was modeled. The imperfection was found to have the greatest influence when modeled in the negative y-axis direction (La Poutré, 1999). The analyses included geometric and material nonlinearities, geometric imperfections and residual stresses and is referred to as GMNIA (Geometric and Material Non-linear Imperfect Analysis). In Table 1 and 2, the ultimate bending moments for these analyses are listed.

4 DESIGN

From the State of the Art, it was found that three methods were proposed in the literature to design for stability. A Merchant-Rankine related method (Eq. 1) by La Poutré, et al., 2002, an interaction formula (Eqs. 2-3) by Linder & Glitsch, 2004, and a method based on modified buckling curves (Eq. 4) by Kindmann & Frickel, 2002. These methods will be applied on the channel sections studied in this paper. In addition, a fourth method, the Overall Method from Eurocode 3, will be examined. The Overall Method allows the design for stability of structures under general loading and was, for example, applied to the in-plane stability of arches (La Poutré, 2007) for which no design provisions exist. Backgrounds on the Overall Method can be found in Greiner, 2003.

With the analytical eigenvalue $M_{eig,loc}$ and the numerical plastic strength M_{MNA}, determined in Section 3.2, a non-dimensional slenderness $\bar{\lambda}_{ov}$ (Eq. 5) was determined. The index loc stands for the location of load application at the web (top flange, axis of symmetry, or bottom flange). With the FE-simulated ultimate bending moment M_{GMNIA}, the non-dimensional reduction factor χ (Tables 1 and 2) was determined with Equation 6.

$$\bar{\lambda}_{ov,loc} = \sqrt{\frac{M_{MNA}}{M_{eig,loc}}} \qquad (5)$$

$$\chi_{loc} = \frac{M_{GMNIA,loc}}{M_{MNA}} \qquad (6)$$

Table 1. Results for UPE 200 Sections.

L	$M_{cr,top}$	$M_{cr,symm}$	$M_{cr,bot}$	M_{MNA}	b_w	$\lambda_{ov,top}$	$\lambda_{ov,symm}$	$\lambda_{ov,bot}$	χ_{top}	χ_{symm}	χ_{bot}
[m]	[kNm]	[kNm]	[kNm]	[kNm]	[m]	[-]	[-]	[-]	[-]	[-]	[-]
1.2	161.1	252.9	397	33.5	0.023	0.46	0.36	0.29	0.87	0.96	1.11
2.4	63.3	88	122.3	41.5	0.014	0.81	0.69	0.58	0.71	0.83	0.93
3.6	41.0	52.5	67.3	46.8	0.01	1.07	0.94	0.83	0.59	0.68	0.77
4.8	31.0	37.7	45.8	50.4	0.007	1.27	1.16	1.05	0.5	0.56	0.63
6.0	25.1	29.5	34.6	50.3	0.006	1.41	1.31	1.21	0.44	0.49	0.54
7.2	21.2	24.3	27.7	50.4	0.005	1.54	1.44	1.35	0.4	0.42	0.47

Table 2. Results for UPE 400 Sections.

L	$M_{cr,top}$	$M_{cr,symm}$	$M_{cr,bot}$	M_{MNA}	b_w	$\lambda_{ov,top}$	$\lambda_{ov,symm}$	$\lambda_{ov,bot}$	χ_{top}	χ_{symm}	χ_{bot}
[m]	[kNm]	[kNm]	[kNm]	[kNm]	[m]	[-]	[-]	[-]	[-]	[-]	[-]
2.4	517.8	780.3	1176	231.7	0.025	0.67	0.54	0.44	0.75	0.86	0.97
4.8	219.9	290.7	384.4	274.3	0.014	1.12	0.97	0.84	0.57	0.65	0.72
7.2	146.0	178.8	219.1	286.0	0.01	1.4	1.26	1.14	0.41	0.47	0.53
9.6	111.0	130.0	152.2	285.4	0.007	1.6	1.48	1.37	0.32	0.37	0.4
12.0	90.1	102.4	116.4	285.9	0.006	1.78	1.67	1.57	0.27	0.29	0.32
14.4	76.0	84.6	94.3	286.2	0.005	1.94	1.84	1.74	0.21	0.23	0.24

The plastic capacity for a UPE 200 is $M_{y,pl}$ = 51.7 kNm and for a UPE 400 it is $M_{y,pl}$ = 297 kNm (steel grade S235). Comparing to the plastic capacity for bending and torsion M_{MNA}, it becomes clear that torsion reduces the bending capacity considerably for short spans.
In the interaction equation by Lindner & Glitsch, the plastic bi-moment capacity is used. For a UPE 200 section the plastic bi-moment capacity is $B_{w,pl}$ = 0.89 kNm^2 and for a UPE 400 it is $B_{w,pl}$ = 5.8 kNm^2. The bi-moment can be found as follows: $B_w = b_w \cdot M_y$ in which b_w is given in Tables 1 and 2 and M_y is the bending moment.

Figure 7 shows the non-dimensional reduction factors χ plotted against the non-dimensional slenderness λ. At the left hand side, this is done for the UPE 200 sections and at the right hand side for the UPE 400 sections. At the top, the figures for top flange loading, at the middle for loading at the axis of symmetry on the web, and at the bottom for bottom flange loading are shown. In these figures, the eigenvalue (elastic buckling) curve is shown as a reference.

The results are compared with two buckling curves. In Section 6.3.2.2 of Eurocode 3 the general design for LTB for all members, and in Section 6.3.2.3 the specific design for LTB of hot-rolled sections is treated. With the given dimensions of the channels, buckling curve B should be used for the general design and buckling curve C for the specific design. However, the buckling curves of the general design start to deviate from unity at a non-dimensional slenderness of 0.2 and of the specific design at $\lambda = 0.4$, which allows for higher applicable loads. When the results from the Overall Method (labeled OM) are compared to these two buckling curves, it emerges that they are larger than buckling curve B from 6.3.2.2 for nearly all non-dimensional slendernesses, and larger than buckling curve C from 6.3.2.3 for most slenderneesses. Only for very short spans (L/h = 6) they fall below curve B.

For the UPE 200 sections loaded at the bottom flange a non-dimensional reduction factor larger than unity was found. Normally, a structure cannot be stronger than the plastic strength ($\chi = 1$). In this particular case, the plastic strength was determined with geometric linearity and the ultimate load M_{GMNIA} with geometric non-linearity. The load at the bottom flange reduces the initial torsion which is accounted for in the geometric non-linear analysis and produces the higher ultimate loads.

The design method of La Poutré, et al., 2002, (Eq. 1) uses constants μ to improve the results of the Merchant-Rankine equation. The constants were determined for UPE 160 sections and prove to be too large for UPE 200 and 400 sections at higher non-dimensional slendernesses.

The design by Kindmann & Frickel, 2002, underestimates the capacity of channels at low slendernesses but approaches buckling curve B at larger slendernesses. The design by Linder & Glitsch, 2004, underestimates the capacity for all slendernesses.

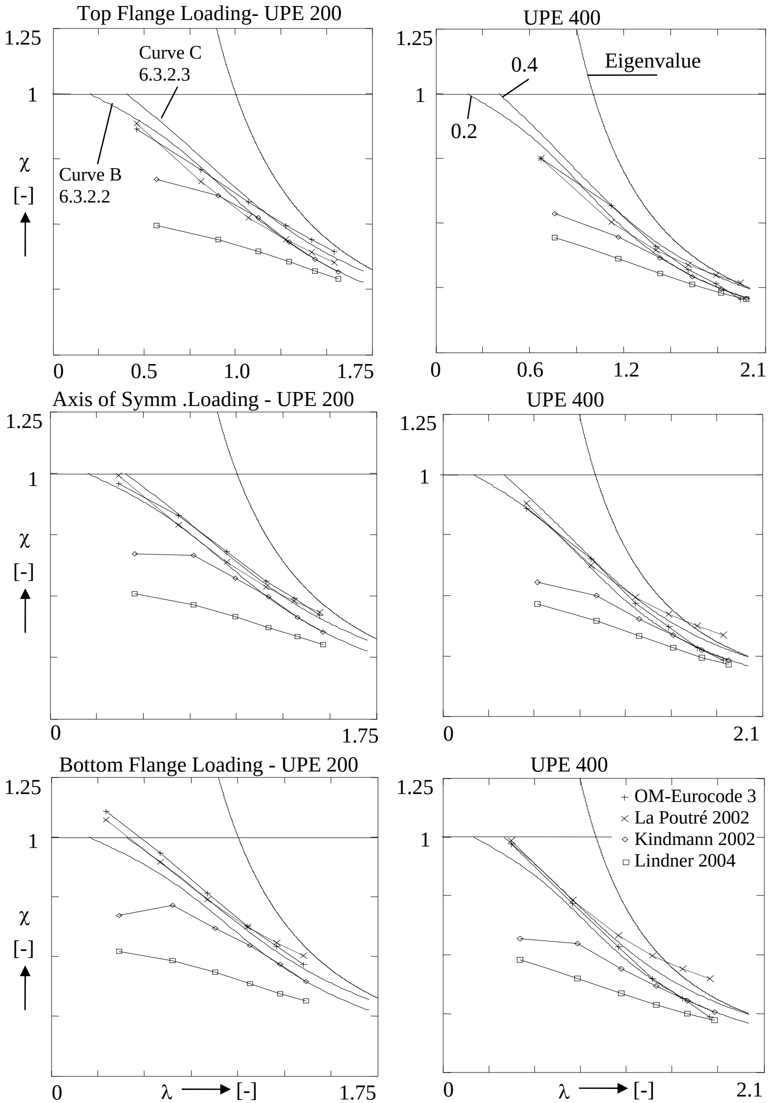

Figure 7. Design for stability of channel sections.

5 DISCUSSION

The Overall Method from Eurocode 3 works well, especially with buckling curve B of Section 6.3.2.2. Ony for very short spans (L/h=6) or slenderness $\lambda < 0.8$ the results fall below the buckling curve, which means that a design using buckling curves overestimates the actual ultimate load. For these very short spans, the results should be adjusted. A drawback of the Overall Method is that currently the plastic strength for channels loaded by torsion and major axis bending needs to be determined with FEA.

The design proposed by La Poutré, et al., 2002, is similar to the Overall Method in that the analytical eigenvalue and the numerical plastic strength for bending and torsion is used. The constants, originally proposed for UPE 160 sections, are not generally applicable to other sections. Therefore, section specific constants would be needed and a maximum slenderness should be imposed in order to keep the results below the buckling curves. A table with section specific constants is not a desirable approach for a design method to be adopted in a structural steel standard.

The design of Kindmann & Frickel, 2002, is based on current design practice. It has as benefit that all parameters can be determined by hand analysis. The method works well for larger spans (slendernesses) but is conservative for short spans.

The Linder & Glitsch, 2004, proposal is rather complex. Determining the bi-moment and bi-moment capacity is not standard practice for stability design of steel structures. The interaction expression (Eq. 2) cannot directly be solved for the maximum applicable bending moment M_y. Finally, the reduction related to the bi-moment seems too severe when applied on the design of channel sections. Possible modifications could solve this problem.

6 CONCLUSIONS

This paper set out to investigate available design criteria for lateral torsional buckling of channel sections loaded in bending and torsion.
It was found from the literature that centrically loaded channel sections (i.e. load applied at the shear center) can be designed with the provisions of steel design standards for wide flanges beams.
For eccentrically loaded channel sections (i.e. load applied in the plane of the web), no standard gives design criteria. In the literature, three design criteria were found. In this paper, a fourth design criterion was explored and compared with the three other design criteria. It was found that the current design proposal proves to the convenient and accurate and is similar to standard design practice for wide flange beams. It has as disadvantage that computer analysis is needed to determine the plastic strength for the interaction of torsion and major axis bending. The design method proposed by Kindmann & Frickel, 2002, proves to be a good alternative.

A recommendation for future research is to derive closed form analytical solutions for the plastic strength of channels loaded in bending and torsion. This would greatly facilitate the design for stability.

REFERENCES

Beedle, L. S. (Ed.) (1990). *Stability of metal structures, a world view*. 2nd edition. 921 p.

DIN 18800 Teil 2 (1990). *Stahlbauten.* Berlin: Beuth Verlag GmbH.

A 6/A 6M (1993). *Standard specification for general requirements for rolled steel plates, shapes, sheet piling and bars for structural use.* Philadelphia: ASTM.

SCI-P-210 (1996). *Parallel flange channels, section properties and member capacities to BS 5950: Part 1: 1990.* Ascot: The Steel Construction Institute.

Galambos, T. V. (Ed.) (1998). *Guide to Stability Design Criteria for Metal Structures*. 5th edition. New York: John Wiley & Sons. 911 p.

AISC Manual of Steel Construction (1999). *Load and resistance factor design*

(Metric). Chicago: American Institute of Steel Construction Inc.

EN 10279 (2000). *Hot rolled steel channels - Tolerances on shape, dimensions and mass.* Brussels: European Committee for Standardization.

EN 1993-1-1 (2006). *Eurocode 3: Design of steel structures. Part 1-1: General rules and rules for buildings.* Brussels: European Committee for Standardisation (CEN).

B 1993-1-1 (2007). *Eurocode 3: Design of steel structures. Part 1-1: General rules and rules for buildings.* Vienna: ON Österreichisches Normungsinstitut.

Boon (2001). *Restspanningen in stalen UPE 160 profielen*. Report nr. TUE BCO 01.22,Technische Universiteit Eindhoven. 77 p.

Gijben (2000). *Influence of supports on lateral buckling of channel and I shaped sections*. Report nr. TUE.BCO 20.12, Eindhoven: Technische Universiteit Eindhoven. 107 p.

Greiner, R. (2003). Concept of the numerically-based buckling check of steel structures. *Steel struct and bridges conf* Prague, 17 Sept. 2003. Prague: Czech Technical University. pp. 511-516

Hill, H. N. (1953). Lateral Buckling of Channels and Z-beams. *American Society of Civil Engineers Transactions,*(Paper No. 2700), 829-841

Höß, P., Heil, W., & Vogel, U. (1992). Traglasten für drehgebettete Träger aus U-profilen. *Stahlbau,* 61(3), 85-91

Kindmann (1996). *Die neuen UPE 80-400, Konstruktion und Bemessung*. Peine, Germany: Preussag Stahl. 55 p.

Kindmann, R. & Frickel, J. (1999). Grenztragfähigkeit von häufig verwendeten Stabquerschnitten für beliebige Schnittgrößen. *Stahlbau,* 68(10), 817-828

Kindmann, R. & Wolf, C. (2004). Ausgewählte Versuchsergebnisse und Erkenntnisse zum Tragverhalten von Stäben aus I- und U-Profilen. *Stahlbau,* 73(9), 683-692

Kindmann, R. & Frickel, J. (2002). Tragfähigkeit von U-Profilen bei Biegung und Torsion. *Rubstahl,*(1), 1-2

Kraus, M. (2005). Genaue Torsionskenngrößen von UPE- und UAP-Profilen auf Grundlage der FE-Methode. *Rubstahl,*(3), 1-4

La Poutré (1999). *Strength and stability of channel sections used as beam*. Report nr. TUE BCO 99.31, Eindhoven: Technische Universiteit Eindhoven. 190 p.

La Poutré, D. B. (2007). In-plane stability of circular steel arches with varialble subtended angles. In W. S. Easterling (Eds.), *Annual Stability* (*SSRC).* New Orleans, 18 Apr. 2007. University of Missouri-Rolla, Rolla, MO, USA: Structural Stability Research Council (SSRC). pp. 201-219

La Poutré, D. B., Snijder, H. H., and Hoenderkamp, J. C. D. (2000). Lateral torsional buckling of channel shaped beams: Experimental research. In D. Camotim, D. Dubina, & J. Rondal (Eds.), *Coupled Instabilities in Metal*

Structures Conf (*CIMS).* Lisbon, 21 Sept. 2000. London: Imperial College Press. pp. 265-272

La Poutré, D. B., Snijder, H. H., and Hoenderkamp, J. C. D. (2002). Design method for lateral torsional buckling of channel sections. In N. Iwankiw (Eds.), *Annual Stability Conf* (*SSRC).* Seattle, 24 Apr. 2002. Gainesville, FL, USA: Structural Stability Research Council (SSRC). pp. 311-326

La Poutré, D. B., Snijder, H. H., and Hoenderkamp, J. C. D. (2003). An FE-model for analyzing spatial stability of steel arches. *Annual technical session & meeting* (*SSRC).* Baltimore, 2 Apr. 2003. Gainesville, FL, USA: Structural Stability Research Council (SSRC). pp. 279-298

Lindner, J. & Glitsch, T. (2004). Vereinfachter Nachweis für I- und U-Träger beansprucht durch doppelte Biegung und Torsion. *Stahlbau,* 73(9), 704-715

Melcher, J. J. (1994). Note to the buckling of beams with monosymmetric section loaded transversely to its plane of symmetry. *Annual Stability conf* (*SSRC).* Bethlehem, Lehigh University, Bethlehem, PA, USA: Structural Stability Research Council (SSRC). pp. 61-75

Melcher, J. J. (1999). Kippen von Trägern als Stabilitätsproblem zweier Gruppen von Querschnittypen. *Stahlbau,* 68(1), 24-29

Roes, M. G. L. (2001). *Plastische doorsnedecapaciteit van stalen profielen.* MSc-thesis. Eindhoven: Technische Universiteit Eindhoven. 212 p.

Rubin, H. (1978). Interaktionsbeziehungen für doppeltsymmetrische I- und Kastenquerschnitte. *Stahlbau,* 47(5), 145-151

Sedlacek, Stangenberg, Lindner, Glitsch, Kindmann, and Wolf (2004). *Untersuchungen zum Einfluss der Torsionseffekte auf die plastische Querschnittstragfähigkeit und die Bauteiltragfähigkeit von Stahlprofilen*. Report nr. P 554, Düsseldorf: Verlag und Vertriebsgesellschaft mbH. 557 p.

Timoshenko, S. P. & Gere, J. M. (1961). *Theory of elastic stability*. 2nd edition. Tokyo: McGraw-Hill. 541 p.

Wagner, W., Sauer, R., & Gruttmann, F. (1999). Tafeln der Torsionskenngrößen von Walzprofilen unter Verwendung von FE-Diskretisierungen. *Stahlbau,* 68(2), 102-111

Wagner, Heil, and Höß (1996). *Bemessung von Einfeld- und Durchlaufträgern aus rundkantigem U-Stahl (DIN 1026) nach dem Traglastverfahren unter Berücksichtigung einer Drehbettung und einer Normalkraftbelastung*. Report nr. P 251, Düsseldorf: Verlag und Vertriebsgesellschaft mbH. 69 p.

Young, W. C. (1989). *Roark's Formulas for Stress and Strain*. 6th int. student edition. London: McGraw-Hill. 624 p.

ON THE INELASTIC STRENGTH OF BEAM-COLUMNS UNDER BIAXIAL BENDING

Ronald D. Ziemian[1], Dong-Woo Seo[2], and William McGuire[3]

ABSTRACT

The application of a tangent modulus, plastic hinge approach to the analysis of the torsional-flexural stability of wide flange, compact section beam-columns subjected to various combinations of axial force and biaxial bending is considered. Nonuniform torsion effects are included. The modulus is a modification of one used by the authors in prior studies and incorporated in the structural analysis program MASTAN2. Results are compared with resistances predicted by design equations appearing in the 2005 AISC *Specification for Structural Steel Buildings* and the more refined finite element program ADINA. The objective is to illustrate the potential of this approach in expanding relatively simple frame analysis programs to model inelastic out-of-plane instabilities.

[1]Professor, Department of Civil and Environmental Engineering, Bucknell University, Lewisburg, PA 17837
[2]Graduate Student, Department of Civil and Environmental Engineering, Bucknell University, Lewisburg, PA 17837
[3]Professor Emeritus, School of Civil and Environmental Engineering, Cornell University, Ithaca, NY 14850

INTRODUCTION

In the latest edition of the Structural Stability Research Council's (SSRC) *Guide to Stability Design Criteria for Metal Structures* it is stated that "standard frame analysis software is incapable of modeling out-of-plane member instabilities and it is primarily for this reason that SSRC Technical Memorandum No. 5 recommends that separate checks be made for frame and member instabilities" (*Guide*, 1998). Four years later, this assessment was further supported by Trahair and Chan (2002) who commented in a University of Sydney research report "it appears at present to be too difficult to develop a practical method of advanced analysis for biaxial bending and torsion." Some progress may have been made since the Guide and Sydney report were published, but that is still, essentially, the state of the art. Even where the theory may exist there remain key areas – most notably in the inelastic domain – in which it has not been reduced to a form simple and reliable enough for routine design. The tasks ahead require consideration of the three-dimensional behavior of structural systems in all of their physical and mechanical variability, including section properties, member interaction, loading patterns, imperfections, residual stresses, and so on.

From the earliest attempts to explain elementary column behavior, variations on the "reduced", "effective", or "tangent" modulus concept have been used to quantify inelastic instability (Salmon, 1921; Bleich, 1952). In more recent years, the concept has been applied to the more complex problem of flexural-torsional buckling (Kim and Chen, 1996; Wongkew and Chen, 2002; Trahair and Hancock, 2004). This paper is in that category and follows two previously published papers. The first by McGuire and Ziemian (2000) treats both in- and out-of-plane instability, but only the elastic case of the latter. The second by Ziemian and McGuire (2002) deals with inelastic, in-plane stability but not out-of-plane effects, which are the chief concerns of this paper.

All of these works are reasoned attempts to interpret some aspect of real behavior. They are valid to the extent that they can be supported by unassailable theory or conclusive experimental verification. Generally, they invoke parameters intended to account for effects that can vary widely, such as residual stresses and initial imperfections. They are useful to the extent that a limited number of sets of parameters can be established by systematic sorting and analysis of the relevant data, as in ways that a few column curves have been developed and accepted for the design of the wide variety of columns encountered in practice (Bjorhovde, 1988; *Australian Standard ASA4100,* 1998). It is in this context that the authors' current concept for modeling flexural-torsional instabilities is presented in this paper.

DESCRIPTION OF ANALYSIS PROGRAM - MASTAN2

The MASTAN2 (2007) analysis program used in this study employs the finite element method with the key incremental stiffness equation

$$[K_t]\{d\Delta\} = \{dP\} \tag{1a}$$

where $[K_t]$ is a tangent stiffness matrix that reflects the current state of the deformed structure, and $\{d\Delta\}$ contains the displacements corresponding to an increment of loading $\{dP\}$. Using one-dimensional (line) elements, it has routines that can calculate realistic limit state responses for two- and three-dimensional steel frames subjected to static loads. Nonlinear geometric behavior is included by use of element geometric stiffness matrices combined with an updated Lagrangian formulation. Material nonlinear behavior is included primarily through an elastic-plastic hinge component of the analytical model that admits full cross-section yielding at element ends. Definition and response of the zero-length plastic hinges is controlled by a stress-resultant yield surface that accounts for axial force and both major- and minor-axis bending. Hence, the tangent stiffness matrix is

$$[K_t] = [K_e] + [K_g] + [K_m] \tag{1b}$$

where $[K_e]$, $[K_g]$, and $[K_m]$ are the linear elastic, geometric, and plastic reduction matrices, respectively. The program's supporting theories and solution methods are presented in the textbook *Matrix Structural Analysis* (McGuire, et al. 2000).

The linear elastic and geometric stiffness matrices in MASTAN2 are formulated for a 14 degree of freedom framework element that includes axial, shear, flexural, and warping components. Warping at the element ends can be specified as free, fixed, or continuous. In previous studies, this formulation has been shown to adequately capture elastic flexural buckling of columns, elastic lateral-torsional buckling of beams, and elastic flexural-torsional buckling of beam-columns.

The basis for the plastic reduction matrix is a yield surface defined by

$$\Phi = p^2 + m_x^2 + m_y^4 + 3.5p^2m_x^2 + 3p^6m_y^2 + 4.5m_x^4m_y^2 = 1 \qquad (2)$$

where, $p=P/P_y$, $m_x=M_x/M_{px}$, $m_y=M_y/M_{py}$, and P_y, M_{px}, and M_{py} are the axial yield load and the major- and minor-axis plastic moments, respectively.

To approximate the material nonlinear effects of residual stresses on member behavior, the elastic modulus E used in computing the coefficients in the element's elastic stiffness matrix may be set to the following tangent modulus provision

$$E_t = \tau\, E_o \quad \text{with} \quad \begin{array}{ll} \tau = 1.0 & \text{for } p \le 0.5 \\ \tau = 4p(1-p) & \text{for } 0.5 < p \le 1.0 \end{array} \qquad (3)$$

where, E_o is the initial elastic modulus (i.e. 29,000ksi for steel). Eq. (3) is a frequently used empirical expression designed to represent the performance of steel columns in the inelastic range (*Guide*, 1998). Implicit in it is the assumption of a residual stress pattern that will result in an effective proportional limit equal to half the yield stress of the material.

In McGuire and Ziemian (2000) and then later in Ziemian and McGuire (2002) attempts are made to improve the ability of the MASTAN2 program to simulate the behavior of systems of small redundancy in which the spread of yielding may have a direct impact on limit state behavior, particularly in cases of minor-axis bending. The latter paper, which only deals with in-plane instability, uses the following modified tangent modulus

$$E_{tm} = \tau\, E_o \;\; \text{with} \;\; \tau = \min\begin{pmatrix} 1.0 \\ (1+2p)\left[1-\left(p+\alpha_y m_y\right)\right] \end{pmatrix} \tag{4}$$

where, the factor α_y is an empirical one, which after calibration with a series of comparative plastic zone analyses was set at 0.65. This value provided good results for typical wide-flange shapes.

Use of the basic MASTAN2 formulation in conjunction with the above tangent modulus or modified tangent modulus approaches provides the opportunity to accurately capture in-plane inelastic flexural buckling of columns.

With this in mind, and especially considering the simplicity of this approach, the potential for using an expression similar to Eq. (4) but with the ability to further capture inelastic out-of-plane buckling was explored.

A subsequent parametric study suggested that a term representing the influence of major-axis bending on inelastic behavior be added to Eq. (4). The resulting expression is

$$E_{tm} = \tau \, E_o \text{ with } \tau = \min\left(\frac{1.0}{(1+2p)\left[1-\left(p+\alpha_y m_y + \alpha_x m_x^2\right)\right]} \right) \quad (5)$$

The potential for this expanded version of the modified tangent modulus approach will be demonstrated through a few comparative examples presented later in this paper.

COMPARATIVE PROGRAM - ADINA

As a basis for comparison, the more refined and commercially available finite element program ADINA (ADINA, 2007) was employed. Fully integrated, 4-node shell elements (MITC4) are used to model the wide flange sections investigated in this study. The cross section was modeled with a mesh density of 10 elements across the flange width and 10 elements through web depth. The number of elements along the length of the member was varied to maintain an element aspect ratio of approximately one. A typical model includes approximately 6000 shell elements. All models considered both geometric (large rotation/small strain) and material (multilinear plasticity) nonlinear effects. An elastic-perfectly-plastic stress-strain response and a parabolic residual stress pattern were explicitly incorporated. Initial imperfections, including out-of-straightness, were included by distorting the original finite element mesh. Using a sinusoidal distribution, a maximum mid-span out-of-straightness of L/1000 and initial twist of 1/1000 radian were used. By employing a system of rigid line elements, axial loading and bending moments are applied at the member ends through a set of concentrated forces distributed over the cross-section. These rigid line elements also provided for modeling member ends as either warping free or warping fixed.

OVERVIEW OF STUDIES

As part of this investigation, separate column, beam, and beam-column studies were completed. For each, several representative wide-flange cross sections of varying major to minor cross section stiffness ratios (r_{major}/r_{minor}) were included. A summary of the studies completed is provided in Table 1. Specific details and complete results of this study are provided in Seo (2008). In the following sections, example results obtained for a W14x53 member fabricated from A992 steel (E=29,000 ksi, F_y=50ksi) are presented.

Table 1. Summary of studies completed.

Study	Condition	Section	r_{major}/r_{minor}	F_{res}/F_y
Column	Major-axis flexural buckling	W10x45 W12x65 **W14x53** W14x176	2.15 1.75 3.07 1.60	0.30 0.50 0.30 0.50
	Minor-axis flexural buckling	W10x45 W12x65 **W14x53** W14x176	2.15 1.75 3.07 1.60	0.30 0.50 0.30 0.50
Beam (major-axis flexure)	Warping free at ends	**W14x53** W24x68	3.07 5.11	0.30 0.30
	Warping fixed at ends	**W14x53** W24x68	3.07 5.11	0.30 0.30
Beam-column (warping free at ends)	Compression plus bi-axial bending	W6x25 W14x43 **W14x53**	1.78 3.08 3.07	0.50 0.30 0.30

COLUMN STUDY – W14X53

For each section investigated, the major-axis and minor-axis column strengths were calculated for a wide range of slenderness ratios (L/r from 10 to 170). MASTAN2 results were developed using the E_t and E_{tm} models given in Eqs (3), (4), and (5). The parabolic residual stress distribution used in ADINA had a maximum value of 0.3 or 0.5 depending on the height-to-width ratio of the section investigated (see Table 1). For both the MASTAN2 and ADINA analysis models, a sinusoidal initial out-of-straightness with a maximum value of L/1000 was used.

Nominal strengths using the AISC (2005) column curve were also obtained.

A comparison of the column strengths is presented in Figures 1 and 2. As shown in Figure 1, the predicted major-axis buckling strengths are all in fairly close agreement. The E_t (Eq. 3) and original E_{tm} (Eq. 4) models better match the ADINA results, while the new E_{tm} (Eq. 5) model, which includes a reduction for major-axis bending moment, more closely resembles the AISC column curve.

The minor-axis buckling strengths predicted by ADINA, AISC, and the E_{tm} model of Eq. 5 (which in the absence of major-axis bending is equivalent to Eq. 4) are in remarkably close agreement. The E_t model (Eq. 3) is obviously less conservative and hence, was one of the main reasons for developing the E_{tm} models.

BEAM STUDY – W14X53

The major-axis flexural strength was investigated for two sections; a W24x68 which would be representative of a typical beam geometry, and a W14x53 which may be more typical of a beam-column cross section. Although the compactness ratios of the sections prevented the possibility of local flange and/or web buckling, a wide range of unbraced lengths provided failure modes that included full yielding and inelastic or elastic lateral-torsional buckling (LTB). For both sections, the MASTAN2 and ADINA analytical models were studied for free- and fixed-end

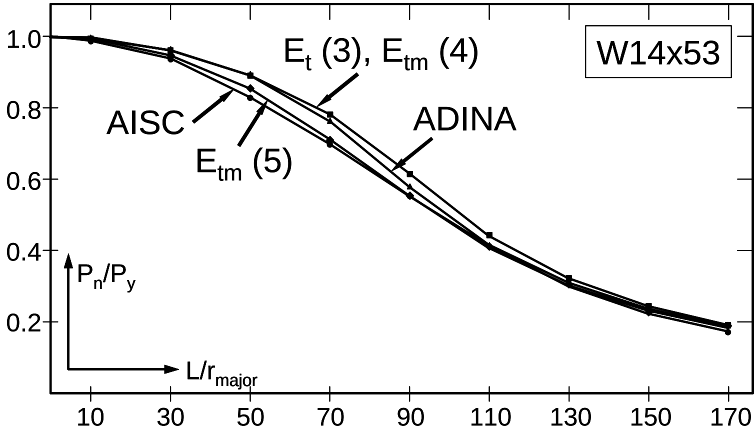

Figure 1. Comparison of **major-axis** compressive strength.

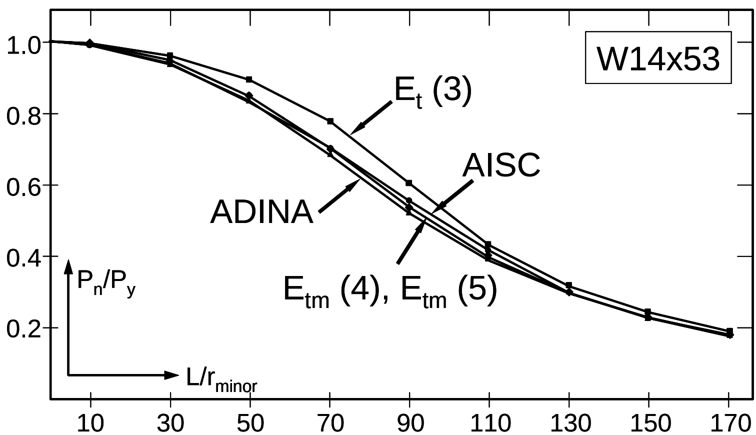

Figure 2. Comparison of **minor-axis** compressive strength.

warping conditions while St. Venant twist was in all cases restrained at member ends. In all cases, the member was assumed as warping continuous and free to twist along its span. Residual stresses and initial geometric imperfections (including a maximum out-of-plane lateral displacement of L/1000 and maximum twist of 1/1000 radian) were incorporated in the MASTAN2 and ADINA analysis models. In all cases, members were subjected to equal end moments that produce single curvature (uniform bending).

A comparison of predicted flexural strengths is shown in Figures 3 and 4. As expected, the original MASTAN2 E_t (Eq. 3) model only captures full cross section yielding (plastic hinge) or elastic LTB strength limit states. Hence, this model can be quite unconservative, especially for the mid-range unbraced length ($L_p<L<L_r$). On the other hand, the use of the E_{tm} (Eq. 5) model allows for the possibility of inelastic LTB and hence, more closely agrees with the refined ADINA results. It is interesting to note that the AISC predicted nominal strengths are fairly unconservative for the warping free condition and much more conservative for warping fixed. Similar results were observed for the W24x68 section.

BEAM-COLUMN STUDY – W14X53

Applying a wide range of combinations of axial force and major- and minor-axis bending moments, the behavior of a W14x53 beam-column was studied. The length of the member was 15’-0” with major- and minor-axis slenderness ratios of L/r_x=30.6 and L/r_y=93.8, respectively.

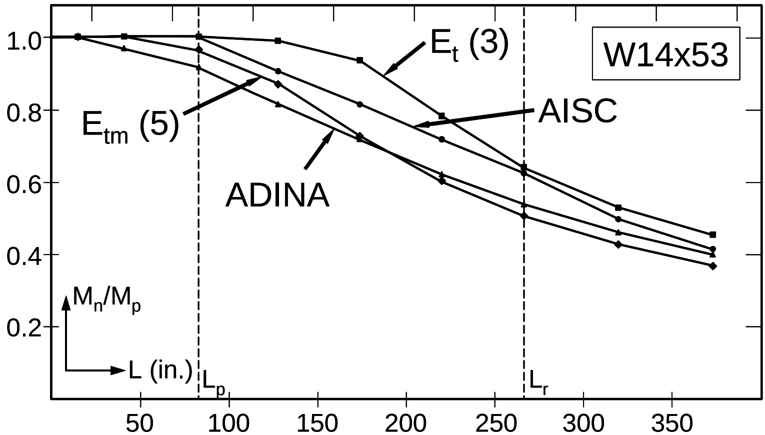

Figure 3. Comparison of major-axis bending strength (**warping free** at ends and continuous along span).

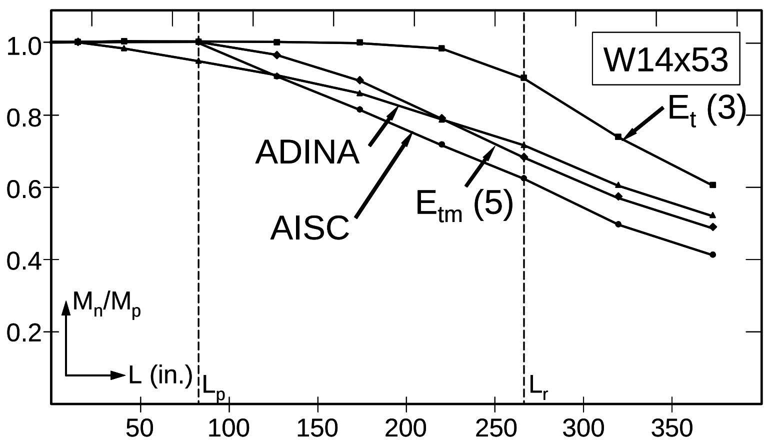

Figure 4. Comparison of major-axis bending strength (**warping fixed** at ends and continuous along span).

Axial forces and uniform moments were proportionally applied at the member ends, with the latter producing single curvature. The support conditions, initial imperfections (in the direction to produce the largest effect), and residual stresses were the same as those used in the beam study (see previous section for details). The member was modeled as warping free at its ends and continuous along its span.

The specific values of axial force and moments studied were purposely selected to result in the AISC interaction equation equaling unity. For example, the interaction equation math (considering nominal strengths, no resistance factors) with P_u/P_y=0.158, M_{ux}/M_{px}=0.234, and M_{uy}/M_{py}=0.370 yields:

Applied Member End Actions	AISC Nominal Resistance
$P_u = 0.158P_y = 123.2kip$	$P_n = 410kip$
$M_{ux} = 0.234M_{px} = 1019in \cdot k$	$M_{nx} = 3480in \cdot k$
$M_{uy} = 0.370M_{py} = 407in \cdot k$	$M_{nx} = 1100in \cdot k$

$$B_{1x} = 1/(1 - 123.2/4779) = 1.026 \quad \text{with } P_{ex} = 4779kip$$

$$B_{1y} = 1/(1 - 123.2/510) = 1.319 \quad \text{with } P_{ey} = 510kip$$

AISC Eq. H1-1a :

$$\frac{123.2}{410} + \frac{8}{9}\left(\frac{1.026 \times 1019}{3480} + \frac{1.319 \times 407}{1100}\right) = 1.00$$

A comparison of the predicted beam-column strengths computed by ADINA and MASTAN2 is provided in Table 2. Continuing with the above example, an ADINA analysis would indicate that the limit of resistance would be reached when a ratio of 0.971 (97.1%) of the member end actions of P_u=123.2kips, M_{ux} =1019in-k, and M_{uy}=407in-k are proportionally applied. Similarly, MASTAN2 analyses with E_{tm} (Eq. 5) and E_t (Eq. 3) would indicate failure load ratios of 1.045 and 1.303, respectively.

In general, there is good agreement observed between the AISC, ADINA, and MASTAN2 E_{tm} (Eq. 5) models. It is apparent that the original E_t (Eq. 3) model can be quite unconservative. In some cases, the ADINA and E_{tm} (Eq. 5) failure load ratios are much lower than the AISC predicted strength. This could be partially explained by the differences in beam strength previously noted. Regardless, it is clear that the E_{tm} (Eq. 5) model does more accurately capture the rather complex limit state behavior of beam-columns subjected to axial force and uni- or bi-axial bending.

SUMMARY AND CONCLUSIONS

This paper presents a modified tangent modulus approach which is intended to overcome shortcomings in plastic hinge analysis programs when inelastic lateral- and flexural-torsional buckling of beams and beam-columns are dominant modes of failure. Using a relatively simple expression that reduces the modulus of elasticity of structural members according to the axial force and major-

Table 2. Comparison of strength of beam-columns under biaxial bending.

Applied End Actions			Load Ratios at Failure			
P_u/P_y	M_{ux}/M_{px}	M_{uy}/M_{py}	AISC	ADINA	E_{tm} (5)	E_t (3)
0.000	0.000	1.000	1.000	1.000	1.000	1.000
0.000	0.800	0.000	1.000	0.871	0.885	1.153
0.053	0.079	0.782	1.000	0.982	1.050	1.115
0.053	0.238	0.598	1.000	1.024	1.129	1.247
0.053	0.397	0.414	1.000	0.919	1.071	1.250
0.053	0.556	0.230	1.000	0.843	0.960	1.182
0.053	0.754	0.000	1.000	0.846	0.880	1.163
0.105	0.079	0.671	1.000	0.966	1.008	1.127
0.105	0.236	0.503	1.000	0.965	1.067	1.244
0.105	0.393	0.336	1.000	0.886	1.005	1.240
0.105	0.551	0.168	1.000	0.816	0.925	1.178
0.105	0.708	0.000	1.000	0.828	0.875	1.161
0.152	0.624	0.000	1.000	0.856	0.920	1.217
0.158	0.078	0.522	1.000	0.998	1.010	1.197
0.158	0.234	0.370	1.000	0.971	1.045	1.303
0.158	0.390	0.218	1.000	0.883	1.000	1.285
0.158	0.546	0.066	1.000	0.843	0.940	1.226
0.158	0.614	0.000	1.000	0.860	0.925	1.224
0.210	0.077	0.390	1.000	1.015	0.995	1.255
0.210	0.232	0.254	1.000	1.035	1.035	1.348
0.210	0.386	0.119	1.000	0.889	1.000	1.320
0.210	0.522	0.000	1.000	0.891	0.970	1.280
0.245	0.461	0.000	1.000	0.911	1.000	1.314
0.263	0.077	0.276	1.000	1.016	0.989	1.298
0.263	0.230	0.157	1.000	0.958	1.035	1.374
0.263	0.383	0.037	1.000	0.915	1.015	1.340
0.263	0.431	0.000	1.000	0.922	1.015	1.328

Table 2 (cont.). Comparison of strength of beam-columns under biaxial bending.

Applied End Actions			Load Ratios at Failure			
P_u/P_y	M_{ux}/M_{px}	M_{uy}/M_{py}	AISC	ADINA	E_{tm} (5)	E_t (3)
0.315	0.076	0.181	1.000	1.008	0.985	1.320
0.315	0.228	0.078	1.000	0.962	1.040	1.380
0.315	0.342	0.000	1.000	0.968	1.045	1.357
0.339	0.302	0.000	1.000	0.961	1.050	1.361
0.368	0.075	0.104	1.000	1.003	0.985	1.320
0.368	0.226	0.016	1.000	1.061	1.045	1.361
0.368	0.254	0.000	1.000	0.973	1.055	1.357
0.421	0.075	0.045	1.000	1.000	0.980	1.293
0.421	0.149	0.009	1.000	0.991	1.020	1.316
0.421	0.168	0.000	1.000	0.990	1.030	1.317
0.432	0.149	0.000	1.000	0.991	1.020	1.302
0.473	0.074	0.003	1.000	1.008	0.965	1.231
0.473	0.083	0.000	1.000	0.989	0.970	1.233
		Average	1.000	0.945	0.998	1.263

and minor-axis bending moments being resisted, it has been demonstrated that a second-order inelastic hinge analysis can provide results that are in close agreement with more sophisticated nonlinear finite element programs.

Since the focus of this research was aimed at showing the potential for this approach, and hence only used a limited number of wide flange shapes, additional studies are recommended for the purpose of establishing terms, empirical constants, and limits of applicability. The authors believe that the proposed modified tangent modulus approach (or some similar variation) can be used to qualify second-order inelastic hinge analysis as a viable analysis method for use in performance based design of three-dimensional frames of compact sections.

REFERENCES

ADINA (2007), *Theory Manual*, ADINA R and D, Inc., Watertown, MA.

AISC (2005), *Specification for Structural Steel Buildings*, American Institute of Steel Construction, Inc., Chicago, IL.

Australian Standard, Steel Strucures, AS4100 (1998) Standards Association of Australia, Sydney, Australia.

Bleich, F. (1952), *Buckling Strength of Metal Structures*, McGraw-Hill, New York, NY.

Bjorhovde, R. (1988), "Columns: From Theory to Practice", *AISC Eng J., Vol* 23(1).

Guide to Stability Design Criteria for Metal Structures (1998), 5th edition, T.V. Galambos, editor, John Wiley and Sons, Inc., New York, NY.

Kim, S. E., and Chen, W. F. (1996), "Practical Advanced Analysis For Unbraced Steel Frame Design", *J. Struct. Eng.*, ASCE, Vol. 122(11).

MASTAN2 (2007), developed by R.D. Ziemian and W. McGuire, Version 3.0, www.mastan2.com

McGuire, W., Gallagher, R.H., and Ziemian, R.D. (2000), *Matrix Structural Analysis*, 2nd edition, John Wiley and Sons, Inc., New York, NY.

McGuire, W., and Ziemian, R D. (2000), "Steel Frame Stability, Out-of-Plane Effects", Proceedings, *First Intl. Conf. on Structural Stability and Dynamics*, Nat. Taiwan Univ., Taipei.

Salmon, E.H. (1921), *Columns, a treatise on the strength and design of compression members*, H. Frowde, London.

Seo, Dong Woo (2008) "A Tangent Modulus Approach for Modeling Inelastic Lateral-Torsional Buckling," MS Thesis, Department of Civil and Environmental Engineering, Bucknell University, Lewisburg, PA (to be submitted in May).

Trahair, N.S., and Chan, S.L. (2002), "Out-of-Plane Advanced Analysis of Steel Structures," Research Report No. R823, Centre for Advanced Structural Engineering, The University of Sydney, Sydney, Australia.

Trahair, N. S., and Hancock, G. J. (2004), "Steel Member Strength by Inelastic Lateral Buckling", *J. Struct. Eng.*, ASCE, Vol. 130(1).

Wongkaew, K., and Chen, W. F. (2002), "Consideration Of Out-Of-Plane Buckling In Advanced Analysis For Planar Steel Frame Design," *J. Constr. Steel Res.*, Vol. 58.

Ziemian, R D. and McGuire, W. (2002), "Modified Tangent Modulus Approach, A Contribution to Plastic Hinge Analysis", *J. Struct Eng.*, ASCE Vol. 128(10).

STABILITY CONSIDERING PERMANENT METAL DECK FORMS DURING CONSTRUCTION OF LONG SPAN BRIDGES

Shekhar S. Patil[1], Ramy S. Abdalla[2], and James S. Davidson[3]

ABSTRACT: This paper presents results from the initial phase of analytical research whose goals are to develop recommendations for considering metal deck formwork for wind load stability and vibratory effects during construction of long span bridges. The effort resulted from vibration and stability challenges encountered by the Alabama Department of Transportation from high wind events during construction of a plate girder bridge spanning a waterway. This first phase of the effort leverages recent testing and analytical research conducted by others, and is essentially an orientation of existing literature. A design method example is presented. The paper also discusses the influence of connection details between girder top flange and metal deck forms on lateral stiffness and stability. Finite element analyses are underway that will simulate the contribution of metal deck form systems in stabilizing bridge girders against wind during construction. Later phases of the effort will consider the effects of PMDFs on vibration characteristics of the bridge superstructure.

[1]Graduate Research Assistant, Department of Civil and Environmental Engineering, The University of Alabama at Birmingham, Birmingham, Alabama 35294.

[2]Civil Engineer, Alabama Department of Transportation, Montgomery, Alabama 36110.

[3]Associate Professor, Department of Civil Engineering, Auburn University, Alabama 36849. Email: *jim.davidson@auburn.edu*

INTRODUCTION

The phenomenon of sudden lateral displacement coupled with rotation of girder length that is not sufficiently braced often controls the design of steel bridge girders during construction. Elastic lateral buckling is a possible means of failure for I-shaped girders during construction. An estimate of load causing such failure must be made by determining an effective length or reducing laterally unsupported length. The susceptibility of I-shaped plate girders to instability during construction is largely due to the fact that plate girders are optimized to carry vertical load in the composite traffic bearing configuration of the completed bridge structure, but have inherently weak torsion resistance during the various phases of construction prior to hardening of the concrete deck.

Designers have traditionally stipulated cross-frames and/or diaphragms (discrete point bracing) at close spacing intervals to minimize the susceptibility of individual girders to instability during construction. Prior to the most recent AASHTO LRFD specifications for highway bridges, the maximum spacing between cross-frames and diaphragms was limited to 25 feet. However, following recent increase in awareness and incidence of fatigue problems encountered around discrete brace connections, the maximum spacing requirement was removed from the LRFD bridge design specifications. Furthermore, cross-frames and diaphragms complicate girder fabrication and erection, which leads to increased construction and inspection costs. For these reasons, among others, alternative bracing systems and engineering methodology are needed.

Traditionally, permanent metal deck forms (PMDF) are used to support wet concrete during construction in both buildings and bridge industries. The metal deck sheeting acting with structural beams possess high in-plane stiffness that resists lateral deformations from wind load as well as provides bracing to the beams in the manner of short deep beams [Yura and Phillips 1992]. These steel deck panels carry loads normal to their plane with the help of in-built bending strength and can resist in-plane shear deformations. Because of this inherent shear resistance, such diaphragms are used as wind bracing for buildings. However, in the bridge industry, AASHTO does not permit PMDF to be utilized for bracing of steel bridge girders, primarily due to the flexible connections between the girders and deck forms.

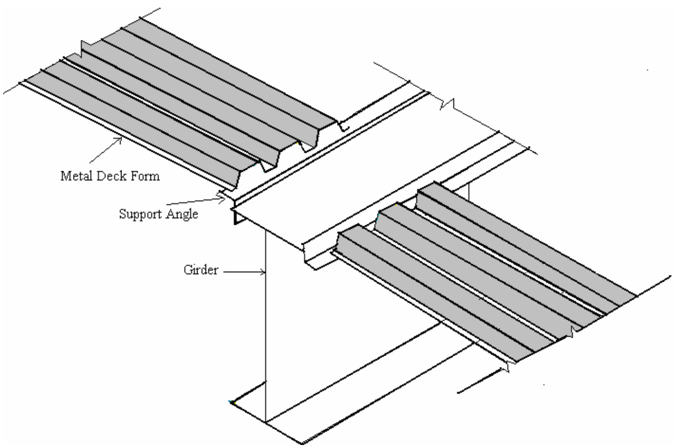

Figure 1: Deck form and girder connection for bridges

Extensive research has been done on the use of metal deck forms for stability of bridge girders during construction. These studies have demonstrated the stability advantage provided by metal deck forms during construction of span lengths typical of highway overpass bridges, but additional work may be needed to determine whether this method can be used for very long, deep bridge girders. This first phase of the project largely leverages recent stability research conducted by others, but with interest towards application to very long, deep bridge girders. Future phases of the work will focus on the use of finite element modeling to validate application to very long, deep bridge girders, and also, due to vibration phenomena encountered by the Alabama Department of Transportation, will consider the influence of PMDF on vibration characteristics of bridge superstructures.

LITERATURE REVIEW

The building industry considers metal deck forms as shear diaphragms for stability of beams during construction. To define the bracing effectiveness of metal deck forms for bridges, researchers at the University of Texas at Austin and the University of Houston have recently performed comprehensive experimental and analytical studies.

Winter [1960] demonstrated that adequate stability bracing must satisfy both stiffness and strength criteria. Effective bracing is achieved by preventing lateral movement or twist of the girder cross-section. In building and bridge industries, the permanent metal deck form is considered as a shear diaphragm system that restrains the lateral movement of girder top flanges. Currah [1993] evaluated the shear strength and shear stiffness of bridge permanent metal deck forms using the Diaphragm Design Manual [SDI 1995]. This work revealed that significant shear stiffness is provided by the metal decking.

Soderberg [1994] and Helwig [1994] studied the lateral bracing ability of permanent metal deck forms commonly used in steel bridge construction. Finite element analyses showed that the lateral bracing provided by the deck form diaphragm system is significant. Expressions were developed based on analyses of beams with an initial twist, $\theta_0 = L/(500d)$ to estimate stiffness requirements and buckling capacity of the girder system. These expressions were used to develop a design approach for single span and continuous girders braced by the permanent metal deck forms. It was found that this design approach reduces the number of cross-frames required to laterally brace the girders. Helwig et al. [1997] showed that there is significant effect of transverse load and moment gradient on the buckling capacity of the girder cross-section.

Helwig [1994] defined the failure of deck panels with maximum eccentricity as due to severe deformation of the support angles at the corners of the panel. To control this angle deformation, Jetann et al. [2002] placed a transverse stiffening angle that spans between adjacent girders to coincide with a side-lap seam so that the deck could be fastened directly to the angle. The shear stiffness and shear strength of the metal deck form systems with modified connection details were measured. Jetann et al. [2002] concluded that including the stiffening angle can significantly improve shear strength and stiffness.

CONNECTION DETAILS AND RECOMMENDATIONS

Currah [1993] suggested that the deck form panel ends must be fastened at every rib trough, and that side lap fasteners be kept as close as possible. For girders braced by shear diaphragms, the most important parameter is the shear rigidity, Q (force per unit radian, KN/rad or kip/rad). The shear rigidity is calculated as the product of effective shear modulus (G') and tributary width of deck (S_d). The effective shear modulus is the ratio of average applied shear stress divided by the diaphragm's shear strain and can be calculated using the following expression [Currah 1993]:

$$G' = \frac{\tau'}{\gamma} \tag{1}$$

Where G' is the effective shear modulus, τ' is the effective shear stress, and γ is the shear strain.

The diaphragm shear stiffness is important in assessing how forces are transferred from one bridge girder to another. The tributary width of the deck (S_d) is the width of the deck effective for a single girder. In a bridge with n girders, n-1 metal deck forms would be used.

$$S_d = (S_g - b_f)\,(n - 1) / n \tag{2}$$

Where n is the number of girders, S_g is the spacing between girders, and b_f is the width of the girder top flange. The shear rigidity is calculated using:

$$Q = G'\ S_d \tag{3}$$

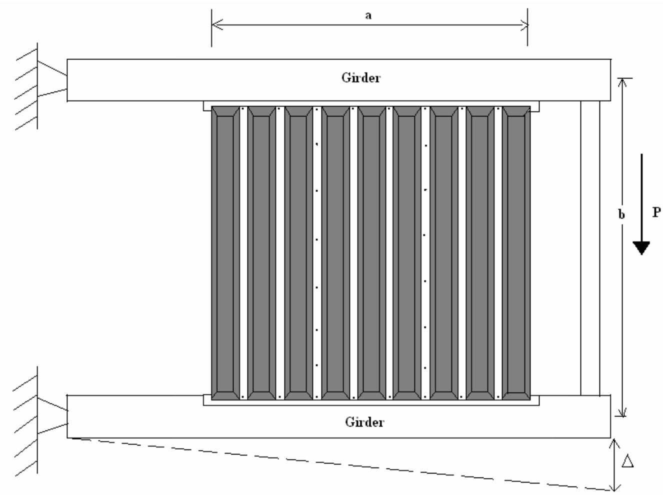

Figure 2: Typical shear test frame

The Steel Deck Institute Design Manual provides equations that can be used to evaluate the effective shear modulus (G') for a given metal deck form. Based on laboratory testing, Currah [1993] showed that SDI expressions provide a reasonable estimate of the effective shear modulus. The shear rigidity will increase as girder spacing increases. For bridges with multiple girders, the shear rigidity will increase since there are more metal deck forms per girder [Egilmez et al. 2005].

In the building industry, the forms are typically attached directly to the top flange of the beam using welds or mechanical fasteners. This allows the decking to be fabricated in long lengths that span over several beams. Although the support angles provide convenience with respect to constructability, issues such as adjusting the form elevation to account for differential camber between adjacent girders or changes in flange thickness along the girder length result in connection eccentricity that can substantially reduce the stiffness and strength of the deck form system. The typical support details of deck/girder system in bridge industry are illustrated in Figure 3.

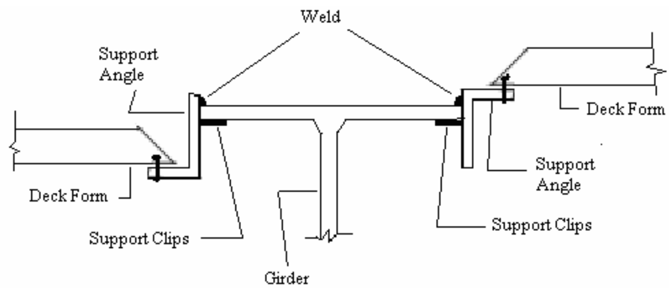

Figure 3: Typical bridge girder and deck form connection

In shear tests performed at the University of Houston, PMDFs showed tendency to produce fields of tension and compression within the panel system (Figure 4). This causes the support angle to pull away from the tension flange and push the angle under the compression flange. The effective angle eccentricity in the region subjected to compression is therefore decreased by an amount equal to the thickness of the flange. The connection stiffness is therefore higher than the corresponding connection in the tension region [Jetann et al. 2002].

Due to the eccentricity that can lead to severe deformation of the support angle, the shear stiffness of metal deck forms reduces substantially. The equation for springs in series can be used as an analytical basis for the reduction in shear stiffness:

$$\frac{1}{\beta_{sys}} = \frac{1}{\beta_{deck}} + \frac{1}{\beta_{conn}} \tag{4}$$

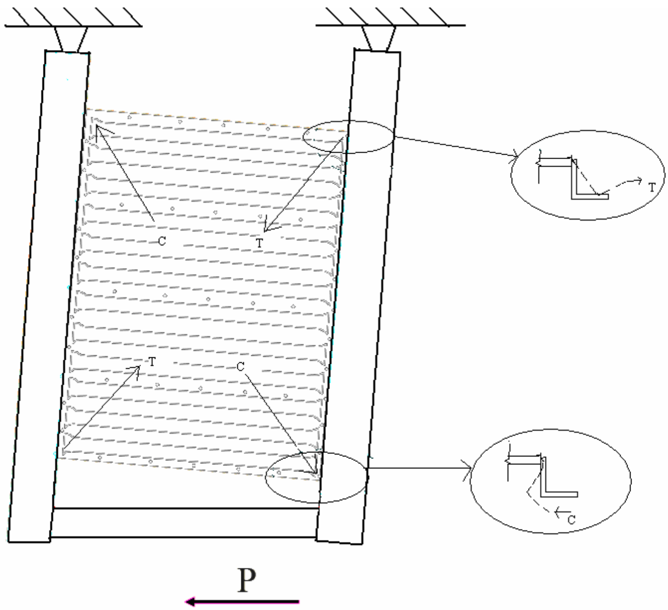

Figure 4: Support angle failure

Hence to control this support angle deformation, a transverse stiffening angle that spans between adjacent girders has been used to fasten the deck directly to the angle [Jetann et al. 2002]. In addition to controlling the deformation of the support angle, transverse stiffening angles also provide support to decks at panel ends (Figure 5).

By comparing experimental results for stiffened and unstiffened connections with zero and maximum support angle eccentricity, Egilmez et al. [2003] observed that there is excessive reduction in the stiffness due to extreme angle deformation, but that there is no drastic change in the ultimate capacity of the PMDF system. Lateral displacement tests with and without modified connection details on a 50 ft twin girder system were conducted to determine the lateral stiffness of PMDF systems subjected to a variety of lateral deformation profiles. A measure of the lateral stiffness of the system was obtained by dividing the turnbuckle or FEA force by the corresponding lateral deflection at that point. The comparison of experimental and FEM tests showed that the actual PMDF systems have a greater in-plane capacity than predicted by a shear diaphragm model [Egilmez and Helwig 2004]. As a result of the in-plane flexural stiffness, the metal deck form system will be more efficient as a bracing element. The stiffened diaphragm model controlled deformation substantially as compared to the unstiffened diaphragm model and showed smaller brace forces. The Steel Deck Diaphragm Design manual provides a truss analogy procedure for calculating the lateral deformation of the metal deck form system. For known dimensions of truss and shear stiffness of the PMDF system, the deflection of the analogous truss model can be obtained using following relationship:

$$\Delta = \frac{P}{G'}\frac{H}{B} \tag{5}$$

Where *P* is the axial force, *H* is the panel width, *B* is the panel length, and *G'* is the PMDF system shear stiffness.

Jetann [2002] also compared the buckling behavior of girders braced with permanent metal deck forms with the buckling behavior that would be expected from conventional discrete bracing systems. To consider the effect of the imperfections on the bracing system, the girders were loaded with an eccentricity that would simulate the girder system that had a straight bottom flange and a displaced top flange equal to $L_b/500$, which is the critical imperfection displacement for torsional bracing systems in beams. The comparison between laboratory and FEA results revealed that permanent metal deck form systems with stiffened connections approaches twice the moment capacity compared to conventional cross-frame systems. After comparing the laboratory and FEA values of effective shear modulus (*G'*) for eccentric unstiffened and stiffened connections, it was concluded that providing stiffening angles to this system increases the stiffness by more than a factor of four [Jetann 2002].

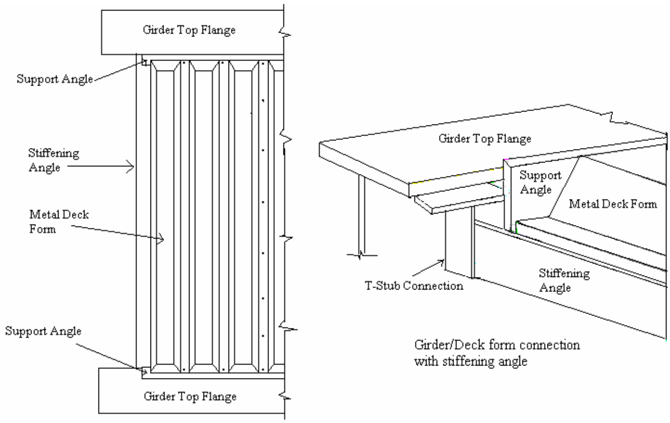

Figure 5: PMDF system with stiffened angle connection

DESIGN METHODOLOGY

A lateral buckling check of the first stage of construction is necessary. Therefore, the girder capacity must be calculated using the AASHTO specifications for lateral torsional buckling:

$$M_{AASHTO} = 91\times 10^{6}\left(\frac{I_{yc}}{L_b}\right)\sqrt{0.772\left(\frac{J}{I_{yc}}\right)+9.87\left(\frac{d}{L_b}\right)^2} \qquad (6)$$

The resulting moment capacity is then calculated for girders without contribution of the metal deck form. For a girder subjected to moment gradient, the buckling capacity is calculated as the product of the corresponding C_b^* values and the buckling moment predicted by one of the lateral torsional buckling formula. This will provide the estimated girder capacity without the metal deck form.

$$M_{cr} = C_b^* M_{AASHTO} \qquad (7)$$

The moment capacity for girders with contribution of deck forms as a bracing element was developed by Helwig [1994] and is shown in the following equation.

$$M_{cr} = C_b^* M_{AASHTO} + mQd \tag{8}$$

Where M_{cr} is the moment capacity of girder/PMDF system, M_{AASHTO} is the buckling moment capacity, Q is the shear rigidity of the decking system, C_b^* is the moment gradient factor, m is the constant that depends on loading, and d is the depth of the girder cross-section. The term "mQd" represents the contribution of the PMDF/support angle connection, which is a function of girder depth and deck shear rigidity, as well as the constant m that depends on the type of loading, intermediate bracing, and the web slenderness (Table 1). For uniform moment, m = 1.0. The values of m are also applicable for concentrated loads applied at the top flange; however, if the load point is also a braced point (no twist), m = 1.0 may be used.

Table 1: Values of *m*

Web Slenderness	Top Flange Loading without Midspan Torsional Brace [Helwig and Frank 1999]	Top Flange Loading with Midspan Torsional Brace [Egilmez et al. 2003]
$h/t_w < 60$	0.5	0.85
$h/t_w > 60$	0.375	0.625

The buckling capacity of diaphragm–braced beams is defined by the lowest value based on the limit states of web bend buckling, shear buckling or lateral-torsional buckling given by Equation 8, which can be rearranged to solve the ideal effective shear modulus in terms of maximum moment, M_{cr}, and the buckling capacity of the girder without diaphragm bracing, $C_b^* M_{AASHTO}$, between points of zero twist:

$$G'_{ideal} = (M_{cr} - C_b^* M_{AASHTO}) / (S_d md) \qquad (9)$$

The expressions presented so far represent the capacity for perfectly straight beams braced by a shear diaphragm. For a particular maximum moment, the diaphragm stiffness derived from these expressions would represent the "ideal stiffness".

Egilmez et al. [2003] conducted large displacement finite element analyses on girders with initial imperfections. They found that providing four times the ideal stiffness could effectively control deformations and brace forces. For design considerations, Equation 9 becomes:

$$G'_{ideal} = 4(M_{cr} - C_b^* M_{AASHTO}) / (S_d md) \qquad (10)$$

The stiffness requirement for the shear diaphragm given is based on an analysis of beams with an initial twist, $\theta_0 = L / (500\ d)$, where d = section depth.

The buckling moment capacity equation derived by Helwig [1994] was developed for girders braced by a deck form that was fastened on only two sides (i.e. at the support angle). The stability bracing contributions from the stiffening angles provide a different type of bracing than the restraint provided by the PMDF connection through the support angle. Since these systems have panels that are connected on four sides, they tend to be more effective than a shear diaphragm supported on only two sides.

The PMDF with stiffened connections provides restraint of two points relative to one another, which is similar to a relative bracing system. Bracing ability increased by a stiffening angle can be accounted by using 50% of the buckling moment capacity computed using half of the spacing (L_b / 2), where L_b is the spacing between the cross-frames. This approach is conservative since the stiffening angles probably provide significantly higher bracing. Therefore, Equation 8 becomes:

$$M_{cr} = \frac{C_b^* M_{AASHTO(L_b/2)}}{2} + mQd \tag{11}$$

The effective shear stiffness of the decks used in the field will usually be greater than the least value obtained from laboratory test results. The laboratory tests used the largest possible eccentricity all along the girder length. In the field, the eccentricities will often be smaller at several locations along the girder length.

The strength requirement for shear diaphragm bracing is a function of the span length and depth of the girder. If a diaphragm with stiffness G'_{reqd} is provided, the required bracing moment $M_{br}^{'}$ per unit length of the girder can be approximated as:

$$M'_{br} = k\frac{(M_u L)}{d^2} \tag{12}$$

Where L is the total span length and d is the girder depth.

The magnitudes of brace moments tend to increase with the depth of the individual girder and the L/d ratio for specific girder depth. The recommended value of brace stiffness of $4Q_{ideal}$ was used to establish the strength requirements. For unstiffened connections, permanent metal deck form bracing is supported only along two sides, therefore the recommended value for k is 0.0011. For stiffened connections, the above equation shows very conservative estimates. Based upon the large displacement solutions, the values of k for the stiffened-deck braced girders can be chosen from following table [Egilmez et al. 2005].

Table 2: *k* values for stiffened deck brace girders

Web Slenderness	Top Flange Loading without Midspan Torsional Brace
h/t_w<60	0.00015
h/t_w>60	-

The brace moment represents the warping restraint provided to the top flange of the girder per unit length of the span and can be resolved into forces on the diaphragm and connection. The brace moment can be used to determine the forces in the fasteners that connect the shear diaphragm to the beams. Although a shear diaphragm model predicts relatively large fastener forces, the magnitude of fastener forces in actual PMDF braced systems are probably not as high because deck contributions to bracing come from shear-flexural behavior [Egilmez et al. 2005].

DESIGN EXAMPLE

The example considers a bridge with continuous girders. Figure 6 represents a four-girder bridge over the Tombigbee River on Alabama state route 114 at Naheola station in Choctaw and Marengo counties. The bridge consists of three spans with exterior spans of 320 ft and center span of 405 ft.

This example will concentrate on the design of bracing for the center 405 ft span. The original design used 15 intermediate cross-frames spaced at 25 ft. The factored dead load moment M_u is 55654 K-ft. Due to presence of intermediate braces, C_b^* is taken as 1. It was observed that, for an unbraced length L_b of 25 ft, $C_b^* M_{AASHTO}$ is much greater than the factored dead load moment. Therefore stiffness calculations are not necessary and decking with stiffening angle with relative low stiffness will be able to brace the girders. This is generally the case in most long span deep bridge girders since the magnitudes of moments tend to increase with the depth of the individual girder.

An unbraced length L_b of 50 ft is considered and $C_b^* M_{AASHTO}$ is calculated as 26095 K-ft, which is less than the factored dead load moment M_u. To provide enough stability, the girders must be checked for erection moment. In this case, the erection moment required for girder self weight and part of construction load ($W_e = 388 + 10 \times 10 = 488$ K/ft) would be,

$$M_e = \frac{1.3 \times 0.488 \times 405^2}{8} = 13007 \text{ K-ft} < 26095 \text{ K-ft}$$

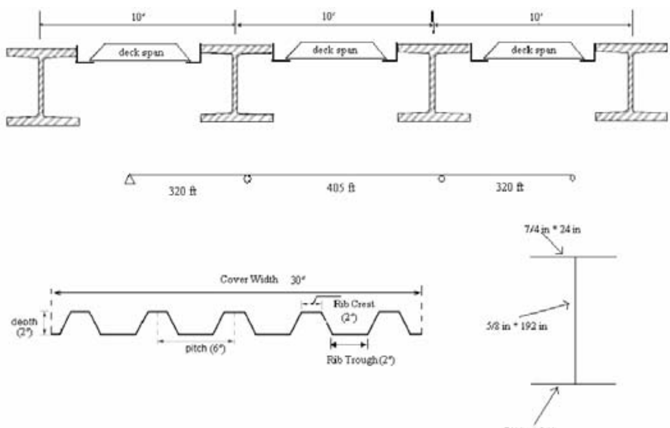

Figure 6: Bridge Layout

The girder is able to support the self weight and a portion of construction loading. There are four girders laterally spaced at 9 ft and connected by metal deck formwork. Considering the metal deck form system as a bracing element, the buckling moment capacity can be evaluated using Equation 11. Due to application of loading on the top flange, the value of m will be taken as 0.375. Rearranging the equation to estimate required shear stiffness,

$$G'_{required} = \frac{4(M_u - (1/2)C_b^* M_{AASHTO(L_b/2)})}{s_d md}$$

Where s_d is tributary width of the deck bracing a single girder.

$$s_d = \frac{(s_g - b_f)(n-1)}{n} = \frac{(10 \times 12 - 24)(4-1)}{4} = 72in$$

L_b = 50 ft; C_b^* = 1.0; d=192 in

Here $(1/2)C_b^* M_{AASHTO(L_b/2)} = (1/2)C_b^* M_{AASHTO(25ft)}$ = 51404 K-ft

Therefore, to control deformations, the required shear stiffness of the metal deck form system is,

$$G'_{required} = \frac{4(55654 \times 12 - 51404 \times 12)}{72 \times 0.375 \times 192} = 39.35K/in$$

The metal deck form system with effective shear stiffness of the 39.35 K/in provides enough bracing to girders to eliminate 8 cross frames along the 405 ft girder length. The distance between cross frames is now equal to 50 ft, which is twice the original design of intermediate cross-frames spaced at 25 ft.

SUMMARY

This paper reflects an initial phase of research whose overall objectives are to investigate the ability of metal deck forms to enhance the lateral stability of plate girders during the construction of very long span bridges. The effort leverages recent research conducted by others, particularly important works conducted at the University of Texas at Austin and the University of Houston. These other programs have demonstrated the ability of permanent metal deck forms to brace moderate-length bridge girders, and that transverse stiffening angles can substantially increase stiffness provided by PMDFs. A design example based on methodology formulated by others was presented for a long span bridge. Future phases of the research will use finite element analyses to validate applicability to very long span bridges, and will investigate the effect of PMDF on vibration characteristics of bridge superstructures during construction. Finite element analyses are currently underway that focus on the ability of metal deck forms with modified connection details to brace deep long span bridge girders during construction.

ACKNOWLEDGEMENTS
The research represented herein was partially funded by USDOT Contract DTRS98-G-0028 as Grant 06210 of the University Transportation Center for Alabama (UTCA). The opinions and conclusions expressed or implied in the paper are those of the authors and not necessarily those of the USDOT, UTCA, or other contributors.

REFERENCES
Currah, R.M., (1993). "Shear Strength and Shear Stiffness of Permanent Steel Bridge deck Forms," M.S. Thesis, The University of Texas at Austin, Austin, Texas.

Egilmez, O.O., Jetann, C.J., Helwig, T.A. (2003). "Bracing Behavior of Permanent Metal Deck Forms," Proceedings of the Annual Stability Conference, Baltimore, ML, April 2-5, pp.133-152.

Egilmez, O.O., Helwig, T.A. (2004). "Buckling Behavior of Steel Bridge Girders by Permanent Metal Deck Forms," Proceedings of the Annual Stability Conference, Long Beach, CA.

Egilmez, O.O., Helwig, T.A. and Herman, R. (2005). "Strength of Metal Deck Forms Used for Stability Bracing of Steel Bridge Girders," Proceedings of the Annual Stability Conference, Montreal, Canada.

Helwig, T.A. (1994). "Lateral bracing of bridge girders by metal deck forms," Ph.D dissertation, University of Texas at Austin, Austin, Tex.

Helwig, T.A., Frank, K.H., and Yura, J.A. (1997). "Lateral-torsional buckling of singly-symmetric I-beams." J. Struct. Engr., ASCE, 123(9), 1172–1179.

Helwig, T.A. and Frank, K.H. (1999). “Stiffness Requirements for Diaphragm Bracing of Beams” J. of Structural Engineering, ASCE, Vol.125, No.11, pp.1249-1256.

Jetann, C.J. (2003). “Stiffness and Strength of Metal Bridge Deck Forms with Stiffened Connection Details,” MS thesis, University of Houston, Houston, TX.

Jetann, C. J., Helwig, T. A., and Lowery, R. (2002). “Lateral Bracing of Bridge Girders by PMDF,” Proceedings of the SSRC Annual Stability Conference, Seattle, WA, April, pp.291-310.

Steel Deck Institute Diaphragm Design Manual (1995), Second Ed., Canton, Ohio.

Soderberg, E. (1994). “Strength and stiffness of stay-in-place metal deck form systems,” MS thesis, University of Texas at Austin, Austin, TX.

Yura, J.A, Phillips, B. (1992). “Bracing Steel Beams in Bridges” Final Report submitted to Texas Dept. of Transportation, Austin, Texas.

Winter, G. (1960). “Lateral Bracing of Columns and Beams,” J. the Structural Div., ASCE, Vol. 84.